TOPOLOGY OF DISORDERED NETWORKS AND THEIR APPLICATIONS

EDITED BY: Punit Boolchand and Matthieu Micoulaut
PUBLISHED IN: Frontiers in Materials

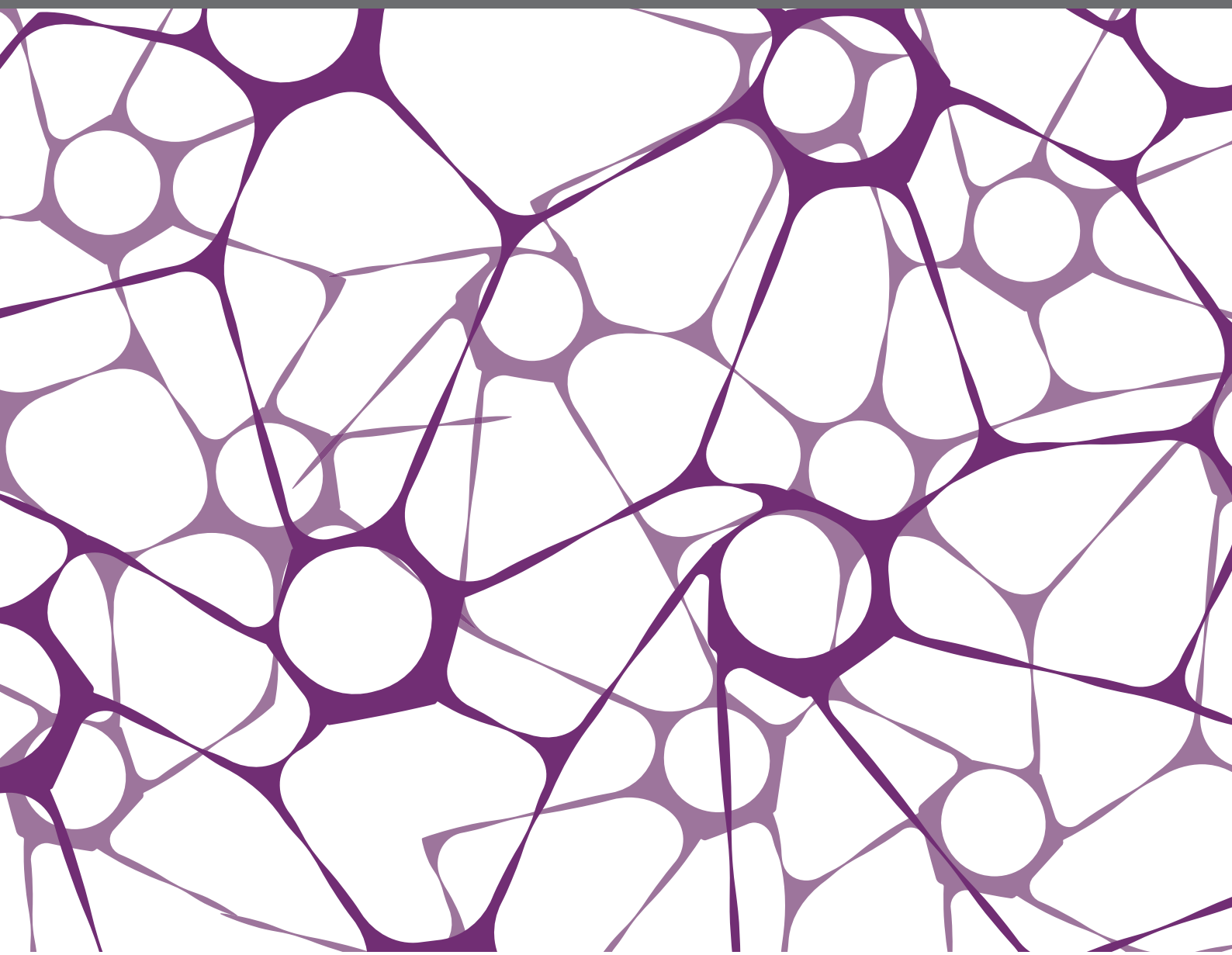

frontiers Research Topics

frontiers

ISSN 1664-8714
ISBN 978-2-88963-987-8
DOI 10.3389/978-2-88963-987-8

About Frontiers

Frontiers is more than just an open-access publisher of scholarly articles: it is a pioneering approach to the world of academia, radically improving the way scholarly research is managed. The grand vision of Frontiers is a world where all people have an equal opportunity to seek, share and generate knowledge. Frontiers provides immediate and permanent online open access to all its publications, but this alone is not enough to realize our grand goals.

Frontiers Journal Series

The Frontiers Journal Series is a multi-tier and interdisciplinary set of open-access, online journals, promising a paradigm shift from the current review, selection and dissemination processes in academic publishing. All Frontiers journals are driven by researchers for researchers; therefore, they constitute a service to the scholarly community. At the same time, the Frontiers Journal Series operates on a revolutionary invention, the tiered publishing system, initially addressing specific communities of scholars, and gradually climbing up to broader public understanding, thus serving the interests of the lay society, too.

Dedication to Quality

Each Frontiers article is a landmark of the highest quality, thanks to genuinely collaborative interactions between authors and review editors, who include some of the world's best academicians. Research must be certified by peers before entering a stream of knowledge that may eventually reach the public - and shape society; therefore, Frontiers only applies the most rigorous and unbiased reviews.
Frontiers revolutionizes research publishing by freely delivering the most outstanding research, evaluated with no bias from both the academic and social point of view. By applying the most advanced information technologies, Frontiers is catapulting scholarly publishing into a new generation.

What are Frontiers Research Topics?

Frontiers Research Topics are very popular trademarks of the Frontiers Journals Series: they are collections of at least ten articles, all centered on a particular subject. With their unique mix of varied contributions from Original Research to Review Articles, Frontiers Research Topics unify the most influential researchers, the latest key findings and historical advances in a hot research area! Find out more on how to host your own Frontiers Research Topic or contribute to one as an author by contacting the Frontiers Editorial Office: researchtopics@frontiersin.org

TOPOLOGY OF DISORDERED NETWORKS AND THEIR APPLICATIONS

Topic Editors:
Punit Boolchand, University of Cincinnati, United States
Matthieu Micoulaut, Sorbonne Universités, France

Citation: Boolchand, P., Micoulaut, M., eds. (2020). Topology of Disordered Networks and their Applications. Lausanne: Frontiers Media SA. doi: 10.3389/978-2-88963-987-8

Table of Contents

frontiers in Materials

EDITORIAL
published: 17 July 2020
doi: 10.3389/fmats.2020.00175

Editorial: Topology of Disordered Networks and Their Applications

Punit Boolchand[1*†] *and Matthieu Micoulaut*[2†]

[1] Department of Electrical Engineering and Computer Science, University of Cincinnati, Cincinnati, OH, United States,
[2] Laboratoire de Physique Theorique de la Matiere Condensee, Sorbonne Université, Paris, France

Keywords: topological constraint theory (TCT), topological phases, fragility index, modulated-DSC, molecular dynamics, Raman scattering, chalcogenides, statistical mechanics

Editorial on the Research Topic

Topology of Disordered Networks and Their Applications

Understanding the physicochemical properties of glasses has attracted widespread interest over the entire twentieth century. Glasses form disordered network structures and cannot be treated as regular lattices on an atomic scale. It has led not only to contributions in basic science such as the improved description of the glass transition phenomenon but also to contributions in materials science, and these have stimulated worldwide applications as smart window glass, flat panel displays, touch screens, protective sheets for cell phones, realization of high-K Dielectrics in standard 3-Terminal devices (Lucovsky et al., 2003), and phase change memories for information storage. The latter two applications alone represent a $1.6 billion market worldwide in 2020.

A profound step forward in understanding network glasses and amorphous materials at an atomic level began nearly 40 years back as the foundations of topolocial constraint theory (TCT) emerged, and interest in manifestations of the theory has continued to grow. The beginnings of the theory started with an innocent query—what optimizes the glass-forming tendency of a melt—and led to the finding (Phillips, 1979) that such melts possess an "ideal" connectivity. In this approach, a glass network is broadly viewed as a network of chemical bonds linking atoms, with the bonds between nearest neighbor (nn) atoms, and bond-angles between second nn atoms serving as *mechanical constraints*. The network as a whole is then viewed to be either in a *flexible phase* (FP) or an *isostatically rigid intermediate phase* (IP) or a *stressed-rigid phase* (SRP) if the number of constraints per atom, n_c, is, respectively, lower than, equal to, or higher than the number of degrees of freedom per atom, i.e., $n_d = 3$ for 3D networks. These three topological phases (TPs) have now been observed in scores of network glasses (Yildirim et al., 2016; Chbeir et al.). The term "ideal" connectivity was traced to the basic condition $n_c = n_d$, which for the case of group IV (Si, Ge)-based chalcogenides corresponds to Corner-Sharing $GeSe_4$ tetrahedra percolating in the network at a mean coordination number of $<r> = 2.40$. The structure of such systems continues to be investigated using diffraction techniques including use of isotopically enriched glasses in neutron diffraction (Rowlands et al.). For the case of group V (P, As)-based chalcogenides, the same condition, $n_c = n_d$ led to $<r> = 2.28$ for the quasi-tetrahedral [$Se = P(Se_{1/2})_3$] local structures (Boolchand et al., 2009) and to 2.40 for pyramidal $(PSe_{1/2})_3$ local structures percolating through the network. Such geometrical motifs seem to have specific spectroscopic signatures (Micoulaut and Boolchand). The condition,

Edited and reviewed by:
Morten M. Smedskjaer, Aalborg University, Denmark

***Correspondence:**
Punit Boolchand
boolchp@ucmail.uc.edu

†These authors have contributed equally to this work

Specialty section:
This article was submitted to Ceramics and Glass, a section of the journal Frontiers in Materials

Received: *08 April 2020*
Accepted: *12 May 2020*
Published: *17 July 2020*

Citation:
Boolchand P and Micoulaut M (2020) Editorial: Topology of Disordered Networks and Their Applications. Front. Mater. 7:175. doi: 10.3389/fmats.2020.00175

$n_c = n_d$, was originally envisaged by Maxwell (1864) in understanding the mechanical stability of macroscopic structures such as bridges and trusses. Such a rigidity treatment can also be undertaken using a polytope approach (Sen and Mason).

Some of the objectives of the research within our Topic have included issues such as how pervasive is the notion of topological phases across the wide array of glass-forming systems? What challenges does one face in probing them, both experimentally and theoretically? What applications can these phases/materials be put to use for? And finally, what new science links the picture above T_g to the one below T_g? On all these scores, new information has emerged from the contributions we received for the Collection.

The inclusion of T-dependent bonding constraints for bond-bending and bond-stretching forces opened an entirely new domain in TCT in 2011 (Gupta and Mauro, 2009; Bauchy and Micoulaut, 2011). It made feasible to model structure and dynamics of glassy melts using molecular dynamics (MD) simulations (Bauchy, 2012). By establishing the variance in bond lengths and bond angles as a function of temperature, one could establish constraints that are either fully or partially intact. For Na^+ in sodium silicate glasses, the approach showed that even though the count of O near-neighbors of a Na^+ cation typically varies between 5 and 6, the variance in Na-O bond lengths demonstrated that the bond-stretching constraint is intact for only one of those five or six oxygen neighbors, underscoring (Bauchy and Micoulaut, 2011) that the "mechanically effective" coordination number of Na^+ is 1 consistent with its chemical valence. Here, additional numerical tools are provided and tested for the case of dense liquids, and these suggest dynamical gaps for the transverse part of viscoelastic transport, which have permitted evaluating a constraint density (Toledo-Marín and Naumis).

Melts of stoichiometric glass compositions where an underlying crystalline phase or phases occur apparently homogenize quicker than their non-stoichiometric counterparts do. Non-stoichiometric melts/glasses in the $2.0<<r><2.7$ range of connectivity undergo "delayed" homogenization, a feature discovered in 2011 (Bhosle et al., 2012a,b), which appears to be tied to the super-strong character of IP melts formed (Chakravarty et al.; Chbeir et al.; Mohanty et al.), with the fragility index m in the range of $20>\times>15$, in the fragile-strong classification. The latter can also alternatively be analyzed from a chalcogenide deficiency viewpoint (Lucas et al.). The feature emerged only once homogenized melts became available, thereby altering the landscape of fragility index results. The rigidity—and stress—elastic phase transitions are percolative in nature and first order in 3D (Jacobs and Thorpe, 1995), and experiments show that once the variance ($<\Delta x>$) in Ge content "x," across a batch composition of a binary GexSe100-x glass for example, is $<0.1\%$, the rigidity and stress transitions are found to be rather abrupt since the network connectivity $<r> = 2\ (1 + x)$ is tied to the variance $<\Delta x>$. Smearing of these two phase transitions was noted in melts/glasses in which the variance $<\Delta x>>2\%$. In modified oxides such as the sodium phosphates, the observation of the three TPs posed more challenges—melts/glasses had to be dry as well as homogeneous (Mohanty et al.). The existence of IPs with remarkable properties such as nearly reversible glass transitions, weak aging, forming compacted networks with reduced molar volumes, forming networks than can adapt, minimum creep, maximum fracture toughness (Bauchy et al., 2011) has come to the fore in more than scores of glass systems (Bauchy and Micoulaut, 2015) and has opened new awareness of the notion of self-organization.

There are three contributions on statistical mechanics origin of the IP and the application to network glasses. In one contribution, the role of topological fluctuations is considered in determining the compositional width of the IP (Kirchner and Mauro). In the second (Toledo-Marín and Yan), a prediction for the existence of a liquid–liquid phase transition in IP phase melts is made. If confirmed, the authors suggest that IPs will represent a new thermodynamic phase of disordered condensed matter. In the third one, a statistical mechanics modeling leads to the prediction of composition–structure relations in alkali borosilicate glasses (Bødker et al.).

Striking suggestions for existence of an IP in calcium-silicate hydrates was presented from numerical simulations by Zhou et al., who have identified the appropriate experimental observables to establishing the rigidity—and stress—elastic phase transitions.

Although TCT has been widely used to describe network glasses composed of atoms, the case of icosahedral borocarbide forming highly coordinated networks of "superatoms" whose connectivity can be controlled by hydrogenation is considered by Nordell et al.. The group has synthesized thin films of hydrogenated icosahedral borocarbide over a wide range of hydrogen contents and examined these in Young's modulus experiments. They observe evidence of rigidity onset near $<r> = 2.40$, and the Young's modulus is found to increase as a power-law in $<r>$ with a value of 1.50 in the stressed-rigid regime in harmony with simulations.

The fragility index variations with mean coordination number $<r>$, in the GexAsxSe100-2x chalcogenide and the modified oxide (Na2O)x(P2O5)100-x (SPGs), led Sidebottom to recognize TPs using a coarse graining model (CGM) approach. In the CGM approach, one excludes the P-O_t dangling ends in SPGs and estimates network connectivity, $<r>$, by the count of P-$O_{bridging}$ contacts defining the backbone. In this approach, the onset of rigidity is expected near $<r> = 2.40$, or 37.5% of Na_2O, a prediction that is confirmed by the observation of the rigidity transition at that composition by Mohanty et al. from modulated-differential scanning calorimetry (MDSC) experiments. The observation is consistent with dangling ends playing no role at the rigidity transition. However, such is not the case for compositions away from the rigidity transition (Boolchand et al., 1996). The presence of dangling ends in stressed-rigid (flexible) networks softens (stiffens) the networks. Indeed, Mohanty et al. also observe the stress transition to occur near $x = 46.0\ (2)\%$ of Na_2O, underscoring that compositions at $x > 37.5\%$ are in the rigid phase, while in the CGM, one views such compositions to be in the flexible phase since $<r> < 2.40$. Thus, the TPs in the SPGs deduced using the CGM approach are found to be inverted with respect to those obtained using the complete network when dangling ends are explicitly included.

Peak force quantitative nanoindentation modulus (NIM) on ternary bulk Agx(GeySe1-y) alloy glasses over a wide range of Ag alloying "x," and base glass "y" chemistry measurements have permitted mapping of NIM and correlating it with the Ag content of the glasses, thus providing new insights into the topologically segregated nature of the ternary glass system.

AUTHOR CONTRIBUTIONS

All authors listed have made a substantial, direct and intellectual contribution to the work, and approved it for publication.

FUNDING

PB acknowledges support from NSF grant DMR 08-53957. MM acknowledges support from Agence Nationale de la Recherche (ANR) grant no. ANR-11-BS08-10012 from American Fullbright Commission and International Materials Institute (H. Jain).

ACKNOWLEDGMENTS

We thank all authors, reviewers, and editors who assisted in the Collection. We thank Dr. Ralph Chbeir who assisted the Topic Editors.

REFERENCES

Bauchy, M. (2012). Topological constraints and rigidity of network glasses from molecular dynamics simulations. *Am. Ceramic Soc. Bull.* 91, 34A−38A. Available online at: https://arxiv.org/abs/1506.06483

Bauchy, M., and Micoulaut, M. (2011). Atomic scale foundation of temperature-dependent bonding constraints in network glasses and liquids. *J. Non Cryst. Solids* 357, 2530–2537. doi: 10.1016/j.jnoncrysol.2011.03.017

Bauchy, M., and Micoulaut, M. (2015). Densified network glasses and liquids with thermodynamically reversible and structurally adaptive behaviour. *Nat. Commun.* 6:6398. doi: 10.1038/ncomms7398

Bauchy, M., Micoulaut, M., Celino, M., Le Roux, S., Boero, M., and Massobrio, C. (2011). Angular rigidity in tetrahedral network glasses with changing composition. *Phys. Rev. B* 84:054201. doi: 10.1103/PhysRevB.84.054201

Bhosle, S., Gunasekera, K., Boolchand, P., and Micoulaut, M. (2012a). Melt homogenization and self?organization in chalcogenides-part I. *Int. J. Appl. Glass Sci.* 3, 189–204. doi: 10.1111/j.2041-1294.2012.00093.x

Bhosle, S., Gunasekera, K., Boolchand, P., and Micoulaut, M. (2012b). Melt homogenization and self?organization in chalcogenides-part II. *Int. J. Appl. Glass Sci.* 3, 205–220. doi: 10.1111/j.2041-1294.2012.00092.x

Boolchand, P., Chen, P., and Vempati, U. (2009). Intermediate phases, structural variance and network demixing in chalcogenides: the unusual case of group V sulfides. *J. Non Cryst. Solids* 355, 1773–1785. doi: 10.1016/j.jnoncrysol.2008.11.046

Boolchand, P., Zhang, M., and Goodman, B. (1996). Influence of one-fold-coordinated atoms on mechanical properties of covalent networks. *Phys. Rev. B Condensed Matter* 53, 11488–11494. doi: 10.1103/PhysRevB.53.11488

Gupta, P. K., and Mauro, J. C. (2009). Composition dependence of glass transition temperature and fragility. I. A topological model incorporating temperature-dependent constraints. *J. Chem. Phys.* 130:094503. doi: 10.1063/1.3077168

Jacobs, D. J., and Thorpe, M. F. (1995). Generic rigidity percolation: the pebble game. *Phys. Rev. Lett.* 75, 4051–4054. doi: 10.1103/PhysRevLett.75.4051

Lucovsky, G., Phillips, J. C., and Boolchand, P. (2003). A new approach to gate dielectric integrity based on differences between i) strained and ii) strain-free interfacial regions: applications to devices with alternative high-k dielectrics. *Int. Conf. Solid State Devices Mater*, 422–423. doi: 10.7567/SSDM.2003.P2-6

Maxwell, J. C. (1864). L. On the calculation of the equilibrium and stiffness of frames. *Philos. Magaz. Ser.* 27, 294–299. doi: 10.1080/14786446408643668

Phillips, J. C. (1979). Topology of covalent non-crystalline solids.1. Short-range order in chalcogenide alloys. *J. Non Cryst. Solids* 34, 153–181. doi: 10.1016/0022-3093(79)90033-4

Yildirim, C., Raty, J.-Y., and Micoulaut, M. (2016). Revealing the role of molecular rigidity on the fragility evolution of glass-forming liquids. *Nat. Commun.* 7:11086. doi: 10.1038/ncomms11086

Conflict of Interest: The authors declare that the research was conducted in the absence of any commercial or financial relationships that could be construed as a potential conflict of interest.

frontiers in Materials

ORIGINAL RESEARCH
published: 14 February 2019
doi: 10.3389/fmats.2019.00011

Statistical Mechanical Model of the Self-Organized Intermediate Phase in Glass-Forming Systems With Adaptable Network Topologies

*Katelyn A. Kirchner and John C. Mauro**

Department of Materials Science and Engineering, The Pennsylvania State University, University Park, PA, United States

Non-equilibrium systems continuously evolve toward states with a lower free energy. For glass-forming systems, the most stable structures satisfy the condition of isostaticity, where the number of rigid constraints is exactly equal to the number of atomic degrees of freedom. The rigidity of a system is based on the topology of the glass network, which is affected by atomistic structural rearrangements. In some systems with adaptable network topologies, a perfect isostatic condition can be achieved over a range of compositions, i.e., over a range of different structures, giving rise to the intermediate phase of optimized glass formation. Here we develop a statistical mechanical model to quantify the width of the intermediate phase, accounting for the rearrangement of the atomic structure to relax localized stresses and to achieve an ideal, isostatic state.

Keywords: glass, intermediate phase, topological constraint theory, statistical mechanics, modeling

OPEN ACCESS

Edited by:
Matthieu Micoulaut, Sorbonne Universités, France

Reviewed by:
Stefan Karlsson, RISE Research Institutes of Sweden, Sweden
Guglielmo Macrelli, Independent Researcher, Este, Italy

****Correspondence:***
John C. Mauro
jcm426@psu.edu

Specialty section:
This article was submitted to Glass Science, a section of the journal Frontiers in Materials

Received: *27 November 2018*
Accepted: *25 January 2019*
Published: *14 February 2019*

Citation:
Kirchner KA and Mauro JC (2019) Statistical Mechanical Model of the Self-Organized Intermediate Phase in Glass-Forming Systems With Adaptable Network Topologies. Front. Mater. 6:11. doi: 10.3389/fmats.2019.00011

INTRODUCTION

Within the field of topological constraint theory, there is growing interest in the ability of a glass network to adapt its topology to achieve isostaticity. A glass network is isostatic when the number of rigid constraints per atom, n, equals the number of translational degrees of freedom (Phillips, 1979). For a system in three-dimensional space, each atom has three degrees of freedom; hence, $\langle n \rangle = 3$ is the condition for achieving an isostatic network (Thorpe, 1983). If $\langle n \rangle > 3$ the system is overconstrained (stressed rigid), and if $\langle n \rangle < 3$ the system is underconstrained (floppy) (Thorpe, 1983). In the overconstrained region, additional rigidity, beyond $\langle n \rangle = 3$, creates localized stresses. Elimination of these stresses can be achieved through an imposition of crystalline order, which drives the network out of the glassy state (Thorpe, 1983).

When topological constraint theory of glass was originally proposed by Phillips and Thorpe, the isostatic state was predicted to be achieved at a single composition, viz., the rigidity percolation threshold (Phillips and Thorpe, 1985). However, in 1999, Raman scattering and temperature-modulated differential scanning calorimetry (MDSC) experiments by Punit Boolchand et al. revealed a finite width of isostatic compositions in which the system can maintain stability, called the *intermediate phase* (IP) (Selvanathan et al., 1999; Boolchand et al., 2001b; Micoulaut, 2007; Moukarzel, 2013). Thorough investigations, particularly in chalcogenide systems, have revealed a difference between the onset of rigidity and the onset of stress, creating a finite width of compositions that enable the most stable, isostatic state (Selvanathan et al., 1999; Boolchand et al., 2001b). One of the most pronounced signatures of the intermediate phase was detected using MDSC measurements (Feng et al., 1997), which measures the non-reversible enthalpy of relaxation, ΔH. The difference between the original

Phillips-Thorpe single percolation threshold result and Boolchand's intermediate phase can be visualized in **Figures 1A,B**, respectively, where the blue circles indicate the lowest energy states of ΔH and hence the isostatic composition(s).

Although a consensus within the glass community has still not been reached regarding the existence of the intermediate phase, over the past 18 years understanding of the phenomenon has greatly advanced. Evidence of the IP has been found through numerical studies (Thorpe et al., 2000), analysis of finite size clusters (Micoulaut and Phillips, 2003), and thorough analyses using MDSC (Selvanathan et al., 1999, 2000; Boolchand et al., 2001b; Vaills et al., 2005; Novita et al., 2007) and Raman scattering (Selvanathan et al., 1999, 2000; Boolchand et al., 2001a; Wang et al., 2001; Novita et al., 2007). These studies all reveal two distinct thresholds marking the boundaries of the intermediate phase: the rigidity transition (the lower bound, below which there are floppy modes in the network) and the stress transition (the upper bound, above which the network is stressed-rigid). Between the two thresholds, fluctuations in the system can enable self-organization, as visualized in **Figure 2**.

A challenge when studying the intermediate phase is the apparent irreproducibility of some of the experiments, causing the physical origins and very existence of the phase to be controversial. Careful sample preparation is necessary in order to detect the IP due to the experiment's high sensitivity to impurities, inhomogeneities, and the thermal history of the glass (Bhosle et al., 2011, 2012). Some critics of the intermediate phase attribute the observed finite widths as possible experimental artifacts (Golovchak et al., 2008; Lucas et al., 2009; Shpotyuk and Golovchak, 2011). During MDSC experiments on Ge-Se glasses, the non-reversible enthalpy was shown to decrease in the IP domain, inferring a need for Ge-Se-Se isostatic structural fragments to account for the rigid but unstressed network (Micoulaut and Phillips, 2003; Massobrio et al., 2007; Sartbaeva et al., 2007). However, an extensive high-temperature nuclear magnetic resonance study revealed that these fragments were missing from the structure (Lucas et al., 2009). To account for this discrepancy, Lucas et al. disagreed with the existence of the intermediate phase and instead hypothesized that the previously observed phase could be an experimental artifact resulting from the use of a single modulation frequency in the MDSC experiments. However, subsequent modeling work showed that the frequency correction used in the analysis of the MDSC experiments provided non-reversing heat flows independent of the particular choice of modulation frequency (Guo et al., 2012).

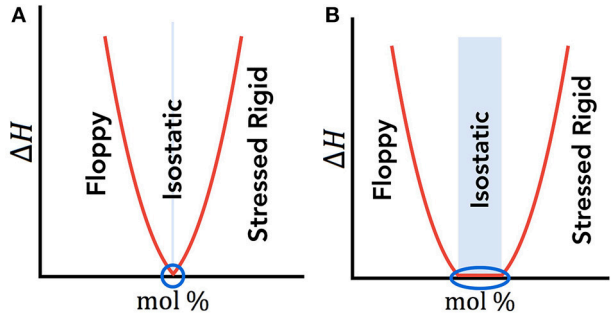

FIGURE 1 | (A) Phillips-Thorpe theory based on a single isostatic point. **(B)** Boolchand intermediate phase where the isostatic region encompasses a finite width. In both **(A)** and **(B)**, the isostatic region is shown as the blue shaded region, and the blue circle identifies the compositions with the lowest enthalpy, ΔH, therefore indicating the energetically preferred and isostatic composition(s).

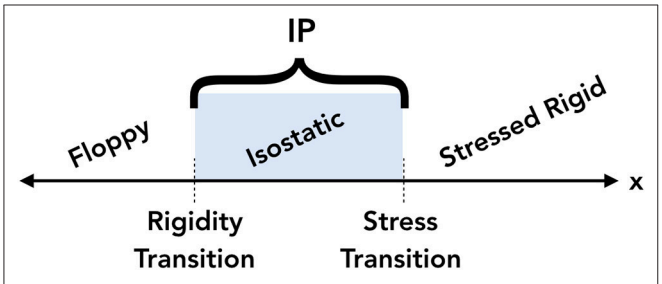

FIGURE 2 | A visual representation of the two thresholds bounding the intermediate phase (IP) for varying compositions, x. The rigidity transition and stress transition separate the floppy, isostatic, and stressed rigid compositions, as shown.

Another claim against the existence of the intermediate phase is the observation of physical aging in the intermediate phase glasses (Golovchak et al., 2006, 2008, 2011; Shpotyuk et al., 2008; Elabbar and Adu-Sehly, 2011). The intermediate phase is reported to be characterized by high stability and a lack of physical aging. However, when differential scanning calorimetry was used to investigate the kinetics associated with the glass transition, results showed that all samples had evidence of physical aging behavior (Zhao et al., 2013). These inconsistencies in the physical understanding of glass adaptability and isostaticity sparked the glass community's growing interest in this field.

Further work is therefore required to elucidate the origin of the intermediate phase. Considering that a finite width of isostatic compositions is indeed possible, the second point of debate is the underlying mechanisms (structure, dynamics, interaction, etc.) enabling the two-threshold intermediate phase. Typically, studies emphasize the central role of fluctuations (Thorpe et al., 2000; Barré et al., 2005; Chubynsky et al., 2006; Micoulaut, 2006). More specifically, it is proposed that the fluctuations in the system enable the atoms to self-organize into a stress-free state while still maintaining a non-crystalline structure of the glass. These structural rearrangements relieve additional stresses, driving the system back toward a lower free energy state (Selvanathan et al., 1999; Boolchand et al., 2001b). The network mitigates the stresses by adapting its topology, thereby affecting the number of rigid constraints in the network.

Topological fluctuations in a glassy system are based on the distribution in rigid constraints, $n(x,T,P)$ (Micoulaut, 2016). Given the non-linear behavior of coordination changes with pressure, pressure dependence is out of the scope in this simplified topological model, i.e., here we will only explore the dependence on composition and temperature. Additionally, this paper considers the network's ability to adapt its topology to eliminate stresses, without considering the kinetics of this adaptation process.

This paper explores both the statistical mechanical origin of the intermediate phase, as well as the role of topological fluctuations in governing its width. The proposed mechanism for the intermediate phase is based on the ability of the network to self-organize, i.e., to eliminate localized stress due to the adaptability of the network. This adaptability is made possible by the localized fluctuations in the glass network's structure and topology, with localized stresses as the driving force for these rearrangements. Modeling the distribution of topological fluctuations was made possible in prior work by linking statistical mechanics and topological constraint theory (Kirchner et al., 2018). Extending this previous work, the current investigation analyzes the degree of self-organization enabled through these structural and topological fluctuations to create a generalized approach for modeling the width of the intermediate phase of an arbitrary glass-forming system. The model is used to quantify the width of the intermediate phase, which can be defined either in units of constraints, n, or composition, x. In both representations, the width is analyzed as a function of composition and temperature. These results are then discussed in relation to localized topological fluctuations. Utilizing the general approach outlined in this paper, the structure of a glass-forming system could potentially be designed to achieve a desired intermediate phase width.

CALCULATION OF THE TOPOLOGICAL FLUCTUATIONS

The width of the intermediate phase is dependent on the adaptability of the glass network, which is enabled by the distribution of rigidity fluctuations. Prior work by the authors established a general approach for calculating the distribution of the number of rigid constraints per atom by linking statistical mechanics and topological constraint theory (Kirchner et al., 2018). Through statistical mechanics, the probability of site occupation is given by Mauro (2013); Mauro and Smedskjaer (2014)

$$p_{i,m} = \frac{1}{Q_{m-1}} \left(g_i - a_{i,m-1}\right) \exp\left(-\frac{\Delta H_i}{kT}\right) \tag{1}$$

where Q_{m-1} is the path-dependent partition function calculated after occupation of modifier $m-1$ (which normalizes the distribution at each step), g_i is the population size of network former sites of type i, and $a_{i,m-1}$ is the number of type i sites previously occupied after modifier $m-1$. ΔH_i is the enthalpy change associated with occupying site type i, k is Boltzmann's constant, and T is the absolute temperature. To account for thermal history effects in a glass, the temperature can be set equal to the fictive temperature of the system.

This statistical mechanical approach calculates the probability density of $N_i(x)$, the mole fraction of network-forming species i in composition x, which serves as an input for the distribution of the number of atomistic constraints, given by Mauro et al. (2009); Mauro (2011)

$$n\,(T,x) = \sum\nolimits_i N_i(x) \sum\nolimits_\alpha w_{i,\alpha}\, q_\alpha(T). \tag{2}$$

In Equation (2) the outer summation is over the network-forming species i and the inner summation is over the various constraints α. $w_{i,\alpha}$ is the number of constraints of type α associated with the species type i and $q_\alpha(T)$ is the temperature-dependent rigidity of constraint α, given by

$$q_\alpha\,(T) = \left[1 - \exp\left(-\frac{\Delta F_\alpha^*}{kT}\right)\right]^{\nu t_{obs}}. \tag{3}$$

The rigidity for each constraint, α, is an independent function of the absolute temperature, T, where ν is the vibrational attempt frequency, t_{obs} is the observation time, and $\Delta F_\alpha{}^*$ is the activation free energy for breaking the α constraint, given by

$$F_\alpha^* = -kT_\alpha \ln\left(1 - 2^{-\frac{1}{\nu t_{obs}}}\right) \tag{4}$$

where T_α is the onset temperature for constraint α. The onset temperature, T_α, is defined as the temperature at which the probability of breaking the constraint is exactly 1/2 (Mauro, 2011). Linking Equations (1,2) results in the

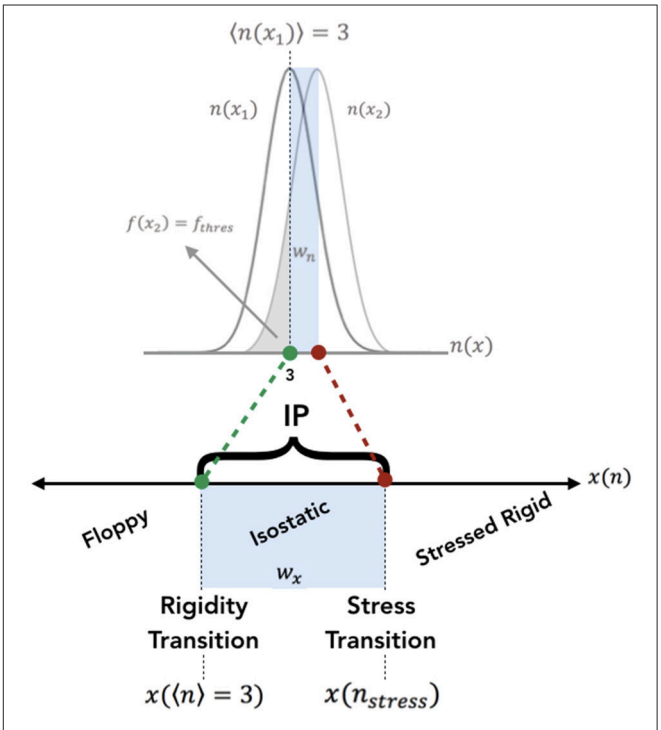

FIGURE 3 | A visual representation of the thresholds that determine the width of the IP, both in terms of the atomic constraints, $n(x)$, and the composition, $x(n)$. Within his paper, the constraints are given as a distribution, hence incorporating the statistical fluctuations of constraints. The rigidity transition is determined by the composition in which the constraint distribution satisfies $\langle n \rangle = 3$. The stress transition is determined by the composition corresponding to the constraint distribution of n_{stress}.

distribution of local constraints, which quantifies the topological fluctuations dictating the width of the intermediate phase (Kirchner et al., 2018).

THE INTERMEDIATE PHASE

The width of the intermediate phase is defined by two boundaries: the rigidity transition and the stress transition. The rigidity transition occurs when the average number of atomic constraints, $\langle n \rangle$, equals the number of degrees of freedom; this represents the transition from a flexible to an isostatic network. Since here we consider a three-dimensional network, the rigidity transition occurs when $\langle n \rangle = 3$. Note that the number of rigid constraints per atom, n, is typically presented as a single mean value; however, this investigation explores the distributions of fluctuations, and hence, the full distribution of n. Therefore, in the context of this paper, $\langle n \rangle$ refers to the mean, while n refers to the distribution of the number of atomistic constraints.

TABLE 1 | The arbitrary model's starting conditions, prior to varying the concentration of network former, B, the network modifier, M, or the temperature, T.

$w_{A,un}$	6
$w_{A,oc}$	6
$w_{B,un}$	6
$w_{B,oc}$	6
$T_{A,un}$ (K)	590
$T_{A,oc}$(K)	565
$T_{B,un}$(K)	590
$T_{B,oc}$(K)	615
T (K)	600
[B]	0.5
[M]	0.5
vt_{obs}	1,000

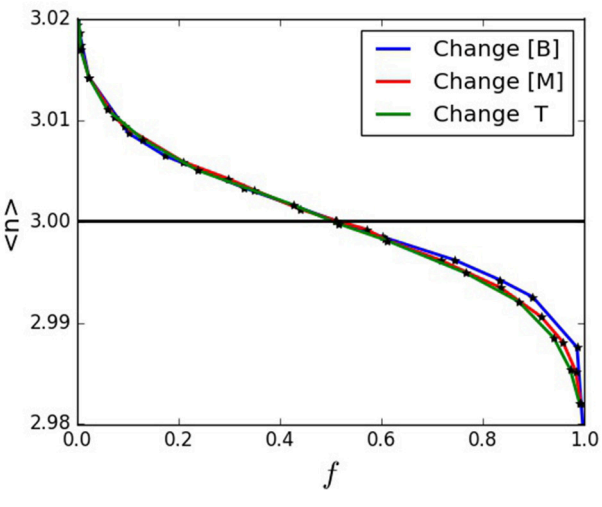

FIGURE 4 | $\langle n \rangle$ vs. f when varying the concentration of network formers, B, modifiers, M, and temperature, T.

Since the dimensionality of the system remains constant, the rigidity transition in a 3D network is defined by

$$\langle n \rangle = 3 \tag{5}$$

The second threshold, the stress transition, occurs when the overconstrained system can no longer rearrange itself into a stress-free state. This boundary is defined by the low-rigidity tail of the distribution, which we quantity with the floppy mode probability, f, given by

$$f = \int_0^3 P(n)\ dn \tag{6}$$

where $P(n)$ is the probability density function of the rigidity distribution n. The quantity f therefore gives the probability of the system having an atomic rigidity less than or equal to three.

It is important to note that not all systems will enable rearrangement, and to model the obtainable intermediate phase within a glass-forming system we need to incorporate a reasonable threshold for rearrangement. Using the definition of f in Equation (6), we can define a material property, f_{thres}, which is the threshold probability for the system to be able to rearrange its structure and topology. In other words, we can define f_{thres} as a minimum threshold for which the system can remain isostatic by relaxing the localized stresses in a stressed-rigid network through structural rearrangements. As long as $f > f_{thres}$ the structure can rearrange itself to eliminate the stresses, viz., by biasing the structure toward the stress-free isostatic configurations. The driving force for this network adaptability is the localized stress generated in the overconstrained, stressed-rigid configurations. Once $f < f_{thres}$ the isostatic configurations are no longer considered to be accessible, i.e., the stresses in the network are too high to fully relax. Therefore, $f = f_{thres}$ marks the stress transition, i.e., the second boundary of the intermediate phase, which can be given in terms of the corresponding constraint distribution, n_{stress}, and is defined as

$$n_{stress} = \langle\, n\,(x, f_{thres})\,\rangle\,. \tag{7}$$

The difference between the two boundaries, given by Equations (5,7), dictates the maximum allowed width, w, of the intermediate phase. The width can be given either in units of the difference in number of constraints,

$$w_n = n_{stress}(x, f_{thres}) - 3 \tag{8}$$

or more typically by the corresponding compositional width,

$$w_x = x\,(n_{stress}, f_{thres}) - x\,(3), \tag{9}$$

where $w_n > 0$ and $w_x > 0$. **Figure 3** illustrates the thresholds and corresponding parameters that determine this maximum width of constraints or compositions enabling self-organization with a disordered network. Given that f_{thres} can vary for different systems, here we consider the intermediate phase width as a function of this material property, f_{thres}.

RESULTS AND DISCUSSION

The scope of the current investigation considers a simplified glass network with composition $A_{1-x}B_x\ M_y$, where A and B are the two network formers and M is the network modifier. Given that there are two types of network formers and one type of modifier, there are four possible structural motifs within the system, based on whether a network-forming site is either unoccupied (denoted as A_{un} and B_{un}) or occupied (A_{oc} and B_{oc}) by a modifier. Following Equation (1), the probability of site occupation is based on the competition between entropic and enthalpic effects. The compositions of A, B, and M determine the entropic preferences, while the enthalpic preferences are determined by the relative energies associated which each state. In our model, we arbitrarily specify the B site to be enthalpically favored for modifier association, i.e., $H_{A,oc} > H_{B,oc}$.

The set of parameter values is provided in **Table 1**, including the number of constraints, $w_{i,\alpha}$, the onset temperatures, T_α (hence, dictating the rigidity, $q_\alpha(T)$, of each constraint), the temperature, the concentration of network formers and network modifiers, and the value of vt_{obs}, i.e., the complete set of variables necessary to solve Equations (1–4). The model's parameters were arbitrarily chosen to make $\langle n \rangle \approx 3$ near $[A] = [B] \approx 0.5$. $[B]$, $[M]$, T were then altered to find the thresholds for the IP.

As addressed in Equations (8,9), the width of the intermediate phase can be expressed either in units of constraints, n, or composition, x. In both representations, the constraints and compositions defining the intermediate phase width are based on the network's composition and temperature.

IP Widths in Units of *n*

The concentration of network former B, the concentration of network modifier M, and the absolute temperature of the system, T, dictate the distribution of n, and therefore, the intermediate phase width in units of n. **Figure 4** illustrates these variables altering the distribution of n, thereby influencing f and $\langle n \rangle$. Given $w_n > 0$ and Equation (8), the IP width in units of n can only be applied to data from $\langle n \rangle \geq 3$. **Figures 5A,B** use Equation (8) to then plot the IP widths in units of n in terms of f_{thres} or $\ln(f_{thres})$, respectively. Both figures show that changing $[B]$, $[M]$, or T result in similar widths for a given f_{thres}.

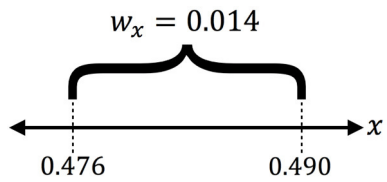

FIGURE 6 | An example IP for $f_{thres} = 0.1$ in terms of composition. This figure shows that the model can quantify the theoretical IP, as given in **Figure 2**.

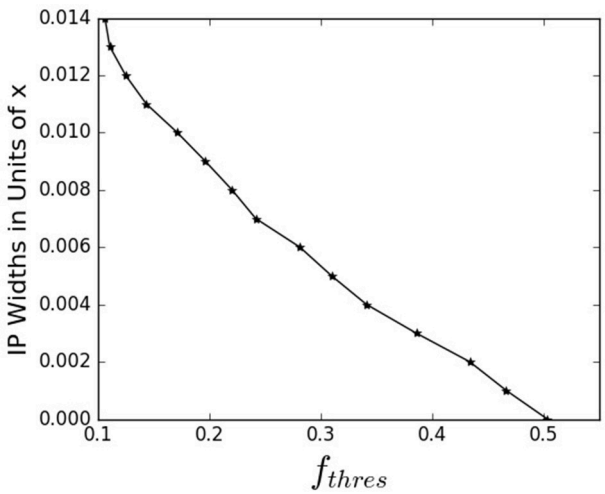

FIGURE 7 | The width of the IP in terms of composition, x, based on f_{thres}. Given an f_{thres}, which is a material property, this graph allows us to determine the corresponding w_x if the system enables adaptable network topologies.

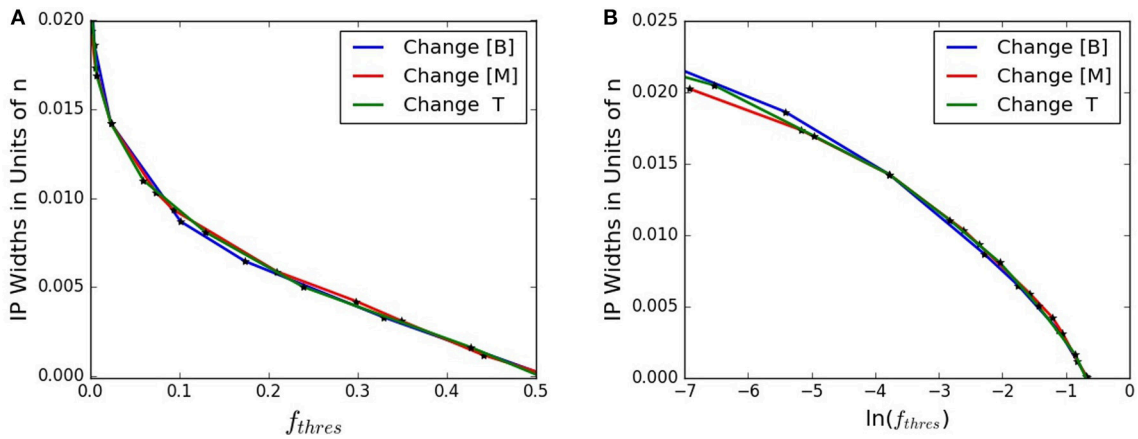

FIGURE 5 | (A) The IP width, w_n, given by Equation (8), based on f_{thres}. **(B)** The IP width, w_n, given by Equation (8), based on $\ln(f_{thres})$.

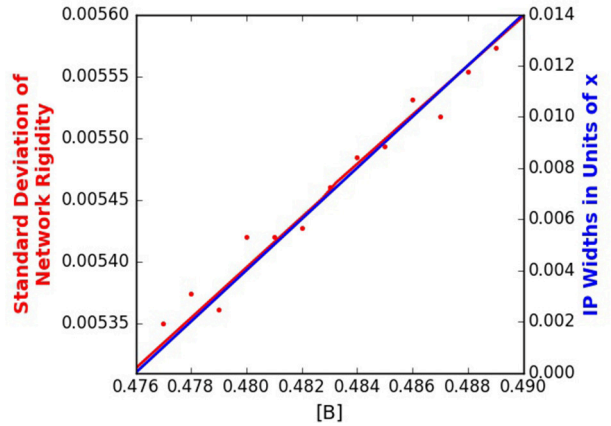

FIGURE 8 | The standard deviation of the distribution of constraints, n, and the resulting intermediate phase width, w_x, for $f_{thres} = 0.1$.

IP Widths in Units of *x*

As shown with w_n, altering composition dictates the width between the two IP thresholds. To measure w_x, the intermediate phase width in terms of the glass composition $A_{1-x}B_x\ M_y$, we determine the composition x at each of the IP thresholds. As defined in Equation (9), the difference between these the composition at $\langle n \rangle = 3$ and the composition at n_{stress} determines the width w_x. Given a sample's material property f_{thres}, this approach enables us to quantify the threshold proposed in **Figure 2**, as shown in **Figure 6** for an arbitrary f_{thres}= 0.1. A more general representation of w_x for each f_{thres} is plotted in **Figure 7**. From these results, with a known rearrangement threshold for a given glass-forming system, we can approximate the width of the intermediate phase.

The proposed mechanism for self-organization, and hence the intermediate phase, is topological fluctuations, which depend on the standard deviation of the distribution of constraints. **Figure 8** plots the magnitude of fluctuations (quantified using the standard deviation of n, calculated over the ensemble of configurations resulting from the combined statistical mechanical/topological model) compared to the intermediate phase width for an arbitrary value of f_{thres}= 0.1. Details of the procedure for calculating the standard deviation of n are provided in our previous work (Kirchner et al., 2018). The results in **Figure 8** show a direct correlation between the maximum fluctuations and the maximum intermediate phase width, hence supporting the proposed mechanism of topological fluctuations enabling the adaptability of glass-forming systems. Increased fluctuations thereby enable a greater width for the intermediate phase.

While this research focuses on the topological origin of the intermediate phase, we have not addressed the important question of the kinetics of the topological changes that enable intermediate phase formation. Moreover, while we have considered the temperature dependence of the constraint rigidity, pressure effects have not yet been investigated. Both of these subjects will be suitable topics for future studies.

CONCLUSION

In this paper we have established a general approach for calculating the boundaries of the intermediate phase for an arbitrary glass-forming system. Our calculation is based on topological fluctuations in the network, which allow for the ability of the glass to relax localized stresses from a stressed-rigid condition. The width of the intermediate phase increases with the level of topological fluctuations, since these fluctuations allow for self-organization of the network, i.e., the ability of the glass to dynamically adapt its topology to alleviate localized stresses. The distribution of fluctuations, as dependent on composition and temperature, was modeled by linking statistical mechanics and topological constraint theory, which can then be used to quantify the width of the intermediate phase in an arbitrary glass-forming system. This theory could also be extended to incorporate the pressure dependence of the intermediate phase boundaries. Future work may also include an in-depth study of the kinetics of the topological reconfigurations enabling the adaptability of the network.

AUTHOR CONTRIBUTIONS

All authors listed have made a substantial, direct and intellectual contribution to the work, and approved it for publication.

FUNDING

We are grateful for funding from the U.S. National Science Foundation (CMMI 1762275).

ACKNOWLEDGMENTS

We are grateful for valuable discussions with Dr. Seong H. Kim of Penn State.

REFERENCES

Barré, J., Bishop, A. R., Lookman, T., and Saxena, A. (2005). Adaptability and "intermediate phase" in randomly connected networks. *Phyis. Rev. Lett.* 97:208701. doi: 10.1103/PhysRevLett.94.208701

Bhosle, S., Gunasekera, K., Boolchand, P., and Micoulaut, M. (2012). Melt homogenization and self-organization in chalcogenides-part 1. *Int. J. Appl. Glass Sci.* 3, 189–205. doi: 10.1111/j.2041-1294.2012.00093.x

Bhosle, S., Gunasekera, K., Chen, P., Boolchand, P., Micoulaut, M., and Massobrio, C. (2011). Meeting experimental challenges to physics of network glasses: assessing the role of sample homogeneity. *Solid State Comm.* 151, 1851–1855. doi: 10.1016/j.ssc.2011.10.016

Boolchand, P., Feng, X., and Bresser, W.J., (2001a). Rigidity transitions in binary Ge-Se glasses and the intermediate phase. *J. Non Cryst. Solids* 293–295, 348–356. doi: 10.1016/S0022-3093(01)00867-5

Boolchand, P., Georgiev, D.G., and Goodman, B., (2001b). Discovery of the intermediate phase in chalcogenide glasses. *J. Optoelectro. Adv. Mat.* 3, 703–720.

Chubynsky, M. V., Brière, M.-A., and Mousseau, N. (2006). Self-organization with equilibration: A model for the intermediate phase in rigidity percolation. *Phys. Rev.* E74:016116. doi: 10.1103/PhysRevE.74.016116

Elabbar, A. A., and Adu-Sehly, A. A. (2011). Structural relaxation and rigidity transition in aged and rejubenated As_xSe_{100-x} glasses. *Phys. B.* 406, 4261–4265. doi: 10.1016/j.physb.2011.08.039

Feng, X., Bresser, W., and Boolchand, P. (1997). Direct evidence for stiffness threshold in chalcogenide glasses. *Phys. Rev. Lett.* 78, 4422–4425. doi: 10.1103/PhysRevLett.78.4422

Golovchak, R., Gorecki, C.z., Koxdras, A., and Shpotyuk, O. I. (2006). Physical ageing effects in vitreous arsenic selenides. *Solid State Comm.* 137(1–2), 67–69. doi: 10.1016/j.ssc.2005.10.009

Golovchak, R., Jain, H., Shpotyuk, O., Kozdras, A., Saiter, A., and Saiter, J-M. (2008). Experimental verification of the reversibility window concept in binary As-Se glasses subjected to a long-term physical aging. *Phys. Rev. B.* 78:014202. doi: 10.1103/PhysRevB.78.014202

Golovchak, R., Kozdras, A., Shpotyuk, O., Gorecki, C. Z., Kovalskiy, A., and Jain, H. (2011). Temperature-dependent structural relaxation in $As_{40}Se_{60}$ glass. *Phys. Lett. A.* 375, 3032–3036. doi: 10.1016/j.physleta.2011.06.056

Guo, X., Mauro, J. C., Allan, D. C., and Yue, Y. (2012). On the frequency correction in temperature-modulated differential scanning calorimetry of the glass transition. *J. Non Crystal. Solids* 358, 1710–1715. doi: 10.1016/j.jnoncrysol.2012.05.006

Kirchner, K. A., Kim, S. H., and Mauro, J. C. (2018). Statistical mechanics of topological fluctuations in glass-forming liquids. *Phys. A.* 510, 787–801. doi: 10.1016/j.physa.2018.07.028

Lucas, P., King, E. A., Gulbiten, O., Yarger, J. L., Soignard, E., and Bureau, B. (2009). Bimodal phase percolation model for the structure of Ge-Se glasses and the existence of the intermediate phase. *Phyis. Rev. B.* 80:214114. doi: 10.1103/PhysRevB.80.214114

Massobrio, C., Celino, M., Salmon, P. S., Martin, R. A., Micoulaut, M., and Pasquarello, A. (2007). Atomic structure of the two intermediate phase glasses $SiSe_4$ and $GeSe_4$. *Physic. Rev. B.* 79:174201. doi: 10.1103/PhysRevB.79.174201

Mauro, J. C. (2011). Topological constraint theory of glass. *Am. Ceramic Soc. Bull.* 90, 31–37.

Mauro, J. C. (2013). Statistics of modifier distributions in mixed network glasses. *J. Chem. Phys.* 138:12A522. doi: 10.1063/1.4773356

Mauro, J. C., Gupta, P. K., and Loucks, R. J. (2009). Composition dependence of glass transition temperature and fragility. II. a topological model of alkali borate liquids. *J. Chem. Phys.* 130:234503. doi: 10.1063/1.3152432

Mauro, J. C., and Smedskjaer, M. M. (2014). Statistical mechanics of glass. *J. Non Crystal. Solids* 396–397, 41–53. doi: 10.1016/j.jnoncrysol.2014.04.009

Micoulaut, M. (2006). Rigidity and intermediate phases in glasses driven by speciation. *Phys. Rev. B.* 74:184208. doi: 10.1103/PhysRevB.74.184208

Micoulaut, M. (2007). Simple clues and rules for self-organized rigidity in glasses. *J. Optoelectr. Adv. Mat.* 9, 3235–3240.

Micoulaut, M. (2016). Concepts and applications of rigidity in non-crystalline solids: a review on new developments and directions. *Adv. Phys. X.* 1, 147–175. doi: 10.1080/23746149.2016.1161498

Micoulaut, M., and Phillips, J. C. (2003). Rings and rigidity transitions in network glasses. *Phys. Rev. B.* 67:104204. doi: 10.1103/PhysRevB.67.104204

Moukarzel, C. F. (2013). Two rigidity-percolation transitions on binary Bethe networks and the intermediate phase in glass. *Phys. Rev. E* 88:062121. doi: 10.1103/PhysRevE.88.062121

Novita, D. I., Boolchand, P., Malki, M., and Micoulaut, M. (2007). Fast-Ion conduction and flexibility of glassy networks. *Phys. Rev. Lett.* 98:195501. doi: 10.1103/PhysRevLett.98.195501

Phillips, J. C. (1979). Topology of covalent non-crystalline solids I: short-range order in chalcogenide alloys. *J. Non Crystal. Solids* 34, 153–181. doi: 10.1016/0022-3093(79)90033-4

Phillips, J. C., and Thorpe, M. F. (1985). Constraint theory, vector percolation and glass formation. *Solid State Comm.* 53, 699–702. doi: 10.1016/0038-1098(85)90381-3

Sartbaeva, A., Wells, S. A., Huerta, A., and Thorpe, M. F. (2007). Local structural variability and the intermediate phase window in network glasses. *Phys. Rev. B.* 75:224204. doi: 10.1103/PhysRevB.75.224204

Selvanathan, D., Bresser, W. J., and Boolchand, P. (2000). Stiffness transitions in Si_xSe_{1-x} glasses from Raman scattering and temperature-modulated differential scanning calorimetry. *Phys. Rev. B.* 61:15061. doi: 10.1103/PhysRevB.61.15061

Selvanathan, D., Bresser, W. J., Boolchand, P., and Goodman, B. (1999). Thermally reversing window and stiffness transitions in chalcogenide glasses. *Solid State Comm.* 111, 619–624. doi: 10.1016/S0038-1098(99)00248-3

Shpotyuk, O., and Golovchak, R. (2011). Pseudo-self-organized topological phases in glassy selenides for IR photonics. *Phys. Status Solidi C* 8:2572. doi: 10.1002/pssc.201084136

Shpotyuk, O., Hyla, M., Boyko, V., and Golovchak, R. (2008). Reversibility windows in selenide-based chalcogenide glasses. *Phys. B.* 403, 3830–3837. doi: 10.1016/j.physb.2008.07.024

Thorpe, M. F. (1983). Continuous deformations in random networks. *J. Non Crystal. Solids* 57, 355–370. doi: 10.1016/0022-3093(83)90424-6

Thorpe, M. F., Jacobs, D. J., Chubynsky, M. V., and Phillips, J. C. (2000). Self-organization in network glasses. Part II. Chalcogenide and organic semiconductors. *J. Non Crystal. Solids* 266–269, 859–866. doi: 10.1016/S0022-3093(99)00856-X

Vaills, Y., Qu, T., Micoulaut, M. , Chaimbault, F., and Boolchand, P. (2005). Direct evidence of rigidity loss and self-organization in silicate glasses. *J. Phys. Condensed Mat.* 17, 4889–4896. doi: 10.1088/0953-8984/17/32/003

Wang, Y., Wells, J., Georgieve, D. G. , and Boolchand, P. (2001). Sharp rigid to floppy phase transition induced by dangling ends in a network glass. *Phys. Rev. Lett.* 87:185503. doi: 10.1103/PhysRevLett.87.185503

Zhao, H. Y., Koh, Y. P., Pyda, M., Sen, S., and Simon, S. L. (2013). The kinetics of the glass transition and physical aging in germanium selenide glasses. *J. Non Crystal. Solids* 368, 63–70. doi: 10.1016/j.jnoncrysol.2013.02.025

Conflict of Interest Statement: The authors declare that the research was conducted in the absence of any commercial or financial relationships that could be construed as a potential conflict of interest.

frontiers in Materials

ORIGINAL RESEARCH
published: 14 May 2019
doi: 10.3389/fmats.2019.00069

Linking Melt Dynamics With Topological Phases and Molecular Structure of Sodium Phosphate Glasses From Calorimetry, Raman Scattering, and Infrared Reflectance

*Chandi Mohanty[1], Avik Mandal[2], Vamshi Kiran Gogi[2], Ping Chen[2], Deassy Novita[2], Ralph Chbeir[2], Mathieu Bauchy[3], Matthieu Micoulaut[4] and Punit Boolchand[2]**

[1] Department of Mechanical and Materials Engineering, University of Cincinnati, Cincinnati, OH, United States, [2] Department of Electrical Engineering and Computer Science, University of Cincinnati, Cincinnati, OH, United States, [3] Physics of AmoRphous and Inorganic Solids Laboratory (PARISlab), Department of Civil and Environmental Engineering, University of California, Los Angeles, Los Angeles, CA, United States, [4] Sorbonne Université, CNRS, Laboratoire de Physique Théorique de la Matière Condensée, Paris, France

OPEN ACCESS

Edited by:
Jincheng Du,
University of North Texas,
United States

Reviewed by:
William LaCourse,
Alfred University, United States
Stefan Karlsson,
RISE Research Institutes of Sweden,
Sweden

***Correspondence:**
Punit Boolchand
boolchp@ucmail.uc.edu

Specialty section:
This article was submitted to Glass Science, a section of the journal Frontiers in Materials

Received: 21 February 2019
Accepted: 01 April 2019
Published: 14 May 2019

Citation:
Mohanty C, Mandal A, Gogi VK, Chen P, Novita D, Chbeir R, Bauchy M, Micoulaut M and Boolchand P (2019) Linking Melt Dynamics With Topological Phases and Molecular Structure of Sodium Phosphate Glasses From Calorimetry, Raman Scattering, and Infrared Reflectance. Front. Mater. 6:69. doi: 10.3389/fmats.2019.00069

Scores of especially dry and homogeneous $(Na_2O)_x(P_2O_5)_{100-x}$ glass compositions over a wide range, $0 < x < 61\%$, are synthesized and examined in modulated Differential Scanning Calorimetry (m-DSC) , Raman scattering, infrared reflectance, and molar volume experiments. The glass transition temperature variation, $T_g(x)$, displays three regimes; at low x ($0 < x < 15\%$), Na serves to produce non-bridging oxygens as T_gs decrease. At higher x, $15\% < x < 50\%$, Na continues to serve as a network modifier, but now chains of Q^2 species steadily grow and $T_g(x)$ increases. In this regime, we observe a square-well-like, thermally reversing window, bordered by abrupt rigidity transition near $x_r = 37.5\%$ and stress transition near $x_s = 46.0\%$ defining the intermediate phase (IP). The rigidity transition near $x_r = 37.5\%$ occurs near the percolation of rigidity predicted by the coarse graining model. Variations of melt fragility index, m(x), established from complex C_p measurements show m(x =0) to be 15(1) and to increase monotonically with x to display a square-well-like fragility window ($m < 20$) in the $37.5(3)\% < x < 46.0(2)\%$ range, a range which coincides with the reversibility window. These results show that melt dynamics encode glass topological phases. At still higher x (>50%), $T_g(x)$ mildly decreases with increasing x, as pyrophosphate units decouple from the backbone and glasses segregate. Raman scattering measurements show that the fraction of the local structural species $f(Q^3(x))$, $f(Q^2(x))$, and $f(Q^1(x))$ tracks the mean-field behavior based on glass stoichiometry (x), as noted earlier from ^{31}P Nuclear Magnetic Resonance (NMR) experiments. Raman scattering also shows that the Q^2 structural species always display a triad of modes, a majority mode and two satellite modes, that serve as topological defects. For the two highest frequency optic modes, infrared specular reflectance measurements show that the frequency difference between the longitudinal optic (LO) and transverse optic (TO)

response displays a global minimum in the IP. The local minimum of molar volumes, a global minimum in the LO–TO mode splitting, a fragility window that coincides with the reversibility window, each observation provides persuasive evidence of the singular role of the IP in present glasses.

Keywords: raman scattering, modulated Differential Scanning Calorimetry (m-DSC), topological phases, reversibility window, fragility window, volumetric window, infrared reflectance, intermediate phase

INTRODUCTION

Sodium phosphate glasses (SPGs) have been widely examined by a variety of probes including neutron scattering (Hoppe et al., 1996; Suzuya et al., 1998; Brow, 2000), ^{31}P NMR (Brow et al., 1994, 1995, 2017; Alam and Brow, 1998; Brow, 2000; Click et al., 2002), X-ray photo electron spectroscopy (Gresch et al., 1979; Sammet et al., 1980), calorimetric experiments (Brow et al., 1994; Hudgens, 1994), Raman scattering (Hudgens, 1994; Hudgens et al., 1998; Brow, 2000), IR reflectance (Hudgens and Martin, 1993; Hudgens, 1994; Moustafa and El-Egili, 1998), and dynamic light scattering experiments (Fabian and Sidebottom, 2009). The base oxide, P_2O_5, is composed of a network of P-centered quasi-tetrahedral units, O_t=P($O_{1/2}$)$_3$, that have three bridging and one non-bridging oxygen near neighbor, generally specified as a Q^3 species in the NMR notation. The base glass is unusual, extremely hygroscopic, and also isostatically rigid in having three chemical bonding constraints per atom. The T_g of the base glass is extremely sensitive to not only its preparation but also to its handling while sealing in an Al pan for a calorimetric experiment. T_gs can easily decrease from 430 to 397°C as the enthalpy of relaxation (ΔH_{nr}) builds up from 0.06(2) to 0.40(2) cal/gm if even traces of water are picked up if the Al pans are not dry or if the relative humidity of the ambient environment in which samples are handled is not <0.01%. Water doping converts a bridging oxygen site into a pair of dangling OH ends, lowering the global network connectivity that is reflected in a decrease of T_g, and an increase of ΔH_{nr} due to the opening of a new degree of freedom of glass relaxation. Alloying Na_2O in the base glass at first decreases the glass transition temperature T_g(x) up to 15 mole % of soda, but then increases it thereafter at higher x to display a maximum near x = 50 mole % of soda, corresponding to $NaPO_3$. The change in slope, dT_g/dx, from negative at low x (<15%) to positive at high x (>15%) underscores that the Na_2O additive serves as a network modifier both at low x and high x. Stoichiometric $NaPO_3$ glass is composed of long P-O-P-O-P chains in which P atoms are tetrahedrally coordinated to two bridging oxygens (O_b) in a chain and two terminal oxygens (O_t) that are charge compensated by a Na^+ cation, a Q^2 species in the NMR notation. The molecular structure of these ultraphosphate glasses, in the 0 < x < 50% composition range, has been broadly described (Brow, 2000) as composed of Q^2 and Q^3 species, with the fraction of Q^2 species, f(Q^2) monotonically growing at the expense of the Q^3 ones (f(Q^3)) as x increases to 50%. In the coarse graining model (Sidebottom and Schnell, 2013) of these glasses, one excludes counting dangling ends, and the Q^2 and Q^3 species then take on a two- and three-fold coordination. The mean coordination number <r> = 2.40, as x increases to 37.5% at the rigidity percolation transition (Thorpe et al., 2000).

We have synthesized especially dry and homogeneous SPGs in the 0 < x < 60% range of soda and examined them in m-DSC, Raman scattering, infrared reflectance, and molar volume measurements. The nature of the glass transition examined in m-DSC experiments reveals the non-reversing enthalpy of relaxation at T_g, ΔH_{nr}(x) and shows a square-well-like variation in the 37.5% < x < 46% range. The observation identifies the composition range with formation of isostatically rigid networks (Phillips, 1979), i.e., networks belonging to the intermediate phase (IP). The onset of the IP near 37.5% coincides closely with the prediction of the coarse graining model (Sidebottom and Schnell, 2013). The increase of T_g(x) in the 20% < x < 50% range suggests that glass compositions at x < 37.5% are in the flexible phase, while those at x > 46% are in the stressed rigid phase.

The increase in viscosity (η) of a glass-forming melt as its T is lowered to T_g to an astronomically high value near 10^{12} Pa.s results in a frozen solid or glass that supports shear (Debenedetti and Stillinger, 2001). In addition, one defines (Williams et al., 1955; Angell, 1988) the fragility index m as the slope d(Log η)/ d(T/T_g) as T approaches T_g. Upon cooling melts across T_g and examining the resulting glass transition exotherm in m-DSC experiments, one can establish m (Carpentier et al., 2003; Thomas, 2005a). In the present work, such experiments show a square-well-like minimum in m with m < 20 as a function of melt composition in the 37.5% < x < 46% compositional window. Thus, the window in fragility apparently *coincides* with the window across which T_g becomes thermally reversing. The finding leads us to the key central finding of the present work, *viz.*, there exists an *intimate linkage between melt fragility index and glass topological phases in the phosphates*. Parallel results were recently reported (Gunasekera et al., 2013a; Chakraborty and Boolchand, 2014) in several binary chalcogenides, underscoring that melt dynamics encode the topological phases of the resulting glasses.

In Raman scattering and IR reflectance experiments, one observes modes characteristic of the Q^3, Q^2, and Q^1 local structural species. Here, Q^n represents a P atom having n-bridging O near-neighbors in the NMR notation. The observed variation in mode frequency and mode scattering strength with glass composition reveals new insights into the structure evolution of glasses. The glass structure near x = 50% is dominated by long -O-P-O-P-O- chains (composed of Q^2 species) that form the extended range structure of the glasses also in the 35% < x < 60% range. In the chains characteristic of the glass, Q^2 species always display a triad of modes, a majority mode

and two lower-frequency satellite modes, henceforth labeled as a minority mode and a defect mode. Evidence shows that the local structures corresponding to the minority and defect modes, function as topological defects. They serve to relieve stress in the flexible and stressed rigid phases but are weakly populated in the stress-free IP. Raman scattering along with IR reflectance show that the highest frequency optic modes display an LO-TO mode frequency splitting (Galeener and Lucovsky, 1976) that displays a global minimum in the IP. Thus, many experimental observables in the calorimetric, Raman scattering, infrared reflectance, and volumetric measurements undertaken here display anomalies in the IP.

Finally we have put the present results on glass structure in context with earlier reports (Cormia et al., 1963; Angell and Rao, 1972; He and Thorpe, 1985; Martin and Angell, 1986; Wäsche and Brückner, 1986; Angell, 1990; Sales, 1990; Hudgens and Martin, 1993; Brow et al., 1994; Hudgens, 1994; Hoppe, 1996; Hudgens et al., 1998; Angell et al., 1999; Brow, 2000; Sidebottom and Changstrom, 2008; Fabian and Sidebottom, 2009; Gupta and Mauro, 2009; Mauro et al., 2009; Sidebottom and Schnell, 2013; Hermansen et al., 2014, 2015; Sidebottom, 2014; Sidebottom et al., 2014) on the subject. By synthesizing especially dry glasses, new insights into the physics of glasses have emerged, and these developments are likely to have important consequences on the applications of these materials.

MATERIALS AND METHODS

Synthesis of $(Na_2O)_x(P_2O_5)_{100-x}$ Glasses

Synthesis of P_2O_5 Glass

The base P_2O_5 starting material is extremely hygroscopic and requires rather special handling for the synthesis of the bulk glass. Fortunately, it sublimes at 340°C into a monomeric form and can be synthesized as a rather pure and dry bulk glass (Hudgens and Martin, 1993) as follows. The starting material in a powder form was transferred in a quartz tube in model HE-493/MO-5 Glove box from Vacuum Atmospheres, which is continuously flushed with dry N_2 gas and with a relative humidity of <0.01%. An assembly made of Swagelok valve connected to an 8-mm-diameter tube supporting connector was used to evacuate the quartz tubing. The quartz tubing was evacuated using a high-vacuum pumping system with a liquid nitrogen trapped diffusion pump. The quartz tube was then gently heated to 340°C, and a deposit sublimed on the cold end of a long quartz tube while pumping on it. Next, the quartz tube was sealed off, and the bulk glass was realized by heating the sublimed P_2O_5 to 350°C and water quenched. Since the thermal expansion of the glass and quartz differs, water quenching leads to a fracture of the quartz tube a few minutes after the water quench. Bulk glass shards are collected and immediately transferred into the glove box. TA Instruments T_{zero} pans that could be hermetically sealed were dried by gently heating to 80°C in a quartz tube while being pumped on by a high-vacuum line overnight and transferred into the glove box. Pans and lids were paired and weighed with a digital balance placed in the glove box. A 10- to 15-mg quantity of the bulk glass was transferred in the pans and hermetically sealed and weighed. This process was repeated several times, and in each synthesis, several bulk glass specimens were synthesized and examined in the m-DSC experiments. The T_g, enthalpy of relaxation, and fragility index of these glasses were measured, and these results are presented in section Calorimetric Results on T_g, ΔH_{nr}, and m.

Synthesis of Bulk $(Na_2O)_x(P_2O_5)_{100-x}$ Glasses in the 20% < x < 61% Range of Soda

Stoichiometric sodium metaphosphate glass, $NaPO_3$, corresponding to x = 50%, was synthesized by heating finely crushed and intimately mixed Na_2CO_3 and P_2O_5 powders as starting materials. In each case, the batch size was kept at 2 g. Two synthesis procedures were employed. **Sample A** was obtained by mixing the fine powders in a Pt crucible for 5 min using a spatula in the glove box. **Sample B** was synthesized by mixing the starting materials in an agate mortar and pestle for about 25 min, and the mixture was transferred to a Pt crucible with a lid in the glove box. Mixtures were then placed in a box furnace at 120°C and heated to 420°C to decarbonize the precursor and taken to 700°C for 2 h, and then to 900°C for 30 min, and the melt was poured over a steel plate to realize the bulk glass. The glass was immediately transferred to the glove box. The stoichiometric glass was crystallized by heating to 420°C, and a powder X-ray diffraction scan confirmed the crystalline phase formed to be indexed on an orthorhombic structure (JCPDS file 011-0648). Micro-Raman scattering results show that while glass **samples A** were heterogeneous, glass **samples B** were homogeneous (Mohanty, 2018) as will be noted in the segment on Results. Although a full range of glass **sample A** compositions were synthesized and their calorimetric properties measured (Mohanty, 2018), in the present work, we will largely report results on the homogeneous glass **samples B.**

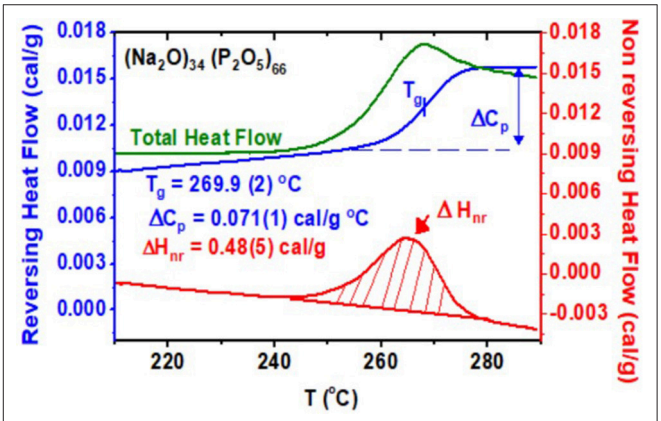

FIGURE 1 | m-DSC scan of a $(Na_2O)_x(P_2O_5)_{100-x}$ glass at x = 34% showing the total (green), reversing (blue), and non-reversing (red) heat flow terms in the heating cycle. The T_g deduced from the inflection point of the reversing heat flow is 269.9(2)°C. The non-reversing enthalpy at T_g deduced after a frequency correction is 0.48(5) cal/gm. The cooling cycle heat flow scans are not shown.

We repeated the processing described above at the metaphosphate composition by extending synthesis to lower values of x, but with some changes; we reduced the alloying temperature from 700 to 600°C as x was lowered from 50 to 20%. This was necessary to avoid loss of P_2O_5 as it was alloyed with Na_2O at lower x (<40%). Glass stoichiometry "x" was independently established by energy dispersive analysis X-ray (EDAX) measurements (Goldstein et al., 2003; Mohanty, 2018), and these values of x were used to define the stoichiometry of glasses. The EDAX-deduced compositions showed a steadily higher soda content than the one based on weighed ones as x decreased in the 30% > x > 20% range. At x > 50%, homogeneous bulk glasses were realized in the 50% < x < 61% range following the processing used at x = 50%. At x > 61%, quenched glasses were found partially crystalline. Micro-Raman scattering measurements, taken at a 1-μm spatial resolution, revealed regions that showed narrow vibrational features characteristic of a partially crystalline sample and broad bands characteristic of a glass. Thus, only results on the fully glassy range at x < 61% will be presented here.

Glass Transition Temperature T_g, Enthalpy of Relaxation of Glasses at T_g (ΔH_{nr}), and Melt Fragility Index (m) From m-DSC

Glass transition endotherms were analyzed by m-DSC in one of two methods. In one method, the endotherm is analyzed in terms of the reversing and non-reversing heat flow terms (Thomas, 2005b). This method was used to establish the T_g and ΔH_{nr}. In the second method, one analyzes the endotherm in terms of the complex specific heat (C_p) with in-phase part, C_p^{ip}, akin to the reversing heat flow, while the out-of-phase part, C_p^{op}, akin to the non-reversing heat flow. The second method lends itself well to establish the fragility index of melts.

All bulk glass samples were examined using a model Q2000 m-DSC from TA Instruments Inc. In a typical measurement, about 10–15 mg of the glass was sealed in T_{zero} pans of the hermetically sealed type. All Al pans and lids were first dried by pumping for at least a day or longer in a vacuum oven held at 80°C. All glass samples were sealed in Al pans in a dry nitrogen ambient environment using the vacuum atmospheres glove box.

Glass Transition Temperature T_g and Enthalpy of Relaxation at T_g, ΔH_{nr}

The typical operating parameters were as follows: scan rate: 3°C/min, modulation amplitude: ±1°C, modulation time: 100 s. The calorimeter was calibrated using indium metal T-calibration, sapphire C_p calibration. In each case, a melt-quenched bulk glass was first rejuvenated by heating past T_g and cooled back to the starting temperature to dissipate stress frozen upon a thermal quench of the melt. Next, a second heating scan initiated to establish the total heat flow, the "reversing" and "non-reversing" heat flow. Next, a cooling cycle followed to establish the frequency-corrected non-reversing heat flow term, $\Delta H_{nr}(x)$, as described elsewhere (Thomas, 2005b; Dash et al., 2017). In **Figure 1**, we show an actual scan of a glass at x = 34%, and find a T_g of 269.9(5)°C, as the average value of the inflection point of the reversing heat flow signal in the heating and cooling cycles. The frequency-corrected non-reversing heat flow $\Delta H_{nr}(x)$ is found to be 0.48(5)cal/gm. Such experiments were systematically undertaken at several glass compositions x to establish trends in $T_g(x)$, $\Delta C_p(x)$, and $\Delta H_{nr}(x)$. Results are presented in section Results.

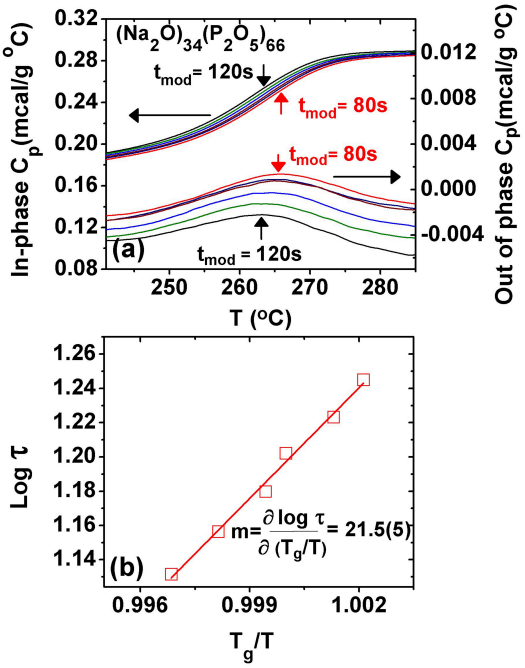

FIGURE 2 | (a) Observed variation of the in-phase C_p^{ip} and the out-of-phase C_p^{op} specific heat as a function of modulation frequency. Note that as the frequency increases, the peak in C_p^{op} shifts to higher temperatures as the glass must relax faster so $\omega\tau = 1$. **(b)** A plot of the enthalpic relaxation time τ as a function of T/T_g displaying an Arrhenius variation, with a slope that fixes the fragility index m = 21.5(5). T_g is determined from the inflection point of the C_p^{ip} at a modulation time period of 100 s.

Melt Fragility Index (m) and Activation Energy (E_A) for Enthalpy Relaxation

Upon cooling a melt past the glass transition, an exotherm is manifested, which can be analyzed in terms of a complex C_p formalism: an in-phase-specific heat, C_p^{ip}, that shows a step-like feature akin to the reversing heat flow, and an out- of-phase specific heat, C_p^{op}, which shows a Gaussian-like peak. In these experiments, one tracks the shift of C_p^{op} peak as the modulation frequency is systematically changed (Bustin and Descamps, 1999; Carpentier et al., 2003), and one establishes the melt fragility index, m, as illustrated next with an example at the composition x = 34% in the present SPGs (**Figure 2**).

These results were obtained as a function of modulation time period t_m in the range 60 s < t_m < 120 s as the melt T is lowered from 285 to 235°C. One finds that the step in C_p^{ip} steadily shifts to higher T as the modulation frequency $\omega = 2\pi/t_m$ is increased. On the other hand, C_p^{op} displays a peak that steadily shifts to

higher T as ω increases. At the peak location, the glass enthalpic relaxation tracks the programmed modulated T-profile, i.e., $\omega\tau = 1$. By establishing the peak location, one fixes the enthalpic relaxation time τ at a given modulation frequency (ω), and from the abscissa of the C_p^{op}, the T at which that enthalpic relaxation time τ was realized. By plotting log of τ as a function of T_g/T (**Figure 2b**), one obtains the fragility index (Böhmer et al., 1993; Bhosle et al., 2012b).

$$m = \left[\frac{d\log(\tau)}{dT_g/T}\right]_{T\to T_g} \quad (1)$$

Given the fragility index m, one then obtains the activation energy E_A for enthalpic relaxation using the following relation (Gunasekera et al., 2013a),

$$E_A = m.T_g.\ln(10) \quad (2)$$

Traditionally melt fragility index of glasses has been measured in DSC experiments following the method introduced by Moynihan et al. (1974). The scan rate ("q") dependence of T_g is measured, and one expects a linear variation of ln "q" against $1/T_g$. We performed such experiments on **samples of set B** with the scan rate varied in the range 5°C/min < q < to 30°C/min. In the present modified oxides, we could not observe a unique slope $d(\ln q)/d(1/T_g)$ over the range of q used. The variation was found to be non-linear and displayed a continuously variable slope with a high slope at low scan rates (q < 10°/min) but a low slope at high scan rates (20°C < q < 30°C), and with the high slope nearly twice that of the low slope in all the samples examined (Mohanty, 2018). On the other hand, the complex C_p approach using m-DSC yielded quite reproducible melt fragility index results that varied systematically with glass composition x, as described in the present work.

Raman Scattering

We used a model T64000 Dispersive Raman system from Horiba Jobin Yvon Inc, with a microscope attachment, and 514.5-nm excitation from an Argon ion laser to excite Raman scattering from bulk SPGs. All spectra were least-squares fit in terms of Voight lineshapes using the Peakfit Software, and keeping the Lorentzian/Gaussian mix fixed at 57%/43%.

As an example of a Raman scattering measurement, we compare in **Figure 3** the observed lineshape of crystalline (Exarhos and Risen, 1974) $NaPO_3$ with its bulk glass counterpart. These spectra show remarkable similarities: features 1, 2, and 3 characteristic of the long P-O-P-O-P chains (Brow et al., 1994, 2017; Hudgens et al., 1998; Brow, 2000) are present in both the crystal and the glass. The prominent **feature 1** near 1,166 cm^{-1}, ascribed to the symmetric stretch mode of $P\text{-}O_t$ bonds in a Q^2-like species (Brow et al., 1994; Hudgens, 1994; Hudgens et al., 1998; Click et al., 2002; Novita and Boolchand, 2007, 3), is observed in both the glass and the crystal. The mode is extremely narrow (Full Width at Half Maximum (FWHM) = 4.6 cm^{-1}) in the crystal but is much broader in the glass (FWHM = 14.1 cm^{-1}). In the two panels below, we highlight the observed lineshape of **Feature 1** in glass **sample A** with the one in glass **sample B** profiled across the glass specimen.

A perusal of the observed lineshapes shows the 1,167 cm^{-1} mode frequency in **sample A** (lower left) is found to shift by as much as 2.0 cm^{-1} as one moves from spot 1 to 4 in the micro-Raman experiments. Furthermore, at spot 1, the lineshape shows evidence of the 1,012 cm^{-1} mode ascribed to Q^1-like species (Brow et al., 1995; Velli et al., 2005) being formed, a feature expected only at x > 50.0%. On the other hand, the Raman spectrum of glass **sample B** shows the mode frequency of the Q^2 species to be steady at 1,167.0(2) cm^{-1} with a variance of <0.3 cm^{-1} as the sample was profiled at five spots. The spots were typically separated by 2 to 3 mm. These spectra illustrate that while **sample A** was heterogeneous, **sample B** was homogenous. Details of synthesis are presented in section Synthesis of $(Na_2O)_x(P_2O_5)_{100-x}$ Glasses.

Infrared Reflectance

An FTIR Model Nexus 870 from Thermo-Nicolet Inc. with a Seagull accessory for specular reflectance studies from bulk glasses was used. The system was set up for mid-IR response (400–6,000 cm^{-1}) using a DTGS detector with KBr window and KBr beam splitter. In a typical measurement, 200 scans were recorded at 4-cm^{-1} resolution. The system as well as glass samples were thoroughly purged with dry air circulating inside the Seagull chamber to flush traces of water on the surface of platelet-like samples. A polished stainless-steel flat disc was used as a reference to normalize the reflected light. The normalized reflectance was then Kramers–Kronig transformed (Galeener et al., 1983) to obtain absorbance, transverse optic (TO), and longitudinal optic (LO) response using Grams 32 software.

Molar Volumes

Molar volumes of bulk glasses were deduced from mass density using the Archimedes' principle. A 125-mg glass sample or larger was weighed in air and in 200 proof alcohol using a quartz fiber suspended from a digital balance with a resolution of 0.1 mg. To calibrate the density of 200 proof alcohol, a Si single crystal wafer of known density ($\rho_{Si} = 2.33$ g/cm^3) was used. To ascertain the accuracy and reproducibility of the method, the density of a single crystal of Ge was measured and found to be 5.322(6)/cm^3, which may be compared to the known standard value of 5.323 g/cm^3. With glass samples weights exceeding 125 mg, the density could be measured to an accuracy of 0.25%.

RESULTS

Calorimetric Results on T_g, ΔH_{nr}, and m

We begin by presenting results for the base P_2O_5 glass corresponding to x = 0. Next, we present calorimetric results on the **SPGs** in the 20% < x < 60% range.

T_g, ΔH_{nr}, and ΔC_p of Base P_2O_5 Glass

Following the synthesis of the base P_2O_5 glass described in section Materials and Methods, at least 10 different glass samples were examined in m-DSC experiments to establish trends in T_g, ΔH_{nr}, and ΔC_p. An m-DSC scan of one of the driest P_2O_5 glass with a $T_g = 430$°C is shown in **Figure 5A**. A summary of the m-DSC results on all other samples is given in **Figure 5B** as a

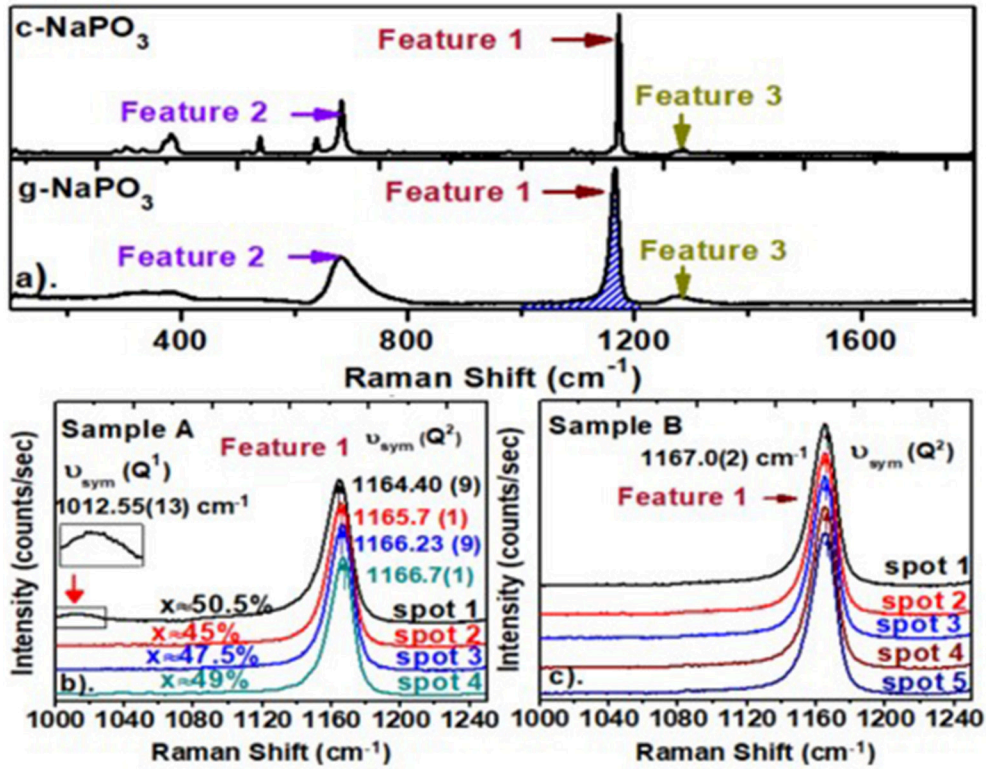

FIGURE 3 | (a) Raman scattering in c-$NaPO_3$ compared to the one in g- $NaPO_3$. In the two panels below **(a)**, we compare the micro-Raman profiling of feature 1 in a glass from **sample A (b)** with the one of a glass **sample B (c)**. The results show the variance in x for **sample A** is 5.5%, but the variance in x for **sample B** is vanishing. In **(b)**, note that the Q^1-related mode near 1,012 cm^{-1} is observed at spot 1, showing the composition to be x = 50.5%. Global variation of feature 1 mode-width and mode-frequency of **sample B** appear in **Figure 7A**. Details of the glass synthesis appear in section Synthesis of $(Na_2O)_x(P_2O_5)_{100-x}$ glasses.

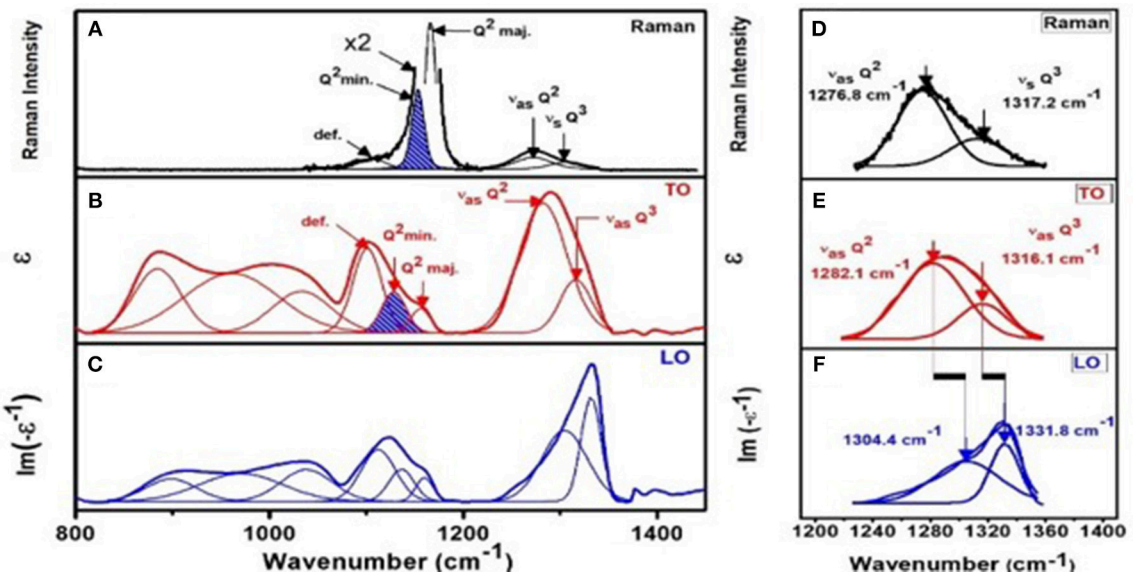

FIGURE 4 | Correlating **(A)** Raman scattering with **(B)** IR TO response (ε) and **(C)** IR LO response [Im (-1/ε)] for $NaPO_3$ glass. Note that the two minority modes (Q^2 min. mode and def. mode) associated with the majority mode near 1,166 cm^{-1} mode are weakly excited in Raman scattering but strongly in IR response **(B,C)**. Please note we have enhanced the two minority modes by a factor of 2 in plotting the data to make these features visible in **(A)**. **(D)** shows a blow up of the two high frequency optic modes from **(A)** while **(E)** and **(F)** give the same two optic modes from **(B)** and **(C)** respectively. Note, one observes an LO-TO splitting associated with the two highest frequency optic modes, Q^2 asymmetric and Q^3 asymmetric as shown in **(E)** and **(F)**.

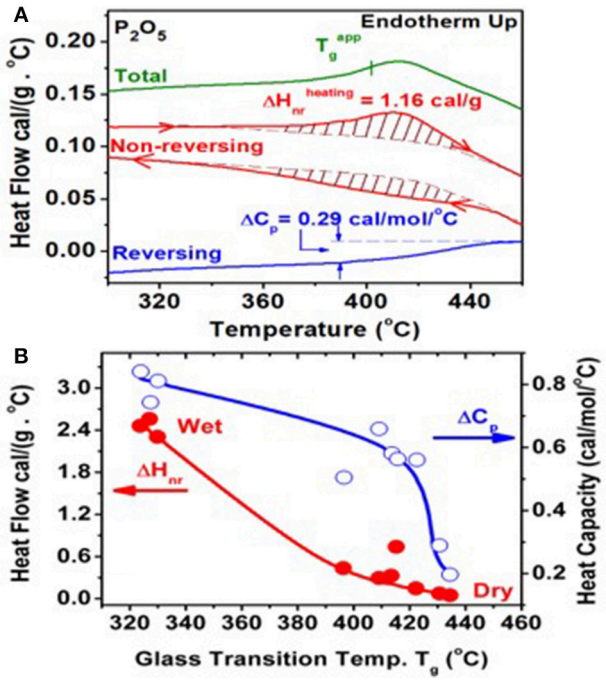

FIGURE 5 | (A) An m-DSC scan of one of the driest P_2O_5 glass synthesized. The total, reversing, and non-reversing heat flows in the heating up cycles are displayed **(B)**. A plot of ΔH_{nr} on the left ordinate as a function of T_g, and ΔC_p on the right ordinate as a function of T_g for the 10 samples measured. The glass sample with the highest T_g of 435(2)°C is identified with dry P_2O_5 glass. This particular glass sample has a vanishing $\Delta H_{nr} \sim 0$, consistent with its isostatically rigid nature.

plot of ΔH_{nr} on the left ordinate as a function of T_g, and ΔC_p on the right ordinate as a function of T_g. Because of the extreme hygroscopicity of the glass, these 10 different glass preparations had apparently varying water impurity content. The presence of water impurity doping leads to the conversion of bridging O into NBO (Walter et al., 1997; Brow, 2000), lowering the global network connectivity, which is reflected in an increase of ΔH_{nr} and a decrease of T_g. Thus, we identify the T_g of dry P_2O_5 glass at 435°C and associate the vanishing $\Delta H_{nr} \sim 0$ with such a sample. The vanishing of ΔH_{nr} is fully consistent with the isostatic nature (Georgiev and Boolchand, 2000) of the quasi-tetrahedral local structure, which contributes three constraints per atom. Our results also show that ΔC_p systematically decreases as glass samples get drier.

T_g, ΔH_{nr}, and ΔC_p of Ultra- and Pyrophosphate Glasses

m-DSC results on bulk $(Na_2O)_x(P_2O_5)_{100-x}$ glasses (**SPGs**) in the 20% < x < 60% range are summarized in **Figure 6**. The three panels (**Figures 6A–C**) plot glass compositional trends in $T_g(x)$, ΔH_{nr} (x), and $\Delta C_p(x)$, respectively. The $T_g(x)$ trends are suggestive that glass structure evolution displays three distinct regions: **I**, **II**, and **III.** In **region I**, 0% < x < 15%, $T_g(x)$ decrease at a rate of near 20°C/mole of Na_2O suggests that Na^+ ions serve to convert BO into NBO, thus lowering the global connectivity of the network that is reflected in the decrease of T_g. This requires that in a P-centered quasi-tetrahedral local structure of P_2O_5 base glass, Na^+ ions bond only to one of the three available BO sites (Wazer, 1958). Remarkably, the slope dT_g/dx of 20.0°C/mole % of Na_2O observed in the experiments is almost identical to the value Micoulaut (1998) predicted if one of the three BO were to be replaced by a NBO, thus lowering the network connectivity as we discuss later. In **region II**, 15% < x < 50%, increase of $T_g(x)$ with x suggests broadly that the Na_2O additive now serves to increase network cohesion as Na^+ ions donate a −ve charge to the P-centered tetrahedra, leading to the two double-bonded terminal (O_t) bonds and two bridging oxygen bonds facilitating growth of the Q^2 species (Wazer, 1958; Brow et al., 1994, 2017; Alam and Brow, 1998; Brow, 2000). In **region III**, 50% < x < 60%, one finds $T_g(x)$ to mildly decrease with x, with a clear evidence of a kink near x = 50%. In **region III**, the network is steadily fragmented as pyro-phosphate dimers form, by the conversion of Q^2 species into a pair of Q^1 species by uptake of 2 Na^+ ions, and as the backbone steadily decouples (Brow et al., 1995; Alam and Brow, 1998; Velli et al., 2005).

Most remarkable are the trends in $\Delta H_{nr}(x)$ (**Figure 6B**) that steadily increase in the 0 < x < 37.5% range to show a square-well-like local minimum in the 37.5(3)% < x < 46.0(2)% range, and then continue to increase in the 46.0% < x < 50.0% range, and to finally decrease in region III, 50% < x < 60% for the pyro-phosphates. We also examined the aging effect of the enthalpy of relaxation $\Delta H_{nr}(x)$ term (Tonchev and Kasap, 2002; Chakravarty, 2003; Micoulaut, 2016) in the 37.5(3)% < x < 46.0(2)% range by heating the glasses at 100°C for a week and found the term to age (black filled data points) for compositions outside but not inside the IP. The square-well-like shape and the absence of any measurable aging in that window are features that are characteristic of the reversibility window (Boolchand, 2006), as we discuss in section Fragmentation of Q^2 Bearing Chains by Q^1 Dimers in the Pyrophosphates (50% < x < 60%). An interesting aspect of the reversibility window is that it sits on a finite background of $\Delta H_{nr} = 0.50$ cal/gm. In fact, the background term progressively increases almost monotonically in the 0.05 cal/gm < ΔH_{nr} < 0.50 cal/gm range as the glass composition increases in the 0 < x < 37.5% range.

In the less homogenous glass **samples A** (Mohanty, 2018), we also observed a reversibility window. But in sharp contrast to the abrupt and square-well like nature of the window seen in **samples B**, the window in **samples A** was narrower and Gaussian like. It appears that the litmus test of ideally homogeneous samples is the observation of a square-well-like reversibility window, wherein one has an abrupt rigidity- and stress-elastic phase transitions (Jacobs and Thorpe, 1995).

Fragility Index of P_2O_5, Ultra-, and Pyro-sodium Phosphate Glasses

In section Glass Transition Temperature T_g, Enthalpy of Relaxation of Glasses at T_g (ΔH_{nr}), and Melt Fragility Index (m) From m-DSC, we outlined the procedure in which m-DSC can be used to deduce melt fragility index (m) and the activation energy for enthalpic relaxation (E_a). The compositional variations of these melt-related calorimetric observables are shown in

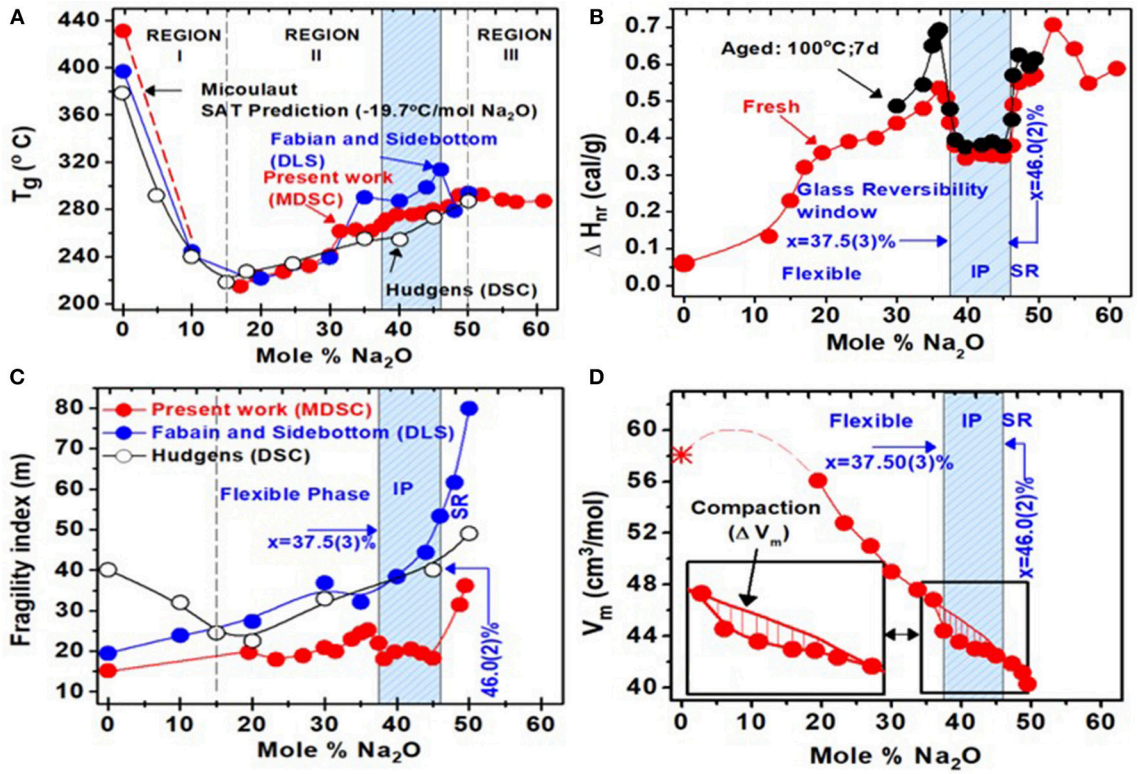

FIGURE 6 | Calorimetric results on sodium phosphate glasses obtained from present work and two earlier reports (Hudgens, 1994; Fabian and Sidebottom, 2009). Compositional trends in **(A)** $T_g(x)$ **(B)** in the non-reversing enthalpy of relaxation, $\Delta H_{nr}(x)$, **(C)** melt fragility index m(x), and **(D)** molar volumes $V_m(x)$. The light blue panel represents the glass composition range across which a glass reversibility window and a melt fragility window are observed, and it is identified with the isostatically rigid intermediate phase. Compositions at $x < 37.5(3)\%$ are in the flexible phase, while those at $x > 46.0(2)\%$ are in the stressed rigid phase. At $x > 50\%$, glasses steadily fragment with the decoupling of pyrophosphate units. In the intermediate phase, molar volumes show a local minimum consistent with the compacted nature of networks formed therein. The composition $x = 37.5\%$ represents the rigidity elastic phase transition in these glasses, and it coincides with the percolation of rigidity in the Sidebottom coarse graining model (D. L. Sidebottom and Schnell 2013) of these glasses.

Figure 6. The fragility index of the base P_2O_5 melt is near m = 15.0(5), and it is suggestive of a super-strong melt. Upon alloying soda, m progressively increases in the $0 < x < 37\%$ range, and then shows a square-well-like minimum in the $37.5(3)\% < x < 46.0(2)\%$ range. Note that in this square-well range, m acquires a value of <20, suggesting that melts formed in the well are super strong. The composition range $37.5(3)\% < x < 46.0\%$, in which melts acquire an $m < 20$, will henceforth be denoted as the **fragility window**. We also note that the compositional width of the **fragility window** in **Figure 6C** within experimental error coincides with that of the **reversibility window** in **Figure 6B**. This is not an accident as we shall discuss in section Discussion.

Raman Scattering

The similarity in Raman scattering of crystalline with glassy meta-phosphate (**Figure 3**) stems from features common to their molecular structures. In both cases, long chains of P-centered tetrahedral units having two bridging oxygen atoms (O_b) and two terminal oxygen atoms (O_t) comprise the local structure. In the glass, **feature 1** near 1,167 cm^{-1} represents a symmetric stretch of P-O_t bonds, **feature 2** near 760 cm^{-1} is a symmetric stretch of P-O_b bonds, while **feature 3** near 1,250 cm^{-1} is an asymmetric stretch of P–O_t bonds. The chains are infinitely long close to 10,000 tetrahedral units (Walsh et al., 1992; Brow, 2000) in the crystalline phase but are estimated to be about 400 tetrahedral units (Wazer, 1958; Bunker et al., 1984; Walsh et al., 1992; Brow, 2000) long in the glassy phase. But, there are also other striking differences in Raman scattering of the glass from that of the crystalline $NaPO_3$. In the crystal, one observes (**Figure 3**) a single optical phonon, with a frequency of 1,172 cm^{-1} with a rather narrow linewidth of 4.8 cm^{-1}. In g-$NaPO_3$, one observes a triad of modes (Velli et al., 2005; Novita and Boolchand, 2007): a majority mode near 1,167 cm^{-1}, and two satellite ones on the low-frequency side of the majority mode. One of these satellites is centered near 1,151 cm^{-1}, while the second one near 1,105 cm^{-1} (**Figure 7**).

The centroid of these satellite modes could be localized by Raman polarization measurements on g-$NaPO_3$ (**Figure 7B**). In **Figure 7B**, we show both the I_{VV} and I_{VH} scattering. In I_{VV} scattering, the E-field vector of the incident light and that of the scattered light are kept vertical. In I_{VH} scattering, the incident laser light E-field was vertical, but the scattered light E-field polarization was horizontal. In the I_{VH} configuration, one can clearly discern the majority mode from the two satellite modes

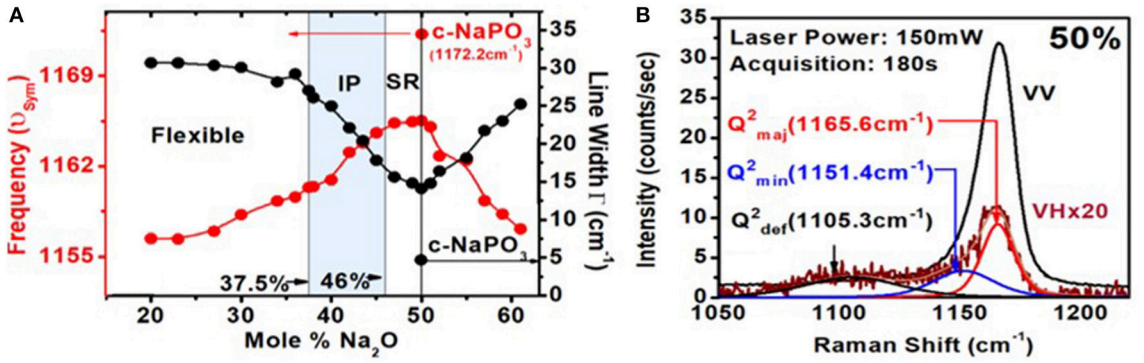

FIGURE 7 | (A) Variations in the Raman P–O_t symmetric stretch mode frequency and linewidth (FWHM) as a function of glass composition. **(B)** Raman polarization results on g-$NaPO_3$ showing both the I_{VV} and I_{VH} scattering of Q^2 species. Note that in the I_{VH} scattering, one observes two satellite modes on the low-frequency wing near 1,151 cm^{-1} and near 1,105 cm^{-1} of the majority mode near 1,166 cm^{-1}. The scattering strengths of the triad of modes associated with the Q^2 species vary with x in a rather systematic fashion (**Figure 10**).

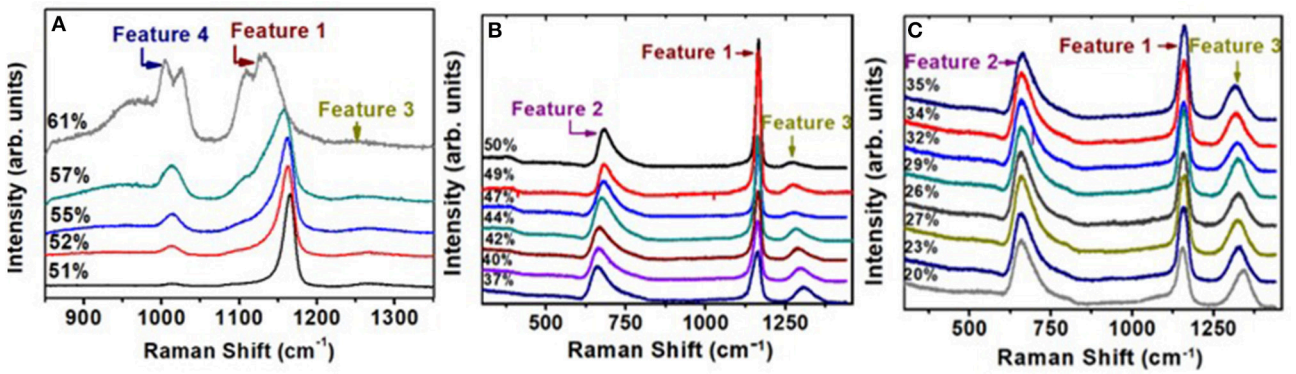

FIGURE 8 | Observed Raman scattering in $(Na_2O)_x(P_2O_5)_{100-x}$ glasses as a function of soda content "x." Spectra **(A)** are those in the pyrophosphate range, 50% < x < 61% range, while spectra **(B,C)** are those in the ultraphosphate range, 20% < x 50%. In the 40% < x < 45% range, we do not observe a shoulder near 1,200 cm^{-1} to the majority mode near 1,166 cm^{-1}, as noted by Hudgens et al. (1998) in their ultraphosphate glasses.

and localize the centroid of the latter two for detailed Raman lineshape analysis.

In **Figure 8**, we provide a global summary of the Raman scattering lineshapes observed in the glasses in the 20% < x < 60% range of soda. Examples of lineshape deconvolution of **feature 1** associated with the triad of modes related to Q^2 local structures (Velli et al., 2005; Novita and Boolchand, 2007) are included in **Figure 9**. The scattering strength and mode frequency variation as a function of glass composition for the triad of modes associated with Q^2 local structures are included in **Figure 10**. The triad of modes henceforth will be labeled as a majority mode, Q^2_{maj}, near 1,166 cm^{-1}, a minority mode, Q^2_{min}, near 1,151 cm^{-1}, and a broad mode that we believe is a defect mode, Q^2_{def}, near 1,105 cm^{-1}. The triad of modes are observed at non-stoichiometric glass compositions as well, and their scattering strengths and frequency change in a rather systematic fashion as a function of glass composition. In particular, one finds the minority mode, Q^2_{min}, shaded blue (**Figure 9**), to steadily increase in scattering strength as the soda content increases in the 47% < x < 50% range. In the ultraphosphate range, the minority and defect modes grow at the expense of the majority mode. There are features of the data that suggest that the minority and majority modes in the ultraphosphates are intrinsic to the Q^2 local structure in the glass, while the defect mode, Q^2_{def}, is most likely stabilized with the presence of an additional Na^+ cation in the vicinity of the Q^2 species. The minority and defect Q^2 site act, we suspect, functionally as topological defects in the ultraphosphates. Finally, in our Raman scattering experiments, we do not observe a high-frequency shoulder to the Q^2 majority mode near 1,200 cm^{-1} (**Figures 8**, **9**) that was noted by Hudgens (1994), in the 40% < x < 45% range of soda concentration. The shoulder mode was traced by Hudgens (1994) to the presence of strained tetrahedral units in their glass samples at room temperature.

We have also analyzed **features 3 and 4** as a super-position of requisite number of Voight lineshapes. In **Figures 11A–D**, we illustrate some examples of these fits. The observed variation of the scattering strength and mode frequency of Q^3 local

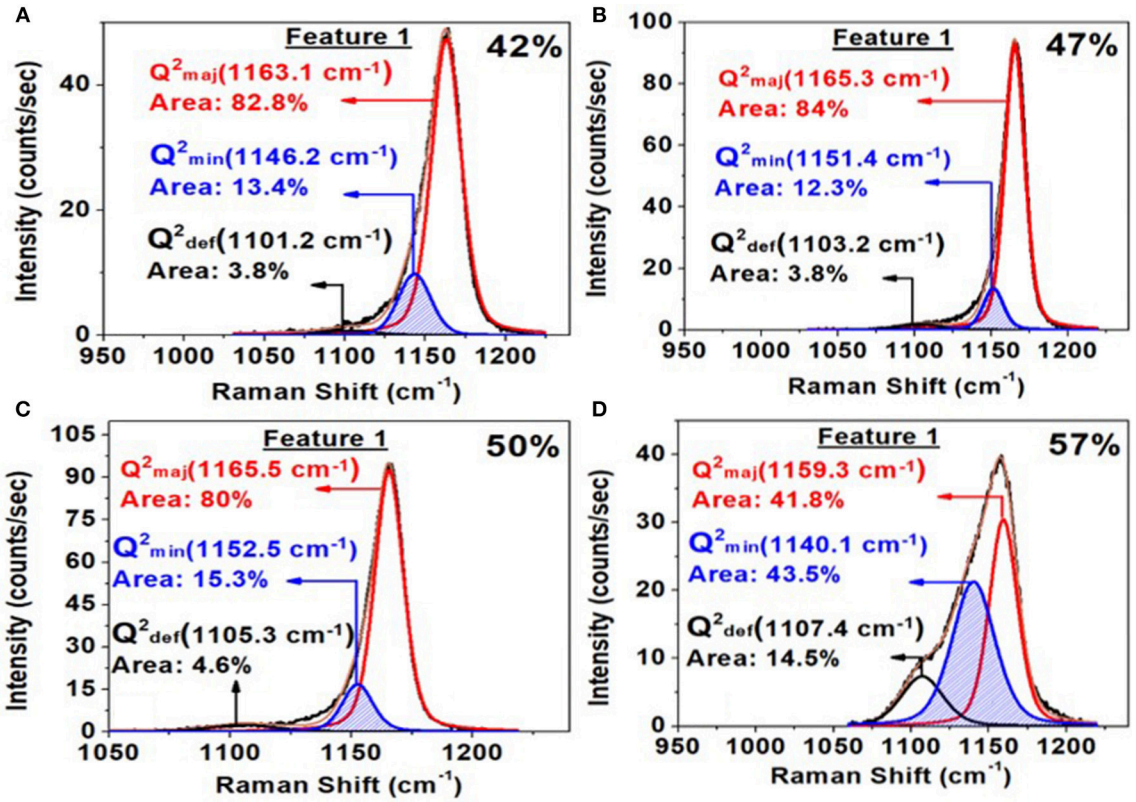

FIGURE 9 | Deconvolution of the triad of modes associated with feature 1 near 1,166 cm^{-1} observed in the Raman scattering at x = 42% in **(A)**; at x = 47% in **(B)**; at x = 50% in **(C)** and at x = 57% in **(D)**. Also noteworthy in these spectra is the complete absence of a shoulder near 1,200 cm^{-1} noted by Hudgens et al. (1998) in Raman scattering of their glass samples in the 40% < x < 45% range.

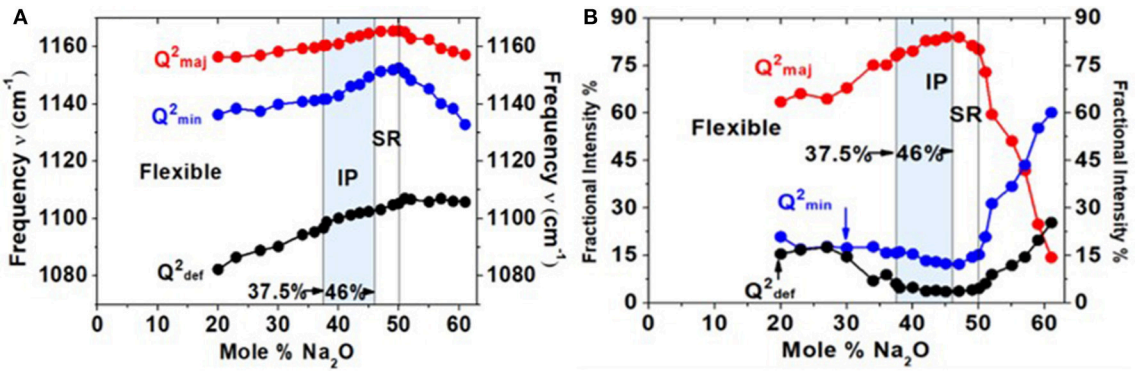

FIGURE 10 | (A) Mode frequency and **(B)** mode scattering strength variation of the triad of modes associated with the Q^2 local structure as a function of x. All modes blue-shift with glass composition in the 20% < x < 50% range. The scattering strength variation **(B)** shows that the majority mode (red dataset) increases in scattering strength with x; the minority mode (blue dataset) and defect band (black dataset) show a global minimum in the intermediate phase.

structure associated with **feature 3** can be observed in the results. In **Figures 11E–H**, we provide the lineshape deconvolution of **feature 4** associated with Q^1 local structure species, and here again, the results reveal a triad of modes (Tatsumisago et al., 1992): a majority mode, $Q^1_{maj,}$ near 1,014 cm^{-1}, a minority mode, Q^1_{min}, near 1,005 cm^{-1}, and a defect mode, Q^1_{def}, near 960 cm^{-1} displaying a rather broad band. With increasing soda content in the 50% < x < 60% range, we observe the minority and defect modes to grow at the expense of the majority mode. In addition to features 1, 2, and 3 visible in the ultraphosphates, we also have analyzed **feature 4** observed near 1,012 cm^{-1} associated with the Q^1 local structure in the pyrophosphate

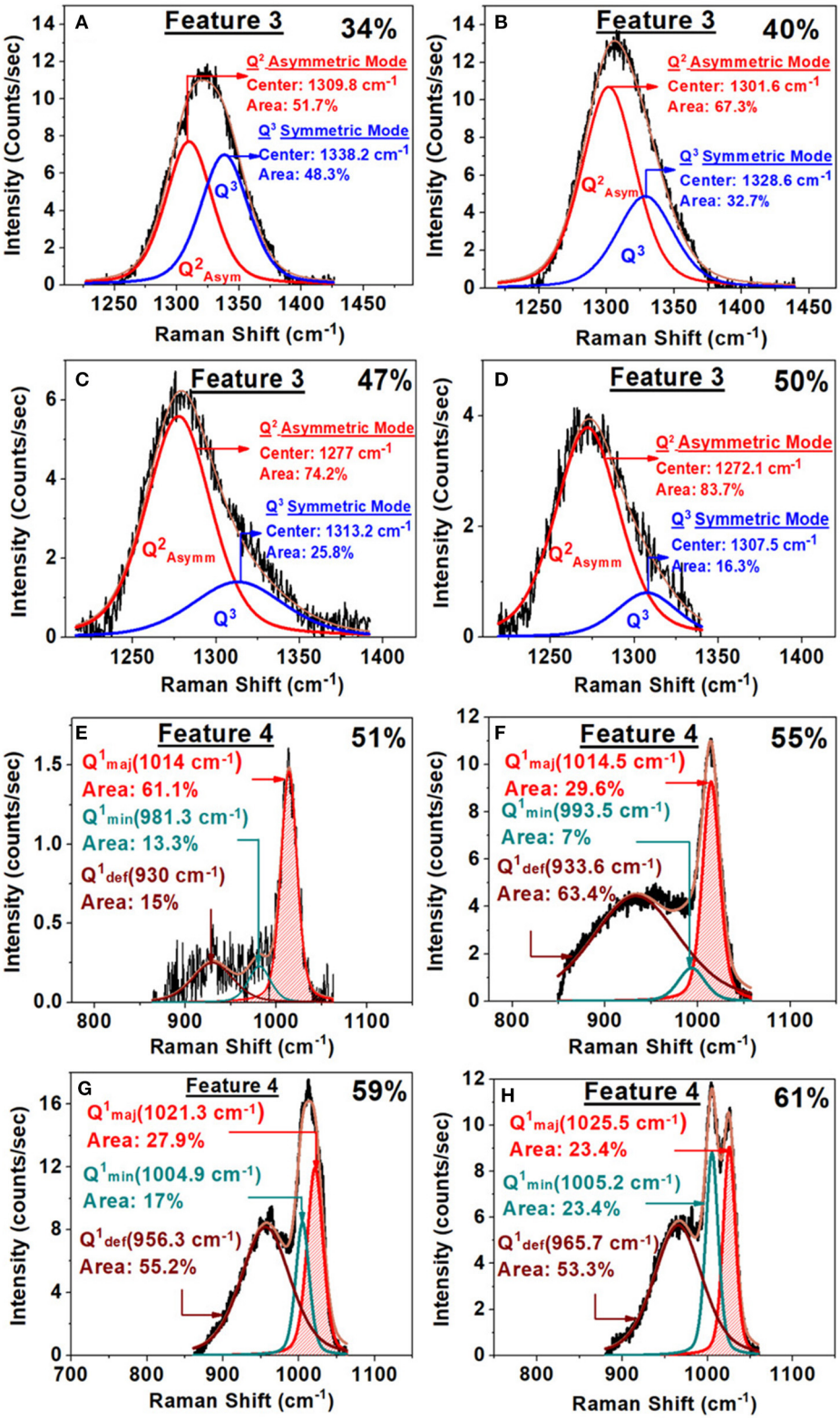

FIGURE 11 | (A–D) Examples of a Raman lineshape analysis of **feature 3** associated with the Q^3 local structure in SPGs with increasing x. Note that as x increases the Q^3 related vibrational mode scattering strength steadily decreases. **(E–H)** Examples of Raman lineshape **feature 4** deconvolution associated with the Q^1 local structure (mode near 1,012 cm^{-1}) in SPGs as a function of glass composition. Note that the scattering strength of the mode in question increases steadily with composition in the $50\% < x < 59\%$.

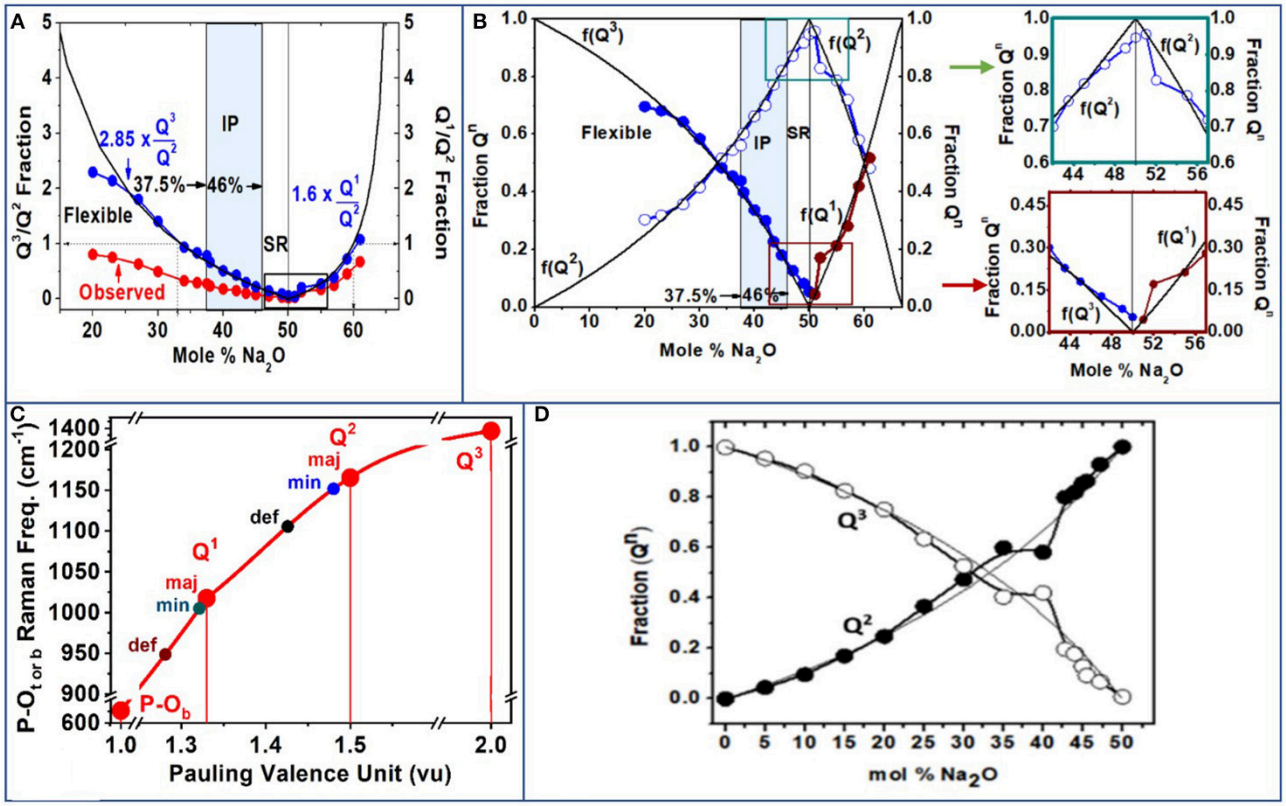

FIGURE 12 | (A) Observed Q^3/Q^2 fractions and Q^1/Q^2 fractions (red data points) obtained from Raman scattering **features 1, 3, and 4** (**Figures 8**, **9**, **11**). The blue data points are obtained after the Raman scattering strengths are corrected for Raman cross sections (see text). **(B)** The $f(Q^3)$ and $f(Q^2)$ and $f(Q^1)$ fractions are plotted as a function of x. The variations in the fractions $f(Q^3)$ and $f(Q^2)$ near x = 50% deviate measurably from the mean-field behavior as shown in the two insets of **(B)**. See text for details. **(C)** Raman P–O_t mode frequency for the Q^3 species and the triad of Q^2 and Q^1 species as a function of Pauling valence unit (PVU). For completeness, we include Raman P–O_b mode frequency with a PVU of 1. **(D)** Fractions of Q^2 and Q^3 species deduced from ^{31}P NMR results of Brow et al. (1994, 1995); Brow (2000).

glass compositions. These results are included in the plots of **Figure 11**.

A summary of the observed scattering strength ratio of Q^2 species-related modes (majority plus minority (**feature 1**) and Q^3 species-related mode (**feature 3**) is plotted in **Figure 12A** as the red filled data points in the 20% < x < 50% range. The scattering strength ratio of the Q^1 mode (majority plus minority) is displayed in **Figure 12A** as the red data points in the 50% < x < 61% range of composition. For the ultraphosphate compositions (**Figure 12A**), it became clear that the observed scattering strength ratio of Q^3/Q^2 fraction was low compared to the expected variation based on glass stoichiometry (thin black line in **Figure 12A**) considerations. This suggests that the Raman scattering cross sections of the two modes in question are different. By requiring that the observed Q^3/Q^2 fraction to equalize near x = 33.33%, as the glass stoichiometry requires, one finds that the Raman cross section for the Q^2 mode exceeds that of the symmetric stretch mode of Q^3 species by a factor of 2.85. The suggestion is qualitatively supported by Naval Research Laboratory Molecular Orbital Library (NRLMOL) calculations (Porezag and Pederson, 1996, 1999; Neugebauer et al., 2002; Park et al., 2006). The normalized Q^3/Q^2 fraction, plotted in **Figure 12A** as the blue data points, then becomes a good representation of the concentrations of the two species in the ultraphosphates.

The observed Q^1/Q^2 fraction, deduced by taking the scattering strength ratio of the sum of the majority and minority modes of Q^1 species and Q^2 species, respectively, (**Figures 9**, **11E–H**, **12A**), are plotted as the red data points in the pyrophosphate range of compositions, 50% < x < 61%. Here again we find that the observed scattering strength ratios are systematically lower than the expected $\mathbf{Q^1/Q^2}$ concentration ratio based on glass stoichiometry considerations. These results suggest that the Raman cross section of the Q^2 species exceeds that of the Q^1 species by a factor 1.60. The Raman cross-section ratio is deduced by requiring the concentration $f(Q^1)/f(Q^2) = 1$ at x = 60%, as required by stoichiometric considerations (Wazer, 1958; Brow, 2000).

From the normalized Q^3/Q^2 ratio, one could cast the results in terms of the individual fractions $f(Q^3)$ and $f(Q^2)$, since the sum of the two fractions must equal 1. Thus, $f(Q^2) = [1 + Q^3/Q^2]^{-1}$; $f(Q^3) = 1 - f(Q^2)$. For the pyrophosphates (x > 50%), by

establishing the normalized Q^1/Q^2 from the Raman experiments, we obtained $f(Q^2) = [1 + Q^1/Q^2]^{-1}$, and $f(Q^1) = 1 - f(Q^2)$.

The observed $f(Q^3)$, $f(Q^2)$, and $f(Q^1)$ fractions from the present Raman scattering (**Figure 12B**) broadly track the expected fractions (thin black lines in **Figure 12B**), based on glass stoichiometry considerations. In the ultraphosphates (Wazer, 1958; Brow, 2000), $0 < x < 50\%$ range, $f(Q^3) = (1 - 2x)/(1 - x)$, and $f(Q^2) = x/(1 - x)$. In the pyrophosphates (Wazer, 1958; Brow, 2000), $50\% < x < 66.6\%$, $f(Q^1) = (2x - 1)/(1 - x)$, and $f(Q^2) = (2 - 3x)/(1 - x)$. Nevertheless, there are deviations from the mean-field behavior that appear near $x = 50\%$. These deviations are small but finite and systematic (**Figure 12B** insets). For example, we find that the concentration of the Q^3 species does not go to zero at $x = 50\%$, but it does so closer to 52%. Furthermore, Q^2 species concentration never reaches its expected maximum value of 1.0 near $x = 50\%$. These deviations are due to the presence of the defect Q^2 and defect Q^1, local structures that are formed, and drain away some of the alloyed soda, leading to the scattering strength anomalies near $x = 50\%$.

A useful perspective on the local structures of the triad of Q^2 and Q^1 species observed in Raman scattering can be obtained by plotting the P–O_t or P–O_b stretch mode frequency as a function of Pauling valence unit (PVU; **Figure 12C**; Brow, 2000). For a Q^3 species, the PVU would be 2.0 since for the three BO bonds each possessing a PVU of 1 leaves the P=O_t bond with a PVU count of $5 - 3 = 2$, given the pentavalent nature of the P cation. For a Q^2 and a Q^1 species, one can show that the PVU would respectively be 1.50 and 1.33. We have included in the plot of **Figure 12C** the case of P–O_b stretch mode frequency since these bonds by definition have a PVU of 1.0. On the plot of **Figure 12C**, one can see a quasi-linear variation of the P=O_t or P–O_b mode frequency with the PVU. Both the majority and minority modes of Q^2 and Q^1 species have mode frequencies that are quite close to each other. On the other hand, the defect band shifts measurably to lower frequency and has a substantially larger width. We discuss this issue in section Discussion. For completeness, we include in **Figure 12D** the ^{31}P NMR results on the $f(Q^3)$ and $f(Q^2)$ fractions reported by Brow et al. (1994); Brow (2000) in the ultraphosphate glasses. The correlation between the NMR results and the Raman scattering is most encouraging.

Infrared Reflectance

Infrared as Probe of Water Traces in Sodium Phosphate Glasses

The presence of water impurity atoms creates dangling ends of P–H and P–OH as the P–O–P–O chains are cut. The vibrational modes of the proposed dangling ends have been identified (Novita and Boolchand, 2007; Colthup, 2012) to be as follows: the P↔$(OH)^-$ stretch (Colthup, 2012) at 1,654 cm^{-1}, the P↔H stretch (Daasch and Smith, 1951) at 2,370 cm^{-1}, and the O↔H stretch (Novita and Boolchand, 2007) at 2,850 cm^{-1}. These were used as a test of bonded water in the chains characteristic of these glasses. In almost all glasses synthesized, we could not detect these vibrational modes. But in select glasses, we did observe these and also found that the T_g of these glasses were measurably lower than their dry counterparts. These results gave us confidence that glasses synthesized in the present work are rather dry. Furthermore, in general, presence of water enhances the IR absorption because of the high dipole moment of H_2O molecule that stains the chains. That feature is readily apparent when we compare the response of a wet glass sample with the dry one. All glass **samples B** synthesized in the present work were examined by FTIR and revealed no evidence of free or bonded water in the glasses.

Complementary Role of Infrared and Raman Activity in Sodium Phosphate Glasses

Confidence in the assignment of triad of modes associated with the Q^2 and Q^1 species emerged by comparing the IR response of the glasses in **Figures 4B,C** with the Raman response as illustrated in **Figure 4A** for the case of the stoichiometric $NaPO_3$ glass. Although the minority and defect modes of the Q^2 species are weakly excited in Raman scattering (**Figure 4A**), the IR response from these excitations is rather high (**Figures 4B,C**). Specifically, if one compares the scattering strength of the minority mode near 1,150 cm^{-1}, one finds it is weakly excited in Raman but strongly in IR–TO response (**Figure 4B**). In the case of the defect mode near 1,105 cm^{-1}, the enhancement is qualitatively higher when one compares the results of **Figure 4A** with **Figure 4B**. The complementary response of Raman and IR response in SPGs were observed, in general, at non-stoichiometric compositions as well, and it was helpful in better understanding the nature of the triad of modes associated with the Q^2 and Q^1 species.

Longitudinal Optic–Transverse Optic Splitting in Sodium Phosphate Glasses

Raman scattering, FTIR-TO response (ε), and FTIR-LO response $[\mathrm{Im}(-\varepsilon^{-1})]$ for all SPGs were obtained, the latter two from specular reflection data on flat disc-like specimen. We show an example at $x = 50\%$ in **Figure 4**. The two highest frequency optic modes in $NaPO_3$ glass appear near 1,276.8 cm^{-1} (ν_{as} Q^2) and near 1,317.2 cm^{-1} (ν_{as} Q^3) in Raman scattering (**Figure 4D**). The corresponding TO mode frequency (ν_{TO}) and LO mode frequency (ν_{LO}) were also measured (**Figures 4E,F**; Galeener and Lucovsky, 1976). In fact, we established the general variation in ν_{TO} and ν_{LO} mode frequency with glass composition "x" (**Figures 13A,C**) and found that $\nu_{TO}(x)$ mode frequency is generally lower than $\nu_{LO}(x)$ as expected, but in the IP, $\nu_{TO}(x)$ blue-shifts to nearly equal ν_{LO} (x), leading to the ν_{LO}-ν_{TO} frequency difference to display a global minimum in that special phase. Furthermore, we find that the variation in both the LO and TO mode frequency displays a rather abrupt blue shift in going from $x = 36\%$ to $x = x_r = 37.5\%$, near the rigidity transition, and a general softening of these excitations as one goes across the IP (**Figure 13**). It is generally acknowledged that LO-TO mode frequency splitting (ν_{LO}-ν_{TO}) provides a measure of the internal E-fields setup in the polar glasses made of positive (P^{5+}, Na^+) cations and negative (O^{2-}) anions. Most noteworthy is the finding that the ν_{LO}-ν_{TO} splitting shows a global minimum in the IP (**Figure 13**) for both the Q^2 asymmetric mode and the Q^3 asymmetric mode (**Figure 4A**).

Trends in Molar Volumes

Compositional trends in the variation of molar volumes [$V_m(x)$] of the present SPGs are summarized in **Figure 6D**. With increasing soda content, one finds $V_m(x)$ steadily decreases from a value near 56.0 cm^3/mol to about 40 cm^3/mol in the 20% $< x <$ 50% range. The reported value (Hudgens, 1994) of V_m in c-$NaPO_3$ is close to 41.1 cm^3/mole, in reasonable accord with the value we obtained in the corresponding metaphosphate glass. The baseline variation $V_m(x)$ is sketched by the smooth curve drawn through the data in **Figure 6D**. A closer perusal of the results show that IP glass compositions reveal evidence of an additional reduction in V_m or compaction of the glassy network from the average behavior that is illustrated by the vertical hash marks in the inset of **Figure 6D**. The compaction remarkably coincides with the reversibility window range of 37.5% $< x <$ 46.0%. Compaction of IP glass compositions has been noted in chalcogenides (Bhosle et al., 2012b; Chakraborty and Boolchand, 2014) previously. The effect is generally ascribed (Boolchand et al., 2013) to the consequence of the balance of near-neighbor covalent bonding interactions exhausting the available degrees of freedom in the isostatically rigid backbone formed in the IP. That balance promotes weaker but longer range Coulombic forces to additionally compact networks formed in the IP, displaying evidence of molar volume window.

DISCUSSION

Linking Melt Fragility Index With Glass Topological Phases

Topological Phases

The calorimetric results on SPGs obtained in the present work along with those reported earlier (Cormia et al., 1963; Angell and Rao, 1972; He and Thorpe, 1985; Martin and Angell, 1986; Wäsche and Brückner, 1986; Angell, 1990; Sales, 1990; Hudgens and Martin, 1993; Hudgens, 1994; Hoppe, 1996; Angell et al., 1999; Brow, 2000; Sidebottom and Changstrom, 2008; Fabian and Sidebottom, 2009; Gupta and Mauro, 2009; Mauro et al., 2009; Sidebottom and Schnell, 2013; Hermansen et al., 2014, 2015; Sidebottom, 2014; Sidebottom et al., 2014) are summarized in **Figure 6**. In addition, we have included in **Figure 6** the compositional trends in molar volumes $V_m(x)$ obtained in the present glasses. The central finding of the present work is the existence of a reversibility window in the 37.5(3)% $< x <$ 46.0(2)% range of soda across which glass transitions become thermally reversing. The square-well-like (Chakravarty, 2003; Chen et al., 2008; Bhosle et al., 2012a,b; Gunasekera et al., 2013b; Chakraborty and Boolchand, 2014; Chakraborty et al., 2017) variation of the non-reversing heat flow $\Delta H_{nr}(x)$ in the indicated range is a direct evidence of the isostatically rigid IP formed in the present glasses. Micoulaut (Micoulaut, 2010; Mantisi et al., 2015) has shown that the enthalpy of relaxation at T_g of a glass constitutes a measure of n_c-3, i.e., departure of the glass network from isostaticity ($n_c = 3$). The increasing T_g in the 20% $< x <$ 50% range shows that glasses at $x <$ 37.5%(3) are in the flexible phase, while those at $x >$ 46.0(2)% are in the stressed rigid phase, thus fixing the three glass topological phases in the present glasses.

In several publications, Sidebottom has developed a coarse graining model of these glasses by considering only the bridging oxygen atoms serving to define the glass backbone. In this approach, one excludes the terminal oxygen atoms and the Na^+ ions in evaluating constraints. In this approach, the mean coordination number of the glass backbone is taken as 3 at $x = 0$ and as 2 at $x = 50\%$, and, in general, one can show,

$$<r(x)> = (3 - 4x)/(1 - x) \quad (3)$$

A mean coordination number of <r> of 2.40 is realized when $x = 37.5\%$ in Equation 3. Thus, in the coarse graining (Sidebottom et al., 2014) approach, one expects the percolation of rigidity to occur when x increases to $x = 37.5\%$, and that prediction is in harmony with our observation of the rigidity transition near that composition in the present SPGs.

Dangling ends of a network play no role near the rigidity transition, but they soften a stressed rigid network and stiffen a flexible network as suggested earlier (Mamedov et al., 2003; Qu and Boolchand, 2005; Boolchand and Goodman, 2017). If one considers the dangling ends of the base P_2O_5 glass, a count of the bond-bending and bond-stretching constraints (Georgiev and Boolchand, 2000) shows the quasi-tetrahedral local structure to be isostatically rigid ($n_c = 3$). The vanishing of $\Delta H_{nr}(x)$ term (**Figure 6**) at $x = 0$ is in harmony with its isostatic character of the base glass. The increase of $T_g(x)$ in the 15% $< x <$ 50% range would, of course, be in conflict with the coarse graining model, which predicts <r> to steadily decrease in the indicated glass range. So, one does not expect the topological phase assignment of the coarse graining model to be in harmony with the observed findings. But since the percolation of rigidity near <r> = 2.40 is independent of the count of dangling ends, the onset of rigidity is correctly predicted by the coarse graining model.

Correlating Melt Dynamics With Glass Topological Phases

The second key finding of the present work is the observation of a melt fragility window in the 37.5(3)% $< x <$ 46.0(2)% range, where the fragility index m displays a square-well-like variation with the fragility index in the well acquiring a value m somewhat lower than 20. The finding underscores the super-strong characteristic of melts (Gunasekera et al., 2013a; Chakraborty and Boolchand, 2014) formed in the fragility window (**Figure 6C**). The correlation between the variation of $\Delta H_{nr}(x)$ (**Figure 6B**) and m(x) (**Figure 6C**) underscores that super-strong melts upon cooling (Boolchand and Goodman, 2017) will give rise to isostatically rigid glasses, while fragile melts formed at $x <$ 37.5(3)% and at $x >$ 46.0(2)% will form flexible and stressed rigid glasses. For stressed rigid glasses, one thus observes T_g to increase with fragility index. For flexible glasses, on the other hand, the reverse is the case, i.e., m(x) increases as T_g decreases at least close to the rigidity transition near $x = 37.5\%$ (**Figure 6C**).

The correlation between melt dynamics and glass topological phases has been observed recently in the chalcogenides such as

Ge–Se (Bhosle et al., 2012a,b) and Ge–S (Chakraborty et al., 2017). The present case of SPG is one of the first on a modified oxide where melt dynamics correlate with glass topological phases. These findings strongly suggest that the dynamics of glass-forming melts may well encode the glass topological phases, as a general principle of glass science.

Challenges of Synthesis and Handling Sodium Phosphate Glasses

The fragility index reported by Fabian and Sidebottom (2009) show m = 80 at x = 50%, and the term to steadily decrease as x decreases to 0 to display a value of m = 20 for the base P_2O_5 melt in their dynamic light scattering measurements. That trend is broadly similar to the one observed by us in our melts, although the absolute values of m observed by us are systematically lower. It is encouraging to see that for the base glass (at x = 0), the fragility index reported in ref. (Fabian and Sidebottom, 2009) is actually quite close to the one observed in the present work by m-DSC. These fragility index results differ qualitatively from those of Hudgens (1994) and Martin (Martin and Angell, 1986; Hudgens and Martin, 1993). Hudgens and Martin (1993) were the first group to demonstrate how P_2O_5 could be dried and purified by sublimation, and we as well as Fabian and Sidebottom followed that procedure. The results in **Figure 5** presented in the present work on calorimetric properties of the base P_2O_5 glass highlight some of the challenges in working with and handling of the base P_2O_5 glass in DSC and m-DSC experiments. Not only must the bulk glass be dry but the Al pans and lids must be especially dry and have the capability to be hermetically sealed to get reliable calorimetric results. The lower $T_g(x)$ (**Figure 6A**) and higher fragility index for the base P_2O_5 glass at x = 0% (**Figure 6B**) reported by Hudgens and Martin in their DSC experiments compared to those reported by us in the present m-DSC ones, particularly at x < 20%, are suggestive that these large differences probably come from inadvertent traces of water impurity doping of these P_2O_5-rich bulk glasses.

Glass Molecular Structure Evolution With Composition From Calorimetric, Raman Scattering, and ^{31}P NMR Studies in Sodium Phosphate Glasses

Three Regimes of Structure Evolution

The $T_g(x)$ variation in the present SPGs displays three distinct regimes of variation. At low x, 0 < x < 15% range, soda serves as a network modifier cutting BO bonds to create NBO ones, leading to a reduction of $T_g(x)$ at a rate that is fully consistent with the predicted slope equations based on the stochastic agglomeration theory (SAT) (Micoulaut, 1998; Georgiev et al., 2001).

$$T_g = T_o\left[1 + \frac{x}{(1-x)\ln\frac{2}{3}}\right] \quad (4)$$

In Equation 4, T_o represents the T_g of the base P_2O_5 glass, and the slope dT_g/dx = 19.7°C/mole % of Na_2O, taking T_g to be 704 K. The observed slope of 20°C/mol% of Na_2O is in harmony with the SAT predicted slope (Micoulaut, 1998). If Na^+ ions were to bond with the terminal O_t of the P-centered quasi-tetrahedral local structure, O_t=$P(O_{1/2})_3$, the network connectivity would remain unaltered and $T_g(x)$ would remain unchanged. The Micoulaut slope equations have been calculated for a variety of modified oxides such as $(Na_2O)_x(SiO_2)_{100-x}$ and $(Na_2O)_x(GeO_2)_{100-x}$. In each case, the $T_g(x)$ decrease with soda content can be traced to the reduced network connectivity as bridging oxygen atoms are converted into non-bridging ones. The observed and calculated slopes, $dT_g(x)/dx$, are in remarkable accord with each other (Micoulaut, 1998; Micoulaut and Naumis, 1999).

Returning to SPGs, at intermediate x, 15% < x < 50%, the additive continues to serve as a network modifier but adds to the cohesion by promoting the growth of the Q^2 species forming part of a P–O–P–O– chains. Na^+ ions now charge compensate the P-centered tetrahedral unit having two bridging oxygen (O_b) and two terminal oxygen (O_t) permitting the P=O_t bond to form. At higher x, 50% < x < 60% range, the Q^2-bearing chains are fragmented by pairs of Q^1 species forming the pyrophosphate units. The loss of backbone structure is reflected in both T_g (x) and $\Delta H_{nr}(x)$ to steadily decrease at x > 50%. This broad picture of glass structure evolution suggested by the trends in $T_g(x)$ variation finds support in Raman scattering and IR reflectance results.

Fraction of Q^n Species and Molecular Structure of the Intermediate Phase From Raman Scattering

Raman scattering (**Figure 8A**) results in the present glasses reveal the three **features 1, 3, and 4**. Analysis of **feature 1** near 1,150 cm^{-1}, associated with the Q^2 local structure, shows a triad of modes (**Figures 9**, **10**), a majority mode, a minority mode, and a defect mode. **Feature 3** near 1,300 cm^{-1} was analyzed in terms of two modes (**Figures 11A–D**). The highest frequency mode represents the symmetric stretch mode of Q^3 species. **Feature 4** near 1,012 cm^{-1} is identified with Q^1 species, and its scattering strength steadily increases as x > 50% as shown in **Figures 12A,B**. These results were cast in terms of the compositional dependence of the fractions $f(Q^2)$, $f(Q^3)$, and $f(Q^1)$ species deduced from Raman scattering (**Figure 12B**) and show that they correlate well with the ^{31}P NMR results of **Figure 12D**. It is encouraging that two independent probes of glass structure, one nuclear, the other optical, have converged to provide closely similar details of local structure in terms of the Q^n species of these SPGs. Recently, Bødker et al. (2018) have successfully reproduced the Q^n speciation in SPGs (**Figures 12B,D**) using a purely statistical mechanical approach by using the experimentally known populations at one select composition, *viz.*, $NaPO_3$.

The Raman mode frequency and mode scattering strength variation for the triad of Q^2 species displays other rather striking features (**Figures 10A,B**) that provide new clues to the formation of the IP. All three modes steadily blue-shift with increasing x, giving unambiguous evidence of a stiffening of the glass network in the 20% < x < 50% range. Furthermore, the minority and the defect mode of the Q^2 species show a global minimum in concentration in the IP range, wherein the majority Q^2 mode

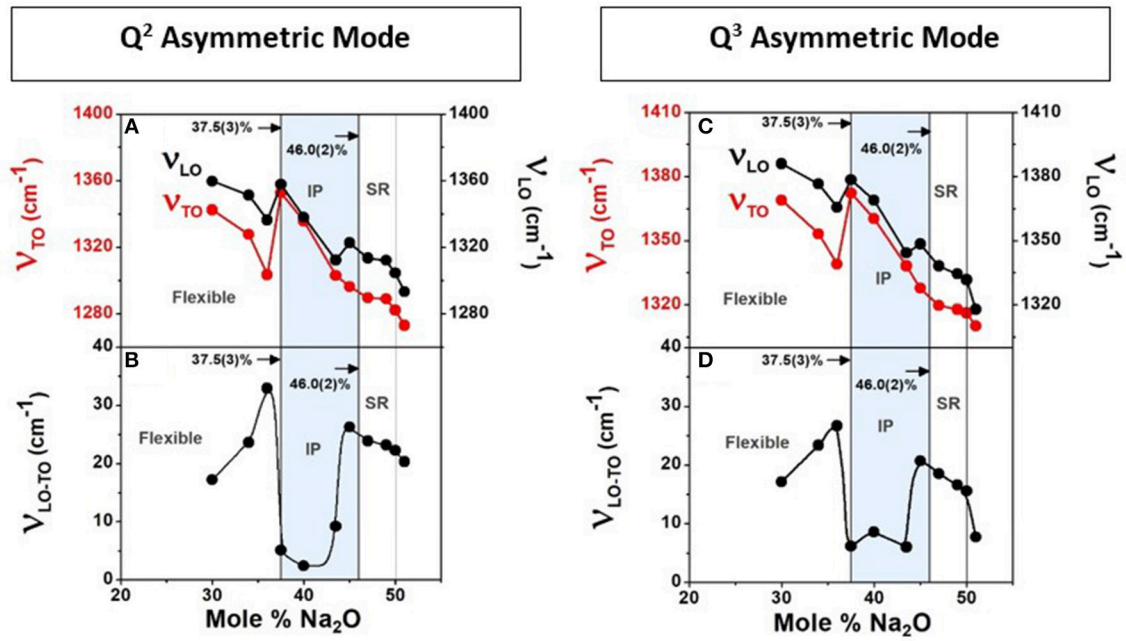

FIGURE 13 | The observed LO and TO mode frequency variation with glass composition for the Q^2 asymmetric mode **(A)** and the Q^3 asymmetric mode **(C)** in $(Na_2O)_x(P_2O_5)_{100-x}$ glasses (**Figure 4**) in the 30% < x < 60% range. The frequency difference $\nu_{LO} - \nu_{TO}$ displays a broad minimum in the IP **(B)** for the Q^2 asymmetric mode and **(D)** for the Q^3 asymmetric mode. The reduction in LO–TO splitting or internal Electric fields in the IP could be the consequence of the absence of network stress and network compaction that leads to a redistribution of charges in these ionic glasses.

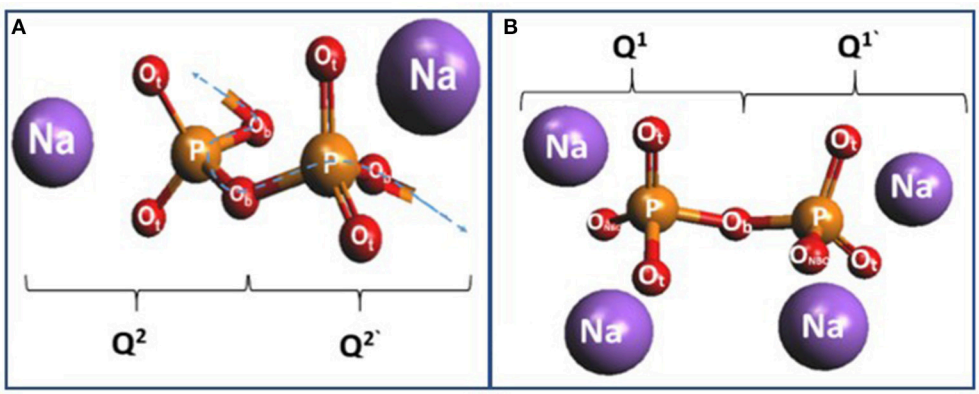

FIGURE 14 | (A) A pair of Q^2 species forming the building block of P–O–P–O chains near x = 50%. **(B)** The uptake of two Na^+ ions with a pair of Q^2 leads to the formation of a Q^1 dimer (pyrophosphate) in the right panel.

near 1,166 cm^{-1} steadily increases in scattering strength with x. These features, i.e., a minimum in the concentration of the minority mode and defect mode along with an average Q^2/Q^3 fraction of near 4 (**Figure 12B**), serve to define the characteristic structural features of the stress-free backbone of the IP.

The generic connection between the triad of modes of the Q^2 species is made more quantitative by PVU considerations (**Figure 12C**; Brow et al., 1995). The plot of the Raman active P–O_t-related stretch mode frequency scaling with the PVU parameter (**Figure 12C**) provides a quantitative measure of the P–O_t bond strengths in each of these species. The majority and minority modes of the Q^2 species possess P–O_t Raman frequency that are quite close to each other and illustrate how local structural disorder is intrinsically built in the chain-bearing glass backbone. The defect mode, on the other hand, is rather broad and is suggestive that its local structure is more distorted, most likely because of the presence of an additional Na^+ cation in the vicinity of the Q^2 local structure. Inclusion of Na^+ ion is suggested by the anomalies in the fraction of Q^2 and Q^3 species manifested near x = 50% when the concentration of the

defect site is high in the stressed rigid glass. We alluded to these anomalies earlier in section Raman Scattering and **Figure 12B**.

We view the minority mode and the defect mode of Q^2 species to functionally serve as stress relief entities of the chain-bearing backbone. Their minimum in the IP range is consistent with the stress-free nature (Wang et al., 2005) of that phase, and their presence a reminder of the role of fluctuations that build the configurational entropy of that phase (Yan, 2018). The minority mode and defect mode represent topological defects that assist self-organization.

At $x > 50\%$, the continued growth in concentration of the minority mode and defect mode at the expense of the majority mode of Q^2 species (**Figure 10B**) constitutes signature of the loss in integrity of the P-O-P-chains. But a far more significant structural change occurs, *viz.*, formation of Q^1 species (1,012 cm^{-1}). The Q^1 species break up the Q^2-bearing chains as schematically illustrated (**Figure 12B**). The scattering strength variation of the Raman mode with x (**Figure 12B**) shows that the Q^1 species become the majority species at $x > 60\%$ rapidly fragmenting the backbone and leading T_gs to mildly decrease as the network connectivity lowers upon growth of Q^1 dimers.

Fragmentation of Q^2-Bearing Chains by Q^1 Dimers in the Pyrophosphates ($50\% < x < 60\%$)

By bringing two additional Na^+ cations next to the P–O–P– chain (**Figure 14A**), one converts the two bridging oxygen atoms (O_b) into two terminal ones (O_t), thus forming the building block of a Q^1 dimer or a pyrophosphate (**Figure 14B**) as schematically illustrated in **Figure 14**. The three P-O_t bonds in the Q^1 species are nearly equivalent as suggested by simulations NRLMOL (Porezag and Pederson, 1996, 1999; Neugebauer et al., 2002; Park et al., 2006) and PVU estimates (Brow et al., 1995; Brow, 2000). The cluster calculations also reveal the Raman cross section of the P–O_t stretch vibration of Q^2 species exceeds that of the corresponding vibration of Q^3 species by a factor of 4.5, a factor that compares reasonably with the experimental deduced value of 2.85 as mentioned earlier in section Raman Scattering.

Simple constraint counting algorithms show that while Q^3 species and Q^2 species are nearly isostatic ($n_c = 3$), the Q^1 species is under constrained ($n_c = 2.69$).

It is useful to mention that the observed scattering strength ratio of the Q^1/Q^2 species deduced from the Raman measurements appear to be somewhat lower than the expected ratio based on stoichiometry considerations (**Figure 12A**). The latter considerations also place the Q^1/Q^2 fraction to equalize at $x = 60\%$. By imposing that condition, one finds the Raman scattering cross section of the Q^2 species to exceed that of the Q^1 species by a factor of 1.60. Our NRLMOL estimates of the Raman cross section of the 1,166 cm^{-1} mode (Q^2) to the 1,012 cm^{-1} mode (Q^1) is found to be 1.93. The correlation between theory and experiment on the Raman cross sections of the modes due to Q^3, Q^2, and Q^1 species is, thus, in reasonable accord with each other.

We had noted earlier that the square-well-like lowering in the enthalpy of relaxation $\Delta H_{nr}(x)$ is the signature of the IP (**Figure 6B**). But we also find that the window sits on a slopping baseline in $\Delta H_{nr}(x)$ that increases monotonically with x in the $20\% < x < 50\%$ range, and furthermore, within the window, the $\Delta H_{nr}(x)$ term remains finite and constant near 0.35 cal/gm. How can we understand this rather peculiar result? Such a result was not observed in chalcogenides, where we always find the reversibility window to possess a nearly vanishing enthalpy of relaxation in the window (Novita and Boolchand, 2007; Chen et al., 2008; Bhosle et al., 2012a,b; Gunasekera et al., 2013b).

The presence of a finite concentration of both minority mode and defect mode of the Q^2 species (**Figure 10B**) that coexist with the main local structures (Q^2 and Q^3 species), we conjecture, contributes a finite contribution to the $\Delta H_{nr}(x)$ term from the presence of these under constrained local structures that form part of the backbone. These under constrained topological defects contribute to the $\Delta H_{nr}(x)$ term over the broad $20\% < x < 50\%$ range as their concentration suggests (**Figure 10B**). In the IP, a local minimum in the $\Delta H_{nr}(x)$ term comes as the right mix of Q^2 (majority mode) and Q^3 species come together to self-organize the network backbone.

Infrared Reflectance, Longitudinal Optic, and Transverse Optic Response

A significant finding from the IR measurements is that the LO and TO mode frequency splitting, ν_{LO}-ν_{TO}, shows a global minimum in the IP (**Figure 13**) for both the two highest-frequency optic modes, Q^2 asymmetric mode and the Q^3 asymmetric mode (**Figure 4A**). The result is most likely related to the stress-free nature of networks formed in the isostatically rigid IP. That speculation clearly needs to be tested theoretically, and it is beyond the scope of the present work.

Here, we would like to draw attention to the fact that the blue shift of the TO mode frequency, ν_{TO}, in the IP where molar volumes decrease (**Figure 6D**) leads in a natural fashion to a mode Gruneisen parameter, $\gamma = -(V/\nu)d\nu/dV$ of 0.75(10). The magnitude of γ suggests (Zallen, 1974) an underlying mode stiffness that is characteristic of covalent bonds. That result appears reasonable given that for a TO mode of the predominantly Q^2-like chains formed in the IP glasses, one expects the P-O_t bonds, locally transverse to the chains, to be involved. And these are the very bonds that will be compressed as the glass backbone compacts (**Figure 6D**) and the interchain spacing decreases. We attribute the blue shift of the TO vibrational excitation in the IP to the underlying network compaction. The LO mode, on the other hand, must involve displacement of P and O_b atoms locally along the chain axis. The P–O_b bonds are softer than the P–O_t ones by almost a factor of 0.60, as suggested by the Raman mode frequency ratio of 670 cm^{-1}/1,160 cm^{-1}. For that reason, we believe the LO mode frequency may remain largely unaffected by compaction of the network structure in the IP.

The global reduction in local electric fields observed in the present polar glass in the IP is reminiscent of a parallel finding in sodium germanate glasses (Rompicharla et al., 2008). The finding may well be a general feature of glasses. We hope the present results stimulates further discussion of the subject.

CONCLUSIONS

We have examined scores of especially dry and homogeneous $(Na_2O)_x(P_2O_5)_{100-x}$ glass compositions over a wide range, $0 < x < 61\%$, in m-DSC, Raman scattering, infrared reflectance, and molar volume experiments. The glass transition temperature variation $T_g(x)$ displays three regimes; at low x ($0 < x < 15\%$), the additive serves as a network modifier converting bridging oxygen atoms (BO) of the parent base material into non-bridging oxygen atoms (NBO) lowering the network connectivity reflected in $T_g(x)$. At higher x, $15\% < x < 50\%$, the additive serves as a network modifier but adds to the cohesion of the network with $T_g(x)$ monotonically increasing as chains of Q^2 species steadily grow at the expense of quasi-tetrahedral units $O_t{=}P(O_{1/2})_3$ of the base glass. In this regime, we observe a thermally reversing, square-well-like window, bordered by an abrupt rigidity transition near $x_r = 37.5\%$ and a stress transition near $x_s = 46.0\%$. Between these two transitions, glasses are viewed to form an isostatically rigid network, the IP. Melt fragility index, established using the complex C_p formalism, reveals $m(x = 0)$ to be 15, to increase monotonically with x, and to display a square-well-like fragility window in the $37.5(3)\% < x < 46.0(2)\%$ range. That range coincides with that of the reversibility window. The fragility window coinciding with the reversibility window underscores that melt dynamics encode glass topological phases. At still higher x ($> 50\%$), $T_g(x)$ mildly decreases with increasing x, confirming that glasses steadily segregate as pyrophosphate units emerge as revealed by the Q^1 structural species in Raman scattering.

Raman scattering measurements also show that the fraction of $f(Q^3(x))$, $f(Q^2(x))$, and $f(Q^1(x))$ generally tracks the mean field behavior based on stoichiometry of glasses. These trends are quite similar to those reported earlier by Brow et al. (1994) and Brow (2000). Raman scattering also shows that the Q^2 structural species always appear with two satellite modes on the low-frequency side. These satellite modes are viewed as topological defects present in glasses.

Infrared specular reflectance measurements on bulk glasses confirm the dryness of glass samples synthesized. Furthermore, these measurements also reveal the LO and TO mode frequencies to change with glass composition in a rather systematic fashion. One finds that the LO–TO mode frequency difference shows a global minimum in the intermediate phase. The observation may be a consequence of the compactness and stress-free nature of glasses prevailing in the IP. Taken together, in the IP, we observe the existence of a reversibility window, a fragility window, a local minimum in molar volumes, a global minimum in the LO–TO mode splitting, and a global minimum in the concentration of the topological defects in the IP. These extrema in physical properties may well be the clearest signature of network self-organization in a network glass.

AUTHOR CONTRIBUTIONS

CM took the lead in the synthesis of glasses and the m-DSC experiments. AM in performing and analyzing the Raman scattering results, and VG in performing and analyzing infrared reflectance results, on the SPGs. Earlier, PC and DN took the lead in the synthesis of the base P_2O_5 glass and its characterization by m-DSC. RC assisted in the Raman and m-DSC experiments and took the lead in numerical simulations using the NRLMOL package. MB and MM assisted with the numerical simulations and discussions on topological phases, melt dynamics, and the coarse graining model approach. PB coordinated the experimental work performed at University of Cincinnati, and assisted in writing the manuscript.

FUNDING

PB acknowledges support from NSF grant DMR 08-53957. MM acknowledges the support of Agence Nationale de la Recherche (ANR) grant no. ANR-11-BS08-10012 from the American Fulbright Commission and the International Materials Institute (H. Jain). MB acknowledges support from NSF grants 1562066, 1762292, and 1826420.

ACKNOWLEDGMENTS

It is a pleasure to thank Dr. Koblar Alan Jackson for assistance with the simulation package NRLMOL to calculate the Raman and infrared vibrations from characteristic local structures, and Dr. Bernard Goodman and Dr. Sergey Mamedov for the many useful discussions on glass science. It is also a pleasure to thank Dr. Warren Huff for the numerous discussions on glass science and particularly for the EDAX measurements.

REFERENCES

Alam, T., and Brow, R. K. (1998). Local structure and connectivity in lithium phosphate glasses: a solid-state ^{31}P MAS NMR and 2D exchange investigation. *J. Non-Cryst. Solids* 223, 1–20. doi: 10.1016/S0022-3093(97)00345-1

Angell, C. A. (1988). Perspective on the glass transition. *J. Phys. Chem. Solids* 49, 863–871. doi: 10.1016/0022-3697(88)90002-9

Angell, C. A. (1990). Dynamic processes in ionic glasses. *Chem. Rev.* 90, 523–542. doi: 10.1021/cr00101a006

Angell, C. A., and Rao, K. J. (1972). Configurational excitations in condensed matter, and the "bond lattice" model for the liquid–glass transition. *J. Chem. Phys.* 57, 470–481. doi: 10.1063/1.1677987

Angell, C. A., Richards, B. E., and Velikov, V. (1999). Simple glass-forming liquids: their definition, fragilities, and landscape excitation profiles. *J. Phys. Condens. Matter* 11:A75. doi: 10.1088/0953-8984/11/10A/005

Bhosle, S., Gunasekera, K., Boolchand, P., and Micoulaut, M. (2012a). Melt Homogenization and self-organization in chalcogenides—part I. *Int. J. Appl. Glass Sci.* 3, 189–204. doi: 10.1111/j.2041-1294.2012.00093.x

Bhosle, S., Gunasekera, K., Boolchand, P., and Micoulaut, M. (2012b). Melt homogenization and self-organization in chalcogenides—part II. *Int. J. Appl. Glass Sci.* 3, 205–220. doi: 10.1111/j.2041-1294.2012.00092.x

Bødker, M. S., Mauro, J. C., Goyal, S., Youngman, R. E., and Smedskjaer, M. M. (2018). Predicting Q-speciation in binary phosphate glasses using statistical mechanics. *J. Phys. Chem. B* 122, 7609–7615. doi: 10.1021/acs.jpcb.8b04604

Böhmer, R., Ngai, K. L., Angell, C. A., and Plazek, D. J. (1993). Nonexponential relaxations in strong and fragile glass formers. *J. Chemi. Phys.* 99, 4201–4209. doi: 10.1063/1.466117

Boolchand, P. (2006). Intermediate phases, reversibility windows, stress-free and non-aging networks, and strong liquids. *Chalcogenide Lett.* 3, 29–31.

Boolchand, P., and Goodman, B. (2017). Glassy materials with enhanced thermal stability. *MRS Bull.* 42, 23–28. doi: 10.1557/mrs.2016.300

Boolchand, P., Mauro, J. C., and Phillips, J. C. (2013). A note on compacted networks. *Phys. Today* 66:10. doi: 10.1063/PT.3.1932

Brow, R. K. (2000). Review: the structure of simple phosphate glasses. *J. Non-Cryst. Solids* 263, 1–28. doi: 10.1016/S0022-3093(99)00620-1

Brow, R. K., Alam, T. M., Tallant, D. R., and Kirkpatrick, R. J. (2017). Spectroscopic studies on the structures of phosphate sealing glasses. *MRS Bull.* 23, 63–67.doi: 10.1557/S088376940003102X

Brow, R. K., Tallant, D. R., Hudgens, J. J., Martin, S. W., and Irwin, A. D. (1994). The short-range structure of sodium ultraphosphate glasses. *J. Non-Cryst. Solids* 177, 221–228. doi: 10.1016/0022-3093(94)90534-7

Brow, R. K., Tallant, D. R., Myers, S. T., and Phifer, C. C. (1995). The short-range structure of zinc polyphosphate glass. *J. Non-Cryst. Solids* 191, 45–55. doi: 10.1016/0022-3093(95)00289-8

Bunker, B. C., Arnold, G. W., and Wilder, J. A. (1984). Phosphate glass dissolution in aqueous solutions. *J. Non-Cryst. Solids* 64, 291–316. doi: 10.1016/0022-3093(84)90184-4

Bustin, O., and Descamps, M. (1999). Slow structural relaxations of glass-forming Maltitol by modulated DSC calorimetry. *J. Chem. Phys.* 110, 10982–10992. doi: 10.1063/1.478041

Carpentier, L., Desprez, S., and Descamps, M. (2003). From strong to fragile glass-forming systems: a temperature modulated differential scanning calorimetry investigation. *Phase Trans.* 76, 787–799. doi: 10.1080/01411590310001603708

Chakraborty, S., and Boolchand, P. (2014). Topological origin of fragility, network adaptation, and rigidity and stress transitions in especially homogenized nonstoichiometric binary GeS glasses. *J. Phys. Chem. B* 118, 2249–2263. doi: 10.1021/jp411823j

Chakraborty, S., Boolchand, P., and Micoulaut, M. (2017). Structural properties of Ge–S amorphous networks in relationship with rigidity transitions: an *ab initio* molecular dynamics study. *Phys. Rev. B* 96:094205. doi: 10.1103/PhysRevB.96.094205

Chakravarty, S. (2003). *Self-Organization and Aging in Network Glasses*. Ph.D. thesis, University of Cincinnati, (Unpublished).

Chen, P., Holbrook, C., Boolchand, P., Georgiev, D. G., Jackson, K. A., and Micoulaut, M. (2008). Intermediate phase, network demixing, boson and floppy modes, and compositional trends in glass transition temperatures of binary As-S system. *Phys. Rev. B* 78:224208. doi: 10.1103/PhysRevB.78.224208

Click, C. A., Brow, R. K., and Alam, T. M. (2002). Properties and structure of cesium phosphate glasses. *J. Non-Cryst. Solids* 311, 294–303. doi: 10.1016/S0022-3093(02)01417-5

Colthup, N. (2012). *Introduction to Infrared and Raman Spectroscopy*. San Diego, CA: Elsevier.

Cormia, R. L., Mackenzie, J. D., and Turnbull, D. (1963). Viscous flow and melt allotropy of phosphorus pentoxide. *J. Appl. Phys.* 34, 2245–2248. doi: 10.1063/1.1702721

Daasch, L., and Smith, D. (1951). Infrared spectra of phosphorus compounds. *Anal. Chem.* 23, 853–868. doi: 10.1021/ac60054a008

Dash, S., Chen, P., and Boolchand, P. (2017). Molecular origin of aging of pure Se glass: growth of inter-chain structural correlations, network compaction, and partial ordering. *J. Chem. Phys.* 146:4983480. doi: 10.1063/1.4983480

Debenedetti, P. G., and Stillinger, F. H. (2001). Supercooled liquids and the glass transition. *Nature* 410, 259–267. doi: 10.1038/35065704

Exarhos, G. J., and Risen, W. M. (1974). Raman study of isothermal devitrification kinetics of $NaPO_3$ glass. *J. Am. Ceram. Soc.* 57, 401–405. doi: 10.1111/j.1151-2916.1974.tb11422.x

Fabian, R., and Sidebottom, D. L. (2009). Dynamic light scattering in network-forming sodium ultraphosphate liquids near the glass transition. *Phys. Rev. B* 80:064201. doi: 10.1103/PhysRevB.80.064201

Galeener, F. L., Leadbetter, A. J., and Stringfellow, M. W. (1983). Comparison of the neutron, Raman, and infrared vibrational spectra of vitreous SiO_2, GeO_2, and BeF_2. *Phys. Rev. B* 27:1052. doi: 10.1103/PhysRevB.27.1052

Galeener, F. L., and Lucovsky, G. (1976). Longitudinal optical vibrations in glasses: GeO_2 and SiO_2. *Phys. Rev. Lett.* 37, 1474–1478. doi: 10.1103/PhysRevLett.37.1474

Georgiev, D. G., and Boolchand, P. (2000). Rigidity transitions and molecular structure of As_xSe_{1-x} glasses. *Phys. Rev. B* 62, 9228–9231. doi: 10.1103/PhysRevB.62.R9228

Georgiev, D. G., Mitkova, M., and Boolchand, P. (2001). Molecular structure, glass transition temperature variation, agglomeration theory, and network connectivity of binary P–Se glasses. *Phys. Rev. B* 64, 1–11. doi: 10.1103/PhysRevB.64.134204

Goldstein, J., Newbury, D. E., Joy, D. C., Lyman, C. E., Echlin, P., Lifshin, E., et al. (2003). *Scanning Electron Microscopy and X-ray Microanalysis*. 3rd ed. Springer US. Available online at://www.springer.com/us/book/9780306472923 (accessed December 21, 2018). doi: 10.1007/978-1-4615-0215-9

Gresch, R., Muller-Warmuth, W., and Dutz, H. (1979). X-ray photoelectron spectroscopy of sodium phosphate glasses. *J. Non-Cryst. Solids* 34, 127–136. doi: 10.1016/0022-3093(79)90012-7

Gunasekera, K., Bhosle, S., Boolchand, P., and Micoulaut, M. (2013a). Superstrong nature of covalently bonded glass-forming liquids at select compositions. *J. Chem. Phys.* 139:164511. doi: 10.1063/1.4826463

Gunasekera, K., Boolchand, P., and Micoulaut, M. (2013b). Elastic phases of GeSbSe ternary glasses driven by topology. *J. Phys. Chem. B* 117, 10027–10034. doi: 10.1021/jp404565d

Gupta, P. K., and Mauro, J. C. (2009). Composition dependence of glass transition temperature and fragility. I. A topological model incorporating temperature-dependent constraints. *J. Chem. Phys.* 130:094503. doi: 10.1063/1.3077168

He, H., and Thorpe, M. F. (1985). Elastic properties of glasses. *Phys. Rev. Lett.* 54:2107. doi: 10.1103/PhysRevLett.54.2107

Hermansen, C., Mauro, J. C., and Yue, Y. (2014). A model for phosphate glass topology considering the modifying ion sub-network. *J. Chem. Phys.* 140:154501. doi: 10.1063/1.4870764

Hermansen, C., Mauro, J. C., and Yue, Y. (2015). Response to "Comment on 'A model for phosphate glass topology considering the modifying ion sub-network'". *J. Chem. Phys.* 142:107103. doi: 10.1063/1.4913761

Hoppe, U. (1996). A structural model for phosphate glasses. *J. Non-Cryst. Solids* 195, 138–147. doi: 10.1016/0022-3093(95)00524-2

Hoppe, U., Walter, G., Stachel, D., and Hannon, A. C. (1996). Short-range order in KPO_3 glass studied by neutron and X-ray diffraction. *Z. Naturforsch.* 51a, 179–186. doi: 10.1515/zna-1996-0308

Hudgens, J. J. (1994). *The Structure and Properties of Anhydrous, Alkali Ultra-Phosphate Glasses*. Available online at: https://lib.dr.iastate.edu/rtd/11267.

Hudgens, J. J., Brow, R. K., Tallant, D. R., and Martin, S. W. (1998). Raman spectroscopy study of the structure of lithium and sodium ultraphosphate glasses. *J. Non-Cryst. Solids* 223, 21–31. doi: 10.1016/S0022-3093(97)00347-5

Hudgens, J. J., and Martin, S. W. (1993). Glass Transition and infrared spectra of low-alkali, anhydrous lithium phosphate glasses. *J. Am. Ceram. Soc.* 76, 1691–1696. doi: 10.1111/j.1151-2916.1993.tb06636.x

Jacobs, D. J., and Thorpe, M. F. (1995). Generic rigidity percolation: the pebble game. *PRL* 75, 4051–4054. doi: 10.1103/PhysRevLett.75.4051

Mamedov, S., Georgiev, D. G., Qu, T., and Boolchand, P. (2003). Evidence for nanoscale phase separation of stressed–rigid glasses. *J. Phys. Condens. Matter.* 15:S2397. doi: 10.1088/0953-8984/15/31/315

Mantisi, B., Bauchy, M., and Micoulaut, M. (2015). Cycling through the glass transition: evidence for reversibility windows and dynamic anomalies. *Phys. Rev. B* 92:134201. doi: 10.1103/PhysRevB.92.134201

Martin, S. W., and Angell, C. A. (1986). On the glass transition and viscosity of phosphorus pentoxide. *J. Phys. Chem.* 90, 6736–6740. doi: 10.1021/j100283a030

Mauro, J. C., Gupta, P. K., and Loucks, R. J. (2009). Composition dependence of glass transition temperature and fragility. II. A topological model of alkali borate liquids. *J. Chem. Phys.* 130, 234503–234508. doi: 10.1063/1.3152432

Micoulaut, M. (1998). The slope equations: a universal relationship between local structure and glass transition temperature. *Eur. Phys. J. B* 294, 277–294. doi: 10.1007/s100510050184

Micoulaut, M. (2010). Linking rigidity transitions with enthalpic changes at the glass transition and fragility: insight from a simple oscillator model. *J. Phys.* 22:285101. doi: 10.1088/0953-8984/22/28/285101

Micoulaut, M. (2016). Relaxation and physical aging in network glasses: a review. *Rep. Progr. Phys.* 79:066504. doi: 10.1088/0034-4885/79/6/066504

Micoulaut, M., and Naumis, G. G. (1999). Glass transition temperature variation, cross-linking and structure in network glasses: a stochastic approach. *Europhys. Lett.* 47:568. doi: 10.1209/epl/i1999-00427-7

Mohanty, C. (2018). *Direct Evidence for Topological Phases in Sodium Phosphate Glasses From Raman Scattering, Infrared Reflectance and Modulated DSC,* Master's thesis, University of Cincinnati, August 2018 *(Unpublished).*

Moustafa, Y. M., and El-Egili, K. (1998). Infrared spectra of sodium phosphate glasses. *J. Non-Cryst. Solids* 240, 144–153. doi: 10.1016/S0022-3093(98)00711-X

Moynihan, C. T., Easteal, A. J., Wilder, J., and Tucker, J. (1974). Dependence of the glass transition temperature on heating and cooling rate. *J. Phys. Chem.* 78, 2673–2677. doi: 10.1021/j100619a008

Neugebauer, J., Reiher, M., Kind, C., and Hess, B. A. (2002). Quantum chemical calculation of vibrational spectra of large molecules—Raman and IR spectra for buckminsterfullerene. *J. Comput. Chem.* 23, 895–910. doi: 10.1002/jcc.10089

Novita, D. I., and Boolchand, P. (2007). Synthesis and structural characterization of dry $AgPO_3$ glass by Raman scattering, infrared reflectance, and modulated differential scanning calorimetry. *Phys. Rev. B* 76:184205. doi: 10.1103/PhysRevB.76.184205

Park, K., Pederson, M. R., Boyer, L. L., Mei, W. N., Sabirianov, R. F., Zeng, X. C., et al. (2006). Electronic structure and vibrational spectra of C2 B10-based clusters and films. *Phys. Rev. B* 73:035109. doi: 10.1103/PhysRevB.73.035109

Phillips, J. C. (1979). Topology of covalent non-crystalline solids.1. Short-range order in chalcogenide alloys. *J. Non-Cryst. Solids* 34, 153–181. doi: 10.1016/0022-3093(79)90033-4

Porezag, D., and Pederson, M. R. (1996). Infrared intensities and Raman-scattering activities within density-functional theory. *Phys. Rev. B Phys.* 54, 7830–7836. doi: 10.1103/PhysRevB.54.7830

Porezag, D., and Pederson, M. R. (1999). Optimization of Gaussian basis sets for density-functional calculations. *Phys. Rev. A* 60, 2840–2847. doi: 10.1103/PhysRevA.60.2840

Qu, T., and Boolchand, P. (2005). Shift in elastic phase boundaries due to nanoscale phase separation in network glasses: the case of $Ge_xAs_xS_{1-2x}$. *Philos. Mag.* 85, 875–884. doi: 10.1080/14786430412331463636

Rompicharla, K., Novita, D. I., Chen, P., Boolchand, P., Micoulaut, M., and Huff, W. (2008). Abrupt boundaries of intermediate phases and space filling in oxide glasses. *J. Phys. Condens. Matter.* 20:202101. doi: 10.1088/0953-8984/20/20/202101

Sales, B. C. (1990). Structural relaxation dynamics of phosphate glasses: the effects of network topology on the glass transition. *J. Non-Cryst. Solids* 119, 136–150. doi: 10.1016/0022-3093(90)90837-C

Sammet, R. B., Chun, H. U., and Goretzki, H. (1980). XPS measurements and structural aspects of silicate and phosphate glasses. *J. Non-Cryst. Solids* 42, 49–60. doi: 10.1016/0022-3093(80)90007-1

Sidebottom, D. L. (2014). Comment on "A model for phosphate glass topology considering the modifying ion sub-network". *J. Chem. Phys.* 140:154501. doi: 10.1063/1.4913760

Sidebottom, D. L., and Changstrom, J. R. (2008). Viscoelastic relaxation in molten phosphorus pentoxide using photon correlation spectroscopy. *Phys. Rev. B* 77:020201. doi: 10.1103/PhysRevB.77.020201

Sidebottom, D. L., and Schnell, S. E. (2013). Role of intermediate-range order in predicting the fragility of network-forming liquids near the rigidity transition. *Phys. Rev. B* 87:054202. doi: 10.1103/PhysRevB.87.054202

Sidebottom, D. L., Tran, T. D., and Schnell, S. E. (2014). Building up a weaker network: the effect of intermediate range glass structure on liquid fragility. *J. Non-Cryst. Solids* 402, 16–20. doi: 10.1016/j.jnoncrysol.2014.05.010

Suzuya, K., Price, D. L., Loong, C.-K., and Martin, S. W. (1998). Structure of vitreous P_2O_5 and alkali phosphate glasses. *J. Non-Cryst. Solids* 232, 650–657. doi: 10.1016/S0022-3093(98)00529-8

Tatsumisago, M., Kowada, Y., and Minami, T. (1992). Raman spectra of rapidly quenched glasses and melts containing large amounts of Li_2O. *J. Non-Cryst. Solids* 150, 207–211. doi: 10.1016/0022-3093(92)90124-3

Thomas, L. (2005a). *TA Instruments Modulated DSC Technology, Chapter 1–9.*

Thomas, L. C. (2005b). Modulated DSC®paper 3 modulated DSC®basics; optimization of MDSC®experimental conditions. *T.A. Instruments* 1–10.

Thorpe, M. F., Jacobs, D. J., Chubynsky, M. V., and Phillips, J. C. (2000). Self-organization in network glasses. *J. Non-Cryst. Solids*, 266–269. doi: 10.1016/S0022-3093(99)00856-X

Tonchev, D., and Kasap, S. O. (2002). Effect of aging on glass transformation measurements by temperature modulated *DSC* 328, 62–66. doi: 10.1016/S0921-5093(01)01668-9

Velli, L. L., Varsamis, C. P. E., Kamitsos, E. I., Möncke, D., and Ehrt, D. (2005). Structural investigation of metaphosphate glasses. *Phys. Chem. Glasses* 46, 178–181.

Walsh, E. N., Griffith, E. J., Parry, R. W., and Quin, L. D. (1992). *Phosphorus Chemistry*. Washington, DC: American Chemical Society. doi: 10.1021/bk-1992-0486

Walter, G., Hoppe, U., Baade, T., Kranold, R., and Stachel, D. (1997). Intermediate range order in $MeO–P_2O_5$ glasses. *J. Non-Cryst. Solids* 217, 299–307. doi: 10.1016/S0022-3093(97)00220-2

Wang, F., Mamedov, S., Boolchand, P., Goodman, B., and Chandrasekhar, M. (2005). Pressure Raman effects and internal stress in network glasses. *Phys. Rev. B* 71:174201. doi: 10.1103/PhysRevB.71.174201

Wäsche, R., and Brückner, R. (1986). The structure of mixed alkali phosphate melts as indicated by their non-Newtonian flow behaviour and optical refringence. *Phys. Chem. Glasses* 27, 87–94.

Wazer, J. R. (1958). Phosphorous and its compounds. Vol I Chemistry. *J. Chem. Educ.* 36:531. doi: 10.1021/ed036p531.2

Williams, M. L., Landel, R. F., and Ferry, J. D. (1955). The temperature dependence of relaxation mechanisms in amorphous polymers and other glass-forming liquids. *J. Am. Chem. Soc.* 77, 3701–3707. doi: 10.1021/ja01619a008

Yan, L. (2018). Entropy favors heterogeneous structures of networks near the rigidity threshold. *Nat. Commun.* 9:1359. doi: 10.1038/s41467-018-03859-9

Zallen, R. (1974). Pressure-Raman effects and vibrational scaling laws in molecular crystals: S_8 and As_2S_3. *Phys. Rev. B* 9, 4485–4496. doi: 10.1103/PhysRevB.9.4485

Conflict of Interest Statement: The authors declare that the research was conducted in the absence of any commercial or financial relationships that could be construed as a potential conflict of interest.

frontiers in Materials

ORIGINAL RESEARCH
published: 13 June 2019
doi: 10.3389/fmats.2019.00133

Structure of the Intermediate Phase Glasses $GeSe_3$ and $GeSe_4$: The Deployment of Neutron Diffraction With Isotope Substitution

Ruth F. Rowlands[1], *Anita Zeidler*[1,2], *Henry E. Fischer*[3] *and Philip S. Salmon*[1,2]*

[1] Department of Physics, University of Bath, Bath, United Kingdom, [2] Science and Technology Division, Corning Incorporated, Corning, NY, United States, [3] Diffraction Group, Institut Laue Langevin, Grenoble, France

The method of neutron diffraction with isotope substitution was used to measure the full set of partial pair-correlation functions for each of the network-forming glasses $GeSe_3$ and $GeSe_4$, which lie at the boundaries of the so-called intermediate phase in the Ge-Se system. The results show the formation of chemically ordered networks, where selenium chains are cross-linked by $Ge(Se_4)_{1/2}$ tetrahedra, in contrast to glassy $GeSe_2$ where the chemical order is broken. In all of these materials, the Ge-centered structural motifs are distributed unevenly on an intermediate length scale, as indicated by the appearance of a first sharp diffraction peak in the Bhatia-Thornton concentration-concentration partial structure factor. The new experimental work provides benchmark results for guiding in the development of realistic structural models, which can be used to explore the network rigidity and other structure-related properties of the glass. In this context, there are discrepancies between experiment and the predictions of first-principles molecular dynamics simulations that are particularly marked in respect of the Ge-Ge correlation functions, which are sensitive to the connectivity of the Ge-centered structural motifs.

Keywords: chalcogenide glass, glass structure, neutron diffraction, rigidity percolation, intermediate phase

OPEN ACCESS

Edited by:
Matthieu Micoulaut, Sorbonne Universités, France

Reviewed by:
Pál Jóvári, Wigner Research Centre for Physics, Hungarian Academy of Sciences, Hungary
Cristian Fernando Moukarzel, Centro de Investigacion y de Estudios Avanzados – Unidad Mérida, Mexico

***Correspondence:**
Philip S. Salmon
p.s.salmon@bath.ac.uk

Specialty section:
This article was submitted to Glass Science, a section of the journal Frontiers in Materials

Received: *02 April 2019*
Accepted: *20 May 2019*
Published: *13 June 2019*

Citation:
Rowlands RF, Zeidler A, Fischer HE and Salmon PS (2019) Structure of the Intermediate Phase Glasses $GeSe_3$ and $GeSe_4$: The Deployment of Neutron Diffraction With Isotope Substitution. Front. Mater. 6:133. doi: 10.3389/fmats.2019.00133

1. INTRODUCTION

The Ge_xSe_{1-x} ($0 \leq x \leq 1$) system is a prototype for understanding the atomic-scale organization in covalently-bonded network glass-forming materials (Tronc et al., 1973; Bresser et al., 1986; Sugai, 1987; Penfold and Salmon, 1991; Zhou et al., 1991; Salmon and Liu, 1994; Feng et al., 1997; Wang et al., 1998; Petri et al., 1999a,b, 2000; Bureau et al., 2003; Salmon and Petri, 2003; Salmon, 2007a; Sartbaeva et al., 2007; Shatnawi et al., 2008; Inam et al., 2009; Lucas et al., 2009; Gjersing et al., 2010a,b; Bauchy et al., 2011; Hosokawa et al., 2011; Micoulaut et al., 2013; Salmon and Zeidler, 2015; Kaseman et al., 2016; Zeidler et al., 2017; Whittaker et al., 2018), where the network-forming motifs provide some of the essential building-blocks for technologically relevant chalcogenide glasses (Hilton, 1966; Seddon and Laine, 1997; Zakery and Elliott, 2003, 2007; Gopinath et al., 2004; Lezal et al., 2004; Kohoutek et al., 2008; Troles et al., 2009; Eggleton et al., 2011). According to mean-field constraint-counting theory, the glass network will undergo the transition with increasing x from an under-constrained elastically floppy phase to an over-constrained stressed-rigid phase at $x = 0.2$, where the mean number of Lagrangian bonding constraints per atom $\bar{N}_c = 3$, the number of degrees of freedom per atom in three dimensions (Phillips, 1979; Thorpe, 1983). At the $x = 0.2$ composition the mean nearest-neighbor coordination number $\bar{n} = 2.4$. In comparison,

spectroscopic and calorimetric measurements on the Ge_xSe_{1-x} system suggest that the floppy and stressed-rigid phases are separated by an 'intermediate phase' that extends over the finite composition range $0.20 \leq x \leq 0.26$ (Boolchand et al., 2001a,b; Bhosle et al., 2011, 2012). For this range, it is argued that the system lowers its free energy on glass formation by self-organizing to incorporate structural configurations that minimize the occurrence of either over or under constrained regions, to give a glass network that is isostatically rigid and stress-free (Thorpe et al., 2000). Here, self-organization is facilitated by structural variability, i.e., an ability of the system to accommodate different atomic conformations (Sartbaeva et al., 2007; Massobrio et al., 2009). The intermediate phase should therefore have a structural origin, but its signature has not been identified from diffraction or extended X-ray absorption fine structure (EXAFS) spectroscopy experiments (Shatnawi et al., 2008; Zeidler et al., 2017), or from molecular dynamics simulations (Micoulaut et al., 2013). From a dynamical perspective in the Ge_xSe_{1-x} system, intermediate phase compositions correspond to a maximum in the viscosity at the liquidus temperature, and to a minimum in the fragility index (Zeidler et al., 2017).

In this paper we take advantage of recent advances in neutron diffraction instrumentation to investigate the structure of two glasses that delimit the intermediate phase. Specifically, neutron diffraction with isotope substitution (NDIS) (Fischer et al., 2006; Salmon and Zeidler, 2013) is combined with singular valued decomposition (SVD) (Ludwig et al., 1987; Zeidler et al., 2010) to measure the full set of partial structure factors for glassy $GeSe_3$ ($x = 0.25$) and $GeSe_4$ ($x = 0.20$). These structure factors represent the maximal information that can be extracted from experiment at the pair-correlation function level. The results are compared to those obtained from high resolution ^{77}Se magic angle spinning (MAS) nuclear magnetic resonance (NMR) (Gjersing et al., 2010b) or two-dimensional ^{77}Se NMR (Kaseman et al., 2016) spectroscopy. The results are also compared to those obtained from recent density-functional-theory based first-principles molecular dynamics (FPMD) simulations (Kibalchenko et al., 2011; Bouzid and Massobrio, 2012; Micoulaut et al., 2013; Wezka et al., 2014; Bouzid et al., 2015; Chaker et al., 2018). This simulation approach is favored when modeling the structure of materials in the Ge_xSe_{1-x} system on account of the similarity between the electronegativity values for Ge and Se, although there are issues regarding the sensitivity of FPMD models to the size of the simulated system, and to the protocol used to prepare a glass from the liquid state (Bouzid et al., 2015; Le Roux et al., 2016).

The paper is organized as follows. The essential theory for the NDIS experiments is given in section 2. The experimental methods are then described in section 3, where the choice of neutron diffractometer enabled the diffraction patterns to be measured with excellent count-rate stability over a wide range of scattering vectors. The results are presented in section 4 at both the first-difference function and partial structure factor levels in order to check for self-consistency in the measured parameters. The results are discussed in section 5 by reference to those obtained from other experiments and FPMD simulations, where issues include the nature and connectivity of the structural motifs, and whether there is a structural signature of the intermediate phase (Shatnawi et al., 2008; Zeidler et al., 2017). Conclusions are drawn in section 6.

2. THEORY

In a neutron diffraction experiment on glassy $GeSe_3$ or $GeSe_4$, the total structure factor (Fischer et al., 2006)

$$F(k) = \sum_{\alpha}\sum_{\beta} c_\alpha c_\beta b_\alpha b_\beta \left[S_{\alpha\beta}(k) - 1\right], \tag{1}$$

is measured, where α and β denote the chemical species, c_α and b_α represent the atomic fraction and coherent neutron scattering length of chemical species α, respectively, $S_{\alpha\beta}(k)$ is a Faber-Ziman (Faber and Ziman, 1965) partial structure factor, and k is the modulus of the scattering vector. Consider the case of four samples that are identical in every respect, except for their isotopic compositions. Let the Ge-Se isotope combinations be represented by nat-nat, nat-mix, 70-nat, and 73–76, where nat denotes the natural isotopic abundance and mix denotes a mixture of Se isotopes, with enrichments (see section 3.1) that give coherent scattering lengths of $b_{^{\mathrm{nat}}\mathrm{Ge}} = 8.185(20)$, $b_{^{70}\mathrm{Ge}} = 9.93(10)$, $b_{^{73}\mathrm{Ge}} = 5.16(4)$, $b_{^{\mathrm{nat}}\mathrm{Se}} = 7.970(9)$, $b_{^{\mathrm{mix}}\mathrm{Se}} = 10.10(5)$, and $b_{^{76}\mathrm{Se}} = 12.19(10)$ fm (Sears, 1992). Then, if the total structure factors are denoted by ${}^{\mathrm{nat}}_{\mathrm{nat}}F(k)$, ${}^{\mathrm{nat}}_{\mathrm{mix}}F(k)$, ${}^{70}_{\mathrm{nat}}F(k)$, and ${}^{73}_{76}F(k)$, respectively, it follows that

$$\begin{pmatrix} {}^{\mathrm{nat}}_{\mathrm{nat}}F(k) \\ {}^{\mathrm{nat}}_{\mathrm{mix}}F(k) \\ {}^{70}_{\mathrm{nat}}F(k) \\ {}^{73}_{76}F(k) \end{pmatrix} = \mathbf{W} \begin{pmatrix} S_{\mathrm{GeGe}}(k) - 1 \\ S_{\mathrm{SeSe}}(k) - 1 \\ S_{\mathrm{GeSe}}(k) - 1 \end{pmatrix}. \tag{2}$$

In the case of $GeSe_3$ the weighting factor matrix is given by

$$\frac{\mathbf{W}}{\mathrm{barn}} = \begin{pmatrix} 0.0419(2) & 0.3573(8) & 0.2446(8) \\ 0.0419(2) & 0.574(6) & 0.310(2) \\ 0.0616(12) & 0.3573(8) & 0.297(4) \\ 0.0166(2) & 0.836(14) & 0.236(4) \end{pmatrix} \tag{3}$$

(1 barn $= 10^{-28}$ m^2), and in the case of $GeSe_4$ the weighting factor matrix is given by

$$\frac{\mathbf{W}}{\mathrm{barn}} = \begin{pmatrix} 0.0268(1) & 0.4065(9) & 0.2088(7) \\ 0.0268(1) & 0.653(7) & 0.265(2) \\ 0.0394(8) & 0.4065(9) & 0.253(3) \\ 0.0106(2) & 0.951(16) & 0.201(3) \end{pmatrix}. \tag{4}$$

The partial structure factors $S_{\alpha\beta}(k)$ are related to the partial pair-distribution functions $g_{\alpha\beta}(r)$ via the Fourier transform relation

$$g_{\alpha\beta}(r) = 1 + \frac{1}{2\pi^2 \rho\, r}\int_0^\infty \mathrm{d}k\, k \left[S_{\alpha\beta}(k) - 1\right] \sin(kr) \tag{5}$$

where ρ is the atomic number density and r is a distance in real space. The mean coordination number of atoms of type β,

contained in a volume defined by two concentric spheres of radii r_1 and r_2 centered on an atom of type α, is given by

$$\bar{n}_{\alpha}^{\beta} = 4\pi\ \rho\ c_{\beta} \int_{r_1}^{r_2} \mathrm{d}r\, r^2 g_{\alpha\beta}(r). \tag{6}$$

It is possible to eliminate one of the partial structure factors by combining two total structure factors. For example, $S_{\mathrm{SeSe}}(k)$ can be eliminated by forming a first-difference function such as

$$\begin{aligned}\Delta F_{\mathrm{Ge}}(k) \equiv\ & {}^{70}_{\mathrm{nat}}F(k) - \left(b^2_{\mathrm{nat}_{\mathrm{Se}}} / b^2_{{}^{76}\mathrm{Se}}\right) {}^{73}_{76}F(k) \\ =\ & c^2_{\mathrm{Ge}}\left(b^2_{{}^{70}\mathrm{Ge}} - b^2_{{}^{73}\mathrm{Ge}} b^2_{\mathrm{nat}_{\mathrm{Se}}} / b^2_{{}^{76}\mathrm{Se}}\right)\left[S_{\mathrm{GeGe}}(k) - 1\right] \\ & + 2c_{\mathrm{Ge}}c_{\mathrm{Se}}\left(b_{{}^{70}\mathrm{Ge}} b_{\mathrm{nat}_{\mathrm{Se}}} - b_{{}^{73}\mathrm{Ge}} b^2_{\mathrm{nat}_{\mathrm{Se}}} / b_{{}^{76}\mathrm{Se}}\right) \\ & \left[S_{\mathrm{GeSe}}(k) - 1\right].\end{aligned} \tag{7}$$

Similarly, $S_{\mathrm{GeSe}}(k)$ can be eliminated by forming a first-difference function such as

$$\begin{aligned}\Delta F(k) \equiv\ & {}^{73}_{76}F(k) - \left(b_{{}^{73}\mathrm{Ge}} b_{{}^{76}\mathrm{Se}} / b_{{}^{70}\mathrm{Ge}} b_{\mathrm{nat}_{\mathrm{Se}}}\right) {}^{70}_{\mathrm{nat}}F(k) \\ =\ & c^2_{\mathrm{Ge}}\left(b^2_{{}^{73}\mathrm{Ge}} - b_{{}^{70}\mathrm{Ge}} b_{{}^{73}\mathrm{Ge}} b_{{}^{76}\mathrm{Se}} / b_{\mathrm{nat}_{\mathrm{Se}}}\right)\left[S_{\mathrm{GeGe}}(k) - 1\right] \\ & + c^2_{\mathrm{Se}}\left(b^2_{{}^{76}\mathrm{Se}} - b_{{}^{73}\mathrm{Ge}} b_{\mathrm{nat}_{\mathrm{Se}}} b_{{}^{76}\mathrm{Se}} / b_{{}^{70}\mathrm{Ge}}\right)\left[S_{\mathrm{SeSe}}(k) - 1\right].\end{aligned} \tag{8}$$

The corresponding real-space functions, denoted by $\Delta G_{\mathrm{Ge}}(r)$ and $\Delta G(r)$, are obtained from Equations (7) and (8), respectively, by replacing each $S_{\alpha\beta}(k)$ by the corresponding $g_{\alpha\beta}(r)$ function. The weighting factors for the Ge-Ge and Ge-Se partial structure factors in Equation (7) are 0.054(1) and 0.196(3) barn for $GeSe_3$ vs. 0.0349(8) and 0.167(3) barn for $GeSe_4$, respectively. The weighting factors for the Ge-Ge and Se-Se partial structure factors in Equation (8) are −0.0323(6) and 0.552(12) barn for $GeSe_3$ vs. −0.0207(4) and 0.628(14) barn for $GeSe_4$, respectively. The first-difference functions are obtained from pairs of measured $F(k)$ functions, whereas the partial structure factors are obtained by combining all of the measured $F(k)$ functions. Self-consistent results are expected if systematic errors are small (Salmon and Petri, 2003).

It is also informative to decompose a total structure factor into its contributions from the Bhatia-Thornton (Bhatia and Thornton, 1970) number-number, concentration-concentration, and number-concentration partial structure factors denoted by $S_{\mathrm{NN}}(k)$, $S_{\mathrm{CC}}(k)$ and $S_{\mathrm{NC}}(k)$, respectively, where

$$\begin{aligned}F(k) = \langle b\rangle^2\left[S_{\mathrm{NN}}(k) - 1\right] + c_{\mathrm{Ge}}c_{\mathrm{Se}}(b_{\mathrm{Ge}} - b_{\mathrm{Se}})^2\left\{\left[S_{\mathrm{CC}}(k) / c_{\mathrm{Ge}}c_{\mathrm{Se}}\right]\right. \\ \left. -1\right\} + 2\langle b\rangle(b_{\mathrm{Ge}} - b_{\mathrm{Se}})S_{\mathrm{NC}}(k)\end{aligned} \tag{9}$$

and $\langle b\rangle = c_{\mathrm{Ge}}b_{\mathrm{Ge}} + c_{\mathrm{Se}}b_{\mathrm{Se}}$ is the mean coherent scattering length. Equation (2) can then be re-written as

$$\begin{pmatrix} {}^{\mathrm{nat}}_{\mathrm{nat}}F(k) \\ {}^{\mathrm{nat}}_{\mathrm{mix}}F(k) \\ {}^{70}_{\mathrm{nat}}F(k) \\ {}^{73}_{76}F(k) \end{pmatrix} = \mathbf{W}' \begin{pmatrix} S_{\mathrm{NN}}(k) - 1 \\ \left[S_{\mathrm{CC}}(k) / c_{\mathrm{Ge}}c_{\mathrm{Se}}\right] - 1 \\ S_{\mathrm{NC}}(k) \end{pmatrix}, \tag{10}$$

where in the case of $GeSe_3$ the weighting factor matrix is given by

$$\frac{\mathbf{W}'}{\mathrm{barn}} = \begin{pmatrix} 0.644(1) & 0.00009(2) & 0.035(1) \\ 0.926(7) & 0.0069(4) & -0.369(11) \\ 0.716(4) & 0.0072(7) & 0.331(2) \\ 1.088(16) & 0.093(3) & -1.468(31) \end{pmatrix}, \tag{11}$$

and in the case of $GeSe_4$ the weighting factor matrix is given by

$$\frac{\mathbf{W}'}{\mathrm{barn}} = \begin{pmatrix} 0.642(1) & 0.00007(2) & 0.034(2) \\ 0.945(8) & 0.0059(3) & -0.373(11) \\ 0.699(3) & 0.0061(6) & 0.327(2) \\ 1.16(2) & 0.079(2) & -1.518(33) \end{pmatrix}. \tag{12}$$

The corresponding partial pair-distribution functions are denoted by $g_{IJ}(r)$ $(I, J = \mathrm{N}, \mathrm{C})$, and are related to the $g_{\alpha\beta}(r)$ functions via the relations

$$g_{\mathrm{NN}}(r) = c^2_{\mathrm{Ge}}g_{\mathrm{GeGe}}(r) + c^2_{\mathrm{Se}}g_{\mathrm{SeSe}}(r) + 2c_{\mathrm{Ge}}c_{\mathrm{Se}}g_{\mathrm{GeSe}}(r), \tag{13}$$

$$g_{\mathrm{CC}}(r) = c_{\mathrm{Ge}}c_{\mathrm{Se}}\left[g_{\mathrm{GeGe}}(r) + g_{\mathrm{SeSe}}(r) - 2g_{\mathrm{GeSe}}(r)\right], \tag{14}$$

$$g_{\mathrm{NC}}(r) = c_{\mathrm{Ge}}\left[g_{\mathrm{GeGe}}(r) - g_{\mathrm{GeSe}}(r)\right] - c_{\mathrm{Se}}\left[g_{\mathrm{SeSe}}(r) - g_{\mathrm{GeSe}}(r)\right]. \tag{15}$$

Equation (9) shows that $S_{\mathrm{NN}}(k)$ would be measured directly in a diffraction experiment if $b_{\mathrm{Ge}} = b_{\mathrm{Se}}$, which is almost the case for the $^{\mathrm{nat}}\mathrm{Ge}^{\mathrm{nat}}\mathrm{Se}_3$ and $^{\mathrm{nat}}\mathrm{Ge}^{\mathrm{nat}}\mathrm{Se}_4$ samples because Ge and Se of natural isotopic abundance have very similar neutron scattering lengths. It follows that $g_{\mathrm{NN}}(r)$ will describe the sites of the scattering nuclei but cannot distinguish between the chemical species that occupy those sites, i.e., it gives information on the topological ordering. The mean coordination number $\bar{n}$ is given by

$$\bar{n} = 4\pi\rho\int_{r_1}^{r_2} \mathrm{d}r\, r^2 g_{\mathrm{NN}}(r) = c_{\mathrm{Ge}}\bar{n}_{\mathrm{Ge}} + c_{\mathrm{Se}}\bar{n}_{\mathrm{Se}}, \tag{16}$$

where the mean coordination number of Ge atoms $\bar{n}_{\mathrm{Ge}} \equiv \bar{n}^{\mathrm{Ge}}_{\mathrm{Ge}} + \bar{n}^{\mathrm{Se}}_{\mathrm{Ge}}$ and the mean coordination number of Se atoms $\bar{n}_{\mathrm{Se}} \equiv \bar{n}^{\mathrm{Se}}_{\mathrm{Se}} + \bar{n}^{\mathrm{Ge}}_{\mathrm{Se}}$. According to the "8-N" rule, in which $\bar{n}_{\mathrm{Ge}} = 4$ and $\bar{n}_{\mathrm{Se}} = 2$, it follows that $\bar{n} = 2.5$ for $GeSe_3$ and $\bar{n} = 2.4$ for $GeSe_4$. In comparison, $S_{\mathrm{CC}}(k)$ will give information on the chemical ordering and, according to Equation (14), there will be a positive peak or negative trough in $g_{\mathrm{CC}}(r)$ if there is a preference at a given distance for like or unlike chemical species, respectively. Finally, $g_{\mathrm{NC}}(r)$ will describe the cross-correlation between sites and their occupancy by a given chemical species. A full description of the Bhatia-Thornton formalism as applied to binary network glass-forming systems is given elsewhere (Salmon, 1992, 2007b).

Equations (2) and (10) can be solved to give the full set of $S_{\alpha\beta}(k)$ or $S_{IJ}(k)$ functions by using the SVD method, which is described by Ludwig et al. (1987) and Zeidler et al. (2010). In the case of Equation (2), the two-norm condition number for the normalized weighting factor matrix is $\kappa'_2 = 144$ for $GeSe_3$ vs. $\kappa'_2 = 236$ for $GeSe_4$, respectively, i.e., the weighting

factor matrix for $GeSe_3$ is better conditioned (Zeidler et al., 2010). In the case of Equation (10), $\kappa_2' = 63$ for $GeSe_3$ vs. $\kappa_2' = 76$ for $GeSe_4$, respectively, i.e., the weighting factor matrices for the $S_{IJ}(k)$ functions are better conditioned than those for the $S_{\alpha\beta}(k)$ functions.

We note that if Equation (2) is re-written to include only the total structure factors for the nat-mix, 70-nat and 73-76 samples, then the two-norm condition number for the normalized weighting factor matrix becomes $\kappa_2' = 133$ for $GeSe_3$ vs. $\kappa_2' = 221$ for $GeSe_4$. The resultant $S_{\alpha\beta}(k)$ functions are in agreement with those obtained by using all four of the total structure factors and the SVD method (Rowlands, 2015). Inclusion of the total structure factor for the nat-nat sample does not improve the conditioning of the weighting factor matrix because ${}^{\rm nat}_{\rm nat}F(k)$ does not contain information on the chemical ordering in the glass: As $b_{^{\rm nat}{\rm Ge}} \simeq b_{^{\rm nat}{\rm Se}}$ it follows from Equation (9) that ${}^{\rm nat}_{\rm nat}F(k) \simeq \langle b \rangle^2 \left[S_{\rm NN}(k) - 1\right]$.

In practice, a diffractometer can measure over only a finite scattering vector range up to a maximum value $k_{\rm max}$, which is equivalent to the multiplication of the ideal diffraction pattern by a window function $M(k)$ where $M(k \leq k_{\rm max}) = 1$ and $M(k > k_{\rm max}) = 0$. The Fourier transform of this window function is given by

$$M(r) = \frac{1}{\pi}\int_0^{k_{\rm max}} {\rm d}k \cos(kr) = \frac{k_{\rm max}}{\pi}{\rm sinc}\left(k_{\rm max}r\right) \tag{17}$$

where ${\rm sinc}(y) \equiv \sin(y)\,/\,y$. To help in identifying those features in a measured $g_{\alpha\beta}(r)$ function that are an artifact of $M(r)$, it is convenient to consider the density function

$$\begin{aligned} d'_{\alpha\beta}(r) &= \frac{2}{\pi}\int_0^{\infty} {\rm d}k \left[S_{\alpha\beta}(k) - 1\right] k\, M(k)\, \sin(kr) \\ &= d_{\alpha\beta}(r) \otimes M(r), \end{aligned} \tag{18}$$

where $d_{\alpha\beta}(r) \equiv 4\pi\rho r\left[g_{\alpha\beta}(r) - 1\right]$ and $\otimes$ denotes the one-dimensional convolution operator. A least-squares fit to $d'_{\alpha\beta}(r)$ can then be made by using a sum of Gaussian functions, representing the peaks in $d_{\alpha\beta}(r)$, convolved with $M(r)$ (Martin et al., 2003; Salmon and Petri, 2003). A similar procedure can also be adopted for the first-difference density functions $\Delta D'_{\rm Ge}(r) \equiv 4\pi\rho r\left[\Delta G_{\rm Ge}(r) \,/\, |\Delta G_{\rm Ge}(r \to 0)|\right] \otimes M(r)$ and $\Delta D'(r) \equiv 4\pi\rho r\left[\Delta G(r) \,/\, |\Delta G(r \to 0)|\right] \otimes M(r)$. Other window functions can be used to reduce the severity of Fourier transform artifacts.

3. EXPERIMENTAL

3.1. Synthesis and Characterization of Glassy $GeSe_3$ and $GeSe_4$

The Ge isotopes used for the sample preparation were processed in order to remove oxide impurities. Finely powdered isotope was loaded into a glass crucible, with a fritted glass bottom of 3 μm pore size, and placed within a reduction furnace. The furnace was flushed with Ar gas to remove air, and the gas flow was switched to hydrogen. Next, the furnace temperature was increased to 873 K at a rate of 4 K $\rm min^{-1}$, left for 48 h, and reduced to ambient at a rate of 1 K $\rm min^{-1}$. The gas flow was then switched back to Ar. This procedure gave a yield of ∼83% and delivered Ge powder that had changed in appearance from black to metallic grey. Infra-red transmission spectroscopy experiments on the powder showed no indication of the Ge-O absorption band at ∼879 $\rm cm^{-1}$ (Madon et al., 1991; Micoulaut et al., 2006), consistent with test experiments in which the reduction procedure was used to remove the oxygen from crystalline GeO_2, or the oxygen impurities from crystalline Ge.

Two diffraction experiments were performed, the first on glassy $GeSe_4$ and the second on glassy $GeSe_3$. Each $GeSe_4$ sample was prepared by loading elemental $^{\rm nat}$Ge (99.999%, Alfa Aesar), ^{70}Ge (95.30% ^{70}Ge, 4.10% ^{72}Ge, 0.51 % ^{76}Ge, 0.05% ^{74}Ge and 0.04% ^{73}Ge, Isoflex USA), or ^{73}Ge (95.60% ^{73}Ge, 2.34% ^{72}Ge, 2.03% ^{74}Ge, 0.025% ^{70}Ge and 0.005% ^{76}Ge, Isoflex USA) together with $^{\rm nat}$Se (99.999+%, Sigma Aldrich), ^{76}Se (99.8 % ^{76}Se and 0.20 % ^{77}Se, Isoflex USA), or $^{\rm mix}$Se (a 49.5:50.5 mixture by mass of $^{\rm nat}$Se and ^{76}Se) in the required mass ratio into a silica ampoule within a high-purity argon-filled glove box. The ampoule, of 5 mm inner diameter and 1 mm wall thickness, had previously been etched using a 48 wt% solution of hydrofluoric acid, rinsed using water then acetone, and baked dry under vacuum at 1073 K for 2 h. Once loaded, the ampoule was isolated using a Young's tap, and transferred to a vacuum line where it was sealed under a pressure of 10^{-5} Torr. The sealed ampoule was placed in a furnace that was rocked at a rate of 0.57 rpm with a maximum rocking angle of 30° to the horizontal. The furnace was heated at a rate of 1 K $\rm min^{-1}$ from ambient to a temperature $T = 1{,}248$ K, dwelling for 4 h each at $T = 494$ K, $T = 958$ K, and $T = 1{,}211$ K, near to the melting and boiling points of Se and the melting point of Ge, respectively. The highest temperature was maintained for 48 h before the rocking motion was stopped, the furnace was placed vertically and left for 4 h, and the furnace was then cooled at a rate of 1 K $\rm min^{-1}$ to $T = 928$ K (∼100 K above the melting point of $GeSe_4$) where the sample was left to equilibrate for 4 h. The ampoule was then dropped into an ice/water mixture. The glassy samples separated cleanly from the their silica ampoules, which were broken open in a high-purity argon-filled glove box. The $GeSe_3$ samples were prepared from the $GeSe_4$ samples by adding elemental Ge of matched isotopic abundance, quenching from 1,027 K, and otherwise following the same method. The mass of the prepared samples was ∼1.5–2.2 g, and the precise sample stoichiometry, as determined by mass, was 0.2496(3) Ge: 0.7504(3) Se for $GeSe_3$ vs. 0.1998(3) Ge: 0.8002(3) Se for $GeSe_4$.

The measured infrared transmission spectra for the $GeSe_3$ and $GeSe_4$ glasses showed no indication of Ge-O or Se-O impurity bands, e.g., in the region around 735–781 $\rm cm^{-1}$ (Savage and Nielsen, 1965). A similarly prepared sample of $GeSe_4$ glass, but with only 12 h of rocking, was characterized using energy dispersive X-ray spectroscopy and Raman spectroscopy, and was found to be homogeneous on a sub-micron to centimeter length scale (Lucas et al., 2019). The mass density, as measured using a helium pycnometer, was 4.309(3) g $\rm cm^{-3}$ or 4.334(4) g $\rm cm^{-3}$ for the $GeSe_3$ and $GeSe_4$ glasses, respectively, corresponding to an atomic number density of $\rho = 0.03353(2)$ $\rm Å^{-3}$ or $\rho = 0.03359(3)$ $\rm Å^{-3}$, respectively. A single glass transition temperature of $T_g = 523(3)$ K for $GeSe_3$ or $T_g = 463(3)$ K for

$GeSe_4$ was measured by using modulated differential scanning calorimetry with a scan rate of 3 K min^{-1} and modulation of 1 K per 100 s.

3.2. Neutron Diffraction Experiments

The diffraction experiments were performed using the D4c instrument at the Institut Laue-Langevin (Fischer et al., 2002). The Cu(220) reflections from a monochromator gave an incident neutron wavelength $\lambda = 0.4990(1)$ Å, and the $\lambda/2$ reflections were suppressed by using a Rh filter. The monochromator crystals were orientated to focus the neutron beam in both the horizontal and vertical directions, thus maximizing the flux of neutrons at the sample position. The same cylindrical vanadium container, of inner diameter 4.8 mm and wall thickness 0.1 mm, was used for each set of experiments to ensure a reproducible scattering geometry. The samples were loaded into the container within a high-purity argon-filled glove box. Diffraction patterns were measured at room temperature ($\simeq$298 K) for each of the samples in its container, the empty container, the empty instrument, and a cylindrical vanadium rod of diameter 6.08 mm for normalization purposes. The diffraction pattern was also measured for a slab of neutron absorbing $^{10}B_4C$ of dimensions similar to the sample in order to estimate the effect of the sample's attenuation on the background count-rate at small scattering angles (Bertagnolli et al., 1976). The relative counting times for the sample-in-container and empty container measurements were optimized in order to minimize the statistical error on the container-corrected intensity (Salmon et al., 2016). The counting times for each of the sample-in-container measurements was ~18 h for the $GeSe_3$ experiment vs. ~22 h for the $GeSe_4$ experiment. The count-rate stability was checked by saving the measured intensity for a given setup at regular intervals, and a comparison between these intensities showed no deviation within the statistical error. The count-rate stability of the D4c instrument is measured to be ±0.012(8)% (Zeidler et al., 2012).

The total structure factors were obtained by following the data analysis procedure described by Salmon et al. (1998), and self-consistency checks were made to assess the reliability of the measured functions. For instance, it is necessary that (i) the measured intensities are greater than or equal to zero which leads to the condition $S_{NN}(k)S_{CC}(k) \geq S_{NC}(k)^2$; (ii) each of the Faber-Ziman partial structure factors satisfies the sum-rule relation $\int_0^\infty dk\, k^2 \left[S_{\alpha\beta}(k) - 1\right] = -2\pi^2\rho$ as found by taking the low-r limit of Equation (5); (iii) the measured $g_{\alpha\beta}(r)$ functions oscillate about zero at r-values smaller than the distance of closest approach between two atoms; and (iv) when these oscillations in $g_{\alpha\beta}(r)$ are set to zero, the back Fourier transform should be in good overall agreement with the original partial structure factor.

4. RESULTS

There is significant contrast between the total structure factors $F(k)$ measured for the different isotopically enriched samples of glassy $GeSe_3$ or $GeSe_4$ (**Figure 1**). A so-called first sharp diffraction peak is observable at $k_{FSDP} = 1.06(1)$ Å^{-1} for $GeSe_3$ vs. $k_{FSDP} = 1.12(2)$ Å^{-1} for $GeSe_4$, and is a signature of ordering on an intermediate length scale (Salmon, 1994). As

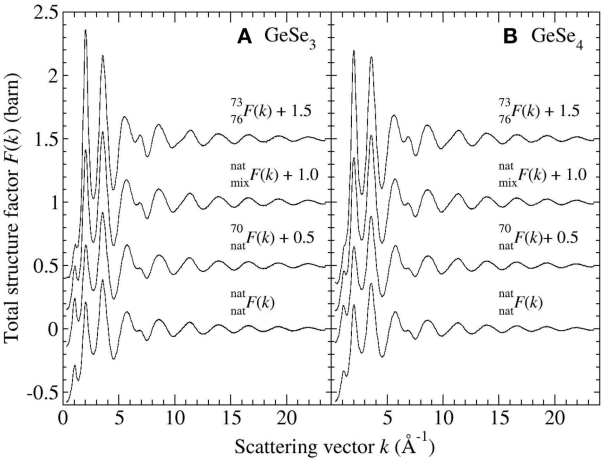

FIGURE 1 | The total structure factors $F(k)$ for glassy **(A)** $GeSe_3$ and **(B)** $GeSe_4$. The solid curves with vertical error bars represent the measured functions, where the size of an error bar is smaller than the curve thickness at most k values.

shown in **Figure 2**, the FSDP appears as a peak in $\Delta F_{Ge}(k)$, for which the Ge-Ge and Ge-Se partial structure factors receive positive weighting factors [Equation (7)], and as a trough in $\Delta F(k)$, for which the Ge-Ge and Se-Se partial structure factors receive negative and positive weighting factors, respectively [Equation (8)]. These observations are consistent with the FSDP having contributions from both $S_{GeGe}(k)$ and $S_{GeSe}(k)$.

Figure 3 shows the $\Delta D'_{Ge}(r)$ and $\Delta D'(r)$ functions for glassy $GeSe_3$ and $GeSe_4$, obtained by Fourier transforming the spline-fitted reciprocal-space functions shown in **Figure 2** with $k_{max} = 23.5$ Å^{-1}. The first peaks in $\Delta D'_{Ge}(r)$ and $\Delta D'(r)$ were assumed to have contributions solely from Ge-Se and Se-Se nearest-neighbors, respectively, i.e., homonuclear Ge-Ge bonds were assumed to be rare. The first peak in each function was then fitted to a single Gaussian function convoluted with the modification function $M(r)$. In the case of $GeSe_3$, the fits gave a Ge-Se nearest-neighbor distance $\bar{r}_{GeSe} = 2.37(2)$ Å with $\bar{n}^{Se}_{Ge} = 4.02(2)$ and a Se-Se nearest-neighbor distance $\bar{r}_{SeSe} = 2.35(2)$ Å with $\bar{n}^{Se}_{Se} = 0.72(2)$, corresponding to a goodness-of-fit parameter R_χ (Wright, 1993) of 0.055 or 0.048, respectively, for a fitted range of 1.5–3.0 Å. In the case of $GeSe_4$, the fits gave $\bar{r}_{GeSe} = 2.37(2)$ Å with $\bar{n}^{Se}_{Ge} = 4.02(5)$ and $\bar{r}_{SeSe} = 2.35(2)$ Å with $\bar{n}^{Se}_{Se} = 1.01(2)$, corresponding to an R_χ value of 0.022 or 0.044, respectively, for a fitted range of 1.5–3.0 Å.

Figure 4 shows the full set of partial structure factors $S_{\alpha\beta}(k)$ for glassy $GeSe_3$, as extracted from the total structure factors shown in **Figure 1A** by using the SVD method. The results show that $S_{GeGe}(k)$ has the most prominent FSDP at $k_{FSDP} = 1.01(1)$ Å^{-1}, and that $S_{GeSe}(k)$ also has a small FSDP at $k_{FSDP} = 1.11(1)$ Å^{-1}. The density functions $d'_{\alpha\beta}(r)$ of **Figure 5A** were obtained by Fourier transforming the spline fitted $S_{\alpha\beta}(k)$ functions of **Figure 4** with $k_{max} = 23.5$ Å^{-1}, where a Lorch window function (Lorch, 1969; Salmon, 2006) was also applied to $S_{GeGe}(k)$ in order to reduce Fourier transform artifacts. The

first peak in $d'_{GeSe}(r)$ and $d'_{SeSe}(r)$ was fitted to a single Gaussian function convoluted with $M(r)$. The fits gave $\bar{r}_{GeSe} = 2.37(2)$ Å with $\bar{n}^{Se}_{Ge} = 4.00(2)$ and $\bar{r}_{SeSe} = 2.35(2)$ Å with $\bar{n}^{Se}_{Se} = 0.70(2)$, corresponding to an R_χ value of 0.048 or 0.047, respectively, for a fitted range of 1.5–3.0 Å. These values are consistent with those obtained from the first-difference functions, and point to a network structure that is built from $Ge(Se_4)_{1/2}$ tetrahedra and Se_n chains (n is an integer ≥ 2) where the homonuclear Se-Se bond distance is 2.35(2) Å. The peak in $d'_{GeGe}(r)$ at 2.70(2) Å has a position that is larger than expected for homonuclear Ge-Ge bond distances of 2.33–2.42 Å (Salmon, 2007a), and it was therefore discounted as a real feature. In the structure of high-temperature crystalline $GeSe_2$, the Ge-Ge distances for edge-sharing (ES) and corner-sharing (CS) $Ge(Se_4)_{1/2}$ tetrahedra are 3.05 and 3.51–3.60 Å, respectively (Dittmar and Schäfer, 1976). The peaks in $d'_{GeGe}(r)$ at 3.04(3) and 3.58(2) Å were therefore assigned to the Ge-Ge distances for ES and CS $Ge(Se_4)_{1/2}$ tetrahedra, respectively.

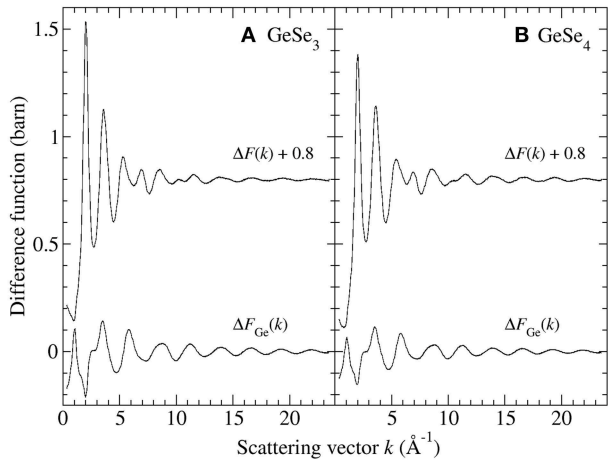

FIGURE 2 | The first-difference functions $\Delta F_{Ge}(k)$ and $\Delta F(k)$ for glassy **(A)** $GeSe_3$ and **(B)** $GeSe_4$. The solid curves with vertical error bars represent the measured functions, where the size of an error bar is smaller than the curve thickness at most k values.

Figure 6 shows the full set of partial structure factors $S_{\alpha\beta}(k)$ for glassy $GeSe_4$, as extracted from the total structure factors shown in **Figure 1B** by using the SVD method. The results show that $S_{GeGe}(k)$ has the most prominent FSDP at $k_{FSDP} = 0.97(2)$ Å^{-1}, and that $S_{GeSe}(k)$ also has a small FSDP at $k_{FSDP} = 1.08(2)$ Å^{-1}. The density functions $d'_{\alpha\beta}(r)$ of **Figure 5B** were obtained by Fourier transforming the spline fitted $S_{\alpha\beta}(k)$ functions of **Figure 6** with $k_{max} = 23.5$ Å^{-1}, where a cosine window function was also applied to $S_{GeGe}(k)$ over the range $21.45 \leq k$ (Å^{-1}) ≤ 23.5 in order to reduce Fourier transform artifacts. The first peak in $d'_{GeSe}(r)$ and $d'_{SeSe}(r)$ was fitted to a single Gaussian function convoluted with $M(r)$. The fits gave $\bar{r}_{GeSe} = 2.37(2)$ Å with $\bar{n}^{Se}_{Ge} = 4.04(5)$ and $\bar{r}_{SeSe} = 2.35(2)$ Å with $\bar{n}^{Se}_{Se} = 1.00(2)$, corresponding to an R_χ value of 0.055

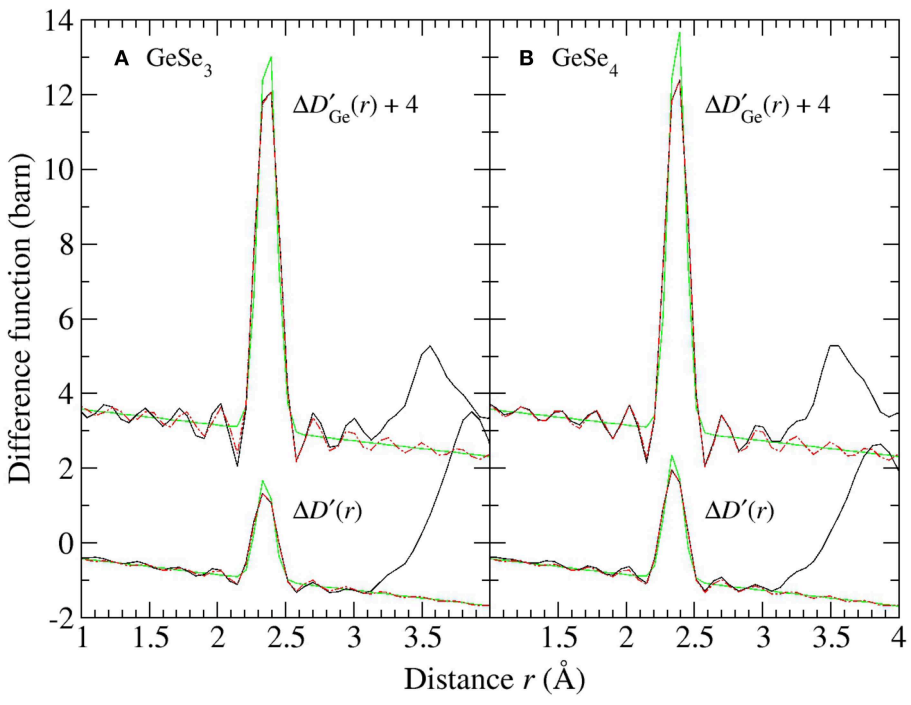

FIGURE 3 | The first-difference density functions $\Delta D'_{Ge}(r)$ and $\Delta D'(r)$ for glassy **(A)** $GeSe_3$ and **(B)** $GeSe_4$ where the solid (black) curves were obtained by spline-fitting and Fourier transforming the $\Delta F_{Ge}(k)$ and $\Delta F(k)$ functions shown in **Figure 2**. In each case, the chained (red) curve shows a fit of the first peak in the measured function to a single Gaussian function [light solid (green) curve] convoluted with $M(r)$.

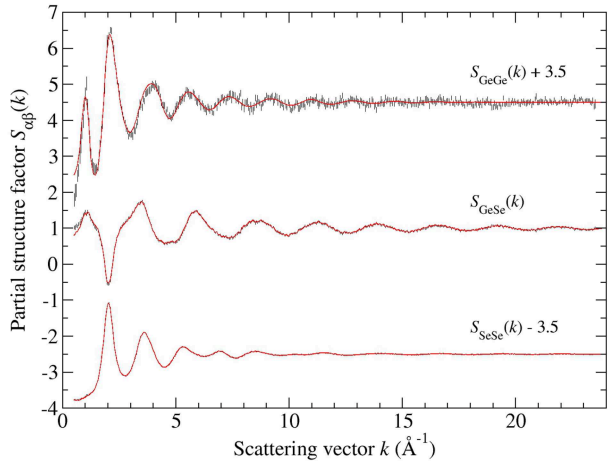

FIGURE 4 | The Faber-Ziman partial structure factors $S_{\alpha\beta}(k)$ for glassy $GeSe_3$, obtained from the measured total structure factors of **Figure 1A** by using the SVD method. The vertical error bars represent the measured data points with statistical errors. The solid (red) curves are the back Fourier transforms of the corresponding partial pair-distribution functions $g_{\alpha\beta}(r)$ given by the solid curves in **Figure 7**.

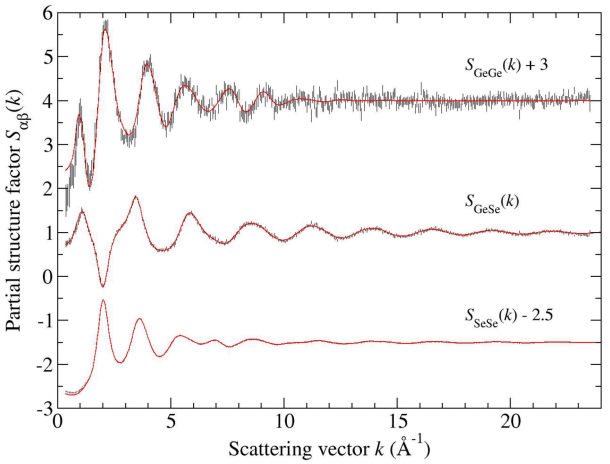

FIGURE 6 | The Faber-Ziman partial structure factors $S_{\alpha\beta}(k)$ for glassy $GeSe_4$, obtained from the measured total structure factors of **Figure 1B** by using the SVD method. The vertical error bars represent the measured data points with statistical errors. The solid (red) curves are the back Fourier transforms of the corresponding partial pair-distribution functions $g_{\alpha\beta}(r)$ given by the solid curves in **Figure 8**.

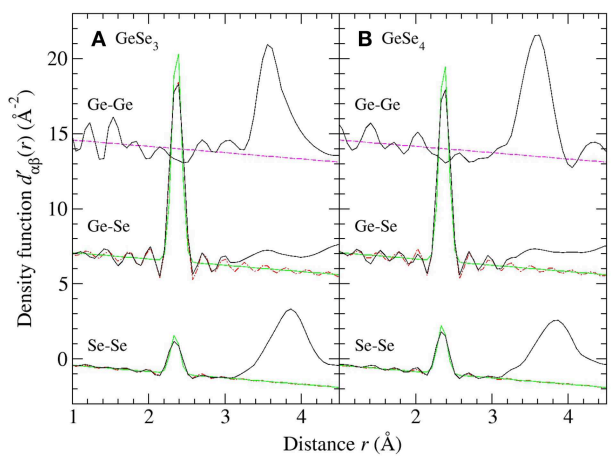

FIGURE 5 | The density functions $d'_{\alpha\beta}(r)$ for glassy **(A)** $GeSe_3$ and **(B)** $GeSe_4$ where the solid (black) curves were obtained by Fourier transforming the spline-fitted $S_{\alpha\beta}(k)$ functions shown in **Figures 4**, **6**, respectively. For $d'_{GeGe}(r)$, the broken (magenta) line gives the locus of points for which $d'_{GeGe}(r) = -4\pi\rho r$. For $d'_{GeSe}(r)$ and $d'_{SeSe}(r)$, the chained (red) curve shows a fit of the first peak to a single Gaussian function [light solid (green) curve] convoluted with $M(r)$. The Ge-Se and Ge-Ge data sets have been shifted vertically for clarity of presentation.

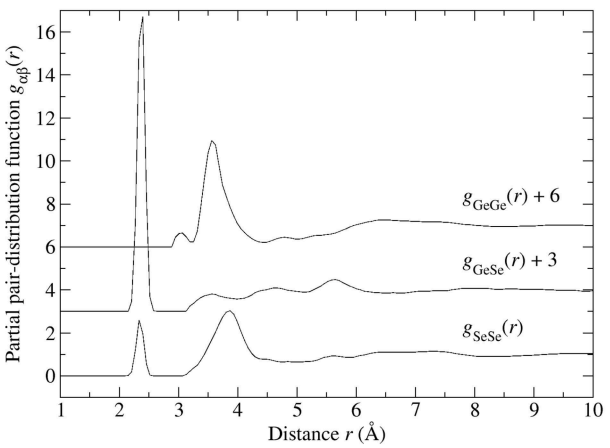

FIGURE 7 | The partial pair-distribution functions $g_{\alpha\beta}(r)$ for glassy $GeSe_3$ after the effect of $M(r)$ has been removed.

or 0.052, respectively, for a fitted range of 1.5–3.0 Å. These values are consistent with those obtained from the first-difference functions, and point to a network structure that is built from $Ge(Se_4)_{1/2}$ tetrahedra and Se_n chains. The $d'_{GeGe}(r)$ function shows no evidence of homonuclear Ge-Ge bonds, and does not display a peak at ≃3.04 Å that can be assigned to ES $Ge(Se_4)_{1/2}$ tetrahedra. The first peak at 3.59(1) Å is, however, broader than the corresponding feature for $GeSe_3$, with a low-r cutoff of 3.07(3) Å that is typical of ES tetrahedral distances.

The final Ge-Se and Se-Se $d_{\alpha\beta}(r)$ functions were obtained by merging smoothly the Gaussian representation of $d_{GeSe}(r)$ or $d_{SeSe}(r)$ in the first-peak region, where the effect of $M(r)$ on $d'_{GeSe}(r)$ and $d'_{SeSe}(r)$ is measurable, with the $d'_{\alpha\beta}(r)$ functions at higher-r values. The $d'_{GeSe}(r)$ function at these higher-r values was smoothed by the application of a Lorch window function. In comparison, $d_{GeGe}(r)$ was set equal to the measured $d'_{GeGe}(r)$ function at all r values. In each case, the unphysical oscillations at r values less than the distance of closest approach between the centers of two atoms were set to $d_{\alpha\beta}(r) = -4\pi\rho r$. The final $d_{\alpha\beta}(r)$ functions were then converted to the $g_{\alpha\beta}(r)$ functions shown in **Figures 7**, **8** for glassy $GeSe_3$ and $GeSe_4$, respectively. The back Fourier transforms of these $g_{\alpha\beta}(r)$ functions are

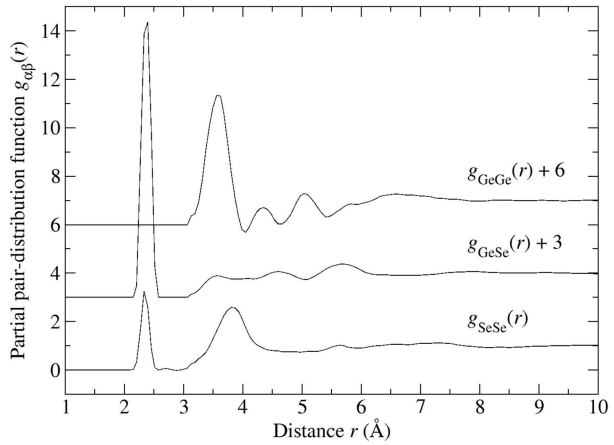

FIGURE 8 | The partial pair-distribution functions $g_{\alpha\beta}(r)$ for glassy $GeSe_4$ after the effect of $M(r)$ has been removed.

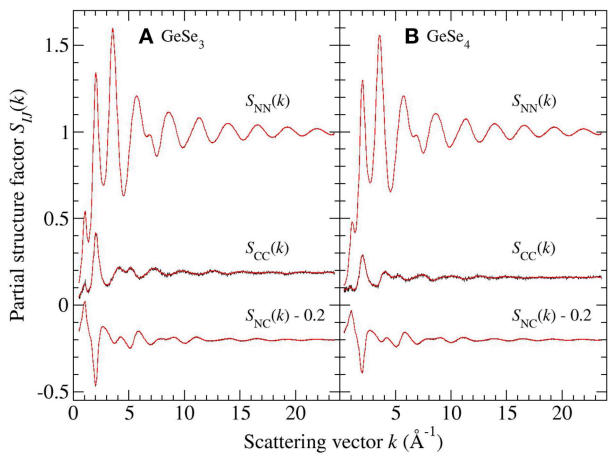

FIGURE 9 | The Bhatia-Thornton partial structure factors $S_{IJ}(k)$ for glassy **(A)** $GeSe_3$ and **(B)** $GeSe_4$, obtained from the measured total structure factors of **Figure 1** by using the SVD method. The vertical error bars represent the measured data points with statistical errors. The solid (red) curves are spline fits used to obtain the partial pair-distribution functions $g_{IJ}(r)$ shown in **Figure 10**.

compared to the measured partial structure factors for glassy $GeSe_3$ and $GeSe_4$ in **Figures 4**, **6**, respectively.

The Bhatia-Thornton partial structure factors $S_{IJ}(k)$ and corresponding partial pair-distribution functions $g_{IJ}(r)$ are shown in **Figures 9**, **10**, respectively. As discussed in section 2, the weighting factor matrix used to obtain the $S_{IJ}(k)$ functions is better conditioned than the matrix used to obtain the $S_{\alpha\beta}(k)$ functions, which accounts for the reduction in size of the error bars for $S_{CC}(k)$ as compared to $S_{GeGe}(k)$. For each material, the inequality relation $S_{NN}(k)S_{CC}(k) \geq S_{NC}(k)^2$ is fulfilled within the statistical error at all k values (section 3.2). Each set of partial structure factors shows an FSDP in the range 1.01(2)–1.05(2) Å^{-1} for $GeSe_3$ vs. 0.91(2)–1.11(2) Å^{-1} for $GeSe_4$, and a principal peak or trough in the range 2.01(2)–2.04(2) Å^{-1} for $GeSe_3$ vs. 1.99(2)–2.03(2) Å^{-1} for $GeSe_4$.

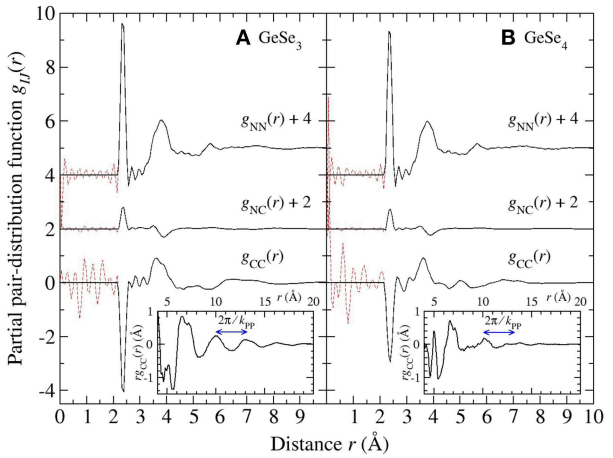

FIGURE 10 | The Bhatia-Thornton partial pair-distribution functions $g_{IJ}(r)$ for glassy **(A)** $GeSe_3$ and **(B)** $GeSe_4$. The solid black curves were obtained by Fourier transforming the spline fitted partial structure factors shown in **Figure 9** and setting the unphysical oscillations at r values smaller than the distance of closest approach between the centers of two atoms [broken (red) curves] to the $g_{IJ}(r \rightarrow 0)$ limit. The insets show the larger-r features in $rg_{CC}(r)$, and the arrowed lines indicate the periodicity expected from the position of the principal peak in $S_{CC}(k)$ at $k_{PP} \simeq 2.03$ Å^{-1}.

As in the case of glassy $GeSe_2$, the FSDP in $S_{CC}(k)$ for glassy $GeSe_3$ and $GeSe_4$ indicates the presence of concentration fluctuations on an intermediate length scale (Penfold and Salmon, 1991; Salmon, 1992). This feature arises from the Ge-Ge and Ge-Se pair-correlation functions, in keeping with the relation

$$S_{CC}(k) = c_{Ge}c_{Se}\{1 + c_{Ge}c_{Se}\left[S_{GeGe}(k) + S_{SeSe}(k) - 2S_{GeSe}(k)\right]\} \quad (19)$$

and the measured $S_{\alpha\beta}(k)$ functions shown in **Figures 4**, **6**. From the properties of Fourier transforms, a sharp peak in $S_{CC}(k)$ at k_i is associated with real-space ordering of periodicity $2\pi/k_i$ that decays with a correlation length of $2\pi/\Delta k_i$, where Δk_i is the peak width (Salmon, 1994). The most prominent feature in $S_{CC}(k)$ is the principal peak at $k_{PP} \simeq 2.03$ Å^{-1} with a height that decreases in the order from $GeSe_2$ to $GeSe_3$ to $GeSe_4$. The Fourier transform of $S_{CC}(k)$ shows oscillations of periodicity $2\pi/k_{PP}$ that are readily discernable for $GeSe_2$ (Salmon, 2006) and $GeSe_3$ (inset to **Figure 10A**). Similarly, the small FSDP in $S_{CC}(k)$ at k_{FSDP} will originate from a real-space length scale that is commensurate with $2\pi/k_{FSDP}$, i.e., the Ge atoms in the network structures are not distributed uniformly on an intermediate length scale. In the context of FPMD simulations, the appearance of this FSDP is significant because its reproduction has necessitated the use of exchange and correlation energy functionals that enhance charge transfer between the Ge and Se atoms (Massobrio et al., 1999, 2000, 2010; Micoulaut et al., 2009, 2013).

5. DISCUSSION

5.1. Network Structure

The measured Ge-Se coordination numbers for glassy $GeSe_2$ (Petri et al., 2000; Salmon and Petri, 2003), $GeSe_3$ and $GeSe_4$

indicate the formation of $Ge(Se_4)_{1/2}$ tetrahedra (**Table 1**). The Ge-Se:Se-Se distance ratio, obtained from the nearest-neighbor Ge-Se and next-nearest-neighbor Se-Se peak positions, is 0.607(6), 0.616(6), or 0.619(6) for $GeSe_2$, $GeSe_3$, and $GeSe_4$, respectively, and the intra-tetrahedral Se-Ge-Se bond angle obtained from these peak positions is 111(1)°, 109(1)°, or 108(1)°, respectively. In comparison, for a regular tetrahedron, the Ge-Se:Se-Se distance ratio is $\sqrt{3/8} = 0.612$, and the intra-tetrahedral Se-Ge-Se bond angle is 109.47°. The Ge-Se-Se bond angle, estimated from the first and second peak positions in $g_{GeSe}(r)$, is 98(2)° for both $GeSe_3$ and $GeSe_4$.

For all of the glasses, the peak in $g_{SeSe}(r)$ at $\bar{r}_{SeSe} \simeq 2.34$ Å originates from homonuclear Se-Se bonds, and the corresponding coordination number increases with the Se content of the glass. A comparison of the $\bar{n}_{Se}^{Se}$ values with those found from ^{77}Se NMR experiments (Gjersing et al., 2010b; Kaseman et al., 2016) is given in **Table 2**. Here, the NMR experiments provide the fractions of Se atoms in Se-Se-Se vs. Ge-Se-Se connections, and the corresponding Se-Se coordination numbers follow from $\bar{n}_{Se}^{Se}(\text{Se-Se-Se}) = \left(N_{Se,Se\text{-}Se\text{-}Se} / N_{Se}\right) \times 2$ and $\bar{n}_{Se}^{Se}(\text{Ge-Se-Se}) = \left(N_{Se,Ge\text{-}Se\text{-}Se} / N_{Se}\right) \times 1$, where $N_{Se,Se\text{-}Se\text{-}Se}$ is the number of Se atoms bound to two other Se atoms in a Se-Se-Se connection, $N_{Se,Ge\text{-}Se\text{-}Se}$ is the number of Se atoms bound to one Ge atom and one Se atom in a Ge-Se-Se connection, and N_{Se} is the total number of Se atoms in the glass.

For $GeSe_2$, the peak in $g_{GeGe}(r)$ at $\bar{r}_{GeGe}$=2.42(2) Å originates from homonuclear Ge-Ge bonds, but there is no evidence of these bonds in either $GeSe_3$ or $GeSe_4$. For $GeSe_2$ and $GeSe_3$, the peak in $g_{GeGe}(r)$ at $\bar{r}_{GeGe} \simeq 3.02$–3.04 Å originates from ES $Ge(Se_4)_{1/2}$ tetrahedra, but this feature is absent for $GeSe_4$. The associated inter-tetrahedral Ge-Se-Ge bond angle, estimated from the nearest-neighbor Ge-Se and ES Ge-Ge distances, is 80(1)°.

For all of the glasses, the peak in $g_{GeGe}(r)$ at $\bar{r}_{GeGe} \simeq 3.57$ Å will have a contribution from CS $Ge(Se_4)_{1/2}$ tetrahedra (Petri et al., 2000; Salmon and Petri, 2003), and the associated inter-tetrahedral Ge-Se-Ge bond angle, estimated from the nearest-neighbor Ge-Se and CS Ge-Ge distances, is 98(2)°. In comparison, for the high-temperature crystalline phase of $GeSe_2$ (Dittmar and Schäfer, 1976), the Ge-Se-Ge bond angle is in the range of 80.2–80.6° for ES tetrahedra vs. 96.2–100.1° for CS tetrahedra.

For $GeSe_3$ and $GeSe_4$, there will be contributions to $g_{GeGe}(r)$ from the Ge-Ge distances within Ge-Se_n-Ge connections. For instance, in the case of $GeSe_4$ there are peaks at 4.34(2) Å and 5.06(2) Å that do not appear to be Fourier transform artifacts, with coordination numbers of $\bar{n}_{Ge}^{Ge} = 0.33(2)$ and $\bar{n}_{Ge}^{Ge} = 1.28(2)$, respectively. If these peaks originate from Ge-Se-Se-Ge connections, then the associated Ge-Ge distance will depend on the relative rotation of these Ge atoms about the Se-Se bond, i.e., on the dihedral angle ϕ between two planes that contain both of the Se atoms and either the first or the second Ge atom in a Ge-Se-Se-Ge connection. For a Ge-Se-Se bond angle of 98° and bond distances of $\bar{r}_{GeSe} = 2.37$ Å and $\bar{r}_{SeSe} = 2.35$ Å, a Ge-Ge distance of 4.34 Å is obtained for $\phi \simeq 84°$, and a Ge-Ge distance of 5.06 Å is obtained for $\phi \simeq 120°$.

For each glass, the NDIS experiments give $\bar{n}_{Ge} = 4$ and $\bar{n}_{Se} = 2$ within the experimental error (**Table 2**), and the overall mean coordination numbers $\bar{n}$ are in agreement with those obtained from the first peak in the $g_{NN}(r)$ functions of **Figure 10** [see Equation (16)]. The NDIS results are therefore consistent with the expectations of the "8-N" rule (Zeidler et al., 2017). In comparison, the fraction of Se atoms in Ge-Se-Ge connections has been measured for several Ge_xSe_{1-x} glasses with $x \leq 1/3$ by using ^{77}Se NMR spectroscopy (Gjersing et al., 2010b; Kaseman et al., 2016). The Se-Ge coordination numbers for CS and ES connections are given by the expressions $\bar{n}_{Se}^{Ge}(\text{CS}) = \left(N_{Se,CS} / N_{Se}\right) \times 2$ and $\bar{n}_{Se}^{Ge}(\text{ES}) = \left(N_{Se,ES} / N_{Se}\right) \times 2$, respectively, where $N_{Se,CS}$ and $N_{Se,ES}$ are the numbers of Se atoms in CS and ES connections, respectively. The $\bar{n}_{Se}^{Ge}$ values extracted from the ^{77}Se NMR results for glassy $GeSe_2$ and $GeSe_4$ are compared to the NDIS results in **Table 2**. Both techniques give a mean coordination number $\bar{n}_{Se} = \bar{n}_{Se}^{Se} + \bar{n}_{Se}^{Ge} = 2$, although there is a discrepancy for $GeSe_4$ between the relative contributions to $\bar{n}_{Se}$ from $\bar{n}_{Se}^{Se}$ vs. $\bar{n}_{Se}^{Ge}$. A similar set of findings was obtained by re-interpreting the measured ^{77}Se MAS NMR spectra for glassy $GeSe_2$ and $GeSe_4$ (Gjersing et al., 2010b) by using the isotropic chemical shifts calculated for the ^{77}Se nucleus via density-functional-theory based NMR calculations for amorphous model structures generated by FPMD (Kibalchenko et al., 2011) (**Table 2**). The associated Ge-Se coordination numbers are given by $\bar{n}_{Ge}^{Se} = (c_{Se} / c_{Ge})\, \bar{n}_{Se}^{Ge} = [(1-x)/x]\, \bar{n}_{Se}^{Ge}$, and are also shown in **Table 2**. For the case of $GeSe_4$, the $\bar{n}_{Ge}^{Se}$ values extracted from the ^{77}Se NMR results are larger than expected from the "8-N" rule.

Within the framework of the "8-N" rule, the chemically ordered network (CON) and random covalent network (RCN) models provide simple but contrasting viewpoints of the network structures (Salmon, 2007a). In the CON, Ge-Se bonds are favored. It follows that only Ge-Se and Se-Se bonds are allowed for compositions with $x < 1/3$ such that $\bar{n}_{Ge}^{Se} = 4$, $\bar{n}_{Se}^{Se} =$

TABLE 1 | The positions $\bar{r}_{\alpha\beta}$ and coordination numbers $\bar{n}_{\alpha}^{\beta}$ found from the first few peaks in the partial pair-distribution functions $g_{\alpha\beta}(r)$ measured by NDIS in the work of Petri et al. (2000) and Salmon and Petri (2003) for glassy $GeSe_2$, and in the present work for glassy $GeSe_3$ and $GeSe_4$.

Glass	α–β	$\bar{r}_{\alpha\beta}$ (Å)	$\bar{n}_{\alpha}^{\beta}$	$\bar{r}_{\alpha\beta}$ (Å)	$\bar{n}_{\alpha}^{\beta}$	$\bar{r}_{\alpha\beta}$ (Å)	$\bar{n}_{\alpha}^{\beta}$
$GeSe_2$	Ge–Ge	2.42(2)	0.25(5)	3.02(2)	0.34(5)	3.57(2)	3.2(3)
	Ge–Se	2.36(2)	3.7(1)				
	Se–Se	2.32(2)	0.20(5)	3.89(2)	9.3(2)		
$GeSe_3$	Ge–Ge	–	–	3.04(3)	0.16(5)	3.57(2)	3.2(1)
	Ge–Se	2.37(2)	4.00(2)	3.57(3)			
	Se–Se	2.34(2)	0.70(2)	3.85(2)	9.2(2)		
$GeSe_4$	Ge–Ge	–	–	–	–	3.58(2)	2.5(2)
	Ge–Se	2.37(2)	4.04(5)	3.57(2)			
	Se–Se	2.35(2)	1.00(2)	3.83(2)	9.0(2)		

The coordination numbers were obtained from Equation (6) with r_1 set at the position of the minimum on the low-r side of a given peak in $g_{\alpha\beta}(r)$, and r_2 set at the position of either the minimum or shoulder on the high-r side of that peak.

TABLE 2 | The composition dependence of the nearest-neighbor coordination numbers.

Glass	Origin	$\bar{n}_{Ge}^{Se}$	$\bar{n}_{Ge}^{Ge}$	$\bar{n}_{Ge}$	$\bar{n}_{Se}^{Ge}$	$\bar{n}_{Se}^{Se}$	$\bar{n}_{Se}$	$\bar{n}$
$GeSe_2$	NDIS[a]	3.7(1)	0.25(5)	3.95(11)	1.85(5)	0.20(5)	2.05(7)	2.68(6)
	^{77}Se NMR[b]	3.68(13)	–	–	1.84(6)	0.160(8)	2.00(6)	–
	FPMD/^{77}Se NMR[c]	3.6	–	–	1.8	0.2	2	–
	FPMD[d]	3.55	0.25	3.80	1.77	0.3	2.07	2.65
	FPMD[e]	3.65	0.29	3.94	1.82	0.2	2.02	2.66
	CON	4	0	4	2	0	2	8/3 = 2.67
	RCN	2	2	4	1	1	2	8/3 = 2.67
$GeSe_3$	NDIS[f]	4.00(2)	0	4.00(2)	1.333(7)	0.70(2)	2.03(2)	2.52(3)
	FPMD[d]	3.87	0.13	4.00	1.29	0.71	2.00	2.5
	CON	4	0	4	4/3 = 1.333	2/3 = 0.667	2	2.5
	RCN	2.4	1.6	4	0.8	1.2	2	2.5
$GeSe_4$	NDIS[f]	4.04(5)	0	4.04(5)	1.01(1)	1.00(2)	2.01(2)	2.42(2)
	^{77}Se NMR[b]	4.32(15)	–	–	1.08(4)	0.90(2)	1.98(4)	–
	^{77}Se NMR[g]	4.37(19)	–	–	1.09(4)	0.91(2)	2.00(5)	–
	FPMD/^{77}Se NMR[c]	4.52	–	–	1.13	0.87	2	–
	FPMD[d]	3.92	0	3.92	0.98	1.00	1.98	2.368
	FPMD ($N = 120$)[h]	3.96	0	3.96	0.99	0.99	1.98	2.376
	FPMD ($N = 480$)[h]	3.85	0.36	4.21	0.96	1.04	2	2.442
	FPMD ($N = 480$)[i]	3.96	0.04	4.00	0.99	1.01	2	2.4
	FPMD ($N = 480$)[j]	3.94	0.04	3.98	0.99	1.02	2.01	2.396
	CON	4	0	4	1	1	2	2.4
	RCN	8/3 = 2.667	4/3 = 1.333	4	2/3 = 0.667	4/3 = 1.333	2	2.4

The results from NDIS experiments are compared to those found from (i) the fractions of Se atoms in Se-Se-Se, Ge-Se-Se, or Ge-Se-Ge connections measured by using ^{77}Se NMR (section 5.1) or (ii) FPMD simulations (section 5.2). The predictions of the CON and RCN models are also listed (Salmon, 2007a). [a]Petri et al., 2000; Salmon and Petri, 2003 [b]Gjersing et al., 2010b [c]Kibalchenko et al., 2011 [d]Micoulaut et al., 2013 [e]Bouzid and Massobrio, 2012; Wezka et al., 2014 [f]Present work [g]Kaseman et al., 2016 [h]Bouzid et al., 2015 [i]vdW$_G$: Chaker et al., 2018 [j]vdW$_W$: Chaker et al., 2018.

$2\,(1-3x)\,/\,(1-x)$, and $\bar{n}_{Ge}^{Ge}=0$, whereas only Ge-Se and Ge-Ge bonds are allowed for compositions with $x > 1/3$ such that $\bar{n}_{Ge}^{Se}$=$2\,(1-x)\,/x$, $\bar{n}_{Se}^{Se}=0$, and $\bar{n}_{Ge}^{Ge}$=$2\,(3x-1)\,/\,x$. By contrast, in the RCN there is a purely statistical distribution of bond types such that Se-Se bonds are allowed for $x > 1/3$ and Ge-Ge bonds are allowed for $x < 1/3$. In this case, the coordination numbers are given by $\bar{n}_{Ge}^{Se}=4\,(1-x)\,/\,(1+x)$, $\bar{n}_{Se}^{Se}=2\,(1-x)\,/\,(1+x)$ and $\bar{n}_{Ge}^{Ge}=8x\,/\,(1+x)$. **Table 2** shows that the coordination numbers from the NDIS method are consistent with the CON for $GeSe_3$ and $GeSe_4$, and that there is a breakdown of the chemical ordering for $GeSe_2$.

The fraction of Ge atoms in ES tetrahedral motifs can be estimated by assuming that there are no extended chains of ES motifs. Then, each ES conformation will involve two ES Ge atoms, two ES Se atoms and four other Se atoms, i.e., each ES Ge atom will be associated with one other ES Ge atom. The corresponding Ge-Ge coordination number is given by $\bar{n}_{Ge}^{Ge}=\left(N_{Ge,ES}\,/\,N_{Ge}\right)\times 1$, where $N_{Ge,ES}$ is the number of Ge atoms in ES motifs and N_{Ge} is the total number of Ge atoms in the glass. In order to make a quantitative comparison with the results from ^{77}Se MAS NMR experiments (Gjersing et al., 2010b), the fraction of Se atoms in ES Ge-Se-Ge connections needs to be estimated from the NDIS results. With the assumption that there are no extended chains of ES motifs, each pair of ES Ge atoms will be associated with two ES Se atoms, i.e., $N_{Ge,ES}=N_{Se,ES}$ such that $N_{Se,ES}/N_{Se}=(N_{Ge}/N_{Se})\,\bar{n}_{Ge}^{Ge}=x\,\bar{n}_{Ge}^{Ge}\,/\,(1-x)$. Hence, the measured NDIS $\bar{n}_{Ge}^{Ge}$ values give $N_{Se,ES}\,/\,N_{Se}=0.17(3)$ for $GeSe_2$ vs. $N_{Se,ES}\,/\,N_{Se}=0.05(2)$ for $GeSe_3$. In comparison, the ^{77}Se MAS NMR experiments give $N_{Se,ES}\,/\,N_{Se}$ values of 0.23(3) and 0.10(3) for $GeSe_2$ and $GeSe_{3.78}$, respectively. For the case of $GeSe_4$, there is no evidence of ES conformations from the NDIS experiments, although the low-r tail on the first peak in $g_{GeGe}(r)$ does cover part of the distance range expected for ES tetrahedra. In comparison, ^{77}Se MAS NMR experiments give $N_{Se,ES}\,/\,N_{Se}=0.08(3)$ for $GeSe_4$ (Gjersing et al., 2010b), and Raman spectroscopy experiments report the existence of ES tetrahedra over the entire composition range $0.1 \leq x \leq 0.33$ (Sugai, 1987; Wang et al., 1998; Lucas et al., 2009; Gjersing et al., 2010b; Bhosle et al., 2012).

We note that the presence of ES conformations and the appearance of an FSDP in $S_{CC}(k)$ (**Figure 9**) are in contradiction with the chain-crossing model for Ge_xSe_{1-x} glasses with x <1/3 in which a uniform distribution of Ge-centered structural motifs is hypothesized (Tronc et al., 1973; Bureau et al., 2003).

5.2. Comparison With FPMD Models

In **Figures 11–13**, the measured $S_{\alpha\beta}(k)$ and $g_{\alpha\beta}(r)$ functions are compared to those obtained from $N = 120$ atom FPMD simulations of $GeSe_2$ (Bouzid and Massobrio, 2012; Micoulaut et al., 2013; Wezka et al., 2014), $GeSe_3$ (Micoulaut et al.,

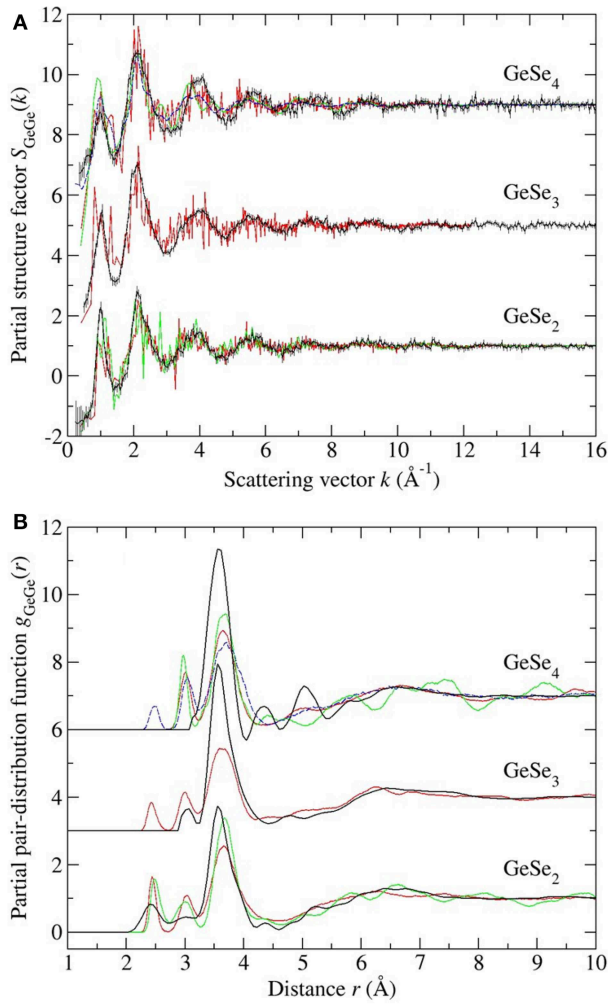

FIGURE 11 | The measured vs. simulated **(A)** $S_{GeGe}(k)$ and **(B)** $g_{GeGe}(r)$ functions for glassy $GeSe_2$, $GeSe_3$ and $GeSe_4$. The measured functions [dark (black) curves] are from the work of Petri et al. (2000) and Salmon and Petri (2003) in the case of $GeSe_2$, or from the present work in the cases of $GeSe_3$ and $GeSe_4$. In **(A)** the vertical bars represents the statistical uncertainty on the measured data points. The FPMD results are from (i) Micoulaut et al. (2013) with $N = 120$ [solid (red) curves], (ii) Bouzid and Massobrio (2012) and Wezka et al. (2014) for $GeSe_2$ with $N = 120$ [solid (green) curves], and (iii) Bouzid et al. (2015) for $GeSe_4$ with either $N = 120$ [solid (green) curves] or $N = 480$ [broken (blue) curves]. The data sets for $GeSe_3$ and $GeSe_4$ are offset vertically for clarity of presentation.

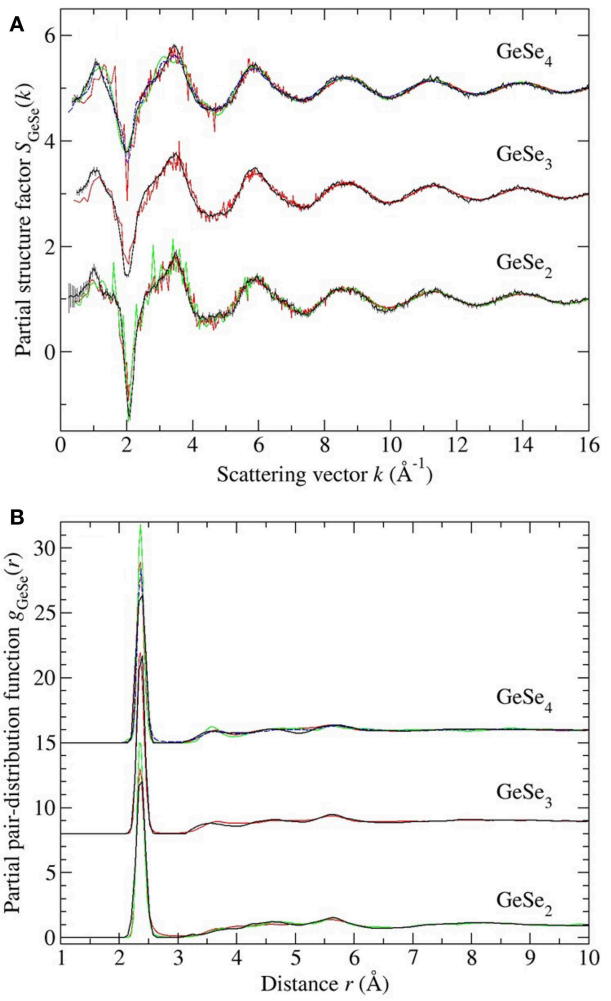

FIGURE 12 | The measured vs. simulated **(A)** $S_{GeSe}(k)$ and **(B)** $g_{GeSe}(r)$ functions for glassy $GeSe_2$, $GeSe_3$, and $GeSe_4$. The measured functions [dark (black) curves] are from the work of Petri et al. (2000) and Salmon and Petri (2003) in the case of $GeSe_2$, or from the present work in the cases of $GeSe_3$ and $GeSe_4$. In **(A)** the vertical bars represent the statistical uncertainty on the measured data points. The FPMD results are from (i) Micoulaut et al. (2013) with $N = 120$ [solid (red) curves], (ii) Bouzid and Massobrio (2012) and Wezka et al. (2014) for $GeSe_2$ with $N = 120$ [solid (green) curves], and (iii) Bouzid et al. (2015) for $GeSe_4$ with either $N = 120$ [solid (green) curves] or $N = 480$ [broken (blue) curves]. The data sets for $GeSe_3$ and $GeSe_4$ are offset vertically for clarity of presentation.

2013), and $GeSe_4$ (Micoulaut et al., 2013; Bouzid et al., 2015) and from $N = 480$ atom simulations of $GeSe_4$ (Bouzid et al., 2015). In all of this FPMD work, the Becke-Lee-Yang-Parr (BLYP) exchange and correlation energy functional was employed (Becke, 1988; Lee et al., 1988), and steps were taken to ensure that the simulated systems were free from residual pressure (Bouzid and Massobrio, 2012). The simulated nearest-neighbor coordination numbers are compared to the measured values in **Table 2**.

Each model gives a good account of the measured Ge-Se and Se-Se correlation functions, but agreement with the measured Ge-Ge correlation functions is less impressive. In general, it is precisely the Ge-Ge correlations that show the greatest sensitivity to the details of the modeling procedure (Salmon and Zeidler, 2015), e.g., to the exchange and correlation energy functional used in the simulations (Massobrio et al., 1999, 2000, 2010; Micoulaut et al., 2009, 2013), to the effect on the structure of any residual pressure (Bouzid and Massobrio, 2012), and to the effect on the structure of both the system size and quench protocol that is employed, especially for small Ge content glasses (Bouzid et al., 2015; Le Roux et al., 2016).

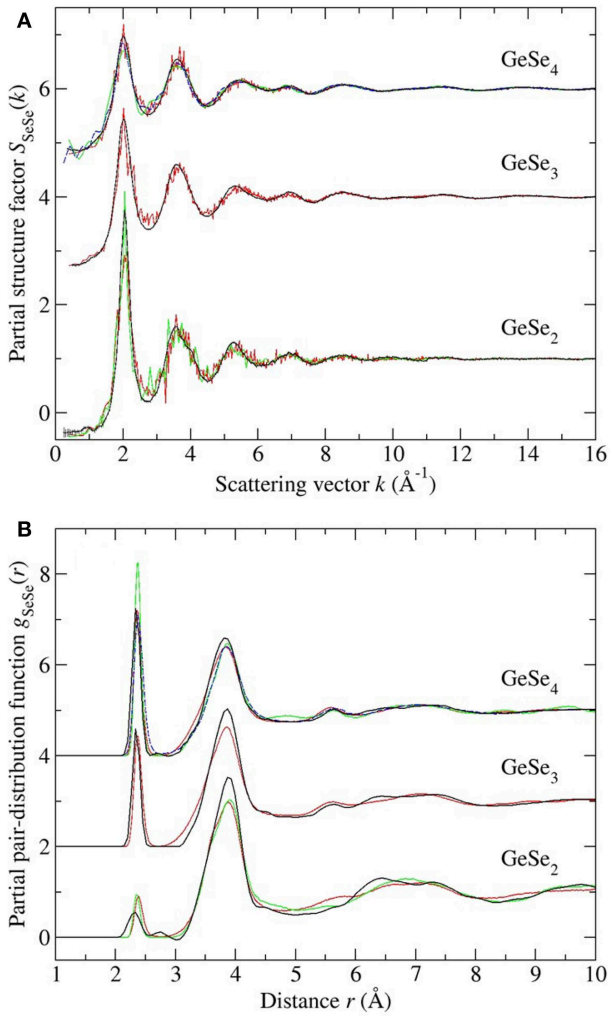

FIGURE 13 | The measured vs. simulated **(A)** $S_{SeSe}(k)$ and **(B)** $g_{SeSe}(r)$ functions for glassy $GeSe_2$, $GeSe_3$, and $GeSe_4$. The measured functions [dark (black) curves] are from the work of Petri et al. (2000) and Salmon and Petri (2003) in the case of $GeSe_2$, or from the present work in the cases of $GeSe_3$ and $GeSe_4$. In **(A)** the vertical bars represent the statistical uncertainty on the measured data points. The FPMD results are from (i) Micoulaut et al. (2013) with $N = 120$ [solid (red) curves], (ii) Bouzid and Massobrio (2012) and Wezka et al. (2014) for $GeSe_2$ with $N = 120$ [solid (green) curves], and (iii) Bouzid et al. (2015) for $GeSe_4$ with either $N = 120$ [solid (green) curves] or $N = 480$ [broken (blue) curves]. The data sets for $GeSe_3$ and $GeSe_4$ are offset vertically for clarity of presentation.

In the case of $GeSe_2$, the models reproduce all of the measured features in $g_{GeGe}(r)$, although the CS tetrahedral peak at $\bar{r}_{GeGe}$ ~3.66 Å is shifted toward a larger-r value as compared to experiment. In the case of $GeSe_3$, the model gives homonuclear Ge-Ge bonds in addition to ES and CS tetrahedral motifs, but homonuclear bonds were not found in the NDIS results, and the height of the CS peak in the simulated $g_{GeGe}(r)$ function is smaller than the measured value. In the case of $GeSe_4$, homonuclear Ge-Ge bonds were found in one FPMD model but not in the others, connections that were not found by experiment. Each model features a clearly defined ES tetrahedral peak in $g_{GeGe}(r)$ at $\bar{r}_{GeGe}$ ~3.0 Å that is absent in the measured function, although there is some overlap of the modeled ES peak with the low-r tail of the first peak in the measured $g_{GeGe}(r)$ function. The height of the CS peak in the simulated $g_{GeGe}(r)$ function is smaller than the measured value. These general findings from the NDIS experiments on $GeSe_3$ and $GeSe_4$ support those obtained from reverse Monte Carlo (RMC) models that were used to analyze the results obtained from anomalous X-ray scattering (AXS) experiments (Hosokawa et al., 2011).

The inclusion of dispersion or van der Waals (vdW) forces in FPMD simulations has recently been considered by Chaker et al. (2018) for the case of glassy $GeSe_4$. Two different theoretical schemes were used for the description of these forces, one based on the work of Grimme (2006) (vdW_G) and the other based on a Wannier function analysis (vdW_W) (Silvestrelli, 2008). The results were compared to those obtained for the $N = 480$ atom FPMD model of Bouzid et al. (2015) in which dispersion forces were not included. The main effect of dispersion forces is to (i) increase the height of the CS tetrahedral peak in $g_{GeGe}(r)$ at $\bar{r}_{GeGe}$ ≃3.6 Å, making it comparable to the height found in the FPMD simulations of Micoulaut et al. (2013), and (ii) either leave constant or increase the height of the second peak in $g_{SeSe}(r)$ at $\bar{r}_{SeSe}$ ≃3.8 Å, depending on the theoretical scheme. The dispersion corrections lead to $\bar{n}_{Ge}$ values that are in better accord with the "8-N" rule (**Table 2**).

5.3. Intermediate Phase

High-energy X-ray diffraction, neutron diffraction and EXAFS spectroscopy experiments have been performed to look for a structural signature of the intermediate phase in Ge_xSe_{1-x} glass (Shatnawi et al., 2008; Zeidler et al., 2017). The composition dependence of several parameters was investigated across the stiffness transition. These parameters included descriptors of the local structure such as (i) the first peak position and width in the total pair-distribution function, (ii) the mean coordination number $\bar{n}$, and (iii) the Debye-Waller factor describing the root-mean-square displacement (static or thermal) of atoms about their equilibrium positions. They also included descriptors of the non-local structure on length scales that are associated with the FSDP and principal peak in the measured total structure factors, where ordering associated with the principal peak can persist to a nanometer length scale (Salmon et al., 2005; Salmon, 2006). All of these parameters were found to evolve smoothly with the glass composition, i.e., a structural signature of the intermediate phase was not identified.

The present work provides benchmark results for guiding in the development of accurate models for the structures of glassy $GeSe_3$ and $GeSe_4$, which can be used to explore the network rigidity and other structure-related properties of the glass. The investigated glasses lie at the boundaries of the intermediate phase in the Ge_xSe_{1-x} system, which is reported for the composition range $0.20 \leq x \leq 0.26$ (section 1). Often, models for the glass structure are provided by FPMD simulations, and the onset of a stressed-rigid phase has been attributed to a substantial change in the distribution of bond

angles associated with Ge-centered tetrahedra, such that bond-angle constraints are broken for $x > 0.25$ (Micoulaut et al., 2013). However, as emphasized by the discussion of section 5.2, there is mismatch between the measured and FPMD results that is particularly noticeable in respect of the Ge-Ge correlation functions, which are sensitive to the connectivity of the Ge-centered structural motifs. In addition, different FPMD models can lead to different conclusions about the network structure. Thus, it will be interesting to see the predictions of FPMD models for intermediate phase glasses that are consistent with all of the measured partial pair-correlation functions.

6. CONCLUSIONS

Full sets of partial structure factors for glassy $GeSe_3$ ($x = 0.25$) and $GeSe_4$ ($x = 0.20$) were measured by using the NDIS method. These glass compositions lie at the boundaries of the intermediate phase in the Ge_xSe_{1-x} system. The results are consistent with chemically ordered network structures, in contrast to $GeSe_2$ where the chemical ordering is broken by the formation of homonuclear Ge-Ge and Se-Se bonds (Petri et al., 2000; Salmon and Petri, 2003). For all of these compositions, the nearest-neighbor Ge and Se coordination numbers are given by $\bar{n}_{Ge} = 4$ and $\bar{n}_{Se} = 2$ within the experimental error (**Table 2**), in accordance with the expectations of the "8-N" rule. In the case of $GeSe_4$, larger $\bar{n}_{Ge}$ values are deduced from ^{77}Se MAS NMR experiments (**Table 2**), which suggests the need for a re-interpretation of the spectroscopy results. A distinct peak in $g_{GeGe}(r)$ at $\bar{r}_{GeGe} \sim 3.03$ Å that originates from ES tetrahedra was observed for both $GeSe_2$ and $GeSe_3$, but was not found for $GeSe_4$. This finding appears to contradict the results obtained from both ^{77}Se MAS NMR (Gjersing et al., 2010b) and Raman spectroscopy (Sugai, 1987; Wang et al., 1998; Lucas et al., 2009; Gjersing et al., 2010b; Bhosle et al., 2012) experiments, although the low-r tail on the first peak in the measured $g_{GeGe}(r)$ function does have a contribution in the distance range associated with ES tetrahedra. The appearance of an FSDP in $S_{CC}(k)$ indicates a non-uniform distribution of Ge-centered tetrahedra on an intermediate length scale, in contradiction to the chain-crossing model (Tronc et al., 1973; Bureau et al., 2003).

The new experimental work provides benchmark results for aiding in the development of realistic structural models for establishing the network rigidity and other structure-related properties of the glass. A comparison of the NDIS results for $GeSe_3$ and $GeSe_4$ with those from recent FPMD simulations shows mismatch that is particularly marked in respect of the Ge-Ge correlation functions, i.e., there is an ingredient missing from the FPMD simulations that may be related to the system size.

DATA AVAILABILITY

The data sets created during this research are openly available from the University of Bath Research Data Archive at https://doi.org/10.15125/BATH-00664 (Salmon and Zeidler, 2019). Raw neutron diffraction data sets for $GeSe_3$ and $GeSe_4$ are available at https://doi.ill.fr/10.5291/ILL-DATA.6-05-922 (Salmon et al., 2013).

AUTHOR CONTRIBUTIONS

PSS and AZ designed the research. AZ prepared the samples. All authors contributed to the neutron diffraction experiments. RFR and AZ analyzed the data. PSS wrote the paper.

FUNDING

The Bath group received support from the EPSRC via Grant No. EP/J009741/1 and from the University of Bath for a PhD studentship (RFR). AZ and PSS are grateful to Corning Inc. for the award of Gordon S. Fulcher Distinguished Scholarships, during which this work was completed. AZ is supported by a Royal Society — EPSRC Dorothy Hodgkin Research Fellowship.

ACKNOWLEDGMENTS

We thank Annalisa Polidori (Bath) for help with the diffraction experiments, and Sabyasachi Sen (UC Davis) for pointing out (Kaseman et al., 2016).

REFERENCES

Bauchy, M., Micoulaut, M., Celino, M., Le Roux, S., Boero, M., and Massobrio, C. (2011). Angular rigidity in tetrahedral network glasses with changing composition. *Phys. Rev. B* 84:054201. doi: 10.1103/PhysRevB.84.054201

Becke, A. D. (1988). Density-functional exchange-energy approximation with correct asymptotic behavior. *Phys. Rev. A* 38, 3098–3100. doi: 10.1103/PhysRevA.38.3098

Bertagnolli, H., Chieux, P., and Zeidler, M. D. (1976). A neutron-diffraction study of liquid acetonitrile I. $CD_3C^{14}N$. *Mol. Phys.* 32, 759–773. doi: 10.1080/00268977600102201

Bhatia, A. B., and Thornton, D. E. (1970). Structural aspects of the electrical resistivity of binary alloys. *Phys. Rev. B* 2, 3004–3012. doi: 10.1103/PhysRevB.2.3004

Bhosle, S., Gunasekera, K., Boolchand, P., and Micoulaut, M. (2012). Melt homogenization and self-organization in chalcogenides - part II. *Int. J. Appl. Glass Sci.* 3, 205–220. doi: 10.1111/j.2041-1294.2012.00092.x

Bhosle, S., Gunasekera, K., Chen, P., Boolchand, P., Micoulaut, M., and Massobrio, C. (2011). Meeting experimental challenges to physics of network glasses: assessing the role of sample homogeneity. *Solid State Commun.* 151, 1851–1855. doi: 10.1016/j.ssc.2011.10.016

Boolchand, P., Feng, X., and Bresser, W. J. (2001a). Rigidity transitions in binary Ge-Se glasses and the intermediate phase. *J. Non-Cryst. Solids* 293–295, 348–356. doi: 10.1016/S0022-3093(01)00867-5

Boolchand, P., Georgiev, D. G., and Goodman, B. (2001b). Discovery of the intermediate phase in chalcogenide glasses. *J. Optoelectron. Adv. Mater.* 3, 703–720.

Bouzid, A., Le Roux, S., Ori, G., Boero, M., and Massobrio, C. (2015). Origin of structural analogies and differences between the atomic structures of $GeSe_4$ and GeS_4 glasses: A first principles study. *J. Chem. Phys.* 143:034504. doi: 10.1063/1.4926830

Bouzid, A., and Massobrio, C. (2012). Note: accounting for pressure effects on the calculated equilibrium structure of glassy $GeSe_2$. *J. Chem. Phys.* 137:046101. doi: 10.1063/1.4739953

Bresser, W., Boolchand, P., and Suranyi, P. (1986). Rigidity percolation and molecular clustering in network glasses. *Phys. Rev. Lett.* 56, 2493–2496. doi: 10.1103/PhysRevLett.56.2493

Bureau, B., Troles, J., Floch, M. L., Guénot, P., Smektala, F., and Lucas, J. (2003). Germanium selenide glass structures studied by ^{77}Se solid state NMR and mass spectroscopy. *J. Non-Cryst. Solids* 319, 145–153. doi: 10.1016/S0022-3093(02)01911-7

Chaker, Z., Ori, G., Tugène, C., Le Roux, S., Boero, M., Massobrio, C., et al. (2018). The role of dispersion forces on the atomic structure of glassy chalcogenides: the case of $GeSe_4$ and GeS_4. *J. Non-Cryst. Solids* 499, 167–172. doi: 10.1016/j.jnoncrysol.2018.07.012

Dittmar, G., and Schäfer, H. (1976). Die kristallstruktur von Germaniumdiselenid. *Acta Crystallogr. B* 32, 2726–2728. doi: 10.1107/S0567740876008704

Eggleton, B. J., Luther-Davies, B., and Richardson, K. (2011). Chalcogenide photonics. *Nat. Photon.* 5, 141–148. doi: 10.1038/nphoton.2011.309

Faber, T. E., and Ziman, J. M. (1965). A theory of the electrical properties of liquid metals. III. The resistivity of binary alloys. *Philos. Mag.* 11, 153–173. doi: 10.1080/14786436508211931

Feng, X., Bresser, W. J., and Boolchand, P. (1997). Direct evidence for stiffness threshold in chalcogenide glasses. *Phys. Rev. Lett.* 78, 4422–4425. doi: 10.1103/PhysRevLett.78.4422

Fischer, H. E., Barnes, A. C., and Salmon, P. S. (2006). Neutron and x-ray diffraction studies of liquids and glasses. *Rep. Prog. Phys.* 69, 233–299. doi: 10.1088/0034-4885/69/1/R05

Fischer, H. E., Cuello, G. J., Palleau, P., Feltin, D., Barnes, A. C., Badyal, Y. S., et al. (2002). D4c: A very high precision diffractometer for disordered materials. *Appl. Phys. A* 74, S160–S162. doi: 10.1007/s003390101087

Gjersing, E. L., Sen, S., and Youngman, R. E. (2010a). Mechanistic understanding of the effect of rigidity percolation on structural relaxation in supercooled germanium selenide liquids. *Phys. Rev. B* 82:014203. doi: 10.1103/PhysRevB.82.014203

Gjersing, E. L., Sen, S., and Youngman, R. E. (2010b). Structure, connectivity, and configurational entropy of Ge_xSe_{100-x} glasses: Results from ^{77}Se MAS NMR spectroscopy. *J. Phys. Chem. C* 114, 8601–8608. doi: 10.1021/jp1014143

Gopinath, J. T., Soljačić, M., Ippen, E. P., Fuflyigin, V. N., King, W. A., and Shurgalin, M. (2004). Third order nonlinearities in Ge-As-Se-based glasses for telecommunications applications. *J. Appl. Phys.* 96, 6931–6933. doi: 10.1063/1.1805182

Grimme, S. (2006). Semiempirical GGA-type density functional constructed with a long-range dispersion correction. *J. Comput. Chem.* 27, 1787–1799. doi: 10.1002/jcc.20495

Hilton, A. R. (1966). Nonoxide chalcogenide glasses as infrared optical materials. *Appl. Opt.* 5, 1877–1882. doi: 10.1364/AO.5.001877

Hosokawa, S., Oh, I., Sakurai, M., Pilgrim, W.-C., Boudet, N., Bérar, J.-F., et al. (2011). Anomalous x-ray scattering study of Ge_xSe_{1-x} glassy alloys across the stiffness transition composition. *Phys. Rev. B* 84:014201. doi: 10.1103/PhysRevB.84.014201

Inam, F., Tafen, D. N., Chen, G., and Drabold, D. A. (2009). Competing stoichiometric phases and the intermediate phase in Ge_xSe_{1-x} glasses. *Phys. Stat. Solid B* 246, 1849–1853. doi: 10.1002/pssb.200982016

Kaseman, D. C., Oliveira, K. M., Palazzo, T., and Sen, S. (2016). Selenium chain length distribution in Ge_xSe_{100-x} glasses: insights from ^{77}Se NMR spectroscopy and quantum chemical calculations. *J. Phys. Chem. B* 120, 4513–4521. doi: 10.1021/acs.jpcb.6b02747

Kibalchenko, M., Yates, J. R., Massobrio, C., and Pasquarello, A. (2011). Structural composition of first-neighbor shells in $GeSe_2$ and $GeSe_4$ glasses from a first-principles analysis of NMR chemical shifts. *J. Phys. Chem. C* 115, 7755–7759. doi: 10.1021/jp201345e

Kohoutek, T., Wagner, T., Orava, J., Krbal, M., Ilavsky, J., Vlcek, M., et al. (2008). Multilayer planar structures prepared from chalcogenide thin films of As-Se and Ge-Se systems and polymer thin films using thermal evaporation and spin-coating techniques. *J. Non-Cryst. Solids* 354, 529–532. doi: 10.1016/j.jnoncrysol.2007.07.057

Le Roux, S., Bouzid, A., Kim, K. Y., Han, S., Zeidler, A., Salmon, P. S., et al. (2016). Structure of amorphous $GeSe_9$ by neutron diffraction and first-principles molecular dynamics: impact of trajectory sampling and size effects. *J. Chem. Phys.* 145:084502. doi: 10.1063/1.4961265

Lee, C., Yang, W., and Parr, R. G. (1988). Development of the Colle-Salvetti correlation-energy formula into a functional of the electron density. *Phys. Rev. B* 37, 785–789. doi: 10.1103/PhysRevB.37.785

Lezal, D., Pedlikova, J., and Zavadil, J. (2004). Chalcogenide glasses for optical and photonics applications. *J. Optoelectron. Adv. Mater.* 6, 133–137.

Lorch, E. (1969). Neutron diffraction by germania, silica and radiation-damaged silica glasses. *J. Phys. C Solid State Phys.* 2, 229–237. doi: 10.1088/0022-3719/2/2/305

Lucas, P., Coleman, G. J., Sen, S., Cui, S., Guimond, Y., Calvez, L., et al. (2019). Structural and chemical homogeneity of chalcogenide glass prepared by melt-rocking. *J. Chem. Phys.* 150:014505. doi: 10.1063/1.5054704

Lucas, P., King, E. A., Gulbiten, O., Yarger, J. L., Soignard, E., and Bureau, B. (2009). Bimodal phase percolation model for the structure of Ge-Se glasses and the existence of the intermediate phase. *Phys. Rev. B* 80:214114. doi: 10.1103/PhysRevB.80.214114

Ludwig, K. F. Jr., Warburton, W. K., Wilson, L., and Bienenstock, A. I. (1987). Liquid $GeBr_4$. I. A test of the anomalous x-ray scattering method as applied to disordered materials. *J. Chem. Phys.* 87, 604–612. doi: 10.1063/1.453553

Madon, M., Gillet, P., Julien, C., and Price, G. D. (1991). A vibrational study of phase transitions among the GeO_2 polymorphs. *Phys. Chem. Miner.* 18, 7–18. doi: 10.1007/BF00199038

Martin, R. A., Salmon, P. S., Fischer, H. E., and Cuello, G. J. (2003). Structure of dysprosium and holmium phosphate glasses by the method of isomorphic substitution in neutron diffraction. *J. Phys. Condens. Matter* 15, 8235–8252. doi: 10.1088/0953-8984/15/49/003

Massobrio, C., Celino, M., Salmon, P. S., Martin, R. A., Micoulaut, M., and Pasquarello, A. (2009). Atomic structure of the two intermediate phase glasses $SiSe_4$ and $GeSe_4$. *Phys. Rev. B* 79:174201. doi: 10.1103/PhysRevB.79.174201

Massobrio, C., Micoulaut, M., and Salmon, P. S. (2010). Impact of the exchange-correlation functional on the structure of glassy $GeSe_2$. *Solid State Sci.* 12, 199–203. doi: 10.1016/j.solidstatesciences.2009.11.016

Massobrio, C., Pasquarello, A., and Car, R. (1999). Intermediate range order and bonding character in disordered network-forming systems. *J. Am. Chem. Soc.* 121, 2943–2944. doi: 10.1021/ja9808447

Massobrio, C., Pasquarello, A., and Car, R. (2000). Concentration fluctuations on intermediate range distances in liquid $GeSe_2$: the critical role of ionicity. *Comput. Mater. Sci.* 17, 115–121. doi: 10.1016/S0927-0256(00)00007-0

Micoulaut, M., Cormier, L., and Henderson, G. S. (2006). The structure of amorphous, crystalline and liquid GeO_2. *J. Phys. Condens. Matter* 18, R753–R784. doi: 10.1088/0953-8984/18/45/R01

Micoulaut, M., Kachmar, A., Bauchy, M., Le Roux, S., Massobrio, C., and Boero, M. (2013). Structure, topology, rings, and vibrational and electronic properties of Ge_xSe_{1-x} glasses across the rigidity transition: a numerical study. *Phys. Rev. B* 88:054203. doi: 10.1103/PhysRevB.88.054203

Micoulaut, M., Vuilleumier, R., and Massobrio, C. (2009). Improved modeling of liquid $GeSe_2$: impact of the exchange-correlation functional. *Phys. Rev. B* 79:214205. doi: 10.1103/PhysRevB.79.214205

Penfold, I. T., and Salmon, P. S. (1991). Structure of covalently bonded glass-forming melts: a full partial-structure-factor analysis of liquid $GeSe_2$. *Phys. Rev. Lett.* 67, 97–100. doi: 10.1103/PhysRevLett.67.97

Petri, I., Salmon, P. S., and Fischer, H. E. (1999a). Structure of the liquid semiconductor GeSe. *J. Phys. Condens. Matter* 11, 7051–7060. doi: 10.1088/0953-8984/11/37/302

Petri, I., Salmon, P. S., and Fischer, H. E. (2000). Defects in a disordered world: the structure of glassy $GeSe_2$. *Phys. Rev. Lett.* 84, 2413–2416. doi: 10.1103/PhysRevLett.84.2413

Petri, I., Salmon, P. S., and Howells, W. S. (1999b). Change in the topology of the glass forming liquid $GeSe_2$ with increasing temperature. *J. Phys. Condens. Matter* 11, 10219–10227. doi: 10.1088/0953-8984/11/50/314

Phillips, J. C. (1979). Topology of covalent non-crystalline solids I: short-range order in chalcogenide alloys. *J. Non-Cryst. Solids* 34, 153–181. doi: 10.1016/0022-3093(79)90033-4

Rowlands, R. F. (2015). *The role of structural disorder in crystalline, glassy and liquid materials*. (Ph.D. thesis), University of Bath, Bath, United Kingdom.

Salmon, P. S. (1992). The structure of molten and glassy 2:1 binary systems: an approach using the Bhatia-Thornton formalism. *Proc. R. Soc. Lond. A* 437, 591–606. doi: 10.1098/rspa.1992.0081

Salmon, P. S. (1994). Real space manifestation of the first sharp diffraction peak in the structure factor of liquid and glassy materials. *Proc. R. Soc. Lond. A* 445, 351–365. doi: 10.1098/rspa.1994.0065

Salmon, P. S. (2006). Decay of the pair correlations and small-angle scattering for binary liquids and glasses. *J. Phys. Condens. Matter* 18, 11443–11469. doi: 10.1088/0953-8984/18/50/004

Salmon, P. S. (2007a). Structure of liquids and glasses in the Ge-Se binary system. *J. Non-Cryst. Solids* 353, 2959–2974. doi: 10.1016/j.jnoncrysol.2007.05.152

Salmon, P. S. (2007b). The structure of tetrahedral network glass forming systems at intermediate and extended length scales. *J. Phys. Condens. Matter* 19:455208. doi: 10.1088/0953-8984/19/45/455208

Salmon, P. S., Fischer, H. E., Rowlands, R. F., and Zeidler, A. (2013). Structure of intermediate phase glasses. doi: 10.5291/ILL-DATA.6-05-922

Salmon, P. S., and Liu, J. (1994). The relation between the melt topology and glass-forming ability for liquid Ge-Se alloys. *J. Phys. Condens. Matter* 6, 1449–1460. doi: 10.1088/0953-8984/6/8/004

Salmon, P. S., Martin, R. A., Mason, P. E., and Cuello, G. J. (2005). Topological vs. chemical ordering in network glasses at intermediate and extended length scales. *Nature* 435, 75–78. doi: 10.1038/nature03475

Salmon, P. S., and Petri, I. (2003). Structure of glassy and liquid $GeSe_2$. *J. Phys. Condens. Matter* 15, S1509–S1528. doi: 10.1088/0953-8984/15/16/301

Salmon, P. S., Xin, S., and Fischer, H. E. (1998). Structure of the glassy fast-ion conductor $AgPS_3$ by neutron diffraction. *Phys. Rev. B* 58, 6115–6123. doi: 10.1103/PhysRevB.58.6115

Salmon, P. S., and Zeidler, A. (2013). Identifying and characterising the different structural length scales in liquids and glasses: an experimental approach. *Phys. Chem. Chem. Phys.* 15, 15286–15308. doi: 10.1039/c3cp51741a

Salmon, P. S., and Zeidler, A. (2015). "Chapter 1: The atomic-scale structure of network glass-forming materials," in *Molecular Dynamics Simulations of Disordered Materials*, Springer Series in Materials Science 215, eds C. Massobrio, J. Du, M. Bernasconi, and P. S. Salmon (Cham: Springer), 1–31. doi: 10.1007/978-3-319-15675-0_1

Salmon, P. S. and Zeidler, A. (2019). Data sets for the Frontiers in Materials article entitled "Structure of Ge-Se glass and network rigidity: The deployment of neutron diffraction with isotope substitution". doi: 10.15125/BATH-00664

Salmon, P. S., Zeidler, A., and Fischer, H. E. (2016). Optimizing the counting times for sample-in-container scattering experiments. *J. Appl. Cryst.* 49, 2249–2251. doi: 10.1107/S160057671601493X

Sartbaeva, A., Wells, S. A., Huerta, A., and Thorpe, M. F. (2007). Local structural variability and the intermediate phase window in network glasses. *Phys. Rev. B* 75:224204. doi: 10.1103/PhysRevB.75.224204

Savage, J. A., and Nielsen, S. (1965). Chalcogenide glasses transmitting in the infrared between 1 and 20 μ - a state of the art review. *Infrared Phys.* 5, 195–204. doi: 10.1016/0020-0891(65)90023-0

Sears, V. F. (1992). Neutron scattering lengths and cross sections. *Neutron News* 3, 26–37. doi: 10.1080/10448639208218770

Seddon, A. B., and Laine, M. J. (1997). Chalcogenide glasses for acousto-optic devices. II. As-Ge-Se systems. *J. Non-Cryst. Solids* 213–214, 168–173. doi: 10.1016/S0022-3093(96)00665-5

Shatnawi, M. T. M., Farrow, C. L., Chen, P., Boolchand, P., Sartbaeva, A., Thorpe, M. F., et al. (2008). Search for a structural response to the intermediate phase in Ge_xSe_{1-x} glasses. *Phys. Rev. B* 77:094134. doi: 10.1103/PhysRevB.77.094134

Silvestrelli, P. L. (2008). Van der Waals interactions in DFT made easy by Wannier functions. *Phys. Rev. Lett.* 100:053002. doi: 10.1103/PhysRevLett.100.053002

Sugai, S. (1987). Stochastic random network model in Ge and Si chalcogenide glasses. *Phys. Rev. B* 35, 1345–1361. doi: 10.1103/PhysRevB.35.1345

Thorpe, M. F. (1983). Continuous deformations in random networks. *J. Non-Cryst. Solids* 57, 355–370. doi: 10.1016/0022-3093(83)90424-6

Thorpe, M. F., Jacobs, D. J., Chubynsky, M. V., and Phillips, J. C. (2000). Self-organization in network glasses. *J. Non-Cryst. Solids* 266–269, 859–866. doi: 10.1016/S0022-3093(99)00856-X

Troles, J., Shiryaev, V., Churbanov, M., Houizot, P., Brilland, L., Desevedavy, F., et al. (2009). $GeSe_4$ glass fibres with low optical losses in the mid-IR. *Opt. Mater.* 32, 212–215. doi: 10.1016/j.optmat.2009.07.024

Tronc, P., Bensoussan, M., Brenac, A., and Sebenne, C. (1973). Optical-absorption edge and Raman scattering in Ge_xSe_{1-x} glasses. *Phys. Rev. B* 8, 5947–5956. doi: 10.1103/PhysRevB.8.5947

Wang, Y., Matsuda, O., Inoue, K., Yamamuro, O., Matsuo, T., and Murase, K. (1998). A Raman scattering investigation of the structure of glassy and liquid Ge_xSe_{1-x}. *J. Non-Cryst. Solids* 232-234, 702–707. doi: 10.1016/S0022-3093(98)00553-5

Wezka, K., Bouzid, A., Pizzey, K. J., Salmon, P. S., Zeidler, A., Klotz, S., et al. (2014). Density-driven defect-mediated network collapse of $GeSe_2$ glass. *Phys. Rev. B* 90:054206. doi: 10.1103/PhysRevB.90.054206

Whittaker, D. A. J., Giacomazzi, L., Adroja, D., Bennington, S. M., Pasquarello, A., and Salmon, P. S. (2018). Partial vibrational density of states for amorphous solids from inelastic neutron scattering. *Phys. Rev. B* 98:064205. doi: 10.1103/PhysRevB.98.064205

Wright, A. C. (1993). The comparison of molecular dynamics simulations with diffraction experiments. *J. Non-Cryst. Solids* 159, 264–268. doi: 10.1016/0022-3093(93)90232-M

Zakery, A., and Elliott, S. R. (2003). Optical properties and applications of chalcogenide glasses: a review. *J. Non-Cryst. Solids* 330, 1–12. doi: 10.1016/j.jnoncrysol.2003.08.064

Zakery, A., and Elliott, S. R. (2007). *Optical Nonlinearities in Chalcogenide Glasses and Their Applications*. Springer Series in Optical Sciences 135. Berlin: Springer. doi: 10.1007/978-3-540-71068-4

Zeidler, A., Salmon, P. S., Fischer, H. E., Neuefeind, J. C., Simonson, J. M., and Markland, T. E. (2012). Isotope effects in water as investigated by neutron diffraction and path integral molecular dynamics. *J. Phys. Condens. Matter* 24:284126. doi: 10.1088/0953-8984/24/28/284126

Zeidler, A., Salmon, P. S., Martin, R. A., Usuki, T., Mason, P. E., Cuello, G. J., et al. (2010). Structure of liquid and glassy $ZnCl_2$. *Phys. Rev. B* 82:104208. doi: 10.1103/PhysRevB.82.104208

Zeidler, A., Salmon, P. S., Whittaker, D. A. J., Pizzey, K. J., and Hannon, A. C. (2017). Topological ordering and viscosity in the glass-forming Ge-Se system: the search for a structural or dynamical signature of the intermediate phase. *Front. Mater.* 4:32. doi: 10.3389/fmats.2017.00032

Zhou, W., Paesler, M., and Sayers, D. E. (1991). Structure of germanium-selenium glasses: an X-ray-absorption fine-structure study. *Phys. Rev. B* 43, 2315–2321. doi: 10.1103/PhysRevB.43.2315

Conflict of Interest Statement: PSS and AZ were employed by Corning Inc. during the time this work was completed.

The remaining authors declare that the research was conducted in the absence of any commercial or financial relationships that could be construed as a potential conflict of interest.

frontiers in Materials

REVIEW
published: 25 June 2019
doi: 10.3389/fmats.2019.00144

Connecting Glass-Forming Fragility to Network Topology

*David L. Sidebottom**

Department of Physics, Creighton University, Omaha, NE, United States

Glass fragility is a byproduct of early attempts to apply law of corresponding states scaling to the temperature dependent thickening of glass forming liquids. Efforts to plot the logarithm of the viscosity vs. inverse temperature scaled to the glass transition point (T_g) fail to collapse data to a common, universal curve but instead display an informative pattern: at one extreme, many "strong" oxide glasses exhibit a single Arrhenius dependence, and at the other extreme, many "fragile" molecular liquids display a highly non-Arrhenius pattern in which the viscosity increases far more rapidly just in advance of T_g. In this regard, network-forming glasses composed of 3D networks of covalently bonded atoms are of interest as they undergo systematic changes in both T_g and fragility depending on the topology of the network and display variations of the fragility index spanning from strong ($m \approx 17$) to fragile ($m \approx 90$) depending on the level of network connectivity. Here we review the merits of a special, coarse-grained definition for the topological connectivity of network-forming glasses that differs from conventional constraint-counting approaches but which allows the fragility of over 150 different network-forming glasses (both oxides and chalcogenides) to be collapsed onto a single function of the average network connectivity. We also speculate on what role this coarse-grained connectivity might play in determining the glass transition temperature.

Keywords: fragility, viscosity, networks, oxide glass, universality

OPEN ACCESS

Edited by:
Matthieu Micoulaut, Sorbonne Universités, France

Reviewed by:
Sabyasachi Sen, University of California, Davis, United States
Yann Gueguen, University of Rennes 1, France

***Correspondence:**
David L. Sidebottom
sidebottom@creighton.edu

Specialty section:
This article was submitted to Glass Science, a section of the journal Frontiers in Materials

Received: *17 April 2019*
Accepted: *07 June 2019*
Published: *25 June 2019*

Citation:
Sidebottom DL (2019) Connecting Glass-Forming Fragility to Network Topology. Front. Mater. 6:144. doi: 10.3389/fmats.2019.00144

INTRODUCTION

Through the ages, glass manufacturing has profited from an appreciation for the delicate balance between glass composition and properties. Ease of glass formation from the melt is closely tied to the working "length" of the glass composition; essentially a measure of how gradually the viscosity of the melt changes with changes in temperature just above the glass transition point. A "long" glass suffers only minor changes in viscosity and so can be manipulated for a longer period of time before needing to be reheated. Early glass research naturally focused on how glass chemistry might function to control the viscosity of the melt across a wide variety of glass compositions. Although similar efforts predated it (Oldekop, 1957; Laughlin and Uhlmann, 1972; Nemilov, 2007), it was a seminal paper by Austen Angell (1984) that really emphasized the deep pattern to how chemical structure of both traditional oxide glasses and simple glass-forming liquids might dictate viscous dynamics in the melt. His now famous plot (Angell, 1984, 1991), reproduced here as **Figure 1**, is in many ways reminiscent of an attempt to apply the "law of corresponding

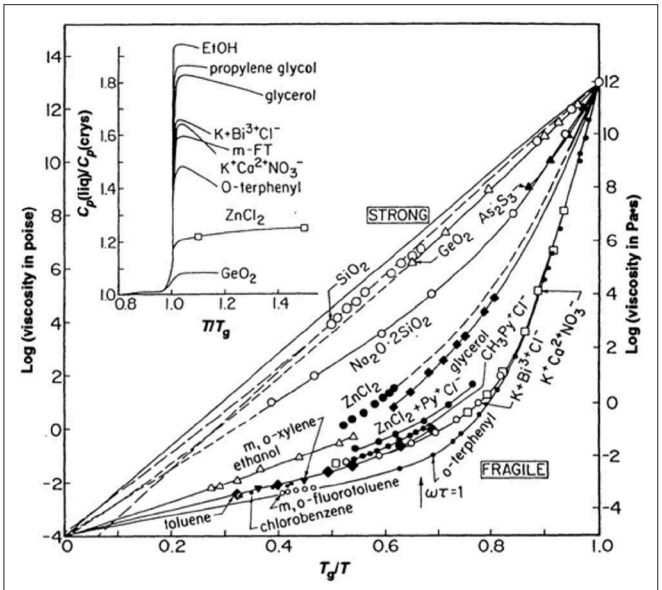

FIGURE 1 | Fragility plot as originally published (Angell, 1984). The viscosity of a variety of glass-forming melts is plotted against inverse temperature scaled to the glass transition temperature where the viscosity equals 10^{12} Pa s. Inset illustrates the jump in specific heat of selected melts which is partly correlated to the degree of fragility from (Angell, 1991) with permission.

states" (Stanley, 1971) to the viscosity of glass-forming melts by scaling the data to the glass transition temperature, T_g, defined as that temperature where the viscosity reaches 10^{12} Pas. However, unlike the law of corresponding states that governs the liquid-vapor transition near the critical point (Stanley, 1971), the viscosity of these glass-forming materials fail to collapse to a single universal scaling curve in this scaled representation. Instead, one finds a pattern that is largely bimodal and for which Angell categorized (Angell, 1991) as either "strong" or "fragile" on the basis of whether the viscosity is highly Arrhenius or highly non-Arrhenius, respectively. Oxide glasses, like SiO_2, are highly Arrhenius over their entire temperature range. These strong glass-formers are composed of a network of relatively strong covalent bonds and typically require refractory-level temperatures to produce a melt. At the opposite extreme are several fragile glass-forming liquids that are held together by weaker, non-directional, van der Waals forces which often exhibit a T_g well below ambient room temperature. Alongside this pattern of non-Arrhenius viscosity, Angell (1991) drew attention to an important correlation of the fragility with the magnitude of the change in specific heat that occurs upon crossing the glass transition point (see inset to **Figure 1**). In thermodynamics this specific heat is the (logarithmic) slope of the entropy with temperature and many have speculated (Adam and Gibbs, 1965; Debenedetti and Stillinger, 2001; Sidebottom, 2015) that the increase in viscosity with cooling is closely associated with how rapidly the entropy of the liquid decreases.

As can be seen from closer inspection of **Figure 1**, the pattern is not exactly bimodal but rather includes a number of intermediates such as $ZnCl_2$ and sodium disilicate whose fragilities lie in between the extremes. The *fragility index* defined by the "steepness" of the limiting slope of the data in **Figure 1** as:

$$m = \lim_{T \to T_g} \frac{d\log_{10} \eta}{d\left(T_g/T\right)}, \tag{1}$$

has often been employed to characterize the specific level of fragility for any given glass-forming material and data in **Figure 1**, for example, range in fragility index from roughly $m = 18$ to $m \approx 85$. With the exception of B_2O_3 whose fragility is intermediate ($m \approx 32$), all of the other traditional network forming oxides (e.g., SiO_2, GeO_2, P_2O_5, As_2O_3) predicted by Zachariasen (1932) to form amorphous states have very low fragilities ranging from $m = 17$ to 20 which boarder on the strong limit in Angell's classification. Unlike the van der Waals liquids, these oxide glasses are constructed of highly directional covalent bonds with strict chemical rules regarding the number of bonds per atom (Zachariasen, 1932). As such, they are often modeled as a network of "balls" (the atoms) connected by "sticks" (the discrete bonds) for which simple topological analyses are applied (Phillips, 1979; He and Thorpe, 1985). For example, in SiO_2 the rule is that every Si atom is connected by sticks to four oxygen atoms and every oxygen atom is connected by sticks to 2 Si atoms.

An important measure of this network topology would be the average number of bonds per atom, $\langle r \rangle$. In the case of SiO_2 where one-third of the atoms are Si (with $r = 4$ bonds each) and two-thirds are O (with $r = 2$ bonds each), the bond density would be $\langle r \rangle = \frac{1}{3} \times 4 + \frac{2}{3} \times 2 = 2.67$. In many topological theories (Phillips, 1979; He and Thorpe, 1985), $\langle r \rangle$ is a mean field parameter that represents a measure of how rigid the network is against applied stresses. Simple constraint-counting arguments indicate that networks with $\langle r \rangle = 2.4$ have a number of atomic constraints equal to the degrees of freedom and that this specific bond density marks a separation between networks (with $\langle r \rangle < 2.4$) that are "floppy" and networks (with $\langle r \rangle > 2.4$) that are "rigid."

While this atomic-weighted bond density appears frequently in many topological studies of glass forming materials, including many concerning the mechanical properties of network-forming chalcogenide glasses (Halfpap and Lindsay, 1986; Tatsumisago et al., 1990), we propose that the *viscosity* of network-forming oxide glasses is better described using an alternative metric of network connectivity. Unlike the chalcogenides which generally permit homo-polar bonding, oxide networks have strict chemical rules against such bonding. These additional rules result in a well-defined *short-range* order (SRO) in oxide glasses for which the structure is better viewed as one of polyhedra "hinged" to neighboring polyhedra through bridging oxygen vertices. For example, in SiO_2 the structure is most commonly viewed as one of SiO_4 tetrahedra that are connected by bridging oxygen (BO) bonds to form a continuous random network. Under low frequency stress relevant to viscous flow, deformation of the bulk network is chiefly achieved by bending and bond-breaking near these vertices as opposed to any substantial internal deformation of the SiO_4 tetrahedron. Thus, in regards to viscous flow the network is better characterized by a *coarse-grained* connectivity, such as the average BOs per polyhedron, $\langle n \rangle$, that

better incorporates these (and other) *rigid structural units* (RSUs) as autonomous elements within the network.

In a series of previous publications (Sidebottom and Schnell, 2013; Sidebottom et al., 2014; Sidebottom, 2015, 2019) we have investigated the potential ties between fragility of an oxide glass and its network connectivity. Our investigations have included alkali-modified phosphates, borates, germanates and, most recently, silicates and each study not only built upon but also refined and sometimes corrected the one previous. With the benefit of hindsight, we are now in a position to paint more broadly with a single, seamless brushstroke the picture of how the fragility of *all* network-forming glasses might be described solely by an appropriately coarse-grained network connectivity. In this paper we review these studies using a single consistent nomenclature for discussing how coarse-graining is to be performed. In addition, we close by offering some speculation as to the influence coarse-grained connectivity may have on the glass transition temperature itself.

DISCUSSION

Alkali Phosphate Melts

Our story begins with efforts to measure the fragility of phosphorous pentoxide, P_2O_5, using dynamic light scattering techniques (Sidebottom and Changstrom, 2008). Although P_2O_5 is among the list of oxides likely to form a glass (Zachariasen, 1932), its extreme hygroscopic nature has rendered it largely useless for any practical application (Zarzycki, 1991). The structure of P_2O_5 consists of PO_4 tetrahedra that are interlinked by only $n = 3$ bridging oxygen bonds to neighboring tetrahedra; one oxygen on the tetrahedron is double bonded and so is non-bridging (Brow, 2000). Like SiO_2, the addition of alkali oxides results in the formation of non-bridging oxygens (Zarzycki, 1991) that depolymerize the network until the metaphosphate (50 mol% alkali oxide) composition is reached where all tetrahedra have $n = 2$ bridging oxygen. Here, the oxide structure of the metaphosphate can be characterized as one of polymeric $[PO_3]_n$ chains. The average BO connectivity per PO_4 unit can thus be determined (Brow, 2000) from the mole fraction of alkali oxide, x, as:

$$\langle n \rangle = 2 \times f_2 + 3 \times f_3 = 2 \times [x/(1-x)] + 3 \times [(1-2x)/(1-x)], \quad (2)$$

where the fractions of PO_4 with $n = 2$ BOs increases as $f_2 = x/(1-x)$ while those with $n = 3$ BOs decrease as $f_3 = (1-2x)/(1-x)$.

In the dynamic light scattering study (Sidebottom and Changstrom, 2008) of P_2O_5, great care was exercised in eliminating the presence of unwanted water. Samples of P_2O_5 were sublimed under vacuum into an ampoule that could be flame sealed while still under vacuum and then used *in situ* to carry out photon correlation spectroscopy (PCS) of the viscous relaxation present in the melt above T_g. In this instance, PCS records the dynamic structure factor of the molten liquid to produce a view of the intrinsic structural relaxation occurring near the glass transition point. It provides a measure of the structural relaxation time which itself is proportional to the viscosity and which reaches values of roughly 100 s at T_g. The proportionality factor is the shear modulus which varies only slightly over the range of temperatures probed by PCS. This correspondence can be exploited to generate a plot of relaxation times as a function of inverse scaled temperature like that shown in **Figure 2** that mirrors the Angell plot (**Figure 1**) and which provides an equivalent measure of the fragility index based on the corresponding steepness of the relaxation time.

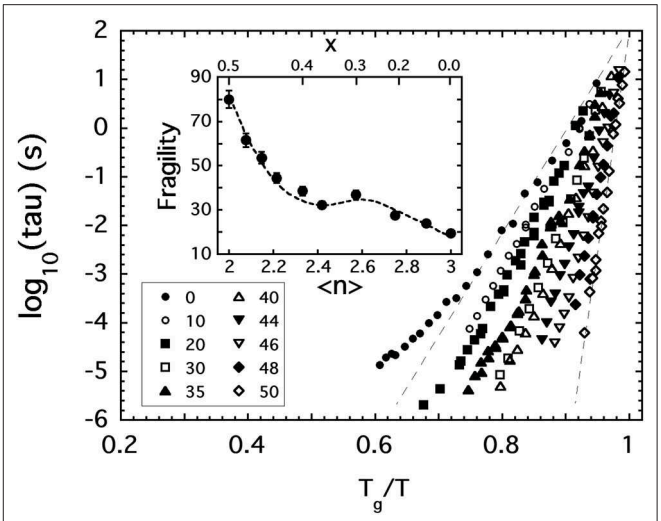

FIGURE 2 | The structural relaxation time (tau) of various $[Na_2O]_x[P_2O_5]_{1-x}$ glass melts plotted against inverse temperature scaled to the glass transition temperature where tau = 100 s. Key shows values of x expressed as a mole % of Na_2O. Inset shows how the fragility index of these melts depends on $\langle n \rangle$, the average BO per phosphate unit.

In addition to P_2O_5, **Figure 2** includes the results of PCS measurements (Fabian and Sidebottom, 2009) conducted on a selection of sodium-modified phosphate melts, $[Na_2O]_x[P_2O_5]_{1-x}$, spanning from $x = 0$ to the metaphosphate composition ($x = 0.5$). The variation of the fragility index, shown in the inset to **Figure 2**, increases with increasing depolymerization of the oxide network in a reasonably monotonic fashion and encompasses the two extremes of fragility ($m = 20$ to $m \approx 85$) seen in **Figure 1**. Moreover, the variation with $\langle n \rangle$ shown in the inset again highlights the potential significance of the $\langle n \rangle = 2.4$ rigidity threshold: this value is near the center of a fragility plateau (where $m \approx 35 \pm 5$) spanning from $\langle n \rangle \approx 2.2$ (below which the network is "floppy" and the fragility increases rapidly) and $\langle n \rangle \approx 2.7$ (beyond which glass melts are highly overconstrained and become less fragile).

The variation of the glass transition temperature over this same range of sodium phosphate glasses is presented in **Figure 3** and shows a rapid decrease with the initial addition of alkali oxide followed at higher concentrations by a more gradual increase on approach to the metaphosphate. Moreover, the glass transition temperature of the metaphosphate depends on the specific alkali species and some (Eisenberg et al., 1966) have suggested it may be correlated to the ionic strength (charge per radius) of the alkali ion as shown in the inset to **Figure 3**. A

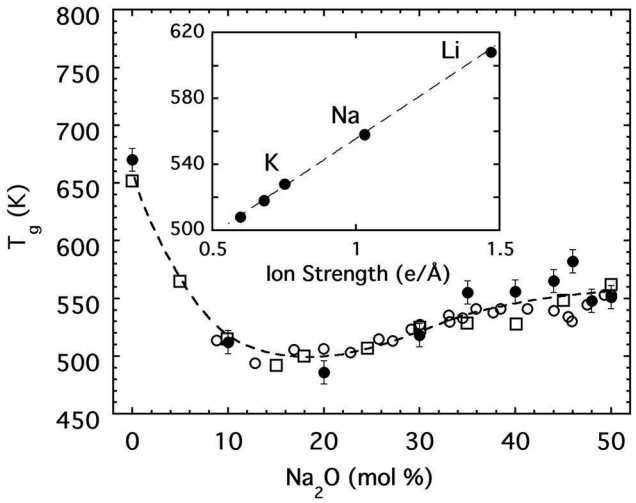

FIGURE 3 | The glass transition temperature for $[Na_2O]_x[P_2O_5]_{1-x}$ glasses. Closed circles are values obtained from dynamic light scattering. Open symbols are literature values [(Eisenberg et al., 1966) (circles); (Hudgens et al., 1998) (squares)]. Dashed line is a guide for the eyes. The inset shows the glass transition temperature for metaphosphate glasses (x = 0.5) as a function of the ion strength.

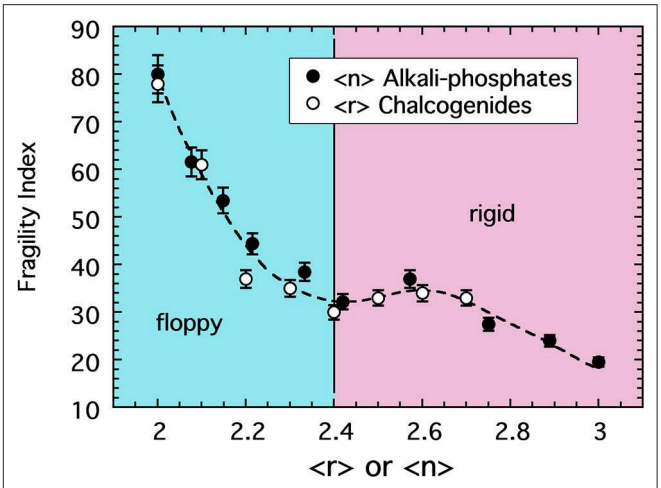

FIGURE 4 | The fragility index of alkali phosphate melts (closed circles) plotted as a function of the average number of bridging oxygen per PO_4 tetrahedra alongside the fragility index of chalcogenide melts (Tatsumisago et al., 1990) plotted as a function of the average bond per atom. The value of $\langle r \rangle = 2.4$ marks the rigidity transition separating under-constrained floppy networks from over-constrained rigid ones.

satisfying interpretation for the anomalous minimum in T_g has been offered by Hoppe (Brow, 2000; Hoppe et al., 2000) on the basis of how the coordination requirements of the alkali ion are satisfied in different ways at low and high concentrations. Below about 20 mol%, alkali ions are able to satisfy their oxygen coordination in *isolated* regions within the 3d network but above 20 mol% they must *share* non-bridging oxygen between multiple phosphate tetrahedra to satisfy the coordination. The result is analogous to a frozen "lake" in which a great many "holes" are punched. At low concentrations the ions sit in isolated holes and their ionic bonds to the non-bridging oxygen of the oxide network surrounding the hole are ineffective in strengthening the overall structure. But, at higher concentrations the holes begin to percolate such that the structure develops into a great many separated rigid regions for which the ionic bonding by the alkali ion is now helpful in strengthening the overall network.

At this junction it is worth stressing again that fragility and glass transition temperature are generally disconnected quantities. This is clearly the case for the alkali phosphates where the compositions ($0.4 < x < 0.5$) for which the greatest changes in fragility occur are those at which almost no change in glass transition temperature is occurring and, reversely, those compositions ($0 < x < 0.2$) were T_g is changing most dramatically are those for which the fragility is changing the least. This disconnect is not unexpected but is consistent with the law of corresponding states perspective raised earlier: there is no *a priori* reason for the scaled slope of the viscosity [Equation (1)] to be directly related to the temperature used in the scaling.

Chalcogenides

Chalcogenide glasses based, for example, on the crosslinking of Se or S chains ($r = 2$) by either Ge ($r = 4$) or As ($r = 3$) share a change in topology from 2d chains to 3d networks similar with that in the alkali phosphate discussed above (He and Thorpe, 1985; Tatsumisago et al., 1990; Böhmer and Angell, 1992). There too, the glass transition temperature decreases with decreasing connectivity ($\langle r \rangle$) but, owing to the absence of any modifier ions or non-bridging oxygens, the decrease is largely monotonic unlike that of the phosphates. Remarkably, the fragility of these two systems is also very similar. This similarity is shown in **Figure 4** where data for the sodium phosphate study plotted as a function of $\langle n \rangle$ are included with the fragility of a series of $Se_{1-2x}As_xGe_x$ melts (Tatsumisago et al., 1990; Böhmer and Angell, 1992) plotted as a function of $\langle r \rangle$.

The coincidence of these two data sets draws us again back to the notion of a law of corresponding states where hidden universalities often emerge when data are appropriately scaled. In determining the fragility, data were scaled by a glass transition temperature that is largely disconnected with the fragility itself. Akin to way the critical point temperature in a liquid-vapor phase transition is set largely by the interaction energy and so differs among different non-ideal gases, the glass transition temperature is an energy scale that differs among different glass compositions. But we see in **Figure 4** the possibility that some additional scaling of the mean field connectivity of the network might expose a common pattern in the fragility of network-forming glasses. Only when the connectivity of the oxide network is defined through a coarse-graining over the RSUs of which it is constructed [i.e., $\langle n \rangle$] does this hidden universality seem appear. Fragility is a measure of viscous flow of the melt and this flow takes place through collective deformations under shear stress (in a zero-frequency limit). In the oxides, the persistence of SRO forces deformations and bond breaking to take place at the weakest linkages and this effectively renormalizes the network to one of rigid polyhedra

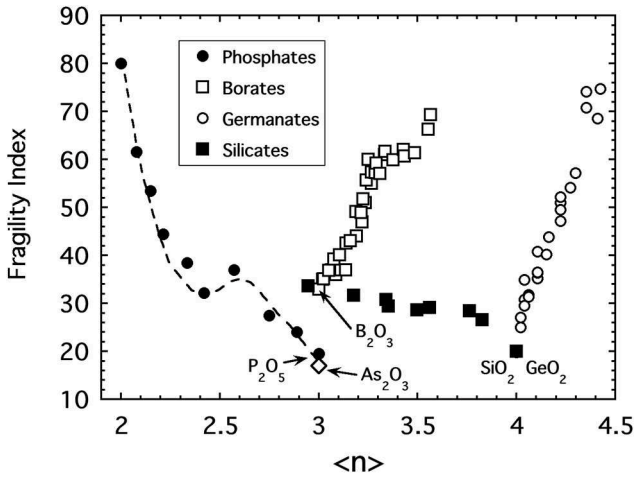

FIGURE 5 | A compilation of fragility indices of various alkali oxide glasses including sodium phosphates (Fabian and Sidebottom, 2009), lithium and sodium borates (Nemilov, 1966; Chryssikos et al., 1994) sodium, potassium and rubidium germanates (Nemilov, 1970; Shelby, 1974), sodium and potassium silicates (Poole, 1949) and arsenic trioxide (Yannopoulos et al., 1999; Sidebottom et al., 2007) as a function of the average bridging oxygen per network-forming cation.

hinged at vertices for which $\langle n \rangle$ becomes the more relevant mean field measure of connectivity.

Other Oxides

The fundamental problem with our idea that $\langle n \rangle$ is the relevant metric of connectivity for oxide networks is that it fails to produce a universal pattern for all the other major oxide glasses! This is evident in **Figure 5** where the fragility of various commercially-relevant glass forming oxides including borates (Nemilov, 1966; Chryssikos et al., 1994), germanates (Nemilov, 1970; Shelby, 1974), and silicates (Poole, 1949) are plotted together as a function of $\langle n \rangle$ the average bridging oxygen connectivity per network-forming cation (i.e., Si, B, Ge, P, and As). In the case of alkali silicates, the fragility behaves like that of the phosphate melts in that it increases with the depolymerization of the network as alkali oxide is introduced. The data shown extend from SiO_2 to the sodium disilicate composition, $Na_2O{:}2SiO_2$, where ∼80% of the SiO_4 tetrahedra possess $n = 3$ bridging bonds while 10% each have $n = 4$ or $n = 2$, respectively (Maekawa et al., 1991).

Sharply at odds with the silicate and phosphate glasses, the fragility of both the alkali borate and alkali germanate glasses display an unanticipated *increase* with increasing network connectivity. They appear to become "floppier" despite the addition of more constraints. In both of these systems, the initial addition of alkali oxide does not produce non-bridging oxygens leading to depolymerization but rather produce increased network polymerization via the formation of polyhedra with higher coordination numbers. In the borate system (Griscom, 1978), trigonal BO_3 units in B_2O_3 are transformed to 4-coordinated, BO_4 tetrahedra when alkali oxide is added (up to about 30 mol%). Similarly, in the germanate system (Henderson and Fleet, 1991) 4-coordinated GeO_4 units are converted to 5-coordinated units as alkali oxide is added (up to about 20 mol%). Only at higher alkali concentrations do substantial numbers of non-bridging oxygens form in either system. The initial increase of network connectivity followed by a decrease causes a number of glass properties to display "anomalous" behavior (Henderson, 2007) with either a maximum or minimum occurring near 30 and 20 mol%, respectively. A prime example is the glass transition temperature (discussed later) which exhibits a maximum.

In the following section, we examine each of these other oxide glass systems to demonstrate how *additional* RSUs that appear in these materials *beyond* that of the short-range order alone can influence the mean field connectivity. Coarse-graining must be extended for these materials to include intermediate range order (IRO) structures when present and we emphasize how a consistent coarse-graining procedure places the fragility of these and other network-forming glasses onto a common master curve as a function of a generalized network connectivity.

Alkali Borates

In comparison with all the other primary oxide glasses whose fragility indices range between $m \approx 17$ and 20, boron trioxide (B_2O_3) has an anomalously high value ($m \approx 32$). Oddly, the fragility of B_2O_3 is far greater than that of arsenic trioxide, an otherwise chemically identical material that likewise favors trigonal (AsO_3) units in its network structure (Galeener et al., 1979) and this suggests that something in B_2O_3 is structurally amiss. Owing in part to the superb NMR properties of the ^{11}B nucleus, the literature (Krogh-Moe, 1962; Griscom, 1978; Youngman and Zwanziger, 1996) has developed an unparalleled understanding of the structure of boron trioxide and its alkali-modified variations that is summarized in **Figure 6** for potassium borate glasses (Youngman and Zwanziger, 1996). It is now well established that roughly two-thirds of the trigonal BO_3 units in B_2O_3 join together into larger-scaled RSUs known as "boroxol rings." These small, 3-membered ring structures exhibit a very sharp Raman band associated with the breathing mode of the ring (Galeener et al., 1978; Walrafen et al., 1980) and this identifies the ring itself as a separate, autonomous rigid structure within the network likely to resist internal deformations under viscous flow. In addition to rings, both diborate and tetraborate structures are also observed (Krogh-Moe, 1962) and the distributions of these RSUs exhibit a complex variation with alkali concentration (see **Figure 6**).

In order to coarse-grain the connectivity, an accounting scheme is needed that can be faithfully applied whereby the connections in the network are properly enumerated on the same per network forming cation basis but with an accommodation made for the presence of these larger, IRO structures. The central ingredient is recognizing how the topological connectivity of a trigonal unit that participates in a ring (or other unit) is generally reduced when compared with a unit that is "free" of such IRO structures. In the case of the boroxol ring for example, the $n = 3$ connectivity of a trigonal unit is reduced to $n = 2$ since each such trigonal unit functions only to connect the external network to the ring itself. In other words, each trigonal unit employs two BO

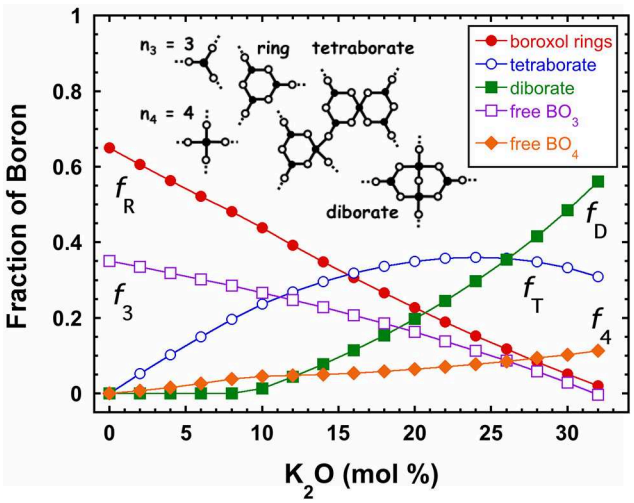

FIGURE 6 | The fraction of boron atoms in various structural units in potassium borate glasses. Values are derived from an NMR investigation (Youngman and Zwanziger, 1996) and include five basic configurations illustrated as cartoons in the figure. These include free boron units of either 3 or 4 coordination as well as boroxol rings, diborate, and tetraborate structures discussed in the text.

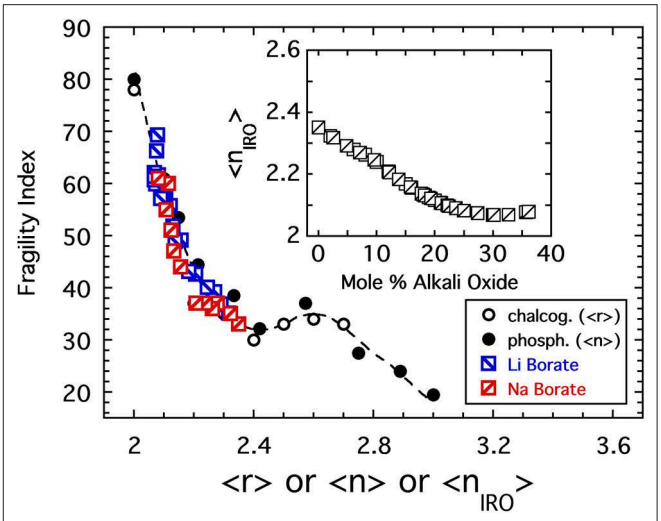

FIGURE 7 | The fragility index of lithium and sodium borate glasses (Nemilov, 1966; Chryssikos et al., 1994) is plotted as a function of the connectivity coarse-grained to include IRO structures. Also shown are the data from **Figure 4** for both the chalcogenides (plotted as a function of the average bond per atom) and the alkali phosphates (plotted as a function of the average BO per phosphate). The inset shows how the coarse-grained connectivity of the borates decreases with increasing alkali oxide addition.

bonds to connect itself to the ring of which one is topologically redundant. Using this accounting scheme for B_2O_3 in which only $f_R = 65\%$ of the trigonal units are in rings while the remaining $f_F = 35\%$ are free, we obtain an adjusted connectivity $\langle n_{IRO}\rangle = 0.65 \times 2 + 0.35 \times 3 = 2.35$, that is reduced in comparison to the BO-only connectivity ($\langle n\rangle$) and which relocates the fragility index of B_2O_3 onto the fragility pattern highlighted in **Figure 4**.

In the alkali-modified borates, addition of alkali oxide drives the production of 4-coordinated boron tetrahedra which, as seen in **Figure 6**, almost exclusively participate in either diborate or tetraborate structures illustrated in that figure. Using the same accounting scheme, we conclude that each of the borate units in a diborate structure (two BO_3 units and two BO_4 units) have a reduced connectivity of $n = 2$, while in a tetraborate structure, six of the eight borate units located on the periphery of the structure have connectivity of $n = 2$, while the other two units that are internal provide no connectivity with the external network ($n = 0$). Thus, the average connectivity of boron in a tetraborate structure is $n = \frac{6}{8} \times 2 + \frac{2}{8} \times 0 = 1.5$ and we arrive at a formula for the coarse-grained connectivity in alkali borates:

$$\langle n_{IRO}\rangle = 4 \times f_4 + 3 \times f_3 + 2 \times \left(f_R + f_D\right) + 1.5 \times f_T, \qquad (3)$$

where f_4 is the fraction of free 4-coordinated boron, f_3 the fraction of free 3-coordinated boron, f_R the fraction of boron in boroxol rings, f_D the fraction of boron in diborate units, and f_T the fraction of boron in tetraborate units. Since these fractions are taken directly from the NMR results (Youngman and Zwanziger, 1996) of **Figure 6**, the coarse-graining formula in Equation (3) contains *no adjustable parameters* and is seen in **Figure 7** to reposition the fragility indices of all the alkali borates coincident with fragility pattern of both the chalcogenide and alkali phosphate glass melts discussed earlier. As seen in the inset, this happens because the coarse-grained connectivity of the network actually decreases from a value near 2.35 for B_2O_3 to values near 2.05 for glasses with 33 mol% despite the increasing density of bridging oxygen. This decrease is a consequence of formation of diborate and tetraborate structures that promote a lowering of the effective network connectivity.

Alkali Germanates

Given the success in relocating the fragility index of alkali borates, we might anticipate that RSUs are also present in alkali germanates and similarly decrease the coarse-grained network connectivity despite the increasing formation of BO bonds. Here, evidence for such structures is gleaned from Raman spectroscopy (Henderson and Fleet, 1991) in which one of two vibrational modes in the range between 350 and 650 cm^{-1} has been interpreted as being caused by 3-membered rings. The Raman spectra obtained by Henderson for sodium germanate glasses with compositions <20 mol% Na_2O are shown in the inset to **Figure 8** where one observes a progressive growth in the 520 cm^{-1} ring mode at the expense of the non-ring mode at lower energy. Unlike NMR, the extraction of quantitative populations of RSUs from Raman bandshapes is less accurate. Nevertheless, using data provided by Henderson, we have performed an analysis of the integrated area beneath these two modes to generate an estimate of the fraction, f_R, of rings. The result is plotted in **Figure 8** and indicates a rapid increase in rings from a starting value near 40 (±10)%; a value which is also supported by estimates taken from a molecular dynamics simulation (Giacomazzi et al., 2005) of GeO_2.

Given that a large fraction of rings might be present in these alkali-germanate glasses, coarse-graining efforts need to

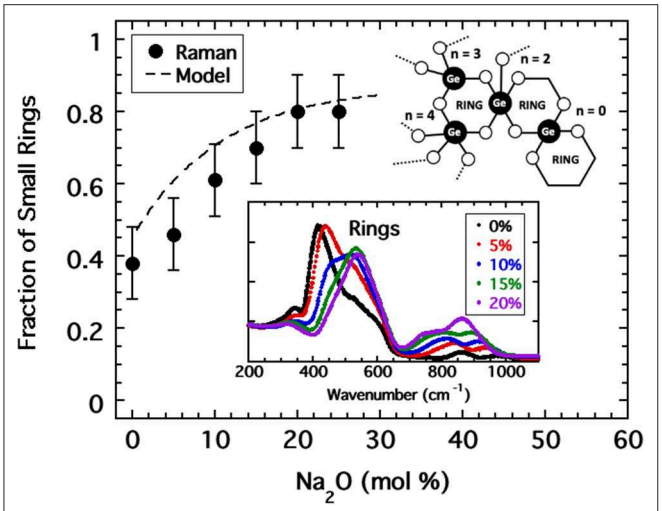

FIGURE 8 | A curve fitting analysis of the low energy Raman band (shown as inset) of sodium germanate glasses (Henderson and Fleet, 1991) provided an estimate of the fraction of this band which is associated with 3-membered rings plotted as solid circles. The dashed line is the corresponding fraction of rings modeled as a continuous function of sodium oxide content by Equation (5) for which parameters were adjusted to best produce a collapse of fragility indices in **Figure 9**. Inset includes a cartoon illustration of various possible RSUs that occur as a consequence of 3-membered rings.

TABLE 1 | Coarse-grained connectivity of six possible RSUs found in alkali germanate glasses as discussed in the text.

	$(\mathbf{1}-\mathbf{f_R})$	$\mathbf{f_R}\,(\mathbf{1}-\mathbf{f_R})$	$\mathbf{f_R^2}$
$\boldsymbol{f_4}$	$n = 4$	$n = 3$	$n = 0$
$\boldsymbol{f_5}$	$n = 5$	$n = 4$	$n = 2$

Each row and column combination represent a single RSU species whose likelihood is proportional to the product of the row by column headings and whose connectivity is given by the table entry. The parameters, $f_{i\,=\,4,5,R}$, represent the fraction of germanium that are 4-, 5-coordinated or participants in 3-membered rings, respectively.

account for all the potential configurations that might appear in any substantial amounts. In addition to dividing the Ge units up by their coordination states where the fraction of four-coordinated units, $f_4 = (1-3x)/(1-x)$, and the fraction of five-coordinated units, $f_5 = 2x/(1-x)$, are established by requirements for charge neutrality, we also must divide these units with regards to the probability that a given unit will be participating in one *or more* ring structures. An added complication not seen in the case of boroxol rings is the possibility for a GeO_4 (or GeO_5) unit to participate in two rings simultaneously forming a "double ring" structure. Including this new possibility, one finds six possible configurations whose corresponding connectivities are summarized in **Table 1**.

If f_R is again defined as the fraction of Ge participating in 3-membered rings, then, regardless of coordination state, a fraction $(1-f_R)$ of the Ge will be "free" in the sense that they do not participate in any ring structure. Such a free Ge will have a connectivity of $n = 4$ if 4-coordinated and $n = 5$ if 5-coordinated, respectively. Likewise, a fraction $f_R(1-f_R)$ of the Ge will participate in a single ring but not in two rings simultaneously. In accord with the rules established for boroxol rings, each such Ge will suffer a reduction in connectivity owing to a single redundant BO bond. Finally, some Ge will be found that participte in two rings simultaneously with the joint probability f_R^2. When a GeO_5 unit participates in two rings simultaneously it functions topologically as $n = 2$ since three of the four BOs being contributed to the rings are redundant. However, when a GeO_4 unit participates in two rings simultaneously it functions analogously to the BO_4 unit in the *interior* of a tetraborate structure and so provides no topological connection to the external network whatsoever.

The coarse-grained connectivity is then given by the weighted average:

$$\langle n_{IRO}\rangle = (1-f_R)(4f_4+5f_5) + f_R\left[(1-f_R)(3f_4+4f_5) + f_R(2f_5)\right]. \quad (4)$$

To model the rapid increase in the fraction of Ge in rings at arbitrary alkali concentrations, an inverted exponential decay function of the form:

$$f_R = f_{SAT} + (f_o - f_{SAT})\,e^{-x/x_o}, \quad (5)$$

was chosen (Sidebottom et al., 2014) in which f_{SAT}, f_o, and x_o are parameters adjusted to maximize the coincidence of the fragility index with the pattern established in **Figure 4**. Values of $f_o = 0.45$, $f_{SAT} = 0.87$, and $x_o = 10.5\%$ were found to provide good coincidence as shown in **Figure 9**. These parameters predict a fraction of rings plotted as a dashed line in **Figure 8** that falls within the error of that estimated from analysis of the Raman modes.

Alkali Silicates

Like the alkali phosphates, addition of alkali oxide to the SiO_2 network results in network depolymerization through the production of NBOs and NMR studies (Stebbins, 1987; Maekawa et al., 1991) have developed a reasonably clear understanding of the fractions of SiO_4 tetrahedra (f_4, f_3, f_2, f_1, and f_0) with $n = 4$, 3, 2, 1, or zero BO bonds, respectively. Less prominent in the literature is a discussion of possible IRO structures that might serve to reduce the effective connectivity of the network. Only rather recently has there emerged a handful of publications (Kalampounias et al., 2006a,b; Malfait et al., 2007) which suggest such structures exist and that provide quantitative indications for their numbers. Among these is a recent NMR study (Malfait et al., 2007) where the authors observed an additional resonance attributed to 3-membered rings in highly modified potassium, rubidium and cesium silicate glasses but which was absent in both lithium, and sodium silicates. The intensity of this additional mode was reported to increase exponentially with increasing potassium oxide and was used to estimate (Malfait et al., 2007) that as many as $f_R \approx 20\%$ of SiO_4 tetrahedra participate in 3-membered rings for $x = 40$ mol% K_2O.

Small 3-membered rings are virtually absent in SiO_2 (Galeener, 1982), but a recent Raman study (Kalampounias

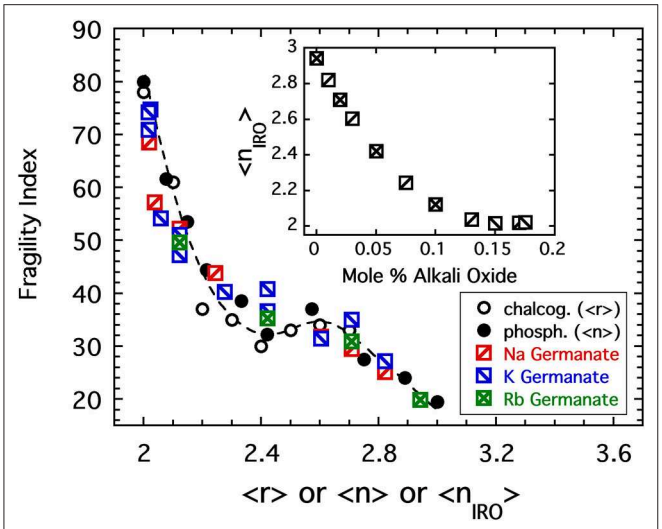

FIGURE 9 | The fragility index of sodium, potassium, and rubidium germanate glasses (Nemilov, 1970; Shelby, 1974), is plotted as a function of the connectivity coarse-grained to include IRO structures as described in the text. Also shown are the data from **Figure 4** for both the chalcogenides (plotted as a function of the average bond per atom) and the alkali phosphates (plotted as a function of the average BO per phosphate). The inset shows how the coarse-grained connectivity decreases rapidly with increasing alkali oxide addition.

et al., 2006a,b) of molten silica near T_g revealed the existence of other rigid structural units. In what had previously been assessed as a single broad symmetric stretching band the authors resolved three separately distinct modes. Drawing heavily upon a similar band structure found in $ZnCl_2$, the authors have assigned these separated modes to represent fractions of SiO_4 tetrahedra that are either "free" (f_F), edge-sharing (f_{ES}), or participants in a so-called "super-tetrahedron" cluster (f_{ST}) consisting of four SiO_4 tetrahedra combined into a larger replica tetrahedron.

Limiting the analysis only to compositions below 40 mol% alkali oxide for which $f_1 = f_0 = 0$, we arrive at 13 possible configurations that a SiO_4 tetrahedron could adopt that are summarized in **Table 2**. The connectivity assignments in the table for free units and rings follow directly from the previous discussion on coarse-graining of the alkali germanates but must be augmented slightly to allow for SiO_4 units in rings *with* NBOs. The presence of NBOs in the alkali silicates raises the topological complication of so-called "dangling bonds" (Thorpe, 1983; Boolchand and Thorpe, 1994) which arise when, for example, a SiO_4 tetrahedra with two NBOs participates in a 3-membered ring. Our approach to these situations is to assign zero connectivity to the unit as others have advocated (Thorpe, 1983). This reflects the impression that the unit no longer provides connectivity to the external network but rather has been fully consumed into the RSU itself much in the way a GeO_4 unit in a double ring is internalized and so assigned $n = 0$ (see **Table 1**). As for the super-tetrahedron, each SiO_4 tetrahedron must complete 3 BO connections to this RSU of which two are redundant. An SiO_4 unit with just 3 BO will

TABLE 2 | Coarse-grained connectivity of 13 allowed configurations found in alkali silicate glass networks with <40 mol% alkali oxide as discussed in the text.

	f_F	f_{ST}	$f_{ES}(1-f_{ES})$	$f_R(1-f_R)$	f_{ES}^2	f_R^2
f_4	$n=4$	$n=2$	$n=3$	$n=3$	$n=2$	$n=0$
f_3	$n=3$	$n=0$	$n=2$	$n=2$	NA	NA
f_2	$n=2$	NA	$n=0$	$n=0$	NA	NA

Each row and column combination represent a single RSU species whose likelihood is proportional to the product of the row by column headings and whose connectivity is given by the table entry. Entries with NA denote situations that are not possible. The parameters, $f_{i=4,3,2,R,ES,ST,F}$, represent the fraction of silicon that have 4, 3, 2 bridging oxygen, are participants in 3-membered rings, edge-sharing connections, supertetrahdrons, or uninvolved in any RSU, respectively.

be entirely consumed by the super-tetrahedron and have no remaining connection to the external network (so $n = 0$) while an SiO_4 unit with only 2 BO would be incapable of existing in a super-tetrahedron at all. Although a pair of edge sharing SiO_4 tetrahedra do not technically generate a RSU (in the sense that a RSU is by definition an autonomous object able to resist internal deformation under the low frequency stress associated with viscous flow), each SiO_4 unit suffers a reduction in connectivity owing to the presence of a redundant BO bond. In the rarer instances for which a SiO_4 tetrahedra participates in two edge sharing connections simultaneously, the unit functions, in a topological sense, as the linkage of a 2d chain ($n = 2$).

Coarse-graining the connectivity of these alkali silicate melts is thus an ambitious effort involving a properly-normalized weighted average of the form:

$$\begin{aligned}\langle n_{IRO}\rangle = \frac{1}{Z}\{f_4[4f_F + 2f_{ST} + 3f_{ES}(1-f_{ES}) + 3f_R(1-f_R) \\ +2f_{ES}^2] + f_3[3f_F + 2f_{ES}(1-f_{ES}) \\ +2f_R(1-f_R)] + 2f_2f_F\},\end{aligned} \tag{6}$$

where

$$\begin{aligned}Z = \sum f_4[f_F + f_{ST} + f_{ES}(1-f_{ES}) + f_R(1-f_R) + f_{ES}^2 + f_R^2] \\ + f_3[f_F + f_{ST} + f_{ES}(1-f_{ES}) + f_R(1-f_R)] \\ + f_2[f_F + f_{ES}(1-f_{ES}) + f_R(1-f_R)].\end{aligned}$$

Not only is the greater diversity of potential structural motifs a challenge, so too is the limited availability of quantitative values of the compositional dependence of the fractions (f_F, f_{ST}, f_{ES}, and f_R) of these motifs needed to complete the calculations. In principle, these fractions together with the fractions of BO per Si (f_4, f_3, and f_2) would present an ill-advised curve fitting exercise with seven adjustable parameters. In an effort to avoid a result that to the reader might appear to be merely contrived from some arbitrary, free adjustment of these parameters, the parameters have been *fixed* to values dictated by the literature sources cited earlier. The values of f_4, f_3, and f_2, for example, are set by values taken directly from data tables in the NMR study (Maekawa et al., 1991). For the SiO_2 glass, the minute fraction of rings ($f_R = 0$) is ignored while the values of $f_F = 20\%$, $f_{ST} = 30\%$, and $f_{ES} =$

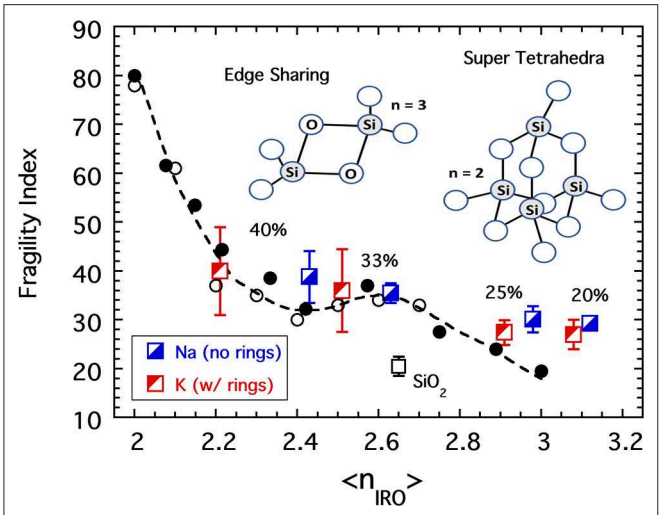

FIGURE 10 | The fragility indices of SiO_2 and selected sodium and potassium silicate glasses (Poole, 1949; Nascimento and Aparicio, 2007; Nemilov, 2007) plotted as a function of the connectivity coarse-grained to include IRO structures as described in the text. Also shown are the data from **Figure 4** for both the chalcogenides (plotted as a function of the average bond per atom) and the alkali phosphates (plotted as a function of the average BO per phosphate). Cartoons illustrate two of the structures, edge-sharing tetrahedra and a super-tetrahedron unit, reported (Kalampounias et al., 2006a) to be present in silicate melts.

50% are assigned the corresponding fractions of areas under the three curve fit bands based on analysis of a figure published in the Raman study (Kalampounias et al., 2006a). For alkali modified silicates with 20–40 mol% alkali, $f_{ES} = 0$ based on the absence of this band reported in the second Raman study (Kalampounias et al., 2006b). Here the values of f_R for the potassium silicates are taken from an extrapolation published as a figure in (Malfait et al., 2007) while for the sodium silicates this fraction is set to $f_R = 0$ and the values for f_F and f_{ST} were set to make up the balance with the ratio $\frac{f_F}{f_{ST}} \approx 5.5$ fixed to the value quoted in the Raman study of 20 mol% potassium silicate (Kalampounias et al., 2006b). Further details of this analysis, including alternative model distributions that avoid any substantial edge-sharing species in SiO_2, may be found elsewhere (Sidebottom, 2019). Results of coarse graining for the fragility of the alkali silicates is shown in **Figure 10**, and given that no adjustment of parameters has been attempted, the collapse to the earlier master curve is deemed to be reasonably successful.

Network-Forming Intermediates

Throughout our analysis of network connectivity in alkali-modified oxide glasses, we have not attached any connectivity to the alkali ion itself. This decision stems from evidence that alkali ions are only weakly tethered to their charge-compensating site on the network (either a NBO or a higher coordinated unit, e.g., GeO_5 or BO_4) and remain considerably mobile in the glassy state well below T_g. Many impedance spectroscopy studies (Dyre et al., 2009) of ion-containing glasses observe relaxation processes associated with the hopping diffusion of the ion between charge compensating sites through the voids in the (frozen) oxide network. Unlike Si^{4+}, Ge^{4+}, and B^{3+} which are identified (Zachariasen, 1932) as *network-forming* cations, alkali ions are described as *network-modifying* cations (Zarzycki, 1991) as they often depolymerize the network via the formation of NBOs without actually participating in the oxide network itself. In between these extremes are several divalent and trivalent ions (e.g., Zn^{2+}, Ca^{2+}, Al^{3+}) that are referred to as *intermediates* as they are capable of functioning either as a network-former or modifier.

In the sodium metaphosphate glass, $NaPO_3$, the oxide structure consists of chains of PO_4 tetrahedra with $n = 2$ BO connections each (Brow, 2000). The sodium ion is charge-compensated by the remaining two NBOs of which each shares half the negative charge and provides a weak crosslinking to the network (as was discussed earlier in regards to the glass transition temperature in **Figure 3**). In both Zn metaphosphate and Al metaphosphate glasses the structure continues to develop from chains of PO_4 tetrahedra each making two BO connections with neighboring PO_4 tetrahedra (Brow, 1993, 2000; Brow et al., 1993). However, these glass melts are stronger than that of $NaPO_3$ (i.e., much lower fragility) and this is suggestive that both Zn^{2+} and Al^{3+} are functioning as network-forming ions that forge increasing connectivity most likely as a consequence of their greater ionic strength (Rodrigues and Wondraczek, 2014; Xia et al., 2019). Indeed, dynamic light scattering measurements (Tran and Sidebottom, 2013; Sidebottom and Vu, 2016) of the fragility in binary mixtures of both $[Zn(PO_3)_2]_y[NaPO_3]_{1-y}$ and $[Al(PO_3)_3]_y[NaPO_3]_{1-y}$ confirm a monotonic decrease in fragility with the substitution for Na by either Zn or Al.

If we treat Zn^{2+} and Al^{3+} as network-forming cations, we must presume that these cations form BO connections with PO_4 tetrahedra that increase the connectivity of the network. In the instance of $Zn(PO_3)_2$ there are, in one chemical formula, two PO_4 polyhedra associated with each Zn^{2+} cation allowing Zn^{2+} to complete its desired coordination of $n = 4$. Meanwhile each of the PO_4 tetrahedra already maintain two BO connections to neighboring PO_4 tetrahedra (to create a chain structure of polymeric $[PO_3]_n$) while the remaining two oxygen are free to coordinate to the Zn^{2+} cation. We assume that the Zn^{2+} cation can be coordinated either in a *corner sharing* fashion or an *edge sharing* fashion to the surrounding PO_4 tetrahedra with equal likelihood and so arrive at three ways in which the Zn^{2+} cation in one chemical formula could be connected with the network. These are illustrated in the inset to **Figure 11**. Firstly, the Zn^{2+} cation could bond with four separate PO_4 tetrahedra via corner sharing connections only. In this case both the ZnO_4 tetrahedron and the two PO_4 tetrahedra (per chemical formula) would be assigned a connectivity of $n = 4$. On a per chemical formula basis the average connectivity per network-forming cation of such a configuration would then be:

$$n_{avg}^{CSCS} = \frac{2}{3} \times 4 + \frac{1}{3} \times 4 = \frac{12}{3}.$$

Secondly, it could bond with just two separate PO_4 tetrahedra via edge sharing connections only. In this case the ZnO_4 tetrahedron

would have a connectivity of $n = 2$ (one redundant BO bond to each PO_4), while each PO_4 tetrahedra would have $n = 3$ (one redundant BO bond to the Zn). In this instance the average connectivity would be:

$$n_{avg}^{ESES} = \frac{2}{3} \times 3 + \frac{1}{3} \times 2 = \frac{8}{3}.$$

Lastly, the Zn^{2+} could form a corner sharing connection to two PO_4 tetrahedra and an edge sharing connection to another. In this last case, the ZnO_4 tetrahedron would have a connectivity of $n = 3$ (one redundant bond to one PO_4 unit) while one PO_4 unit would have connectivity of $n = 3$ and the other $n = 4$. In this last scenario there are two permutations each with the same average connectivity:

$$n_{avg}^{ESCS} = n_{avg}^{CSES} = \frac{1}{3} \times 4 + \frac{1}{3} \times 3 + \frac{1}{3} \times 3 = \frac{10}{3}.$$

If we now add to this the reasonable assumption of a purely random distribution in which the probability for corner sharing equals that for edge sharing (i.e., $f_{CS} = f_{ES} = 50\%$), then $f_{CS}f_{CS} = f_{ES}f_{ES} = f_{CS}f_{ES} = 1/4$ and the coarse-grained connectivity of zinc metaphosphate glass would be:

$$\langle n_{Zn(PO_3)_2} \rangle = \frac{1}{4} \left\{ \frac{12}{3} + 2 \times \frac{10}{3} + \frac{8}{3} \right\} = 3.33, \quad (7)$$

and (assuming ideal mixing) the connectivity of mixtures of the form $[Zn(PO_3)_2]_y[NaPO_3]_{1-y}$ would have a connectivity given by:

$$\langle n(y) \rangle = y \langle n_{Zn(PO_3)_2} \rangle + (1-y) \langle n_{NaPO_3} \rangle = 3.33y + 2(1-y). \quad (8)$$

A similar analysis (Sidebottom and Vu, 2016) for the four possible configurations of a 6-fold coordinated Al^{3+} cation predicts the connectivity of aluminum metaphosphate to be:

$$\langle n_{Al(PO_3)_3} \rangle = \frac{1}{8} \left\{ \frac{18}{4} + 3 \times \frac{16}{4} + 3 \times \frac{14}{4} + \frac{12}{4} \right\} = 3.75, \quad (9)$$

with mixtures of the form $[Al(PO_3)_3]_y[NaPO_3]_{1-y}$ having connectivity:

$$\langle n(y) \rangle = y \langle n_{Al(PO_3)_3} \rangle + (1-y) \langle n_{NaPO_3} \rangle = 3.75y + 2(1-y). \quad (10)$$

Using Equations (9) and (11), the fragility of both Zn-Na and Al-Na metaphosphate melts is plotted together with the master curve in **Figure 11** and again show good coincidence.

Glass Transition Temperature

In this final section we turn attention to the nature of the glass transition temperature in network-forming oxides. The glass transition temperature should be viewed as a relevant energy scale associated with the average thermal energy needed to generate sufficient bond breaking so as to facilitate a viscous flow

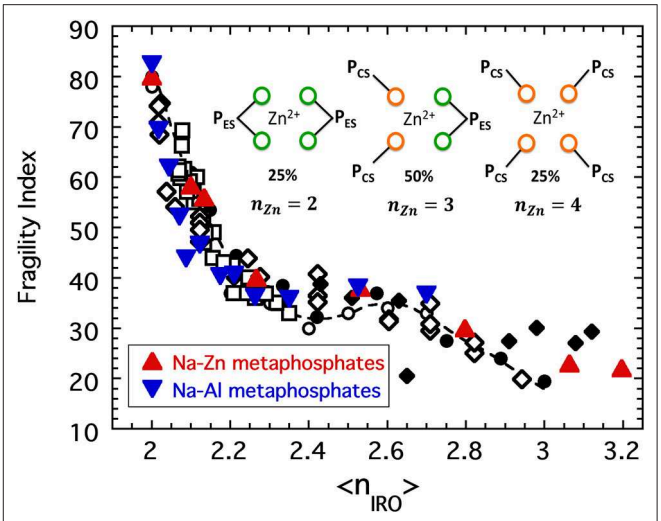

FIGURE 11 | The fragility indices of $[Al(PO_3)_3]_y[NaPO_3]_{1-y}$ and $[Zn(PO_3)_2]_y[NaPO_3]_{1-y}$ plotted as a function of the connectivity coarse-grained to include both edge-sharing and corner-sharing configurations as described in the text. Also shown are the collective data from previous figures: sodium phosphates (solid circles), chalcogenides (open circles), alkali borates (open squares), alkali germanates (open diamonds), and alkali silicates (solid diamonds). The inset shows the three possible configurations of a Zn cation in $Zn(PO_3)_2$ glass.

of 10^{12} Pas (as the T_g is commonly defined) and this identification is further supported by the well-known empirical "2/3 rule" (Wang et al., 2006) that for a large number of glassforming materials T_g is typically about 2/3 of the melting temperature. In light of our earlier theme regarding a law of corresponding states, this T_g need not have any formal relation to the fragility of the melt. One would not anticipate T_g to mimic the compositional variations in fragility and, indeed, we already have acknowledged this to be the case for alkali phosphate melts whose glass transition temperature is influence by both depolymerization of the oxide network and by the restorative effects of crosslinking by alkali ions. Nevertheless, there are a handful of examples that suggest the glass transition temperature may still be influenced by the network connectivity and we explore these here. Admittedly, the evidence presented here is largely anecdotal and so the discussion should be regarded as only a starting point for further investigations.

Firstly, consider the glass transition temperature of both the alkali borates and germanates which are plotted in **Figure 12** as a function of the alkali oxide content just up to the levels where substantial numbers of NBOs would begin to develop. The general increase in the glass transition would suggest that this energy scale is mainly influenced by the degree of network polymerization (characterized either by $\langle r \rangle$ or $\langle n \rangle$) which initially increases as a result of increasing coordination. This suspicion is also supported at higher alkali concentrations (beyond that plotted in **Figure 12**) where the T_g of both systems begins to decrease due to the formation of NBOs that then depolymerize the network. In both cases, the initial absence of NBOs in the

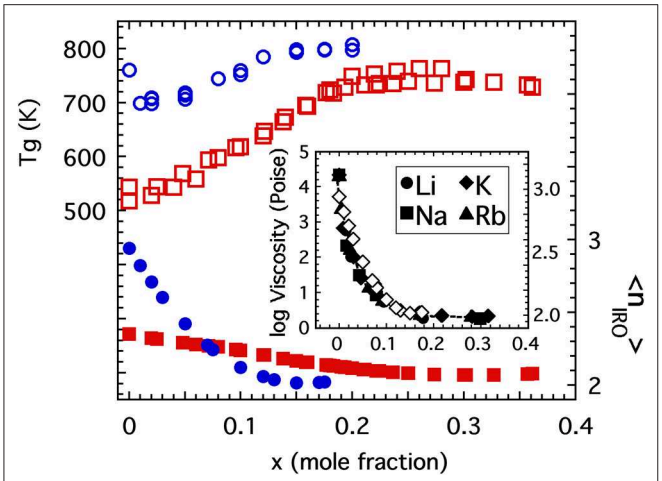

FIGURE 12 | The glass transition temperature of alkali germanates (Shelby, 1974; open circles) and alkali borates (Gupta and Mauro, 2009; open squares) as a function of the mole fraction of alkali oxide with scale on the left side. Also plotted are the coarse-grained connectivity (discussed in the text) for alkali germanates (solid circles) and alkali borates (solid squares) with scale on the right side. Inset shows the close correspondence between the rapid decrease in 1,300°C viscosity of alkali germanate melts (Riebling, 1963; solid symbols) and the rapid decrease in coarse-grained connectivity (open diamonds).

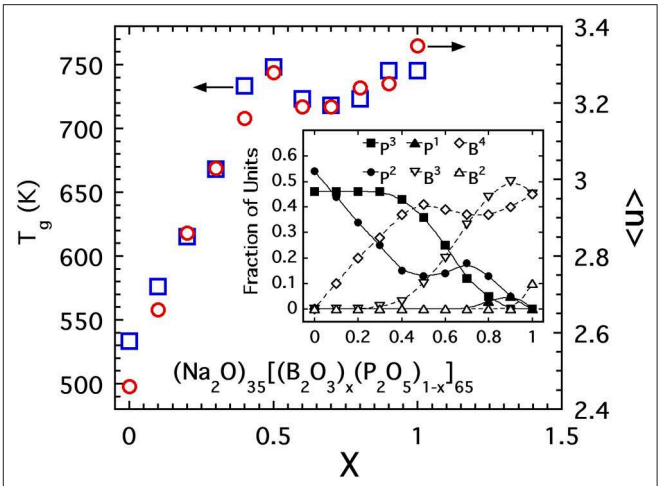

FIGURE 13 | The glass transition temperature (open squares, scale on left side) and average bridging oxygen per network forming cation (open circles, scale on right side) of sodium borophosphate glasses (Christensen et al., 2012). Inset shows the fraction of boron and phosphate units with a given bridging oxygen coordination number used in computing $\langle n \rangle$.

network preclude the possibility for the alkali ions to function as crosslinks between separate "patches" of disconnected oxide network and so the restorative effect seen in the alkali phosphate is not present at these lower concentrations and would not be anticipated until large numbers of NBOs have formed. This tie between network constraints and T_g has long been suggested as the cause for the borate and germanate "anomalies" (Henderson, 2007).

Secondly, we highlight results of a study of borophophate glasses (Christensen et al., 2012) with a fixed alkali content. Extensive NMR investigations of this specific glass system provide a clear picture of the fractions of species with a given number of BO connections. The compositional variation of these fractions is presented as an inset to **Figure 13** and shows a rather complex variation with exchange of P by B across the series. Using these fractions, one can compute the average connectivity per network forming cation and this has been plotted in **Figure 13** along with the measured glass transition temperatures. The scale for T_g has been adjusted to best overlay the data points with those of $\langle n \rangle$ in the intermediate range of compositions and the match is quite reasonable over a range from $0.2 < x < 0.9$. While this matching procedure is somewhat contrived, the agreement is rather remarkable especially as it captures the peculiar "peak and dip" that occurs for *both* $\langle n \rangle$ and T_g in the range $0.4 < x < 0.8$. The ability for both quantities to capture this non-monotonic clearly indicates that T_g is dominated by $\langle n \rangle$ in this borophosphate series.

Lastly, we reflect on the possibility for the coarse-grained connectivity, $\langle n_{IRO} \rangle$, to influence the glass transition temperature. Returning to the glass transition temperatures of the alkali borates and alkali germanates in **Figure 12**, one sees that although the T_g of both generally increases with the polymerization of these oxide networks, the T_g of the alkali germanates actually *decreases* by some 80 degrees K with the initial addition of just 1 or 2 mol% alkali oxide (Shelby, 1974). This drop has long been associated with a rapid drop in the high temperature viscosity of these same melts (Riebling, 1963; Henderson, 2007) shown in the inset to **Figure 12**. Although some (Shelby, 1974) have speculated the drop could be the result of sample contamination by small amounts of water or due to formation of non-bridging oxygens with initial alkali addition, we suggest here an alternative explanation. As seen in the inset to **Figure 12** the drop off of the high temperature viscosity is very closely mimicked by the rapid decrease in coarse-grained connectivity $\langle n_{IRO} \rangle$ and so the drop in T_g might be a reflection of the rapid change in IRO structure taking place in these low alkali germanate glasses. By comparison, the decrease of $\langle n_{IRO} \rangle$ in the alkali borates is far less rapid and this could explain why the T_g of these melts exhibits no initial drop off. Thus, we propose that while $\langle n \rangle$ is likely the most dominant structural influence for setting the glass transition temperature, the presence of larger-sized RSUs that comprise the IRO may also produce a significant influence in the right circumstances.

These examples support the general notion that the glass transition temperature increases with increasing network connectivity. This makes intuitive sense. Our view of $k_B T_g$ is that of a level of thermal energy needed to break (and reform) sufficient numbers of bridging bonds to achieve a bulk viscosity of 10^{12} Pas. Increasing the density of these bridging bonds implies that a higher level of energy would be needed in order to re-establish the same transition-level viscosity. What might be more speculative is the notion that the generation of IRO structures could lower the glass transition temperature by virtue

of lowering the density of those bridging bonds that matter to viscous flow. Despite an increasing number of BO per cation, the formation of IRO is accompanied by larger-scale rigid elements that flex primarily through bridging oxygen at their vertices and it is only these weaker linkages that need be broken to facilitate viscous flow. As we have witnessed in the alkali germanate glasses, the density of these weaker linkages can decrease very rapidly causing a similar drop in viscosity (see **Figure 12**) along with a drop in T_g.

CONCLUSIONS

The equilibrium viscosity of some glass forming materials can change by over 10 orders of magnitude for as little as a 10% increase in thermal energy and this sensitivity to temperature changes near the glass transition point is characterized by the fragility. The fragility varies quite appreciably among glasses across a spectrum of chemical compositions including traditional network-forming oxides and simple molecular liquids but appears to be most closely correlated to the nature of the structural bonding present in the glass. In the instance of network-forming materials, this then allows one to consider the role of network topology in determining the fragility. Here, we have demonstrated how the fragility of a great many network-forming oxide glasses is seen to follow a very common dependence on the topological connectivity of the network provided this connectivity is adjusted to reflect the presence of larger-scaled rigid structural units that form in some systems. Throughout, we have emphasized how the needed coarse-graining of these structural units is achieved in like fashion for several alkali oxide glasses using a single method.

The collapse of the fragility for a great many oxide glasses considered here suggests that fragility is determined only by a single, mean field parameter—either $\phi = \langle r \rangle, \langle n \rangle$ *or* $\langle n_{IRO} \rangle$–whichever captures the connectivity of *weakest linkages* present in the network structure. This result is in accord with our viewpoint that the sort of network deformations required for bulk viscous flow need not involve all the covalent bonds present but can be achieved while certain rigid structural units remain largely undeformed. An understanding for why this universality exists is not fully certain, but we have speculated that it is deeply rooted in the nature of the configurational entropy, S_C, of cross-linked networks (Sidebottom, 2015). Simple thermodynamic arguments coupled with the Adam-Gibbs entropy picture (Adam and Gibbs, 1965) predict that fragility is proportional to the square of $\frac{dS_C}{d\phi}$, the slope of the configurational entropy with respect to network connectivity. That is, fragility is a reflection of the sensitivity of the network's configurational entropy to small changes in network connectivity of weakest links. The very fragile glasses at $\phi < 2.2$ are under-constrained networks resembling cross-linked polymer chains whose number of accessible conformations—the logarithm of which is the configurational entropy—can be greatly increased by even a small reduction in constraints. By contrast, strong glasses with $\phi > 2.8$ are highly over-constrained and find little or no entropic benefit from the removal of a few constraints many of which are topologically redundant at these high levels of connectivity. In future work we hope to explore this entropic connection in more detail by employing computer modeling in an effort to reproduce the specific shape of the master curve.

AUTHOR CONTRIBUTIONS

The author confirms being the sole contributor of this work and has approved it for publication.

ACKNOWLEDGMENTS

The author is grateful to Dr. G. S. Henderson for his willingness to share data files of Raman spectra in a series of sodium germanate glasses and provide advice on the analysis.

REFERENCES

Adam, G., and Gibbs, J. H. (1965). On the temperature dependence of cooperative relaxation properties in glass-forming liquids. *J. Chem. Phys.* 43, 139–146. doi: 10.1063/1.1696442

Angell, C. A. (1984). *Strong and Fragile Liquids Relaxations in Complex Systems*. National Technical Information Service, US Department of Commerce, 3–11.

Angell, C. A. (1991). Relaxation in liquids, polymers and plastic crystals - strong/fragile patterns and problems. *J. Non-Cryst. Sol.* 131–133, 13–31. doi: 10.1016/0022-3093(91)90266-9

Böhmer, R., and Angell, C. A. (1992). Correlations of the nonexponentiality and state dependence of mechanical relaxations with bond connectivity in Ge-As-Se supercooled liquids. *Phys. Rev. B* 45:10091. doi: 10.1103/PhysRevB.45.10091

Boolchand, P., and Thorpe, M. F. (1994). Glass-forming tendency, percolation of rigidity, and onefold-coordinated atoms in covalent networks. *Phys. Rev. B* 50, 10366–10368. doi: 10.1103/PhysRevB.50.10366

Brow, R. K. (1993). Nature of alumina in phosphate glass I: properties of sodium aluminophosphate glass. *J. Am. Ceram. Soc.* 76, 913–918. doi: 10.1111/j.1151-2916.1993.tb05315.x

Brow, R. K. (2000). Review: the structure of simple phosphate glasses. *J. Non-Cryst. Sol.* 263–264, 1–28. doi: 10.1016/S0022-3093(99)00620-1

Brow, R. K., Kirkpatrick, R. J., and Turner, G. L. (1993). Nature of alumina in phosphate glass II: structure of sodium aluminophosphate glass. *J. Am. Ceram. Soc.* 76, 919–928. doi: 10.1111/j.1151-2916.1993.tb05316.x

Christensen, R., Byer, J., Olson, G., and Martin, S. W. (2012). The glass transition temperature of mixed glass former 0.35 Na_2O+ 0.65 [xB_2O_3+(1– x) P_2O_5] glasses. *J. Non-Cryst. Sol.* 358, 826–831. doi: 10.1016/j.jnoncrysol.2011.12.068

Chryssikos, G. D., Duffy, J. A., Hutchinson, J. M., Ingram, M. D., Kamitsos, E. I., and Pappin, A. J. (1994). Lithium borate glasses: a quantitative study of strength and fragility. *J. Non-Cryst. Sol.* 172, 378–383. doi: 10.1016/0022-3093(94)90460-X

Debenedetti, P. G., and Stillinger, F. H. (2001). Supercooled liquids and the glass transition. *Nature* 410, 259–267. doi: 10.1038/35065704

Dyre, J. C., Maass, P., Roling, B., and Sidebottom, D. L. (2009). Fundamental questions relating to ion conduction in disordered solids. *Rep. Prog. Phys.* 72:046501. doi: 10.1088/0034-4885/72/4/046501

Eisenberg, A., Farb, H., and Cool, L. G. (1966). Glass transitions in ionic polymers. *J. Polymer Sci. A-2* 4, 855–868. doi: 10.1002/pol.1966.160040603

Fabian, R. Jr., and Sidebottom, D. L. (2009). Dynamic light scattering in network-forming sodium ultraphosphate liquids near the glass transition. *Phys. Rev. B* 80:064201. doi: 10.1103/PhysRevB.80.064201

Galeener, F. L. (1982). Planar rings in vitreous silica. *J. Non-Cryst. Sol.* 49, 53–62. doi: 10.1016/0022-3093(82)90108-9

Galeener, F. L., Lucovsky, G., and Geils, R. H. (1979). Raman and infrared spectra of vitreous As_2O_3. *Phys. Rev. B* 19, 4251–4258. doi: 10.1103/PhysRevB.19.4251

Galeener, F. L., Mikkelsen, J. C. Jr., Geils, R., and Mosby, W. J. (1978). The relative Raman cross sections of vitreous SiO_2, GeO_2, B_2O_3, and P_2O_5. *Appl. Phys. Lett.* 32, 34–36. doi: 10.1063/1.89823

Giacomazzi, L., Umari, P., and Pasquarello, A. (2005). Medium-range structural properties of vitreous germania obtained through first-principles analysis of vibrational spectra. *Phys. Rev. Lett.* 98:075505. doi: 10.1103/PhysRevLett.95.075505

Griscom, D. L. (1978). "Borate glass structure," in *Borate Glasses: Structure, Properties and Applications,* Vol. 12. eds L. D. Pye, V. D. Frechette, and N. J. Kreidel (New York, NY: Materials Science Research), 11–138. doi: 10.1007/978-1-4684-3357-9_2

Gupta, P. K., and Mauro, J. C. (2009). Composition dependence of glass transition temperature and fragility. I. A topological model incorporating temperature-dependent constraints. *J. Chem. Phys.* 130:094503. doi: 10.1063/1.3077168

Halfpap, B. L., and Lindsay, S. M. (1986). Rigidity percolation in the germanium-arsenic-selenium alloy system. *Phys. Rev. Lett.* 57:847. doi: 10.1103/PhysRevLett.57.847

He, H., and Thorpe, M. F. (1985). Elastic properties of glasses. *Phys. Rev. Lett.* 54:2107. doi: 10.1103/PhysRevLett.54.2107

Henderson, G. S. (2007). The germanate anomaly: what do we know? *J. Non-Cryst. Sol.* 353, 1695–1704. doi: 10.1016/j.jnoncrysol.2007.02.037

Henderson, G. S., and Fleet, M. E. (1991). The structure of glasses along the Na_2O - GeO_2 join. *J. Non-Cryst. Sol.* 134, 259–269. doi: 10.1016/0022-3093(91)90384-I

Hoppe, U., Walter, G., Kranold, R., and Stachel, D. (2000). Structural specifics of phosphate glasses probed by diffraction methods: a review. *J. Non-Cryst. Sol. I*, 29–47. doi: 10.1016/S0022-3093(99)00621-3

Hudgens, J. J., Brow, R. K., Tallant, D. R., and Martin, S. W. (1998). Raman spectroscopy study of the structure of lithium and sodium ultraphosphate glasses. *J. Non-Cryst. Sol.* 223, 21–31. doi: 10.1016/S0022-3093(97)00347-5

Kalampounias, A. G., Yannopoulos, S. N., and Papatheodorou, G. N. (2006a). Temperature-induced structural changes in glassy, supercooled, and molten silica from 77 to 2150 K. *J. Chem. Phys.* 124:014504. doi: 10.1063/1.2136878

Kalampounias, A. G., Yannopoulos, S. N., and Papatheodorou, G. N. (2006b). A high-temperature Raman spectroscopic investigation of the potassium tetrasilicate in glassy, supercooled, and liquid states. *J. Chem. Phys.* 125:164502. doi: 10.1063/1.2360275

Krogh-Moe, J. (1962). New evidence on the boron coordination in alkali borate glasses. *Phys. Chem. Glasses* 3, 1–6.

Laughlin, W. T., and Uhlmann, D. R. (1972). Viscous flow in simple organic liquids. *J. Phys. Chem.* 76, 2317–2325. doi: 10.1021/j100660a023

Maekawa, H., Maekawa, T., Kawamura, K., and Yokokawa, T. (1991). The structural groups of alkali silicate glasses determined from 29Si MAS-NMR. *J. Non-Cryst. Sol.* 127, 53–64. doi: 10.1016/0022-3093(91)90400-Z

Malfait, W. J., Halter, W. E., Morizet, Y., Meier, B. H., and Verel, R. (2007). Structural control on bulk melt properties: Single and double quantum 29Si NMR spectroscopy on alkali-silicate glasses. *Geochim. Cosmochim. Acta* 71, 6002–6018. doi: 10.1016/j.gca.2007.09.011

Nascimento, M. L. F., and Aparicio, C. (2007). Viscosity of strong and fragile glass-forming liquids investigated by means of principal component analysis. *J. Phys. Chem. Sol.* 68, 104–110. doi: 10.1016/j.jpcs.2006.09.013

Nemilov, S. V. (1966). A structural investigation of glasses in the B_2O_3-Na_2O system by the viscosimetric Method. *Izv. Akad. Nauk SSSR, Neorg. Mater.* 2, 349–359.

Nemilov, S. V. (1970). Viscosity and structure of binary germanate glasses in the softening range. *J. Appl. Chem. USSR* 43, 2644–2651.

Nemilov, S. V. (2007). Structural aspect of possible interrelation between fragility (length) of glass forming melts and Poisson's ratio of glasses. *J. Non-Cryst. Sol.* 353, 4613–4632. doi: 10.1016/j.jnoncrysol.2007.08.045

Oldekop, W. (1957). Theoretical discussion of the viscosity of glasses. *Glastech. Ber.* 30, 8–14.

Phillips, J. C. (1979). Topology of covalent non-crystalline solids I: short-range order in chalcogenide alloys. *J. Non-Cryst. Sol.* 34, 153–181. doi: 10.1016/0022-3093(79)90033-4

Poole, J. P. (1949). Low-temperature viscosity of alkali silicate glasses. *J. Am. Ceram. Soc.* 32, 230–233. doi: 10.1111/j.1151-2916.1949.tb18952.x

Riebling, E. F. (1963). Structure of molten oxides. I. Viscosity of GeO_2 and binary germanates containing Li_2O, Na_2O, K_2O, and Rb_2O. *J. Chem. Phys*. 39, 1889–1895. doi: 10.1063/1.1734549

Rodrigues, B. P., and Wondraczek, L. (2014). Cationic constraint effects in metaphosphate glasses. *J. Chem. Phys.* 140:214501. doi: 10.1063/1.4879559

Shelby, J. E. (1974). Viscosity and thermal expansion of alkali germanate glasses. J. *Am. Ceram. Soc.* 57, 436–439. doi: 10.1111/j.1151-2916.1974.tb11376.x

Sidebottom, D. L. (2015). Fragility of network-forming glasses: a universal dependence on the topological connectivity. *Phys. Rev. E* 92:062804. doi: 10.1103/PhysRevE.92.062804

Sidebottom, D. L. (2019). The fragility of alkali silicate glass melts: part of a universal topological pattern. *J. Non-Cryst. Sol.* 516, 53–66. doi: 10.1016/j.jnoncrysol.2019.04.033

Sidebottom, D. L., and Changstrom, J. R. (2008). Viscoelastic relaxation in molten phosphorus pentoxide using photon correlation spectroscopy. *Phys. Rev. B* 77:020201. doi: 10.1103/PhysRevB.77.020201

Sidebottom, D. L., Rodenburg, B. V., and Changstrom, J. R. (2007). Connecting structure and dynamics in glass forming materials by photon correlation spectroscopy. *Phys. Rev. B* 75:132201. doi: 10.1103/PhysRevB.75.132201

Sidebottom, D. L., and Schnell, S. E. (2013). The role of intermediate range order in predicting fragility of network-forming liquids near the rigidity transition. *Phys. Rev. B* 87:054202. doi: 10.1103/PhysRevB.87.054202

Sidebottom, D. L., Tran, T. D., and Schnell, S. E. (2014). Building up a weaker network: the effect of intermediate range glass structure on liquid fragility. *J. Non-Cryst. Sol.* 402, 16–20. doi: 10.1016/j.jnoncrysol.2014.05.010

Sidebottom, D. L., and Vu, D. (2016). Assessing the network connectivity of modifier ions in metaphosphate glass melts: a dynamic light scattering study of Na-Zn mixtures. *J. Chem. Phys.* 145:164503. doi: 10.1063/1.4965815

Stanley, H. E. (1971). *Introduction to Phase Transitions and Critical Phenomena*. New York, NY: Oxford University Press.

Stebbins, J. F. (1987). Identification of multiple structural species in silicate glasses by 29Si NMR. *Nature* 330, 465–467. doi: 10.1038/330465a0

Tatsumisago, M., Halfpap, B. L., Green, J. L., Lindsay, S. M., and Angell, C. A. (1990). Fragility of Ge-As-Se glass-forming liquids in relation to rigidity percolation, and the Kauzmann paradox. *Phys. Rev. Lett.* 64:1549. doi: 10.1103/PhysRevLett.64.1549

Thorpe, M. F. (1983). Continuous deformations in random networks. *J. Non-Cryst. Sol.* 57, 355–370. doi: 10.1016/0022-3093(83)90424-6

Tran, T. D., and Sidebottom, D. L. (2013). Glass-Forming dynamics of aluminophosphate melts studied by photon correlation spectroscopy. *J. Am. Ceram. Soc.* 96, 2147–2154. doi: 10.1111/jace.12444

Walrafen, G. E., Samanta, S. R., and Krishnan, P. N. (1980). Raman investigation of vitreous and molten boric oxide. *J. Chem. Phys*. 72, 113–120. doi: 10.1063/1.438894

Wang, L. M., Angell, C. A., and Richert, R. (2006). Fragility and thermodynamics in nonpolymeric glass-forming liquids. *J. Chem. Phys*. 125:074505. doi: 10.1063/1.2244551

Xia, Y., Zhu, W., Lockhart, M., Aitken, B., and Sen, S. (2019). Fragility and rheological behavior of metaphosphate liquids: Insights into their chain vs. network characters. *J. Non-Cryst. Sol.* 514, 77–82. doi: 10.1016/j.jnoncrysol.2019.03.036

Yannopoulos, S. N., Papatheodorou, G. N., and Fytas, G. (1999). Light-scattering study of slow and fast dynamics in a strong inorganic glass former. *Phys. Rev. B* 60, 15131–15142. doi: 10.1103/PhysRevB.60.15131

Youngman, R. E., and Zwanziger, J. W. (1996). Network modification in potassium borate glasses: structural studies with NMR and Raman spectroscopies. *J. Phys. Chem.* 100, 16720–16728. doi: 10.1021/jp961439+

Zachariasen, W. H. (1932). The atomic arrangement in glass. *J. Am. Chem. Soc.* 54 3841–3851. doi: 10.1021/ja01349a006

Zarzycki, J. (1991). *Glasses and the Vitreous State*. Great Britain: Cambridge University Press.

Conflict of Interest Statement: The author declares that the research was conducted in the absence of any commercial or financial relationships that could be construed as a potential conflict of interest.

frontiers in Materials

ORIGINAL RESEARCH
published: 09 July 2019
doi: 10.3389/fmats.2019.00164

Testing Rigidity Transitions in Glass and Crystal Forming Dense Liquids: Viscoelasticity and Dynamical Gaps

*J. Quetzalcóatl Toledo-Marín and Gerardo G. Naumis**

Departamento de Sistemas Complejos, Instituto de Física, Universidad Nacional Autónoma de México (UNAM), Mexico, Mexico

A computational study of rigidity for dense fluids of monodisperse and bidisperse hard-disks near a phase and a glass transition respectively is presented. To achieve this goal, the transversal part of the dynamical structure factor is calculated. In both cases, a viscoelastic behavior is obtained, with a dynamical gap determined by a critical wavevector k_c. Transversal waves exist for $k > k_c$ while the maximal correlations happens at frequency $\omega = 0$ for $k < k_c$. In both cases k_c goes to zero as the freezing point is approached. Both systems are able to fulfill a scaled dynamical law as a power law is found for the critical k_c as a function of the packing. The obtained results indicate that this method gives an alternative to study rigidity and constraint theory in dense fluids, since it is possible to assign a number of floppy modes or broken constraints in the liquid by computing the number of modes below k_c, as well as an effective average coordination number. Also, this suggests that the critical wavevector k_c can serve as a suitable order parameter.

Keywords: dynamical-gap, rigidity, relaxation, hard-disks, viscoelasticity

OPEN ACCESS

Edited by:
Punit Boolchand, University of Cincinnati, United States

Reviewed by:
Mathieu Bauchy, University of California, Los Angeles, United States
Matteo Baggioli, Institute of Theoretical Physics, Faculty of Science, Autonomous University of Madrid, Spain

****Correspondence:***
Gerardo G. Naumis
naumis@fisica.unam.mx

Specialty section:
This article was submitted to Glass Science, a section of the journal Frontiers in Materials

Received: *14 May 2019*
Accepted: *24 June 2019*
Published: *09 July 2019*

Citation:
Toledo-Marín JQ and Naumis GG (2019) Testing Rigidity Transitions in Glass and Crystal Forming Dense Liquids: Viscoelasticity and Dynamical Gaps. Front. Mater. 6:164. doi: 10.3389/fmats.2019.00164

1. INTRODUCTION

Over the last years it has become clear that rigidity topology of glass melts is intimately related with its relaxation properties (Selvanathan et al., 2000; Boolchand et al., 2001, 2018; Novita et al., 2007; Rompicharla et al., 2008; Bhosle et al., 2012; Gunasekera et al., 2013; Yildirim et al., 2016), as for example the relationship with fragility, which determines if a compound is good or bad glass former (Mauro et al., 2009, 2014).

Phillips and Thorpe's constraint theory of rigidity gives good insights on how such problems are related to network topology (Phillips, 1979; Thorpe, 1983). These ideas were eventually extended to include thermodynamics (Huerta and Naumis, 2002a,b, 2003; Huerta et al., 2004; Naumis, 2005; Flores-Ruiz and Naumis, 2012; Yan, 2018) and even the Boson peak (Flores-Ruiz and Naumis, 2009, 2011; Flores-Ruiz et al., 2010). Molecular dynamics in realistic systems has been of invaluable help regarding this point (see for instance Bauchy and Micoulaut, 2011). Stochastic models gave similar results (Naumis and Kerner, 1998; Kerner and Naumis, 2000). Boolchand and coworkers have made different studies concerning rigidity in melts and glass aging using optical, mechanical and thermodynamical properties (Selvanathan et al., 2000; Gunasekera et al., 2013).

Rigidity also plays a role in usual thermodynamic phase transitions as any transition involves the development of a generalized rigidity to keep phase order against thermal fluctuations (Chaikin and Lubensky, 1995). In spite of this, even for the usual thermodynamical phase transitions the understanding of the rigidity transition that takes place is not well understood. One of the aims

of this paper is precisely this, to study how rigidity evolves for dense fluids near a phase and a glass transition.

Experimentally, rigidity is usually calculated through the average coordination number, obtained from the relative concentration and corresponding valence of each chemical ingredient (Phillips, 1979). Although this is a clear defined protocol in a solid, in a liquid it is more difficult to have such a picture. A simple procedure to surmount such problem is to look not only at the average coordination number, but also to the elastic properties. In fact, the lack of elastic behavior against shear stress turns out to be the main defining feature of a Newtonian fluid. A striking consequence is the absence of transversal waves in fluids at low frequencies and wavenumbers (Trachenko and Brazhkin, 2015; Baggioli et al., 2019). However, elasticity of liquids depends upon the time and spatial scales in which the system is probed or perturbed. Thus, viscoelasticity will contain very valuable information concerning the rigidity of dense liquids close to a glass transition. For organic glasses, there are some early works concerning the study of flexible and rigid polymer models and how this is related with relaxation (Bartenev, 1970; Picu and Weiner, 1998; Picu et al., 1999). For inorganic glasses, this area is still open in many important aspects (Scopigno et al., 2007; Gueguen et al., 2015; Zhou et al., 2017; Zhu et al., 2018; Sen et al., 2019). In this article we will concentrate on how to test rigidity in simple fluids by using the information concerning transversal waves. Such information is encoded in the dynamical structure factor. Here we will compare glass and crystal forming fluids, both in its most elementary aspects.

As previously mentioned, the main feature that defines a rigid system is the resistance to shear-stress. Rigidity relates to the propagation of transversal waves. Thus, a natural starting point is to look at wave propagation, which involves a frequency ω and a wavevector $\boldsymbol{k}$. Therefore, rigidity of liquids involves time and space density-density and velocity-velocity fluctuations, which are well-described by the dynamical structure factor. Here we are concerned with the transversal part of the dynamical structure factor, defined as (Boon and Yip, 1991),

$$S(k,\omega) = \int_0^\infty dt e^{-\imath\omega t} C_T(k,t) \ . \tag{1}$$

where $C_T(k,t)$ is the transversal current density-density correlation function,

$$C_T(k,t) = \langle J_T^*(k,t) J_T(k,0)\rangle \ , \tag{2}$$

and the brackets $\langle ...\rangle$ represent an ensemble average. $J_T(k,t)$ is the transversal density current averaged over the different directions of $\boldsymbol{k}$ given the wavenumber $k = |\boldsymbol{k}|$,

$$J_T(k,t) = \frac{1}{\sqrt{2N}k} \sum_{i=1}^{N} \boldsymbol{k} \times \boldsymbol{v}_i(t) \exp\left(\imath \boldsymbol{k}\cdot \boldsymbol{r}_i(t)\right) \ . \tag{3}$$

Here, $\boldsymbol{v}_i(t)$ and $\boldsymbol{r}_i(t)$ are the velocity and position of the ith particle of a given system at time t. The $1/\sqrt{2}$ factor takes into account the two transverse currents in three-dimensional systems. This factor is replaced by one in two dimensions.

The resulting correlations functions can also be used to find the complex susceptibility $\xi(k,z)$ (where $z = \omega + i\epsilon$) when an external field probe $F(t)$ is appplied to the system. It can be proved that the susceptibility is given by (Boon and Yip, 1991),

$$\xi(k,z) = iz\beta S(k,z) - \beta C_T(k,0) \tag{4}$$

where $\beta = 1/k_B T$ with T the temperature and k_B the Boltzmann constant.

Let us now apply this test to different systems. In particular, here we will start with the most simple fluids able to produce glasses and crystals. One system is made from two dimensional hard-disks and the other is a bidispersive mixture of hard disks. In the monodisperse hard-disks system, the diameter of the disks is σ, while in the bidisperse case there are two kinds of disks, $\mathcal{A}$ and $\mathcal{B}$, each with diameters $\sigma_\mathcal{A}$ and $\sigma_\mathcal{B}$, respectively. For the monodisperse system, the packing fraction is given by $\eta = N\pi\sigma^2/A$ where A is the area. For the bidisperse system $\eta = [N\pi(x\sigma_\mathcal{A}^2 + (1-x)\sigma_\mathcal{B}^2]/A$, where x is the relative concentration of disks $\mathcal{A}$. In our simulation, we take $x = 1/2$ and $\sigma_A = 1.4\sigma_\mathcal{B}$. The monodisperse hard-disk system is interesting in many senses as crystallization takes place by two phase transitions. First the liquid goes into coexistence at $\eta \approx 0.70$ with the hexatic phase at $\eta \approx 0.7175$. This is captured by the orientational order parameter, such that in the hexatic phase orientational order appears and the transition is characterized by the Mayer-Wood loop in the $P-v$ diagram (Engel et al., 2013). As the packing fraction increases, a second order transition from hexatic to solid is observed at $\eta \approx 0.72$ (Engel et al., 2013; Russo and Wilding, 2017). While the hexatic phase has short range positional order and quasi-long-range orientational order, the solid has quasi-long range positional order and long-range orientational order. In this regard, positional order parameter is used to distinguish between the hexatic and solid phase (Engel et al., 2013). Recently it has been observed that a small polydispersity destroys the hexatic phase (Russo and Wilding, 2017). Moreover, the bidisperse system at $x = 1/2$ is able to generate a glass (Isobe, 2016; Russo and Wilding, 2017; Russo et al., 2018). In fact, there is a nice correlation between disk's mismatch, glass forming ability, configurational and vibrational entropy (Russo et al., 2018).

In **Figure 1**, we present the evolution of the compressibility factor $P/\rho k_B T$ where $\rho = N/A$ as a function of η. Such results were obtained from an Event-Driven Molecular Dynamics simulation with $N = 2,500$ hard-disks. An event driven molecular dynamics simulation called *DynamO* (Bannerman et al., 2011) was used while, in the case of bidisperse, the initial configuration was generated using the code developed by Skoge et al. (2006). For hard potentials, particles interact only when the distance between them is equal to the sum of their radius. While this condition is not fulfilled, the velocity of the particles remain the same. Event-Driven Molecular Dynamics takes advantage of this by locating the next collision (i.e., the time when the collision will occur and the pair of particles that will collide), evolving the simulation up to that time and implementing the collision dynamics (Allen and Tildesley, 2017). The hydrostatic pressure is computed from the trace of the pressure tensor and divided by 3. However, since we are simulating 2D systems, the element

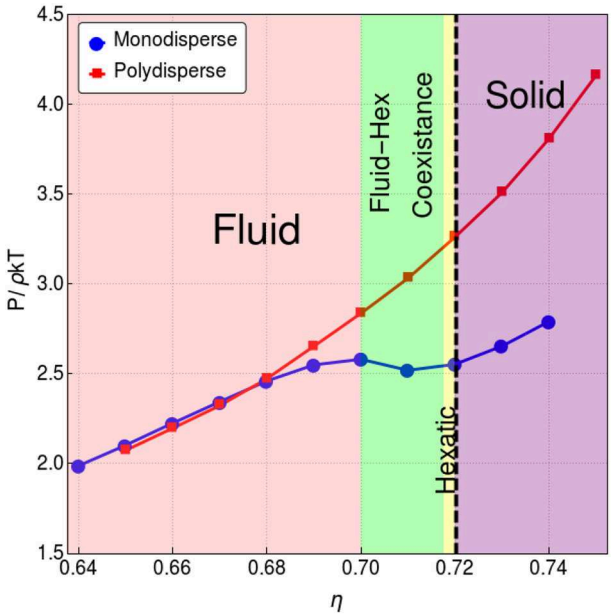

FIGURE 1 | Pressure vs. packing fraction in the studied region for monodisperse hard-disks (blue curve) and bidisperse hard-disks (red curve) as shown in the plot legend. For the case of monodisperse hard-disks, below $\eta \approx 0.7$ the system is in the fluid phase (colored pink), between $\eta \approx 0.7$ and $\eta \approx 0.7175$ the fluid coexist with the hexatic phase (colored green). Above $\eta \approx 0.7175$ the system is in a hexatic phase (colored yellow). At $\eta \approx 0.72$, a second order phase transition from hexatic to solid occurs (marked with a dashed line), and above $\eta \approx 0.72$ the system is in the solid phase (colored purple) (Russo and Wilding, 2017). This plot was obtained from a simulation with $N = 2,500$ hard-disks.

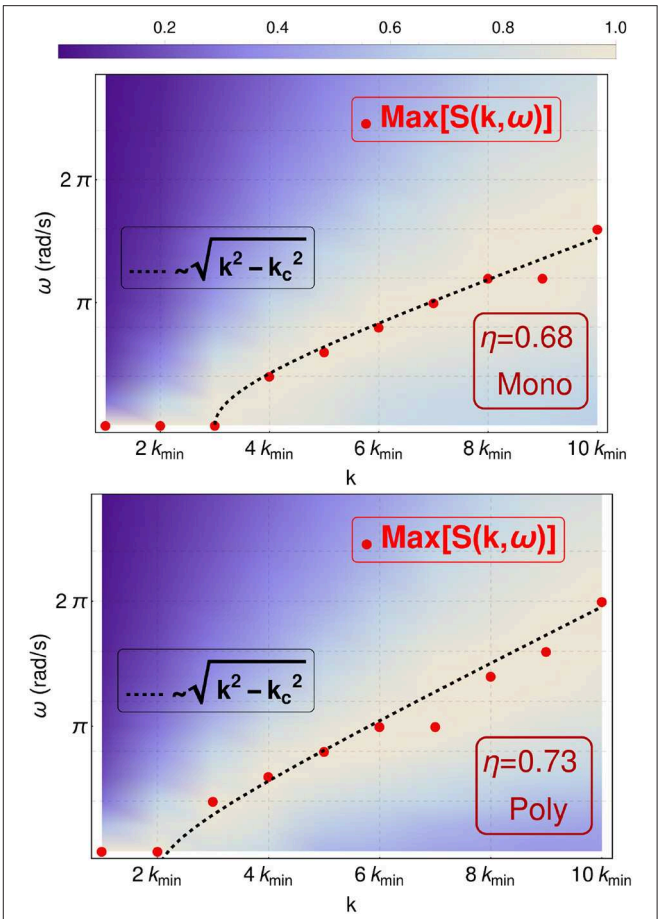

FIGURE 2 | Countour plot of the transversal dynamical structure factor $S(k, \omega)$ for $N = 2,500$ in the case of (**Upper panel**) monodisperse hard-disk system with packing fraction is $\eta = 0.68$ and (**Lower panel**) polydisperse hard-disk system with packing fraction is $\eta = 0.73$. The red dots are the observed maximums. The dotted curve allows to compare with the indicated functional form. Notice the presence of the dynamical gap located at $k < 3k_{min}$ and $k < 2k_{min}$ for packing fraction 0.68 monidisperse and packing fraction 0.73 polydisperse, respectively.

$P_{zz} = 0$, therefore, we have rescale by 3/2. The way in which DynamO computes this tensor is from the kinetic and interaction contributions, i.e., the kinetic contribution is defined as

$$\boldsymbol{P}^{kinetic} = \frac{1}{V}\sum_{i=1}^{N} m_i \boldsymbol{v}_i \boldsymbol{v}_i \,, \tag{5}$$

where V is the volume, N the number of disks, $m_i = 1$ is mass, $\boldsymbol{v}_i$ is the velocity of disk i and $\boldsymbol{v}_i\boldsymbol{v}_i$ is the dyadic product which yields a matrix. The interaction contribution is defined as

$$\boldsymbol{P}^{interaction} = \frac{1}{Vt_{sim}}\sum_{i,j}^{event} \Delta \boldsymbol{p}_i \boldsymbol{r}_{ij} \,, \tag{6}$$

where t_{sim} is the total time of the simulation, the summation is over each two-particle event (collision), i and j indicate the two particles involved in the event, $\Delta \boldsymbol{p}_i$ is the momentum impulse on particle i, and $\boldsymbol{r}_{ij} = \boldsymbol{r}_i - \boldsymbol{r}_j$ is the separation vector between the interacting particles.

Figure 1 allows to confirm that, in the case of monodisperse hard-disks, the system is undegoing a first order phase transition, while the bidisperse hard-disk system is not. Our aim is now to look at the viscoelastic response of both systems. In the upper panel of **Figure 2**, we present the transversal part of the dynamical structure factor $S(k, \omega)$ for the monodisperse system near the phase transition. The colors here represent the values of $S(k, \omega)$ for different wavenumbers k given in terms of the lowest wavenumber $k_{min} = 2\pi/L$, where $L = \sqrt{\pi\eta/N}4/\sigma$. As k increases, the peaks in $S(k, \omega)$ shift to larger values of ω. A gap is seen between the peaks for $k \leq 2k_{min}$. Also, in **Figure 2**, we compare with the function $\omega(k) \approx \sqrt{k^2 - k_c^2}$, which shows a good agreement with a recent theoretical solid-state approach to liquids (Trachenko and Brazhkin, 2015; Baggioli and Trachenko, 2018a,b) (see Baggioli et al., 2019 for a recent review on the subject). The lower panel of **Figure 2** shows that the bidisperse melt also shows a similar transversal branch with a gap and a critical k_c. Recently, this phenomena has been called the dynamical gap (Trachenko and Brazhkin, 2015).

Figure 2 gives a nice glimpse of the viscoelasticity and how a transition from a fluid-like to a solid-like behavior is revealed by

the presence of a dynamical gap. What is most important to us, is the observation that for $k < k_c$ all peaks of $S(k,\omega)$ are at $\omega = 0$. Thus, in this region $S(k,\omega) \approx \delta(\omega)$, where $\delta(\omega)$ is the Dirac delta function. Since for $k < k_c$ we have $\omega = 0$, we can consider these states, in terms of rigidity, as floppy, i.e., the system is flexible. Another way to see this result is by observing that here the rigidity transition will depend upon the time-scale of observation.

To test these ideas, we further follow the behavior of k_c as a function of η up to the freezing packing fraction for the monodisperse case. **Figure 3** shows the evolution of k_c. As expected, $k_c \to 0$ as $\eta \to \eta_m$, where $\eta_m = 0.7$ is the packing fraction where the system becomes solid for this system size. We should stress that for a larger system, $k_c \to 0$ at a packing fraction equal to ≈ 0.72 in the case of monodisperse hard-disks, in agreement with the hexatic-to-solid phase transition (Russo and Wilding, 2017). **Figure 3** also shows the evolution of k_c for the bidisperse case. It is observed that $k_c \to 0$ as $\eta \to \eta_p$, where $\eta_p = 0.75$.

Thus, **Figure 3** clearly shows that a rigidity transition will take place as the fluid density increases. **Figure 3** has other interesting features. The first is that the bidisperse fluid presents a bigger dynamical gap for the same given packing fraction. From a rigidity point of views this is expected as the effective number of contacts is reduced. In fact, a previous test in solids showed how one can, by decreasing the size of some disks in a monodisperse system, create a Boson peak (Flores-Ruiz and Naumis, 2009, 2011; Flores-Ruiz et al., 2010). Thus, **Figure 3** gives a nice alternative to test in a quantitative way the underlying rigidity of the solid.

Another revealing aspect of **Figure 3** is that the critical k_c seems to follow the law,

$$k_c \sim (\eta_\gamma - \eta)^\alpha \tag{7}$$

where $\gamma = m$ or $\gamma = p$ depending whether the system is monodisperse (m) or polydisperse (p). As k_c is the inverse of a dynamical length scale, α represents the scaling of this rigidity, suggesting to be a critical exponent for the size of rigid clusters. Thus, it is expected to depend upon the dimensionality of the system (Toledo-Marín and Naumis, unpublished).

To test this possibility we fitted the curves shown in **Figure 3** to the functional from given in Equation (7). We obtained $\alpha = 0.8 \pm 0.1$ in both cases. We, further, fitted k_c *vs* $(\Delta\eta/\eta_\gamma)^\alpha$, where $\Delta\eta = \eta_\gamma - \eta$. In **Figure 4**, we show the fits and the legend shows the slope values.

In the hydrodynamic regime, $C_L(k,t)$ Equation (2) satisfies the transverse part of the linearized Navier-Stokes equation. Under very general arguments, it can be proved that the expression for $S(k,\omega)$ is given by Boon and Yip (1991),

$$S(k,\omega) = \frac{2v_0^2 k^2 \Gamma(k)/\tau(k)}{\left(\omega^2 - \left(k^2\Gamma(k) - \frac{1}{2\tau^2(k)}\right)\right)^2 + \left(k^2\Gamma(k) - \frac{1}{4\tau^2(k)}\right)\frac{1}{\tau^2(k)}} \tag{8}$$

Here $\Gamma(k) = G_\infty(k)/\rho$, where $G_\infty(k)$ is the wavenumber-dependent high-frequency shear modulus, ρ is the density, $v_0^2 = C_T(k, t=0)$ and $\tau(k)$ is the wavenumber-dependent relaxation time (Boon and Yip, 1991).

The condition for shear wave propagation is obtained from equating to zero the derivative of Equation (8) with respect to ω. The resulting inequality for shear wave propagation is,

$$k^2\Gamma(k) > \frac{1}{2\tau^2(k)} \, . \tag{9}$$

As k decreases, $\Gamma(k)$ decreases much faster than $\tau(k)$. Thus, the inequality in (9) eventually breaks at a certain k_c, such that

$$k_c^2 \approx \frac{1}{2\tau^2(k_c)\Gamma(k_c)} \, . \tag{10}$$

In fact, Trachenko and Brazhkin (2015) and Baggioli et al. (2019) studied the dynamical gap and provided a variation to the Navier-Stokes equation, which in turn leads to the well-known telegraph's equation, from that they obtain the following equation for ω,

$$\omega^2 + \imath\frac{\omega}{\tau} - V_t^2 k^2 = 0 \, . \tag{11}$$

where τ is a relaxation time. Solving for ω yields

$$\omega_\pm = -\frac{\imath}{2\tau} \pm V_t\sqrt{k^2 - k_c^2} \, , \tag{12}$$

the energy dispersion with a damping and a gap determined by $k_c = 1/2\tau V_t$, a result similar to Equation (10) as $V_t \approx \sqrt{G_\infty(k)/\rho}$ for $k >> k_c$.

Notice that ω has a finite imaginary part. In **Figure 2**, the frequency corresponds to the real part. Now, from linear response theory, it is easy to see that the inverse of the left-hand-side of Equation (11) is proportional to the susceptibility, hence, by Equation (4) we would expected the imaginary part being encoded in the width of the peaks of the transverse density current correlation function. In **Figure 5**, we have plotted $S(k,\omega)$ *vs* ω for different values of k, while in **Figure 6** we have plotted the width of the transverse density current correlation function vs. the wavenumber, for 2,500 hard disks with packing fractions $\eta = 0.68$ monodisperse and $\eta = 0.73$ polydisperse, respectively. As k increases, the width becomes larger, which would imply smaller relaxation times, in agreement with Boon and Yip (1991), Trachenko and Brazhkin (2015), and Baggioli et al. (2019).

To test numerically Equation (12) we proceed as follows. Consider for example the case of the polydisperse system for $\eta = 0.68$. First V_t is obtained from considering $k >> k_c$ from where $\omega = V_t k$. This is the slope of the dotted line in **Figure 2**, from where $V_t \approx 0.24\pi/k_{min}$. Next from **Figure 6**, we obtain that $1/(2\tau) \approx 0.68\pi$. Using Equation (12) we find that $k_c \approx 2.83k_{min}$, in good agreement with **Figure 2**, in which $k_c \approx 2k_{min}$.

It is worthwhile to remark that our data satisfy Equation (8), which contains the Maxwell relaxation relationship for viscoelasticity, as it can be proved that in the long wavelength limit, the relaxation time $\tau(k)$ is given by Boon and Yip (1991),

$$\tau(0) = \frac{\nu}{G_\infty(0)} \tag{13}$$

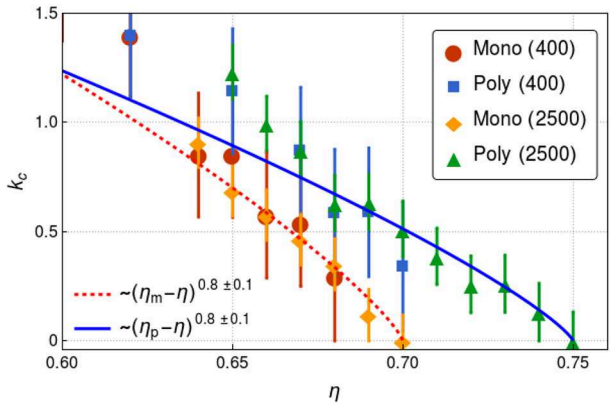

FIGURE 3 | Dynamical gap vs. reduced packing fraction η/η_C where η_C es the packing fraction such that $k_C = k_{min}$. The data points correspond to the simulations while the dashed lines corresponds to fits (see legends). For monodisperse disks $\eta_C = 0.7$ while for polydisperse disks $\eta_C = 0.75$. The computations were made for systems with $N = 400$ and $N = 2,500$ disks as indicated in the labels.

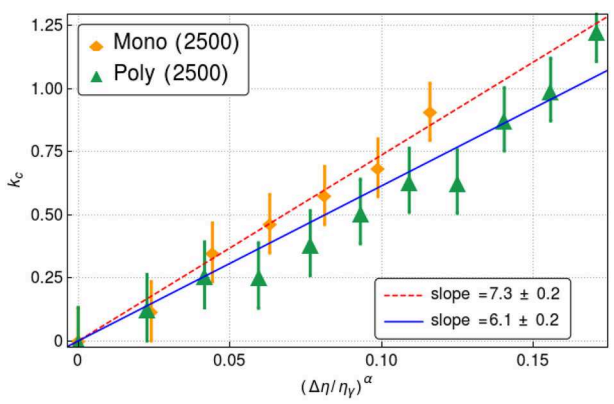

FIGURE 4 | Plot of the dynamical gap vs reduced packing fraction $(\Delta\eta/\eta_C)^\alpha$. The data points correspond to the simulations while the dashed lines corresponds to fits (see legends). The computations were made for systems with $N = 2,500$ disks.

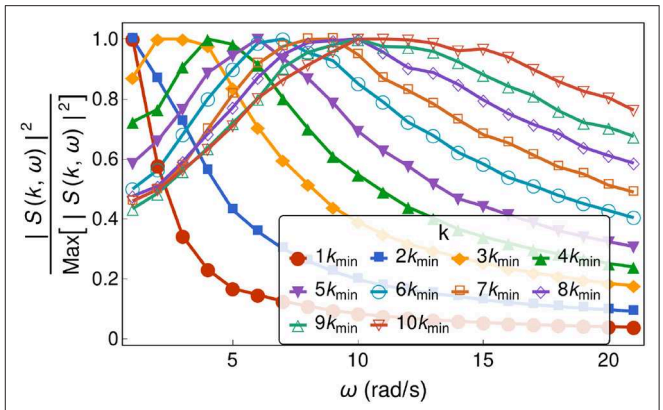

FIGURE 5 | The transverse density current correlation function as a function of ω for different wavenumbers. This was obtained for polydisperse hard-disks at a packing fraction 0.73. Notice that for all curves where $k < 3k_{min}$, the maximum is located at $\omega = 0$. For $k \geq 3k_{min}$, the peak moves to higher frequencies as k increases, indicating transversal wave propagation although with an increased damping.

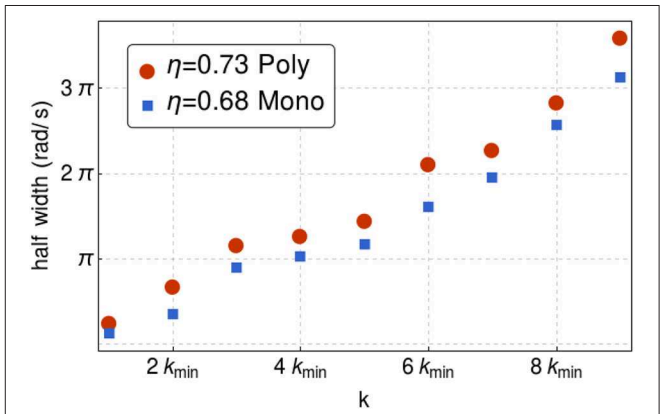

FIGURE 6 | Half-width of the transverse density current correlation function as a function of the wavenumber for packing fraction $\eta = 0.68$ monodisperse and $\eta = 0.73$ polydisperse for 2, 500 hard disks. As k increase, the width becomes larger which is qualitatively consistent with (Trachenko and Brazhkin, 2015; Baggioli et al., 2019).

where ν is the viscosity. This relation holds for any k dependence of $\tau(k)$, even if we make the crude assumption of taking $\tau(k) = \tau(0) = \tau$.

Let us know return to investigate the connection of constraint theory with the dynamical gap. As the fluid is isotropic, we can obtain a relationship between k_c and the number of floppy modes as follows. First we can approximate the behavior for $k < k_c$ by a delta function, resulting in a simplified version of $S(k, \omega)$,

$$S_f(k, w) \approx \delta(\omega)\Theta(k_c - k) + \Theta(k - k_c)S(k, \omega) \tag{14}$$

where $\Theta(x)$ is the Heaviside function. The total number of modes with zero frequency in three dimensions is proportional to the volume of a sphere with radius k_c in the k-space,

$$N_f(k_c) \approx 2\int_0^{k_c} 4\pi k^2 dk = \frac{8\pi}{3}k_c^3 \tag{15}$$

where the factor 2 comes from the possible transversal waves polarizations. In 2D we have $N_f(k_c) \approx \pi k_c^2$.
The fraction of floppy modes (f) with respect to the total number of modes is obtained by normalization,

$$f_{3D} \approx \frac{2}{3}\left(\frac{k_c}{k_D}\right)^3, f_{2D} \approx \frac{1}{2}\left(\frac{k_c}{k_D}\right)^2 \tag{16}$$

The normalization factor k_D ($\gg k_c$) is the Debye wavevector (Yang et al., 2017) while the subscripts $3D$ and $2D$ refer

to the dimensionality of the system. We can conclude that floppy modes are related with the dynamical gap seen in the viscoelastic properties.

Using Equation (7), one can obtain a relationship between η and f valid for the monodisperse and polydisperse system,

$$f_{2D} \sim \frac{1}{2k_D^2}\left(\frac{\Delta\eta}{\eta_\gamma}\right)^{2\alpha} \tag{17}$$

In principle, we can go further by relating the previous results to obtain a dynamical average coordination. However, the lattice may have a strong heterogeneous character as floppy regions favor the maximization of vibrational entropy (Naumis, 2005) and care must be taken since it is possible that the system may gain structure and order (Frenkel, 2014) as in the case of the network studied in Yan (2018) where floppy regions appear in a given coordination number window above the rigidity threshold. Relaxation is affected by this heterogeneity (Glasstone et al., 1941; Hänggi et al., 1990; Toledo-Marín and Naumis, 2017, 2018). Yet it is tempting to go further and define a mean dynamical coordination number $\langle Z\rangle$. For angular and radial forces are present, is known that $f_{3D} = 2-5\langle Z\rangle/6$, while $f_{3D} = 1-\langle Z\rangle/6$ for radial forces (Thorpe, 1983). In $2D$, we have for pure radial forces $f_{2D} = 1 - \langle Z\rangle/4$. Using Equation (16), for pure radial forces and in 2D we have,

$$\langle Z\rangle_{2D} \sim 4\left(1 - \frac{1}{2k_D^2}\left(\frac{\Delta\eta}{\eta_\gamma}\right)^{2\alpha}\right) \tag{18}$$

This number can be compared with results obtained from the first-neighbor-counting obtained from collisions (Wyart, 2005). In particular, we observe that for $k_c = 0$ we recover the condition for rigidity, and as k_c grows, the coordination number decreases as expected for a fluid system. Furthermore, it is known that the coordination number may be obtained integrating the radial distribution function in a small sphere of radius equal to the distance between two particles. The radial distribution function is related to the structure factor which in turn may be put in terms of the current density correlation function (Boon and Yip, 1991). Thus, it seems plausible to relate the coordination number with the current density correlation function and, in particular, with the dynamical gap. However, we leave that for future work.

In conclusion, here we observed that for simple dense fluids near a glass or a crystal phase transition there is a dynamical gap and above a certain critical wavevector, k_c, there are transversal propagating modes although with strong damping. Modes with k below to k_c have zero frequency. This critical k_c goes to zero as a power law with exponent close to 0.8 as the fluid goes into a solid in the vicinity where this phase transition occurs.

In fact, this sole observation opens new avenues for future research. For example, quite recently it was shown that the hexatic-to-solid phase transition in the case of monodisperse hard-disks, as well as with a small concentration of bidispersity, is a KT transition (Russo and Wilding, 2017). This was proven on the basis of a prediction made within the KTHNY-theory framework, in which the elastic constant, K, should be zero in the hexatic phase and have a jump to 16π in the solid (Strandburg, 1988). This elastic constant K may be expressed in terms of the transverse and longitudinal speed of sound denoted as V_t^2 and V_l^2, respectively, which yields

$$K = 4\rho V_t^2\left(1 - \frac{V_t^2}{V_l^2}\right). \tag{19}$$

When k_c goes to zero, shear waves propagate in the system as a whole and the transverse speed of sound changes from zero to some finite value. Hence, in the case of monodisperse hard-disks, we speculate that k_c may serve as an order parameter for the hexatic-to-solid transition.

An even more interesting aspect is that, although the hexatic phase disappears for even a small concentration of small hard-disks, the KT transition should still happen theoretically (Strandburg, 1988; Russo and Wilding, 2017). In this sense, the dynamical-gap may serve as a tool to locate it.

Finally, by assuming isotropy of the liquid, one can count zero frequency modes to assign a number of floppy modes to the fluid. Thus, a dynamical average coordination number and a certain number of broken constraints can be defined from this count. Our study suggest that viscoelasticity can serve as a powerful tool to characterize rigidity in the fluid phase.

DATA AVAILABILITY

The datasets generated for this study are available on request to the corresponding author.

AUTHOR CONTRIBUTIONS

GN proposed the work. JT-M did the simulations. JT-M and GN analyzed the results and wrote the manuscript.

FUNDING

This work was partially supported by DGAPA-UNAM project IN102717. JT-M acknowledges a doctoral fellowship from CONACyT.

ACKNOWLEDGMENTS

We thank Christian Moukarzel, Le Yan, Adrian Huerta, and John Russo for discussions. We thank the editors for the invitation in order to publish these results.

REFERENCES

Allen, M. P., and Tildesley, D. J. (2017). *Computer Simulation of Liquids*. New York, NY: Oxford University Press.

Baggioli, M., Brazhkin, V., Trachenko, K., and Vasin, M. (2019). Gapped momentum states. *arXiv preprint arXiv:1904.01419*.

Baggioli, M., and Trachenko, K. (2018a). Maxwell interpolation and close similarities between liquids and holographic models. *arXiv preprint arXiv:1808.05391*. doi: 10.1103/PhysRevD.99.106002

Baggioli, M., and Trachenko, K. (2018b). Solidity of liquids: how holography knows it. *arXiv preprint arXiv:1807.10530*.

Bannerman, M. N., Sargant, R., and Lue, L. (2011). Dynamo: a free \calo (n) general event-driven molecular dynamics simulator. *J. Comput. Chem.* 32, 3329–3338. doi: 10.1002/jcc.21915

Bartenev, G. M. (1970). *The Structure and Mechanical Properties of Inorganic Glasses*. Transl. by P. Jaray and F. F. Jaray. Groningen: Wolters-Noordhoff Groningen.

Bauchy, M., and Micoulaut, M. (2011). Atomic scale foundation of temperature-dependent bonding constraints in network glasses and liquids. *J. Non-Crystall. Solids* 357, 2530–2537. doi: 10.1016/j.jnoncrysol.2011.03.017

Bhosle, S., Gunasekera, K., Boolchand, P., and Micoulaut, M. (2012). Melt homogenization and self-organization in chalcogenides-part II. *Int. J. Appl. Glass Sci.* 3, 205–220. doi: 10.1111/j.2041-1294.2012.00092.x

Boolchand, P., Bauchy, M., Micoulaut, M., and Yildirim, C. (2018). Topological phases of chalcogenide glasses encoded in the melt dynamics (phys. status solidi b 6/2018). *Phys. Status Solidi* 255:1870122. doi: 10.1002/pssb.201870122

Boolchand, P., Georgiev, D., and Goodman, B. (2001). Discovery of the intermediate phase in chalcogenide glasses. *J. Optoelectron. Adv. Mater.* 3, 703–720.

Boon, J. P., and Yip, S. (1991). *Molecular Hydrodynamics*. New York, NY: Courier Corporation.

Chaikin, P. M., and Lubensky, T. C. (1995). *Principles of Condensed Matter Physics*. Cambridge: Cambridge University Press.

Engel, M., Anderson, J. A., Glotzer, S. C., Isobe, M., Bernard, E. P., and Krauth, W. (2013). Hard-disk equation of state: first-order liquid-hexatic transition in two dimensions with three simulation methods. *Phys. Rev. E* 87:042134. doi: 10.1103/PhysRevE.87.042134

Flores-Ruiz, H. M., and Naumis, G. G. (2009). Excess of low frequency vibrational modes and glass transition: a molecular dynamics study for soft spheres at constant pressure. *J. Chem. Phys.* 131:154501. doi: 10.1063/1.3246805

Flores-Ruiz, H. M., and Naumis, G. G. (2011). Boson peak as a consequence of rigidity: a perturbation theory approach. *Phys. Rev. B* 83:184204. doi: 10.1103/PhysRevB.83.184204

Flores-Ruiz, H. M., and Naumis, G. G. (2012). Mean-square-displacement distribution in crystals and glasses: an analysis of the intrabasin dynamics. *Phys. Rev. E* 85:041503. doi: 10.1103/PhysRevE.85.041503

Flores-Ruiz, H. M., Naumis, G. G., and Phillips, J. C. (2010). Heating through the glass transition: a rigidity approach to the boson peak. *Phys. Rev. B* 82:214201. doi: 10.1103/PhysRevB.82.214201

Frenkel, D. (2014). Order through entropy. *Nat. Mater.* 14:9. doi: 10.1038/nmat4178

Glasstone, S., Eyring, H., and Laidler, K. J. (1941). *The Theory of Rate Processes*. New York, NY: McGraw-Hill.

Gueguen, Y., Keryvin, V., Rouxel, T., Fur, M. L., Orain, H., Bureau, B., et al. (2015). A relationship between non-exponential stress relaxation and delayed elasticity in the viscoelastic process in amorphous solids: illustration on a chalcogenide glass. *Mech. Mater.* 85, 47–56. doi: 10.1016/j.mechmat.2015.02.013

Gunasekera, K., Bhosle, S., Boolchand, P., and Micoulaut, M. (2013). Superstrong nature of covalently bonded glass-forming liquids at select compositions. *J. Chem. Phys.* 139:164511. doi: 10.1063/1.4826463

Hänggi, P., Talkner, P., and Borkovec, M. (1990). Reaction-rate theory: fifty years after kramers. *Rev. Modern Phys.* 62:251. doi: 10.1103/RevModPhys.62.251

Huerta, A., and Naumis, G. (2002a). Relationship between glass transition and rigidity in a binary associative fluid. *Phys. Lett. A* 299, 660–665. doi: 10.1016/S0375-9601(02)00519-4

Huerta, A., and Naumis, G. G. (2002b). Evidence of a glass transition induced by rigidity self-organization in a network-forming fluid. *Phys. Rev. B* 66:184204. doi: 10.1103/PhysRevB.66.184204

Huerta, A., and Naumis, G. G. (2003). Role of rigidity in the fluid-solid transition. *Phys. Rev. Lett.* 90:145701. doi: 10.1103/PhysRevLett.90.145701

Huerta, A., Naumis, G. G., Wasan, D. T., Henderson, D., and Trokhymchuk, A. (2004). Attraction-driven disorder in a hard-core colloidal monolayer. *J. Chem. Phys.* 120, 1506–1510. doi: 10.1063/1.1632893

Isobe, M. (2016). Hard sphere simulation in statistical physics-methodologies and applications. *Mol. Simul.* 42, 1317–1329. doi: 10.1080/08927022.2016.1139106

Kerner, R., and Naumis, G. G. (2000). Stochastic matrix description of the glass transition. *J. Phys.* 12:1641. doi: 10.1088/0953-8984/12/8/306

Mauro, J. C., Philip, C. S., Vaughn, D. J., and Pambianchi, M. S. (2014). Glass science in the united states: current status and future directions. *Int. J. Appl. Glass Sci.* 5, 2–15. doi: 10.1111/ijag.12058

Mauro, J. C., Yue, Y., Ellison, A. J., Gupta, P. K., and Allan, D. C. (2009). Viscosity of glass-forming liquids. *Proc. Natl. Acad. Sci. U.S.A.* 106, 19780–19784. doi: 10.1073/pnas.0911705106

Naumis, G. G. (2005). Energy landscape and rigidity. *Phys. Rev. E* 71:026114. doi: 10.1103/PhysRevE.71.026114

Naumis, G. G., and Kerner, R. (1998). Stochastic matrix description of glass transition in ternary chalcogenide systems. *J. Non-Crystall. Solids* 231, 111–119. doi: 10.1016/S0022-3093(98)00417-7

Novita, D. I., Boolchand, P., Malki, M., and Micoulaut, M. (2007). Fast-ion conduction and flexibility of glassy networks. *Phys. Rev. Lett.* 98:195501. doi: 10.1103/PhysRevLett.98.195501

Phillips, J. C. (1979). Topology of covalent non-crystalline solids I: short-range order in chalcogenide alloys. *J. Non-Crystall. Solids* 34, 153–181. doi: 10.1016/0022-3093(79)90033-4

Picu, R. C., Loriot, G., and Weiner, J. H. (1999). Toward a unified view of stress in small-molecular and in macromolecular liquids. *J. Chem. Phys.* 110, 4678–4686. doi: 10.1063/1.478351

Picu, R. C., and Weiner, J. H. (1998). Stress relaxation in a diatomic liquid. *J. Chem. Phys.* 108, 4984–4991. doi: 10.1063/1.475907

Rompicharla, K., Novita, D., Chen, P., Boolchand, P., Micoulaut, M., and Huff, W. (2008). Abrupt boundaries of intermediate phases and space filling in oxide glasses. *J. Phys.* 20:202101. doi: 10.1088/0953-8984/20/20/202101

Russo, J., Romano, F., and Tanaka, H. (2018). Glass forming ability in systems with competing orderings. *Phys. Rev. X* 8:021040. doi: 10.1103/PhysRevX.8.021040

Russo, J., and Wilding, N. B. (2017). Disappearance of the hexatic phase in a binary mixture of hard disks. *Phys. Rev. Lett.* 119:115702. doi: 10.1103/PhysRevLett.119.115702

Scopigno, T., Yannopoulos, S. N., Scarponi, F., Andrikopoulos, K. S., Fioretto, D., and Ruocco, G. (2007). Origin of the λ transition in liquid sulfur. *Phys. Rev. Lett.* 99:025701. doi: 10.1103/PhysRevLett.99.025701

Selvanathan, D., Bresser, W., and Boolchand, P. (2000). Stiffness transitions in si x se 1- x glasses from raman scattering and temperature-modulated differential scanning calorimetry. *Phys. Rev. B* 61:15061. doi: 10.1103/PhysRevB.61.15061

Sen, S., Xia, Y., Zhu, W., Lockhart, M., and Aitken, B. (2019). Nature of the floppy-to-rigid transition in chalcogenide glass-forming liquids. *J. Chem. Phys.* 150:144509. doi: 10.1063/1.5092841

Skoge, M., Donev, A., Stillinger, F. H., and Torquato, S. (2006). Packing hyperspheres in high-dimensional euclidean spaces. *Phys. Rev. E* 74:041127. doi: 10.1103/PhysRevE.74.041127

Strandburg, K. J. (1988). Two-dimensional melting. *Rev. Modern Phys.* 60:161. doi: 10.1103/RevModPhys.60.161

Thorpe, M. (1983). Continuous deformations in random networks. *J. Non-Crystall. Solids* 57, 355–370. doi: 10.1016/0022-3093(83)90424-6

Toledo-Marín, J. Q., and Naumis, G. G. (2017). Short time dynamics determine glass forming ability in a glass transition two-level model: a stochastic approach using kramers– escape formula. *J. Chem. Phys.* 146:094506. doi: 10.1063/1.4977517

Toledo-Marín, J. Q., and Naumis, G. G. (2018). Escape time, relaxation, and sticky states of a softened henon-heiles model: Low-frequency vibrational mode effects and glass relaxation. *Phys. Rev. E* 97:042106. doi: 10.1103/PhysRevE.97.042106

Trachenko, K., and Brazhkin, V. (2015). Collective modes and thermodynamics of the liquid state. *Rep. Progr. Phys.* 79:016502. doi: 10.1088/0034-4885/79/1/016502

Wyart, M. (2005). *On the Rigidity of Amorphous Solids. Price Fluctuations, Conventions and Microstructure of Financial Markets*. Physics and Society [physics.soc-ph]. Ecole Polytechnique X, ffpastel-00001919. Available online at: https://pastel.archives-ouvertes.fr/pastel-00001919/document

Yan, L. (2018). Entropy favors heterogeneous structures of networks near the rigidity threshold. *Nat. Commun.* 9:1359. doi: 10.1038/s41467-018-03859-9

Yang, C., Dove, M., Brazhkin, V., and Trachenko, K. (2017). Emergence and evolution of the k gap in spectra of liquid and supercritical states. *Phys. Rev. Lett.* 118:215502. doi: 10.1103/PhysRevLett.118.215502

Yildirim, C., Micoulaut, M., Boolchand, P., Kantor, I., Mathon, O., Gaspard, J.-P., et al. (2016). Universal amorphous-amorphous transition in ge x se 100- x glasses under pressure. *Sci. Rep.* 6:27317. doi: 10.1038/srep27317

Zhou, T., Zhou, Q., Xie, J., Liu, X., Wang, X., and Ruan, H. (2017). Elastic-viscoplasticity modeling of the thermo-mechanical behavior of chalcogenide glass for aspheric lens molding. *Int. J. Appl. Glass Sci.* 9, 252–262. doi: 10.1111/ijag.12290

Zhu, W., Aitken, B. G., and Sen, S. (2018). Communication: observation of ultra-slow relaxation in supercooled selenium and related glass-forming liquids. *J. Chem. Phys.* 148:111101. doi: 10.1063/1.5022787

Conflict of Interest Statement: The authors declare that the research was conducted in the absence of any commercial or financial relationships that could be construed as a potential conflict of interest.

frontiers in Materials

ORIGINAL RESEARCH
published: 09 July 2019
doi: 10.3389/fmats.2019.00157

Intermediate Phase in Calcium–Silicate–Hydrates: Mechanical, Structural, Rigidity, and Stress Signatures

Qi Zhou[1], *Mengyi Wang*[1,2], *Lijie Guo*[3], *Punit Boolchand*[4] *and Mathieu Bauchy*[1]*

[1] *Physics of AmoRphous and Inorganic Solids Laboratory (PARISlab), Department of Civil and Environmental Engineering, University of California, Los Angeles, Los Angeles, CA, United States,* [2] *Department of Materials Science and Engineering, Massachusetts Institute of Technology, Cambridge, MA, United States,* [3] *BGRIMM Technology Group, Beijing, China,* [4] *Department of Electrical Engineering and Computer Science, University of Cincinnati, Cincinnati, OH, United States*

Topological constraint theory (TCT) classifies disordered networks as flexible, stressed-rigid, or isostatic based on the balance between the number of topological constraints and degrees of freedom. In contrast with the predictions from a mean-field enumeration of the constraints, the isostatic state—wherein the network is rigid but free of stress—has been suggested to be achieved within a range of compositions, the intermediate phase, rather than at a fixed threshold. However, our understanding of the nature and potential structural signatures of the intermediate phase remains elusive. Here, based on molecular dynamics simulations of calcium–silicate–hydrate systems with varying compositions, we seek for some mechanical and structural signatures of the intermediate phase. We show that this system exhibits a composition-driven rigidity transition. We find that the fracture toughness, fracture energy, mechanical reversibility, and creep compliance exhibit an anomalous behavior within a compositional window at the vicinity of the isostatic threshold. These features are argued to constitute a mechanical signature of an intermediate phase. Notably, we identify a clear structural signature of the intermediate phase in the medium-range order of this system, which is indicative of an optimal space-filling tendency. Based on these simulations, we demonstrate that the intermediate phase observed in this system arises from a bifurcation between the rigidity and stress transitions. These features might be revealed to be generic to isostatic disordered networks.

Keywords: intermediate phase, topological constraint theory, rigidity theory, rigidity transition, molecular dynamics, calcium–silicate–hydrate

OPEN ACCESS

Edited by:
Limin Wang,
Yanshan University, China

Reviewed by:
Haizheng Tao,
Wuhan University of Technology, China
Qiuju Zheng,
Qilu University of Technology, China

***Correspondence:**
Mathieu Bauchy
bauchy@ucla.edu

Specialty section:
This article was submitted to Glass Science, a section of the journal Frontiers in Materials

Received: *17 May 2019*
Accepted: *19 June 2019*
Published: *09 July 2019*

Citation:
Zhou Q, Wang M, Guo L, Boolchand P and Bauchy M (2019) Intermediate Phase in Calcium–Silicate–Hydrates: Mechanical, Structural, Rigidity, and Stress Signatures. Front. Mater. 6:157. doi: 10.3389/fmats.2019.00157

INTRODUCTION

Topological constraint theory (TCT), or rigidity theory, offers a convenient framework to describe the network topology of disordered networks (Phillips, 1979, 1981). In this framework, atomic networks are considered as mechanical trusses, wherein some nodes (the atoms) are connected to each other via some constraints (the chemical bonds) (Mauro, 2011; Bauchy, 2019). By simplifying complex disordered networks into simpler mechanical trusses, TCT captures the important network topology while filtering the second-order structural details of the atomic network—which

facilitates the development of predictive composition–property models (Micoulaut and Yue, 2017; Bauchy, 2019).

In atomic networks, relevant topological constraints comprise the 2-body radial bond-stretching (BS) and 3-body angular bond-bending (BB) constraints, which keep the bond distances and bond angles fixed around their average values, respectively. In analogy with the stability of mechanical trusses (Maxwell, 1864), TCT then classifies atomic networks as (i) flexible, when the number of constraints is lower than the number of atomic degrees of freedom, (ii) stressed–rigid, when the number of constraints is larger than the number of atomic degrees of freedom, and (iii) isostatic, when the numbers of constraints and atomic degrees of freedom match each other. Due to the lack of constraints, undercoordinated flexible networks tend to exhibit some internal floppy modes of deformation (Thorpe, 1983; Boolchand et al., 1995). In contrast, overcoordinated stressed–rigid networks are fully locked but exhibit some internal stress since some constraints become mutually redundant and cannot all be satisfied at the same time (Wang et al., 2005; Li et al., 2019). In turn, isostatic networks are rigid but free of any internal stress.

A mean-field enumeration of the topological constraints predicts that the isostatic state should be achieved at a single threshold composition that is characterized by $n_c = 3$, wherein n_c is the number of BS and BB constraints per atom and 3 is the number of degrees of freedom per atom (Phillips, 1979). In a fully connected network wherein all BS and BB are active, this state is achieved when the network exhibits an average coordination number of 2.4 (Mauro, 2011). However, temperature-modulated differential scanning calorimetry tests have suggested that the isostatic character can be achieved within a range of compositions rather than at a fixed threshold—wherein glasses exhibit a nearly zero non-reversible enthalpy at the glass transition (Boolchand et al., 2001; Bhosle et al., 2012a,b). This suggests that the flexible-to-rigid and stressed-to-unstressed transitions may not occur at the same composition threshold, which has been suggested to arise from a self-organization of the network—which adapts its structure to become rigid while avoiding the formation of stress (Thorpe et al., 2000; Chubynsky et al., 2006; Micoulaut and Phillips, 2007). These two transitions define the *intermediate phase* (IP), which separates the flexible and stressed–rigid phases (i.e., the three topological phases of a disordered network).

Interestingly, isostatic chalcogenide glasses belonging to the intermediate phase exhibit some unique properties, namely a reversible glass transition (Boolchand et al., 2001; Chakravarty et al., 2005), weak relaxation and aging (Chakravarty et al., 2005; Chen et al., 2010), low propensity for creep (Bauchy et al., 2017), anomalous mechanical properties (Varshneya and Mauro, 2007; Bauchy et al., 2016a), superstrong behavior (Boolchand et al., 2018), optimal space-filling tendency (Phillips, 2006; Rompicharla et al., 2008), and stress-free character (Wang et al., 2005).

Although the intermediate phase has been observed in several families of chalcogenides (Mantisi et al., 2015; Boolchand and Goodman, 2017) and modified oxides (Vaills et al., 2005; Micoulaut, 2008; Vignarooban et al., 2014; Mohanty et al., 2019), several questions remain unanswered. What role, if any, does the material's synthesis play in the observation of the intermediate phase (Lucas et al., 2009; Boolchand et al., 2011; Zeidler et al., 2017)? Are intermediate phases a generic feature of disordered networks? Does the intermediate phase manifest itself in other properties than the non-reversible enthalpy at the glass transition? In which aspect(s), if any, of the local or intermediate atomic structure is the intermediate phase encoded? In particular, no clear short-range order structural signature of the intermediate phase is presently available. These gaps in knowledge partially arise from the fact that most of the theoretical works investigating the nature of the intermediate phase have thus far focused on model glasses (e.g., triangular lattices), which may not capture the complex structure of real glasses (Thorpe et al., 2000; Chubynsky et al., 2006; Yan and Wyart, 2014; Yan, 2018).

Here, based on molecular dynamics simulations of calcium–silicate–hydrate systems [i.e., $CaO–SiO_2–H_2O$ or C–S–H, the binding phase of concrete (Taylor, 1997)] with varying compositions, we seek some mechanical and structural signatures of the intermediate phase. We show that C–S–H exhibits a composition-driven rigidity transition governed by its Ca/Si molar ratio. We find that a large body of mechanical properties exhibit an anomalous behavior within a range of composition at the vicinity of the isostatic threshold—which are argued to constitute some signatures of an intermediate phase. Based on this system, we identify a structural signature of the intermediate phase in the medium-range order of C–S–H. We demonstrate that the intermediate phase observed in C–S–H arises from a bifurcation between the rigidity and stress transitions.

METHODS

Preparation of the Calcium–Silicate–Hydrate Samples

In the following of this manuscript, we consider a series of C–S–H samples to identify some mechanical, structural, and dynamical signature of the intermediate phase. To this end, we adopt the model introduced by Pellenq et al. to describe the structure and topology of C–S–H with varying Ca/Si molar ratios (Pellenq et al., 2009; Abdolhosseini Qomi et al., 2014b). Although fine structural details of this model have been discussed (Richardson, 2013, 2014; Scrivener et al., 2015), this model remains the only model that is capable of describing the structure of C–S–H systems across a wide range of Ca/Si molar ratios. In addition, we do not expect the overall atomic topology of C–S–H to strongly depend on the fine structural details of the chosen model.

In detail, the C–S–H atomic models developed by Pellenq et al. are obtained by introducing some defects in an 11 Å tobermorite configuration (Hamid, 1981) following a combinatorial approach (Abdolhosseini Qomi et al., 2014b). This initial tobermorite crystal consists of pseudo-octahedral calcium oxide sheets that are surrounded on each side by silicate chains. These negatively charged calcium–silicate layers are separated from each other by both dissociated and undissociated interlayer water molecules and charge-balancing calcium cations. Starting from this structure, the Ca/Si molar ratio is gradually increased

from 1.0 to 1.9 by randomly removing some SiO_2 groups (Qomi et al., 2019). The introduced defects offer some possible sites for the adsorption of extra water molecules, which is performed via the Grand Canonical Monte Carlo method—ensuring equilibrium with bulk water at constant volume and room temperature. Eventually, the ReaxFF potential—a reactive potential—was used to account for the chemical reaction of the interlayer water with the defective calcium–silicate sheets (Manzano et al., 2012a,b). The use of a reactive potential allows us to model the dissociation of water molecules into hydroxyl groups. This model has been shown to predict realistic compositions, structure, mechanical, dynamical, and thermal properties for C–S–H (Abdolhosseini Qomi et al., 2014a,b, 2015; Bauchy et al., 2015a, 2016a). The details of the methodology used for the preparation of the models, as well as multiple validations with respect to experimental data can be found in Abdolhosseini Qomi et al. (2014b) and in previous works (Abdolhosseini Qomi et al., 2013, 2014a, 2015; Bauchy et al., 2014a,b,c, 2015a,b, 2016b; Qomi et al., 2015; Bauchy, 2017; Liu et al., 2018). **Figure 1** shows some snapshots of the C–S–H model herein for select Ca/Si molar ratios.

Simulation Details

The structural, mechanical, and dynamical properties of the C–S–H samples considered herein are studied by MD simulations using the LAMMPS package (Plimpton, 1995). To account for the potential dissociation of water molecules into hydroxyl groups, we adopt the ReaxFF potential parameterized by Manzano et al. with a timestep of 0.25 fs (Manzano et al., 2012b). Unless specified otherwise, all the simulated samples comprise around 500 atoms. All the samples are relaxed under 300 K and zero pressure in the *NPT* ensemble prior to any further characterization. More simulation details can be found in Abdolhosseini Qomi et al. (2014b) and the supplementary material thereof.

Enumeration of the Topological Constraints

Assessing the state of rigidity of the disordered materials requires an accurate knowledge of their atomic structure—which is readily accessible from MD simulations. Here, we use the outcome of the MD simulations to enumerate the number of constraints per atom (n_c) in C–S–H as a function of the Ca/Si molar ratio by following a well-established methodology (Bauchy and Micoulaut, 2011, 2013a,b,c; Bauchy et al., 2011, 2013, 2014d; Bauchy, 2013; Micoulaut and Bauchy, 2013; Micoulaut et al., 2013, 2015; Bauchy and Micoulaut, 2015). This method is based on the idea that topological constraints remove some internal degrees of freedom by preventing some relative motion between atoms. In turn, a large relative motion is indicative of the absence of any underlying constraints. In detail, the number of radial BS constraints acting on a central atom can be assessed by calculating the radial excursion of each neighbor. As detailed in Bauchy et al. (2014a), we observe a clear gap between intact (low radial excursion) and broken constraints (high radial excursions). The limit between intact and broken interatomic BS constraints was found to be at around 7% of relative motion (Bauchy and Micoulaut, 2011; Bauchy et al., 2014a), which is fairly close to the Lindemann criterion (Lindemann, 1910). Similarly, the number of BB constraints created by a central atom can be assessed by computing the excursion of all the angles formed by the central atom 0 and its neighbors 1, 2, 3, etc. (the neighbors are here ranked based on their respective distance from the central atom). Again, as detailed in Bauchy et al. (2014a), we observe a clear gap between intact (low angular excursion) and broken constraints (high angular excursions). Based on previous work, the limit between intact (low angular excursion) and broken (high angular excursion) BB constraints was found to be around 13–15° (Bauchy and Micoulaut, 2011; Bauchy et al., 2014a). Note that, since the excursions associated with intact and broken BS or BB constraints are significantly different from each other, the number of BS and BB constraints computed through this method does not depend on the specific choice of the threshold used to discriminate intact from broken constraints.

Mechanical Properties of Calcium–Silicate–Hydrate

In the following, we use previously reported values of fracture toughness, fracture energy, unrecovered volume, and creep compliance for the C–S–H samples considered herein and argue that such properties offer some signatures of the existence of an intermediate phase in C–S–H.

The fracture toughness and fracture energy of the C–S–H samples considered herein were reported in Bauchy et al. (2016a). To characterize the resistance to fracture of C–S–H, we first prepare some larger C–S–H systems made of around 4,500 atoms by replicating the initial systems into a $3\times1\times3$ supercell. We then create a notch in these configurations by inserting a sharp initial crack into the structure while ensuring that the system remains neutral. The notched systems are then further relaxed in the *NPT* ensemble. The notched configurations are then elongated stepwise along the weakest direction z (i.e., the direction that is orthogonal to the silicate layers) by small 1% increments of the tensile strain. At each step, after an initial equilibration of 50 ps, the stress along the z-axis is averaged for an additional 50 ps—which yields a strain rate of 0.1 ns^{-1}. As detailed in Bauchy et al. (2016a), such a strain rate was found to be low enough to offer an accurate description of the fracture response of the C–S–H samples considered herein. The fracture energy is then computed from the integral of the obtained stress–strain curve (Brochard et al., 2013). The fracture toughness is subsequently calculated based on the Irvin formula (Brochard et al., 2013). More details about the computation of the fracture energy and fracture toughness can be found in Bauchy et al. (2015a).

To assess the mechanical reversibility of the C–S–H samples, we subject them to a loading-unloading cycle and determine the extent of unrecovered volume (Bauchy et al., 2017). To this end, starting from C–S–H configuration relaxed under zero pressure, each system is hydrostatically compressed under 10 GPa. The system is then relaxed under this load for 10 ns in the *NPT* ensemble—which is found to be long enough to ensure a convergence of energy and volume. The system is then subsequently relaxed back to zero pressure for 10 ns in the *NPT*

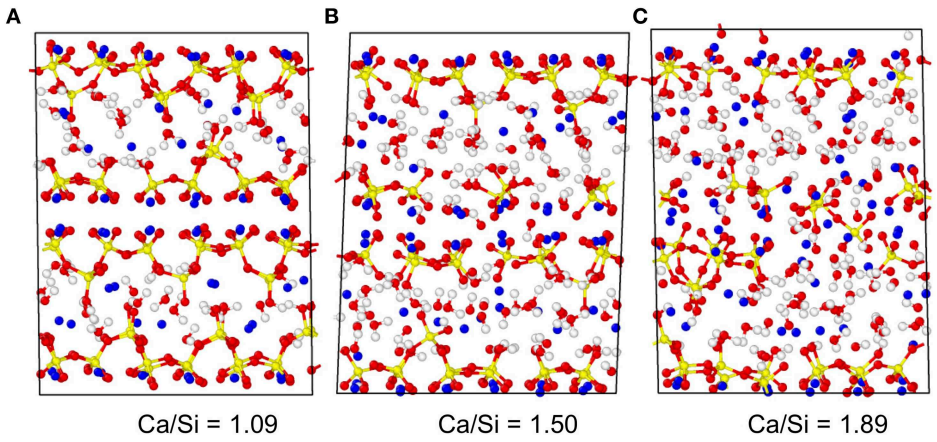

FIGURE 1 | Snapshots of the atomic structure of select calcium–silicate–hydrate systems with **(A)** Ca/Si = 1.09, **(B)** Ca/Si = 1.50, and **(C)** Ca/Si = 1.89. Ca, Si, H, and O atoms are indicated in blue, yellow, white, and red, respectively.

ensemble. We then define the fraction of unrecovered volume ($V_{\text{unrecovered}}$) by comparing the initial volume (V_{i}) of the system to that achieved after the loading-unloading cycle (V_{f}):

$$V_{\text{unrecovered}} = (V_{\text{i}} - V_{\text{f}})/V_{\text{i}} \tag{1}$$

Note that a perfectly elastic/reversible system would not exhibit any unrecovered volume.

Finally, the creep compliance of the C–S–H samples considered herein was reported in Refs. (Pignatelli et al., 2016; Bauchy et al., 2017). Since a direct simulation of the creep dynamics of C–S–H is, at this point, unachievable by conventional MD simulations, we adopt the accelerated relaxation technique (ART), which was recently developed to investigate the relaxation of silicate glasses (Yu et al., 2015, 2017b). This method consists in subjecting the system to small, cyclic perturbations of isostatic stress $\pm\Delta\sigma$. At each stress cycle, a minimization of the energy is performed, wherein the system has the ability to deform (in terms of both shape and volume) in order to reach the target stress. Note that the resulting relaxation does not depend on the choice of $\Delta\sigma$—provided that this stress remains sub-yield (see Bauchy et al., 2017). This method mimics the artificial aging observed in granular materials subjected to vibrations (Boutreux and de Geennes, 1997; Richard et al., 2005)—wherein small vibrations tend to induce the compaction of granular materials, that is, to make the system artificially age. In contrast, large vibrations would tend to randomize the arrangements of the grains, which decreases the overall compactness and, therefore, makes the system rejuvenate (Bauchy et al., 2016b). Here, we mimic the stress condition experienced in deviatoric creep by imposing a constant shear stress τ_0, such that $\Delta\sigma < \tau_0$. As shown in Bauchy et al. (2017), we find that the stress perturbations induce a gradual shear deformation of the C–S–H samples. In detail, the configurations exhibit a shear strain γ that increases linearly with the applied shear stress τ_0 and logarithmically with the number of stress cycles N—in agreement with experimental observations (Vandamme and Ulm, 2009). This allows us to define the creep modulus C as:

$$\gamma = (\tau_0/C)\ \log(1 + N/N_0) \tag{2}$$

where N_0 is a fitting parameter. We then define the creep compliance J as the inverse of the creep modulus C.

Structural Analysis

To seek a structural signature for the intermediate phase, we compute all the partial pair distribution functions. The partial structure factors are then computed from the Fourier transform of the partial pair distribution functions (Bauchy, 2012; Abdolhosseini Qomi et al., 2013). Special focus is placed on the first sharp diffraction peak (FSDP) of the partial structure factor, which captures the existence of medium-range order structural correlations within the structure (Wilson and Madden, 1994; Elliott, 1995). To this end, the position of the FSDP (Q_{FSDP}) is determined by fitting the FSDP with a Lorentzian function (Bauchy, 2012). This allows us to define a typical medium-range repetition distance (d) for each pair of atoms as (Du and Corrales, 2005):

$$d = 2\pi/Q_{\text{FSDP}} \tag{3}$$

Computation of the Internal Stress

To determine the degree of stress acting in the atomic network of the C–S–H, we adopt the concept of "stress per atom." Although stress is ill-defined at the atomic level, we rely here on the formalism proposed by Thompson et al. (2009), which expresses the contribution of each atom to the virial of the system. The local "hydrostatic pressure" applied to each atom is then defined as the ratio of the trace of the calculated local stress tensor divided by the volume of the atom, which is here taken as the

Voronoi volume. Note that, although the network as a whole is at zero pressure, some bonds are under compression while others are under tension—so that they mutually compensate each other. This approach was recently used to quantify the internal stress exhibited by stressed–rigid atomic networks (Li et al., 2019), mixed alkali glasses (Yu et al., 2015, 2017a,b, 2018), and colloidal systems (Liu et al., 2019). It should be noted that, in the thermodynamic sense, stress is only properly defined for a large ensemble of atoms, so that the physical meaning of the "stress per atom" is unclear. Nevertheless, this quantity can conveniently capture the existence of local instabilities within the gel due to competitive interatomic forces (Ioannidou et al., 2017).

Based on this framework, we compute the local stress experienced by each Si atom, since the silicate chains constitute the rigidity backbone of C–S–H. To isolate the contribution of the network connectivity to the stress of each Si atom, the "stress per atom" calculation is repeated in Q_n clusters (n = 0-to-4) that are fully isolated, that is, with no effect of the network connectivity (here, a Q_n unit denotes a SiO_4 tetrahedron that is connected to n other SiO_4 tetrahedra, i.e., with 4 – n terminating O atoms). The isolated clusters are prepared by placing the atoms as perfect SiO_4 tetrahedra, charge-balancing the terminating O atoms by Na cations, and performing an energy minimization prior to the stress calculation. Finally, the internal stress of each Si atom in the system is calculated from the difference between its states of stress in the network and isolated cluster (ensuring a consistent Q_n state in network and isolated cluster). More details about the stress calculation can be found in Li et al. (2019).

Computation of the Internal Mobility

Finally, we estimate the internal rigidity (or mobility) of the system. To this end, we first cool the C–S–H sample to 0 K in the *NPT* ensemble with a cooling rate of 1 K/s to access their inherent configuration. We then apply an instantaneous energy bump of 0.1 eV/atom. Due to the equipartition of the energy, half of the energy is used to increase the temperature while the other half is used to increase the potential energy of the system through some atomic displacements. Note that the energy is here chosen to be high enough to allow some atomic motion over low energy barriers, but low enough to avoid any melting of the system (Bauchy et al., 2014c). Following the energy bump, the system is then allowed to relax in the microcanonical *NVE* ensemble for 100 ps. During this stage, we track the mean square displacement (MSD) of each atom. Although the MSD of H atoms exhibit a diffusive regime and continuously increase over time (Abdolhosseini Qomi et al., 2014a), we note that the MSD of Si and Ca atoms exhibit a plateau. This indicates that the energy bump makes it possible for the Si and Ca atoms to overcome some small energy barriers and to experience some local reorganizations. We then use the final average MSD of Si and Ca atoms as a measure of the internal mobility of the system, whereas a low MSD is indicative of a rigid system, that is, characterized by large energy barriers.

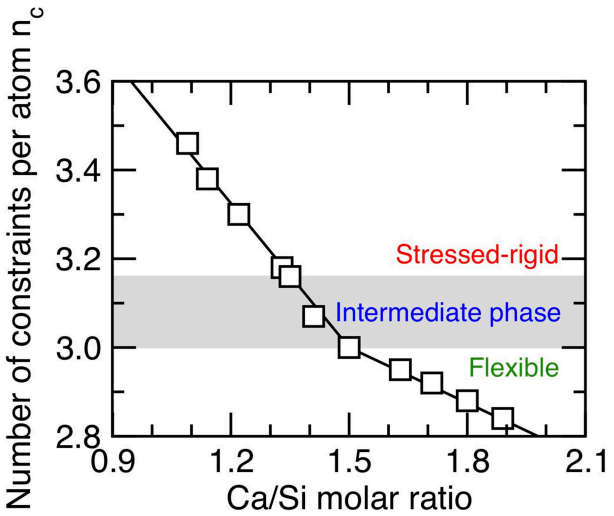

FIGURE 2 | Number of constraints per atom (n_c) in calcium–silicate–hydrate networks as a function of the Ca/Si molar ratio. The gray area indicates the location of the intermediate phase wherein structural and mechanical properties show some anomalous behaviors (see following figures).

RESULTS AND DISCUSSION

Rigidity Transition

We first assess the rigidity state of the C–S–H samples considered herein as a function of composition. **Figure 2** shows the number of constraints per atom (n_c) computed from the MD simulations (see section Enumeration of the Topological Constraints) as a function of the Ca/Si molar ratio. Overall, we find that the number of constraints per atom decreases with increasing Ca/Si molar ratio (Bauchy et al., 2016a), which is in agreement with the fact that the degree of connectivity of the silicate chains (i.e., as captured by the mean chain length) decreases with increasing Ca/Si molar ratio (Abdolhosseini Qomi et al., 2014b). This also echoes the fact that both the stiffness and hardness of C–S–H decrease with increasing Ca/Si molar ratio (Abdolhosseini Qomi et al., 2014b), since these mechanical properties have been shown to scale with the number of topological constraints (Smedskjaer et al., 2010; Bauchy et al., 2015b; Yang et al., 2019).

More specifically, we observe the existence of a rigidity transition in C–S–H that is driven by composition (Bauchy et al., 2016a). Namely, C–S–H is found to be stressed–rigid ($n_c > 3$) at low Ca/Si, flexible ($n_c < 3$) at high Ca/Si, and isostatic ($n_c \approx 3$) at Ca/Si $\approx$ 1.5 (see **Figure 2**). Interestingly, this rigidity transition manifests itself in the structure of C–S–H, as the system is found to be largely crystalline and anisotropic for Ca/Si < 1.5, whereas it is fairly amorphous and isotropic for Ca/Si > 1.5 (see **Figure 1**) (Abdolhosseini Qomi et al., 2014b).

Mechanical Signatures of the Intermediate Phase

Fracture Toughness

Having established the existence of a composition-driven rigidity transition in C–S–H, we now seek some mechanical signatures

associated with this transition. As previously mentioned, we first note that both the stiffness and hardness of C–S–H do not exhibit any anomalous behavior at the vicinity of the rigidity transition—in agreement with the fact that these mechanical properties simply scale with the number of topological constraints (Smedskjaer et al., 2010; Bauchy et al., 2015b; Yang et al., 2019). In contrast, the response to fracture of C–S–H presents a clear signature of the rigidity transition. **Figures 3A,B** shows the computed values of the mode I fracture toughness and fracture energy (see section Mechanical Properties of Calcium–Silicate–Hydrate) as a function of the number of constraints per atom. We observe that both the fracture toughness and fracture energy exhibit a maximum at the vicinity of the isostatic threshold ($n_c \approx 3$) (Bauchy et al., 2016a).

Interestingly, a local maximum of fracture toughness also observed at the vicinity of the isostatic threshold was also reported in sodium silicate and chalcogenide glasses (Guin et al., 2002; Varshneya and Mauro, 2007; Bauchy et al., 2016a; Bauchy, 2019). The harmony among these observations over various families of systems (i.e., oxides and chalcogenides) suggests that this feature might be generic to isostatic disordered materials (Bauchy et al., 2016a). This anomalous behavior has been explained by the fact that flexible networks ($n_c < 3$) have the ability to locally deform due to the existence of some internal degrees of freedom but tend to easily break, and they exhibit a low cohesion due to their low connectivity. In contrast, highly connected stressed–rigid networks ($n_c > 3$) feature higher cohesion but tend to break in a fully brittle fashion due to the existence of some internal stress that prevents any local ductile event (Wang et al., 2016). In turn, isostatic networks ($n_c \approx 3$) feature an optimal balance between cohesion and ability to show ductile deformation since they are rigid but free of internal stress (Bauchy et al., 2016a).

More interestingly, we observe that, rather than presenting a single maximum at the isostatic threshold ($n_c = 3$), both the fracture toughness and fracture energy appear to exhibit a broad maximum within a window of composition ranging from Ca/Si = 1.3-to-1.5 or $n_c = 3.0$-to-3.16. We note that, in turn, both of these properties exhibit a sudden drop at $n_c < 3.0$ and $n_c > 3.16$. These observations suggest that C–S–H may feature an isostatic atomic network (i.e., rigid but free of internal stress) within this range of composition rather than only at a single isostatic threshold ($n_c = 3$). This suggests the existence of an intermediate phase (which separates the flexible and stressed–rigid phases) in C–S–H. As shown below, the fracture toughness and fracture energy are only some of the many features that present an unusual behavior within the compositional window.

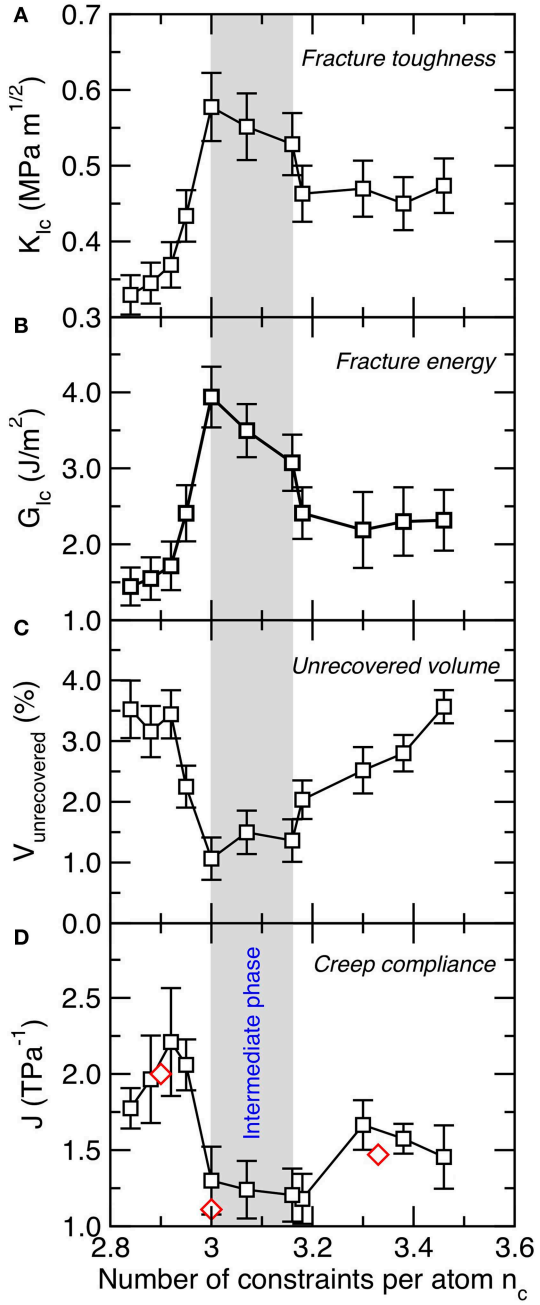

FIGURE 3 | (A) Mode I fracture toughness (K_{Ic}), **(B)** fracture energy, **(C)** unrecovered volume after a loading-unloading cycle, and **(D)** creep compliance as a function of the number of constraints per atom (n_c). The creep compliance values are compared with experimental measurements (red diamonds) obtained by micro-indentation (Nguyen et al., 2014) and nano-indentation (Vandamme and Ulm, 2009). The gray area indicates the location of the intermediate phase wherein structural and mechanical properties show some anomalous behaviors.

Reversibility Under Load

We now assess the degree of mechanical reversibility of the atomic structure. To this end, we subject the C–S–H structure to a loading-unloading cycle and compute the fracture of unrecovered volume (see section Mechanical Properties of Calcium–Silicate–Hydrate). Note that a perfectly reversible, elastic structure would exhibit a zero unrecovered volume. **Figure 3C** shows the fracture of unrecovered volume as a function of the number of constraints per atom. In general, we observe that C–S–H is not mechanically reversible, that is, its volume tends to decrease following a loading-unloading cycle (i.e., C–S–H remains permanently densified even after being relaxed to zero pressure).

Interestingly, we observe that the fracture of unrecovered volume exhibits a minimum at the vicinity of the isostatic threshold (see **Figure 3C**), which indicates that such structures exhibit a nearly fully mechanically reversible structure. This echoes with previous results observed for Ge–Se glasses, wherein isostatic glasses were also found to exhibit minimum unrecovered volume (or maximum recovered volume) (Mauro and Varshneya, 2007). The fact that this feature has been observed both in oxide and chalcogenide systems suggests that it might be generic to isostatic disordered networks. This behavior has been explained from the fact that flexible networks ($n_c < 3$) exhibit some internal floppy modes of deformation, which facilitate some irreversible reorganizations of the atoms upon loading, which, in turn, induce a permanent densification of the network upon loading. In contrast, stressed–rigid networks ($n_c > 3$) tend to remain locked in their densified state, as the presence of internal stress prevents the full relaxation of the network during unloading. In turn, isostatic networks ($n_c \approx 3$), which are both free of internal stress and modes of deformation, tend to feature maximum volume recovery (Mauro and Varshneya, 2007; Bauchy et al., 2017; Bauchy, 2019).

Again, we note that this anomalous behavior (i.e., minimum in unrecovered volume) is observed within a range of composition rather than at a fixed threshold (see **Figure 3C**). Interestingly, this composition matches with that wherein the fracture toughness and fracture energy are found to be maximum (see **Figures 3A,B**), which suggests that the fracture of unrecovered volume may constitute another signature of the existence of an intermediate phase in C–S–H. Interestingly, the mechanical reversibility of isostatic networks evidenced herein echoes the thermodynamic reversibility of isostatic glasses during the glass transition (Bauchy and Micoulaut, 2015; Mantisi et al., 2015).

Creep

We now focus on the response of the C–S–H samples under sustained loading (i.e., creep). **Figure 3D** shows the computed creep compliance of C–S–H (see section Mechanical Properties of Calcium–Silicate–Hydrate) as a function of the number of constraints per atom. Note that low values of creep compliance (or high values of creep modulus) are indicative of a high resistance to creep, that is, low delayed deformations under sustained loading. As reported in Refs. (Pignatelli et al., 2016; Bauchy et al., 2017), we find that C–S–H exhibits minimum creep compliance at the vicinity of the isostatic threshold ($n_c \approx 3$). The existence of a minimum in creep compliance around Ca/Si = 1.5 is also supported by available experimental data obtained by micro-indentation (Nguyen et al., 2014) and nano-indentation (Vandamme and Ulm, 2009). This has been explained from the fact that flexible networks exhibit some internal degrees of freedom, which allow the atom to jump over some low energy barriers during sustained loading, which, in turn, facilitates permanent deformations. In contrast, the presence of internal stress in stressed–rigid systems acts as an elastic energy penalty that stimulates the relaxation (i.e., deformation) of the system toward lower states of energy upon creep. In turn, isostatic networks, which are free of both internal stress and modes of deformation, exhibit maximum resistance to creep deformations (Bauchy et al., 2017).

Once again, we find that, rather than being minimum at a fixed threshold composition, the creep compliance exhibits a broad minimum within a range of composition that matches that wherein the fracture toughness/energy and the unrecovered volume are maximum and minimum, respectively. In turn, the creep compliance presents a sudden jump at lower and higher number of constraints per atom. This suggests that the creep compliance acts as another signature of the intermediate phase evidence herein. The fact that the resistance to creep is maximum within the intermediate phase echoes the fact that intermediate phase chalcogenide glasses have been found to exhibit minimum relaxation at the vicinity of the glass transition and minimum aging at room temperature (Boolchand et al., 2001; Chakravarty et al., 2005).

More generally, the fact that stiffness (which essentially depends on the curvature of the local energy landscape) does not present any signature of the intermediate phase suggests that the nature of the intermediate phase is not encoded in the near-equilibrium topography of the energy landscape, but rather in its far-from-equilibrium topography, i.e., that explored upon fracture and plastic non-reversible deformations (i.e., creep) or densification (i.e., unrecovered volume).

Structural Signatures of the Intermediate Phase

We now seek a structural signature of the intermediate phase in C–S–H, as the question as to whether any structural signature of the intermediate phase can be found in isostatic glasses remains unclear (Wang et al., 2017; Zeidler et al., 2017). We first note that we do not observe any obvious anomalous behavior in the short-range order structure of C–S–H (e.g., partial pair distribution function, bond distance, bond angle, coordination number, etc.) (Abdolhosseini Qomi et al., 2014b). As such, we focus our attention on the medium-range order structure—which is encoded in the FSDP of the structure factor (see section Structural Analysis). **Figure 4A** shows the position of the FSDP of the Si–Si partial structure factor, which captures the existence of some medium-range structural correlations among Si tetrahedra. We observe that the position of the FSDP of the Si–Si partial structure factor shows a maximum at the vicinity of the isostatic threshold ($n_c \approx 3$). Since the position of the FSDP is inversely related to a typical repetition distance in the medium-range order (see Equation 3), the maximum in the position of the FSDP is associated with a minimum of the Si–Si medium-range order repetition distance (see **Figure 4B**). Importantly, we note that the compositional window wherein the position of the Si–Si FSDP is maximum (or the Si–Si repetition distance minimum) matches with that of the intermediate phase, wherein several mechanical properties show anomalous behavior (see **Figure 3**). As shown in **Figures 4C,D**, similar behavior is observed for the Ca–O FSDP. This suggests that the position of the FSDP of partial structure factors offers a structural signature of the intermediate phase in C–S–H.

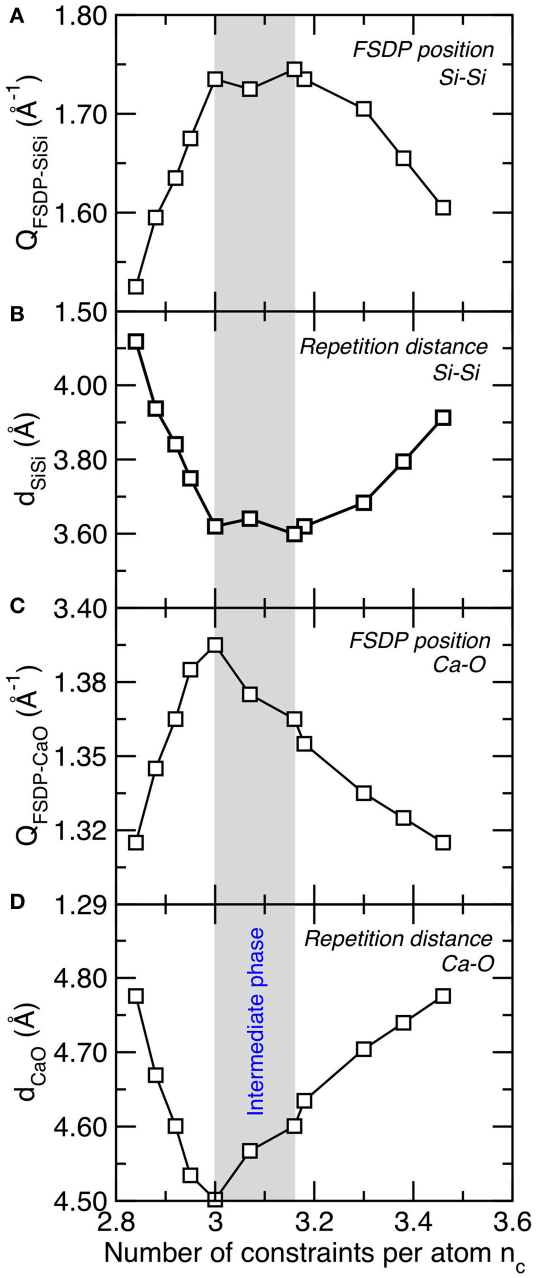

FIGURE 4 | (A) Position of the first sharp diffraction peak (Q_{FSDP}) of the Si–Si partial structure factor and **(B)** corresponding typical repetition distance **(D)**. **(C)** Position of the first sharp diffraction peak of the Ca–O partial structure factor and **(D)** corresponding typical repetition distance. The gray area indicates the location of the intermediate phase wherein structural and mechanical properties show some anomalous behaviors.

Interestingly, such behavior was also previously observed in oxide and chalcogenide glasses. First, the positions of the Si–O and O–O FSDP were also found to be maximum in isostatic densified sodium silicate glasses (Micoulaut and Bauchy, 2013). A weakly defined maximum in the position of the As–Se FSDP was also observed in As–Se chalcogenide glasses (Bauchy et al., 2013). Finally, the rigidity of the network was also found to be encoded in the position of FSDP of the structure factor in irradiated silica samples (Wang et al., 2017). All these observations across various families of materials suggest, once again, that this feature might be a generic signature of isostatic disordered networks.

These results suggest that the intermediate phase is encoded in the medium-range (rather than short-range) order structure of C–S–H. The fact that the typical repetition distance is minimum in the intermediate phase can be related to the fact that intermediate-phase glasses have been shown to exhibit an optimal space-filling tendency (for instance, several chalcogenide glasses exhibit a minimum in molar volume in the intermediate phase) (Rompicharla et al., 2008; Boolchand et al., 2018). This can be understood from the fact that, due to their low connectivity, flexible networks tend to present large rings or terminating bonds, which decreases the packing efficiency of the atoms. In turn, since their structure is fully locked by the high number of constraints, stressed–rigid networks are unable to reorganize their structure to achieve more efficiently packed configurations.

Rigidity and Stress Signatures of the Intermediate Phase

Finally, we investigate the nature of the atomic mechanism giving birth to the intermediate phase in C–S–H reported herein. To this end, we first assess the rigidity of the network by subjecting the C–S–H configurations to an energy bump and tracking the resulting atomic motion (see section Computation of the Internal Mobility). The methodology has presently been used to characterize the topography of the energy landscape of disordered networks (Sastry et al., 1998; Krishnan et al., 2017b). Indeed, configurations featuring small energy barriers (i.e., smooth energy landscape) tend to exhibit some large atomic motion following an energy bump, whereas those presenting large energy barriers (i.e., rough energy landscape) tend to show very limited energy atomic motion since the atoms are trapped in their energy basins.

Figure 5A shows the average final MSD of the Ca and Si atoms after an energy bump of 0.1 eV/atom as a function of the number of constraints per atom. We observe that the computed MSD values remain very small (around 0.2 Å^2) for $n_c > 3$. This indicates that, in this regime, the system is rigid so that the atoms only vibrate around their average position following the energy bump. In contrast, we observe that the MSD presents a sudden increase for $n_c < 3$. This shows that, at this point, the system becomes flexible and features some internal mobility. Similar behavior was observed in flexible irradiated silica samples (Krishnan et al., 2017b; Wang et al., 2017). This can be understood from the fact that, for $n_c < 3$, the configuration presents more internal degrees of freedom (i.e., initially 3 per atom) than constraints, so that the system comprises some internal floppy modes of deformation (whose number of given by $3 - n_c$) (Thorpe, 1983; Boolchand et al.,

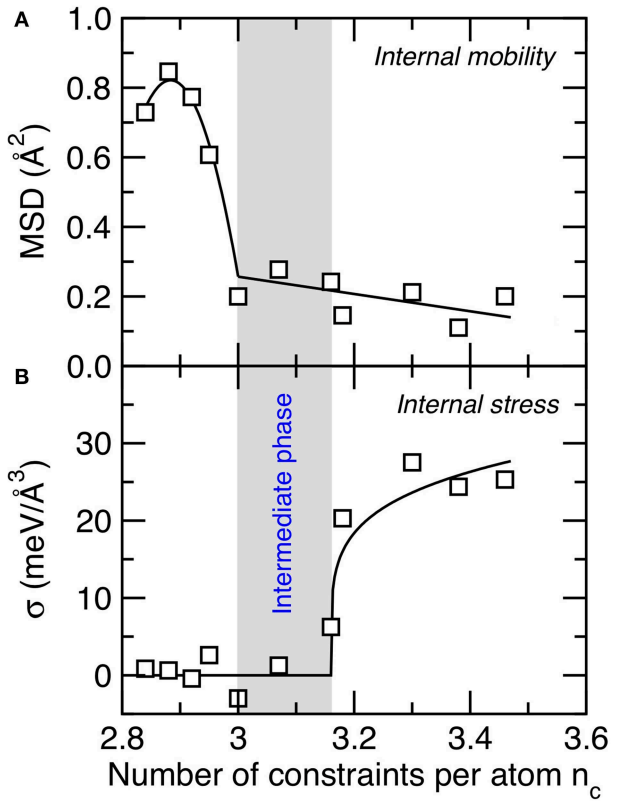

FIGURE 5 | (A) Mean-square displacement of the Ca and Si atoms after an energy bump of 0.1 eV/atom (i.e., a signature of internal mobility within the atomic network) and **(B)** average atomic-level stress undergone by Si atoms (i.e., a signature of internal stress within the atomic network). The gray area indicates the location of the intermediate phase wherein structural and mechanical properties show some anomalous behaviors.

1995). Such floppy modes manifest themselves by the formation of some channels in between the basins of the energy landscape, which enhance the internal mobility of the system.

We now focus on the quantification of the internal stress acting in the network (see section Computation of the Internal Stress). **Figure 5B** shows the average atomic-level internal stress undergone by Si atoms as a function of the number of constraints per atom. We find that, at low n_c, no significant internal stress is observed (Krishnan et al., 2017a). In contrast, we observe a sharp increase in the internal stress at high n_c. This indicates that, in this regime, the configuration experiences some local instability wherein some bonds are under tension, whereas some others are under compression (note that the total pressure remains zero in all the C–S–H systems). The existence of some internal stress in highly connected glasses has also been observed in previous experiments (Wang et al., 2005) and simulations (Li et al., 2019). This arises from the fact that, at high n_c, the system eventually comprises more constraints than degrees of freedom. In this regime, some constraints become mutually dependent, so that the constraints cannot all be satisfied at the same time (just like the angles of a triangle with three fixed edges cannot present arbitrary values). At this point, the weaker constraints yield to the stiffer ones, which results in the formation of some internal stress (Bauchy et al., 2015b).

Importantly, we observe that the rigid-to-flexible (see **Figure 5A**) and stressed-to-unstressed (see **Figure 5B**) transitions do not occur at the same composition. Interestingly, the locations of these two transitions correspond to the beginning and the end of the intermediate phase reported herein (i.e., from n_c = 3.00-to-3.16). This signals that the intermediate phase is characterized by an atomic network that is rigid (i.e., with no significant internal flexibility) but also free of internal stress. Although the location of the rigidity transition (at n_c = 3.00) is expected from a mean-field enumeration of the constraints (i.e., the point at which the constraints completely exhaust the atomic degrees of freedom), that of the stress transition (at n_c = 3.16) cannot be predicted from a mean-field enumeration—which would also predict a stress transition at n_c = 3.00, that is, when the number of constraints exceeds the number of atomic degrees of freedom. The fact that the stress occurs at $n_c > 3$ suggests that the system presents some level of self-organization to avoid the formation of any internal stress—since stress otherwise comes with an energy penalty (Bauchy and Micoulaut, 2015; Yan, 2018). These results suggest that the bifurcation between the rigidity (at n_c = 3.00) and stress (at n_c = 3.16) transitions is at the origin of the intermediate phase reported herein and explain the anomalous behaviors in the mechanical and structural properties of C–S–H in this composition window.

CONCLUSION

Overall, these results present a large array of mechanical, structural, and dynamical signatures of an intermediate phase in calcium–silicate–hydrate systems. We find that configurations belonging to the intermediate phase exhibit maximum fracture toughness and fracture energy, reversibility under load, and minimum propensity for creep relaxation—which might constitute some generic features of the intermediate phase. These results suggest that the nature of the intermediate phase is not encoded in the near-equilibrium topography of the energy landscape, but rather in its far-from-equilibrium topography. In addition, we report the existence of a structural signature of the intermediate phase, which manifests itself as an optimal space-filling tendency in the medium-range (rather than short-range) order structure of the atomic network. Based on these simulations, we demonstrate that the intermediate phase observed in this system arises from the fact that the flexible-to-rigid and stressed-to-unstressed transitions are decorrelated from each other and do not occur at the same compositional threshold. These results offer a unified picture for the intermediate phase. Further, the observation of an intermediate phase in C–S–H (which, despite being disordered, is not a traditional glass) suggests that the intermediate phase might be generic to disordered materials. However, the formation of an intermediate

phase requires some level of structural flexibility (i.e., to enable the network to self-organize to postpone the onset of stress). For instance, although select stoichiometric glasses (e.g., SiO_2 and P_2O_5) present an isostatic network, such monolithic glasses do not appear to have the ability to self-organize to remain isostatic if a small fraction of network modifiers is added (Vaills et al., 2005; Mohanty et al., 2019). Nevertheless, although it has initially been observed in chalcogenide glasses (Boolchand et al., 2001), the intermediate phase has since then been reported to also exist in silicate (Vaills et al., 2005; Bauchy and Micoulaut, 2015; Mantisi et al., 2015) and phosphate glasses (Mohanty et al., 2019)—which suggests that intermediate phases are not restricted to select families of glasses.

DATA AVAILABILITY

The datasets generated for this study are available on request to the corresponding author.

AUTHOR CONTRIBUTIONS

QZ, MW, and MB conducted the simulations presented herein and analyzed the data. QZ, LG, PB, and MB discussed the results and wrote the manuscript. All the authors contributed to revising the manuscript prior to submission.

FUNDING

This work was supported by the National Science Foundation under Grant No. 1562066 and by the Beijing General Research Institute of Mining & Metallurgy (BGRIMM) Technology Group.

ACKNOWLEDGMENTS

We acknowledge fruitful discussion and collaboration with Profs. Gaurav Sant, Matthieu Micoulaut, Mohammad Javad Abdolhosseini Qomi, Roland Pellenq, and Franz-Joseph Ulm.

REFERENCES

Abdolhosseini Qomi, M. J., Bauchy, M., Pellenq, R. J.-M., and Ulm, F.-J. (2013). "Applying tools from glass science to study calcium-silicate-hydrates" in *Mechanics and Physics of Creep, Shrinkage, and Durability of Concrete: A Tribute to Zdenek P. Bazant: Proceedings of the Ninth International Conference on Creep, Shrinkage, and Durability Mechanics (CONCREEP-9),* eds U. Franz-Josef, J. M. Hamlin, and R. J.-M Pellenq (Cambridge, MA: ASCE Publications), 78–85. doi: 10.1061/97807844131 11.008

Abdolhosseini Qomi, M. J., Bauchy, M., Ulm, F.-J., and Pellenq, R. J.-M. (2014a). Anomalous composition-dependent dynamics of nanoconfined water in the interlayer of disordered calcium-silicates. *J. Chem. Phys.* 140:054515. doi: 10.1063/1.4864118

Abdolhosseini Qomi, M. J., Krakowiak, K. J., Bauchy, M., Stewart, K. L., Shahsavari, R., Jagannathan, D., et al. (2014b). Combinatorial molecular optimization of cement hydrates. *Nat. Commun.* 5:4960. doi: 10.1038/ncomms5960

Abdolhosseini Qomi, M. J., Ulm, F.-J., and Pellenq, R. J.-M. (2015). Physical origins of thermal properties of cement paste. *Phys. Rev. Appl.* 3:064010. doi: 10.1103/PhysRevApplied.3.064010

Bauchy, M. (2012). Structural, vibrational, and thermal properties of densified silicates: Insights from molecular dynamics. *J. Chem. Phys.* 137:044510. doi: 10.1063/1.4738501

Bauchy, M. (2013). Structure and dynamics of liquid AsSe4 from ab initio molecular dynamics simulation. *J. Non-Cryst. Solids* 377, 39–42. doi: 10.1016/j.jnoncrysol.2012.12.018

Bauchy, M. (2017). Nanoengineering of concrete via topological constraint theory. *MRS Bull.* 42, 50–54. doi: 10.1557/mrs.2016.295

Bauchy, M. (2019). Deciphering the atomic genome of glasses by topological constraint theory and molecular dynamics: a review. *Comput. Mater. Sci.* 159, 95–102. doi: 10.1016/j.commatsci.2018.12.004

Bauchy, M., Abdolhosseini Qomi, M. J., Bichara, C., Ulm, F.-J., and Pellenq, R. J.-M. (2014a). Nanoscale structure of cement: viewpoint of rigidity theory. *J. Phys. Chem. C* 118, 12485–12493. doi: 10.1021/jp502550z

Bauchy, M., Abdolhosseini Qomi, M. J., Pellenq, R. J. M., and Ulm, F. J. (2014b). Is cement a glassy material? *arXiv:1506.06445.*

Bauchy, M., Abdolhosseini Qomi, M. J., Ulm, F.-J., and Pellenq, R. J.-M. (2014c). Order and disorder in calcium–silicate–hydrate. *J. Chem. Phys.* 140:214503. doi: 10.1063/1.4878656

Bauchy, M., Kachmar, A., and Micoulaut, M. (2014d). Structural, dynamic, electronic, and vibrational properties of flexible, intermediate, and stressed rigid As-Se glasses and liquids from first principles molecular dynamics. *J. Chem. Phys.* 141:194506. doi: 10.1063/1.4901515

Bauchy, M., Laubie, H., Abdolhosseini Qomi, M. J., Hoover, C. G., Ulm, F.-J., and Pellenq, R. J.-M. (2015a). Fracture toughness of calcium–silicate–hydrate from molecular dynamics simulations. *J. Non-Cryst. Solids* 419, 58–64. doi: 10.1016/j.jnoncrysol.2015.03.031

Bauchy, M., and Micoulaut, M. (2011). Atomic scale foundation of temperature-dependent bonding constraints in network glasses and liquids. *J. Non-Cryst. Solids* 357, 2530–2537. doi: 10.1016/j.jnoncrysol.2011.03.017

Bauchy, M., and Micoulaut, M. (2013a). Percolative heterogeneous topological constraints and fragility in glass-forming liquids. *EPL Europhys. Lett.* 104:56002. doi: 10.1209/0295-5075/104/56002

Bauchy, M., and Micoulaut, M. (2013b). Structure of As2Se3 and AsSe network glasses: Evidence for coordination defects and homopolar bonding. *J. Non-Cryst. Solids* 377, 34–38. doi: 10.1016/j.jnoncrysol.2013.01.019

Bauchy, M., and Micoulaut, M. (2013c). Transport anomalies and adaptative pressure-dependent topological constraints in tetrahedral liquids: evidence for a reversibility window analogue. *Phys. Rev. Lett.* 110:095501. doi: 10.1103/PhysRevLett.110.095501

Bauchy, M., and Micoulaut, M. (2015). Densified network glasses and liquids with thermodynamically reversible and structurally adaptive behaviour. *Nat. Commun.* 6:6398. doi: 10.1038/ncomms7398

Bauchy, M., Micoulaut, M., Boero, M., and Massobrio, C. (2013). Compositional thresholds and anomalies in connection with stiffness transitions in network glasses. *Phys. Rev. Lett.* 110:165501. doi: 10.1103/PhysRevLett.110.165501

Bauchy, M., Micoulaut, M., Celino, M., Le Roux, S., Boero, M., and Massobrio, C. (2011). Angular rigidity in tetrahedral network glasses with changing composition. *Phys. Rev. B* 84:054201. doi: 10.1103/PhysRevB.84.054201

Bauchy, M., Qomi, M. J. A., Bichara, C., Ulm, F.-J., and Pellenq, R. J.-M. (2015b). Rigidity transition in materials: hardness is driven by weak atomic constraints. *Phys. Rev. Lett.* 114:125502. doi: 10.1103/PhysRevLett.114.125502

Bauchy, M., Wang, B., Wang, M., Yu, Y., Abdolhosseini Qomi, M. J., Smedskjaer, M. M., et al. (2016a). Fracture toughness anomalies: viewpoint of topological constraint theory. *Acta Mater.* 121, 234–239. doi: 10.1016/j.actamat.2016.09.004

Bauchy, M., Wang, M., Yu, Y., Wang, B., Krishnan, N. M. A., Masoero, E., et al. (2017). Topological control on the structural relaxation of atomic networks under stress. *Phys. Rev. Lett.* 119:035502. doi: 10.1103/PhysRevLett.119.035502

Bauchy, M., Wang, M., Yu, Y., Wang, B., Krishnan, N. M. A., Ulm, F.-J., et al. (2016b). Topological control on atomic networks' relaxation under stress. *arXiv [Preprint]. arXiv:1605.05043.*

Bhosle, S., Gunasekera, K., Boolchand, P., and Micoulaut, M. (2012a). Melt homogenization and self-organization in chalcogenides-part I. *Int. J. Appl. Glass Sci.* 3, 189–204. doi: 10.1111/j.2041-1294.2012.00093.x

Bhosle, S., Gunasekera, K., Boolchand, P., and Micoulaut, M. (2012b). Melt Homogenization and Self-Organization in Chalcogenides-Part II. *Int. J. Appl. Glass Sci.* 3, 205–220. doi: 10.1111/j.2041-1294.2012.00092.x

Boolchand, P., Bauchy, M., Micoulaut, M., and Yildirim, C. (2018). Topological phases of chalcogenide glasses encoded in the melt dynamics. *Phys. Status Solidi B* 255:1800027. doi: 10.1002/pssb.201800027

Boolchand, P., Bhosle, S., Gunasekera, K., Vignarooban, K., and Chakraborty, S. (2011). Glass homogeneity precursive to self-organization. *J. Optoelectron. Adv. Mater.* 13:1353.

Boolchand, P., Bresser, W., Zhang, M., Wu, Y., Wells, J., and Enzweiler, R. (1995). Lamb-mossbauer factors as a local probe of floppy modes in network glasses. *J. Non-Cryst. Solids* 182, 143–154. doi: 10.1016/0022-3093(94)00540-0

Boolchand, P., Georgiev, D. G., and Goodman, B. (2001). Discovery of the intermediate phase in chalcogenide glasses. *J. Optoelectron. Adv. Mater.* 3, 703–720.

Boolchand, P., and Goodman, B. (2017). Glassy materials with enhanced thermal stability. *MRS Bull.* 42, 23–28. doi: 10.1557/mrs.2016.300

Boutreux, T., and de Geennes, P. G. (1997). Compaction of granular mixtures: a free volume model. *Phys. Stat. Mech. Its Appl.* 244, 59–67. doi: 10.1016/S0378-4371(97)00236-7

Brochard, L., Hantal, G., Laubie, H., Ulm, F., and Pellenq, R. (2013). Fracture mechanisms in organic-rich shales: role of Kerogen. *Poromechanics* 2471–2480. doi: 10.1061/9780784412992.288

Chakravarty, S., Georgiev, D. G., Boolchand, P., and Micoulaut, M. (2005). Ageing, fragility and the reversibility window in bulk alloy glasses. *J. Phys. Condens. Matter.* 17:L1. doi: 10.1088/0953-8984/17/1/L01

Chen, P., Boolchand, P., and Georgiev, D. G. (2010). Long term aging of selenide glasses: evidence of sub-Tg endotherms and pre-Tg exotherms. *J. Phys.* 22:065104. doi: 10.1088/0953-8984/22/6/065104

Chubynsky, M. V., Brière, M.-A., and Mousseau, N. (2006). Self-organization with equilibration: a model for the intermediate phase in rigidity percolation. *Phys. Rev. E* 74:016116. doi: 10.1103/PhysRevE.74.016116

Du, J., and Corrales, L. R. (2005). First sharp diffraction peak in silicate glasses: structure and scattering length dependence. *Phys. Rev. B* 72:092201. doi: 10.1103/PhysRevB.72.092201

Elliott, S. R. (1995). Extended-range order, interstitial voids and the first sharp diffraction peak of network glasses. *J. Non-Cryst. Solids* 182, 40–48. doi: 10.1016/0022-3093(94)00539-7

Guin, J.-P., Rouxel, T., Sanglebœuf, J.-C., Melscoët, I., and Lucas, J. (2002). Hardness, toughness, and scratchability of germanium–selenium chalcogenide glasses. *J. Am. Ceram. Soc.* 85, 1545–1552. doi: 10.1111/j.1151-2916.2002.tb00310.x

Hamid, S. (1981). The crystal-structure of the 11-a natural tobermorite. *Z. Krist.* 154, 189–198. doi: 10.1524/zkri.1981.154.3-4.189

Ioannidou, K., Del Gado, E., Ulm F-J, and Pellenq Roland, J.-M. (2017). Inhomogeneity in cement hydrates: linking local packing to local pressure. *J. Nanomech Micromechanics* 7:04017003. doi: 10.1061/(ASCE)NM.2153-5477.0000120

Krishnan, N. M. A., Wang, B., Sant, G., Phillips, J. C., and Bauchy, M. (2017a). Revealing the Effect of irradiation on cement hydrates: evidence of a topological self-organization. *ACS Appl. Mater. Interfaces* 9, 32377–32385. doi: 10.1021/acsami.7b09405

Krishnan, N. M. A., Wang, B., Yu, Y., Le Pape, Y., Sant, G., and Bauchy, M. (2017b). Enthalpy landscape dictates the irradiation-induced disordering of quartz. *Phys. Rev. X* 7:031019. doi: 10.1103/PhysRevX.7.031019

Li, X., Song, W., Smedskjaer, M. M., Mauro, J. C., and Bauchy, M. (2019). Quantifying the internal stress in over-constrained glasses by molecular dynamics simulations. *J. Non-Cryst. Solids X* 1:100013. doi: 10.1016/j.nocx.2019.100013

Lindemann, F. A. (1910). Ueber die berechnung molekularer eigenfrequenzen. *Phys. Z* 11, 609–612.

Liu, H., Dong, S., Tang, L., Krishnan, N. M. A., Sant, G., and Bauchy, M. (2019). Effects of polydispersity and disorder on the mechanical properties of hydrated silicate gels. *J. Mech. Phys. Solids* 122, 555–565. doi: 10.1016/j.jmps.2018.10.003

Liu, H., Du, T., Krishnan, N. M. A., Li, H., and Bauchy, M. (2018). Topological optimization of cementitious binders: advances and challenges. *Cem. Concr. Compos* 101, 5–14. doi: 10.1016/j.cemconcomp.2018.08.002

Lucas, P., King, E. A., Gulbiten, O., Yarger, J. L., Soignard, E., and Bureau, B. (2009). Bimodal phase percolation model for the structure of Ge-Se glasses and the existence of the intermediate phase. *Phys. Rev. B* 80:214114. doi: 10.1103/PhysRevB.80.214114

Mantisi, B., Bauchy, M., and Micoulaut, M. (2015). Cycling through the glass transition: evidence for reversibility windows and dynamic anomalies. *Phys. Rev. B* 92:134201. doi: 10.1103/PhysRevB.92.134201

Manzano, H., Moeini, S., Marinelli, F., van Duin, A. C. T., Ulm, F.-J., and Pellenq, R. J.-M. (2012a). Confined water dissociation in microporous defective silicates: mechanism, dipole distribution, and impact on substrate properties. *J. Am. Chem. Soc.* 134, 2208–2215. doi: 10.1021/ja209152n

Manzano, H., Pellenq, R. J. M., Ulm, F.-J., Buehler, M. J., and van Duin, A. C. T. (2012b). Hydration of calcium oxide surface predicted by reactive force field molecular dynamics. *Langmuir* 28, 4187–4197. doi: 10.1021/la204338m

Mauro, J. C. (2011). Topological constraint theory of glass. *Am. Ceram. Soc. Bull.* 90, 31–37.

Mauro, J. C., and Varshneya, A. K. (2007). Modeling of rigidity percolation and incipient plasticity in germanium–selenium glasses. *J. Am. Ceram. Soc.* 90, 192–198. doi: 10.1111/j.1551-2916.2006.01374.x

Maxwell, J. C. (1864). L. On the calculation of the equilibrium and stiffness of frames. *Philos. Mag. Ser.* 27, 294–299. doi: 10.1080/14786446408643668

Micoulaut, M. (2008). Constrained interactions, rigidity, adaptative networks, and their role for the description of silicates. *Am. Mineral.* 93, 1732–1748. doi: 10.2138/am.2008.2903

Micoulaut, M., and Bauchy, M. (2013). Anomalies of the first sharp diffraction peak in network glasses: evidence for correlations with dynamic and rigidity properties. *Phys. Status Solidi B* 250, 976–982. doi: 10.1002/pssb.201248512

Micoulaut, M., Bauchy, M., and Flores-Ruiz, H. (2015). "Topological constraints, rigidity transitions, and anomalies in molecular networks," in *Molecular Dynamics Simulations of Disordered Materials*, Vol. 215, eds C. Massobrio, J. Du, M. Bernasconi, and P. Salmon (Cham: Springer), 275–311. doi: 10.1007/978-3-319-15675-0_1

Micoulaut, M., Kachmar, A., Bauchy, M., Le Roux, S., Massobrio, C., and Boero, M. (2013). Structure, topology, rings, and vibrational and electronic properties of GeSe glasses across the rigidity transition: a numerical study. *Phys. Rev. B* 88:054203. doi: 10.1103/PhysRevB.88.054203

Micoulaut, M., and Phillips, J. C. (2007). Onset of rigidity in glasses: from random to self-organized networks. *J. Non-Cryst. Solids* 353, 1732–1740. doi: 10.1016/j.jnoncrysol.2007.01.078

Micoulaut, M., and Yue, Y. (2017). Material functionalities from molecular rigidity: maxwell's modern legacy. *MRS Bull.* 42, 18–22. doi: 10.1557/mrs.2016.298

Mohanty, C., Mandal, A., Gogi, V. K., Chen, P., Novita, D., Chbeir, R., et al. (2019). Linking melt dynamics with topological phases and molecular structure of sodium phosphate glasses from calorimetry, raman scattering, and infrared reflectance. *Front. Mater.* 6:69. doi: 10.3389/fmats.2019.00069

Nguyen, D.-T., Alizadeh, R., Beaudoin, J. J., Pourbeik, P., and Raki, L. (2014). Microindentation creep of monophasic calcium–silicate–hydrates. *Cem. Concr. Compos.* 48, 118–126. doi: 10.1016/j.cemconcomp.2013.11.011

Pellenq, R. J.-M., Kushima, A., Shahsavari, R., Vliet, K. J. V., Buehler, M. J., Yip, S., et al. (2009). A realistic molecular model of cement hydrates. *Proc. Natl. Acad. Sci.U.S.A.* 106, 16102–16107. doi: 10.1073/pnas.0902180106

Phillips, J. C. (1979). Topology of covalent non-crystalline solids 1. Short-range order in chalcogenide alloys. *J. Non-Cryst. Solids* 34, 153–181. doi: 10.1016/0022-3093(79)90033-4

Phillips, J. C. (1981). Topology of covalent non-crystalline solids II: medium-range order in chalcogenide alloys and As-Si-Ge. *J. Non-Cryst. Solids* 43, 37–77. doi: 10.1016/0022-3093(81)90172-1

Phillips, J. C. (2006). Microscopic reversibility, space-filling, and internal stress in strong glasses. *arXiv [preprint] cond-Mat0606418*.

Pignatelli, I., Kumar, A., Alizadeh, R., Pape, Y. L., Bauchy, M., and Sant, G. (2016). A dissolution-precipitation mechanism is at the origin of concrete creep in moist environments. *J. Chem. Phys.* 145:054701. doi: 10.1063/1.4955429

Plimpton, S. (1995). Fast parallel algorithms for short-range molecular dynamics. *J. Comput. Phys.* 117, 1–19.

Qomi, M. J. A., Bauchy, M., Ulm, F.-J., and Pellenq, R. (2015). "Polymorphism and Its Implications on Structure-Property Correlation in Calcium-Silicate-Hydrates," in *Nanotechnology in Construction*, eds K. Sobolev and S. P. Shah

(Springer International Publishing), 99–108. Available at: http://link.springer.com/chapter/10.1007/978-3-319-17088-6_12 (accessed May 21, 2015).

Qomi, M. J. A., Masoero, E., Bauchy, M., Ulm, F.-J., Gado, E. D., and Pellenq, R. J.-M. (2019). "C-S-H across Length Scales: From Nano to Micron," in *CONCREEP 10 (American Society of Civil Engineers),* 39–48. Available online at: http://ascelibrary.org/doi/abs/10.1061/9780784479346.006 (accessed July 3, 2016).

Richard, P., Nicodemi, M., Delannay, R., Ribière, P., and Bideau, D. (2005). Slow relaxation and compaction of granular systems. *Nat. Mater.* 4, 121–128. doi: 10.1038/nmat1300

Richardson, I. G. (2013). The importance of proper crystal-chemical and geometrical reasoning demonstrated using layered single and double hydroxides. *Acta Crystallogr. Sect. B Struct. Sci. Cryst. Eng. Mater.* 69, 150–162. doi: 10.1107/S205251921300376X

Richardson, I. G. (2014). Model structures for C-(A)-S-H(I). *Acta Crystallogr. Sect. B Struct. Sci. Cryst. Eng. Mater.* 70, 903–923. doi: 10.1107/S2052520614021982

Rompicharla, K., Novita, D. I., Chen, P., Boolchand, P., Micoulaut, M., and Huff, W. (2008). Abrupt boundaries of intermediate phases and space filling in oxide glasses. *J. Phys. Condens. Matter Inst. Phys. J.* 20:202101. doi: 10.1088/0953-8984/20/20/202101

Sastry, S., Debenedetti, P. G., and Stillinger, F. H. (1998). Signatures of distinct dynamical regimes in the energy landscape of a glass-forming liquid. *Nat. Lond.* 393, 554–557. doi: 10.1038/31189

Scrivener, K. L., Juilland, P., and Monteiro, P. J. M. (2015). Advances in understanding hydration of Portland cement. *Cem. Concr. Res.* 78, 38–56. doi: 10.1016/j.cemconres.2015.05.025

Smedskjaer, M. M., Mauro, J. C., and Yue, Y. (2010). Prediction of glass hardness using temperature-dependent constraint theory. *Phys. Rev. Lett.* 105:115503. doi: 10.1103/PhysRevLett.105.115503

Taylor, H. F. W. (1997). *Cement Chemistry*. Aberdeen: Thomas Telford.

Thompson, A. P., Plimpton, S. J., and Mattson, W. (2009). General formulation of pressure and stress tensor for arbitrary many-body interaction potentials under periodic boundary conditions. *J. Chem. Phys.* 131:154107. doi: 10.1063/1.3245303

Thorpe, M. F. (1983). Continuous deformations in random networks. *J. Non-Cryst. Solids* 57, 355–370. doi: 10.1016/0022-3093(83)90424-6

Thorpe, M. F., Jacobs, D. J., Chubynsky, M. V., and Phillips, J. C. (2000). Self-organization in network glasses. *J. Non-Cryst. Solids* 266, 859–866. doi: 10.1016/S0022-3093(99)00856-X

Vaills, Y., Qu, T., Micoulaut, M., Chaimbault, F., and Boolchand, P. (2005). Direct evidence of rigidity loss and self-organization in silicate glasses. *J. Phys.-Condens. Matter* 17, 4889–4896. doi: 10.1088/0953-8984/17/32/003

Vandamme, M., and Ulm, F.-J. (2009). Nanogranular origin of concrete creep. *Proc. Natl. Acad. Sci. U.S.A.* 106, 10552–10557. doi: 10.1073/pnas.0901033106

Varshneya, A. K., and Mauro, D. J. (2007). Microhardness, indentation toughness, elasticity, plasticity, and brittleness of Ge–Sb–Se chalcogenide glasses. *J. Non-Cryst. Solids* 353, 1291–1297. doi: 10.1016/j.jnoncrysol.2006.10.072

Vignarooban, K., Boolchand, P., Micoulaut, M., Malki, M., and Bresser, W. J. (2014). Rigidity transitions in glasses driven by changes in network dimensionality and structural groupings. *EPL Europhys. Lett.* 108:56001. doi: 10.1209/0295-5075/108/56001

Wang, B., Krishnan, N. M. A., Yu, Y., Wang, M., Le Pape, Y., Sant, G., et al. (2017). Irradiation-induced topological transition in SiO2: structural signature of networks' rigidity. *J. Non-Cryst. Solids* 463, 25–30. doi: 10.1016/j.jnoncrysol.2017.02.017

Wang, B., Yu, Y., Wang, M., Mauro, J. C., and Bauchy, M. (2016). Nanoductility in silicate glasses is driven by topological heterogeneity. *Phys. Rev. B* 93:064202. doi: 10.1103/PhysRevB.93.064202

Wang, F., Mamedov, S., Boolchand, P., Goodman, B., and Chandrasekhar, M. (2005). Pressure Raman effects and internal stress in network glasses. *Phys. Rev. B* 71:174201. doi: 10.1103/PhysRevB.71.174201

Wilson, M., and Madden, P. A. (1994). "'Prepeaks"' and "'first sharp diffraction peaks"' in computer simulations of strong and fragile ionic liquids. *Phys. Rev. Lett.* 72, 3033–3036. doi: 10.1103/PhysRevLett.72.3033

Yan, L. (2018). Entropy favors heterogeneous structures of networks near the rigidity threshold. *Nat. Commun.* 9:1359. doi: 10.1038/s41467-018-03859-9

Yan, L., and Wyart, M. (2014). Evolution of covalent networks under cooling: contrasting the rigidity window and jamming scenarios. *Phys. Rev. Lett.* 113:215504. doi: 10.1103/PhysRevLett.113.215504

Yang, K., Yang, B., Xu, X., Hoover, C., Smedskjaer, M. M., and Bauchy, M. (2019). Prediction of the Young's modulus of silicate glasses by topological constraint theory. *J. Non-Cryst. Solids* 514, 15–19. doi: 10.1016/j.jnoncrysol.2019.03.033

Yu, Y., Mauro, J. C., and Bauchy, M. (2017a). Stretched exponential relaxation of glasses: origin of the mixed-alkali effect. *Am. Ceram. Soc. Bull.* 96, 34–36.

Yu, Y., Wang, M., Anoop Krishnan, N. M., Smedskjaer, M. M., Deenamma Vargheese, K., Mauro, J. C., et al. (2018). Hardness of silicate glasses: Atomic-scale origin of the mixed modifier effect. *J. Non-Cryst. Solids* 489, 16–21. doi: 10.1016/j.jnoncrysol.2018.03.015

Yu, Y., Wang, M., Smedskjaer, M. M., Mauro, J. C., Sant, G., and Bauchy, M. (2017b). Thermometer effect: origin of the mixed alkali effect in glass relaxation. *Phys. Rev. Lett.* 119:095501. doi: 10.1103/PhysRevLett.119.095501

Yu, Y., Wang, M., Zhang, D., Wang, B., Sant, G., and Bauchy, M. (2015). Stretched exponential relaxation of glasses at low temperature. *Phys. Rev. Lett.* 115:165901. doi: 10.1103/PhysRevLett.115.165901

Zeidler, A., Salmon, P. S., Whittaker, D. A. J., Pizzey, K. J., and Hannon, A. C. (2017). Topological ordering and viscosity in the glass-forming Ge–Se system: the search for a structural or dynamical signature of the intermediate phase. *Front. Mater.* 4:32. doi: 10.3389/fmats.2017.00032

Conflict of Interest Statement: The authors declare that the research was conducted in the absence of any commercial or financial relationships that could be construed as a potential conflict of interest.

frontiers in Materials

ORIGINAL RESEARCH
published: 15 July 2019
doi: 10.3389/fmats.2019.00166

Correlating Melt Dynamics and Configurational Entropy Change With Topological Phases of As_xS_{100-x} Glasses and the Crucial Role of Melt/Glass Homogenization

*Soumendu Chakravarty[1], Ralph Chbeir[2], Ping Chen[2], Matthieu Micoulaut[3] and Punit Boolchand[2]**

[1] Department of Mechanical and Materials Engineering, University of Cincinnati, Cincinnati, OH, United States, [2] Department of Electrical Engineering and Computer Science, University of Cincinnati, Cincinnati, OH, United States, [3] Laboratoire de Physique Théorique de la Matière Condensée, CNRS UMR 7600, Sorbonne Université, Paris, France

OPEN ACCESS

Edited by:
Morten M. Smedskjaer,
Aalborg University, Denmark

Reviewed by:
Gerardo Naumis,
National Autonomous University of Mexico, Mexico
Le Yan,
University of California, Santa Barbara, United States

***Correspondence:**
Punit Boolchand
boolchp@ucmail.uc.edu

Specialty section:
This article was submitted to Glass Science, a section of the journal Frontiers in Materials

Received: 13 May 2019
Accepted: 25 June 2019
Published: 15 July 2019

Citation:
Chakravarty S, Chbeir R, Chen P, Micoulaut M and Boolchand P (2019) Correlating Melt Dynamics and Configurational Entropy Change With Topological Phases of As_xS_{100-x} Glasses and the Crucial Role of Melt/Glass Homogenization. Front. Mater. 6:166. doi: 10.3389/fmats.2019.00166

Melt dynamics and glass Topological phases of especially dry and homogenized binary As_xS_{100-x} melts/glasses are examined in Modulated-DSC, Raman scattering, and volumetric experiments. In the S-rich glasses ($12\% < x < 23\%$), direct evidence for the elusive 537 cm^{-1} stretch vibrational mode of the Quasi-Tetrahedral (QT), $S = As(S_{1/2})_3$, local structure is observed in FT-Raman scattering once melts are homogenized and glasses cycled through $T_g+10^{\circ}C$ for an extended period. The enthalpy of relaxation at T_g, $\Delta H_{nr}(x)$, fragility index, m(x), Molar volumes, $V_m(x)$ each display three distinct regimes of variation. Specifically, m(x) displays a Gaussian like global minimum (fragility window), and $\Delta H_{nr}(x)$ displays an abrupt square-well like variation (reversibility window), while $V_m(x)$ displays a Gaussian-like local minimum (Volumetric window) in the isostatically rigid phase ($22.5\% < x < 28.5\%$). At low x (<20%) in the Flexible phase, glasses are segregated with a S_8-rich nanophase that decouples from the As-S glassy backbone. At medium x ($22.5\% < x < 28.5\%$) glassy backbones form an isostatically rigid phase displaying a vanishing $\Delta H_{nr}(x)$ term, and compacted structures with corresponding melts being superstrong ($m < 20$). At high x ($28.5\% < x < 40\%$) in the Stressed-Rigid phase, glasses possess an increasing $\Delta H_{nr}(x)$ term, and melts become increasingly fragile, with m(x) >20 as x increases. Taken together, these results underscore that superstrong melts yield isostatically rigid glasses, while fragile ones form either Flexible or Stressed-rigid glasses upon cooling. The onset of the rigidity transition near $<r> = 2.22$, instead of the usual value of $<r> = 2.40$, is identified with presence of QT local structures in addition to Pyramidal $As(S_{1/2})_3$ local structures in the glassy backbone, and with a small but finite fraction of polymeric S_n chains being decoupled from the backbone.

Keywords: modulated differential scanning calorimeter (MDSC), Raman, molar volume, topological constraint theory, configurational entropy

INTRODUCTION

Chalcogenide glasses continue to be fascinating materials since their inception nearly 4 decades ago. The fascination stems from fundamental investigations into their molecular structure that inherently control glass functionality examined as a function of network connectivity. These considerations have a close bearing on their Topological phases (Mantisi et al., 2015; Boolchand and Goodman, 2017). In recent years these materials have found a niche in select advanced applications as phase change memory materials (Raoux, 2009), in 3D X-point memory[1] (Tang et al., 2009; Malventano, 2017), as materials of choice for optical fibers and waveguides in infrared optics and Supercontinuum emission (Goncalves et al., 2018; Tremblay et al., 2018), amongst many others. In these investigations, it would appear that glass functionality is apparently tied to their chemical composition, and more generally to the underlying Topological phases.

In elemental Selenium, chains are known (Gouda, 2012) to be more stable than Se_8 rings, with the consequence that when a Se-melt is quenched, one obtains a bulk glass composed largely of polymeric Se_n chains. The reverse is the case in elemental Sulfur, S_8 rings are more stable than polymeric S_n chains, with the consequence that when an elemental Sulfur melt is quenched, one invariably obtains a molecular crystal composed of S_8 crowns. And when Sulfur is heated to a T of nearly 159°C, also called T_λ, the S_8 rings open up into chains, leading to the polymerization transition (Tobolsky and Eisenberg, 1959). The T_λ transition in pure S has been more recently examined in Photon correlation spectroscopy (Scopigno et al., 2007), to reveal an underlying chain relaxation process in the millisecond range, validating the Maxwell relation for the increase of viscosity for the polymerization transition. Recent Raman scattering experiments (Bellissent et al., 1990; Kalampounias et al., 2003; Andrikopoulos et al., 2005), have permitted to establish the polymerized Sulfur fraction as a function of T as T>150° C, and compare these to theory (Tobolsky and Eisenberg, 1959). Thus, Se-rich alloyed melts with group IV (Si, Ge) and/or group V (P, As) elements readily form bulk chalcogenide glasses, but their S-rich counterparts invariably demix into a majority S-rich phase composed of S_8 rings, and a minority chalcogenide glass phase composed of the group IV and/or group V additive crosslinking chains of polymeric S_n.

Over the years that foregoing picture of demixing of S-rich glasses has been well-confirmed for the case of As-S binary melts in numerous investigations starting since the late sixtees (Ward, 1968). More recently, Wagner et al. (1998) used Modulated Differential Scannining Calorimetry (MDSC) to show that S-rich ($x < 25\%$) As_xS_{100-x} glasses display bimodal T_g's and are phase separated. Georgiev et al. (2003b) used MDSC and Raman scattering to show that the stoichiometric As_2S_3 glass is also intrinsically phase separated (Boolchand, 2000; Boolchand et al., 2002) into As-rich (As_4S_4 Realgar monomers) and As_2S_3 based S-rich regions (Phillips et al., 1980; Zitkovsky and Boolchand, 1987), with that degree of phase separation determined by the melt-quench temperature used to synthesize the glass. In 2008, Chen et al. confirmed S-rich glasses ($x < 25\%$) to be demixed into a S_8-rich nanophase displaying the T_λ transition near 159°C, and with the base As-S polymeric glass backbone displaying a quasi-linear variation of T_g with x over a wide range $12\% < x < 40\%$. More significantly they (Chen et al., 2008) also showed the existence of a reversibility window in As-S glasses in the $22.5\% < x < 29.5\%$ range using MDSC to establish the three Topological phases; Flexible, Intermediate and Stressed-rigid. In their study, Chen et al., typically used 2 gram sized As-S batches, and alloyed these for 2 to 3 days at 650°C. And as we acquired more experience on learning how glass melts homogenize, it became clear to us in 2018 that such heat treatment was insufficient to fully homogenize melts/glasses in the present binary.

New and recent evidence has accrued on delayed homogenization of Chalcogenide melts. The results show that binary Ge-Se (Bhosle et al., 2011; Gunasekera et al., 2013), As-Se (Ravindren et al., 2014), and Ge-S (Chakraborty and Boolchand, 2014) and ternary $Ge_xAs_xSe_{100-2x}$ (Chbeir et al., 2019) melts of even small (2 gram or less) sized batches typically take 10 days or more to homogenize when alloyed at suitable temperatures. Basic glass science investigations on such homogenized glasses/melts have revealed a rather intimate and detailed correlation between melt properties such as dynamics and glass Topological phases (Boolchand and Goodman, 2017). These considerations became a strong impetus to extend such investigations to the case of the present As-S binary. In this work we have thus chosen to undertake a detailed study on the As-S binary, and have explored amongst other issues the consequences of such homogenization on fundamental correlations between glass Topological phases with melt dynamics.

In the present work, we show direct evidence for presence of Quasi-Tetrahedral $S = As(S_{1/2})_3$ local structures in As_xS_{100-x} glasses from Raman scattering, and the existence of a *window* in glass transition reversibility that coincides with a *window* in melt fragility index established from MDSC experiments, both of which to correlate with a *window* in molar volumes established from density measurements. Each of these windows reside in the $22.5(3)\% < x < 28.5(3)\%$ range which defines the range of compositions across which the Intermediate Phase (IP) is manifested. Our results also show that the window in *molar volumes* encodes in a rather direct manner the homogeneity of glasses. Furthermore, the rigidity- and stress-elastic phase transitions, which border the IP, are found to be abrupt in composition even in the freshly synthesized glasses. Upon room temperature aging of glasses over several months the reversibility window continues to remain sharp but also gets deeper. Furthermore, the rigidity onset in binary As_xS_{100-x} glasses near $<r> = 2.220(5)$ is found to deviate substantially from the $<r> = 2.40$ prediction of Phillips-Thorpe (Thorpe, 1985). We take the result to confirm the participation of both QT $S = As(S_{1/2})_3$ (Boolchand et al., 2009) and Pyramidal $As(S_{1/2})_3$ isostatic local structures to the formation of that special Intermediate phase. The present work also serves to demonstrate that a pre-requisite to observe these elastic phase transitions in network glasses to be sharp, is that the local connectivity of the backbone,

[1]3D XPoint™: A Breakthrough in Non-Volatile Memory Technology. Intel. Available online at: https://www.intel.com/content/www/us/en/architectureand-technology/intel-micron-3d-xpoint-webcast.html (accessed April 17, 2019).

which is determined by the mean coordination number $<r> = (2 + <x>)$, must be well-defined, i.e., the variance in glass stoichiometry ($<\Delta x>$), on a scale of 50 microns or less must be <0.5% across the synthesized batch. After describing the materials and methods (section Materials and Methods), and the experimental results (section Experimental Results), we discuss the several broader issues related to the observed correlation between melt dynamics and glass topological phases (section Discussion). The conclusions from our findings are summarized in section Conclusions.

MATERIALS AND METHODS

Synthesis of Melts/Glasses

Bulk As_xS_{100-x} glasses were synthesized using 99.999% As_2S_3 lumps of typically 3 mm in diameter and 99.999% elemental S flakes from Cerac Inc. as the starting materials. Elemental Sulfur flakes were vacuum dried by pumping to 10^{-6} Torr for 48 h. Both starting materials were weighed and sealed in a N_2 gas purged glove bag with relative humidity of <5%. Appropriate weight ratios of the two starting materials were used to synthesize bulk glasses of 1.5 gram batch size in the 15% < x < 40% range. Quartz tubes were dried in a vacuum oven at 80°C for at least 24 h prior to their use. Starting materials were sealed in quartz tubes of 5 mm ID and 1 mm wall thickness at a pressure of 3×10^{-7} Torr using a Veeco LN_2 trapped diffusion pumping system. The starting materials were next alloyed by heating in a box furnace with quartz tubes held vertical, and with the T slowly increased to 650°C and kept there for varying alloying times, t_r, till melts completely homogenized. Typically, FT-Raman spectra of melts quenched from a temperature 50°C above the liquidus were periodically acquired at 5 locations along the 15 mm long melt column, and the process of alloying continued till spectra at the 5 locations became identical. In the FT-Raman scattering measurements glass samples were mounted on an xyz stage to precisely control the location to probe glass column encapsulated in the quartz tube used for synthesis. These Raman profiling experiments showed that alloying times, t_r, in the range 3 to 6 weeks were required to homogenize melts (section Kinetics of Melt/Glass Homogenization). Such FT-profiling experiments introduced in 2011 (Bhosle et al., 2012a,b; Gunasekera et al., 2013; Chakraborty and Boolchand, 2014) have proved to be remarkably insightful (Bhosle et al., 2012a,b; Gunasekera et al., 2013; Chakraborty and Boolchand, 2014; Chbeir et al., 2019) in understanding the intrinsically slow nature of the kinetics of melt/glass homogenization in chalcogenides.

The stoichiometric glass was synthesized by using As_2S_3 starting material lumps, sealed in evacuated (3×10^{-7} Torr) quartz tube, and heated to 650°C for 3 days. Thereafter, the temperature was slowly lowered to 360°C, i.e., 50°C above the liquidus (310°C), and the melt kept at that temperature for 4 h before a water quench. As established earlier (Georgiev et al., 2003b), As_2S_3 melts when quenched from higher temperatures increasingly nanoscale phase separate into Realgar fragments and a S-rich backbone. FT-Raman profiling measurements confirmed that the As_2S_3 melt/glass so synthesized was homogeneous but also mildly nanoscale phase separated.

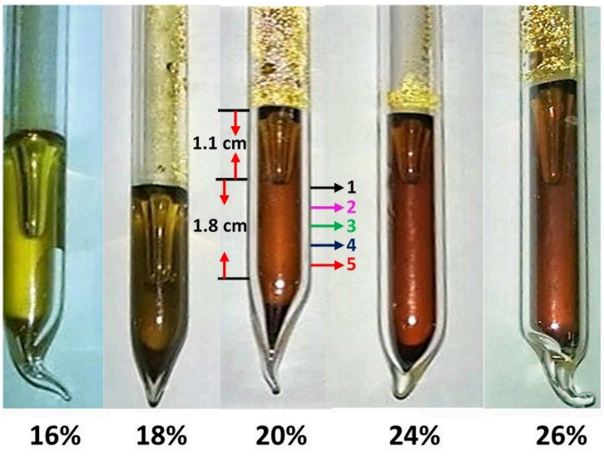

FIGURE 1 | A view of synthesized glasses showing a change of color from a dull yellow at low x (16.0%) transitioning to darker yellow at x = 18%, and to darker orange as x increased to 26.0%. Note that each glass sample displays a meniscus. At x = 20%, we used the 1.8 cm long glass column below the meniscus to acquire *ex-situ* Raman scattering at 5 locations as melts were alloyed. Batch compositions were considered homogeneous when these spectra became identical.

All glass samples synthesized displayed a characteristic color that changed with composition from a lighter yellow (16%) to darker orange (26%) as x increased in the 16% < x < 26% range **(Figure 1)**. Each glass sample displayed a clearly defined meniscus with a glass column below it of about 2 cm in length as illustrated in **Figure 1**, for the glass composition at x = 20%, which was subjected to FT-Raman profiling. The crystalline As_2S_3 specimen used in the present work, and the earlier work of Georgiev, was a gift from Professor Zallen (1974). The c-As_4S_4 specimen used in the present work was synthesized earlier by alloying elemental As with stoichiometric As_2S_3 glass (Georgiev et al., 2003b).

FT-Raman Scattering

A Thermo-Nicolet model 870 FTIR with a Raman module was used to examine the molecular structure of synthesized glasses. Glasses encapsulated in evacuated quartz tube, mounted on an xyz stage of the Raman module, were examined by focusing about 125 mW of the 1,064 nm radiation from a Nd-YAG laser with a 50 micron spot size (the micro-configuration) to excite Raman scattering. Ideally one wants to use the smallest spot size to get a realistic estimate of the glass heterogeneity (Gunasekera et al., 2013). In a typical measurement 200 scans were acquired yielding a 2 cm^{-1} resolution and took typically 15 min of acquisition time. A glass specimen, examined at 5 locations along the length of a melt column, required about 75 min. An InGaAs detector or a Ge detector was used in the measurements. The bandgap of As_xS_{100-x} glasses varies in the 2.3 eV < E_g < 2.8 eV range (Yamaguchi, 1985) across the composition range 0.40 > x > 0.10 of interest studied here. The 1,064 nm (1.16 eV) radiation is transparent to all the glasses examined, and yielded spectra of high signal/noise ratio. To ascertain batch heterogeneity or the lack of it, we found particularly useful to normalize the observed

signals to the vibrational mode with the highest scattering strength, which in our case was either the S_8-ring and -S_n chain mode at low x (<17%), or the broad band centered near 350 cm^{-1} that results from the As-S glass backbone at high x (>17%). The spread in scattering strength of other vibrational modes with sample location, then directly permitted to establish the variance in As content, $<\Delta x>_{As}$ across a 1.5 gram batch composition, and served as a quantitative measure of batch heterogeneity in these Raman profiling experiments (section Experimental Results).

Separately we also used a T64000 Dispersive Raman scattering facility with a microscope attachment. The 514 nm radiation from an Ar-ion laser was used to excite the scattering. Use of the 514 nm excitation in the Dispersive System leads to band-band excitation, and results from these experiments will be compared to the mid-gap excitation ones from the FT-Raman experiments.

Modulated Differential Scanning Calorimetry

A model Q2000 MDSC from TA Instruments Inc, was used to examine the nature of the glass transitions (Thomas, 2005; Bhosle et al., 2012b) in calorimetric measurements. An attractive feature of the method is that both glass and melt properties can be examined using the same glass specimen. For a measurement of T_g and the enthalpy of relaxation of a glass at T_g, the glass transition endotherm is examined in a heating scan and analyzed in terms of reversing- and non-reversing- heat flow components. On the other hand, to establish the fragility index of melts, the T_g exotherm obtained upon cooling a melt across T_g was analyzed in terms of complex C_p formalism as a function of modulation frequency. We illustrate the principle of both methods in the narrative below.

T_g and Enthalpy of Relaxation of Glasses

In DSC one typically examines thermal events, endotherms or exotherms by scanning at a linear T-ramp of 20°C/min. MDSC is an AC calorimetric method in which one superposes a programmed sinusoidal temperature oscillation over a linear T-ramp, and from the resulting modulated heat flow (Thomas, 2005) deduces the component of the heat flow that tracks the T-modulation, also called "reversing heat flow" signal. The difference signal between the heat flow and the reversing heat flow, is labeled as the non-reversing heat flow. That separation uniquely permits one to deduce T_g and the enthalpy of relaxation at T_g. The enthalpy of relaxation at T_g, the ergodicity breaking feature of a glass transition, not only depends on glass composition but also on thermal history, dryness, purity and homogeneity.

Prior to its use, the Q2000 calorimeter system was fully calibrated for T using melting of Indium metal, and the specific heat C_p using a standard sapphire specimen, the cell constant was established and uploaded in the software to undertaking any measurements. The following calibration steps were performed: (i) Baseline calibration—An empty cell is heated through the temperature range required for all our subsequent experiments. The software then automatically applies the required constants to make the baseline flat and zero the heat flow signal. (ii) Cell constant calibration—An Indium standard is heated through its melting transition. The software then automatically calculates the heat of fusion by comparing the calculated value to the theoretical value. The ratio between the two values is dialed in to the software as cell constant. (iii) Temperature calibration—An Indium standard is again heated through its melting transition. The software then automatically extrapolates the onset of recorded melting point of the Indium and compares it to the known melting point. Difference between these two values is used by the instrument as Temperature calibration constant. (iv) Heat capacity signal calibration—A sapphire standard is used here. We run the sapphire under the exact same conditions as our samples. We then calculate the calibration constant with the help of the following equation: Calibration Constant = (Theoretical value/Measured value). The calibration constant is then dialed into the software.

To illustrate a measurement of T_g and the enthalpy of relaxation at T_g, ΔH_{nr}, we show a scan of a $As_{26}S_{74}$ glass in **Figure 2**. About a 10 mg quantity of a glass specimen in a platelet form preferably, was hermetically sealed in T_{zero} Al pans (Thomas, 2005) in an inert ambient and examined in a heating cycle at a scan rate of 3°C/min, and a modulation time period of 100 sec, and a modulation temperature amplitude of 1°C. The heating cycle across T_g was then followed by a cooling cycle as illustrated in **Figure 2**.

The reversing heat flow signal shows **(Figure 2)** a rounded step, permitting one to fix the T_g by recording the inflection point. A T_g of 136.2(2)°C was obtained in the heating cycle, and a T_g of 133.5(2)°C was obtained in the cooling cycle, yielding a mean value of 134.8(3)°C as the scan rate independent

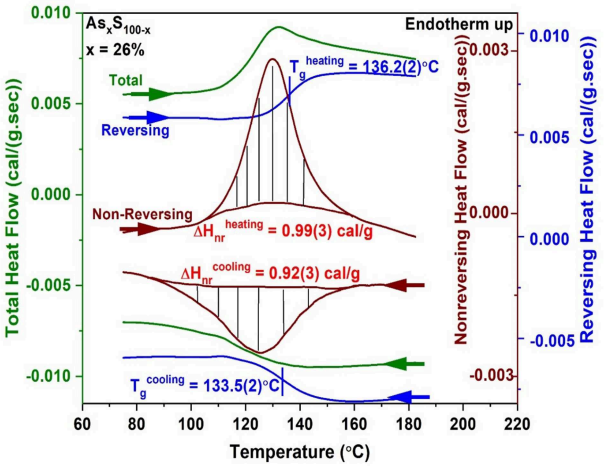

FIGURE 2 | MDSC scan of a $As_{26}S_{74}$ glass showing the heating cycle (top 3 curves) followed by the cooling cycle (bottom 3 curves) across T_g. The total heat flow (green) is deconvoluted into a reversing (blue) and a non-reversing heat flow (brown) signal, with the hashed marked integrated area giving the enthalpy of relaxation in the heating and cooling cycles. The T_g of the glass is taken to be the average value of the inflection point of the reversing heat flow signal in heating and cooling and yields a value of T_g =134.8(3)°C. The frequency corrected enthalpy of relaxation, ΔH_{nr} (Thomas, 2005) is the difference between the endotherm obtained in heating up and the exotherm in cooling down, and yields a value of 0.07(3) cal/gm.

T_g of the $As_{26}S_{78}$ glass. The non-reversing heat flow term shows a Gaussian-like peak in the heating cycle and the hashed marked region yields the enthalpy ΔH_{nr} of 0.99(3) cal/gm. In the cool-down cycle one observes an exotherm with a ΔH_{nr} term of 0.92(3) cal/gm. The frequency corrected ΔH_{nr} term, the difference between the two terms, ΔH_{nr} (heating)—ΔH_{nr} (cooling) yields a value of 0.07(3) cal/gm. There are set procedures to draw baselines as discussed in the manual of the instrument (Thomas, 2005). The baseline function used depends on the observed result, and it could either be a linear variation, or a sigmoidal tangential one or a sigmoidal horizontal one. Calorimetric results on glasses are presented in section Glass Transition Temperature (T_g(x)), Non-reversing Enthalpy of Relaxation (ΔH_{nr}(x)), and Specific Heat Jump (ΔC_p(x)) at T_g.

Fragility Index and Activation Energy for Enthalpic Relaxation Time

As a glass forming melt is cooled to T_g, it's viscosity (η) increases exponentially to reach an astronomically high value of about 10^{12} Pa s. One characterizes the viscous slow down by plotting the Log (η) as a function of T_g/T, and defines the slope m = d(Log (η))/d(T_g/T) as T approaches T_g to be the fragility index, "m." It is widely believed that SiO_2 glass has a fragility index of 20 (Böhmer et al., 1993). Melts characterized by a fragility index m < 20 are thus viewed to be superstrong, while those with m>>20 viewed as fragile. The fragile-strong classification of glassy melts (Williams et al., 1955; Angell, 1991) is thus widely used to characterize dynamics of glass forming melts. The Maxwell relation,

$$\eta = G_\infty \tau \tag{1}$$

connects the viscosity, η to the shear relaxation time τ (Böhmer et al., 1993), where G_∞ is the infinite frequency shear modulus that is independent of T. One thus relates viscosity to the shear relaxation time as,

$$m = \left[\frac{dlog\,(\tau)}{d\mathbf{T}_g/T}\right]_{T\to T_g} \tag{2}$$

When an MDSC instrument is set up to measure the melt fragility index (Carpentier et al., 2003; Thomas, 2005), one examines the glass transition exotherm as a melt is cooled past T_g in terms of a complex specific heat, C_p^*, which is made of an in-phase or real term (C_p^r) and an out-of-phase or imaginary term (C_p^i). The in-phase term displays a rounded step while the out-of-phase term shows a Gaussian-like peak. In these experiments one examines the T_g event as a function of modulation frequency (ω). The peak in C_p^i corresponds to the condition when $\omega\tau = 1$, i.e., the melt completely tracks the impressed T-modulated heat flow signal. Here ω is the modulated frequency and τ the melt enthalpic relaxation time. And as ω is increased the peak in C_p^i shifts to a higher T since the glass must now relax faster (i.e., τ decreases) so that the product $\omega\tau$ remains 1. These observations permit one to establish the variation of τ as a function of T, and thus deduce the fragility index from the slope of such a semilog plot describing enthalpic relaxation.

In **Figure 3,** we illustrate an example of such a measurement for an $As_{26}S_{74}$ melt. The modulation time period t_m was varied in the 80 sec < t_m < 120 sec range. And we find the step in C_p^r steadily shifts to higher T as the modulation frequency $\omega = 2\pi/t_m$ is increased. On the other hand, C_p^i displays a peak that steadily shifts to higher T as ω increases. By establishing the peak location, one establishes the T at which the melt has acquired an enthalpic relaxation time τ. By plotting log of τ as a function of T_g/T one obtains the fragility index as shown in **Figure 3B**.

The activation energy (E_a) for enthalpic relaxation is deduced using equation 3 once m and T_g are established.

$$E_a = m.T_g.\ln\,(10) \tag{3}$$

For our glass at x = 26%, we obtained a fragility index of m = 14.7(8).

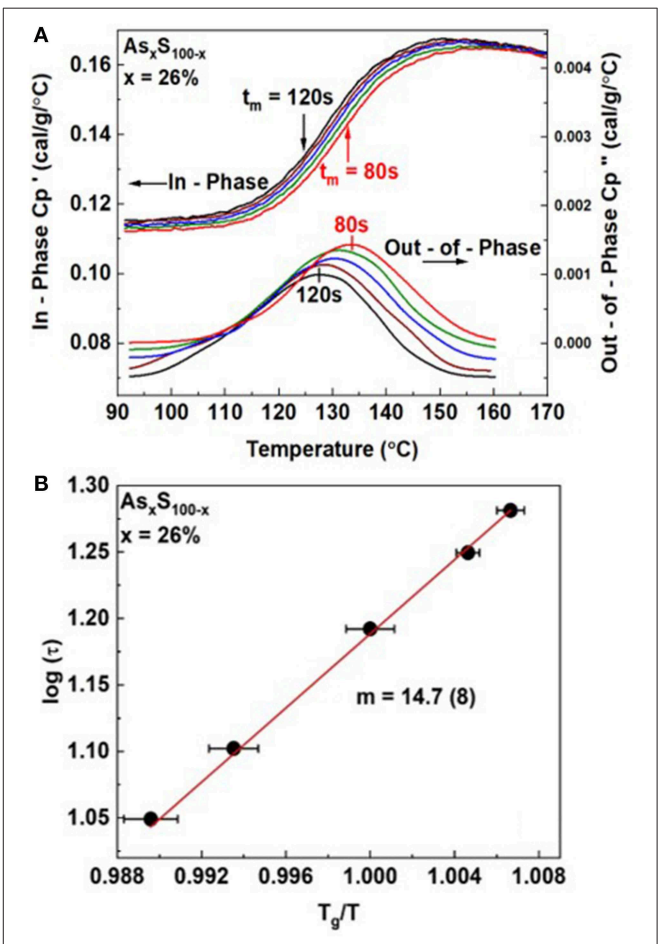

FIGURE 3 | (A) Observed variation in the in-phase C_p^r and out-of phase C_p^i term for an $As_{26}S_{74}$ melt as a function of modulation frequency $\omega = 2\pi/t_m$ showing both terms to shift to higher T as ω is increased. **(B)** By establishing τ from the impressed ω, and measuring the T at which the peak in C_p^i occurs, one establishes the fragility index by plotting log τ against T_g/T to deduce the slope from the semilog Arrhenius plot using equation 2. The deduced value of m = 14.7(8).

Volumetric Measurements

We obtained the mass density "ρ" for our glasses using the Archimedes' Principle by measuring the mass in air and volume by weighing it in a liquid-−200 Proof alcohol in our case. A Model 185 Mettler Toledo digital microbalance with a quartz fiber suspended from the pan with a hook at the bottom to support a sample was used to measure weight in air, followed by weight in the liquid. Typical glass sample size exceeded 125 mg to achieve a 0.25% accuracy in density. Molar volumes "$V_m(x)$" were then obtained from the known molecular weights and measured glass densities. The density of ethyl alcohol was obtained using a Si single crystal wafer of known density (ρ_{Si}) of 2.33 g/cm^3. A Ge single crystal of known density (ρ_{Ge}) 5.323 g/cm^3 was separately used to independently confirm the accuracy of the density measurements. To obtain weight of a glass sample in alcohol, the quartz fiber was submerged in alcohol while being in suspension mode from the digital balance. The balance was then tried to nullify the effect of the buoyant force of alcohol on the fiber (taring) before positioning the glass sample on the quartz fiber hook.

Below we provide typical data on a glass sample permitting V_m to be measured.

Step 1: Measurement of the density of alcohol (ρ_{alc}) using a single crystal Si wafer.

Weight of Si single crystal wafer ($\rho = 2.33$ g/cm^3) in air (W_{Si}^{air}) = 230.2 mg

Weight of Si in alcohol ($W_{Si}^{alcohol}$) = 152.1 mg

$\rho_{alcohol} = [(W_{Si}^{air} - W_{Si}^{alcohol})/W_{Si}^{air}] \times \rho_{Si} = 0.7905$ g/cm^3

The density measurement was repeated four times to check for reproducibility, yielding a mean value of $\rho_{alcohol}$ of 0.7904(2) g/cm^3.

Step 2: Measurement of the density of Ge (ρ_{Ge}).

Weight of Ge in air (W_{Ge}^{air}) = 123.4 mg.

Weight of Ge in alcohol ($W_{Ge}^{alcohol}$) = 105.1 mg;

$\rho_{Ge} = [W_{Ge}^{air}/(W_{Ge}^{air} - W_{Ge}^{alcohol})] \times \rho_{alcohol} = 5.329(5)$ g/cm^3 using the measured density of alcohol of 0.7904(2) g/cm^3; The above measurement was repeated four times and the mean value of ρ_{Ge} was obtained as 5.3295 g/cm^3. This may be compared to the literature value of 5.323 g/cm^3.

Step 3. Calculated density and molar volume of As_xS_{100-x} glass at x = 26%;

W^{air} = 142.4 mg, $W^{alcohol}$ = 103.3 mg, Density of glass sample, $W^{air}/(W^{air} - W^{alcohol}) \times 0.7904(2) = 2.739(4)$ g/cm^3.

Molar volume of the glass specimen V_m = Molecular weight of glass sample/ρ_{sample} = 43.204/2.739 = 15.776(25) cm^3/mol.

EXPERIMENTAL RESULTS

Kinetics of Melt/Glass Homogenization

We have established the kinetics of As_xS_{100-x} melt/glass homogenization across a wide range of compositions, 12% < x < 33%, using FT-Raman profiling experiments (Bhosle et al., 2011). Two broad domains of behavior emerge. At low x, 12% < x < 20%, the kinetics are rather slow and required alloying the 1.5 gram batches at 650°C for about 6 weeks to fully homogenize. At higher x, in the 20% < x < 33% range particularly, the kinetics are faster, and melts/glasses homogenize in about 4 weeks. Broadly, there are several impediments in homogenizing S-rich melts. Elemental S melts at 115.2°C, and acquires a vapor pressure of 1 Atmosphere at 444°C, which increases to 10 atmospheres near 640°C (Lide et al., 2005). Furthermore, Sulfur undergoes a polymerization transition, T_λ transition (Tobolsky and Eisenberg, 1959) near 150°C, with S_8 monomers prevailing at $T < T_\lambda$, slowly opening up and transforming into polymeric S_n chains at $T > T_\lambda$ (Kalampounias et al., 2003), leading to a pronounced increase in viscosity (Tobolsky and Eisenberg, 1959). The presence of the S_8-rich nano-phase acts as a barrier to the growth of the As-S glass backbone, a feature that we believe qualitatively slows down the growth of the As-S backbone, as we demonstrate below using the FT-Raman profiling experiments.

Case 1: S_8-rich As_xS_{100-x} Melts in the 10% < x < 20% Range

In **Figure 4**, we reproduce FT-Raman profiling results of an $As_{18}S_{82}$ melt that was slowly heated at 1°C/min to 650°C in quartz tube held vertically in a box furnace. As the glass was alloyed for t_r = 5d, Raman profiling experiments revealed the variance in S content, $<\Delta(1\text{-}x)>_S$ across the batch to be nearly 5% **(Figure 4A)**. In these experiments, glass heterogeneity is established by taking the scattering strength ratio of the S-rich modes (S_8 + S_n) near 470 cm^{-1} to the broad band centered near 350 cm^{-1} providing a measure of As in the As-S glass backbone. The scattering strength ratio of these modes yields a measure of the S to As content of the melt locally where the laser beam scatters off the vertical glass column in an evacuated quartz tube. And as melt is alloyed longer, the variance in S content, $<\Delta(1\text{-}x)>_S$ steadily decreases to become <0.4% after t_r = 40d. We view this process as due to As diffusing up and S diffusing down the melt column. But even after 40 days of alloying substantial amounts of Sulfur still remained segregated as S_8 rings (features labeled in the spectra). Next we heated the glass to 95°C and held it there for 2 days, and upon Raman profiling such a glass **(Figure 4E),** observed unmistakable evidence of a mode near 537 cm^{-1}, which we believe represents the As=S stretch mode of $S = As(S_{1/2})_3$ quasi-tetrahedral **(Table 1)**. Here we note that the T = 95°C exceeds the T_g (=85°C) of the glass but is less than the T_λ (=159°C) transition of pure Sulfur. In this key heating step the As-S bearing glass backbone softens and flows across the S_8-rich nanophase permitting backbone fragments to coalesce and grow in size. The S_8-rich nanophase remains largely intact at 95°C. In the final step, the glass is taken to 650°C and kept there for 2 additional days and then water quenched. Raman results now provide **(Figure 4F)** clear evidence for a substantial growth of the 537 cm^{-1} mode. Also noteworthy in the spectra of **Figure 4F** is that the scattering strength of the S_8 ring modes has now substantially decreased in relation to the one in spectrum of **Figure 4E**. By heating the glass to 650°C in the final step, a significant fraction of Sulfur apparently alloys in the enlarged As-S backbone, but as we comment later, it also appears that some part of S_n chains decouple from the backbone. These S_n fragments would have to be small, i.e., with $n < 8$, for them not to be part of the S_8 rich nanophase. Closely parallel results are observed at other compositions in the 12% < x < 22%

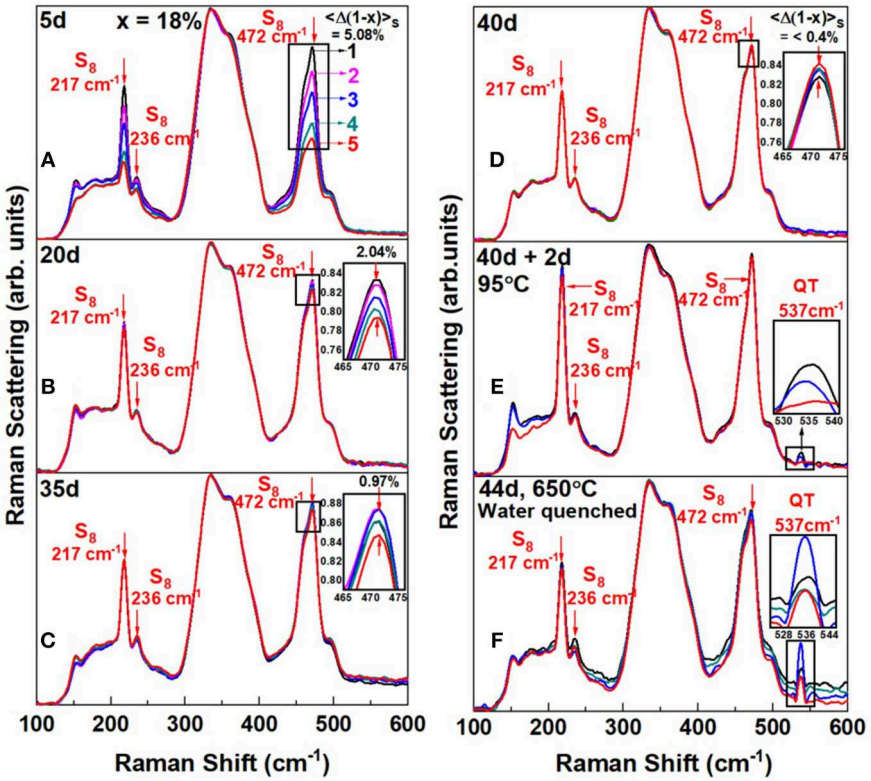

FIGURE 4 | FT—Raman scattering of an $As_{18}S_{82}$ glass alloyed **(A)** for t_r = 5d, displays a Sulfur—variance $<\Delta(1-x)>_S = 5.08\%$, **(B)** for t_r = 20d, that variance decreases to 2.04(5)%, **(C)** for t_r = 20d, it decreases further to 0.97(5)% **(D)** and for t_r = 40d nearly saturates to 0.40(5)%. The reduced Sulfur variance across the 1.5 gram batch composition is taken as evidence of glass homogenizing upon continued alloying. In **(D)**, the homogenized melt/glass upon a thermal quench from 650°C displays a segregated backbone immersed in a sea of S_8–rich fragments. In **(E)** heating the glass at $T_g + 10°C = 95°C$ for 2d, results in fragments of the backbone coalescing, and the observation of the 537 cm^{-1} mode of QT units. In **(F)** by taking the glass of **(E)** to 650°C for 2 days and water quenching it, leads to a precipitous growth of the 537 cm^{-1} mode, and substantial amount of additional Sulfur alloying in the backbone inferred from the qualitative reduction of the S_8 ring—fraction between spectrum **(E,F)**. A schematic representation of the structural changes that underlie in going from **(D)** to **(F)** is shown in **Figure 5**.

range with rather striking evidence of growth of the 537 cm^{-1} mode (see **Supplementary Information**). The slow kinetics of homogenization particularly in the S-rich glasses, x < 18%, is apparently controlled by the segregated S_8-rich nanophase, which inhibits growth of the As-S backbone. The S_8-rich nanophase is easily detected in calorimetric measurements by the T_λ transition (Chen et al., 2008) as we comment later in section Glass Transition Temperature ($T_g(x)$), Non-reversing Enthalpy of Relaxation ($\Delta H_{nr}(x)$), and Specific Heat Jump ($\Delta C_p(x)$) at T_g.

To illustrate the molecular structure consequences of the Raman results of **Figure 4D** through **Figure 4F**, in a schematic fashion, consider **Figure 5**. In step (i) of **Figure 5**, we view the melt to be composed of the As-S backbone fragments, shown as small brown circles, that are connected by the yellow strands that represent polymeric S_n chains when the melt is alloyed at 650°C for 40d, as the glass weighed at x = 18% homogenizes **(Figure 4D)**. A water quench of the homogenized melts, results in the long S_n polymeric chains to break up into the more stable S_8 rings that come together to form an amorphous phase shown as yellow circles in step (ii) of **Figure 5**. Upon heating the glass sample at 95°C for 2d (step (iii) of **Figure 5**), the small brown backbone fragments coalesce to form the larger sized brown rectangular objects. In step (iv) of **Figure 5**, the glass is taken backup to 650°C, the S_8 rings polymerize and assist in growth of the glass backbone (brown rectangular objects). In the final step (v) of **Figure 5**, the melt is water quenched with larger sized backbone fragments forming and being intermixed with the S_8 ring amorphous phase (yellow circles) when in Raman

TABLE 1 | Raman and IR vibrational modes of As-S clusters.

		I^{Ram}				
Cluster	**ω (cm-1)**	**IR**	**Iso**	**Total**	***p***	**Description**
AsS_3H_3	165	0.18	5.0	7.28	0.23	Umbrella
	352	0.18	31.3	34.0	0.06	Symmetric stretch
	355	0.78	0.00	6.63	0.75	Asymmetric stretch
AsS_4H_3	146	0.20	1.10	4.48	0.57	Umbrella
	335	0.21	59.5	60.7	0.01	Symmetric stretch
	365	1.17	0.00	14.3	0.75	Asymmetric stretch
	537	1.58	12.1	21.9	0.34	S = As

The frequencies and Raman/IR cross sections and depolarization ratios for each cluster are given, along with a description of the eigenvectors.

scattering **(Figure 4F)** we find unambiguous evidence of the 537 cm^{-1} mode tied to the growth of the QT local structures in the As-S backbone.

In **Figure 6**, we provide a summary of the homogenization process in a plot of the scattering strength ratio of the Sulfur-band (S_n chains + S_8 rings) near 470 cm^{-1} to the As-related broad band centered near 350 cm^{-1} **(Figure 5)** as a function of the weighed As mole% x. The broad band comprises (Kalampounias et al., 2003) vibrational modes of the glass containing As-Pyramids and As- Quasi-tetrahedra. The red data points in **Figure 6** define an empirical curve made possible by results on the fully homogenized glasses synthesized in the present work. On this empirical curve we then project the observed extremum in scattering strength ratios from the Raman profiling experiments (insets of **Figures 4A–E**) to deduce the S-content variance, $<\Delta(1\text{-}x)>_S$ of a batch composition. This has permitted us to establish the variance $<\Delta(1\text{-}x)>_S$ of a batch composition in real time, t_r, in days, as homogenization of the alloyed melt proceeds. We emphasize that the measured variance is across the whole batch composition, and it is not at a local point in the melt/glass column as one would measure once the glass is extracted from the quartz tube and used in a traditional Raman scattering experiment. In a batch composition, changes in glass stoichiometry at one location will influence the global stoichiometry of the batch as a whole. These Raman profiling experiments thus measure the global homogeneity of a batch composition and not merely homogeneity at a local point in a glass specimen.

Our profiling experiments also show that in S-rich glasses ($x < 20\%$), where a substantial amount of S segregates as S_8 rings, the typical alloying time to achieve homogeneity of the melts is nearly 6 weeks. The variance in S content of a S-rich glass starts out usually near 5% after 5d of alloying, and it decreases by an order of magnitude to <½% after 40 days, when the melt/glass is considered to be homogeneous.

Case II: S_8-deficient As_xS_{100-x} Melts in the 20% < x < 33% Range

The second case of interest occurs at higher As content **(Figure 7)**, when the S_8-ring fraction is minimal. Such glass compositions now homogenize relatively quicker, i.e., after alloying at 650°C for only $t_r = 24d$, as illustrated for a glass at $x = 26\%$ shown in **Figure 7**. At this composition we observe the 537 cm^{-1} mode of QT units once the glass has homogenized. After 4d of alloying the Sulfur-variance of the batch is near 5%. **(Figure 7A)**, it decreases to 1% after 12d **(Figure 7B)**, and it decreases to 0.1% after 24d **(Figure 7D)** when the batch composition has homogenized. The homogenization kinetics documented at $x = 26\%$, is typical of many other glass compositions in the $20\% < x < 33\%$ range, i.e., compositions encompassing the Intermediate Phase and the Stressed-rigid Phase. Nevertheless, in the present case, as in the case of the $x = 26\%$ glass, upon heating the glass to $T_g+10°C = 144°C$ for 2d, one observes clear evidence of the 537 cm^{-1} mode **(Figure 7E)** for the first time. By heating the glass further to 650°C for 2 days followed by a water quench, the scattering strength of the 537 cm^{-1} mode increases **(Figure 7F)** substantially and that of the S_8 ring mode near 217 cm^{-1} decreases.

The variance in S-content across a 1.5 gram sized batch composition, in the initial stages of alloying, derives from the heavier (lighter) As (S) atoms moving to the lower (upper) part of the glass column. The compositional gradient is most helpful in tracking the growth of homogeneity by merely probing <1% of the glass column. If one had rocked the melts, it would have been challenging to completely track the super-strong melt inclusions in a sea of fragile ones without probing more than 50% of the batch composition, and that would have been a formidable task to implement. In a previous study (Chen et al., 2008) of As-S glasses, melts were typically alloyed at 600 to 650°C for 2 to 3 days. We became aware that chalcogenide melts undergo delayed homogenization starting in 2011 (Bhosle et al., 2011; Gunasekera et al., 2013; Chakraborty and Boolchand, 2014). And as we present results from the present work, we shall discuss the present findings in relation to the previous ones bringing out the crucial role of homogenization in elucidating the physics and chemistry of these glasses. Once the physics of homogenization is established, one can always design procedures to expedite homogenization of larger batches over several days rather than several weeks.

Raman Scattering on As_xS_{100-x} Glasses

FT-Raman scattering on the especially homogenized bulk As_xS_{100-x} glasses were acquired using a Thermo-Nicolet Nexus 870 FTIR with Raman module. The observed lineshapes as function of glass composition are summarized in **Figure 8**. In the top panel **(Figure 8A)** we include Raman scattering of the two reference crystalline phases of interest (Georgiev et al., 2003b); c-As_2S_3 and c-As_4S_4. In the middle panel we present Raman spectra of As_xS_{100-x} glasses in the high As content range, $40\% > x > 24\%$ **(Figure 8B)**, while in the bottom panel spectra of glasses in the low As-content range, $20\% < x < 12\%$ **(Figure 8C)**.

Raman Scattering in As_xS_{100-x} Glasses in the High As Range 24% < x < 40%

In glass science one has often been tempted to draw analogies between the Raman spectrum of the stoichiometric glass with its crystalline counterpart. The case of the stoichiometric glass at $x = 40\%$ and c-As_2S_3 (orpiment) is no exception (Ward, 1968), since both are viewed as composed predominantly of a polymeric network of PYR units. But there are glaring differences as well. The stoichiometric glass is actually NSPS into As-rich As_4S_4 Realgar units that decouple from the S-rich polymeric network composed of PYR units in which a finite concentration of S-S bonds persist (Phillips et al., 1980; Zitkovsky and Boolchand, 1987). Furthermore, the degree of segregation of As_2S_3 glass is intimately tied to the melt quench temperature (T_q), with the segregation (Georgiev et al., 2003b) increasing as $T_q > T_{liquidus}$. The evidence of segregation is unmistakable in Raman spectrum of **Figure 8B**, as the triad of modes near 188, and 220 and 352 cm^{-1} labeled R in the stoichiometric glass **(Figure 8B)**, appears at nearly the same frequency (within 2 cm^{-1}) as their counterparts in c-As_4S_4 (Realgar) **(Figure 8A)**. This is as one expects, given

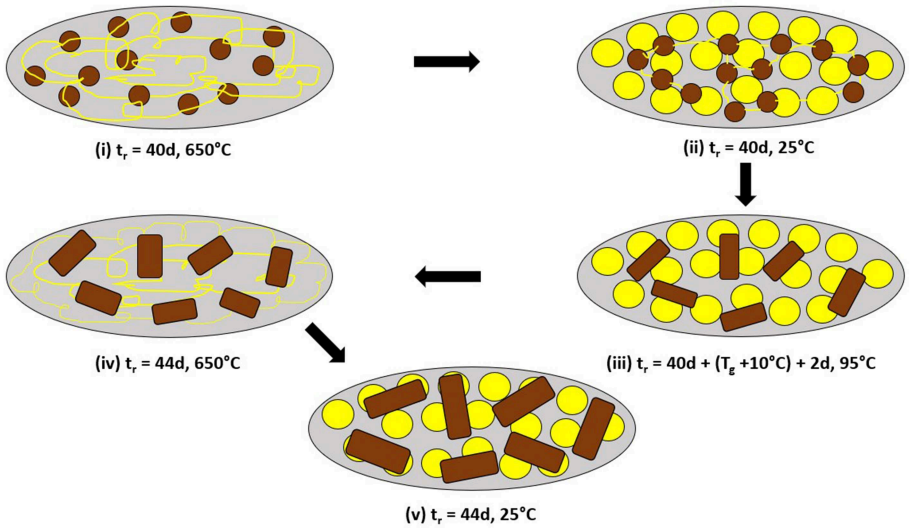

FIGURE 5 | Schematic representation of structural changes underlying the coalescing of backbone fragments (from small brown circles to larger rectangles), and leading to the observation of the 537 cm^{-1} mode in $As_{18}S_{82}$ glass as shown by the Raman scattering results of **Figures 4D–F**. In **(i)** after 40d of alloying at 650°C, the melt is viewed to be composed of $As_{18}S_{82}$–rich circular domains immersed in a sea of polymeric S_n chains (thin yellow lines). **(ii)** After a water quench, the S_n–rich chain regions transform into the more stable S_8 rings, largely decoupled from the glassy backbone. **(iii)** Heating the quenched glass to 95°C for 2d, results in softening and diffusion of the backbone fragments to coalesce and form the larger rectangular domains. **(iv)** Heating the glass to 650°C leads more S_n chains to be alloyed in the backbone, and finally **(v)** Upon a water quench to 25°C leads to their growth. Confirmation is given by Raman scattering that shows the S_8–ring fraction to qualitatively decrease in going from **Figure 4E** → **4F**.

that Realgar is composed of molecular cages composed of 8-atom clusters (Bonazzi et al., 1995) with strong intramolecular interactions mediated by covalent bonds, but weaker inter-cluster ones deriving from non-bonding van der Walls interactions.

A close examination of the Raman lineshape of the stoichiometric glass also reveals a quartet of modes (Georgiev et al., 2003b) labeled O **(Figure 8B)** that are found in c-As_2S_3 but with a notable difference. The modes in the glass are blue shifted by about 14 to 21 cm^{-1} in relation to those of c-As_2S_3 **(Figure 8A)**. This is illustrated by the vertical broken black lines passing through the glass modes, which are found to be systematically shifted to a higher frequency in relation to the quartet of modes in the crystal (see arrows in **Figure 8A**). The blue shift of modes in the glass is viewed to be the consequence (Georgiev et al., 2003b) of the greater molar volume, V_m (15.4 cm^3) of the glass than the crystal V_m (14.10 cm^3) (Robie and Bethke, 1962). The more open structure of the glass promotes intra-molecular interactions due to σ-bonds in PYR and QT local structures at the expense of the intermolecular ones mediated by π-bonds between these local structures.

The range of intermediate range glass compositions in the 24% $< x <$ 35% poses challenges in Raman lineshape deconvolution as we comment in the next section.

Raman Scattering in As_xS_{100-x} Glasses in the Low As Range, 12% < x < 20%

Raman scattering of As-deficient glasses in the 12% $< x <$ 20% range display lineshapes **(Figure 8B)** that reveal the triad of QT modes; QT_1 = 335 cm^{-1}, QT_2 = 390 cm^{-1}, and QT_3 = 537 cm^{-1}, and a pair of closely spaced modes of PYR units (352, 355 cm^{-1}) in the broad band centered near 340 cm^{-1} as illustrated in **Figure 9** for compositions at x = 12, 17, and 18% (see **Supplementary Information**).

All the observed lineshapes **(Figure 9)** at x of 18% or less, were least squares fit to a superposition of Voight profiles, and the observed mode frequencies of the two local structures are found, indeed, quite close to those deduced by the NRLMOL code **(Table 1)**. Even the observed Integrated intensity of the various modes **(Figure 9)** are in reasonable accord with the projected Raman cross-sections of the various modes by the NRLMOL code.

The main band centered near 350 cm^{-1} has contributions from the symmetric stretch (ss), and asymmetric stretch (as) of QT and PYR units. The band near 472 cm^{-1} has contributions from S_n chains and S_8 rings, while the highest frequency mode is the S = As stretch mode of QT units. Least squares fit of the lineshape used the Peakfit software from SPSS Inc. In addition, we observe a mode near 490 cm^{-1}, labeled D in the spectra (**Figures 8C**, **9**), which is observed over a wide range (12% $< x <$ 37%) of As content. The mode is consistent with a stretch vibration of S-S dimers between AsS_3 pyramids, as suggested by the mode scattering strength variation in our Raman lineshapes, which display a global maximum near x = 25% (see **Supplementary Information**). The other modes observed include S_8 ring modes (217 cm^{-1}, 472cm^{-1}) and S_n chain mode (461 cm^{-1}) over a wide range of x, the elusive mode near 537 cm^{-1} from the QT, S = $As(S_{1/2})_3$ local structure, labeled as QT_3. This mode is, indeed, observed in these homogeneous glasses in the 12% $< x <$ 26% range.

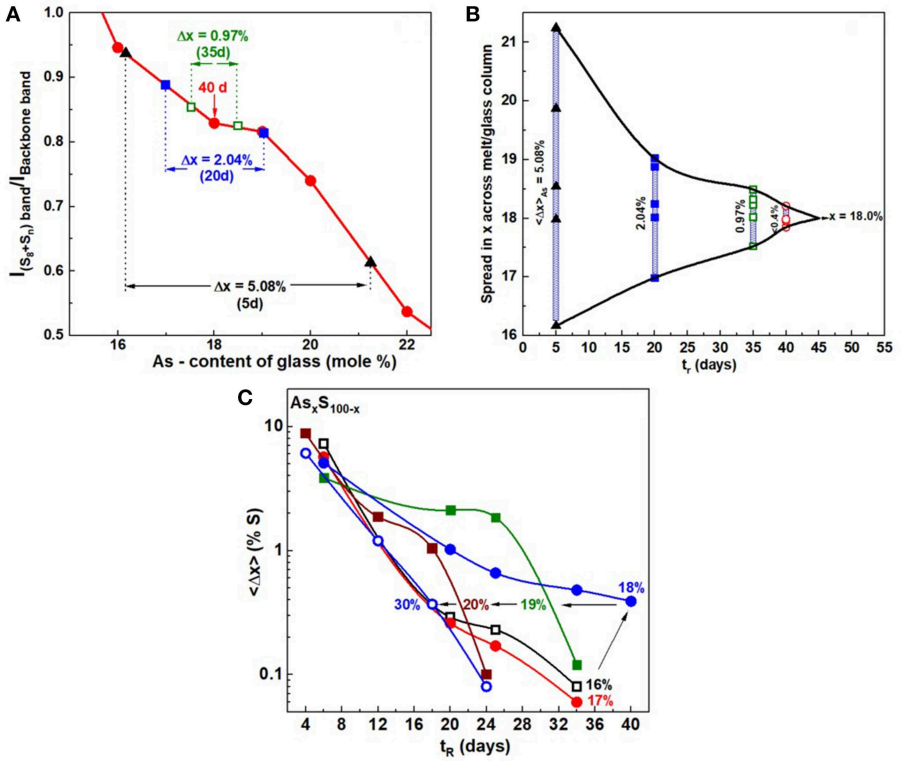

FIGURE 6 | (A) Observed variation in the ratio of the scattering strength of S—related band near 472 cm^{-1} to the backbone band near 340 cm^{-1} plotted against the As content of glasses. The red data points are results obtained on fully homogenized glasses from x = 16% to x = 22%, with the smooth red curve serving as an empirical curve. Superposed on the calibration plot are the results obtained for a glass sample weighed at x = 18% as it was alloyed from 5 to 40d, and the variance in S—concentration to narrow from 5.08% to about 0.4%. In **(B)** the narrowing data of the S—variance, taken to be the same as the As—variance, is plotted as a function of alloying time, t_r, in days for $As_{18}S_{82}$ glass. It provides a pictorial view of the manner in which the weighed glass at x = 18% undergoes delayed homogenization. In **(C)** we provide a global view how the S-variance of the batches decreases with alloying time t_r in days at different As content x. Note that at x = 18%, the kinetics are slowest, and these decrease both at low x (< 18%) and high x (>18%). The x = 18% composition also is the one where the QT fraction is the highest. See **Supplementary Information**.

At lower As content (x < 15%), as the S-content of the glasses increases and the content of the S_8 nanophase grows, formation of the polymeric As-S backbone becomes a challenge as we noted earlier in homogenization studies in section Kinetics of Melt/Glass Homogenization. By a low-T anneal of the homogenized glasses, at $T_g + 10°C$, we could observe the high frequency QT mode even at x = 12% (**Figures 8**, **9**).

In the transition range, 22% <x < 35%, spanning the Intermediate phase and the Stressed-rigid phases of the present As-S binary, evolution of the Raman spectra poses challenges to uniquely deconvolute. This is the case because as the QT local structures deplete and the PYR units grow, one finds that orpiment-like structures must evolve giving rise to the quartet of O-modes, whose frequency closely overlaps with those of the QT local structures formed at low x. In **Figure 8B**, we illustrate the challenge by drawing a continuous red line coming from the PYR mode observed at low x (<20%), to the quartet of O-modes expected at higher As content. Since as many as 7 vibrational modes of the O-species and QT_n-species occur and have overlapping mode frequencies, clearly one can only obtain fits to the spectra of the glasses by imposing several constraints on mode centroids and widths. The procedure raises the obvious questions on the uniqueness of the fitting process.

Dispersive and FT Raman Scattering in As_xS_{100-x} Glass Compared

We have also examined As-S glasses in Dispersive Raman scattering using 514 nm excitation using a T64000 Micro-Raman system from Horiba Inc. As an illustration we show in **Figure 10** spectrum of a $As_{18}S_{82}$ bulk glass examined in FT-Raman scattering excited using 1,064 nm excitation **(Figure 10A)**, and separately in Dispersive Raman **(Figure 10B)**. There are several features common to both spectra including the S_8-ring modes near 151, 217, and 472 cm^{-1}, the As-S backbone band centered near 340 cm^{-1} and the polymeric S_n chain mode near 461 cm^{-1}. But there is also a glaring difference; the 537 cm^{-1} mode is observed in FT-Raman spectrum **Figure 10A** but not in Dispersive Raman spectrum **Figure 10B**.

These results lead us to believe that the electronic states contributing to the QT local structure are most likely resonantly excited in the mid-gap region by the 1,064 nm excitation. The QT are qualitatively suppressed in Dispersive Raman

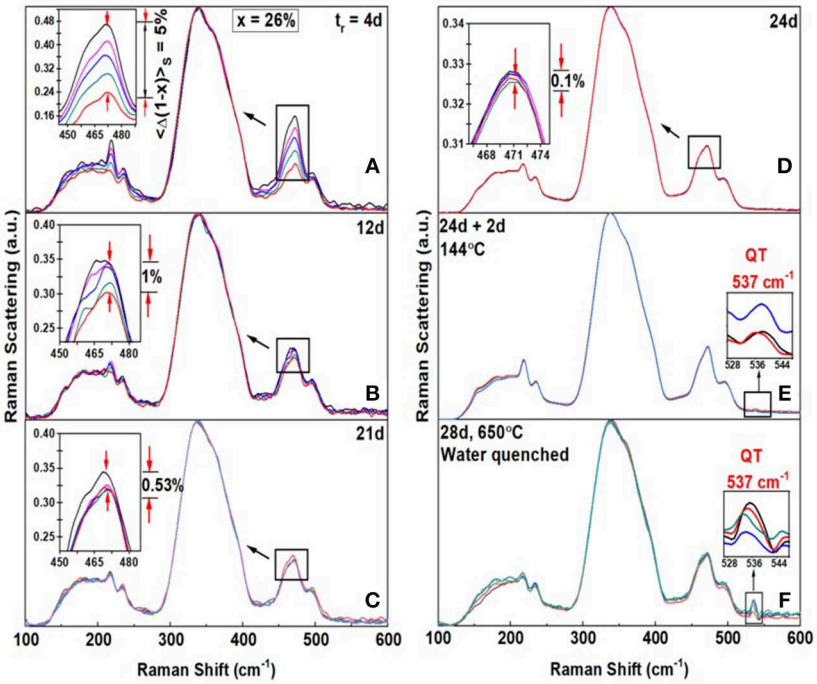

FIGURE 7 | FT—Raman profiling results of an As_xS_{100-x} glass at x = 26% revealing the Sulfur variance $<\Delta(1\text{-}x)>_S$ **(A)** to be 5% after alloying for t_r = 4d **(B)** the variance ∼ 1% after t_r = 12d, **(C)** the variance = 0.53% after 12d **(D)** the variance = 0.1% after t_r = 24d. **(E)** When the glass is heated to 144°C = T_g + 10°C for 2d, evidence of the 537 cm^{-1} mode first appears. **(F)** When glass was next heated to 650°C for 2d and water quenched, the scattering strength of the 537 cm^{-1} mode increased substantially. These changes in Raman lineshapes in going from step **(E)** to **(F)**, closely mimic those seen at x = 18% in **Figure 4**. In particular note that the 217 cm^{-1} mode of S_8 rings decreases in scattering strength in going from **(E)** to **(F)**. These changes in Raman scattering at x = 18% and at x = 26%, particularly the growth of the 537 cm^{-1} upon T_g cycling the glass followed by a heating step to 650°C and a water quench, reinforce the schematic structural changes suggested in the model of **Figure 5**.

making use of the near band gap excitation as schematically illustrated in **Figure 10C**, on a plot of the optical band gap of As_xS_{100-x} glasses reported by Yamaguchi (Yamaguchi, 1985). The pattern is not unique to the glass composition at x = 18%, but is observed at other compositions at x < 24%., Dispersive Raman scattering on As-S glasses have also been reported by Golovchak et al. (2010) and Bychkov et al. (2006). Also see **Supplementary Material**.

Glass Transition Temperature (T_g(x)), Non-reversing Enthalpy of Relaxation (ΔH_{nr}(x)), and Specific Heat Jump (ΔC_p(x)) at T_g

The compositional trends in calorimetric observables such as glass transition temperature, T_g(x), enthalpy of relaxation ΔH_{nr}(x) at T_g, and the specific heat jump at T_g ΔC_p(x), in As_xS_{100-x} glasses deduced from Modulated DSC experiments on the present glasses are summarized in **Figure 11**. Also included in **Figure 11** is the observed variation of Molar volumes (V_m(x)) in glasses. Taken together, both the Calorimetric and Volumetric results provide a global view of the three distinct regimes of variation. At low x (<22%), one observes two endotherms; one near T = 150°C that shifts minimally in T with increasing x, but with an enthalpy of relaxation that steadily decreases with increasing x to vanish near x > 22% (not shown in **Figure 11**). On the other hand, the second endotherm is found to steadily upshift in T almost quasi-linearly with increasing x in the 15% < x < 40% range. These T_g(x) trends **(Figure 11A)** are similar to those reported by Wagner et al. (1998), who were one of the first to employ MDSC to examine As-S glasses. In their work, Wagner et al. identified the endotherm near 150°C as a second glass transition, and viewed the bimodal T_g's observed at x < 25% as evidence of phase separation of these S-rich glasses. In a subsequent study (Chen et al., 2008), examined many more compositions and recognized that the 150°C endotherm is actually the T_λ transition, i.e., presence of S-rich domains composed of S_8 rings that polymerize into S_n chains as T exceeds T_λ, in these S-rich binary As-S glasses. They noted that the T_λ transition, well-established in pure S and is observed near the same temperature of about 150°C.

The nature of the second endotherm observed in As-S glasses became transparent when more detailed compositional trends became available (Chen et al., 2008), and showed a quasi-linear increase of T_g(x) with x **(Figure 11A)** over a wide composition range 10% < x < 40% to represent the glass transition characterizing the As-S network backbone. The enthalpy of relaxation, ΔH_{nr}(x), of the endotherm, one found, displays a rather sharply defined square-well like variation in

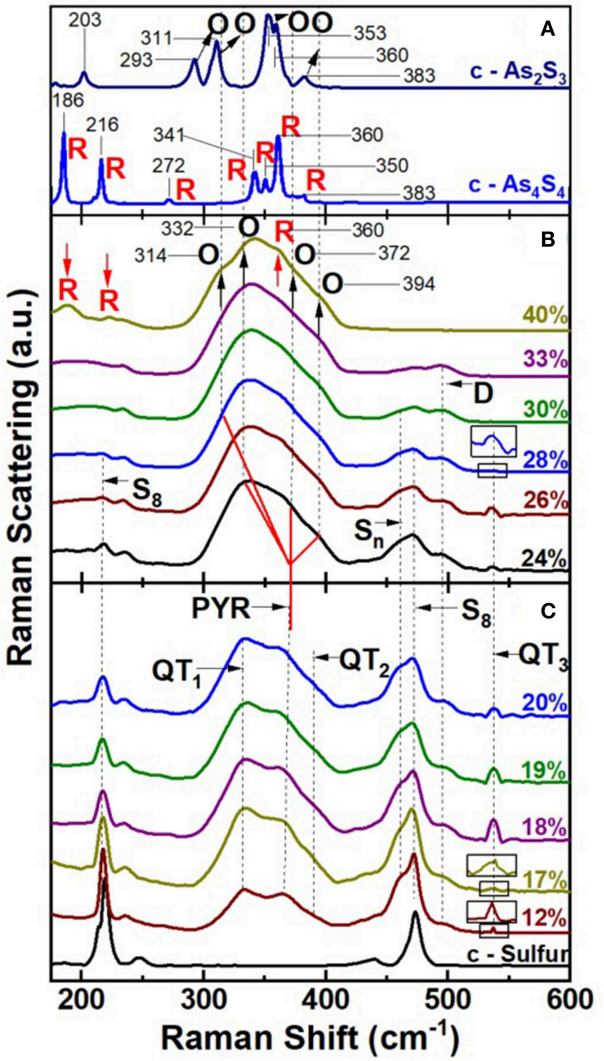

FIGURE 8 | FT Raman results on **(A)** c-As_2S_3 (Orpiment) and c-As_4S_4 (Realgar), **(B)** As_xS_{100-x} bulk glasses at high As content in the 40% < x < 24% range, and in **(C)** at low As content in the range 20% < x < 12% and of crystalline—Sulfur. In **(C)** we observe the three expected modes of QT $S = As(S_{1/2})_3$ local structures labeled QT_1, QT_2, and QT_3, and the modes of PYR $As(S_{1/2})_3$ local structure labeled PYR. These modes occur at frequencies close to those predicted by NRLMOL calculations **(Table 1)**. In **(B)** at x = 40%, the four observed modes labeled O with indicated mode frequencies in cm^{-1} are due to Orpiment—like features, and are systematically blue shifted wrt to the O-modes in c-As_2S_3 in **(A)** by about 14 to 21 cm^{-1}. The stoichiometric glass (x = 40%) also displays 3 modes labeled R that occur at frequencies reasonably close to those observed in c-As_4S_4 as in **(A)**. Feature D near 490 cm^{-1} is observed over a wide range of x, 12% < x < 33%. The observation of R modes in the x = 40% glass shows the stoichiometric glass is mildly NSPS as noted earlier by Georgiev et al. (2003b). In **(B)** modes of QT species steadily go over into those of O—species as x increases from 24 to 40%. Modes of polymeric S_n chains (461 cm^{-1}), and of monomeric S_8 species (217 cm^{-1}, 472 cm^{-1}) are observed as expected. See text.

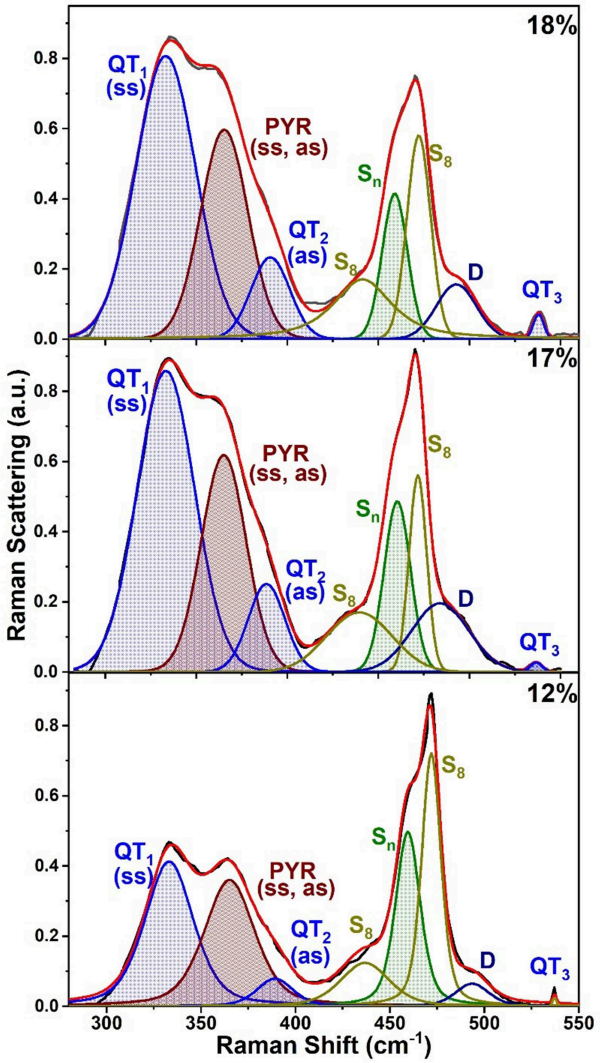

FIGURE 9 | Observed FT Raman scattering in As_xS_{100-x} glasses at low x (< 18%) deconvoluted in terms of a superposition of requisite number of Voight profiles as illustrated in the plots. See text and **Table 1** for the mode assignments.

the composition range, 22.5% < x < 28.5% (Chen et al., 2008). In the present work we confirm the findings of Chen et al., and in addition, now show that in homogenized glasses, the square-well variation of $\Delta H_{nr}(x)$, also known as the reversibility window is observed even in fresh glasses as well as 6-month aged ones **(Figure 11B)**. Reversibility windows have now been widely observed in many glass systems including chalcogenides and oxides (Mantisi et al., 2015; Boolchand and Goodman, 2017). These windows represent signature of the isostatically rigid phases also known as the Intermediate Phases (Boolchand et al., 2001). The abrupt nature of the onset of the window near $x = x_r = 22.5\%$ represents the rigidity transition, and the end of the window near $x = x_s = 28.5\%$ as the onset of the stress-transition (Chen et al., 2008). These two elastic phase transitions in the present As-S binary glasses are found to be particularly abrupt in composition "x" in the present glasses, due to the especially homogenized nature of glasses synthesized as will be discussed later in section Discussion.

Variation of Melt Fragility Index With Glass Composition

One cannot overemphasize the tremendous resource MDSC provides in measuring T_g and $\Delta H_{nr}(x)$ of a glass, and also to establish the fragility index, m(x), from the activation energy E_a of the enthalpy relaxation time of melts using the same glass specimen. The methodology to measure melt fragility index using MDSC was described earlier in section Modulated Differential Scanning Calorimetry. Fragility index are established in viscosity, or flexure, measurements that generally require much larger glass samples than those used in measuring T_g and enthalpy of relaxation using DSC or MDSC. That consideration also raises issues concerning sample homogeneity that is more easily achieved in smaller batch sizes (2 grams or less) than in larger (20 grams or more) ones.

The observed variation in the fragility index, m(x), of As_xS_{100-x} melts reveal a Gaussian-like minimum centered around the reversibility window (blue panel), with $m < 20$ in the window and acquiring values of $m > 20$ outside the window. In **Figure 12A**, we include the fragility index "m" of As_2S_3 glass measured in Dilatometric studies reported by Málek (1997). In **Figure 12A** we also show with a broken line the fragility index of SiO_2 glass near $m = 20$. The super-strong character of melts, i.e., $m < 20$, in the blue panel, defines the fragility window, which coincides with the reversibility window in glass composition "x," and we shall discuss these results in section Discussion. Given the measured m(x), we have projected the expected melt viscosity variation with x using the MYEGA formalism (Mauro et al., 2009), and these results **(Figure 12A)** show that near $x = 25\%$, melt viscosity far exceeds those at $x = 15\%$ or at $x = 35\%$ by nearly 2 orders of magnitudes. The activation energy for enthalpy relaxation $E_a(x)$ deduced from the fragility index results and the inverse of $E_a(x)$ are plotted in **Figures 12B,C**, respectively. Our Raman profiling experiments **(Figures 6, 7)** provide ample evidence that the 1.50 gram sized As_xS_{100-x} melts, in the present work, take several weeks rather than several days to homogenize. That feature of glass forming melts has been noted earlier (Gunasekera et al., 2013; Mohanty, 2018; Chbeir et al., 2019) in other glass systems as well, and is responsible for the delayed homogenization of glass forming melts that encompass a fragility window in general.

Variation of Molar Volumes With Glass Composition

The density of glasses were measured using Archimedes method (section Volumetric Measurements), which permitted one to extract trends in the variation of molar volumes, $V_m(x)$ with x. These compositional trends in $V_m(x)$, for the especially homogenized bulk glasses **(Figure 11D)**, are compared to those reported by Chen et al. (2008) in an earlier investigation of the present binary. In addition, we have summarized $V_m(x)$ results from previous reports (Sundaram et al., 2011) on binary As_xS_{100-x} glasses in **Figure 11D**. These results when taken together reveal a broad pattern; the reported $V_m(x)$ results at x>30% vary significantly between different reports highlighting the challenges in synthesizing reproducible glasses.

It is useful to recall that Chen et al. (2008) used 2 gram sized batches and alloyed them at 650°C for typically 2d or 3d. In 2003, we assumed the glasses were rendered homogenous by that thermal treatment. The present $V_m(x)$ results highlight in a rather unambiguous fashion the intimate role played by glass homogeneity on network packing. The local minimum of $V_m(x)$ in the IP region of the present glasses is localized entirely in the IP presumably because of the homogeneity of the glasses. The smearing of $V_m(x)$ at the rigidity- ($x_r = 22.5\%$) and stress-elastic phase boundaries ($x_s = 28.5\%$) observed in our previous (Chen et al., 2008) report is entirely consistent with the expected variance in S stoichiometry, $<\Delta(1\text{-}x)>_S$ in those set of glass samples. For glasses synthesized in 2008, we estimate the homogeneity, i.e., variance in S stoichiometry, $<\Delta(1\text{-}x)>_S$ across the synthesized batch compositions to be near 3% (see **Figures 4, 5**). Such considerations also have interesting consequences on the measured $V_m(x)$, outside the IP, both in the stressed-rigid phase ($x > x_s$), and the flexible phase ($x < x_r$) where the present V_m values measurably exceed **(Figure 11D)** some earlier reports (Sundaram et al., 2011). These factors underscore in a direct fashion the crucial role of the variation of $V_m(x)$ on glass/melt homogeneity of batch compositions. We comment on these results in section Glass Topological Phases.

DISCUSSION

Glass Topological Phases

Topological Phases of As_xS_{100-x} Glasses

The Calorimetric, Volumetric, and Raman scattering results on the especially homogenized As_xS_{100-x} glasses and melts reported in this work display three distinct regimes of variation as a function of their composition "x." The enthalpy of relaxation at T_g in the glasses, $\Delta H_{nr}(x)$, shows a square-well like behavior **(Figure 13)** with the heat flow term becoming miniscule in the $22.5\% < x < 28.5\%$ range. One of the first attempts to link calorimetric observation of a minuscule enthalpy of relaxation at T_g (ΔH_{nr} term) with flexibility and rigidity of glassy networks was due to Micoulaut (2010), who showed that the vanishing of ΔH_{nr} at T_g is the signature of an isostatically rigid glass, i.e., a glass in which $n_c = n_d$. Here n_c represents the count of mechanical constraints/atom due to bond-stretching and bond-bending covalent forces, while n_d the degrees of freedom/atom $= 3$ in 3D networks. Such networks conform to that Maxwell-Phillips rigidity condition (Maxwell, 1864; Phillips, 1979) and are viewed as rigid but unstressed, and form part of the Intermediate Phase (IP) (Boolchand et al., 2001; Georgiev et al., 2001). The IP is bounded on the low connectivity side, i.e., $x = x_r = 22.5\%$ by the rigidity-transition, and on the high connectivity side, i.e., $x = x_s = 28.5\%$ by the stress-transition. In As-S glasses, since As atoms are 3-fold and Sulfur atoms 2-fold coordinated, the mean coordination number

$$< r >= 3x + 2(1 - x) = 2 + x \tag{4}$$

varies linearly with x. Furthermore, since <r> provides a measure of network connectivity, and since T_g is determined by

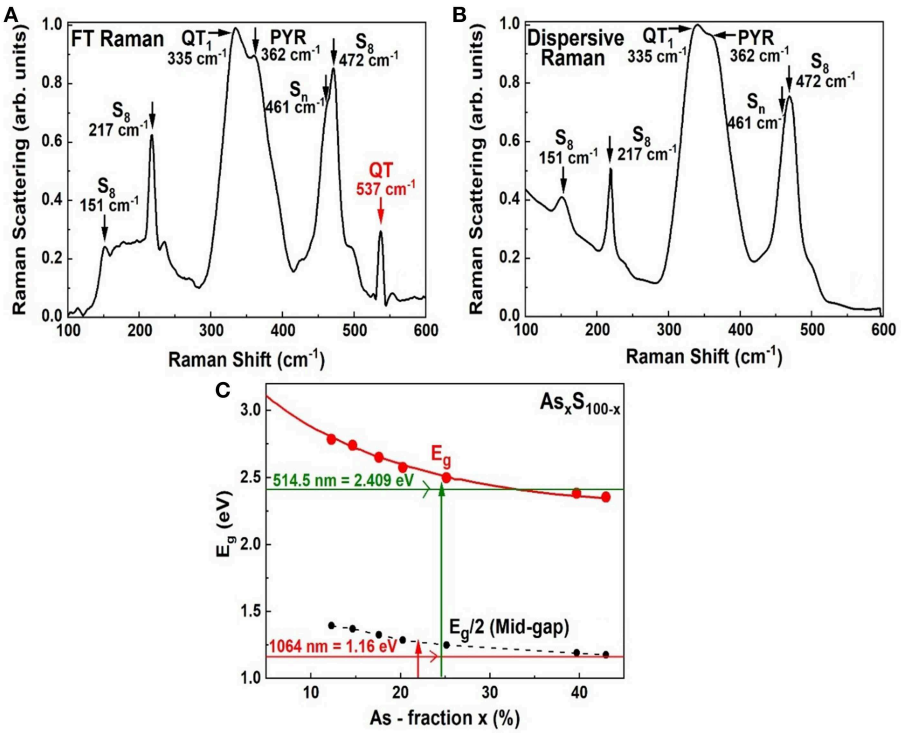

FIGURE 10 | Showing **(A)** FT—Raman spectrum of an $As_{18}S_{82}$ glass as in **Figure 4F**, **(B)** a Dispersive Raman spectrum of the same glass, and **(C)** the variation of the optical band gap in As_xS_{100-x} glasses reported by Yamaguchi (1985). In **(A)** the scattering is excited in the midgap region using the 1,064 nm as shown in **(C)**, while in **(B)** the scattering is excited using 514 nm radiation that excited the scattering in the conduction band region.

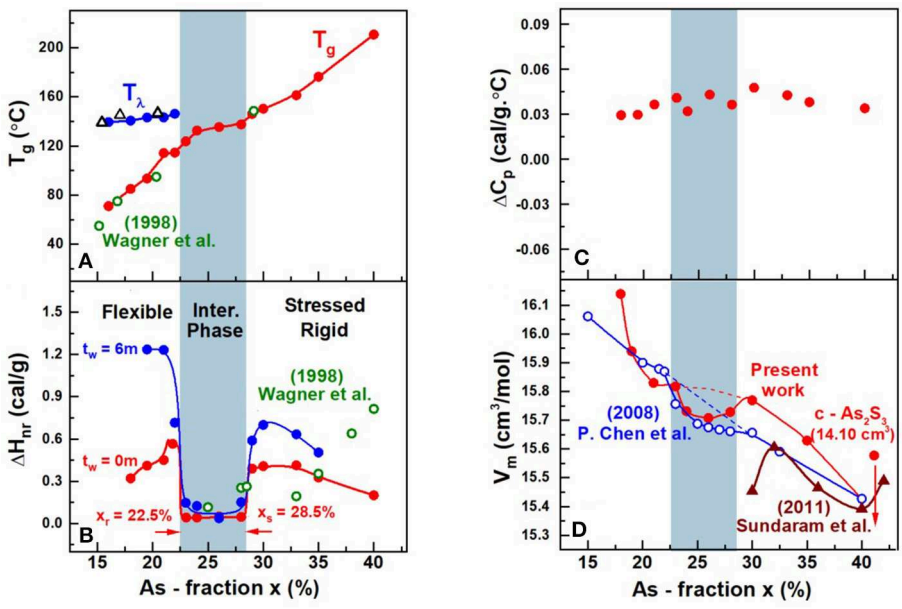

FIGURE 11 | Compositional trends of **(A)** T_λ transition (●) and the glass transition temperature (●) $T_g(x)$ from present work and T_λ transition (Δ) and the glass transition temperature (○) from Wagner et al. (1998) **(B)** the enthalpy of relaxation at T_g, $\Delta H_{nr}(x)$ in the fresh (●) and 6 m aged state (●) from present work and the enthalpy of relaxation (○) from Wagner et al. (1998) **(C)** the specific heat jump at T_g, $\Delta C_p(x)$ and **(D)** molar volumes, $V_m(x)$, in the present As_xS_{100-x} glasses. The $T_g(x)$ increases almost quasi—linearly with x while $\Delta H_{nr}(x)$ shows a square-well like behavior, the reversibility window. $V_m(x)$ displays a local minimum in the IP, the volumetric window that coincides with the IP boundary (light blue panel). Trends in $V_m(x)$ reported by Chen et al. (2008) on glasses (○) that were not as well-homogenized show a smearing of the volumetric window near the edges of the IP where the rigidity and stress transitions occur. The brown data set is from Sundaram et al. (2011) on glasses that were reacted for 12–24 h inside a rocking furnace. See text.

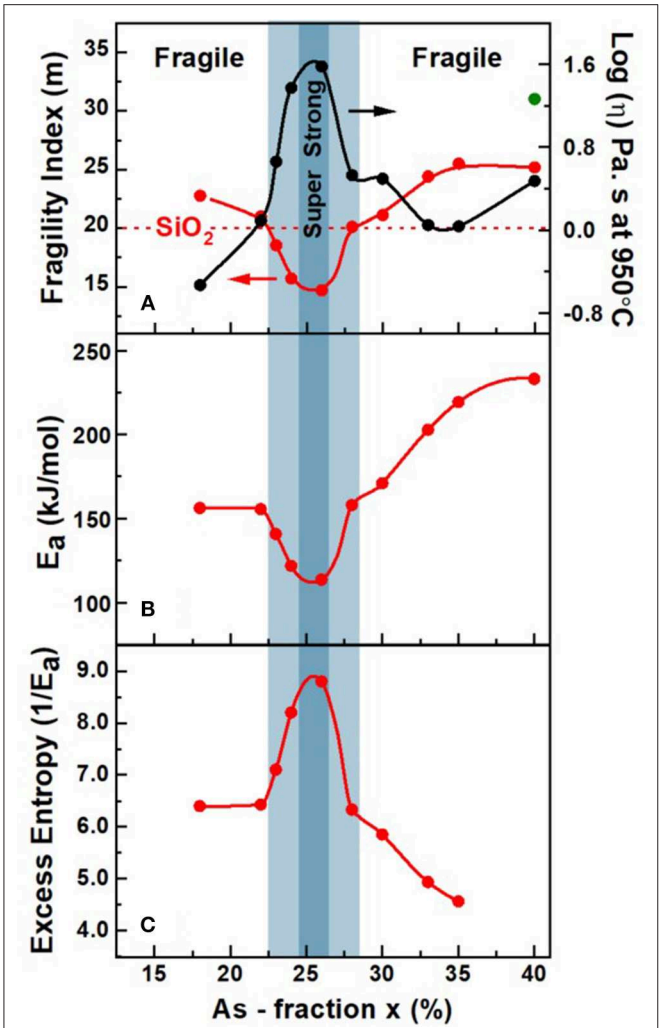

FIGURE 12 | (A) Observed variation in fragility index m(x), **(B)** activation energy of enthalpy relaxation time, $E_a(x)$, and **(C)** the variation in $1/E_a$ with x in As_xS_{100-x} melts obtained using mDSC. Also included in **(A)** is the projected variation (•) of melt viscosity (η) based on the presently measured m(x) and the MYEGA formalism (Mauro et al., 2009). In **(A)** the observed Gaussian—like minimum in m(x) centered around the *reversibility window* (shaded light blue), with $m < 20$ in the window and acquiring values of $m > 20$ outside the window, serves to define the *fragility window*. The super—strong character of melts near $x = 25.0\%$ acquiring an $m = 15.0$, is illustrated with a darker blue color. The green color data for m(x) of 31 at $x = 40\%$ is from Dilatometric measurements of Málek (1997).

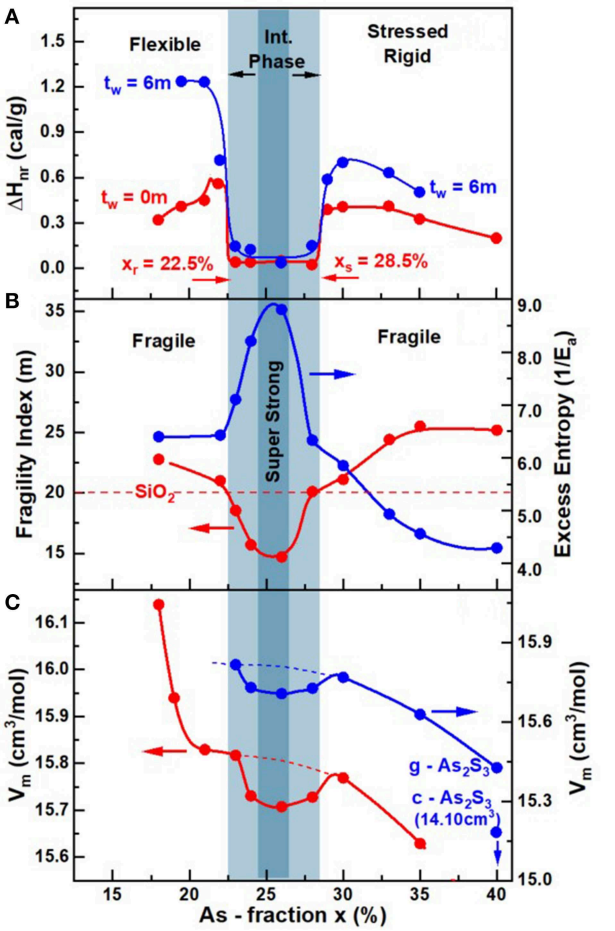

FIGURE 13 | Compositional trends in **(A)** enthalpy of relaxation at T_g (ΔH_{nr}) **(B)** melt fragility index and **(C)** glass molar volumes displaying local minima in the $22.5\% < x < 28.5\%$ range, the light blue panel. In **(B)** we also plot the inverse of the activation energy, E_a, for enthalpy relaxation times. In **(A)** the light blue panel gives the glass reversibility window, **(B)** compositions for which $m < 20$ defines the fragility window, and in **(C)** the local minimum in molar Volumes illustrates the volumetric window in glasses. To better illustrate $V_m(x)$ results at $x > 30\%$, we have redrawn the data on a coarser ordinate scale on the right to illustrate the reduction in V_m in both g- and c- As_2S_3 [14.10(2) cm^3] (Robie and Bethke, 1962).

the connectivity of a glassnetwork (Micoulaut, 1998), one expects $T_g(x)$ to increase linearly with x **(Figure 11A)**.

The increase of $T_g(x)$ with x **(Figure 11A)** and the observation of the reversibility window **(Figure 11B)** uniquely fixes the Topological Phases in the present As-S glasses. Glass compositions at $x < x_r$ with a lower T_g and thus $<r>$, are thus viewed to be in the Flexible phase, compared to those at $x > x_s$ that possess a higher T_g and thus $<r>$ are in the Stressed-rigid phase, while those in between, $x_r < x < x_s$ possess an optimal connectivity $<r>$ to be in the Intermediate Phase (**Figures 11B**, **13A**). The abruptness of the rigidity- and stress-transitions is fundamentally tied to the percolative nature of these elastic phase transitions (Thorpe et al., 2000). And to observe that intrinsic behavior in a laboratory experiment requires that glasses synthesized be homogeneous, ideally on an atomic scale. Experiments have shown that even if the homogeneity of a glass is established on a much larger scale of 50 μm, it is in practice a reasonably sufficient condition for the elastic phase transitions to be sharp (Bhosle et al., 2011). In the experiments, this requires that the variance of As content, $<\Delta x>_{As}$, across an As_xS_{100-x} batch composition, measured on a scale of 50 μm, to be <0.5% (**Figures 4**, **6**, **7**). If the variance $<\Delta x>_{As}$ exceeds 3% or more, one expects the two transitions to be smeared (Bhosle et al., 2012a,b) leading to a Gaussian-like or even triangular shaped reversibility window as noted elsewhere (Bhosle et al.,

2012a,b). Sulfur-rich glasses containing more than 80 mole% of S, in general, pose yet another challenge. A feature peculiar to the chemistry of Sulfur, is that the S_8 ring conformation is more stable than a polymeric S_n chain one. Thus, when melts are cooled S-rich domains condense into a S_8-rich-nanophase once the T < 150°C, the T_λ transition. The segregated S_8-rich nanophase cuts the As-S polymeric backbone and serves as an impediment to the growth of that backbone. In this work (section Kinetics of Melt/Glass Homogenization) we show that once glass/melts are homogenized, an additional step of low-temperature heating above T_g for 24 h or more, is crucial to coalesce fragmented segments of the backbone between the S_8 rich nanophase domains, to observe the elusive mode of the As=S stretch mode near 537 cm^{-1} of the As-centered, S = $As(S_{1/2})_3$ quasi-tetrahedral units.

The assignment of the 537 cm^{-1} mode with the S = $As(S_{1/2})_3$ QT units is in complete agreement with the calculated frequency of that As = S stretch mode using NRLMOL code (Chen et al., 2008). More significantly the compositional variation of the mode scattering strength unambiguously shows a maximum near x = 18%, precursive to the onset of rigidity (see **Supplementary Information**). The QT and PYR units are each isostatically rigid ($n_c = 3$), and their presence in comparable amounts in the backbone assists in stabilizing the IP by the increased configurational entropy (S_c) of the backbone (Yan, 2018). Our FT-Raman scattering results on the present As-S glasses also show (see **Supplementary Information**) that the scattering strength of the 490 cm^{-1} mode shows a maximum near x = 25% in the present binary, in harmony with the assignment as a stretch mode of S-S dimer linking AsS_3 pyramids. Thus, our earlier assignment (Chen et al., 2008) of the 490 cm^{-1} with QT units is clearly not supported by these new results on especially homogenized glasses.

Aging Behavior of $\Delta H_{nr}(x)$ and Network Configurational Entropy S_c

Our aging experiments on As-S glasses performed at RT for 6 months show that the enthalpy of relaxation, $\Delta H_{nr}(x)$, increases nearly 4-folds in the flexible phase (x < 22.5%) and by nearly 2-folds in the stressed-rigid phase (x > 28.5%), and remains unchanged and near vanishing in the Intermediate phase. These results unambiguously show the stability of the Intermediate phase over the neighboring phases in the present glasses. In particular the abrupt nature of the rigidity- and stress- elastic phase transition remains intact upon aging.

In our aging experiments, glasses were held at room temperature (T_a = 25°C). And since the kinetics of aging are determined by the T_a/T_g ratio, one expects aging of $\Delta H_{nr}(x)$, in the flexible phase ($T_a/T_g = 0.80$) to be more pronounced than in the stressed rigid phase ($T_a/T_g = 0.69$), since T_g of glasses in the flexible phase (∼100°C) are lower than those in the stressed rigid ones (∼140°C). Our aging results are clearly in harmony with that expectation.

The vanishing of the $\Delta H_{nr}(x)$ term in the Intermediate phase suggests that network glasses possess melt-like configurational entropy. The aging related increase of the $\Delta H_{nr}(x)$ term outside the IP suggests that there are entropy sinks contributing to the lowering of the configurational entropy in those phases. We view the formation of S_8 rings as entropy sinks in the flexible phase, which lead to an increase of the $\Delta H_{nr}(x)$ term. A perusal of the observed Raman spectra of the glasses **(Figure 8)** shows a rather pronounced growth in scattering strength of the S_8 related vibrational features near 217 cm^{-1} and 472 cm^{-1} as the As content of glasses, x is <24%. In the stressed-rigid glasses formed at x > 28.5%, one expects the entropy of the glassy backbones to steadily reduce since both QT- and PYR-local structures are formed in the IP, but only PYR-local structures persist as x increases to 40%. The steadily decreasing chemical disorder as x increases to 40%, may be viewed as aspects of local and intermediate range structure that contribute to the lowering of configurational entropy. And since V_m of c-As_2S_3 is quite low, one expects $V_m(x)$ in the glasses to also decrease as x increases to the stoichiometric composition, x = 40%. That view is independently corroborated by the configurational entropy, S_c, variation within the Adam Gibbs approach, which is determined by the inverse of the activation energy E_a **(Figure 13B)** of the enthalpy relaxation times (section Ideal Glasses, IP, and Configurational Entropy) deduced from fragility index measurements. Note that in **Figure 13B**, the variation of $1/E_a$ against x, displays a maximum in the IP and $1/E_a$ steadily decreases in the stressed-rigid phase. We revisit the glass network configurational entropy considerations in section Ideal Glasses, IP, and Configurational Entropy in context with the nature of ideal glasses formed in the IP.

We conclude this section with a comment. Although stoichiometric g-As_2S_3 possesses a $<r>$ = 2.40, it is quite noteworthy that no IP forms around that composition (McCloy et al., 2010) as suggested by the finite enthalpy of relaxation observed for the stoichiometric glass. The stoichiometric glass is segregated into an As-rich nano phase and a S-rich $As_2S_3+\delta$. The NSPS structure does not sustain an IP. This result in not peculiar to As_2S_3.

The Rigidity Phase Transition in As_xS_{100-x} Glasses Near x = 22.5%

The Phillips-Thorpe prediction for onset of rigidity in disordered molecular networks (Thorpe et al., 2000; Phillips, 2004) near $<r>$ = 2.40 has been remarkably successful in understanding the Group IV-selenides and sulfides (Selvanathan et al., 1999; Bhosle et al., 2011, 2012a,b; Chakraborty and Boolchand, 2014) [Ge(or Si)]x[Se)]100-x. The elastic phase transition stems from isostatically rigid ($n_c = 3$) local structures, such as $GeSe_4$ or $SiSe_4$ or GeS_4 tetrahedral units that percolate near a mean $<r>$ = 2.40. On the other hand, the case of the group V-chalcogenides, such As-Se, P-Se, drew attention several years ago, when one noticed that onset of rigidity is observed at a measurably lower mean coordination number near $<r>$ = 2.28 (Georgiev et al., 2000; Boolchand et al., 2009). The transition was identified with presence of isostatically rigid (i.e., n_c =3) local structures based on QT (Ch = $Pn(Ch_{1/2})_3$) units formed in Pnictide (P_n = P or As) based chalcogenides (Ch = S or Se). The case of binary P-Se (Georgiev et al., 2001), and ternary (P or As)$_x$Ge$_y$Se$_{100-x-y}$ (Chakravarty et al., 2005; Qu and Boolchand, 2005; Chbeir et al., 2019) have convincingly shown in calorimetric and Raman scattering evidence that the onset of rigidity occurs near $<r>$ of 2.28, suggesting that P_n- centered QT local structures are

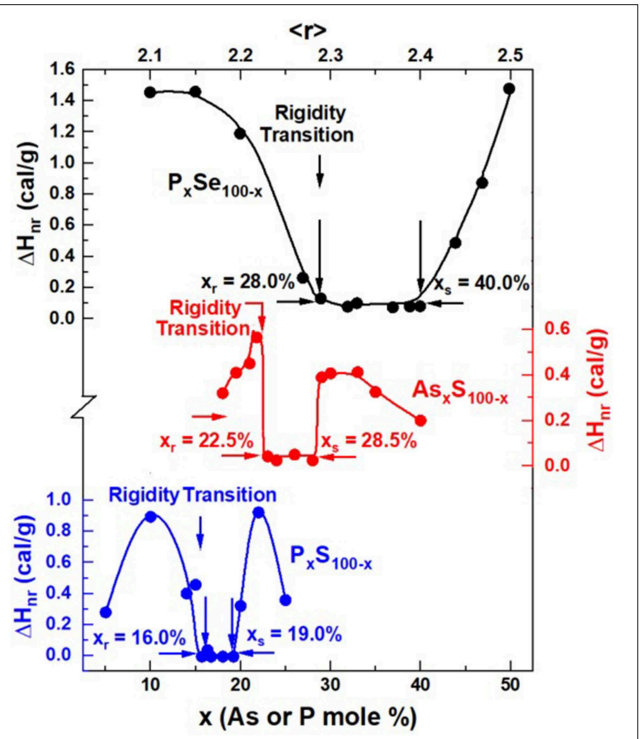

FIGURE 14 | Observed reversibility windows in P_xS_{100-x} (Vempati, 2005), As_xS_{100-x} (**Figure 11B**, t_m = 0, present work), and P_xSe_{100-x} (Chakravarty et al., 2005) glasses. Note that the rigidity transition, x_r = 16% in P_xS_{100-x}, shifts up to x_r = 22.5% in As_xS_{100-x}, and then to x_r = 28% in the P_xSe_{100-x} binary.

implicated in the percolation of rigidity at the lower connectivity. We note that the <*r*> of the QT species is 2.28.

The case of the present As-S binary, where the onset of rigidity transition occurs near <*r*> = 2.22, even lower than the usual circumstance near <*r*> = 2.28, opens the obvious question, how are we understand the shift to an <*r*> to an even lower value of <*r*> than 2.28? We believe these observations have a structural connection, and comment on it next.

MDSC experiments on P_xS_{100-x} glasses show (Vempati, 2005) the reversibility window to occur in the 16% < x < 19% range (**Figure 14**). Raman scattering measurements unequivocally show three well-resolved vibrational modes near 377, 416, and 472 cm^{-1}. These modes are, respectively identified (Vempati, 2005) with the stretch modes of $S = P(S_{1/2})_3$ QT units labeled as P4, $P(S_{1/2})_3$ PYR units labeled as P3, and polymeric S_n chains (Boolchand et al., 2009). And from the observed scattering strength ratio of the QT and PYR modes, one obtains an approximate concentration ratio N_{P4}/N_{P3} of 0.60(5). The stoichiometry of the backbone suggested for onset of the rigidity transition near x = 16% is then found to be near $P_{28}S_{82}$. These data clearly suggest that the polymeric S_n chains are largely decoupled from the backbone in these binary P_xS_{100-x} glasses. It is useful to remind ourselves that the stoichiometry of the P-Se backbone at the onset of the rigidity transitions in P_xSe_{100-x} glasses also occurs near x = 28.0%, except in these binary glasses the polymeric Se_n chains comprise part of the isostatically rigid backbone. Thus, the structural picture that emerges is that while in the P-Se binary glasses the polymeric Se_n chains form part of the backbone, in sharp contrast in binary P-S binary glasses the polymeric S_n chains are nearly completely decoupled from the backbone causing the onset of rigidity to shift down in x rather strikingly. One could not have guessed from the Raman scattering results alone if the polymeric S_n chains are part of or decoupled from the glassy backbone, but when these optical measurements are correlated with the Calorimetric ones, a clear interpretation of the shift in the elastic phase transition to lower x in the P-S binary emerges.

That brings us to the case of the present As-S binary glasses. We note that the onset of rigidity (**Figure 14**) occurs near x_r = 22.5%, shifted down from the case of P-Se binary at x_r = 28% by nearly 6% in x. This is nearly half-way in between the shift in x observed between the onset of rigidity in the P-Se binary near x_r = 28% and the onset of rigidity transition near x_r = 16% in the P-S binary. The case of the As-S binary poses formidable challenges in uniquely fitting the observed Raman lineshapes to deduce the fraction of QT/PYR near x = 22.5% as we eluded to in section Raman Scattering on As_xS_{100-x} Glasses. Nevertheless, from the location of the rigidity transition x_r = 22.5% in As-S glasses, we speculate that in these sulfide glasses nearly half of the polymeric S_n chains are decoupled from the backbone. That observation reminds of the finding in our Raman profiling experiments that showed in the final step of melt quenching after T_g cycling S-rich glasses (x < 22%), one clearly observes (See **Figures 4**, **6** for example) the S_8 ring fraction in glasses to sharply decrease, underscoring that the polymeric S_n fraction has increased. And it would appear that not all these S_n chain fragments become part of the backbone. The behavior needs to be further explored in future work.

Compaction of IP Glassy Networks in Homogeneous As_xS_{100-x} Glasses

The molar volume $V_m(x)$, variation in the present glasses (**Figures 11D**, **13C**) displays three rather distinct regimes; in the flexible phase one observes a pronounced growth in $V_m(x)$ at x < 20% (b) in the IP range one observes a Gaussian-like local minimum, and (c) in the stressed-rigid phase a rather sharp reduction of $V_m(x)$ occurs at x > 29%. Equally striking is the fact that $V_m(x)$ in the IP range systematically exceed those noted earlier in the glasses synthesized by Chen et al. (2008). Furthermore, one cannot miss noting that trends in $V_m(x)$ in the three regions, in the especially homogenized glasses of the present work, are completely distinct. At x < 21%, $V_m(x)$ increases precipitously and at low x, at x > 30%, $V_m(x)$ decreases remarkably, while in the IP, one observes a Gaussian-like minimum. Trends in $V_m(x)$ in our earlier investigations (Chen et al., 2008) showed a clear smearing of the variation near the two elastic phase boundaries (rigidity and stress) separating these three regions. These differences in trends of $V_m(x)$ are most likely connected to the homogeneity of glasses synthesized in the present work.

The pronounced growth of V_m at x < 20% (**Figure 11D**) appears to be closely correlated with the sharp increase in the concentration of S_8 rings observed in Raman scattering

(**Figure 8**). Here we must remember that the inter-ring forces that stabilize the S_8 ring nanophase derive from lone pair interactions. On the other hand, at x > 30%, the sharp reduction in $V_m(x)$ must surely be tied to the pronounced growth of pyramidal $As(S_{1/2})_3$ local units with a $<r>$ of 2.40 that promote increased cross-linking of the glasses as one approaches the stoichiometric glass composition at x = 40%. The crystalline phase (orpiment) that is fully polymerized has the lowest Molar volume of 14.10(2) cm^3 (Robie and Bethke, 1962). The local minimum in $V_m(x)$ observed in the IP, so clearly displayed in the present homogeneous glasses, confirms the role of the weaker long range forces (van der Walls, and Coulombic) that come into play when the strong covalent forces (bond-bending and bond-stretching) are exactly balanced by the degrees of freedom of 3 per atom. Network compaction in the IP is the realization of the Maxwell-Phillips rigidity criteria, $n_c = n_d$, being exactly fulfilled in that special phase. The absence of a smearing of that local minimum near the edges is a direct reflection of the low variance in $<\Delta x>_{As}$ in the presently synthesized bulk glasses.

Correlating Melt Fragility Index With Glass Enthalpy of Relaxation

The key central finding of the present work is that the melt fragility index m(x) in the As_xS_{100-x} binary is found to be closely correlated to the glass enthalpy of relaxation. Specifically, glassy melts examined in the composition range 22.5% < x < 28.5% **(Figure 12A)** display a Gaussian-like minimum of the fragility index m(x). A perusal of the observed variation in m(x) shows that m < 20 in the said range, but increases to m > 20 outside that range. One defines the melt composition range across which m < 20 to be the "fragility window". These fragility index measurements made use of the same especially homogenized bulk glasses that were used to establish the glass enthalpy of relaxation that revealed the square-well like variation defining the "reversibility window" **(Figure 11B)**. The observed trends in the compositional variation of the fragility index, m(x), characteristic of melts, and the enthalpy of relaxation at T_g, $\Delta H_{nr}(x)$, a quantity that characterizes the glasses shows that there exists a rather intimate relationship between melts and glasses. These trends demonstrate that super-strong melts upon cooling to T_g give rise to isostatically rigid glasses in the Intermediate Phase (**Figure 13**). While, fragile melts formed at non-IP compositions upon cooling will give rise to either Flexible glasses or Stressed-rigid ones. Furthermore, one can also distinguish the fragile melts that give rise to Flexible glasses from those that form Stressed-Rigid ones. In Flexible glasses the fragility index decreases with increasing T_g, but in Stressed-rigid ones, the reverse is true, i.e., the fragility index increases with T_g.

The intimate correlation between the fragility window and the reversibility window noted here for the As-S binary is reminiscent of two other recent reports on chalcogenides, one on the Ge-Se binary (Gunasekera et al., 2013) and the other on the Ge-S binary (Chakraborty and Boolchand, 2014), where closely similar results are found. The melt-glass correlation has also been noted in a modified oxide (Mohanty, 2018) the case of—sodium phosphate glasses. These new findings clearly suggest that the correlation between melt dynamics and glass Topological phases may well be a generic feature of the glassy state of matter.

Equilibrium Phase Diagram, Eutectics, and Aging of the Reversibility Window

The equilibrium phase diagram of As-S binary was reported in the year 1981 by Borisova (1981). In the report the author found the existence of a eutectic near an As composition of x = 15% with a eutectic temperature (T_E) of about 150°C. Subsequently the phase diagram was re-investigated in 1990 by Okamoto in Binary Alloy Phase diagram 2nd Edition (Okamoto, 1990). In this later report, interestingly, no evidence of a eutectic was found.

Our results on the aging of the reversibility window in the present As-S binary glass system shown in **Figures 11B**, **13A** is fully compatible with the absence of a eutectic near x = 15%. Indeed, if there was a eutectic near x = 15%, one would expect the rigidity transition to smear with aging time and not to show an abrupt change in the enthalpy of relaxation as documented in **Figures 11B**, **13A**.

We conclude this section with a final remark. In both the As_xSe_{100-x} and P_xSe_{100-x} binary systems, the equilibrium phase diagrams display evidence (Monteil and Vincent, 1975; Okamoto, 2000) of a eutectic near x = 20%. The presence of the eutectic has attracted much interest in glass science. It constitutes signature of phase separation that causes the liquidus to locally decrease. That circumstance assists in rapid cooling of melts and has been used to promote (Richet, 2001) glass formation in metallic systems. The presence of a eutectic in the As-Se and P-Se binary systems has another interesting consequence. In both these binary systems, we have reported evidence of reversibility windows; for the As-Se binary in the 28% < x < 37% range, and for the P-Se binary in the 28% < x < 40% (Georgiev et al., 2003a; Ravindren et al., 2014). However, in both these systems, aging of glasses inevitably leads to the smearing of the rigidity transition and even narrowing of the reversibility window (Chen et al., 2010) since the T_g's of the glasses near the rigidity transition are quite close to the Eutectic Temperature (T_E). It is for this reason the reversibility window does not retain its near square-well shape upon aging of the glasses when heated to T_g. That circumstance needs to be distinguished from the case when no eutectic occurs in the vicinity of the reversibility window, as is the case in the present As-S binary and the rigidity- and stress-transition continue to be abrupt both in the fresh and aged glasses and elsewhere (Bhosle et al., 2011; Chakraborty and Boolchand, 2014; Chbeir et al., 2019).

Ideal Glasses, IP, and Configurational Entropy

Adam-Gibbs (Adam and Gibbs, 1965) suggested that the exponential increase in viscosity of a melt as it is cooled to a temperature T, can be tied to its loss of excess configurational entropy (S_c) by the following equation,

$$\eta = \eta_o \exp\left(\frac{B}{TS_c}\right) \quad (5)$$

Since the viscosity of a melt is viewed to be a thermally–activated process

$$\eta = \eta_o \exp\left(\frac{E_a}{k_B T}\right) \quad (6)$$

One must conclude from equations 5 and 6 that the excess configuration entropy S_c must vary as the inverse of the activation energy of enthalpy $1/E_a$. From MDSC experiments on the present glasses we have established E_a, the activation energy for enthalpy relaxation (**Figure 3** and Equation 3). The compositional variation of $1/E_a$ (**Figure 12C**) displays a pronounced peak centered on the IP. The result implies that IP melts must continue to possess a high configurational entropy even when such melts are cooled to near T_g (Yan, 2018). The excess entropy S_c is defined as the entropy difference between the super cooled liquid at T and the state of the glass at which the entropy can no longer be lost (Bestul and Chang, 1964). The high configurational entropy of IP glass compositions is precisely what is also implied in the minuscule or vanishing enthalpy of relaxation $\Delta H_{nr}(x)$ of these special glass compositions. In contrast the abrupt and sizable increase of the $\Delta H_{nr}(x)$ term in non-IP compositions (flexible and stressed-rigid phase) is due to such networks possessing entropy sinks. In the flexible phase the entropy sinks include S_8 monomers for which direct evidence emerges from not only the Raman vibrational modes of these species (**Figure 8**) but also the pronounced increase of molar volumes at $x < 22.5\%$ (**Figure 13C**) evolving in the flexible phase. In the stressed-rigid phase the entropy sinks include pyramidal $(AsS_{1/2})_3$ units that steadily compact the backbone network into structural configurations akin to those found in orpiment as revealed by Raman scattering (**Figure 8**) as well as the variation of Molar volumes (**Figure 13C**). IP glasses represent ideal glasses. They not only possess a high glass forming tendency, show minimal aging, and form isostatically rigid structures that are adaptive in nature. These ideal glasses also exist only in high configurational entropy structures as found in corresponding melts. These observations on IP glasses as ideal glasses are clearly at variance with the notion advanced many years ago that ideal network glasses possess low configurational entropy and form at T close to the Kauzmann temperature (Angell, 1995).

CONCLUSIONS

We have examined especially homogenized As_xS_{100-x} glasses in Modulated-DSC, Raman scattering and Molar volume experiments over a wide range, $12\% < x < 40\%$, of compositions. Glasses were synthesized by alloying As_2S_3 and elemental S as starting materials in evacuated quartz tubes, and quenched melts Raman profiled as a function alloying time till the observed lineshapes along the length of melt column became identical. Sulfur-rich ($x < 20\%$) melts required about 6 weeks while S-deficient ones ($x > 20\%$) about 4 weeks of alloying time at 650°C to homogenize. In such homogenized glasses the variance in As content, $<\Delta x>_{As}$ across 1.5 gram sized batches reduced by an order of magnitude to become <½%. A second step of heating glasses at $T_g + 10$°C for 2 days, once glasses were homogenized, was found sufficient to observe the elusive 537 cm^{-1} mode of the S=As stretch mode of $S = As(S_{1/2})_3$ local structures at $x < 26\%$ in FT-Raman scattering experiments. In such glasses, the enthalpy of relaxation at T_g, $\Delta H_{nr}(x)$, displays a square-well like variation in the $22.5\% < x < 28.5\%$ composition range even in the fresh state, defining the Reversibility window. The fragility index, m(x), of corresponding melts show a Gaussian-like local minimum with $m < 20$ in the same composition range, thus defining a Fragility window. Molar volumes, $V_m(x)$, of glasses display a local Gaussian like minimum localized entirely in the Reversibility window and underscoring the compacted nature of glasses formed in that composition range defining a Volumetric window. On As_xS_{100-x} glasses that were alloyed for 3 days at 650°C in our previous work (Chen et al., 2008), the $V_m(x)$ window is found to be smeared at its edges by comparison (**Figure 11D**), because of the larger variance in As-stoichiometry $<\Delta x>_{As}$ across the same size batches synthesized. At low x ($< 20\%$) in the Flexible phase, glasses are segregated into a S_8-rich nanophase and an As-S bearing glassy backbone. At medium x ($22.5\% < x < 28.5\%$) glassy backbones composed of both QT and PYR local structures form the building blocks of the isostatically rigid Intermediate Phase (IP) displaying a vanishing $\Delta H_{nr}(x)$ term, and with corresponding melts displaying a super-strong behavior ($m < 20$) that contributes to the delayed homogenization of melts. At high x ($28.5\% < x < 40\%$) glasses exist in a Stressed-rigid phase, possessing an increasing $\Delta H_{nr}(x)$ term, and with corresponding melts becoming increasingly fragile, $m(x)>20$, with increasing x. These results unequivocally demonstrate that superstrong melts yield isostatically rigid glasses, while fragile one's form either Flexible or Stressed rigid glasses upon cooling past T_g. The most exceptional nature of As_xS_{100-x} glasses formed in the $22.5\% < x < 28.5\%$ range, displaying a Reversibility window, a Volumetric window, and their melt counterparts showing a Fragility window, are realization of the self-organized IP formed in these network glasses.

DATA AVAILABILITY

Publicly available datasets were analyzed in this study. This data can be found here: https://pubs.acs.org/doi/abs/10.1021/jp411823j.

AUTHOR CONTRIBUTIONS

SC synthesized glasses and performed Modulated DSC experiments, Raman scattering, and Molar volume experiments, he analyzed these data working closely with RC, PC, and PB. MM assisted with discussions on topological phases, melt dynamics, and ideal glasses. PB coordinated the experimental work performed at University of Cincinnati, and all co-authors including RC, MM, PC, and PB assisted in writing the manuscript.

FUNDING

PB acknowledges support from NSF grant DMR 08-53957. MM acknowledges support of Agence Nationale de la Recherche (ANR) Grant No ANR-11-BS08-10012 from American Fulbright Commission and International Materials Institute (H. Jain).

ACKNOWLEDGMENTS

It is a pleasure to acknowledge discussions with Dr. Richard Zallen and Dr. Jim Phillips on issues of glass science spread over several decades. We thank Dr. Alan Jackson for assistance with simulation package NRLMOL to calculate Raman and Infrared vibrations from characteristic local structures. We have benefitted from discussions with Caleb McDonald, Len Thomas and Steve Hall on the use of the Q2000 TA Instruments MDSC.

SUPPLEMENTARY MATERIAL

The Supplementary Material for this article can be found online at: https://www.frontiersin.org/articles/10.3389/fmats.2019.00166/full#supplementary-material

REFERENCES

Adam, G., and Gibbs, J. H. (1965). On the temperature dependence of cooperative relaxation properties in glass-forming liquids. *J. Chem. Phys.* 43, 139–146. doi: 10.1063/1.1696442

Andrikopoulos, K. S., Kalampounias, A. G., and Yannopoulos, S. N. (2005). Rounding effects on doped sulfur's living polymerization: the case of As and Se. *Phys. Rev. B* 72:014203. doi: 10.1103/PhysRevB.72.014203

Angell, C. A. (1991). Relaxation in liquids, polymers and plastic crystals - strong fragile patterns and problems. *J. Non Cryst. Solids* 131, 13–31. doi: 10.1016/0022-3093(91)90266-9

Angell, C. A. (1995). Formation of glasses from liquids and biopolymers. *Science* 267, 1924–1935. doi: 10.1126/science.267.5206.1924

Bellissent, R., Descotes, L., Boué, F., and Pfeuty, P. (1990). Liquid sulfur: local-order evidence of a polymerization transition. *Phys. Rev. B* 41, 2135–2138. doi: 10.1103/PhysRevB.41.2135

Bestul, A. B., and Chang, S. S. (1964). Excess entropy at glass transformation. *J. Chem. Phys*. 40, 3731–3733. doi: 10.1063/1.1725086

Bhosle, S., Gunasekera, K., Boolchand, P., and Micoulaut, M. (2012a). Melt homogenization and self-organization in chalcogenides-part I. *Int. J. Appl. Glass Sci.* 3, 189–204. doi: 10.1111/j.2041-1294.2012.00093.x

Bhosle, S., Gunasekera, K., Boolchand, P., and Micoulaut, M. (2012b). Melt homogenization and self-organization in chalcogenides-part II. *Int. J. Appl. Glass Sci.* 3, 205–220. doi: 10.1111/j.2041-1294.2012.00092.x

Bhosle, S., Gunasekera, K., Chen, P., Boolchand, P., Micoulaut, M., and Massobrio, C. (2011). Meeting experimental challenges to physics of network glasses: assessing the role of sample homogeneity. *Solid State Commun*. 151, 1851–1855. doi: 10.1016/j.ssc.2011.10.016

Böhmer, R., Ngai, K. L., Angell, C. A., and Plazek, D. J. (1993). Nonexponential relaxations in strong and fragile glass formers. *J. Chem. Phys.* 99, 4201–4209. doi: 10.1063/1.466117

Bonazzi, P., Menchetti, S., and Pratesi, G. (1995). The crystal structure of pararealgar, As 4 S 4. *Am. Mineral.* 80, 400–403. doi: 10.2138/am-1995-3-422

Boolchand, P. (2000). The maximum in glass transition temperature (Tg) near x = 1/3 in GexSe1-x glasses. *Asian J. Phys.* 9, 709–721.

Boolchand, P., Chen, P., and Vempati, U. (2009). Intermediate phases, structural variance and network demixing in chalcogenides: the unusual case of group V sulfides. *J. Non Cryst. Solids* 355, 1773–1785. doi: 10.1016/j.jnoncrysol.2008.11.046

Boolchand, P., Georgiev, D. G., and Goodman, B. (2001). Discovery of the intermediate phase in chalcogenide glasses. *J. Optoelectr. Adv. Mater.* 3, 703–720.

Boolchand, P., Georgiev, D. G., Qu, T., Wang, F., Cai, L., and Chakravarty, S. (2002). Nanoscale phase separation effects near rfl = 2.4 and 2.67, and rigidity transitions in chalcogenide glasses. *Comptes Rendus Chime* 12, 713–724. doi: 10.1016/S1631-0748(02)01440-6

Boolchand, P., and Goodman, B. (2017). Glassy materials with enhanced thermal stability. *MRS Bull.* 42, 23–28. doi: 10.1557/mrs.2016.300

Borisova, Z. (1981). *Glassy Semiconductors*. Springer. Available online at: https://www.springer.com/us/book/9781475708530 (accessed March 31, 2019).

Bychkov, E., Miloshova, M., Price, D. L., Benmore, C. J., and Lorriaux, A. (2006). Short, intermediate and mesoscopic range order in sulfur-rich binary glasses. *J. Non Cryst. Solids* 352, 63–70. doi: 10.1016/j.jnoncrysol.2005.11.002

Carpentier, L., Desprez, S., and Descamps, M. (2003). From strong to fragile glass-forming systems: a temperature modulated differential scanning calorimetry investigation. *Phase Transit.* 76, 787–799. doi: 10.1080/01411590310001603708

Chakraborty, S., and Boolchand, P. (2014). Topological origin of fragility, network adaptation, and rigidity and stress transitions in especially homogenized nonstoichiometric binary GeS glasses. *J. Phys. Chem. B* 118, 2249–2263. doi: 10.1021/jp411823j

Chakravarty, S., Georgiev, D. G., Boolchand, P., and Micoulaut, M. (2005). Ageing, fragility and the reversibility window in bulk alloy glasses. *J. Phys. Condens. Matter* 17, L1–L7. doi: 10.1088/0953-8984/17/1/L01

Chbeir, R., Bauchy, M., Micoulaut, M., and Boolchand, P. (2019). Evidence for a correlation of melt fragility index with topological phases of multicomponent glasses. *Front. Mater*. 6:173. doi: 10.3389/fmats.2019.00173

Chen, P., Boolchand, P., and Georgiev, D. G. (2010). Long term aging of selenide glasses: evidence of sub-Tg endotherms and pre-Tg exotherms. *J. Phys. Condens. Matter* 22. doi: 10.1088/0953-8984/22/6/065104

Chen, P., Holbrook, C., Boolchand, P., Georgiev, D. G., Jackson, K. A., and Micoulaut, M. (2008). Intermediate phase, network demixing, boson and floppy modes, and compositional trends in glass transition temperatures of binary As-S system. *Phys. Rev. B* 78:224208. doi: 10.1103/PhysRevB.78.224208

Georgiev, D. G., Boolchand, P., Eckert, H., Micoulaut, M., and Jackson, K. (2003a). The self-organized phase of bulk P x Se 1 – x glasses. *Europhys. Lett.* 62, 49–55. doi: 10.1209/epl/i2003-00361-2

Georgiev, D. G., Boolchand, P., and Jackson, K. A. (2003b). Intrinsic nanoscale phase separation of bulk As 2 S 3 glass. *Philos. Mag.* 83, 2941–2953. doi: 10.1080/1478643031000151196

Georgiev, D. G., Boolchand, P., and Micoulaut, M. (2000). Rigidity transitions and molecular structure of AsxSe1Àx glasses. *Phys. Rev. B* 4, R9228–R9231.

Georgiev, D. G., Mitkova, M., Boolchand, P., Brunklaus, G., Eckert, H., and Micoulaut, M. (2001). Molecular structure, glass transition temperature variation, agglomeration theory, and network connectivity of binary P-Se glasses. *Phys. Rev. B* 64, 134204-1–134204-11. doi: 10.1103/PhysRevB.64.134204

Golovchak, R., Shpotyuk, O., Mccloy, J. S., Riley, B. J., Windisch, C. F., Sundaram, S. K., et al. (2010). Structural model of homogeneous As-S glasses derived from Raman spectroscopy and high-resolution XPS. *Philos. Mag.* 90, 4489–4501. doi: 10.1080/14786435.2010.510455

Goncalves, C., Kang, M., Sohn, B.-U., Yin, G., Hu, J., Tan, D. T. H., et al. (2018). New candidate multicomponent chalcogenide glasses for supercontinuum generation. *Appl. Sci.* 8:2082. doi: 10.3390/app8112082

Gouda, P. (2012). *Arsenic Selenium Antimony Ultra-trace Analysis Atomic Absorption Spectroscopy, Inductively Coupled Plasma, Bench Chemistry*. 3rd Edn. Bloomington, IN: iUniverse, Inc.

Gunasekera, K., Bhosle, S., Boolchand, P., and Micoulaut, M. (2013). Superstrong nature of covalently bonded glass-forming liquids at select compositions. *J. Chem. Phys.* 139:164511. doi: 10.1063/1.4826463

Kalampounias, A. G., Andrikopoulos, K. S., and Yannopoulos, S. N. (2003). Probing the sulfur polymerization transition *in situ* with Raman spectroscopy. *J. Chem. Phys.* 118, 8460–8467. doi: 10.1063/1.1566938

Lide, D. R., Baysinger, G., Chemistry, S., Berger, L. I., Goldberg, R. N., and Kehiaian, H. V. (2005). *CRC Handbook of Chemistry and Physics*. CRC Press. Available online at: http://www.hbcpnetbase.com

Málek, J. (1997). Dilatometric study of structural relaxation in arsenic sulfide glass. *Thermochimica Acta* 311, 183–198. doi: 10.1016/S0040-6031(97)00466-8

Malventano, A. (2017). *How 3D XPoint Phase - Change Memory Works*. Available online at: https://www.pcper.com/reviews/Editorial/How-3D-XPoint-Phase-Change-Memory-Works

Mantisi, B., Bauchy, M., and Micoulaut, M. (2015). Cycling through the glass transition: evidence for reversibility windows and dynamic anomalies. *Phys. Rev. B* 92:134201. doi: 10.1103/PhysRevB.92.134201

Mauro, J. C., Yue, Y., Ellison, A. J., Gupta, P. K., and Allan, D. C. (2009). Viscosity of glass-forming liquids. *Proc. Natl. Acad. Sci. U. S. A.* 106, 19780–19784. doi: 10.1073/pnas.0911705106

Maxwell, J. C. (1864). L. On the calculation of the equilibrium and stiffness of frames. *Philos. Mag. Ser.* 4, 294–299. doi: 10.1080/14786446408643668

McCloy, J. S., Riley, B. J., Sundaram, S. K., Qiao, H. A., Crum, J. V., and Johnson, B. R. (2010). Structure-optical property correlations of arsenic sulfide glasses in visible, infrared, and sub-millimeter regions. *J. Non Cryst. Solids* 356, 1288–1293. doi: 10.1016/j.jnoncrysol.2010.04.018

Micoulaut, M. (1998). The slope equations: a universal relationship between local structure and glass transition temperature. *Eur. Phys. J. B* 294, 277–294. doi: 10.1007/s100510050184

Micoulaut, M. (2010). Linking rigidity transitions with enthalpic changes at the glass transition and fragility: insight from a simple oscillator model. *J. Phys. Condens. Matter* 22:285101. doi: 10.1088/0953-8984/22/28/285101

Mohanty, C. (2018). *Direct evidence for topological phases in sodium phosphate glasses from Raman scattering, infrared reflectance and modulated dsc* (Master's thesis). University of Cincinnati, Cincinnati, OH.

Monteil, Y., and Vincent, H. (1975). Les seleniures de phosphore. *J. Inorg. Nucl. Chem.* 37, 2053–2056. doi: 10.1016/0022-1902(75)80828-1

Okamoto, H. (1990). *As - S (Arsenic Sulfur)*. Materials Park: ASM International.

Okamoto, H. (2000). *As - Se: Desk Handbook: Phase Diagrams for Binary Alloys*. Materials Park: ASM International.

Phillips, J. C. (1979). Topology of covalent non-crystalline solids.1. Short-range order in chalcogenide alloys. *J. Non Cryst. Solids* 34, 153–181. doi: 10.1016/0022-3093(79)90033-4

Phillips, J. C. (2004). Constraint theory and hierarchical protein dynamics. *J. Phys. Condens. Matter* 16, S5065–S5072. doi: 10.1088/0953-8984/16/44/004

Phillips, J. C., Beevers, C. A., and Gould, S. E. B. (1980). Molecular structure of As2Se3 glass. *Phys. Rev. B* 21, 5724–5732. doi: 10.1103/PhysRevB.21.5724

Qu, T., and Boolchand, P. (2005). Shift in elastic phase boundaries due to nanoscale phase separation in network glasses: the case of Ge x As x S1- 2 x. *Philos. Mag.* 85, 875–884. doi: 10.1080/14786304123314636

Raoux, S. (2009). Phase change materials. *Annu. Rev. Mater. Res.* 39, 25–48. doi: 10.1146/annurev-matsci-082908-145405

Ravindren, S., Gunasekera, K., Tucker, Z., Diebold, A., Boolchand, P., and Micoulaut, M. (2014). Crucial effect of melt homogenization on the fragility of non-stoichiometric chalcogenides. *J. Chem. Phys.* 140:134501. doi: 10.1063/1.4869107

Richet, P. (2001). *The Physical Basis of Thermodynamics*. 1st Edn. New York, NY: Springer.

Robie, R. A., and Bethke, P. M. (1962). *Molar Volumes and Densities of Minerals*. Reston, VA: U.S. Geological Survey.

Scopigno, T., Yannopoulos, S. N., Scarponi, F., Andrikopoulos, K. S., Fioretto, D., and Ruocco, G. (2007). Origin of the λ transition in liquid sulfur. *Phys. Rev. Lett.* 99:025701. doi: 10.1103/PhysRevLett.99.025701

Selvanathan, D., Bresser, W. J., Boolchand, P., and Goodman, B. (1999). Thermally reversing window and stiffness transitions in chalcogenide glasses. *Solid State Commun.* 111, 619–624. doi: 10.1016/S0038-1098(99)00248-3

Sundaram, S. K., McCloy, J. S., Riley, B. J., Murphy, M. K., Qiao, H. A., Windisch, C. F., et al. (2011). Gamma radiation effects on physical, optical, and structural properties of binary As-S glasses. *J. Am. Ceramic Soc.* 95, 1048–1055. doi: 10.1111/j.1551-2916.2011.04938.x

Tang, and, S., Karpov, I. V., Dodge, R., Klehn, B., Kalb, J. A., Strand, J., et al. (2009). "A stackable cross point Phase Change Memory," in *2009 IEEE International Electron Devices Meeting* (Baltimore: IEDM), 1–4.

Thomas, L. (2005). *T.A. Instruments. Modulated DSC Technology, Chapters* (New Castle: TA Instruments), 1–9.

Thorpe, M. F. (1985). Rigidity percolation in glassy structures. *J. Non Cryst. Solids* 76, 109–116. doi: 10.1016/0022-3093(85)90056-0

Thorpe, M. F., Jacobs, D. J., Chubynsky, M. V., and Phillips, J. C. (2000). Self-organization in network glasses. *J. Non Cryst. Solids* 266–269, 859–866. doi: 10.1016/S0022-3093(99)00856-X

Tobolsky, A. V., and Eisenberg, A. (1959). Equilibrium polymerization of sulfur. *J. Am. Chem. Soc.* 81, 780–782. doi: 10.1021/ja01513a004

Tremblay, J.-É., Malinowski, M., Richardson, K. A., Fathpour, S., and Wu, M. C. (2018). Picojoule-level octave-spanning supercontinuum generation in chalcogenide waveguides. *Opt. Express* 26:21358. doi: 10.1364/OE.26.021358

Vempati, U. (2005). *Reversibility Windows, Non-aging and Nano Scale Phase Separation Effects in Bulk Germanium-Phosphorus-Sulfide Glasses* (Master's thesis). University of Cincinnati, Cincinnati, OH.

Wagner, T., Kasap, S. O., Vlček, M., Sklenář, A., and Stronski, A. (1998). The structure of As xS100yx glasses studied by temperature-modulated differential scanning calorimetry and Raman spectroscopy. 5, 5581–5588. doi: 10.1016/S0022-3093(98)00194-X

Ward, A. T. (1968). Raman spectroscopy of sulfur, sulfur-selenium, and sulfur-arsenic mixtures. *J. Phys. Chem.* 72, 4133–4139. doi: 10.1021/j100858a031

Williams, M. L., Landel, R. F., and Ferry, J. D. (1955). The temperature dependence of relaxation mechanisms in amorphous polymers and other glass-forming liquids. *J. Am. Chem. Soc.* 77, 3701–3707. doi: 10.1021/ja01619a008

Yamaguchi, M. (1985). The relationship between optical gap and chemical composition in chalcogenide glasses. *Philos. Mag. B* 51, 651–663. doi: 10.1080/13642818508243153

Yan, L. (2018). Entropy favors heterogeneous structures of networks near the rigidity threshold. *Nat. Commun.* 9:1359. doi: 10.1038/s41467-018-03859-9

Zallen, R. (1974). Pressure-Raman effects and vibrational scaling laws in molecular crystals: S 8 and As 2S 3. *Phys. Rev. B* 9, 4485–4496. doi: 10.1103/PhysRevB.9.4485

Zitkovsky, I., and Boolchand, P. (1987). Strucutural ordering As2S3 Bulk glass: role of quench temperature. *Diffusion Defect Data* 53–54, 167–172. doi: 10.4028/www.scientific.net/DDF.53-54.167

Conflict of Interest Statement: The authors declare that the research was conducted in the absence of any commercial or financial relationships that could be construed as a potential conflict of interest.

frontiers in Materials

ORIGINAL RESEARCH
published: 23 July 2019
doi: 10.3389/fmats.2019.00180

Relative Influence of Topology, Dimensionality and Stoichiometry Toward the Properties of Covalent Network Glasses

*Pierre Lucas**

Department of Materials Science and Engineering, University of Arizona, Tucson, AZ, United States

Trends in density and fragility are analyzed in the Ge-As-Se, As-Se, and Ge-Se systems for the purpose of identifying correlations with structural characteristics related to topology, stoichiometry, and dimensionality. The Ge-As-Se system provides the most revealing testbed as it permits to isolate individual effects. The fragility of Ge-As-Se glasses is clearly controlled by stoichiometric factors while the topological transition at $<r> = 2.4$ is not observed in this system. The density of Ge-As-Se glasses broadly increases with average coordination but show two anomalies centered near $<r> = 2.4$ and 2.67. These anomalies merge into a single extremum corresponding to stoichiometric compositions when plotted against excess/deficiency in Se, thereby revealing their common link to stoichiometric factors. Nevertheless, when stoichiometric factors are fixed, dimensional effects are revealed in the form of a linear dependence upon content of tetrahedral Ge. Similarly, a diffuse maximum at the topological transition of $<r> = 2.4$ is observed when only Se-excess compositions are considered. For the As-Se system, a local maximum in fragility is observed at the two dimensional composition As_2Se_3 contrary to predictions from topological or stoichiometric factors, thereby indicating that dimensional effect control the fragile behavior. Finally, in the Ge-Se system, a topological transition associated with balance of constraints and degrees of freedom is found at $<r> = 2.4$ when contributions from stoichiometry, and dimensionality are absent. In all systems, no case is found where topological effects dominate either stoichiometric or dimensional effects, hence it can be concluded that it is the least predominant contribution while stoichiometry is found to be the prevailing effect.

Keywords: chalcogenide glass, density, fragility, stoichiometry, topology, dimensionality

OPEN ACCESS

Edited by:
Matthieu Micoulaut, Sorbonne Universités, France

Reviewed by:
Andriy Kovalskiy, Austin Peay State University, United States
Yong Gyu Choi, Korea Aerospace University, South Korea

***Correspondence:**
Pierre Lucas
pierre@u.arizona.edu

Specialty section:
This article was submitted to Glass Science, a section of the journal Frontiers in Materials

Received: *15 May 2019*
Accepted: *09 July 2019*
Published: *23 July 2019*

Citation:
Lucas P (2019) Relative Influence of Topology, Dimensionality and Stoichiometry Toward the Properties of Covalent Network Glasses. Front. Mater. 6:180. doi: 10.3389/fmats.2019.00180

INTRODUCTION

Chalcogenide glasses have numerous technological applications due to their excellent transparency in the mid-infrared range (Eggleton et al., 2011; Lucas et al., 2013) but they have also been the subject of much interest for investigating structure-property relationships due to the well-defined nature of their covalent networks. In these glassy networks, each atom generates a clear number of covalent bonds following Mott's 8-N rule (Mott and Davis, 1979) where Ge, As and Se are 4-, 3-, and 2-fold coordinated, respectively. This has led to the development of topological theories based on constraint counting arguments where the glass network properties are estimated from the balance

between the number of constraints and degrees of freedom (Phillips, 1979; Thorpe, 1983). Within this conceptual framework, rigidity is expected to percolate through the structure when the average number of bonds per atom (average coordination) is $<r> = 2.4$. Some studies have shown trends in properties that are consistent with this prediction but they are usually limited to small sets of compositions (Tatsumisago et al., 1990; Senapati et al., 1997) and some show significant scattering (Wang et al., 2009). Other studies did not observe the predicted trends (Aitken, 2001; Yang et al., 2012). Nevertheless, topological principles have often remained the dominant theory for describing the physical properties of chalcogenide glasses (Boolchand et al., 2001; Gupta and Mauro, 2009; Zeidler et al., 2017).

Besides topology, other structural characteristics have been suggested to show correlations with trends in physical properties. Zallen first laid out a description of chalcogenide glasses in terms of network dimensionality where he emphasized the correlation between atomic coordination and the dimensionality of the resulting structure, i.e., 3D character for Ge, 2D for As and 1D for Se (Zallen, 1983). Based on these considerations Tanaka suggested that a transition observed at $<r> = 2.67$ in several chalcogenide systems may be dimensional in nature (Tanaka, 1989). Experimental observations of the effect of structural dimensionality have been reported in several systems (Wang et al., 2009; Yang et al., 2012). Another structural characteristic that appears to have a systematic contribution toward physical properties is the stoichiometry i.e., the relative excess or deficiency of selenium (or sulfur) relative to the metal atoms where stoichiometric compositions have exactly one Se(S) atom between each metal atom. Compositions with excess Se(S) link metal atoms with small chains while deficient compositions contain direct metal-metal bonds in large concentrations. These stoichiometric effects were found to be particularly prominent in ternary systems (Wang et al., 2011, 2014; Yang et al., 2015).

This paper collates a large body of data from the literature to assess the relative contribution of these three structural characteristics toward two fundamental physical properties: the density and the fragility. The present study is purposely limited to glassy systems containing only Ge, As, and Se due to the similarity in size and electronegativity of the three component atoms. This way, the relative effects of topology, stoichiometry and dimensionality can be investigated without interference from steric effects due to atomic radii mismatch, bonding effects due electronegativity mismatch, or density variations due to mismatch in molar mass. Indeed, density trends in systems containing heavier atoms such as Ge-As-Te or Ge-Sb-Se would be invariably dominated by the content of the large atoms and would mask other contributions so as to make interpretations ambiguous. Furthermore, chemical order is known to be largely preserved in the three systems under study (Sen and Aitken, 2002; Kaseman et al., 2013; Deschamps et al., 2015) with the unique exception of $GeSe_2$ (Petri et al., 2000). As a consequence, the effect of stoichiometry can be primarily associated with the presence of structural motives such as flexible Se-chains and rigid metal-metal bonds which are expected to influence the physical properties of the glassy network. In that respect the sulfide counterpart systems are also known to satisfy chemical order (Sen et al., 2001), hence it is expected that similar conclusions may apply to these systems as well. This is supported by the observation of identical stoichiometric trends in Ge-As-Se, and Ge-As-S systems (Wang et al., 2014; Yang et al., 2015). Conversely, systems that do not satisfy chemical order such as Ge-As-Te may not follow the same trends.

Accordingly, systems based on Ge, As, and Se provide the least ambiguous test beds for estimating the relative influence of topology, dimensionality, and stoichiometry. Overall it is found that stoichiometry is the dominant contribution followed by dimensionality and finally topology as a minor contribution.

Ge-As-Se SYSTEM

Density

The Ge-As-Se system is often regarded as the ideal test bed for assessing structure-property relationship due to the similarity of the three component atoms (Tatsumisago et al., 1990). In the present work, density is chosen due to the wide availability of experimental data in the literature. While significant variability may be present due to differences in annealing conditions between studies, clear patterns can be observed. In order to minimize such variability only four large data sets were selected including over a 100 compositions and covering the full range of coordination and stoichiometry. Data set from Borissova (Borisova, 1981), Aitken (Aitken, 2001), Wang (Wang et al., 2009, 2011), and Wang (Wang et al., 2017) were used. All these samples were produced by mechanical melt-rocking which has been shown to yield fully homogeneous glasses (Lucas et al., 2019).

As shown in **Figure 1A**, the density of Ge-As-Se glasses generally increases with bond density ($<r>$) but also shows two anomalous extrema, one near 2.4, and one near 2.67. Tanaka (1989) previously suggested that the maximum near 2.4 is topological in nature and is associated with the balance of constraint and degrees of freedom while the minimum near 2.67 is associated with the dimensionality of the glass network. But contrary to previous observation by Tanaka made on a smaller set of compositions (Tanaka, 1989), the two extrema observed here are rather diffuse with significant scattering. This suggests that average coordination alone is too simple a parameter to predict the glass property over wide composition ranges. This in turn suggests that multiple effects may be in competition to determine the glass properties.

Instead, **Figure 1B** plots the density as a function of the stoichiometric contribution defined as the Se excess/deficiency in the glass [as quantified in (Wang et al., 2014)]. Interestingly it is found that the two extrema observed in **Figure 1A** now merge into one, thereby emphasizing the common origin of these anomalies. Indeed, the compositions showing extreme behaviors in **Figure 1A** are the same as in **Figure 1B**. The anomalous behavior can be clearly associated with the stoichiometric compositions where each metal atom is bridge by exactly one Se.

While the merging of the two extrema in **Figure 1A** suggest that Se% may be the most fundamental variable for describing

structure-property relationship in Ge-As-Se glass, the non-monotonous evolution and the remaining scattering clearly indicate that multiple effects are at play in the relationship between structure and properties.

The relative contribution of each effect may be revealed if the contribution from other structural characteristics can be set to fixed values. For example, when the contribution from stoichiometry is neutralized by selecting only compositions at Se% = 0, the effect of network dimensionality can be clearly revealed as depicted in **Figure 2**. The density decreases linearly with Ge content as the network dimensionality increases, despite the concomitant increase in average coordination (**Figure 2**). This is opposite to the general trend observed in **Figure 1A** where density broadly increases with $<r>$. This seemingly inconsistent trend is the direct result of the dominant role of dimensionality effects where the 4-fold Ge atoms create a more open tetrahedral network despite the highest average coordination.

Similarly, if the network coordination if fixed at $<r> = 2.5$, the density shows a single maximum at the stoichiometric composition Se% = 0 (**Figure 3**) instead of the double extremum shown in **Figure 1B**. At this constant value of $<r>$ the contributions of topology and dimensionality are fixed so that the individual contribution of stoichiometry can be revealed. This suggests that stoichiometry tends to maximize density when all other effects are kept constant.

Finally, if the contribution of stoichiometry is minimized by selecting only Se-rich glasses with Se% > 0, the density shows a single maximum at $<r> = 2.4$, although significant scatter is still present as shown in **Figure 4**.

Fragility

The calorimetric fragility of 34 glasses from the Ge-As-Se system was measured by differential scanning calorimetry (DSC) using the Moynihan cool rate method (Wang et al., 2014). The set of compositions cover the whole range of stoichiometry and average coordination. The variation of the fragility index m with stoichiometry and average coordination are shown in **Figures 5A,B**, respectively.

As in the case of density it clearly appears that stoichiometry is a more fundamental determinant of fragility than topological factors. A well-defined minimum in calorimetric fragility is observed at the stoichiometric compositions Se% = 0. In fact, five distinct compositions superimpose at the Se% = 0 with virtually the same value of fragility. Instead, no clear minimum can be observed as function of $<r>$ expect a general basin centered around $<r> = 2.5$. This emphasizes that stoichiometry is clearly the dominant structural feature in controlling the fragile behavior of Ge-As-Se supercooled liquids.

As-Se SYSTEM

Density

The structure of As-Se glasses can be described by the chain-crossing model where chains of selenium are increasingly cross-linked by the trivalent As atoms thereby increasing the dimensionality of the 1D chain structure into a reticulated network of higher dimension (~3D) (Yang et al., 2010; Deschamps et al., 2015). However, at the stoichiometric composition, the structure is composed entirely of $AsSe_3$ trigonal pyramids and forms a layer-like 2D structure reminiscent of the orpiment crystalline phase (Zallen, 1983; Yang et al., 2012). Upon further introduction of As, sharp Raman peaks indicate that As-rich molecular units are precipitating out of the network, reducing the overall reticulation and bringing back the backbone structure to a higher dimension (~3D). At even higher as concentrations, the network eventually collapses as the concentration of 0D molecular units dominates (Yang et al., 2010, 2012).

The contribution of the different structural characteristics is blurred in binary system because they tend to occur at the same composition. In the case of the As-Se system, the topological rigidity transition ($<r> = 2.4$) occurs at the same composition as the stoichiometry As_2Se_3 and as a minimum in dimensionality (2D). The density of As-Se glasses is shown in **Figure 6** as a function of average coordination number $<r>$. A well-defined single minimum is observed at $<r> = 2.4$ which is consistent with the contributions from stoichiometry and

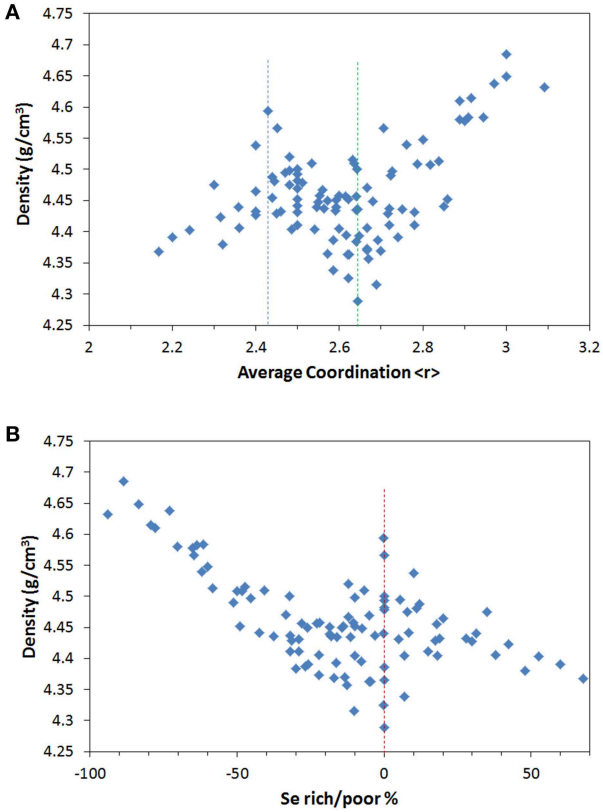

FIGURE 1 | (A) Density of Ge-As-Se glasses as a function of the average coordination number $<r>$. The dashed line indicate the two extrema associated with topological effects near $<r> = 2.4$ and structural dimensionality near $<r> = 2.67$. **(B)** Density of Ge-As-Se glasses as a function of excess/deficiency of Se in the structure. The dashed line indicates the common extremum for stoichiometric composition. Data taken from Borisova (1981), Aitken (2001), Wang et al. (2009), Wang et al. (2011), Wang et al. (2017).

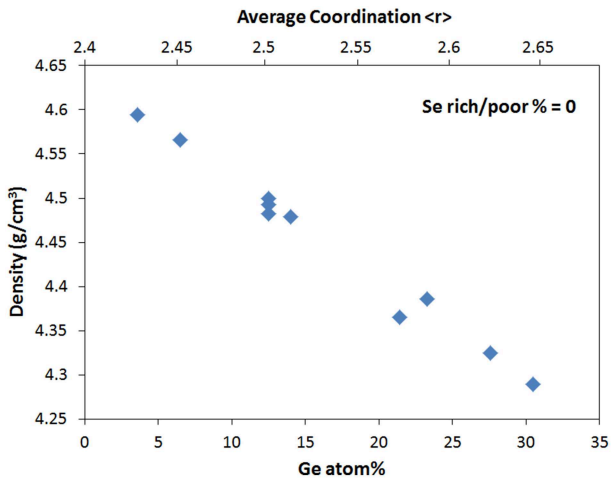

FIGURE 2 | Density of Ge-As-Se glasses with stoichiometric composition (Se rich/poor = 0) as a function of percentage of Ge atoms and average coordination $<r>$. The density varies linearly with Ge% when the effect of stoichiometry is neutralized.

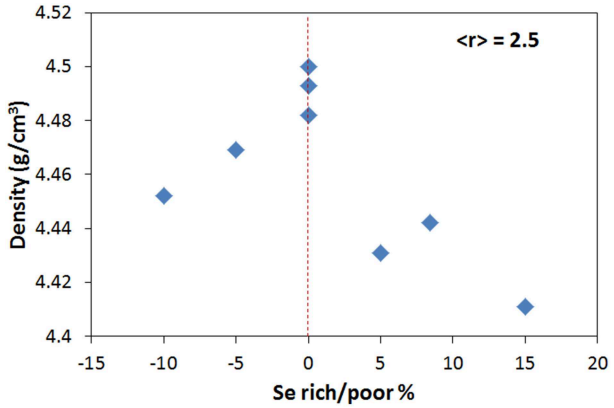

FIGURE 3 | Density of Ge-As-Se glasses with fixed average coordination of $<r> = 2.5$ as a function of excess/deficiency of Se in the structure.

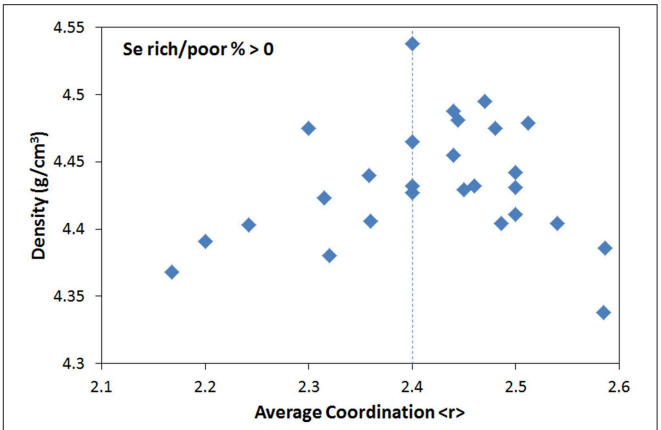

FIGURE 4 | Density of Se-rich Ge-As-Se glasses (Se rich/poor % > 0) as a function of average coordination $<r>$.

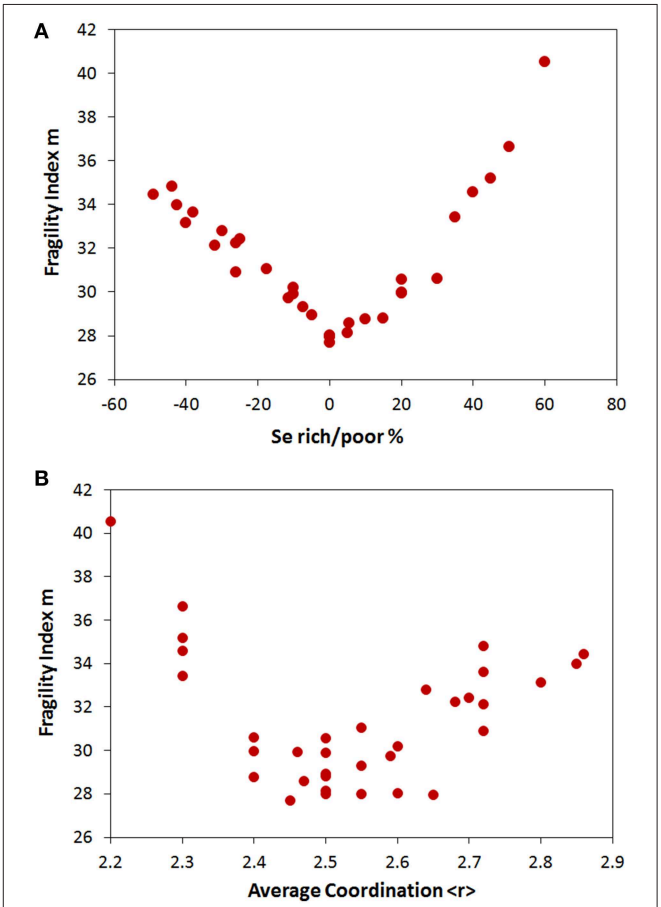

FIGURE 5 | Fragility index *m* of Ge-As-Se glasses as a function of **(A)** excess/deficiency of Se in the structure. **(B)** average coordination $<r>$.

topology observed in **Figures 3**, **4** for the Ge-As-Se system. The dimensionality varies non-monotonically and its contribution to the density appears to be non-dominant.

Fragility

The fragility of glasses from the As-Se system is shown in **Figure 7**. The fragility index is found to change non-monotonically with average coordination $<r>$. The same trend is observed whether the fragility is measured from viscosity, DSC, or modulated DSC (Musgraves et al., 2011; Yang et al., 2012). While the fragility appears to incline toward a minimum at the stoichiometric composition, consistent with **Figure 5A**, the fragility index actually shows a local maximum at the stoichiometry at $<r> = 2.4$. This non-monotonic pattern is not consistent with prediction from either stoichiometric or topological effects. However, it is fully consistent with the evolution of the structural dimensionality in this glass system. This anomaly was actually pointed out by Angell many years ago (Tatsumisago et al., 1990). Fragility is well-known to correlate to structural dimensionality with 3D networks such as silica

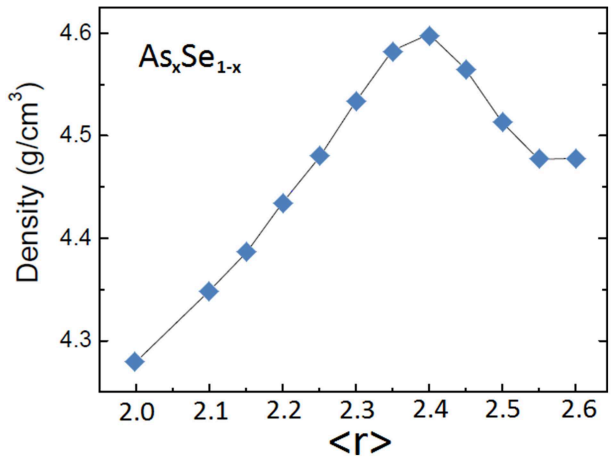

FIGURE 6 | Density of As-Se glasses as a function of average coordination $<r>$. Data from Yang et al. (2010).

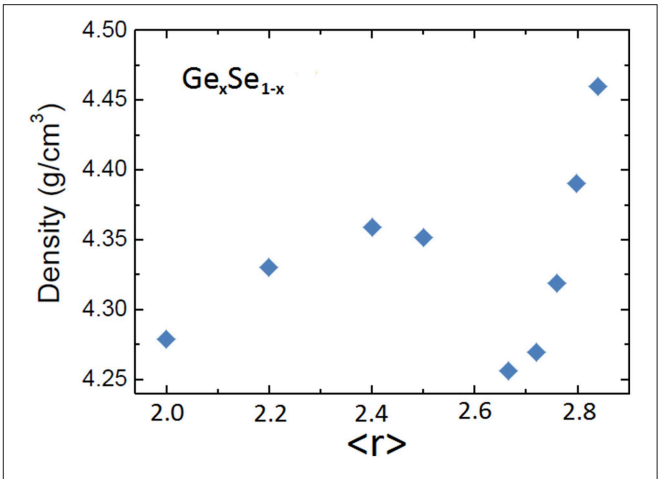

FIGURE 8 | Density of Ge-Se glasses as a function of average coordination $<r>$. Data from Yang et al. (2013).

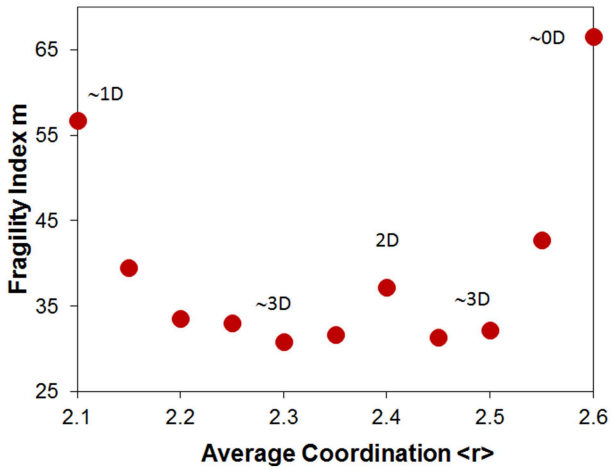

FIGURE 7 | Fragility Index m of glasses from the As-Se system as a function of average coordination $<r>$. Labels identify the dimensionality character of the network. Data from Yang et al. (2012).

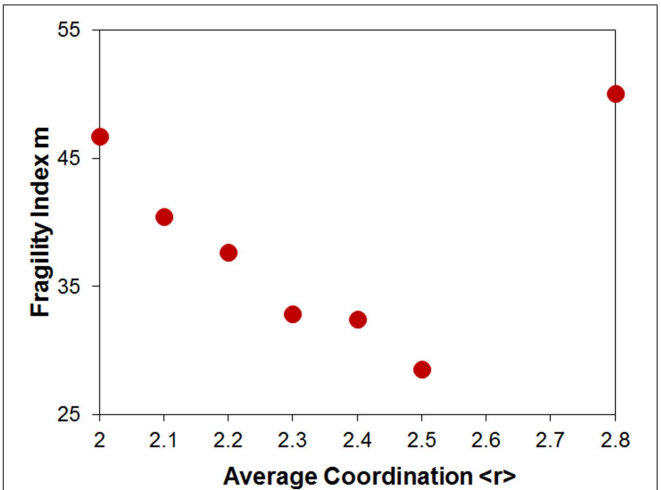

FIGURE 9 | Fragility of Ge-Se glasses as a function of average coordination $<r>$. Data from Senapati and Varshneya (1996). Additional data sets such as that presented in Zeidler et al. (2017) show a collective broad minimum near $<r> = 2.45$.

being the strongest and 0D molecular glasses such as o-terphenyl being the most fragile (Angell, 1991). In the case of As_2Se_3 the sheet structure where layers are only bonded by weak Van der Wall interactions leads to faster collapse of the structure with temperature and a more fragile behavior. Hence, in the case of the As-Se system, dimensionality eventually dominates the fragility behavior.

Ge-Se SYSTEM

Density

Structural effects tend to overlap in the Ge-Se binary in the same way as for As-Se. In the case of Ge-Se, the stoichiometric composition $GeSe_2$ also corresponds to the 3D tetrahedral structure isomorphous of SiO_2. On the other end the topological transition at $<r> = 2.4$ does not overlap with other effects. The density trend shown in **Figure 8** indeed exhibit a maximum near $<r> = 2.4$ which reveals the topological contribution. In the absence of other structural effects, the balance between constraints and degree of freedom can affect the trend in density. The density also shows a sharp minimum at the stoichiometric composition $GeSe_2$ ($<r>$ 2.67). This trend is clearly dominated by structural dimensionality as the glassy network converts to an open tetrahedral framework. The effect of stoichiometry is only a minor contribution in this case.

Fragility

Fragility data derived from viscosity are shown in **Figure 9** for the Ge-Se system (Senapati and Varshneya, 1996). The fragility shows a broad minimum centered near $<r> = 2.5$, however the number of data points in this set is somewhat limited

and broader data sets from the literature have been found to present a collective minimum near $<r> = 2.45$, although they show a considerable amount of scatter (Zeidler et al., 2017). Viscosity data for the stoichiometric composition cannot be obtained as $GeSe_2$ is a poor glass-former that readily crystallizes upon reheating. However, fragility values derived calorimetrically do not indicate any anomalous variation at that composition (Zeidler et al., 2017). Hence the fragility trend appears to be dominated by topological effects.

One point of concern when describing structure-property relationship in the Ge-Se system is the considerable concentration of edge-sharing tetrahedra in the structure, up to ∼35% (Petri et al., 2000; Lucas et al., 2009). This raises concern about the validity of the constraint counting procedure as constraints become interdependent for ring sizes smaller than 6 atoms (Thorpe, 1983). In the case of edge sharing tetrahedra, four member rings would lead to significant overestimates of the number of constraints, and in turn to the actual position of the rigidity transition. But more importantly, this structural segregation leads to very distinct dynamics of the different structural units upon reheating (Lucas et al., 2009; Gjersing et al., 2010) which should have a direct implication to the fragility behavior. This further complicates any structural interpretation of the supercooled liquid behavior in the Ge-Se system.

CONCLUSION

Experimental data for over a 100 glass compositions in the Ge-As-Se as well as As-Se and Ge-Se systems were analyzed to investigate correlations between trends in physical properties and the three structural characteristics: topology, dimensionality and stoichiometry. Two fundamental physical properties were selected for each system: the density for the glassy state and the fragility for the supercooled liquid state. Stoichiometry, i.e., the relative excess or deficiency of selenium relative to the metal atoms is found to be the most universal indicator of physical properties although structural dimensionality can also be a dominating factor. Topological effects based on constraint counting arguments are found to play a minor role and their contribution can only be observed in Se-rich composition when stoichiometric and dimensional effects are absent. This is the case in the Ge-Se system where the fragility exhibits a broad minimum near $<r> = 2.45$ (Zeidler et al., 2017). Sulfide systems that also satisfy chemical order are expected to follow the same trends, as suggested by a previous study (Yang et al., 2015). However, it is not clear that these trends will apply to systems known to violate chemical order such as Ge-As-Te.

DATA AVAILABILITY

This data can be found in the references provided in the manuscript.

AUTHOR CONTRIBUTIONS

PL wrote this manuscript based on an original analysis of literature data.

FUNDING

PL acknowledge financial support from NSF-DMR under grant #: 1832817.

REFERENCES

Aitken, B. G. (2001). "Structure-property relationships in Ge-As selenide and sulphide glasses," in *Proceedings of the International Congress on Glass*, Vol. 1 (Edinburgh).

Angell, C. A. (1991). Relaxation in liquids, polymers and plastic crystals - strong/fragile patterns and problems. *J. Non Cryst. Solids*. 131–133, 13–31. doi: 10.1016/0022-3093(91)90266-9

Boolchand, P., Feng, X., and Bresser, W. J. (2001). Rigidity transitions in binary Ge-Se glasses and the intermediate phase. *J. Non Cryst. Solids*. 293–295, 348–356. doi: 10.1016/S0022-3093(01)00867-5

Borisova, Z. U. (1981). *Glassy Semiconductors*. New York, NY: Plenum Press.

Deschamps, M., Genevois, C., Cui, S., Roiland, C., LePolles, L., Furet, E., et al. (2015). Structure of arsenic selenide glasses studied by NMR: selenium chain length distributions and the flory model. *J. Phys. Chem. C*. 119, 11852–11857. doi: 10.1021/acs.jpcc.5b02423

Eggleton, B. J., Luther-Davies, B., and Richardson, K. (2011). Chalcogenide photonics. *Nat. Photonics*. 5, 141–148. doi: 10.1038/nphoton.2011.309

Gjersing, E. L., Sen, S., and Youngman, R. E. (2010). Mechanistic understanding of the effect of rigidity percolation on structural relaxation in supercooled germanium selenide liquids. *Phys. Rev. B Condens. Matter Mater. Phys.* 82:014203. doi: 10.1103/PhysRevB.82.014203

Gupta, P. K., and Mauro, J. C. (2009). Composition dependence of glass transition temperature and fragility. i. a topological model incorporating temperature-dependent constraints. *J. Chem. Phys*. 130:094503. doi: 10.1063/1.3077168

Kaseman, D. C., Hung, I., Gan, Z., and Sen, S. (2013). Observation of a continuous random network structure in Ge(x)Se(100-x) glasses: results from high-resolution 77Se MATPASS/CPMG NMR spectroscopy. *J. Phys. Chem. B*. 117, 949–954. doi: 10.1021/jp311320t

Lucas, P., Coleman, G. J., Sen, S., Cui, S., Guimond, Y., Calvez, L., et al. (2019). Structural and chemical homogeneity of chalcogenide glass prepared by melt-rocking. *J. Chem. Phys*. 150:014505. doi: 10.1063/1.5054704

Lucas, P., King, E. A., Gulbiten, O., Yarger, J. L., Soignard, E., and Bureau, B. (2009). Bimodal phase percolation model for the structure of Ge-Se glasses and the existence of the intermediate phase. *Phys. Rev. B: Condens. Matter* 80:214114. doi: 10.1103/PhysRevB.80.214114

Lucas, P., Yang, Z., Fah, M. K., Luo, T., Jiang, S., Boussard-Pledel, C. (2013). Telluride glasses for far infrared photonic applications. *Opt. Mater. Express*. 3, 1049–1058. doi: 10.1364/OME.3.001049

Mott, N. F., and Davis, E. A. (1979). *Electronic Processes in Non-Crystalline Materials*. Oxford: Clarendon Press.

Musgraves, J. D., Wachtel, P., Novak, S., Wilkinson, J., and Richardson, K. (2011). Composition dependence of the viscosity and other physical properties in the arsenic selenide glass system. *J. Appl. Phys*. 110:063503. doi: 10.1063/1.3638122

Petri, I., Salmon, P. S., and Fischer, H. E. (2000). Defects in a disordered world: the structure of glassy $GeSe_2$. *Phys. Rev. Lett*. 84, 2413–2416. doi: 10.1103/PhysRevLett.84.2413

Phillips, J. C. (1979). Topology of covalent non-crystalline solids. i. short-range order in chalcogenide alloys. *J. Non Cryst. Solids*. 34, 153–181. doi: 10.1016/0022-3093(79)90033-4

Sen, S., and Aitken, B. G. (2002). Atomic structure and chemical order in Ge-As selenide and sulfoselenide glasses: an x-ray absorption fine structure spectroscopic study. *Phys. Rev. B Condens. Matter* 66:134204. doi: 10.1103/PhysRevB.66.134204

Sen, S., Ponader, C., W., and Aitken, B. G. (2001). Ge and As x-ray absorption fine structure spectroscopic study of homopolar bonding, chemical order, and topology in Ge-As-S chalcogenide glasses. *Phys. Rev. B*. 64:104202. doi: 10.1103/PhysRevB.64.104202

Senapati, U., Firstenberg, K., and Varshneya, A. K. (1997). Structure-property inter-relations in chalcogenide glasses and their practical implications. *J. Non Cryst. Solids*. 222, 153–159. doi: 10.1016/S0022-3093(97)00394-3

Senapati, U., and Varshneya, A. K. (1996). Viscosity of chalcogenide glass-forming liquids: an anomaly in the 'strong' and 'fragile' classification. *J. Non Cryst. Solids*. 197, 210–218. doi: 10.1016/0022-3093(95)00628-1

Tanaka, K. (1989). Structural phase transitions in chalcogenide glasses. *Phys. Rev. B Condens. Matter*. 39, 1270–1279. doi: 10.1103/PhysRevB.39.1270

Tatsumisago, M., Halfpap, B. L., Green, J. L., Lindsay, S. M., and Angell, C. A. (1990). Fragility of germanium-arsenic-selenium glass-forming liquids in relation to rigidity percolation, and the kauzmann paradox. *Phys. Rev. Lett*. 64, 1549–1552. doi: 10.1103/PhysRevLett.64.1549

Thorpe, M. F. (1983). Continuous deformations in random networks. *J. Non Cryst. Solids*. 57, 355–370. doi: 10.1016/0022-3093(83)90424-6

Wang, R. P., Bulla, D., Smith, A., Wang, T., and Luther-Davies, B. (2011). Structure and physical properties of GexAsySe1-x-y glasses with the same mean coordination number of 2.5. *J. Appl. Phys*. 109:023517. doi: 10.1063/1.3544309

Wang, R. P., Smith, A., Luther-Davies, B., Kokkonen, H., and Jackson, I. (2009). Observation of two elastic thresholds in GexAsySe1-x-y glasses. *J. Appl. Phys*. 105:056109. doi: 10.1063/1.3079806

Wang, T., Gulbiten, O., Wang, R., Yang, Z., Smith, A., Luther-Davies, B., et al. (2014). Relative contribution of stoichiometry and mean coordination to the fragility of Ge-As-Se glass forming liquids. *J. Phys. Chem. B*. 118, 1436–1442. doi: 10.1021/jp412226w

Wang, Y., Qi, S., Yang, Z., Wang, R., Yang, A., and Lucas, P. (2017). Composition dependences of refractive index and thermo-optic coefficient in Ge-As-Se chalcogenide glasses. *J. Non Cryst. Solids*. 459, 88–93. doi: 10.1016/j.jnoncrysol.2017.01.004

Yang, G., Bureau, B., Rouxel, T., Gueguen, Y., Gulbiten, O., Roiland, C. et al. (2010). Correlation between structure and physical properties of chalcogenide glasses in the AsxSe1-x system. *Phys. Rev. B Condens. Matter*. 82:195206. doi: 10.1103/PhysRevB.82.195206

Yang, G., Gueguen, Y., Sangleboeuf, J.-C., Rouxel, T., Boussard-Pledel, C., Troles, J., et al. (2013). Physical properties of the GexSe1-x glasses in the $0 < x < 0.42$ range in correlation with their structure. *J. Non Cryst. Solids*. 377, 54–59. doi: 10.1016/j.jnoncrysol.2013.01.049

Yang, G., Gulbiten, O., Gueguen, Y., Bureau, B., Sangleboeuf, J.-C., Roiland, C., et al. (2012). Fragile-strong behavior in the As_xSe_{1-x} glass forming system in relation to structural dimensionality. *Phys Rev. B Condens. Matter* 85:144107. doi: 10.1103/PhysRevB.85.144107

Yang, Y., Zhang, B., Yang, A., Yang, Z., and Lucas, P. (2015). Structural origin of fragility in Ge-As-S glasses investigated by calorimetry and raman spectroscopy. *J. Phys. Chem. B*. 119, 5096–5101. doi: 10.1021/acs.jpcb.5b01768

Zallen, R. (1983). *The Physics of Amorphous Solids*. Weinheim: John Wiley and Sons.

Zeidler, A., Salmon, P. S., Whittaker, D. A. J., Pizzey, K. J., and Hannon, A. C. (2017). Topological ordering and viscosity in the glass-forming Ge–Se system: the search for a structural or dynamical signature of the intermediate phase. *Front. Mater.* 4:32. doi: 10.3389/fmats.2017.00032

Conflict of Interest Statement: The author declares that the research was conducted in the absence of any commercial or financial relationships that could be construed as a potential conflict of interest.

frontiers in Materials

ORIGINAL RESEARCH
published: 24 July 2019
doi: 10.3389/fmats.2019.00173

Evidence for a Correlation of Melt Fragility Index With Topological Phases of Multicomponent Glasses

*Ralph Chbeir[1], Mathieu Bauchy[2], Matthieu Micoulaut[3] and Punit Boolchand[1]**

[1] Department of Electrical Engineering and Computer Science, University of Cincinnati, Cincinnati, OH, United States, [2] Physics of AmoRphous and Inorganic Solids Laboratory (PARISlab), Department of Civil and Environmental Engineering, University of California, Los Angeles, Los Angeles, CA, United States, [3] Sorbonne Université, CNRS UMR 7600, Laboratoire de Physique Théorique de la Matière Condensée, Paris, France

Scores of glass compositions in the equimolar $Ge_xAs_xSe_{100-2x}$ ternary system are synthesized across the $0 < x < 26\%$ range, and their homogeneity tracked by *ex-situ* Raman profiling. In synthesis, we alloyed the starting materials to homogenize until the variance, $<\Delta x>_{Ge}$, in Ge content "x," across a 1.5-g sized batch composition of $<0.01\%$ was realized. We undertook Modulated-DSC, Raman scattering, and molar volume experiments as a function of composition. Trends in $T_g(x)$ increase monotonically with x over the examined range, but the non-reversing enthalpy of relaxation at T_g, $\Delta H_{nr}(x)$, displays a sharp square-well like reversibility window over the $9.5(2)\% < x < 17.0(2)\%$ range even in rejuvenated glasses. Trends in melt fragility index, m(x), established by measuring the T-dependence of the enthalpy relaxation time across T_g, show a Gaussian-like variation with $m(x) < 20$ in the $9.5(2)\% < x < 17.0(2)\%$ range, and $m > 20$ outside that range, thus establishing a fragility window. The close correlation between the variations of m(x) and $\Delta H_{nr}(x)$ underscores that super-strong melts formed in the fragility window form Intermediate Phase (IP) glasses in the reversibility window, while fragile melts formed at non-IP compositions give rise to either flexible or stressed-rigid glasses. Molar volumes of glasses reveal a global reduction for IP glass compositions, thereby underscoring the compacted nature of the isostatically rigid networks formed in that phase. Evidence for specific dynamic features of the different phases is provided by molecular dynamics simulations, which indicate that the diffusivity is minuscule for $x > 17\%$ and increases substantially in the flexible phase. These results show that liquid dynamics and fragility encode glass topological phases in this ternary chalcogenide. The optimization of the glass-forming tendency for IP compositions, the stress-free nature of these networks, and the qualitative suppression of aging, are features that all point to their ideal nature. These ideas of IP glasses as ideal glasses are at variance with the notion that ideal glasses possess a low configurational entropy and form at T_g values that approach the Kauzmann temperature. IP networks display, adaptability, high glass-forming tendency, stress-free nature, and high configurational entropy of networks.

Keywords: modulated DSC (MDSC), Raman scattering, topological constraint theory (TCT), molar volume, ^{129}I Mössbauer spectroscopy, fragility index, enthalpy of relaxation at T_g, melt homogenization

OPEN ACCESS

Edited by:
Joachim Deubener, Clausthal University of Technology, Germany

Reviewed by:
Jean-Marc Delaye, Commissariat à l'Energie Atomique et aux Energies Alternatives (CEA), France
Sindy Fuhrmann, Friedrich Schiller University Jena, Germany

****Correspondence:***
Punit Boolchand
boolchp@ucmail.uc.edu

Specialty section:
This article was submitted to Glass Science, a section of the journal Frontiers in Materials

Received: *09 April 2019*
Accepted: *04 July 2019*
Published: *24 July 2019*

Citation:
Chbeir R, Bauchy M, Micoulaut M and Boolchand P (2019) Evidence for a Correlation of Melt Fragility Index With Topological Phases of Multicomponent Glasses. Front. Mater. 6:173. doi: 10.3389/fmats.2019.00173

INTRODUCTION

Chalcogenide glasses have served as useful test laboratory to examine the predictions of Topological Constraint Theory (TCT) since the theory was first introduced (Phillips, 1979) in 1979 and its vibrational consequences elucidated by M.F. Thorpe (Thorpe, 1983) in 1983. Chalcogenides have also emerged as the materials of choice for 3D-X-point memory devices(Intel[1]; Malventano[2]; Tang et al., 2009), phase-change memory (Raoux and Wuttig, 2009), Continuum emission in the IR (Goncalves et al., 2018; Tremblay et al., 2018), optical fibers, and waveguides (Tang et al., 2015; Chen et al., 2019). The interplay between these applications and underlying basic science including topological phases (TP) now offers new prospects to tune material functionality with applications.

Amongst the chalcogenides, and particularly within the context of TCT, binary Ge_xSe_{100-x} glasses have acquired much notoriety starting from the mid-1980s. Inelastic neutron scattering experiments revealed a low frequency mode near 5 meV (Boolchand et al., 1990; Kamitakahara et al., 1991) and one found that the fractional scattering strength of the mode normalized to the total vibrational density of states acquires a value of nearly 1/3 in pure Se as $x \rightarrow 0$. The result gives confirmation of the floppy mode concept that Thorpe introduced (Thorpe, 1983) to establish the percolation of rigidity near $<r> = 2.40$. This indicates that the elastic phase transition is driven by a control parameter $<r>$, whereas the density of low frequency modes represents the order parameter of the transition. The presence of these low frequency excitations led the ^{119}Sn Mössbauer Debye-Waller factors in Ge_xSe_{100-x} glasses to display a giant softening as $x \rightarrow 0$. This follows because the mean-square displacement ($<r^2>$) relates to the first inverse moment of the vibrational density of states. Measurements of ^{119}Sn mean-square displacement, $<r^2>$ as a function of Ge content x, show a vibrational threshold near $x = 20.0\%$, or $<r>$ of 2.40, in harmony with the notion of percolation of rigidity (Boolchand et al., 1990). And the connection of such floppy modes has been linked to the energy landscape in glasses (Naumis, 2005).

Crucial insights into the molecular structure of binary Ge_xSe_{100-x} glasses emerged from Mössbauer spectroscopy (Bresser et al., 1981; Boolchand et al., 1982; Boolchand, 1985; Boolchand and Bresser, 2000) using both ^{119}Sn absorption and ^{129}I emission spectroscopy. These experiments performed in the $31.5\% < x < 33.3\%$ composition range showed that glassy networks undergo a nanoscale phase separation (NSPS) transition near $x = 31.5\%$ into characteristic Ge-rich and Se-rich clusters, resulting in a 2% concentration of homopolar (Ge-Ge, and Se-Se) bonds in the stoichiometric glass at $x = 33.3\%$ ($GeSe_2$) (Salmon and Petri, 2003; Salmon, 2007). Such NSPS was later confirmed in Calorimetric and Raman scattering measurements on homogeneous glasses (Bhosle et al., 2012b). In these Mössbauer Effect experiments since tracers (^{119}Sn, ^{129m}Te) were doped in a base glass, batch compositions necessarily had to be kept rather small, <¼ g, and the issue of glass heterogeneity was never in doubt.

A significant step forward in the field was the observation of a reversibility window in binary Si_xSe_{100-x} glasses (Selvanathan et al., 1999). In MDSC one observes the enthalpy of relaxation at T_g to show a square-well like minimum (reversibility window), with the walls of the window. Such walls have been identified in a variety of theoretical models as a rigidity and a stress transition (Thorpe et al., 2000; Micoulaut and Phillips, 2003; Barré et al., 2005; Chubynsky et al., 2006). The first transition near $x = 20\%$ ($<r> = 2.40$), the rigidity transition, is followed by the second transition near $x = 27\%$ ($<r> = 2.54$), the stress transition (Thorpe et al., 2000). And it was not until 2010 (Micoulaut, 2010) that one recognized that the near vanishing of the enthalpy of relaxation in the reversibility window constituted a signature of the isostatically rigid nature of glassy networks ($n_c = 3$) formed between the two elastic phase transitions. Such reversibility windows have now been documented in several scores of glasses (Yildirim et al., 2016b), unequivocally demonstrating the generality of the three topological phases, flexible-, intermediate, and stressed-rigid.

As larger batch sizes (2–20 g) of the chalcogenides were synthesized, it emerged in 2011 that such melts undergo delayed homogenization (Bhosle et al., 2012b; Chakraborty and Boolchand, 2014; Ravindren et al., 2014). The behavior can now be traced to the super-strong behavior of Intermediate Phase (IP) melts formed in these binary glass systems. The present equimolar Ge-As-Se ternary drew our attention for two reasons. Although MDSC and Raman scattering results did reveal (Qu et al., 2002) evidence of a reversibility window, the glass samples synthesized in 2002, were not homogeneous, a recognition that emerged only later in 2011. The second reason came from the recognition that the glass transition temperature $T_g(x)$ displayed an almost linear variation with x, even when x exceeded the chemical threshold near $x_c = 18.18\%$. Such is not the case in several binary Selenide and Sulfide glasses such as Ge-Se (or S), and As-Se (or S) where a T_g maximum occurs near the chemical thresholds. The observation suggested (Boolchand et al., 2002) that fully polymerized glassy networks must apparently exist in the $Ge_xAs_xSe_{100-2x}$ ternary over a rather wide range of stoichiometry, $0 < x < 26\%$. That feature of the ternary was appealing (Qu et al., 2002; Qu, 2004), as it suggested the absence of any NSPS at compositions exceeding the chemical threshold. Thus, probing the nature of the topological phases, and especially the underlying rigidity- and stress- elastic phase transitions that separate these phases would be immune from effects due to NSPS.

The finding of delayed homogenization of binary Ge-Se melts/glasses was a strong impetus to re-examine the TPs in the present $Ge_xAs_xSe_{100-2x}$ ternary, and to clarify the role of glass synthesis in relation to the sharpness of the rigidity- and stress-elastic phase transitions that border the Intermediate Phase (IP). The second goal of the present work was to also measure the variation of fragility index in such homogenized melts and to explore if trends in melt dynamics have a bearing on the nature of the glass TPs.

[1] *Intel 3D XPointTM: A Breakthrough in Non-Volatile Memory Technology*. Intel. Available online at: https://www.intel.com/content/www/us/en/architecture-and-technology/intel-micron-3d-xpoint-webcast.html (accessed February 14, 2019).

[2] Malventano, A. *How 3D XPoint Phase-Change Memory Works*. Available online at: https://www.pcper.com/reviews/Editorial/How-3D-XPoint-Phase-Change-Memory-Works

In the present work we report observing a rather abrupt *thermally reversing window* that is square-well-like in nature even in freshly quenched glasses after rejuvenation (T_g cycling) of the especially homogenized $Ge_xAs_xSe_{100-2x}$ ternary glasses. Furthermore, we also examined the variation of fragility index (m(x)), and find evidence of a compositional range across which $m < 20$, which defines the "*fragility window*." Remarkably, the compositional width of the "*fragility window*" observed not only coincides with that of the "*reversibility window,*" but both are somewhat wider in range, $9.5\% < x < 17.0\%$, than the previous report (Qu et al., 2002; Qu, 2004). These experimentally measured anomalies are correlated with dynamic anomalies calculated from molecular dynamics simulations and a huge increase in diffusivity is detected once the glass-forming liquids become flexible.

Why is the homogeneity of a melt/glass so critical to examining topological phases? Previous molecular dynamics simulations have shown that the reversibility window arises from the fact that the flexible-to-rigid and unstressed-to-stressed transitions occur at different compositional thresholds, thereby giving birth to an intermediate phase that is rigid but free of stress (Bauchy, 2019). These two elastic transitions have been shown to be percolative in character (Jacobs and Thorpe, 1995; Thorpe et al., 2000) and, hence, one expects these transitions, in principle, to be intrinsically sharp in the composition space. In binary Ge_xSe_{100-x} glasses, for example, the network connectivity is determined locally by the Ge fraction x. If the variance in Ge stoichiometry "$<\Delta x>_{Ge}$" across a glass specimen were to exceed 1%, one can expect the two elastic phase transitions to be smeared. That is exactly what we observed in our experiments on the $Ge_xAs_xSe_{100-2x}$ ternary in 2003. If the variance in Ge stoichiometry exceeded 3%, the reversibility window could be triangular (Bhosle et al., 2012b) or, worse yet, the window may not be observed. On the other hand, if the variance in Ge stoichiometry is <0.01%, as noted in the present work, one expects and, indeed, observes rather sharp rigidity- and stress-transitions. And, ideally, one would like to establish the Ge variance on an atomic scale. As a practical matter it should be at least on a scale of 50 microns, if not lower. The observation of abrupt elastic phase transitions in a topologically disordered network is not only novel and exciting but also constitutes evidence of the percolative nature of these elastic phase transitions.

MATERIALS AND METHODS

Synthesis of Glasses, and Characterization of Their Homogeneity by *ex situ* Ft-Raman Profiling

The starting materials for the synthesis included small pieces (∼ 3 mm in diameter) of 99.999% pure Se nodules from Alfa Aesar, 99.999% pure Ge lumps from Alfa Aesar and stoichiometric As_2Se_3 from Noah Technologies. We handled these materials in a model HE-493/MO-5 Glove box from Vacuum Atmospheres, which is designed to be flushed with dry N_2 gas continuously and with a relative humidity of <0.01%. We sealed small pieces of the starting materials of about 3 mm in size or less, in the desired weight ratio, in evacuated quartz tubes of 5 mm ID and 1 mm wall thickness. Prior to their use, we dried quartz tubes in a vacuum oven at 80°C for at least 24 h. Batch size were kept at 1.5 g, and the starting materials encapsulated in evacuated quartz tubes at a pressure of 2×10^{-7} Torr using a liquid Nitrogen trapped diffusion pump system. We heated quartz tubes to 950°C for typically 10 days, keeping them vertical in a box furnace. Water impurity doping of chalcogenide glasses, unwittingly assists homogenization of melts, increases the enthalpy of relaxation of glasses, decreases T_g, and increases the fragility index of melts (Bhosle et al., 2012a,b). These extrinsic features are not representative of the dry melts/glasses.

A Thermo-Nicolet Nexus 870 based FT-Raman system, using 1,064 nm radiation from a Nd-YAG laser, focused to a 50 μm spot size (micro-setting), was used to excite the scattering. The collection optics also has provision for a macro-setting with a laser spot size of 1 mm. Glass specimen wetting 5 mm ID evacuated quartz tubes were mounted on a digitally controlled x-y-z stage to focus the laser beam entering along the quartz tube diameter (x-axis adjustment) and onto the quartz tube glass specimen interface (z-axis adjustment) to optimize the signal. The y-axis adjustment of the sample stage permitted to access specific locations along the glass column for recording Raman scattering. Spectra were acquired at typically six locations about 2 mm apart along the glass specimen column of typically 20 mm in length (y-axis adjustment). The software permits comparing observed lineshapes normalized to the highest scattering strength mode, and that facilitated directly variations in glass specimen stoichiometry by comparing the scattering strength of the corner sharing (CS) of $GeSe_4$ tetrahedra (near 200 cm^{-1}) with the broad band of a triad of modes (Dash et al., 2017) associated with Se_n chains-uncorrelated, Se_n chain-correlated, and Se_8 rings (near 250 cm^{-1}). Periodically, quartz tubes were water quenched after lowering their T to 650°C and Raman spectra taken at 6 locations along the 20 mm long melt column. By using a laser beam spot size of 50 μm or less, one probes glass homogeneity to a finer scale, which is essential to get a true representation of glass/melt homogeneity. It is important to emphasize that in these homogeneity studies the full batch composition was profiled. This of course is necessary since the stoichiometry of a small part of the batch is tied to the stoichiometry of the rest of the batch (Gunasekera et al., 2013). **Figure 1** shows a partial summary of the observed spectra; and one finds how the starting melt, which is rich in Ge(Se) atoms at the bottom(top) of the vertical melt column, steadily homogenizes as Ge atoms diffuse up while Se atoms diffuse down the melt column. After 2 days of alloying the variance in Ge stoichiometry, $<\Delta x>_{Ge}$ is found to be about 1.04%, but it systematically decreased by almost three orders of magnitude to nearly 0.01 % or lower after 10.5 days of alloying (**Figure 2**). In these profiling experiments, one could successfully decode the heterogeneity of the batch to a level of 0.01% range in the variance of Ge by merely sampling only a tiny volume fraction of 2% of the batch column. The existence of a gravitationally induced segregation that sets up in the melt column at the beginning of the alloying process as quartz tubes are held vertical, aids in tracking how Ge- and Se-atoms, respectively, diffuse the melt column (Gunasekera et al., 2013) to homogenize with no rocking. Had we rocked the melt column it

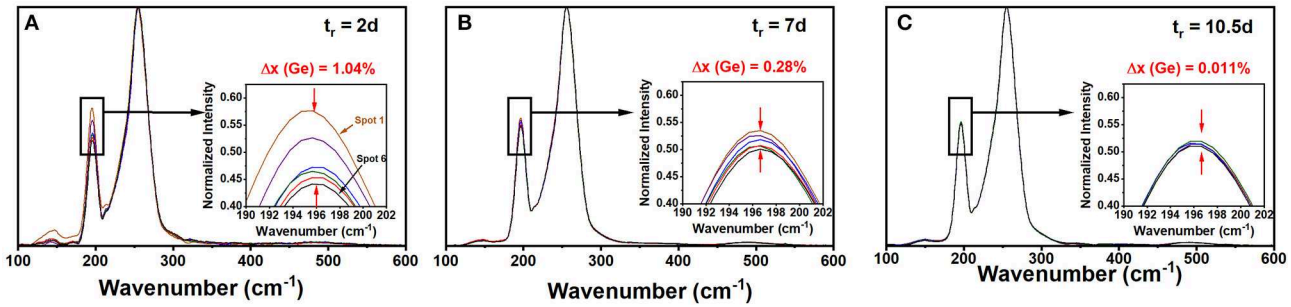

FIGURE 1 | FT-Raman spectra of a $Ge_9As_9Se_{82}$ glass composition profiled after being alloyed at 950°C in **(A)** 2d, in **(B)** 7d, and in **(C)** 10.5 d. The variance $<\Delta x>_{Ge}$ in Ge concentration "x" across the batch decreased from 1.04(5) to 0.28(5) to < 0.05% upon progressive alloying as revealed by the spread in the normalized scattering strength of the Corner-Sharing mode near 200 cm^{-1} in insets. The Omnic software normalizes each spectrum to the most intense peak near 250 cm^{-1} coming from polymeric Se_n chains. The $<\Delta x>_{Ge}$ variance is being probed on a 50 micron scale set by the laser-spot size.

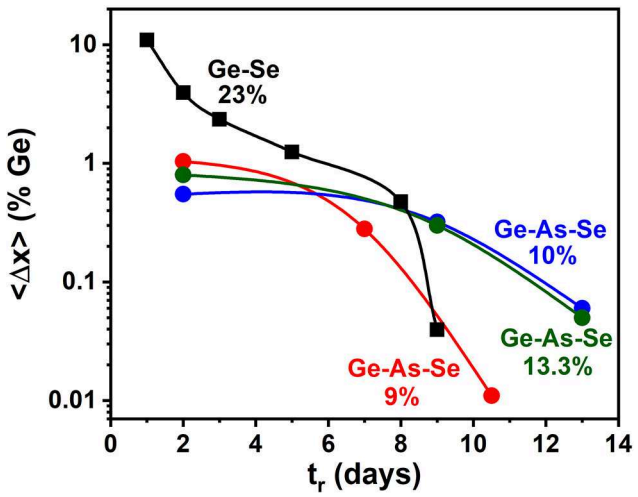

FIGURE 2 | Observed reduction in the Ge variance $<\Delta x>_{Ge}$ of the $Ge_xAs_xSe_{100-2x}$ glasses as a function of alloying time t_r in days at indicated compositions x when probed at a 50 μm resolution determined by the laser spot size. Glass homogeneity steadily increases as $<\Delta x>_{Ge}$ decreases by almost two orders of magnitude upon alloying the starting materials for typically 10–13 days. We show that delayed homogenization is tied to the Super-strong character of melts in the 9.5% < *x* < 17% range, the Intermediate Phase.

would have been difficult to detect the isolated super-strong melt inclusions spread across the melt column unless one probed more like 10–30% or more of the batch volume, which surely would have been an enormous task in itself.

There are other aspects of the homogenization studies that we mention in passing. The scale on which a batch is examined in the Raman profiling experiments matters because TPs are determined by atomic scale network connectivity or mean coordination number <r>, fixed by the local Ge, As, and Se stoichiometry. Furthermore, the scale on which a batch is examined in the Raman profiling experiments matters. A sample may be homogeneous after 2 days of alloying on a spatial scale of 1 mm (laser spot size) but not on a finer scale of 50 μm (laser spot size) as we have noted (Bhosle et al., 2012a). Finally, melt homogenization kinetics are broadly determined by the slowest diffusing species or the species with the highest viscosity, which occurs in the IP. Most compositions in the $Ge_xAs_xSe_{100-2x}$ ternary, at x > 5%, take typically 7–11 days to homogenize in our chosen geometry. The IP compositions such as x = 10 and 13.3% take a few days longer to homogenize than non-IP ones. The fragility index of IP melts apparently controls the kinetics of melt homogenization, as we will comment later in discussion of results. In very select cases where a stoichiometric glass is being synthesized at a composition where there exists a distinct well-defined underlying simple crystalline phase, delayed homogenization could be circumvented. In the present ternary, we are unaware of any crystalline phase or phases that occur and that may expedite the homogenization process.

Finally, in our present efforts we aimed to synthesize the most homogeneous melts to explore the physics of TPs in network glasses. Once these fundamental issues are understood, new strategies can be implemented to reduce the alloying time of glass synthesis by at least an order of magnitude to achieve homogeneous melts/glasses.

Modulated-DSC as a Probe of the Enthalpy of Relaxation of Glasses at T_g and the Fragility Index of Melts

Modulated Differential Scanning Calorimetry (MDSC) has proven to be a reliable (Thomas, 2005; Bhosle et al., 2012b) and rather direct means to independently establish the glass transition temperature T_g, and the modulation frequency corrected enthalpy of relaxation of a glass at T_g (ΔH_{nr}) with minimal scanning-rate-related kinetic upshifts. The procedure for obtaining the frequency corrected enthalpy of relaxation was developed as early as in 1995 by Len Thomas (Thomas, 2005), and more recently confirmed in numerical simulations (Guo et al., 2012). The measured ΔH_{nr} term is a pivotal calorimetric observable of a glass, that characterizes not merely its non-ergodic state but is crucially linked to the flexibility and rigidity of networks (Micoulaut, 2010) provided these are dry and homogenous. Furthermore, MDSC also permits measuring the fragility index "m," of a melt. We illustrate the

principles of both these methods by showing results of ternary $Ge_xAs_xSe_{100-2x}$ glasses at select compositions. We used a Q2000 TA Instruments MDSC with glass samples in hermetically sealed T_{zero} Al pans (Thomas, 2005) to achieve the best baselines in the calorimetric scans.

Enthalpy of Relaxation of a Glass at T_g

A significant advance in understanding the nature of T_g in network glasses has emerged from the use of MDSC over the traditional DSC (Bhosle et al., 2012a,b; Gunasekera et al., 2013). In this approach, one programs a sinusoidal temperature variation on a linear T- ramp, to extract the part of the total heat flow that tracks the sinusoidal oscillations, called the reversing heat flow, and then obtain from them the difference signal between the total heat flow and the reversing heat flow, the non-reversing heat flow. Experiments reveal that the reversing heat flow shows a rounded step (shown in blue), while the non-reversing heat flow, shows a Gaussian-like peak (shown in red) that relates to the overshoot observed in the total heat flow (shown in green) as illustrated in **Figure 3** for the case of a ternary glass at x = 11%. The red shaded area in the endotherm (curve 3, **Figure 3**) gives the enthalpy of relaxation upon heating the glass, and is used to calculate the frequency corrected enthalpy of relaxation (Thomas, 2005) of $\Delta H_{nr}(x = 11\%) = 0.00(3)$ cal/g. The ΔH_{nr} term is closely tied to the physics of the glassy state. The deconvolution of the total endothermic heat flow into the reversing and non-reversing heat flow is of fundamental interest in glass science. The reversing heat flow permits establishing the T_g from the inflection point of the step while the step height ΔC_p yields the change in the specific heat between the melt and the glass. The non-reversing heat flow provides a measure of non-ergodicity of the T_g transition and it's vanishing for the case of a ternary glass at x = 11%, constitutes the signature of an isostatically-rigid glass, i.e., $n_c = 3$ (Micoulaut, 2010). The reversing heat flow provides a measure of vibrational entropy change between the glass and the melt, while the non-reversing heat flow provides a direct measure of the configurational entropy difference between the glass and the melt. The vanishing of the $\Delta H_{nr}(x)$ term suggests that the configurational entropy of the glass is melt-like, in other words the excess entropy of the glass remains high as in the corresponding melt. Excess entropy is defined as the entropy difference between the super cooled liquid at T and the state of the glass at which the entropy can no longer be lost (Bestul and Chang, 1964).

Fragility Index of a Melt

There is broad recognition (Carpentier et al., 2003; Thomas, 2005) that MDSC experiments can be undertaken to analyze the glass transition endotherm either in terms of the reversing and non-reversing heat flow components or in the complex C_p formalism. In the latter approach, the in-phase- part of the complex specific heat, C_p^{ip}, shows a step-like feature akin to the reversing heat flow, while the out- of- phase part of the complex specific heat, C_p^{op}, shows a Gaussian-like peak akin to the non-reversing enthalpy of relaxation. Starting from a T above T_g, as one cools a melt across T_g, one observes a glass transition exotherm. One analyses the thermal event in terms of C_p^{ip} and

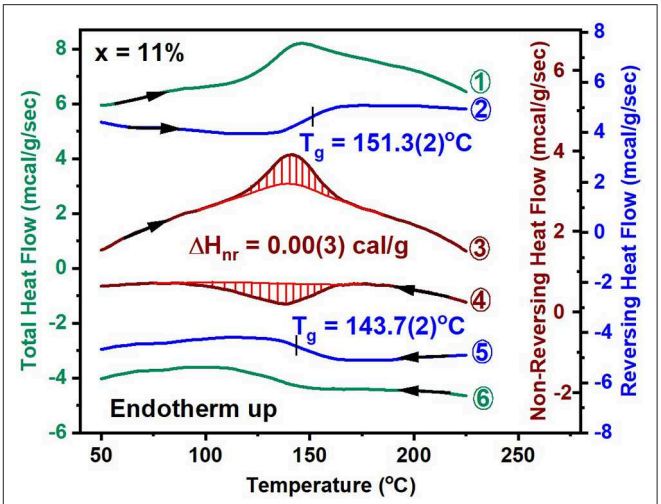

FIGURE 3 | MDSC scan of a $Ge_xAs_xSe_{100-2x}$ glass at $x = 11\%$, showing the total, reversing and non-reversing heat flow as curves labeled 1, 2, and 3 in the heating cycle. The corresponding heat flow terms in the cooling cycle are labeled as curves 4, 5, and 6. See text for the operating parameters. The mean value of T_g of 151.3°C in the heating cycle and of 143.7°C in the cooling cycle yields the scanning rate independent T_g. The frequency corrected enthalpy of relaxation, $\Delta H_{nr}(x)$ is obtained by subtracting the exothermic contribution shaded in red (curve 4) from the endothermic one (in curve 3). The typical operating conditions are as follows; linear T ramp at 3°C/min, modulation time of 100 s, and modulation amplitude at ±1°C.

C_p^{op} as a function of modulation frequency and obtains the melt fragility index. In these experiments, one tracks the shift of C_p^{op} peak as the modulation frequency is systematically changed.

To illustrate the method, we show below (**Figure 4**) the complex C_p results for a $Ge_xAs_xSe_{100-2x}$ melt at x = 14%. These results were obtained as a function of modulation time period t_m in the range $60\text{ s} < t_m < 120\text{ s}$ as the melt T is lowered from 220 to 140°C. One finds that the step in C_p^{ip} steadily shifts to higher T as the modulation frequency $\omega = 2\pi/t_m$ increases. On the other hand, C_p^{op} displays a peak that steadily shifts to higher T as ω increases. At the peak location the glass enthalpy of relaxation tracks the programmed modulated T- profile, i.e., $\omega\tau = 1$. By establishing the peak location of the relaxation peak, one fixes the enthalpy relaxation time τ given the modulation frequency (ω) used, and from the abscissa of the C_p^{op}, the T at which that enthalpy relaxation time τ occurs. By plotting log of τ as a function of T_g/T (**Figure 4** right) one obtains the fragility index.

$$m = \left[\frac{dlog(\tau)}{d(T_g/T)}\right]_{T \to T_g} \quad (1)$$

The following relation then permits deducing the activation energy, E_a, for enthalpy relaxation,

$$E_a = m.T_g.\ln(10) \quad (2)$$

The typical operating parameters are as follows; the cooling rate used was 0.5°C/min, modulation time varied from 120 to 60 s, modulation amplitude was kept at ±1°C. We calibrated

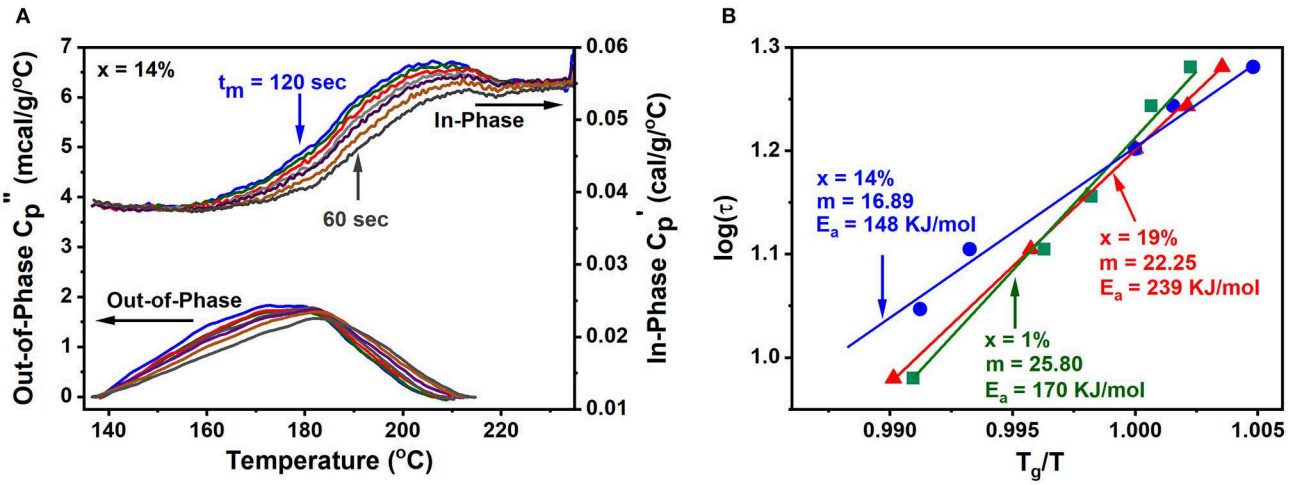

FIGURE 4 | (A) Shows the variation of the C_p^{ip} and C_p^{op} contributions as a function of modulation frequency. As the modulation frequency increases in going from a t_m of 120–60 s, the C_p^{op} peaks corresponding to $\omega \cdot \tau = 1$, steadily shifts to higher temperature underscoring the melt has to relax faster (τ decreases) to track the increased (ω) modulated heat flow. **(B)** Shows a plot of log of τ as a function of T_g/T permitting one to deduce the fragility index from the slope (Equation 1).

the Q2000 MDSC calorimeter for temperature by performing an Indium melting scan. We calibrated the head for specific heat by using a sapphire standard. These are slow experiments typically requiring 48 h of scanning to examine one glass composition.

Analogies between dielectric relaxation studied in electrical measurements and enthalpy relaxation examined in a calorimetric measurement (MDSC) in several glass forming systems, both organic as well as inorganic, show a rather appealing feature (Carpentier et al., 2003; Descamps and Decroix, 2014). Dielectric relaxation involves variation of polarization with a time varying electric field, while enthalpy relaxation relates to the variation of heat flow with a time varying temperature. Dielectric relaxation proceeds at a higher frequency (0.05 Hz−150 KHz) than enthalpy relaxation (0.01–0.1 Hz), and thus occurs at a lower T regime. And if one plots how these relaxation times vary with T, one observes a smooth extrapolation of the dielectric relaxation times to the longer enthalpy relaxation times as T approaches T_g (Carpentier et al., 2003). These results reassure us that melt dynamics probed by two different probes in different relaxation time regimes, show universality of behavior. These observations lend credence to the melt fragility index results on glasses deduced from MDSC.

The increase of viscosity (η) of a glass forming melt as its T is lowered to T_g is often described (Vogel, 1921; Fulcher, 1925; Tammann and Hesse, 1926; Williams et al., 1955; Angell, 1995; Hodge, 1996) by plotting log η against T_g/T. Only select melts display an Arrhenius variation of η on such a plot, such as fused SiO_2, and these are termed *strong*, but a large number of melts display a super-Arrhenius behavior in which the activation energy E_a of viscosity ($\eta = \eta_o \exp E_a/kT$) steadily increases as T approaches T_g. One describes (Angell, 1995; Hodge, 1996) such melts as *fragile*. And, formally, one defines the fragility index of a melt, m, as the dimensionless slope of the log η vs. T_g/T, as T approaches T_g (Equation 3). Within the fragile-strong classification, m varies from about a minimum value near 17 for super-strong melts to a maximum value of about 145 for the fragile ones (Mauro et al., 2009; Gunasekera et al., 2013; Chakraborty and Boolchand, 2014).

$$m = \left[\frac{d\log(\eta)}{d(T_g/T)}\right]_{T \to T_g} \tag{3}$$

The Maxwell relation (Equation 4) connects viscosity to the shear stress relaxation time τ

$$\eta = G_\infty \tau \tag{4}$$

with G_∞ representing the infinite frequency shear modulus. And, since G_∞ is T-independent, one can write the fragility index as shown in Equation 1.

In the calorimetric measurements one measures the enthalpy relaxation time τ_H near T_g to deduce the fragility index (Carpentier et al., 2003).

A wide variety of glass forming melts, both organic as well as inorganic, display a *fragile* behavior (Angell, 1995; Debenedetti and Stillinger, 2001). And one expects that at high T, close to twice T_g, the viscosity of a superstrong melt (m = 17) will exceed that of a fragile melt (m = 35) by one order in magnitude. Most remarkably, for the especially homogenized IP melt compositions examined presently and elsewhere (Gunasekera et al., 2013; Chakraborty and Boolchand, 2014; Mohanty, 2018) the super-strong nature of such melts with m < 20 (**Figure 5C),** leads understandably to a higher viscosity of such melts than those of the flexible phase or stressed-rigid melts. This key finding rests at the base of delayed homogenization of glass forming melts encompassing an IP composition.

Raman Scattering

A Thermo-Nicolet FTIR Nexus 870 research bench with a Raman module was used to record Raman scattering from the bulk

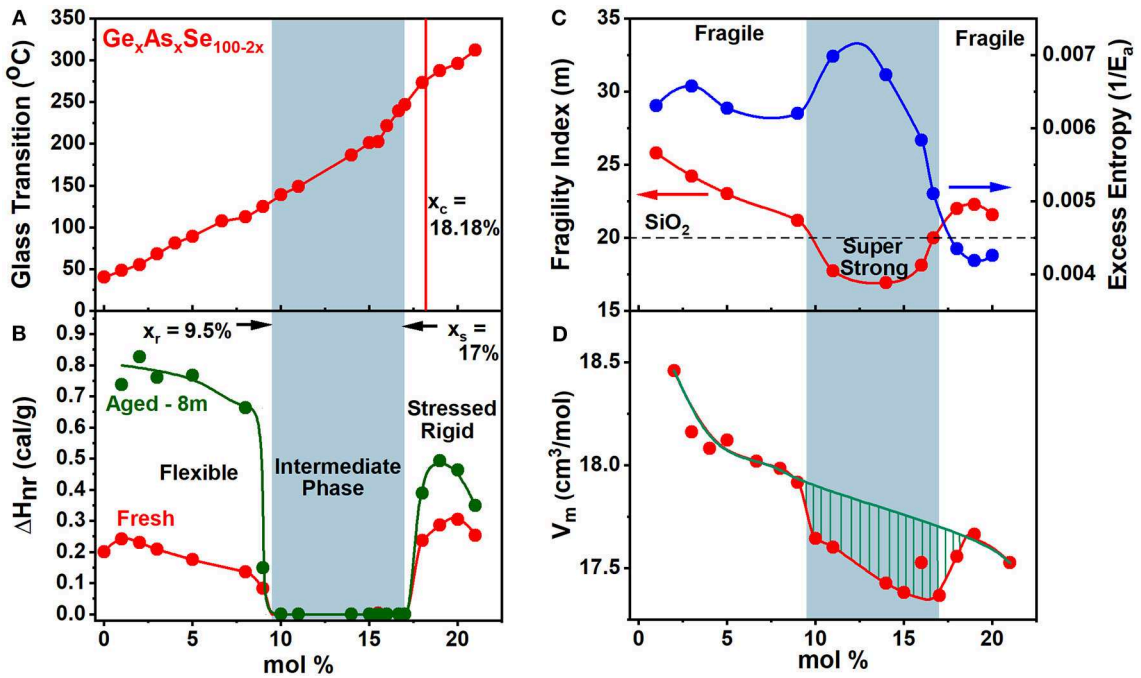

FIGURE 5 | Displays the observed compositional trends in **(A)** glass transition temperature, $T_g(x)$, **(B)** the non-reversing enthalpy of relaxation at T_g, $\Delta H_{nr}(x)$, **(C)** melt fragility index, m(x) and **(D)** Molar Volumes, $V_m(x)$, of especially homogenized $Ge_xAs_xSe_{100-2x}$ ternary glasses. The green striped region represents the volumetric window where the average behavior deviates from the mean behavior showing a compaction in the intermediate phase. The blue panel highlights the IP—compositions spanning the range $9.5\% < x < 17.0\%$.

glasses encapsulated in evacuated quartz tubes. The bulk glass specimen was positioned on an xyz stage of the instrument and the scattering was excited using the 1,064 nm radiation from a Nd-YAG laser tightly focused to a 50 μm spot size. In a typical run 126 mW of laser power was used, the radiation focused at the quartz/ bulk glass interface and an acquisition of 100 cycles took 7 min of acquisition time. In section Quantitative Mapping of melt homogeneity by FT Raman Profiling below, we provide details of the quantitative mapping of glass/melt homogeneity from these Raman scattering data that profiled the bulk glass.

Quantitative Mapping of Melt Homogeneity by FT Raman Profiling

The variance in Ge stoichiometry $<\Delta x>_{Ge}$ of a ternary glass at a composition x = 9%, was deduced from the spectra of **Figure 1** as follows. The scattering strength ratio of the CS mode near 200 cm^{-1} to the broad band observed near 250 cm^{-1}, which has contribution from predominantly Se_n polymeric chains, As-centered pyramids (PYR) and -quasi-tetrahedra (QT) was deduced by analyzing Raman scattering. An empirical correlation of the Raman scattering strength ratios as a function of weighed glass composition in FT-Raman profiling experiments is generated self-consistently by having Raman results (**Figure 1**) from all the fully homogenized glass compositions as shown in **Figure 6** by the red line joining the red filled circles. Next the profiled spectra of the glass specimen at x = 9% after 2 days of alloying was deduced and these data projected in **Figure 6** as the black square data points. These data place the variance in Ge concentration across the batch after 2 days of alloying near 1.04% and provides a visual measure of glass heterogeneity. Upon alloying the glass for 7 days, the variance in Ge content in the batch decreased to 0.28%, and after 10.5 days of alloying became minuscule (<0.01%) when the batch was considered to be homogeneous.

The rigidity- and stress- elastic phase transitions in these disordered molecular networks are intrinsically sharp because of their percolative (Thorpe, 1985) nature, and glasses must be homogenized (Boolchand, 1985) at least to a scale of 50 μm or less to establish the intrinsic nature of these transitions.

Molar Volumes

Densities of our glass samples were determined by using Archimedes principle with 200 proof alcohol being the immersion fluid. We established the density of alcohol by using a Si crystal wafer of a known density (ρ_{si} = 2.323 g/cm^3). We mounted the Si crystal on a quartz fiber that was suspended from a Mettler-Toledo model B154 digital microbalance, with a resolution of 0.1 mg, and weighed it in air. The quartz fiber is then submerged into the fluid and the balance tared to negate the buoyant force on the fiber. The Si crystal was then placed on the quartz fiber hook and submerged into the fluid and the weight of the Si crystal in alcohol recorded. Having the weight of the Si crystal in air and in alcohol then enabled one to calculate the density of the alcohol.

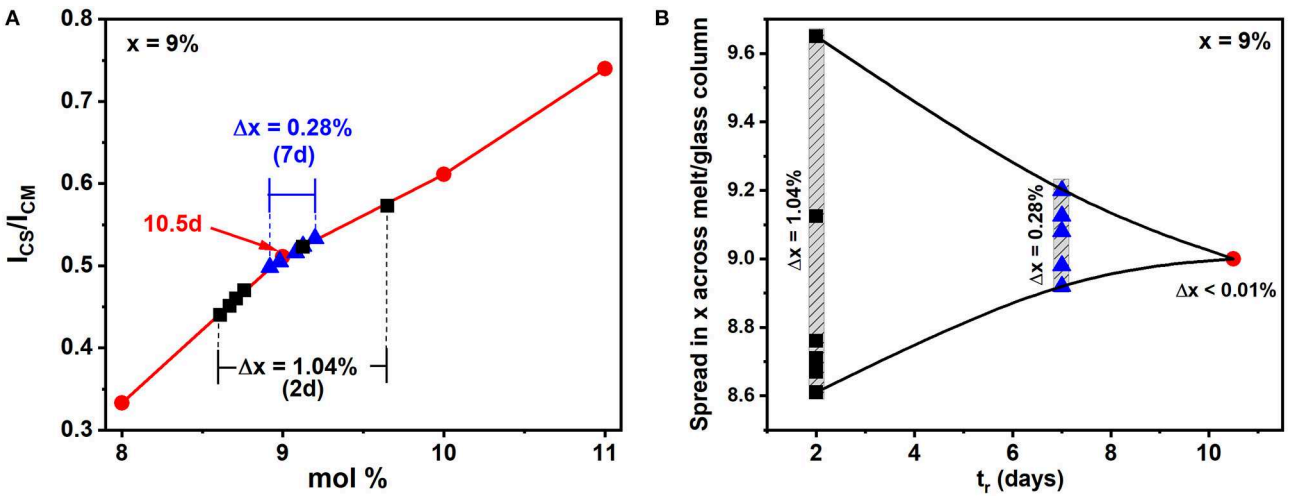

FIGURE 6 | (A) From the fully homogenized glasses we established the red, empirical correlation of the Raman scattering strength ratios with weighed glass composition once that composition has been homogenized in the FT-Raman profiling experiments, describing the variation in the scattering strength ratio of the Corner-Sharing mode near 200 cm^{-1} to the broad Se_n chain band near 250 cm^{-1}. The six spectra plotted in **Figure 1** are normalized to the highest scattering strength band near 250 cm^{-1}, and the spread in the CS mode strength after 2 days of alloying provides a visual measure of glass heterogeneity. These data are plotted as the black squares in the plot above. Upon alloying the glass for 7 days, the variance in Ge content of the glass decreased to 0.28%, and then became minuscule (<0.01%) after 10.5 days of alloying. **(B)** An alternative representation of melt homogenization can be displayed by plotting the variance $<\Delta x>$ in Ge stoichiometry deduced from FT-Raman profiling of a 1.5-g batch composition weighed at $x = 9\%$ and its composition tracked as a function of t_r, the alloying time, at 950°C in days. Note that the variance decreases by 2 orders of magnitude in going from 2d (1.04%) to 10.5d (0.01%) and yields the expected weighed composition at $x = 9\%$.

To establish the accuracy and reproducibility of our method, the density of a Ge single crystal was independently measured, and a value of 5.324(6) g/cm^3 was found, which is comparable to the published standard value of 5.323 g/cm^3.

We emphasize that the glass samples used in density experiments are to be no <100 mg in weight. This allows the density to be measured to an accuracy of 0.25% or less. Each sample's density measurement was repeated 5 times.

We provide, as an example, the calculations used to establish the density of the alcohol, ρ_{alc}, and the density of a $Ge_xAs_xSe_{100-2x}$ glass specimen at x = 14%, ρ_{sample}.

Density of Alcohol

Weight of Silicon in air (w_{air}): 104.8 mg; Weight of Silicon in alcohol (w_{alc}): 69.3 mg; Density of Silicon (ρ_{si}) = 2.323 g/cm^3

$$\rho_{alc} = \frac{(w_{air} - w_{alc})}{w_{air}} * \rho_{Si} = 0.786 g/cm^3$$

Density of $Ge_xAs_xSe_{100-2x}$ x = 14%

Weight of sample in air (w_{air}): 127.2 mg; Weight of sample in alcohol (w_{alc}): 104.7 mg; Density of alcohol ($\rho_{alcohol}$): 0.786 g/cm^3

$$\rho_{sample} = \frac{w_{air}}{(w_{air} - w_{alc})} * \rho_{alc} = 4.45\ g/cm^3$$

The molar volumes of the bulk glass were then deduced from the mass density.

Molar Volume of $Ge_xAs_xSe_{100-2x}$ x = 14%

Molar mass of sample: 77.52 g/mol, Density of sample: 4.45 g/cm^3.

$$V_m = \frac{Molar\ mass}{Density} = 17.43\ cm^3/mol$$

Trends in molar volumes of the ternary glasses are summarized in the next section.

First Principles Molecular Dynamics Simulations

We performed a series of First principles molecular dynamics simulations (Car and Parrinello, 1985), using the canonical (NVT) ensemble, for the computation of the mean square displacement and the diffusion constant, on the same $Ge_xAs_xSe_{100-2x}$ systems containing $N = 249$ atoms at 11 different compositions (2, 4, 5, 8, 9, 10, 15, 17, 18, 19, 21%) with the number of As, Ge and Se atoms fulfilling the desired stoichiometry. A periodically repeated cubic cell was used, whose size changes according to the number density of the glasses (see section Molar Volumes). For the simulation of the present liquids, we used density functional theory (DFT) in combination with plane wave basis sets. The electronic scheme has been chosen after a series of methodological investigations on different liquid chalcogenide glasses and liquids (Micoulaut et al., 2009; Massobrio et al., 2010; Bouzid et al., 2015). These showed that a generalized gradient approximation (GGA) for the exchange correlation energy improves substantially the description of both short and intermediate-range order as

compared to the local density approximation (LDA) (Massobrio et al., 1999). In addition, it was demonstrated that the exchange-correlation functional reducing the metallic character of the bonding (a Becke, Lee, Yang and Parr (BLYP) functional) led to systems with a reduced number of miscoordinated atoms and metallic character (Micoulaut et al., 2009), and improved the reproduction of structure functions obtained from neutron diffusion in the liquid and amorphous state (Bauchy et al., 2013; Micoulaut et al., 2013; Yildirim et al., 2016b).

Using these recipes, the electronic structure of the As-Ge-Se liquids was described within DFT and evolved self-consistently during the motion using a GGA for the exchange and correlation parts of the total energy, according to Becke (B) and LYP, respectively (Becke, 1988; Lee et al., 1988). Valence electrons were treated explicitly, in conjunction with norm-conserving pseudopotentials to account for core-valence interactions. The wave functions were expanded at the γ-point of the supercell and the energy cutoff was set at 20 Ry. Starting configurations were taken from binary Ge-Se liquids (Yildirim et al., 2016b) and As atoms were appropriately inserted in order to meet the desired stoichiometry. Loss of the memory of the initial configurations has been achieved through preliminary runs at 2,000 K over 50 ps. For all investigated compositions and temperatures (1,500 and 1,200 K), statistical averages in the liquid state were obtained over 20–25 ps of trajectory with a time step of $\Delta t = 0.12$ fs and a fictitious mass of 1,000 a.u.

RESULTS

Glass Transition Temperature, Glass Enthalpy of Relaxation, and Melt Fragility Index

The calorimetric results on homogeneous $Ge_xAs_xSe_{100-2x}$ glasses show that $T_g(x)$ increases monotonically with x over a wide range $0 < x < 25\%$ of compositions (**Figure 5A**). These results show that Ge- and As- atoms serve to cross-link (Micoulaut and Naumis, 1999) polymeric Se_n chains as $GeSe_2$ tetrahedra both CS and Edge-Sharing (ES), and $AsSe_{(1/2)3}$ pyramids form in the chemical composition range $8\% << x_c = 18.2\%$. At $x > x_c$ homopolar Ge-Ge and As-As bonds must form part of the same backbone as the one prevailing at $x < x_c$, for $T_g(x)$ to continue to increase at $x > x_c$.

The variation of the non-reversing enthalpy of relaxation at T_g (ΔH_{nr}), in the glasses shows a sharply defined square-well like minimum **(Figure 5B)**, and it is highlighted by the light blue panel, i.e., the **thermally reversing window.** The vanishing of the frequency corrected enthalpy of relaxation at T_g, ΔH_{nr}, in the $9.5\% < x < 17.0$. % range constitutes evidence that it represents the region of phase space (Micoulaut, 2010; Bauchy and Micoulaut, 2015; Mantisi et al., 2015) where glass transitions become thermally-reversing in character. The ΔH_{nr} is minuscule in the IP, which is a clear evidence that the samples are dry and do not contain water impurities (Vaills et al., 2005). The dynamic reversibility of glass transitions corresponds to the overshoot in the endotherm vanishing, and is identified with the formation of isostatically-rigid local structures (Bauchy and Micoulaut, 2015), with the count of bonding constraints per atom, $n_c = 3$, and satisfy the Maxwell-Phillips rigidity criteria (Maxwell, 1864; Phillips, 1979). Such networks are rigid but unstressed and possess a liquid-like entropy.

The variation of the melt fragility index, m(x), displaying a Gaussian like minimum (**Figure 5C**) with $m < 20$ for IP compositions, and serves to define a *fragility window* or, at least, *a fragility minimum*, in which melts are viewed to be super-strong, in the strong-fragile classification (Angell, 1995) of melts. Note that the dashed line drawn in **Figure 5C** marks the fragility index of SiO_2 glass taken as $m = 20$, and it divides the m(x) plot into three regions; (i) a low x region ($x < 9.5\%$) and (ii) a high x region ($x > 17\%$) and (iii) an intermediate x -region. Note that fragility window coincides with the reversibility window in x-space and the three regions mentioned above represent, respectively, the *flexible* phase ($x < 9.5\%$), *stressed-rigid* phase ($x > 17.0\%$), and the intermediate phase ($9.5\% < x < 17.0\%$).

Intermediate phase melts, with $m < 20$, are quite special; these are super-strong and their viscosity at 950°C where we alloyed the starting materials are significantly greater than those of their non-IP composition counterparts. Finally, the close correlation in composition between melt- and glass- properties leads to the central finding of this work, viz, that *melt fragility index encode glass TPs.* Parallel findings have recently been noted in binary Ge-Se (or S) (Bhosle et al., 2012a,b; Gunasekera et al., 2013; Chakraborty and Boolchand, 2014) glasses and are suggestive that the melt-glass correlation could well be a general feature of glass science.

Compacted Nature of Intermediate Phase Networks

The variation in molar volumes of the present ternary glasses as a function of composition is plotted in **Figure 5D**. The average behavior shows V_m to decrease from 18.5 to 17.5 cm^3/mol, reflecting the increased cross-linking of the networks. The plot also shows an additional reduction of V_m in the reversibility window shown by the hashed mark region. These data show that glass compositions are compacted (Boolchand et al., 2013), a feature observed in the IP of other glasses as well (Bhosle et al., 2012a,b; Chakraborty and Boolchand, 2014). The network compaction is broadly viewed as the consequence of the stress-free nature of the glass backbone where the effect of longer range forces such as van der Waals and Coulombic come into play, largely because the strong short-range covalent forces are balanced by the 3D network dimensionality. The average reduction in $V_m(x)$, with increasing x, is a consequence of the increased mean coordination number, $<r> = 2 + 3x$, that increases linearly with x leading to space filling, i.e., more atoms being packed per unit volume. Here the mean coordination number follows if one assumes that Ge, As, and Se atoms are, respectively, 4, 3-, and 2-fold coordinated conforming to the 8-N bonding rule.

Glass Structure Evolution With Composition From Raman Scattering

Raman scattering has been particularly useful in elucidating the glass structure evolution of the present chalcogenides. The observed Raman line shapes as a function of increasing As

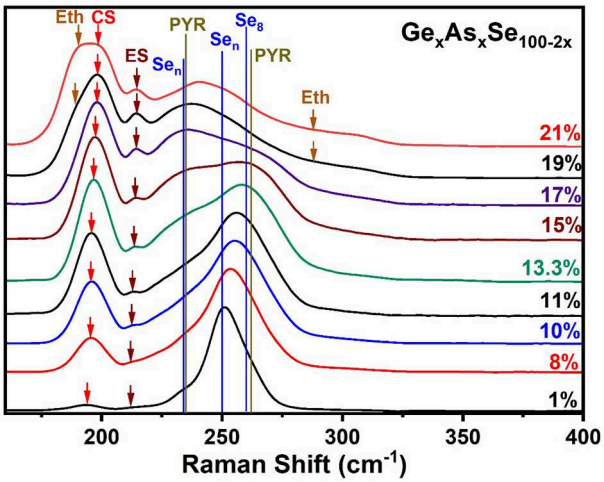

FIGURE 7 | Observed FT-Raman scattering results on $Ge_xAs_xSe_{100-2x}$ ternary glasses as a function of increasing Ge and As content "x." The expected vibrational modes are labeled. Jackson et al. have calculated these normal modes by NRLMOL code summarized in **Table 1**. In the 300 cm^{-1} to the 600 cm^{-1} range we see weakly excited modes that are presented and analyzed in **Figure 8**. The assigned modes are Eth, Ethane; CS, Corner Sharing; ES, Edge Sharing; Se_n, Selenium Chain; PYR, Pyramidal; Se_8, Selenium 8 rings.

TABLE 1 | Vibrational modes of the Ge-centered CS and ES tetrahedra and Ethane like Ge_2Se_6 units are included in the top panel, followed by those of the As-centered local structures base on pyramidal and quasi-tetrahedral local structure in the middle panel, and those of the triad of modes related to polymeric Se_n Chains in the lowest panel (Jackson et al., 1999).

Ge_xSe_{100-x} cluster	$\omega^{Th}(cm^{-1})$	I^{Ram} (Å^4/amu)
Corner sharing (CS)	195	47.9
Edge sharing (ES)	219	40.5
	319	7.7
Ethane-like	179	49.2
	288	3.9
As_xSe_{100-x} cluster	**$\omega^{Th}(cm^{-1})$**	**I^{Ram} (Å^4/amu)**
Pyramidal (PYR)	103	8.0
	235	16.6
	262	3.15
Quasi-tetrahedral	89	3.8
	198	39.4
	271	11.3
	364	9.3
Se cluster	**$\omega^{Th}(cm^{-1})$**	
Correlated	234	
Uncorrelated	250	
Se_8	260	

and Ge alloying content "x" are displayed in **Figure 7**. We are greatly assisted in mode assignments because of the availability (Jackson and Pederson, 1990; Pederson and Jackson, 1990, 1991; Quong et al., 1993; Porezag and Pederson, 1996; Porezag, 1997; Briley and Pederson, 1998; Jackson et al., 1999) of the expected normal mode frequencies of the various As-centered and Ge-Centered local structures from NRLMOL cluster calculations (**Table 1**). Furthermore, Raman scattering in the Ge-Se binary glasses, intensely investigated in previous work (Bhosle et al., 2011, 2012a), have confirmed the Ge-centered local structure mode frequencies. The case of the As-Se binary glasses has also been investigated (Chen et al., 2010; Ravindren et al., 2014), although some ambiguities in mode assignments have persisted, issues that we will address here.

At low x (< 5%), the spectra are dominated by the broad band near 250 cm^{-1} coming from polymeric Se_n chains and some contribution from Se_8 rings and compacted Se_n chains. These display a triad of modes (234, 259, and 260 cm^{-1}) as shown in **Table 1** and have been confirmed in experiments on very dilute Ge doped Se glasses (Yannopoulos and Andrikopoulos, 2004; Dash et al., 2017). Detailed results in binary Ge_xSe_{100-x} glasses (Bhosle et al., 2012a) reveal that the vibrational modes near 197 cm^{-1} comes from Corner-sharing and the one near 217 cm^{-1} from edge sharing $GeSe_2$ tetrahedra. With increasing x, and particularly near x = 15% the square shaped band in the 225–275 cm^{-1} range has contributions from modes of As-centered pyramidal (235 cm^{-1}, 265 cm^{-1}) and quasi-tetrahedral (198, 271 cm^{-1}) units.

Perhaps the most striking result to emerge from these spectra on homogeneous glasses in the present work is the mode near 350 cm^{-1} (shown in the inset of **Figure 8**) that steadily increases with x. Although the increase is slight in QT_1, by comparing it to its bond bending vibrational mode, QT_2, there is undoubtedly an increase in the concentration of the quasi-tetrahedra with increasing x. In a previous study (Qu et al., 2002; Qu, 2004), this particular mode was not observed in glasses probably because these were not especially homogenized. This particular mode is predicted near 364 cm^{-1} (**Table 1**) and involves stretch of the double bonded Se = $As(Se_{1/2})_3$ in a quasi-tetrahedral local structure. With increasing x, the QT mode near 350 cm^{-1} sits at the edge of the more strongly excited mode of Ge ES units near 320 cm^{-1} and is thus eventually masked in the inset of **Figure 8**.

The strongest QT mode occurs at 198 cm^{-1} and it overlaps with the mode of CS tetrahedral units, making a quantitative determination of the QT local structures at best difficult.

Dynamic Anomalies in the Liquid State

In the present contribution, we also focus on the dynamics of the obtained simulations. Structural properties will be considered and discussed elsewhere. The calculation of the mean-square displacement (msd) $<r^2(t)>$ of the three tagged atoms (As, Ge, Se) leads to a usual profile in a log-log plot representing $<r^2(t)>$ with time, i.e., a ballistic regime at short time where the behavior scales as t^2 and a diffusive regime that sets in for most compositions (1,500 K) at around 1–5 ps. Note that, because of the chosen high temperatures considered herein, no cage-like motion is obtained. The diffusion constant D_i (i = As, Ge, Se) can be obtained using the Einstein relation limit:

$$D_i = \lim_{t\to\infty} \frac{\langle r^2(t)\rangle}{6t}$$

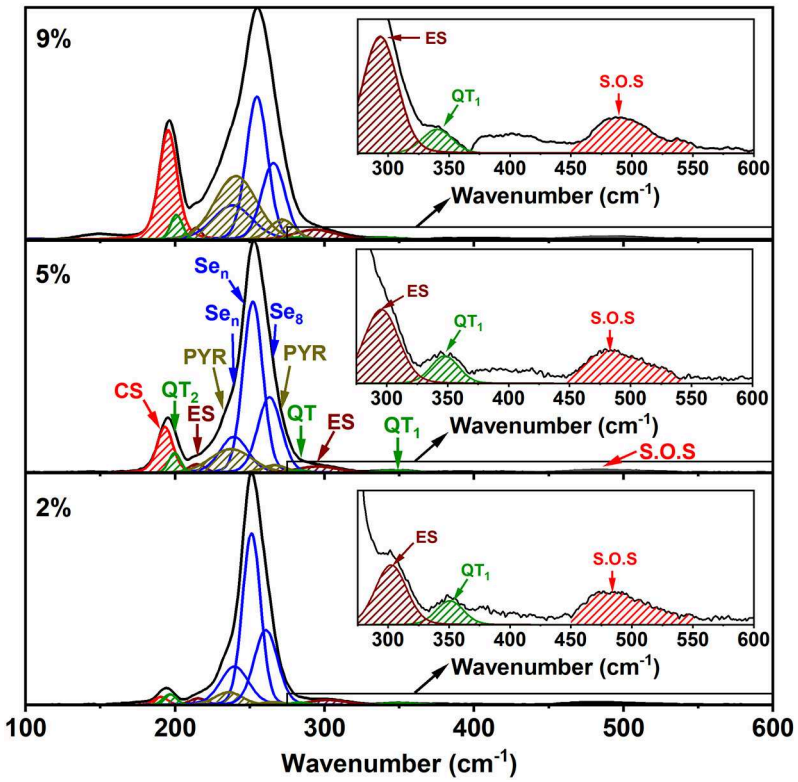

FIGURE 8 | Raman line shape deconvolution at several glass compositions in the low x regime of the present ternary. These modes are in harmony with the expected vibrational modes of the characteristic local structures as shown in **Table 1**. In the high frequency range spanning 300–600 cm^{-1}, we illustrate in the inset evidence of the 350 cm^{-1} mode coming from the As-centered QT units. The red hash-marked mode represents second order scattering from the Se_n chain mode near 250 cm^{-1}. See text.

and both D_{Se} and D_{As} are plotted as a function of content for the isotherms 1,500 and 1,200 K (**Figure 9**). Experimental diffusivity values for such system are unavailable but one can check that the values of D_i are globally compatible with similar systems. For instance, it has been found (Yildirim et al., 2016a) that Ge diffusion is of about 5.10^{-5} $cm^2.s^{-1}$ in $Ge_{20}Se_{80}$ liquids at 1,373 K, i.e., rather close to the value obtained for a similar Se content in the present case ($6.4.10^{-5}$ $cm^2.s^{-1}$ for $Ge_{10}As_{10}Se_{80}$ at 1,500 K). Such values have been found to be compatible with viscosity results (Stølen et al., 2002; Gueguen et al., 2011) at high temperature once a Stokes-Einstein equation is used to estimate the viscosity (Sipp and Richet, 2002).

An inspection of the behavior with composition clearly indicates that the diffusivity results contain features of the underlying TPs. D_i is very small for highly cross-linked melts (x > 17%, e.g., D_{Se} = 2.5 10^{-5} $cm^2.s^{-1}$ for x = 21% and 1,500 K), increases slightly in the IP, and then becomes very large (about 10 times larger at x = 4%), with the substantial increase of D manifesting in the flexible phase. In contrast to the Ge-Se, wherein IP melts were found to display a minimum in diffusivity (Yildirim et al., 2016b), in the present Ge-As-Se, melts in the IP (9–17%) remain nearly constant in diffusivity. However, it should be noted that, for such elevated temperatures, extrema can be barely visible, as noted earlier for high temperature Ge-Se liquids (Yildirim et al., 2016a).

The nature of the dynamics is also very strongly dependent on composition and the distance of motion for the atoms (e.g., Se atoms in the inset of **Figure 9**) increases substantially in liquids that are flexible. For stressed-rigid phase compositions, the msd is rather small, e.g., $<r^2(t)>=19Å^2$ for x = 21% at 1,200 K, corresponding to a distance of several interatomic distances only (4.5 Å) and larger distances can hardly be explored due to the large cross-link density. As the Se content increases, IP compositions seem to lead to a slight increase $<r^2(t)>$, barely visible from the figure. The most noticeable change is obtained at the intermediate to flexible boundary and at both investigated temperatures, $<r^2(t)>$ starts to dramatically increase at 8–9% to reach nearly 200 $Å^2$ for x = 2%.

DISCUSSION

Correlating Melt Dynamics With Glass Topological Phases

Trends in Fragility Index and in Projected Melt Viscosity

In the observed trend of m(x) (**Figure 5C**), we had noted before, that there is a global Gaussian-like variation of m(x) centered

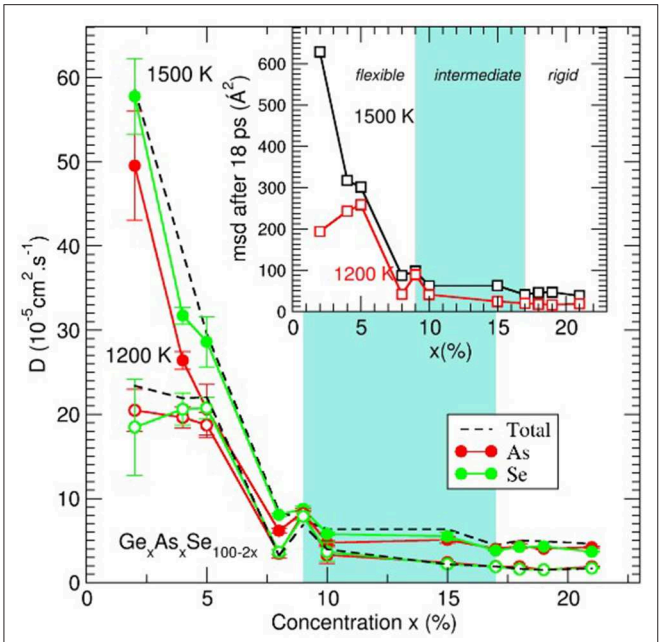

FIGURE 9 | Average self-diffusion constant (broken lines) and species dependent (As, red; Se, green) self-diffusion constant D(x) for two isotherms (1,500 and 1,200 K) as a function of content x in $Ge_xAs_xSe_{100-2x}$ glass-forming liquids. The inset represents the Se average mean-square displacement after 18 ps simulation time. Gray zones represent the location of the intermediate phase.

around the fragility window; with m < 20 in the **fragility window,** 9.5% < x < 17.0%, and m > 20 for compositions outside that window. The implications are that the viscosity of melts in the fragility window would be much greater than those of melt compositions outside that window.

We have used the Mauro, Yue, Allison, Gupta and Alan (MYEGA) model to calculate the viscosity of $Ge_xAs_xSe_{100-2x}$ melts using the following relation,

$$\log_{10}\eta(T) = \log_{10}\eta_\infty + (12 - \log_{10}\eta_\infty)\left(\frac{T_g}{T}\right)\exp\left[\left(\frac{m}{12-\log_{10}\eta_\infty} - 1\right)\left(\frac{T_g}{T} - 1\right)\right] \quad (5)$$

as a function of T_g/T given the measured fragility index, m, the alloying temperature of T = 950°C, and the measured $T_g(x)$ of the glasses. In the Equation (5) above η_∞ is taken as $\log_{10}\eta_\infty = -4$ at m = 60. We project the variation of the viscosity η(x) with melt composition in **Figure 10C** as the green data points. We find η(x) increases by almost two orders of magnitude in going from the fragile melt composition x = 9.0% to the super-strong melt composition at x = 15.0 % in the fragility window. In fragile melts at x > 17% the increase of T_g is responsible for the increased viscosity from Equation (5). The broad implications of these projections are clear, viscosity of melts in the fragility window increases substantially leading melt diffusivity to reduce in that window in relation to diffusivity of fragile melt compositions at x < 9.5%. We believe these considerations are responsible for the delayed homogenization of all chalcogenide melts (**Figure 2**) synthesized presently. As an

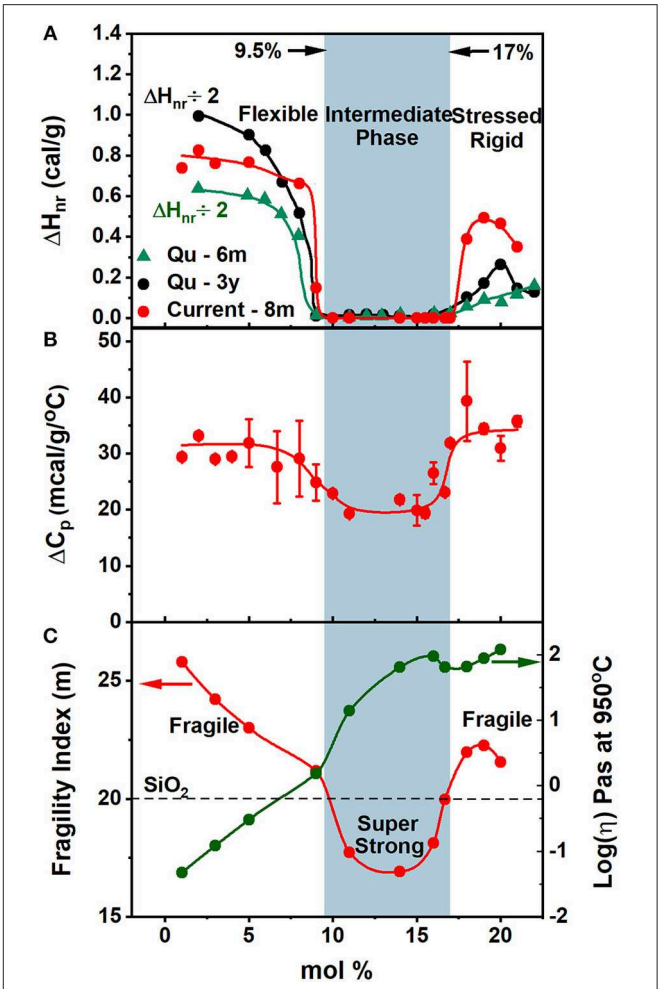

FIGURE 10 | Observed variation of **(A)** the Non-reversing heat flow, $\Delta H_{nr}(x)$ in present glasses (•) compared to previous work of Tao and Boolchand (▲, •), **(B)** the specific change $\Delta C_p(x)$, and **(C)** the fragility index, m, in the especially homogenized ternary $Ge_xAs_xSe_{100-2x}$ glasses in the present work. Also projected is the variation of melt viscosity, η at 950°C expected using the measured *m* and the MYEGA equation.

aside we would like to draw attention of the reader to reference (Gunasekera et al., 2013), wherein one could visually observe the sharply reduced diffusion of Ge_xSe_{100-x} melts (in **Figure 3** of the reference) in the narrow super-strong regime of 21.5% < x < 23.0% where the fragility index reduced to m = 15. This was made possible by recording Raman spectra as a function of alloying time in those profiling experiments.

Trends in Enthalpy of Relaxation at T_g and Configurational Entropy Difference ΔS_{config} Between a Glass and Corresponding Melt

The present calorimetric results (**Figure 10**) unambiguously show the existence of two elastic phase transitions (Boolchand et al., 2001; Qu et al., 2002) rather than a single one, as was suspected several years ago (Thorpe, 1983; Tatsumisago et al., 1990; Böhmer and Angell, 1992), corresponding to the percolation of rigidity near <r> = 2.40. The observation of two

elastic phase transitions in binary Si_xSe_{100-x} glasses (Selvanathan et al., 1999) lead as early as 1998 to the recognition that, in real glasses, the rigidity and stress transitions will, in general, occur at two distinct and separate network connectivity. And it led to the birth of the IP as composed of rigid but unstressed networks formed between these two transitions. In the present ternary these two transitions occur near x = 9.5% or <r> = 2.285, and near x = 17.0% or <r> = 2.51. And we identify these, respectively, with the onset of rigidity and onset of stress in these glasses (Thorpe et al., 2000). The identification is consistent with the vanishing of the frequency corrected enthalpy of relaxation, which has been shown to be the signature (Micoulaut, 2010) of networks being isostatically rigid, $n_c = 3$. Micoulaut (2010) and Bauchy and Micoulaut (2015) were one of the first to link enthalpy of relaxation at T_g in calorimetric measurements with the optimally-constrained nature, $n_c = 3$, of glassy networks. The two transitions are also observed in $\Delta C_p(x)$, which reveals a small step of 0.01 cal/g/°C at both the rigidity- and the stress-transitions (**Figure 10B**). The two transitions are also observed in melt fragility index variation m(x), which show a fragile (m > 20) to superstrong (m < 20) transition near x = 9.5%, and then a superstrong (m < 20) to fragile (m > 20) transition near x = 17.0%, the stress-transition.

Correlating Melt Dynamics With Their Glass Topological Phases

The compositional variation of $\Delta H_{nr}(x)$ and m(x) observed (**Figures 10A,C**) in the present glass system demonstrates that superstrong melts in the fragility window upon cooling to T_g will invariably form IP glasses in the reversibility window. On the other hand, fragile melts formed at non-IP compositions give rise to either flexible or stressed-rigid glasses. Furthermore, one can uniquely distinguish between the two kinds of fragile melts by recognizing that for glasses in the flexible phase the fragility index, m, decreases with an increase of T_g, while the reverse would be the case for glasses in the stressed-rigid phase (see **Figures 5A,C**). The correlation observed between $\Delta H_{nr}(x)$ and m(x) here in the case of the present ternary has, indeed, close parallels to the case of the Ge-Se (or S) binary systems (Gunasekera et al., 2013; Chakraborty and Boolchand, 2014). Taken together, these results on especially homogenized melts/glasses are suggestive that melt dynamics encode the glass topological phases. The result that may well-represent a general principle of glass science.

Correlating Melt Fragility Index From Flexure- and Viscosity- With Present Modulated-DSC Experiments

Three decades ago, ternary $Ge_xAs_xSe_{100-2x}$ melts were investigated in terms of viscosity (Tatsumisago et al., 1990) and flexure measurements (Böhmer and Angell, 1992). Both sets of experiments made use of the same stock of glasses. These were synthesized by alloying the pure elements in evacuated quartz tubes at a T range in the 600–1,150°C range for 24 h. The fragility

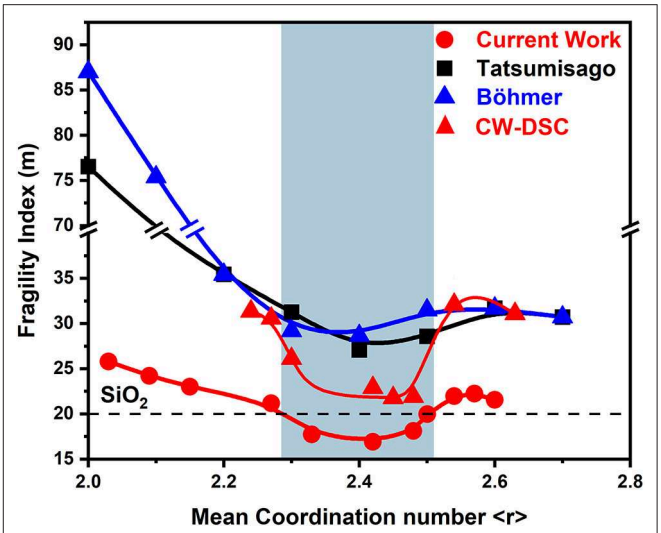

FIGURE 11 | Variations in the fragility index of equimolar $Ge_xAs_xSe_{100-2x}$ ternary melts reported by Tatsumisago et al. (■) and by Böhmer and Angell (▲) compared to those reported in the present work using MDSC (●) and DSC (▲).

index results as a function of glass composition from both sets of experiments (Böhmer and Angell, 1992) yielded remarkably similar results (**Figure 11**). And, for ease of comparison, we have included the present results (**Figure 5C**) in **Figure 11** as well. It is comforting to see that in all three data sets, fragility index of melts within a narrow range of compositions near x = 13.3% or <r> = 2.40 display a strong character, while those at x < 9.5% and x > 17% become increasingly fragile.

On the other hand, the actual values of the fragility index, m, reported in the viscosity and flexure measurements are significantly greater from those measured in the present MDSC work. The difference is as large as 60 units in m near pure Se to about 30 units near <r> = 2.40 or x = 13.3 mole% and about eight units in m near the composition x = 20 in the stressed-rigid phase. We have also measured the fragility index of the present Ge-As-Se glasses using the Moynihan approach (Moynihan et al., 1974). If the Tg's in the DSC measurement are established from the inflection point of the heat flow, trends in m(x) (**Figure 11**) are quite similar to those found using MDSC (**Figure 5C**). In particular in the IP range m approach a value close to 20.

We can think of two possible factors contributing to this large disparity in melt fragility index on the same glass ternary system. The first factor could be the role of the experimental method. In viscosity and flexure, one probes the shear stress relaxation time, while in the calorimetric measurement the enthalpy relaxation time—and it has been suggested that different properties of glasses and melts may exhibit distinct relaxation times (Potuzak et al., 2011; Yu et al., 2015, 2017). On the other hand what is of relevance here is the variation in the T dependence of the relaxation time, and not the relaxation time magnitude itself. For example, fragility index of melts measured by Dielectric spectroscopy (Carpentier et al., 2003), Dynamic Light scattering (Fabian and Sidebottom, 2009), and MDSC (Mohanty et al., 2019), involve measuring different kinds of relaxation times,

but when these are plotted against inverse Temperature close to T_g, yield nearly the same slope, i.e., fragility index. The second factor could be the sample make up. For small (1.5-g) batch sizes, as shown in **Figures 1**, **2**, we noted at least 1.5 mole% spread in Ge stoichiometry near x = 9% for melts alloyed for 24 h at 950°C. In the viscosity (Tatsumisago et al., 1990) and flexure (Böhmer and Angell, 1992) measurements, which require much larger samples than the ones synthesized presently, the synthesis of homogeneous bulk glasses is unlikely to be achieved with the alloying treatment described (Tatsumisago et al., 1990; Böhmer and Angell, 1992). Melt heterogeneity would invariably lead to increased fragility index as noted in recent work as well (Ravindren et al., 2014). The large differences in the magnitude of m between the present work and these earlier reports at the same composition, x, probably result from glass sample make up. Heterogeneity of melts would invariably lead the fragile component to rapidly diffuse through a melt leaving the least mobile super-strong component to be largely localized in small pockets. The delayed homogenization of chalcogenide melts, such as those reported here in the present ternary, may well be a generic factor contributing to the large spread in fragility index at the same melt/glass composition.

Aging of the Reversibility Window in Fully–With Partially–Homogeneous $Ge_xAs_xSe_{100-2X}$ Glasses

The challenges in the synthesis of homogeneous chalcogenide glasses came to the fore when FT-Raman profiling measurements (Bhosle et al., 2012a,b) were first brought to bear on understanding how melt/glass batches actually homogenize in real time upon alloying of the starting materials. The delayed nature of the homogenization over 7–10 days of alloying rather than 1 or 2 days was subsequently found to be a fairly pervasive feature of all chalcogenides examined since. And it was traced to the super-strong nature of melts in the IP with fragility index m < 20 that slow down the diffusive mixing of the batch composition (Gunasekera et al., 2013). In 2003, we had synthesized $Ge_xAs_xSe_{100-2x}$ glasses by alloying the starting materials at 960°C for 48 h, which we now recognize only lead to partially homogeneous glasses- i.e., the variance, $<\Delta x>$, of Ge stoichiometry across the 1.5 g batches are estimated near 1.5 mole% from the results of **Figure 2.** The reversibility window in these glasses displayed edges that were smeared when examined after 1 month of aging (Qu, 2004) for that reason. But upon long term aging (6 months, 3 years) at room temperature the reversibility window evolved and showed that, for glasses at x < 10%, the $\Delta H_{nr}(x)$ term increased and the reversibility window edge near x = 10% sharpened up (**Figure 10A**).The aging induced increase of $\Delta H_{nr}(x)$ at x > 17% was much less pronounced, understandably so because the T_g values of these stressed-rigid glasses are measurably greater than those of the flexible ones at x < 10% (**Figure 5A**), leading to substantially reduced kinetics of aging as determined by the T/T_g ratio. In spite of that limitation, one finds that both the rigidity- and stress-transitions became better defined upon aging, to closely approach the transitions observed in the especially homogenized glasses.

The aging behavior of the homogeneous glasses examined in the present work stands in sharp contrast to the findings on the partially homogenized glasses studied earlier. We could clearly observe sharp rigid- and stress- elastic phase transitions in the fresh rejuvenated glasses (**Figure 5B**). It helps one understand how homogeneity of melts/glasses is intimately tied to the observation of the IP in these glasses. Melt/glass homogenization is precursive to observation of a sharp square-well like reversibility window permitting one to fix the three TPs (Boolchand et al., 2018).

MDSC experiments also show that the non-ergodic enthalpy of relaxation $\Delta H_{nr}(x)$, builds up significantly upon aging of non-IP glass compositions to about 2.0 cal/g after 3 years of room temperature aging (Qu, 2004) **(Figure 10A).** Thus, in fully relaxed glasses the underlying configurational entropy change associated with T_g, ΔS_{conf} exceeds 0.08 cal/g/°C. In the estimate, we take the width of T_g to be 25°C. Finally, the heat capacity change at T_g, $\Delta C_p(x)$ associated with the reversing heat flow of 0.015 cal/g/°C, suggests that the underlying change in vibrational entropy, ΔS_{vib}, is nearly half that of $\Delta C_p(x)$, a value of 0.008 cal/g/°C. Thus ΔS_{conf} (= 80 mcal/g/°C) is an order of magnitude greater than ΔS_{vib} (= 8 mcal/g/°C). A correlation of strong (fragile)- melts with a small (large) magnitude of ΔC_p across T_g has been suggested (Angell, 2000). That correlation is also observed in the present findings (**Figure 10B**). But the present results also show a far more striking correlation of melt fragility with the enthalpy of relaxation, $\Delta H_{nr}(x)$ of the glass.

We note that $\Delta H_{nr}(x)$ is vanishingly small in glasses resulting from superstrong melts, but it increases by several orders of magnitude in glasses that result from fragile melts. The $\Delta H_{nr}(x)$ term results from the non-reversing heat flow and it contributes an entropy change (ΔS_{conf}) that is configurational, which far exceeds ΔS_{vib} resulting from the jump in C_p across T_g, ΔC_p, which comes from the reversing heat flow. We view the presence of the rather high value of ΔS_{conf} term in the IP to suggest that the configurational entropy of IP melts decreases minimally ($\Delta H_{nr}(x) = 0$) for IP glasses, underscoring that networks characterizing the IP have a rather high entropy, i.e., a liquid-like entropy. On the other hand, the much higher value of $\Delta H_{nr}(x)$ in the relaxed non-IP glass compositions constitutes a signature that their phases have undergone substantial reconstruction upon aging and possess a lower configurational entropy than their high-T melt counterparts **(Figure 5C)**.

In the Flexible phase (x < 10%), the large increase in ΔH_{nr} upon aging (**Figure 5B**), and in the projected melt configurational entropy S_c (**Figure 5C**), we trace to the polymeric Se_n chains. As x decreases in the 0% < x < 10% range, the Se_n chains grow in length with $n \sim 250$ in pure Se. The uncorrelated Se_n chains characteristic of the fresh glass, particularly if they are long ($n > 15$) will reconstruct with each other and get correlated (Dash et al., 2017), while some of the long chains will transform to Se_8 rings, as documented (Dash et al., 2017) in the Se-rich (x < 8%) phase of binary Ge_xSe_{100-x} glasses from Raman scattering. Specifically, the broad band near 250 cm^{-1} in Raman scattering of these Se-rich glasses is composed of a triad of modes identified respectively with (i) correlated Se_n chains, (ii) uncorrelated Se_n chains and (iii) Se_8 rings, and aging induced changes in the scattering strength of these modes have assisted in identifying

the microscopic origin of aging (Dash et al., 2017) and would understandably apply to the flexible phase of the present ternary as well.

In the Stressed-rigid phase of the present ternary glasses ($x > 17.0\%$), the glass backbone is composed of high mean coordination number <r> local structures. These include CS- (2.40) and ES- $GeSe_2$ (2.67) tetrahedra and Pyramidal $As(Se_{1/2})_3$ (2.40). The backbone compacts as revealed by the steadily decreasing Molar volumes (**Figure 5D)**. And aging will further lead to a compaction of the network resulting in the configurational entropy to decrease or ΔH_{nr} to increase (**Figure 5B**). On the other hand, in the IP, quite remarkably, the presence of an isostatically rigid and stress-free backbone, endows glasses with a new functionality to adapt and self-organize. And aging is qualitatively suppressed in this phase.

Glass Molecular Structure and Intermediate Phases

One of the more challenging issues in glass science is to predict the compositional windows across which networks can self-organize to display IPs and the underlying molecular structure manifestations. Some important clues on the microscopic origin of self-organization effects can be sought by examining the molecular structure of glasses. The IPs in the Ge-Se and As-Se binary systems, and the present $Ge_xAs_xSe_{100-2x}$ ternary are established. It is useful to inquire if these windows display any correlations, and, if so, what one might learn on the molecular structure of the IP from such correlations. We comment on some of these issues next.

Reversibility Windows of As-Se, Ge-Se Binary Exhaust the Window of the Present $Ge_xAs_xSe_{100-2x}$ Ternary

Upon alloying traces of As- and Ge- in a base Se glass one expects the chains of polymeric Se_n chains to be crosslinked by As-centered quasi-tetrahedra, $Se{=}As(Se_{1/2})_3$ (<r> = 2.28) and As-centered pyramids, $As(Se_{1/2})_3$, (<r> = 2.40), Ge centered corner-sharing (CS)- $GeSe_4$ tetrahedra (<r> = 2.40), and Ge-centered edge sharing (ES)-$GeSe_2$ tetrahedra (<r>= 2.67) progressively. A count of bond-stretching and bond-bending constraints shows that the four local structures, viz., Se = $As(Se_{1/2})_3$, $As(Se_{1/2})_3$, $GeSe_4$, ES-GeSe2 are isostatically rigid ($n_c = 3$). The presence of both As- centered and Ge-centered local structures leads to chemical disorder, increases the configurational entropy of the backbone and thus assists (Yan, 2018), in formation of the IP. The presence of chemical disorder suppresses NSPS effects and thereby a T_g maximum near the chemical threshold. The latter feature is observed in respective binary glasses as eluded earlier. And since the mean coordination numbers of these local structures steadily increase in the $2.28 < <r> < 2.67$ range, one expects As-centered local structures to predominantly form in the $2.28 < <r> < 2.40$ range and, at higher x, the Ge-centered local structures to form in the $2.40 < <r> < 2.51$ range. In a qualitative fashion, one may thus view the superposition of both binary glass reversibility windows to broadly account for the wider reversibility window in the present ternary. What do we know about the IP in Ge-Se binary and As-Se binary glass systems?

Bhosle et al. (2012b), reported upon the reversibility window in homogeneous binary Ge_xSe_{100-x} glasses. They found the window to be abrupt and square-well like with the onset of rigidity near $x_r = 2.39$ and onset of stress, $x_s = 2.52$. That result was the culmination of an effort spread over 15 years, in which the shape of the reversibility window changed from triangular-like, to Gaussian-like to becoming Square-well like as melt/glass specimen were steadily homogenized (Bhosle et al., 2012b), and the variance in Ge-stoichiometry was systematically reduced from about 1.0–0.05% as the alloying time of melts at 950°C was increased from 2 days to about 7 days.

In the first MDSC study of As-Se glasses (Georgiev et al., 2001) where the existence of a reversibility window was observed (**Figure 12**) in the $29\% < x < 37\%$ range, binary melts were alloyed near 700°C for 3 days and then water quenched. The glasses were never T_g cycled after the quench but merely aged at room temperature, thereby offsetting the segregation effect of the eutectic. And the reversibility window observed is characteristic of glasses composed of As-centered pyramidal and quasi-tetrahedral local structures. Here, one must recall that the Eutectic temperature, T_E (= 147 °C) is close to the T_g (= 104 °C) of glasses near x = 20% of As. It is for this reason that in aging studies of the reversibility window in subsequent studies (Golovchak et al., 2008; Ravindren et al., 2014) the integrity of the window was not preserved. In the more detailed study of Ravindren et al. (2014) where glasses were especially homogenized by alloying melts for extended periods, they were T_g cycled after a water quench. In that study, one also found the reversibility window to steadily smear, particularly near x = 20%, the eutectic composition (**Figure 13**), as glasses aged and steadily segregated (Ravindren et al., 2014). In a glass forming system wherein a eutectic is present close to the reversibility window, one expects thermodynamic considerations based on segregation to override self-organization effects, particularly suppression of aging of the enthalpy of relaxation due to segregation effects.

Although the existence of the Eutectic in As-Se binary, as well as P-Se binary, is well-recognized (Okamoto, 2000), the role of the eutectic on self-organization effects has received recognition only recently. And it may be helpful to add a few comments on that topic for completeness. The eutectic is signature of segregation of respective melts into Se-rich and As- rich regions. We believe that the As-rich regions consist of ethylene-like $(As)_2(Se_{1/2})_4$ local structures containing homopolar As-As bonds in a Se-rich glassy matrix. The evidence for these local structures have emerged recently (Ravindren, 2015) from close analogies in Raman scattering of the P-Se and As-Se binary systems. They have suggested that ethylene like $(As)_2(Se_{1/2})_4$ local structure in analogy to $(P)_2(Se_{1/2})_4$ local structure exist, for which independent confirmation is given by MD simulations (Bauchy and Micoulaut, 2013) and ^{31}P NMR (Eckert, 1989).

To summarize, we illustrate in **Figure 13**, Topological phases of the Ge_xSe_{100-x} and As_xSe_{100-x} binary systems and the present $Ge_xAs_xSe_{100-2x}$ ternary on the Ge-As-Se composition triangular plot (Qu et al., 2002; Wang et al., 2009). The IP in As-Se binary (green, label A) and the Ge-Se binary (purple, label B) when

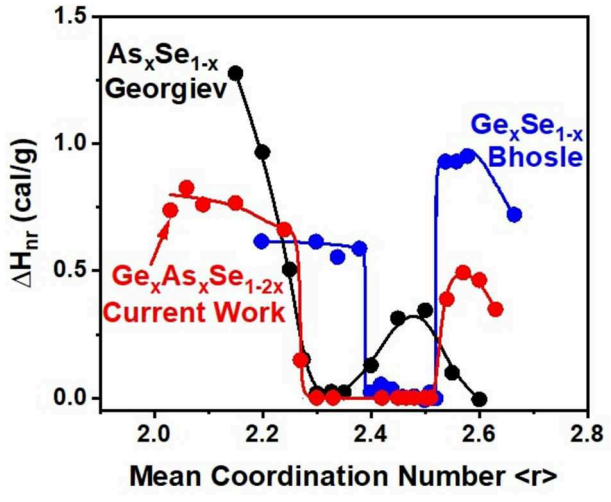

FIGURE 12 | Reversibility window in $Ge_xAs_xSe_{100-2x}$ after 8 months of aging compared to the windows in As-Se and Ge-Se binary glasses taken from Georgiev et al. (2000) and Bhosle et al. (2012b).

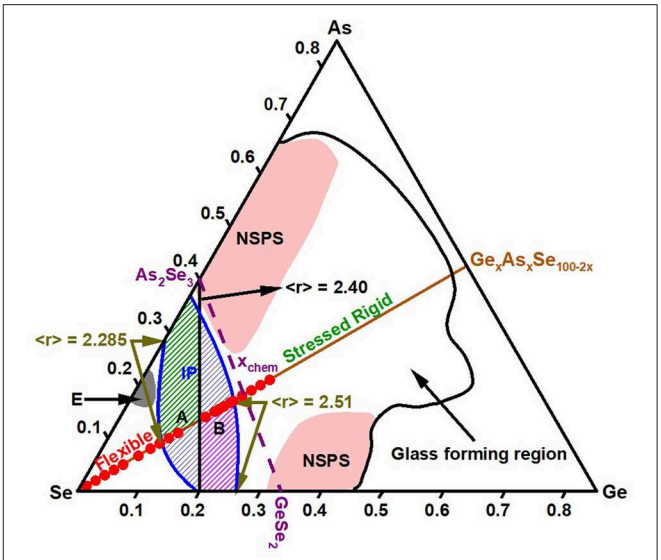

FIGURE 13 | Topological phases observed in Ge_xSe_{100-x} binary (Bhosle et al., 2012b), As_xSe_{100-x} binary (Georgiev et al., 2000) and $Ge_xAs_xSe_{100-2x}$ ternary projected on the Ge-As-Se compositional triangle. The glass forming region is taken from ref. Z.U. Borisova (Borisova, 1981). Starting from pure Se, as we move along the equimolar composition *x*, one spans the Flexible phase ($0 < < r > < 2.285$), the Intermediate Phase ($2.285 < < r > < 2.51$) followed by the stressed-rigid phase ($< r > > 2.51$), and with the red data points showing the 20 glass compositions examined in the present study. Note the black line joining the As_2Se_3 glass composition to the $GeSe_4$ one, is the locus of glass compositions with $< r > = 2.40$, and it splits the IP of the equimolar ternary into almost nearly equal parts, labeled A (hashed green) and B (hashed purple), with the segment A (B) nearly overlapping with IPs observed in As_xSe_{100-x} (Ge_xSe_{100-x}) binary systems, respectively. The broken line of purple color, joining As_2Se_3 to $GeSe_2$ composition, represents the join of chemical threshold compositions (x_{chem}), with NSPS setting in as x approaches x_{chem} in both binary glass systems but not the present equimolar ternary as sketched. Feature E centered near $x = 20\%$ of As in the As_xSe_{100-x} join is the Eutectic in that binary system. See text.

combined add up to the IP of the present ternary as illustrated by the vertical lines delineating the <r> markers at 2.28, 2.40, and 2.51. Noteworthy in the plot is the onset of NSPS in the binary glass systems near the stoichiometric chemical compositions (Boolchand et al., 2002) $GeSe_2$ and As_2Se_3. In these NSPS regions it is unlikely that the network backbone connectivity has a unique value, often estimated by the usual 8-N bonding rule, taking the coordination number of Ge, As, and Se to be 4, 3, and 2, respectively.

Molecular Structure Evolution of Stressed-Rigid Networks in Binary Ge-Se and Ternary $Ge_xAs_xSe_{100-2x}$ Glasses Compared and Contrasted

The unusual nature of glass structure evolution in the binary Ge_xSe_{100-x} displaying molecular clustering in the Se-rich range ($x < 33.3\%$) emerged from Mössbauer spectroscopy experiments using ^{129m}Te tracer (Bresser et al., 1986). Both Te and Se atoms belong to the VIth column of the periodic table, are isovalent and take on a 2-fold coordination here. The larger covalent radius of Te (of 138 pm) than Se (of 120 pm) has profound consequences; Te selectively replaces available Se sites possessing a larger free volume, such as surface sites of characteristic molecular clusters rather than cluster interior sites (Bresser et al., 1986).

In these Mössbauer experiments, the ^{129}I daughter A-site represents the chemically ordered site, formed from a parent ^{129m}Te atom bonded to 2 Ge near neighbors (nns), while the ^{129}I daughter B-site results from a ^{129m}Te parent atom bonded to either two Se nns or a Se and a Ge nn (Bresser et al., 1986). In a continuous random network (CRN) description of these glasses, one expects the site intensity ratio $N_B/N_A(x)$ as a function of Ge content "x" to show a smooth broken-line curve starting from an infinite value at $x = 0$, to approaching 0 at $x = 33.3\%$ for a chemically ordered stoichiometric $GeSe_2$ glass (**Figure 14B**). At $x = 0$, all Te atoms would have two Se nns (i.e., only B sites are possible), while at $x = 33.3\%$ each Te atom would have only Ge nns if the $GeSe_2$ glass is chemically ordered, so that only A sites are possible. In the Mössbauer effect experiments, on the other hand, trends in $I_B/I_A(x)$ mimic the expectation of a CRN model only at low $x < 15\%$ of Ge, but, as x increases ($> 15\%$), the site intensity ratio $I_B/I_A(x)$ displays a local maximum near $x = x_c = 23\%$, corresponding to the centroid of the IP, where molecular clustering has evolved, and the $I_B/I_A(x)$ ratio remains finite at 1.60(4) as $x = 33.3\%$. The results underscore that the stoichiometric glass is not chemically ordered (Bresser et al., 1981, 1986; Boolchand et al., 1982; Boolchand and Bresser, 2000; Salmon and Petri, 2003). It is composed of large Se-rich clusters based on the high–T form of c-$GeSe_2$ (α-$GeSe_2$) (Bridenbaugh et al., 1979; Boolchand, 1985) whose surfaces are intrinsically reconstructed in the glass to form Se-Se dimers, which may be viewed as Topological defects. The late Dr. K. Murase correctly identified that the Raman stretch mode of Se-Se dimers on the surface of reconstructed clusters is near 246 cm^{-1} (Boolchand, 2000a).

Presence of these Se-Se bonds, on grounds of stoichiometry, requires Ge-Ge bonds to exist in stoichiometric $GeSe_2$ glass. Evidence of such bonds in small Ge-rich clusters based

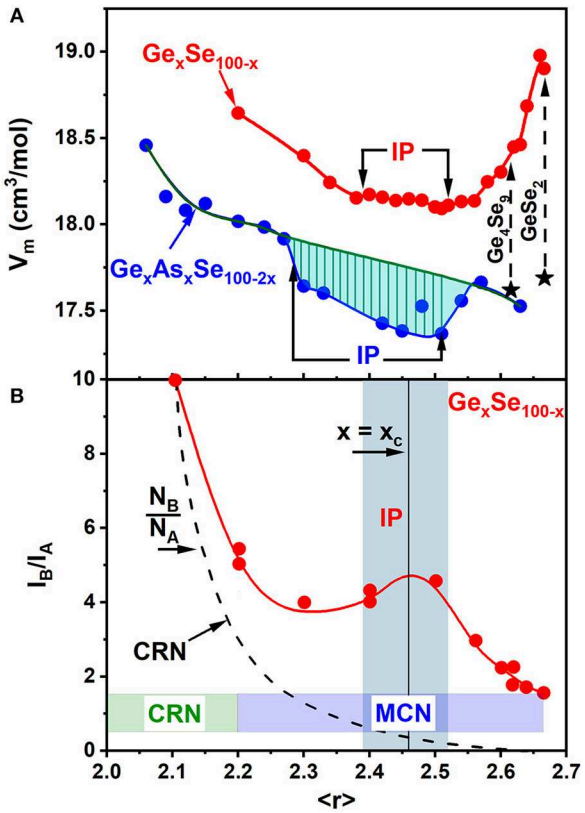

FIGURE 14 | (A) Trends in molar volumes, $V_m(x)$ of binary Ge_xSe_{100-x} glasses compared to those of the present $Ge_xAs_xSe_{100-2x}$ ternary glasses. **(B)** ^{129}I Mössbauer site intensity ratios I_B/I_A (x), deduced from doping ^{129m}Te tracer in Ge_xSe_{100-x} glasses reveal a Continuous Random network (CRN) type of a variation at low *x* (<10%). But at higher *x* (>15%) a Molecular Clustered Network (MCN) prevails as the observed site intensity ratios I_B/I_A (x) far exceed the expected $N_B/N_A(x)$ site concentration ratio based on a CRN (Bresser et al., 1986). See text. Also note that as x increases to 33.3% of Ge, the finite value of the I_B/I_A ratio of 1.66 (10) shows the stoichiometric $GeSe_2$ glass has an intrinsically broken chemical order (Bresser et al., 1986).

on ethane-like Ge_2Se_6 local molecular units, emerged from Raman scattering, and independently from ^{119}Sn Mössbauer effect experiments. Since Sn is isovalent to Ge, ^{119}Sn Mössbauer Effect experiments probe the chemically specific Ge-local structures (Boolchand and Bresser, 2000) formed in the glass, which includes both the tetrahedrally coordinated Ge sites as well as the non-tetrahedrally coordinated Ge sites as in the ethane-like Ge-rich cluster possessing Ge-Ge bonds.

The molecular clustering picture of binary Ge_xSe_{100-x} glasses developed above is elegantly corroborated in the measured $V_m(x)$ results that show a qualitative increase in the stressed-rigid regime at x > 26%. That behavior in $V_m(x)$ in Ge-Se binary differs qualitatively from the one observed in the present ternary chalcogenide. It raises the questions what is so special about the structure of these stressed-rigid binary Ge-Se glass compositions that their network structure leads to packing effects that are so different? The issue was at the center of controversy in the mid-1980s (Bridenbaugh et al., 1979; Bresser et al., 1981, 1986; Murase et al., 1983). In the equilibrium phase diagram of the Ge-Se binary there exist two crystalline phases of relevance here (i) a low T metastable structure of Ge_4Se_9 stoichiometry (x = 30.8%) of $V_m = 17.62$ cm^3 (Fjellvåg et al., 2001), and a high-T form α- $GeSe_2$ (x = 33.33%) of $V_m = 17.69$ cm^3 (Burgeat et al., 1975). The α- $GeSe_2$ phase consist of a stacking of 2D sheets, with each sheet composed of chains of CS $GeSe_2$ tetrahedra that are laterally coupled by a pair of ES units (Phillips et al., 1980). The structure of Ge_4Se_9 is strikingly similar to that of α-$GeSe_2$, except the pair of ES tetrahedra linking the CS chains are altered in a subtle way: these become CS tetrahedral units linked by an additional Se-Se dimer bond. Returning to the binary Ge_xSe_{100-x} glasses, once x > 31.5%, one observes ethane-like Ge-rich cluster to appear in ^{119}Sn Mössbauer spectroscopy (Boolchand et al., 1982; Boolchand and Bresser, 2000), as well as in Raman scattering (Bhosle et al., 2012a) where evidence of a mode near 180 cm^{-1} associated with these Ge-rich cluster is observed. Clearly, as the Ge content of glasses x exceeds 31.5%, much of the Ge additive now goes into forming the Ge-rich clusters that decouple from the Se-rich backbone, thus arresting the growth of $T_g(x)$, and one observes the slope dT_g/dx to display a maximum at that composition (Bhosle et al., 2012b). The onset of backbone demixing as x > 31.5% leads the non-bonding van der Waals interaction between the clusters to grow. And we view the rapid increase of $V_m(x)$ of binary Ge_xSe_{100-x} glasses in the 2.62 < <r> < 2.67 range (**Figure 14A**) as a direct consequence of demixing of the backbone into small Ge-rich and large Se-rich clusters. And as x = 33.3%, $dT_g/dx = 0$, leading to a maximum of T_g, which constitutes direct evidence for the stoichiometric glass to be segregated or NSPS (Boolchand, 2000b; Boolchand et al., 2002). Such segregation is also observed in binary As-Se, Ge-S, and As-S glasses near the chemical threshold, but it notably absent in binary Si-Se glasses (Boolchand, 2000b).

In the present ternary, upon alloying As an additive in the Ge-Se binary, the NSPS effects are also completely suppressed. Trends in $V_m(x)$ are qualitatively reversed. In the present ternary $V_m(x)$ decreases with x (**Figure 14A**), as more connected local structures based on As-centered -QT units and -PYR units, Ge-centered -CS and -ES tetrahedral units emerge, and chemically disorder the network backbone. The presence of this chemical disorder precludes the growth of the 2D layer form of α-$GeSe_2$ fragments or the 2D form As_2Se_3 like 6 membered rings (Kim and Boolchand, 1979; Phillips et al., 1980; Boolchand et al., 1986) to nucleate and form part of the backbone. It is for this reason the glassy backbone evolves in a topology that is Continuous Random Network (CRN) like steadily compacting with increasing x or <r>. And remarkably no evidence of NSPS is evidenced as suggested by the absence of a T_g maximum near the chemical threshold (x = 18.18% or <r> = 2.55). Furthermore, an *additional reduction* of V_m in the IP range (2.28 < <r> < 2.53) (**Figure 14A**) from the average value of $V_m(x)$ outside the IP is observed. It emerges because the strong covalent bonding forces (bond-stretching and bond-bending) due to the known local structures satisfy the Maxwell-Phillips criteria (n_c = 3) for rigidity, permitting the weaker and long range van der Waals forces to come into play and compact (Boolchand

et al., 2013) glassy backbones formed in that isostatically rigid reversibility window (**Figure 14A**).

Intermediate Phase Glasses as Ideal Glasses

Adam-Gibbs (Adam and Gibbs, 1965) suggested that the viscosity of a melt increases as its excess configurational entropy (S_c) decreases as it is cooled to T_g described by the relation,

$$\eta = \eta_o \exp(\frac{B}{TS_c}) \quad (6)$$

Since the viscosity of a melt is viewed to be a thermally-activated process,

$$\eta = \eta_o \exp(\frac{E_a}{k_B T}) \quad (7)$$

and from the two relations above, one must then require that the inverse of the activation energy for shear relaxation time provides a measure of the excess entropy loss (S_c) upon cooling of a melt,

$$\frac{E_a}{k_B T} = \frac{B}{TS_c} \quad (8)$$

$$Or$$

$$S_c = \frac{Bk_B}{E_a} \quad (9)$$

From Equation (9), one recognizes that the inverse of the activation energy for shear relaxation time provides a measure of the excess configurational entropy of the melt as it cools.

Since the fragility index deduced from calorimetric measurements are often correlated with those inferred from viscosity or shear relaxation times, one then expects the inverse activation energy, $1/E_a$, from calorimetric measurements to provide a measure of configurational entropy loss as a melt is cooled.

The inverse activation energy for enthalpy relaxation ($1/E_a$) in the present Ge-As-Se chalcogenide melts as a function of composition, **Figure 5C**, displays a maximum near the center of the IP. The result unambiguously shows that as an IP melt cools from a high T to $T = T_g$, the configurational entropy S_c remains high, and indeed, that is also the reason the resulting glass has a near vanishing non-reversing enthalpy, $\Delta H_{nr}(x)$. Such glass compositions are viewed as possessing liquid-like structures with a high S_c and for that reason show minimal aging (Boolchand and Goodman, 2017). The low propensity for aging of isostatic glasses also echoes the fact that isostatic systems have been shown to exhibit minimum creep deformations under sustained load (Pignatelli et al., 2016; Bauchy et al., 2017). On the other hand, the non-IP glass compositions have their structure evolve with either polymeric Se_n chains (as in t-Se, entropy sinks) forming at $x < 9.5\%$ or CS and ES- $GeSe_2$ tetrahedra and pyramidal $As(Se_{1/2})_3$ units forming at $x > 17\%$, and leading the $\Delta H_{nr}(x)$ term to increase, and thus lower the configurational entropy of the melt/glass (**Figures 5B,C**). IP glass compositions display a high glass-forming tendency, show minimal aging, and are thus Ideal glasses. These ideas of IP glasses as ideal glasses are at variance with the notion that ideal network glasses possess low configurational entropy and form at T close to the Kauzmann temperature (Angell, 1995). On the other hand, the high configurational entropy of IP glass compositions and their functionality to adapt are much closer to the recent ideas of a competition between entropy and energy to stabilize the intermediate phase (Yan, 2018).

CONCLUSIONS

The specially homogenized nature of the bulk $Ge_xAs_xSe_{100-2x}$ glasses synthesized in the present work have lead the frequency corrected Enthalpy of relaxation at T_g, $\Delta H_{nr}(x)$, to display a square-well-like reversibility window even in the fresh (rejuvenated) state. Upon room temperature aging for 8 months, the window gets substantially deeper. The reversibility window is bordered by an abrupt rigidity- transition, near $x_r = 9.5(2)\%$ and an equally abrupt stress-transition near $x_s = 17.0(3)$ %.

The specially homogenized nature of the bulk glasses synthesized in the present work has also led molar volumes (V_m) across the IP composition range, $9.5\% < x < 17\%$, to show an additional small but systematic reduction of 2.5% in V_m in the IP from the average behavior of V_m across the range of compositions examined. The result demonstrates the compacted nature (Boolchand et al., 2013) of the isostatic networks formed in that special phase.

The melt fragility index, m(x), deduced from MDSC experiments show a Gaussian-like global minimum with $m(x) < 20$ for IP compositions, defining the fragility window. The fragility window coinciding with the reversibility window, underscores that super-strong melts give rise to IP glasses, while fragile melts to either flexible or stressed-rigid glasses, leading to the conclusion that melt dynamics encode glass Topological phases.

Trends in the projected melt viscosity, $\eta(x)$ using the measured fragility index, m(x), and the MYEGA formalism, show almost three orders of magnitude increase in $\eta(x)$ in the $0 < x < 20\%$ range. Trends in the inverse of the projected viscosity, $1/\eta(x)$, broadly parallel the melt diffusivities D calculated from ab-initio MD simulation. These results are strongly suggestive that the delayed homogenization of melts during synthesis is due to the low diffusivities or high viscosity of melts at 950°C in the $13\% < x < 25\%$ composition range.

Finally, the inverse of the activation energy for enthalpy relaxation time shows a maximum near $x = 14\%$, the center of the IP melt compositions, strongly suggesting that such melts possess a high liquid-like configurational entropy, S_c, in the Adams-Gibbs picture. The optimization of the glass forming tendency for IP compositions, the stress-free nature of these structures in which three types of isostatically-rigid local structures proliferate, and the qualitative suppression of aging in that phase, the high configurational entropy of IP networks, each point to the ideal nature of glasses formed in the IP. Some of these exceptional functionalities of IP networks observed in experiments, appear to find support in

recent ideas based on Statistical Mechanics modeling of the IP (Yan, 2018).

DATA AVAILABILITY

The datasets for this manuscript are not publicly available because much of the work comes from the Ph.D. dissertation of RC and it will be available when he defends his thesis. Requests to access the datasets should be directed to boolchp@ucmail.uc.edu.

AUTHOR CONTRIBUTIONS

RC synthesized glasses and performed MDSC experiments, Raman scattering, and Molar volume experiments. He analyzed these data working closely with PB. MB and MM assisted with numerical simulations and extensive discussions on topological phases, melt dynamics, and ideal glasses. PB coordinated the experimental work performed at University of Cincinnati, and all co-authors RC, MB, MM, and PB assisted in writing the manuscript.

FUNDING

PB acknowledges support from NSF grant DMR 08-53957. MM acknowledges support of Agence Nationale de la Recherche(ANR) Grant No ANR-11-BS08-10012 from American Fulbright Commission and International Materials Institute (H. Jain). MB acknowledges support from NSF grants 1562066, 1762292, and 1826420.

ACKNOWLEDGMENTS

It is a pleasure to thank Dr. Alan Jackson for assistance with simulation package NRLMOL to calculate Raman and Infrared vibrations from characteristic local structures. We acknowledge with much pleasure continued discussions with Dr. Bernard Goodman, Dr. Jim Phillips, and Dr. Sergey Mamedov on issues of glass science and Dr. Caleb McDonald for issues on MDSC. We are indebted to Leonard Thomas for providing crucial insights on the frequency correction effect of the enthalpy of relaxation at T_g that he discovered and presented at the September, 1995 NATAS Conference, San Francisco, CA.

REFERENCES

Adam, G., and Gibbs, J. H. (1965). On the temperature dependence of cooperative relaxation properties in glass-forming liquids. *J. Chem. Phys.* 43, 139–146. doi: 10.1063/1.1696442

Angell, A. (2000). "Glass formation and the nature of the glass transitions," in *Insulating and Semiconducting Glasses Series on Directions in Condensed Matter Physics*, ed P. Boolchand (Singapore: World Scientific), 1–51. doi: 10.1142/9789812813619_0001

Angell, C. A. (1995). Formation of glasses from liquids and biopolymers. *Science* 267, 1924–1935. doi: 10.1126/science.267.5206.1924

Barré, J., Bishop, A. R., Lookman, T., and Saxena, A. (2005). Adaptability and "intermediate phase" in randomly connected networks. *Phys. Rev. Lett.* 94:208701. doi: 10.1103/PhysRevLett.94.208701

Bauchy, M. (2019). Deciphering the atomic genome of glasses by topological constraint theory and molecular dynamics: a review. *Comput. Mater. Sci.* 159, 95–102. doi: 10.1016/j.commatsci.2018.12.004

Bauchy, M., and Micoulaut, M. (2013). Structure of As_2Se_3 and AsSe network glasses: evidence for coordination defects and homopolar bonding. *J. Non Crystal. Solids* 377, 34–38. doi: 10.1016/j.jnoncrysol.2013.01.019

Bauchy, M., and Micoulaut, M. (2015). Densified network glasses and liquids with thermodynamically reversible and structurally adaptive behaviour. *Nat. Commun.* 6:6398. doi: 10.1038/ncomms7398

Bauchy, M., Micoulaut, M., Boero, M., and Massobrio, C. (2013). Compositional thresholds and anomalies in connection with stiffness transitions in network glasses. *Phys. Rev. Lett.* 110, 165501. doi: 10.1103/PhysRevLett.110.165501

Bauchy, M., Wang, M., Yu, Y., Wang, B., Krishnan, N. M. A., Masoero, E., et al. (2017). Topological control on the structural relaxation of atomic networks under stress. *Phys. Rev. Lett.* 119:035502. doi: 10.1103/PhysRevLett.119.035502

Becke, A. D. (1988). Density-functional exchange-energy approximation with correct asymptotic behavior. *Phys. Rev. A* 38:3098. doi: 10.1103/PhysRevA.38.3098

Bestul, A. B., and Chang, S. S. (1964). Excess entropy at glass transformation. *J. Chem. Phys.* 40, 3731–3733. doi: 10.1063/1.1725086

Bhosle, S., Gunasekera, K., Boolchand, P., and Micoulaut, M. (2012a). Melt homogenization and self-organization in chalcogenides-part I. *Int. J. Appl. Glass Sci.* 3, 189–204. doi: 10.1111/j.2041-1294.2012.00093.x

Bhosle, S., Gunasekera, K., Boolchand, P., and Micoulaut, M. (2012b). Melt homogenization and self-organization in chalcogenides-part II. *Int. J. Appl. Glass Sci.* 3, 205–220. doi: 10.1111/j.2041-1294.2012.00092.x

Bhosle, S., Gunasekera, K., Chen, P., Boolchand, P., Micoulaut, M., and Massobrio, C. (2011). Meeting experimental challenges to physics of network glasses: assessing the role of sample homogeneity. *Solid State Commun.* 151, 1851–1855. doi: 10.1016/j.ssc.2011.10.016

Böhmer, R., and Angell, C. A. (1992). Correlations of the nonexponentiality and state dependence of mechanical relaxations with bond connectivity in Ge-As-Se supercooled liquids. *Phys. Rev. B* 45, 10091–10094. doi: 10.1103/PhysRevB.45.10091

Boolchand, P. (1985). "Mossbauer spectroscopy–a rewarding probe of morphological structure of semiconducting glasses," in *Physical Properties of Amorphous Materials* Institute for Amorphous Studies Series, eds D. Adler, B. Schwartz, and M. C. Steele (Springer). Available online at: https://www.springer.com/us/book/9780306419072 (accessed January 13, 2019). doi: 10.1007/978-1-4899-2260-1_7

Boolchand, P. (2000a). *Insulating and Semiconducting Glasses*. Singapore: World Scientific. doi: 10.1142/9789812813619

Boolchand, P. (2000b). The maximum in glass transition temperature T_g near $x = 1/3$ in Ge_xSe_{1-x} glasses. *Asian J. Phys.* 9, 709–721.

Boolchand, P., Bauchy, M., Micoulaut, M., and Yildirim, C. (2018). Topological phases of chalcogenide glasses encoded in the melt dynamics. *Phys. Status Solidi* 255:1800027. doi: 10.1002/pssb.201800027

Boolchand, P., and Bresser, W. J. (2000). The structural origin of broken chemical order in $GeSe_2$ glass. *Philos. Magazine B* 80, 1757–1772. doi: 10.1080/13642810008216504

Boolchand, P., Bresser, W. J., and Suranyi, P. (1986). The molecular structure of As_2Se_3 glass. *Hyperfine Interact.* 27, 385–388. doi: 10.1007/BF02354787

Boolchand, P., Enzweiler, R. N., Cappelletti, R. L., Kamitakahara, W. A., Cai, Y., and Thorpe, M. F. (1990). Vibrational thresholds in covalent networks. *Solid State Ionics* 39, 81–89. doi: 10.1016/0167-2738(90)90029-Q

Boolchand, P., Georgiev, D. G., and Goodman, B. (2001). Discovery of the intermediate phase in chalcogenide glasses. *J. Optoelectron. Adv. Mater.* 3, 703–720.

Boolchand, P., Georgiev, D. G., Qu, T., Wang, F., Cai, L., and Chakravarty, S. (2002). Nanoscale phase separation effects near r=2.4 and 2.67, and rigidity transitions in chalcogenide glasses. *Comptes Rendus Chimie* 5, 713–724. doi: 10.1016/S1631-0748(02)01440-6

Boolchand, P., and Goodman, B. (2017). Glassy materials with enhanced thermal stability. *MRS Bull.* 42, 23–28. doi: 10.1557/mrs.2016.300

Boolchand, P., Grothaus, J., Bresser, W. J., and Suranyi, P. (1982). Structural origin of broken chemical order in a $GeSe_2$ glass. *Phys. Rev. B* 25, 2975–2978. doi: 10.1103/PhysRevB.25.2975

Boolchand, P., Mauro, J. C., and Phillips, J. C. (2013). A note on compacted networks. *Phys. Today* 66:10. doi: 10.1063/PT.3.1932

Borisova, Z. (1981). *Glassy Semiconductors*. Springer. Available online at: https://www.springer.com/us/book/9781475708530 (accessed April 4, 2019). doi: 10.1007/978-1-4757-0851-6

Bouzid, A., Massobrio, C., Boero, M., Ori, G., Sykina, K., and Furet, E. (2015). Role of the van der Waals interactions and impact of the exchange-correlation functional in determining the structure of glassy $GeTe_4$. *Phys. Rev. B* 92:134208. doi: 10.1103/PhysRevB.92.134208

Bresser, W., Boolchand, P., and Suranyi, P. (1986). Rigidity percolation and molecular clustering in network glasses. *Phys. Rev. Lett.* 56, 2493–2496. doi: 10.1103/PhysRevLett.56.2493

Bresser, W. J., Boolchand, P., Suranyi, P., and de Neufville, J. P. (1981). Direct evidence for intrinsically broken chemical ordering in melt-quenched glasses. *Phys. Rev. Lett.* 46, 1689–1692. doi: 10.1103/PhysRevLett.46.1689

Bridenbaugh, P. M., Espinosa, G. P., Griffiths, J. E., Phillips, J. C., and Remeika, J. P. (1979). Microscopic origin of the companion A_1 Raman line in glassy $Ge(S,Se)_2$. *Phys. Rev. B* 20, 4140–4144. doi: 10.1103/PhysRevB.20.4140

Briley, A., and Pederson, M. R. (1998). Vibrational frequencies and intensities of small molecules: all-electron, pseudopotential, and mixed-potential methodologies. *Phys. Rev. B Condensed Matter Mater. Phys.* 58, 1786–1793. doi: 10.1103/PhysRevB.58.1786

Burgeat, J., le Roux, G., and Brenac, A. (1975). Sur une nouvelle forme cristalline de $GeSe_2$. *J. Appl. Crystallogr.* 8, 325–327. doi: 10.1107/S0021889875010527

Car, R., and Parrinello, M. (1985). Unified approach for molecular dynamics and density-functional theory. *Phys. Rev. Lett.* 55, 2471–2474. doi: 10.1103/PhysRevLett.55.2471

Carpentier, L., Desprez, S., and Descamps, M. (2003). From strong to fragile glass-forming systems: a temperature modulated differential scanning calorimetry investigation. *Phase Trans.* 76, 787–799. doi: 10.1080/01411590310001603708

Chakraborty, S., and Boolchand, P. (2014). Topological origin of fragility, network adaptation, and rigidity and stress transitions in especially homogenized nonstoichiometric binary GeS glasses. *J. Phys. Chem. B* 118, 2249–2263. doi: 10.1021/jp411823j

Chen, P., Boolchand, P., and Georgiev, D. G. (2010). Long term aging of selenide glasses: evidence of sub-T_g endotherms and pre-T_g exotherms. *J. Phys.-Condes. Matter* 22:065104. doi: 10.1088/0953-8984/22/6/065104

Chen, Z., Wang, G., and Wang, X. (2019). Physical mechanism and response characteristics of unsaturated optical stopping-based amorphous arsenic sulfide thin-film waveguides. *IEEE Photon. J.* 11, 1–10. doi: 10.1109/JPHOT.2019.2894741

Chubynsky, M. V., Brière, M.-A., and Mousseau, N. (2006). Self-organization with equilibration: a model for the intermediate phase in rigidity percolation. *Phys. Rev. E* 74:016116. doi: 10.1103/PhysRevE.74.016116

Dash, S., Chen, P., and Boolchand, P. (2017). Molecular origin of aging of pure Se glass: growth of inter-chain structural correlations, network compaction, and partial ordering. *J. Chem. Phys.* 146:224506. doi: 10.1063/1.4983480

Debenedetti, P. G., and Stillinger, F. H. (2001). Supercooled liquids and the glass transition. *Nature* 410, 259–267. doi: 10.1038/35065704

Descamps, M., and Decroix, A. A. (2014). Polymorphism and disorder in caffeine: dielectric investigation of molecular mobilities. *J. Mol. Struct.* 1078, 165–173. doi: 10.1016/j.molstruc.2014.04.042

Eckert, H. (1989). Structural characterization of non-oxide chalcogenide glasses using solid state NMR. *Angew. Chem. Int. Edn. English* 28, 1723–1732. doi: 10.1002/anie.198917231

Fabian, R., and Sidebottom, D. L. (2009). Dynamic light scattering in network-forming sodium ultraphosphate liquids near the glass transition. *Phys. Rev. B* 80:064201. doi: 10.1103/PhysRevB.80.064201

Fjellvåg, H., Kongshaug, K. O., and Stølen, S. (2001). Crystal structure of Ge4Se9: a new germanium selenide with Se2 pairs breaking the edge-sharing GeSe4 tetrahedra in GeSe2. *J. Chem. Soc. Dalton Trans.* 1043–1045. doi: 10.1039/b009794m

Fulcher, G. (1925). Analysis of recent measurements of viscosity of glasses. *J. Am. Ceram. Soc.* 8, 339–355. doi: 10.1111/j.1151-2916.1925.tb16731.x

Georgiev, D. G., Boolchand, P., and Micoulaut, M. (2000). Rigidity transitions and molecular structure of As_xSe_{1-x} glasses. *Phys. Rev. B* 62, R9228–R9231. doi: 10.1103/PhysRevB.62.R9228

Georgiev, D. G., Mitkova, M., Boolchand, P., Brunklaus, G., Eckert, H., and Micoulaut, M. (2001). Molecular structure, glass transition temperature variation, agglomeration theory, and network connectivity of binary P-Se glasses. *Phys. Rev. B* 64:134204. doi: 10.1103/PhysRevB.64.134204

Golovchak, R., Jain, H., Shpotyuk, O., Kozdras, A., Saiter, A., and Saiter, J.-M. (2008). Experimental verification of the reversibility window concept in binary As-Se glasses subjected to a long-term physical aging. *Phys. Rev. B* 78:014202. doi: 10.1103/PhysRevB.78.014202

Goncalves, C., Kang, M., Sohn, B.-U., Yin, G., Hu, J., Tan, D. T. H., et al. (2018). New candidate multicomponent chalcogenide glasses for supercontinuum generation. *Appl. Sci.* 8:2082. doi: 10.3390/app8112082

Gueguen, Y., Rouxel, T., Gadaud, P., Bernard, C., Keryvin, V., and Sangleboeuf, J.-C. (2011). High-temperature elasticity and viscosity of Ge_xSe_{1-x} glasses in the transition range. *Phys. Rev. B* 84:064201. doi: 10.1103/PhysRevB.84.064201

Gunasekera, K., Bhosle, S., Boolchand, P., and Micoulaut, M. (2013). Superstrong nature of covalently bonded glass-forming liquids at select compositions. *J. Chem. Phys.* 139:164511. doi: 10.1063/1.4826463

Guo, X., Mauro, J. C., Allan, D. C., and Yue, Y. (2012). On the frequency correction in temperature-modulated differential scanning calorimetry of the glass transition. *J. Non Crystal. Solids* 358, 1710–1715. doi: 10.1016/j.jnoncrysol.2012.05.006

Hodge, I. M. (1996). Strong and fragile liquids — a brief critique. *J. Non Crystal. Solids* 202, 164–172. doi: 10.1016/0022-3093(96)00151-2

Jackson, K., Briley, A., Grossman, S., Porezag, D. V., and Pederson, M. R. (1999). Raman-active modes of a - $GeSe_2$ and a - GeS_2: a first-principles study. *Phys. Rev. B* 60, R14985–R14989. doi: 10.1103/PhysRevB.60.R14985

Jackson, K., and Pederson, M. R. (1990). Accurate forces in a local-orbital approach to the local-density approximation. *Phys. Rev. B* 42, 3276–3281. doi: 10.1103/PhysRevB.42.3276

Jacobs, D. J., and Thorpe, M. F. (1995). Generic rigidity percolation: the pebble game. *Phys. Rev. Lett.* 75, 4051–4054. doi: 10.1103/PhysRevLett.75.4051

Kamitakahara, W. A., Cappelletti, R. L., Boolchand, P., Halfpap, B., Gompf, F., Neumann, D. A., et al. (1991). Vibrational densities of states and network rigidity in chalcogenide glasses. *Phys. Rev. B* 44, 94–100. doi: 10.1103/PhysRevB.44.94

Kim, C. S., and Boolchand, P. (1979). Chemical bonding in sulfur, selenium, and tellurium from ^{129}I and ^{125}Te Mössbauer investigations. *Phys. Rev. B* 19, 3187–3197. doi: 10.1103/PhysRevB.19.3187

Lee, C., Yang, W., and Parr, R. G. (1988). Development of the Colle-Salvetti correlation-energy formula into a functional of the electron density. *Phys. Rev. B* 37:785. doi: 10.1103/PhysRevB.37.785

Mantisi, B., Bauchy, M., and Micoulaut, M. (2015). Cycling through the glass transition: evidence for reversibility windows and dynamic anomalies. *Phys. Rev. B* 92:134201. doi: 10.1103/PhysRevB.92.134201

Massobrio, C., Micoulaut, M., and Salmon, P. S. (2010). Impact of the exchange-correlation functional on the structure of glassy GeSe2. *Solid State Sci.* 12, 199–203. doi: 10.1016/j.solidstatesciences.2009.11.016

Massobrio, C., Pasquarello, A., and Car, R. (1999). Intermediate range order and bonding character in disordered network-forming systems. *J. Am. Chem. Soc.* 121, 2943–2944. doi: 10.1021/ja9808447

Mauro, J. C., Yue, Y., Ellison, A. J., Gupta, P. K., and Allan, D. C. (2009). Viscosity of glass-forming liquids. *PNAS* 106, 19780–19784. doi: 10.1073/pnas.0911705106

Maxwell, J. C. (1864). L. On the calculation of the equilibrium and stiffness of frames. *Philos. Magazine Ser. 4* 27, 294–299. doi: 10.1080/14786446408643668

Micoulaut, M. (2010). Linking rigidity transitions with enthalpic changes at the glass transition and fragility: insight from a simple oscillator model. *J. Phys.* 22:285101. doi: 10.1088/0953-8984/22/28/285101

Micoulaut, M., Kachmar, A., Bauchy, M., Le Roux, S., Massobrio, C., and Boero, M. (2013). Structure, topology, rings, and vibrational and electronic properties of Ge_xSe_{1-x} glasses across the rigidity transition: a numerical study. *Phys. Rev. B* 88:054203. doi: 10.1103/PhysRevB.88.054203

Micoulaut, M., and Naumis, G. G. (1999). Glass transition temperature variation, cross-linking and structure in network glasses: a stochastic approach. *EPL.* 47:568. doi: 10.1209/epl/i1999-00427-7

Micoulaut, M., and Phillips, J. C. (2003). Rings and rigidity transitions in network glasses. *Phys. Rev. B* 67:104204. doi: 10.1103/PhysRevB.67.104204

Micoulaut, M., Vuilleumier, R., and Massobrio, C. (2009). Improved modeling of liquid $GeSe_2$: Impact of the exchange-correlation functional. *Phys. Rev. B* 79:214205. doi: 10.1103/PhysRevB.79.214205

Mohanty, C. (2018). *Direct evidence for topological phases in sodium phosphate glasses from raman scattering, infrared reflectance and modulated DSC*

(Unpublished master's thesis). University of Cincinnati, Cincinnati, OH, United States.

Mohanty, C., Mandal, A., Gogi, V. K., Chen, P., Novita, D., Chbeir, R., et al. (2019). Linking melt dynamics with topological phases and molecular structure of sodium phosphate glasses from calorimetry, raman scattering, and infrared reflectance. *Front. Mater.* 6, 1–20. doi: 10.3389/fmats.2019.00069

Moynihan, C. T., Easteal, A. J., Wilder, J., and Tucker, J. (1974). Dependence of the glass transition temperature on heating and cooling rate. *J. Phys. Chem.* 78, 2673–2677. doi: 10.1021/j100619a008

Murase, K., Fukunaga, T., Yakushiji, K., Yoshimi, T., and Yunoki, I. (1983). Investigation of stability of (Ge, Sn)-(S, or Se)42 cluster vibrational spectra. *J. Non Crystal. Solids* 59–60, 883–886. doi: 10.1016/0022-3093(83)90311-3

Naumis, G. G. (2005). Energy landscape and rigidity. *Phys. Rev. E* 71:026114. doi: 10.1103/PhysRevE.71.026114

Okamoto, H. (2000). *Desk Handbook: Phase Diagram for Binary Alloys*. Novelty, OH: ASM International.

Pederson, M. R., and Jackson, K. A. (1990). Variational mesh for quantum-mechanical simulations. *Phys. Rev. B* 41, 7453–7461. doi: 10.1103/PhysRevB.41.7453

Pederson, M. R., and Jackson, K. A. (1991). Pseudoenergies for simulations on metallic systems. *Phys. Rev. B* 43, 7312–7315. doi: 10.1103/PhysRevB.43.7312

Phillips, J. C. (1979). Topology of covalent non-crystalline solids I: short-range order in chalcogenide alloys. *J. Non Crystal. Solids* 34, 153–181. doi: 10.1016/0022-3093(79)90033-4

Phillips, J. C., Beevers, C. A., and Gould, S. E. B. (1980). Molecular structure of As_2Se_3 glass. *Phys. Rev. B* 21, 5724–5732. doi: 10.1103/PhysRevB.21.5724

Pignatelli, I., Kumar, A., Alizadeh, R., Pape, Y. L., Bauchy, M., and Sant, G. (2016). A dissolution-precipitation mechanism is at the origin of concrete creep in moist environments. *J. Chem. Phys.* 145:054701. doi: 10.1063/1.4955429

Porezag, D. (1997). *Development of ab-initio and approximate density functional methods and their application to complex fullerene systems* (Master's thesis). Chemnitz University of Technology, Chemnitz, Germany.

Porezag, D., and Pederson, M. R. (1996). Infrared intensities and Raman-scattering activities within density-functional theory. *Phys. Rev. B.* 54, 7830–7836. doi: 10.1103/PhysRevB.54.7830

Potuzak, M., Welch, R. C., and Mauro, J. C. (2011). Topological origin of stretched exponential relaxation in glass. *J. Chem. Phys.* 135:214502. doi: 10.1063/1.3664744

Qu, T. (2004). *Non-Aging And Self-Organization In Network Glasses.* Available online at: https://etd.ohiolink.edu/pg_10?0::NO:10:P10_ACCESSION_NUM:ucin1075233143 (accessed October 12, 2018).

Qu, T., Georgiev, D. G., Boolchand, P., and Micoulaut, M. (2002). The intermediate phase in ternary $Ge_xAs_xSe_{1-2x}$ glasses. *MRS Online Proc. Library Arch.* 754, CC8.1.1–12. doi: 10.1557/PROC-754-CC8.1

Quong, A. A., Pederson, M. R., and Feldman, J. L. (1993). First principles determination of the interatomic force-constant tensor of the fullerene molecule. *Solid State Commun.* 87, 535–539. doi: 10.1016/0038-1098(93)90591-A

Raoux, S., and Wuttig, M. (eds) (2009). *Phase Change Materials: Science and Applications*. Springer. Available online at: https://www.springer.com/us/book/9780387848730 (accessed February 14, 2019). doi: 10.1007/978-0-387-84874-7

Ravindren, S. (2015). *New Insights Into the Glass Structure and Melt Dynamics of Ge-As-Se Alloys: Topological Phases, Eutectic Effects, Slow Homogenization Of Melts And Nanoscale Phase Separation Effects.* Available online at: https://etd.ohiolink.edu/pg_10?0::NO:10:P10_ACCESSION_NUM:ucin1427798415 (accessed April 4, 2019).

Ravindren, S., Gunasekera, K., Tucker, Z., Diebold, A., Boolchand, P., and Micoulaut, M. (2014). Crucial effect of melt homogenization on the fragility of non-stoichiometric chalcogenides. *J. Chem. Phys.* 140:134501. doi: 10.1063/1.4869107

Salmon, P. S. (2007). Structure of liquids and glasses in the Ge–Se binary system. *J. Non Crystal. Solids* 353, 2959–2974. doi: 10.1016/j.jnoncrysol.2007.05.152

Salmon, P. S., and Petri, I. (2003). Structure of glassy and liquid $GeSe_2$. *J. Phys.* 15:S1509. doi: 10.1088/0953-8984/15/16/301

Selvanathan, D., Bresser, W. J., Boolchand, P., and Goodman, B. (1999). Thermally reversing window and stiffness transitions in chalcogenide glasses. *Solid State Commun.* 111, 619–624. doi: 10.1016/S0038-1098(99)00248-3

Sipp, A., and Richet, P. (2002). Equivalence of volume, enthalpy and viscosity relaxation kinetics in glass-forming silicate liquids. *J. Non Crystal. Solids* 298, 202–212. doi: 10.1016/S0022-3093(02)00948-1

Stølen, S., Grande, T., and Johnsen, H.-B. (2002). Fragility transition in GeSe2–Se liquids. *Phys. Chem. Chem. Phys.* 4, 3396–3399. doi: 10.1039/b201396g

Tammann, G., and Hesse, W. (1926). Die abhängigkeit der viscosität von der temperatur bei unterkühlten flüssigkeiten. *Zeitschrift Für Anorganische Und Allgemeine Chemie* 156, 245–257. doi: 10.1002/zaac.19261560121

Tang, S., Karpov, I. V., Dodge, R., Klehn, B., Kalb, J. A., Strand, J., et al. (2009). "A stackable cross point Phase Change Memory," in *2009 IEEE International Electron Devices Meeting* (Baltimore, MD: IEDM), 1–4.

Tang, Z., Furniss, D., Fay, M., Sakr, H., Sójka, L., Neate, N., et al. (2015). Mid-infrared photoluminescence in small-core fiber of praseodymium-ion doped selenide-based chalcogenide glass. *Opt. Mater. Express OME* 5, 870–886. doi: 10.1364/OME.5.000870

Tatsumisago, M., Halfpap, B. L., Green, J. L., Lindsay, S. M., and Angell, C. A. (1990). Fragility of Ge-As-Se glass-forming liquids in relation to rigidity percolation, and the Kauzmann paradox. *Phys. Rev. Lett.* 64, 1549–1552. doi: 10.1103/PhysRevLett.64.1549

Thomas, L. (2005). *T.A. Instruments.* Modulated DSC Technology. Chapters 1–9.

Thorpe, M. F. (1983). Continuous deformations in random networks. *J. Non Crystal. Solids* 57, 355–370. doi: 10.1016/0022-3093(83)90424-6

Thorpe, M. F. (1985). Rigidity percolation in glassy structures. *J. Non Crystal. Solids* 76, 109–116. doi: 10.1016/0022-3093(85)90056-0

Thorpe, M. F., Jacobs, D. J., Chubynsky, M. V., and Phillips, J. C. (2000). Self-organization in network glasses. *J. Non Crystal. Solids* 266–269, 859–866. doi: 10.1016/S0022-3093(99)00856-X

Tremblay, J.-É., Malinowski, M., Richardson, K. A., Fathpour, S., and Wu, M. C. (2018). Picojoule-level octave-spanning supercontinuum generation in chalcogenide waveguides. *Opt. Express OE* 26, 21358–21363. doi: 10.1364/OE.26.021358

Vaills, Y., Qu, T., Micoulaut, M., Chaimbault, F., and Boolchand, P. (2005). Direct evidence of rigidity loss and self-organization in silicate glasses. *J. Phys.* 17, 4889–4896. doi: 10.1088/0953-8984/17/32/003

Vogel, H. (1921). The law of relation between the viscosity of liquids and the temperature. *Zeitschrift für Physik* 22, 645–646.

Wang, R. P., Smith, A., Prasad, A., Choi, D. Y., and Luther-Davies, B. (2009). Raman spectra of GexAsySe1–x–y glasses. *J. Appl. Phys.* 106:043520. doi: 10.1063/1.3204951

Williams, M. L., Landel, R. F., and Ferry, J. D. (1955). The temperature dependence of relaxation mechanisms in amorphous polymers and other glass-forming liquids. *J. Am. Chem. Soc.* 77, 3701–3707. doi: 10.1021/ja01619a008

Yan, L. (2018). Entropy favors heterogeneous structures of networks near the rigidity threshold. *Nat. Commun.* 9:1359. doi: 10.1038/s41467-018-03859-9

Yannopoulos, S. N., and Andrikopoulos, K. S. (2004). Raman scattering study on structural and dynamical features of noncrystalline selenium. *J. Chem. Phys.* 121, 4747–4758. doi: 10.1063/1.1780151

Yildirim, C., Raty, J.-Y., and Micoulaut, M. (2016a). Anomalous diffusion and non-monotonic relaxation processes in Ge-Se liquids. *J. Chem. Phys.* 144:224503. doi: 10.1063/1.4953077

Yildirim, C., Raty, J.-Y., and Micoulaut, M. (2016b). Revealing the role of molecular rigidity on the fragility evolution of glass-forming liquids. *Nat. Commun.* 7:11086. doi: 10.1038/ncomms11086

Yu, Y., Wang, M., Smedskjaer, M. M., Mauro, J. C., Sant, G., and Bauchy, M. (2017). Thermometer effect: origin of the mixed alkali effect in glass relaxation. *Phys. Rev. Lett.* 119:095501. doi: 10.1103/PhysRevLett.119.095501

Yu, Y., Wang, M., Zhang, D., Wang, B., Sant, G., and Bauchy, M. (2015). Stretched exponential relaxation of glasses at low temperature. *Phys. Rev. Lett.* 115:165901. doi: 10.1103/PhysRevLett.115.165901

Conflict of Interest Statement: The authors declare that the research was conducted in the absence of any commercial or financial relationships that could be construed as a potential conflict of interest.

frontiers in Materials

ORIGINAL RESEARCH
published: 26 July 2019
doi: 10.3389/fmats.2019.00175

Predicting Composition-Structure Relations in Alkali Borosilicate Glasses Using Statistical Mechanics

Mikkel S. Bødker[1], *Søren S. Sørensen*[1], *John C. Mauro*[2] *and Morten M. Smedskjaer*[1]*

[1] Department of Chemistry and Bioscience, Aalborg University, Aalborg, Denmark, [2] Department of Materials Science and Engineering, The Pennsylvania State University, University Park, PA, United States

Predicting the atomic-scale structure of multicomponent glasses from their composition and thermal history would greatly accelerate the discovery of new engineering and functional glasses. A statistical mechanics-based approach has recently been applied to predict the composition-structure evolution in binary oxide glasses by determining the relative entropic and enthalpic contributions to the bonding preferences. In this work, we first establish the network modifier-former interaction parameters in sodium silicate and sodium borate glasses to predict the structural evolution in sodium borosilicate glasses. Due to the significant variations in the experimentally determined structural speciation in borosilicate glasses, we perform classical molecular dynamics (MD) simulations to establish and validate our structural model. We also show that the statistical mechanical model naturally accounts for the difference in structural speciation from MD simulations and NMR experiments, which in turn arises from the difference in cooling rate and thus thermal history of the glasses. Finally, we demonstrate the predictive capability of the model by accurately accounting for the structural evolution in potassium borosilicate glasses without using any adjustable model parameters. This is possible, because all the interaction parameters are already established in the potassium silicate, potassium borate, and sodium borosilicate glasses, respectively.

Keywords: glass, borosilicates, modeling, statistical mechanics, structure

OPEN ACCESS

Edited by:
Matthieu Micoulaut, Sorbonne Universités, France

Reviewed by:
Jean-Marc Delaye, Commissariat à l'Energie Atomique et aux Energies Alternatives (CEA), France
Roman Golovchak, Austin Peay State University, United States

***Correspondence:**
Morten M. Smedskjaer
mos@bio.aau.dk

Specialty section:
This article was submitted to Glass Science, a section of the journal Frontiers in Materials

Received: *22 May 2019*
Accepted: *08 July 2019*
Published: *26 July 2019*

Citation:
Bødker MS, Sørensen SS, Mauro JC and Smedskjaer MM (2019) Predicting Composition-Structure Relations in Alkali Borosilicate Glasses Using Statistical Mechanics. Front. Mater. 6:175. doi: 10.3389/fmats.2019.00175

INTRODUCTION

A multitude of applications of oxide glasses exist, including in the fields of construction materials (Almutawa et al., 2013), electronic substrates (Rahman and Padavettan, 2012), medical technology (Day et al., 2011), etc. There is thus a need to continually develop new glass compositions with physical and chemical properties tuned for each specific application (Naumis, 2005; Mauro, 2014; Mauro et al., 2016) while fulfilling a number of criteria related to their production, including glass-forming ability, cost, emissions, toxicity, refractory compatibility, etc. To accelerate the pace of glass composition development, correlations between the atomic-scale structure of glasses and their macroscopic properties need to be established, for example based on topological constraint theory (Mauro, 2011; Micoulaut, 2016; Smedskjaer et al., 2017; Bauchy, 2019).

Oxide glasses are composed of network formers (such as Si, B, or P), which form the structural backbone and are linked together through bridging oxygen (BO). Network modifiers (such as Na or Ca) break the backbone by forming non-bridging oxygen (NBO) or stabilizing negatively

charged network formers. Such short range order (SRO) rearrangements have been intensively investigated using various analytical tools, including solid state nuclear magnetic resonance (NMR) spectroscopy (Youngman, 2018), neutron diffraction (Fischer et al., 2006), and Raman spectroscopy (Neuville et al., 2014). Despite the significant advances within these technologies, the SRO analysis of glasses remains a tedious task due to their non-crystalline nature (Mauro, 2014) and the fact that they feature wide bond angle and length distributions. The SRO of glasses can be accurately characterized in simple compositions with only two to maybe three oxide components, whereas the accuracy drops for multicomponent compositions (Eckert, 2018). Moreover, predicting the structural descriptors (such as average coordination number of network formers) in multicomponent glasses is often impossible with the current models available. Recently, a statistical mechanics based model (Mauro, 2013) has been applied to determine relative enthalpy barriers for modifiers to associate with the various network former units in binary modifier-former glasses (Bødker et al., 2018, 2019). In this work, we attempt to transfer the enthalpy barriers established for binary alkali borate and alkali silicate glasses to predict the structural evolution in ternary alkali borosilicate glasses.

Borosilicate glasses are among the most utilized glasses, e.g., as thermal shock resistant glassware (Lima and Monteiro, 2001) and nuclear waste immobilization (Plodinec, 2000), and their composition-structure relations have thus been intensively investigated (Martens and Müller-Warmuth, 2000). Addition of modifier cations can increase the connectivity of the glass by charge-stabilizing tetrahedral boron (Lelong et al., 2017), but also reduce it by depolymerizing silicon structural units, and at high modifier concentrations also boron. The network formers' competition for modifier cations depends on the Si/B ratio, as described by Bray (1985) and Araujo (1980). However, to our knowledge, a comprehensive composition-structure model, accounting for the quantitative boron and silicon speciation as function of Si/B ratio and modifier content and type(s), has not yet been developed. Knowledge of the evolution of structural units with modifier concentration and Si/B ratio is needed for predicting the properties of borosilicate glasses directly from their composition (for a fixed thermal and pressure history; Smedskjaer et al., 2011).

To gain additional information about the structure of borosilicate glasses, molecular dynamics (MD) simulations have also been conducted based on recent force field developments (Deng and Du, 2018; Wang et al., 2018). The timescales in MD simulations are typically reduced to the nanosecond scale (Micoulaut, 2016), resulting in typical quenching rates in the range of 1–10 K/ps. This leads to a much higher fictive temperature (T_f) in simulated glasses compared to experimental glasses. As a result, the structures of the MD-generated glasses have been frozen in at a higher temperature than the experimental counterparts, giving rise to distributions of structural units that are more entropically dominated (Tomozawa et al., 2005). Despite this disadvantage of the MD simulations, they provide additional structural details, including the complete atomic configuration (Massobrio et al., 2015). Moreover, structural analysis of the experimentally synthesized glasses also comes with some disadvantages, such as uncertainties related to the actual chemical composition (especially if it is not analyzed), inhomogeneity or phase separation, partial crystallization, and thermal history differences. In addition, there are uncertainties related to the data analysis, such as deconvolution of NMR spectra. For alkali borosilicate glasses, we have found that the reported structures (determined by NMR spectroscopy) differ significantly from study to study and even within the same studies for the nominally same glass compositions. For example, the fraction of Si with four BOs in Na_2O-B_2O_3-$2SiO_2$ has been found to be 0 and 57% by Bhasin et al. (1998) and Nanba et al. (2004), respectively, while the fraction of four-fold coordinated boron in Na_2O-B_2O_3-$1.33SiO_2$ has been reported to be both 44 and 62% in the same study (Martens and Müller-Warmuth, 2000).

To overcome these problems in this study, we first show how the statistical mechanics model of SRO structure established based on experimental NMR data can be linked to that based on MD simulations data. With this link established, we will then show that we can predict the structure of MD-simulated ternary sodium borosilicate glasses by first establishing relative enthalpic and entropic bonding preferences in binary sodium borates and silicates. To do so, we only need one additional parameter, namely, the modifiers' relative preference for associating with a silicate structural group relative to a borate structural group. This newly established parameter is then used to predict the structural evolution in potassium borosilicate glasses without any free parameters. These iterations will be based on structural data obtained by NMR experiments and MD simulations, including results from literature (Maekawa et al., 1991; Bhasin et al., 1998; Du and Cormack, 2004; Adkins and Cormack, 2011; Schuch et al., 2011; Deng and Du, 2018) for sodium borate, sodium silicate, and sodium borosilicate glasses as well as new MD simulations performed in this study for potassium borosilicate glasses.

MOLECULAR DYNAMICS SIMULATIONS

Glass Preparation

Twelve glasses in the family of $R$$K_2O$-$B_2O_3$-$K$$SiO_2$ (see **Table S1**) were simulated by MD using LAMMPS (Plimpton, 1995). A combined potential of the Coulomb and Buckingham potential was used in combination with a potential spline for low values of separation to avoid the Buckingham catastrophe. We refer to the work of Deng and Du for details on the potential and potential spline (Deng and Du, 2018). The force field parameters and quenching procedure have also been taken from that study (Deng and Du, 2018). This includes using varying values for the B-O interaction according to the values of R and K. Cut-offs for all short-range interactions were 11 Å while long range Coulombic interactions were computed directly below 11 Å and using the Particle-Particle-Particle-Mesh (PPPM) method with a relative accuracy of 10^{-5} above 11 Å. A timestep of 1 fs was used for all simulations. Initially ∼3,000 atoms were placed randomly in a simulation box with a density ∼2% lower than the experimental value to allow for more realistic dynamics in the melt, while avoiding any unrealistic overlaps. This was followed by a potential energy minimization and 60 ps of equilibration

in the NVT ensemble at 300 K. The temperature was then set to 6,000 K, allowing the system to equilibrate for 100 ps, followed by a step function to 5,000 K and another isothermal equilibration for 100 ps, both in the NVT ensemble. The system was then quenched from 5,000 to 300 K at 5 K/ps in the NVT ensemble, followed by structural relaxation at 300 K for 60 ps at zero pressure in the NPT ensemble. Finally, this was followed by another 60 ps of structural relaxation in the NVT ensemble.

Structural and Thermal Analysis

The number of BOs and NBOs associated with each silicon species was evaluated by first counting the number of oxygens within the first coordination shell of every boron and oxygen atom. In addition to providing the degree of connectivity around the Si atoms, it also yields the coordination number of boron as a function of composition. The potential used in the simulations has already been verified elsewhere (Deng and Du, 2018). This analysis was followed by counting the number of boron and silicon within the first coordination shell of all oxygens, hence categorizing each oxygen as either bridging or non-bridging. These two pieces of information were then combined to yield the number of NBOs associated with every boron and silicon atom in each simulation. All structural characteristics were averages of 10 structures from the final NVT equilibration.

Fictive temperatures (T_f) were found by employing the method of Liu et al. (2018). This method uses local ground-state enthalpy as a function of temperature to estimate T_f, giving very well-defined transitions compared to common methods of temperature-enthalpy plots as the method only considers the enthalpy of the atomic configuration at each temperature, leaving out contributions of atom dynamics.

STATISTICAL MECHANICAL STRUCTURE MODEL

The statistical mechanical model used herein to predict the modifier-former associations in mixed network former glasses was first proposed by Mauro (2013) and later implemented and validated on binary oxide glasses by Bødker et al. (2018, 2019). The model is based on the assumption that the probability for the initially added network modifier to interact with a certain network former atom depends on the relative statistical entropy (i.e., the fraction of microstates consistent with the macrostate of each network former) and the relative enthalpic barrier for the modifier to break the bonds associated with each network former. Here, the microstates refer to the SRO structural units as each of these correspond to a specific potential energy, while the macrostate is the sum of structural units consistent with a given network former. Using Na_2O-B_2O_3-SiO_2 as an example, the probability for sodium to associate with a borate unit depends on the statistical entropy of boron (i.e., the fraction of boron to silicon content) and the enthalpic energy barrier for this interaction, relative to the enthalpic barrier of the sodium-silicon interaction. This is analogous to calculating the probabilities for drawing a red marble from an urn with both red and blue marbles with different sizes. If we know the relative fraction of the red marbles, i.e., the statistical entropy, and their relative size compared to blue marbles (analogous to the enthalpy barrier in the glass system), we can calculate the probability to draw a red marble over a blue using a non-central (weighted) distribution function (Mauro and Smedskjaer, 2014). In the glass system, we assume that the energy barrier for a modifier to interact with the network former is constant regardless of the composition. The statistical entropy of each network former species does, however, change upon interactions with a modifier ion, since a drawn species is not replaced. This results in a hypergeometric distribution that describes the evolution of network former species as a function of the modifier concentration. As the entropy of the system changes with composition, so does the probability for the modifier-former interaction, requiring a numerical solution to predict the structural evolution of network former species.

To establish the model (Mauro, 2013), we first consider the Boltzmann distribution function (Schwabl, 2006) that describes the probability (i.e., the weighting factor) for a system to be in a given state as a function of the system's temperature and the energy of that state,

$$p_i = \frac{e^{-\frac{\varepsilon_i}{kT}}}{\sum_{i=1}^{M} e^{-\frac{\varepsilon_i}{kT}}}, \tag{1}$$

where p_i is the probability of state i, k is the Boltzmann constant, T is the temperature of the system, ε_i is the total energy of state i, and M is the total number of states. Here, p_i describes the probability for a network modifier to interact with a given network former species i, and consequently, ε_i becomes the free energy of this interaction, which may be described by entropic and enthalpic contributions,

$$p_i = \frac{e^{-\frac{H_i - S_i T}{kT}}}{\sum_{i=1}^{M} e^{-\frac{H_i - S_i T}{kT}}}. \tag{2}$$

Next, we introduce the statistical entropy of the system as,

$$S_i = k \ln \Omega_i \tag{3}$$

where, Ω_i is the number of microstates consistent with a given macrostate for species i,

$$p_i = \frac{e^{-\frac{H_i - k \ln \Omega_i T}{kT}}}{\sum_{i=1}^{M} e^{-\frac{H_i - k \ln \Omega_i T}{kT}}}. \tag{4}$$

We then obtain,

$$p_i = \frac{e^{-\frac{H_i}{kT} + \ln \Omega_i}}{\sum_{i=1}^{M} e^{-\frac{H_i}{kT} + \ln \Omega_i}}, \tag{5}$$

or,

$$p_i = \frac{\Omega_i e^{-\frac{H_i}{kT}}}{\sum_{i=1}^{M} \Omega_i e^{-\frac{H_i}{kT}}}. \tag{6}$$

The number of microstates consistent with the macrostate of species i divided by the total number of microstates consistent with the macrostate of the oxide glass will be the same as the relative fraction of species i divided by the total number of species. Since the fraction of a given structural species i in the glass changes with composition, we obtain

$$\Omega_{i,\omega} = (g_i - n_{i,\omega}), \tag{7}$$

where ω represents a given modifier concentration, g_i is the degeneracy (initial fraction) of species i, and $n_{i,\omega}$ is the total fraction of species i that has already interacted at modifier concentration ω. ω represents an absolute quantity of modifier ions, but we have converted it to a relative concentration for easy comparison with the experimental data. When calculating the probability of an interaction with species i at concentration ω, we must use the fraction of species i at the previous concentration step ($\omega-1$),

$$p_{i,\omega} = \frac{(g_i - n_{i,\omega-1})e^{-\frac{H_i}{kT}}}{\sum_{i=1}^{M}\sum_{j=0}^{\omega-1}(g_i - n_{i,j})e^{-\frac{H_i}{kT}}}. \tag{8}$$

The double summation in the denominator is over all species M and the accumulated number of successful interactions of species i after j number of attempts ($n_{i,j}$) up to but not including the current modifier concentration ω. For each concentration step, the fraction $n_{i,\omega}$ of network former species i interacting with the modifier ion can be calculated from the probability of the interaction and its fraction at the previous concentration step $\omega-1$. Then, that fraction is subtracted from the remaining amount of network forming species i at the next concentration, which is used to calculate the new probability and so on. Hence, the probability distribution function in Equation (8) is a type of non-central hypergeometric distribution function, where the relative enthalpy H_i values are the free parameters when fitting to experimental data. We define $e^{-\frac{H_i}{kT}}$ as the weighting factor w_i for a modifier to interact with the structural group i, where T is assumed to be equal to T_f for $T < T_f$, since the structure is assumed to freeze in at the fictive temperature:

$$p_{i,\omega} = \frac{(g_i - n_{i,\omega-1})w_i}{\sum_{i=1}^{M}\sum_{j=0}^{\omega-1}(g_i - n_{i,j})w_i}, \tag{9}$$

where,

$$w_i = e^{-\frac{H_i}{kT_f}}. \tag{10}$$

The application of Equation (9) to predict the structure of binary oxide glasses has been described in detail elsewhere (Bødker et al., 2018, 2019). Here, we will use the M_2O-B_2O_3-SiO_2 system, where M is an alkali metal, to explain the numerical procedure when calculating the compositional dependence of structural units with the present model. The SRO structural units of interest in the silicate part of the borosilicate network are the Q^n units, where n is the number of BO per tetrahedron ($n = 0, 1, 2, 3$, or 4), while those of interest in the borate part are the B^n units, again with $n = 0, 1, 2, 3$, or 4.

First, following our previous study of alkali borate glasses (Bødker et al., 2019), we consider the reaction mechanisms for B^3 and B^4 structural groups when interacting with an alkali modifier oxide (M_2O),

$$2B^3 + M_2O \rightarrow 2B^4, \tag{11}$$

$$2B^3 + M_2O \rightarrow 2B^2. \tag{12}$$

These two reactions describe the boron anomaly, where a three-fold coordinated B^3 structural unit may either form a four-fold coordinated B^4 structural unit without NBOs or a three-fold coordinated B^2 unit with one NBO. Previous studies (Uhlmann and Shaw, 1969; Yiannopoulos et al., 2001) have shown that Equation (11) dominates at low modifier concentration, while Equation (12) dominates at higher modifier concentration. To capture this so-called boron anomaly in this study, we introduce a critical concentration above which a parameter ($\alpha_{B4/B2}$) changes from 1 to 0, allowing only one of the two reactions to occur at any point. This is a structural simplification, but as it will be shown, it enables us to establish a simple model, yet predict the structural evolution with sufficient accuracy. An additional complication occurs when a network modifier interacts with a B^4 unit,

$$2B^4 + M_2O \rightarrow 2B^2 + M_2O. \tag{13}$$

As the modifier concentration increases, the B^4 structural units will begin to become converted to B^2 units, forming new NBOs on either boron or silicon units close to the initial B^4 unit. Then the modifier cations interact with the newly created NBOs. Equation (9) is used to calculate the fraction of the introduced modifier at each concentration step that initiates the conversion of a B^4 structural unit; hence the fraction of free modifier is also known and must be included in the interactions at each ω. Analogous to our work on alkali phosphate glasses[13], the following depolymerization reactions occur for all silicate structural units [and similarly for the B^2 and B^1 structural units (Bødker et al., 2019)],

$$2Q^n + M_2O \rightarrow 2Q^{n-1}. \tag{14}$$

With all the possible modifier interactions established, the fractions of the structural units at concentration ω are calculated as,

$$B^3_\omega = B^3_{\omega-1} - p_{B^3,\omega} - p_{B^4,\omega} \cdot p_{B^3,\omega}, \tag{15}$$

$$B^4_\omega = B^4_{\omega-1} + p_{B^3,\omega} \cdot \alpha_{B^4/B^2} - p_{B^4,\omega}. \tag{16}$$

That is, the fraction of B^3 at modifier concentration step ω ($B^3{}_\omega$) equals the fraction of B^3 at the previous concentration step ($B^3_{\omega-1}$) minus the fraction that reacts at ω ($p_{B^3,\omega}$) and also minus the fraction of B^4 that is converted to B^2 multiplied by the probability for the B^3 to react ($p_{B^4,\omega} \cdot p_{B^3,\omega}$). The

latter is needed, since the extra modifier from a B^4 group (Equation 13) will react according to the bonding preference at this composition. In Equation (16), the number of B^4 units will increase proportionally to the fraction of B^3 units drawn (Equation 11), but only until the critical modifier concentration, where $\alpha_{B4/B2}$ changes from 1 to 0. Additional examples are given for B^2 and Q^3 structural units as,

$$B^2_\omega = B^2_{\omega-1} + p_{B^3,\omega} \cdot \left(1 - \alpha_{B^4/B^2}\right) + p_{B^4,\omega} + p_{B^4,\omega} \cdot p_{B^3,\omega} - p_{B^2,\omega} - p_{B^4,\omega} \cdot p_{B^2,\omega} \quad (17)$$

$$Q^3_\omega = Q^3_{\omega-1} + p_{Q^4,\omega} + p_{B^4,\omega} \cdot p_{Q^4,\omega} - p_{Q^3,\omega} - p_{B^4,\omega} \cdot p_{Q^3,\omega} \quad (18)$$

In Equation (17), the fraction of B^2 units will increase when a B^3 is drawn (Equation 12) only when $\alpha_{B4/B2}$ is 0 and always when B^3 is drawn by the modifiers released by B^4 ($p_{B^4,\omega} \cdot p_{B^3,\omega}$). Additionally, the fraction of B^2 will increase when a B^4 is converted and become reduced when the modifier draws a B^2 either initially ($p_{B^2,\omega}$) or after being released from a B^4 ($p_{B^4,\omega} \cdot p_{B^2,\omega}$). The fractions of Q^4, Q^3,… Q^0, B^1, and B^0 will increase according to the probability of their n+1 species to be drawn, but at the same time decrease according to the probability for the modifier to interact with that unit as shown in the Q^3 example in Equation (18). Further explanation of the modeling procedure is given elsewhere (Bødker et al., 2019). Typically, the fitting parameters of the model would be all the relative H_i values (or w_i, if T_f is unknown), but in this study, the relative H_i values are first established in binary sodium borate glasses and sodium silicate glasses (as demonstrated in section Validating Structure Model for Alkali Silicate and Borate Glasses below). These H_i values are then transferred to predict the structural evolution in the sodium borosilicate glasses with only one free parameter, the conversion factor ($w_{Si,B}$). This parameter is needed, since all enthalpy values are calculated relatively within each system, i.e., the H_{Q3} in the sodium silicate is relative to the H_{Q4} parameter, while the H_{B2} in sodium borate is relative to the H_{B3} parameter.

Modeling of the composition-structure evolution in the binary and ternary systems to obtain the H_i values was performed in the object-oriented programming language Python. Here, the Basinhopping optimization method (part of the SciPy package) is used (Jones et al., 2001), since it attempts to find the global minimum in the parameter space by repeating the optimization with different guessed values of the starting parameters and solving for the structure in a self-consistent fashion. Additionally, all simulations were repeated five to 10 times with different starting values.

RESULTS AND DISCUSSION

Validating Structure Model for Alkali Silicate and Borate Glasses

The statistical mechanical model has previously been established in binary phosphate (Bødker et al., 2018) and borate glasses (Bødker et al., 2019), but not yet in binary silicate glasses. The modeling procedure for silicate glasses is the same as for binary phosphate glasses (Bødker et al., 2018). Here, we apply this approach to sodium silicates (**Figure 1A**) and potassium silicates (**Figure 1B**) based on ^{29}Si MAS NMR data from literature (Schroeder et al., 1973; Maekawa et al., 1991). To obtain relative H_i values for these glasses, we extrapolated the T_g values found in literature (**Table S2**) (Schroeder et al., 1973; MacDonald et al., 1985; Belova et al., 2015) using simple regression to estimate a T_g value for each modifier concentration step (ω). As shown in **Figure 1**, the model accurately captures the evolution of structural Q^n units with the modifier concentration using the fitted H_i values as reported in **Table 1**. Similarly, the modeling of the structure of sodium borate (Shelby, 1983; Schuch et al., 2011) and potassium borate (Zhong and Bray, 1989) systems based on ^{11}B MAS NMR data is shown in **Figures S1a,b**, with the corresponding T_g values from literature in **Table S2**. Only the fraction of B^4 is obtained from ^{11}B MAS NMR so these fits have been made using Equations (15) and (16) in section Statistical Mechanical Structure Model. Due to the limited amount of experimental data, these H_i values are very sensitive to any experimental uncertainties, which is especially the case for H_3 and H_4 of the borate glasses in the high modifier regions.

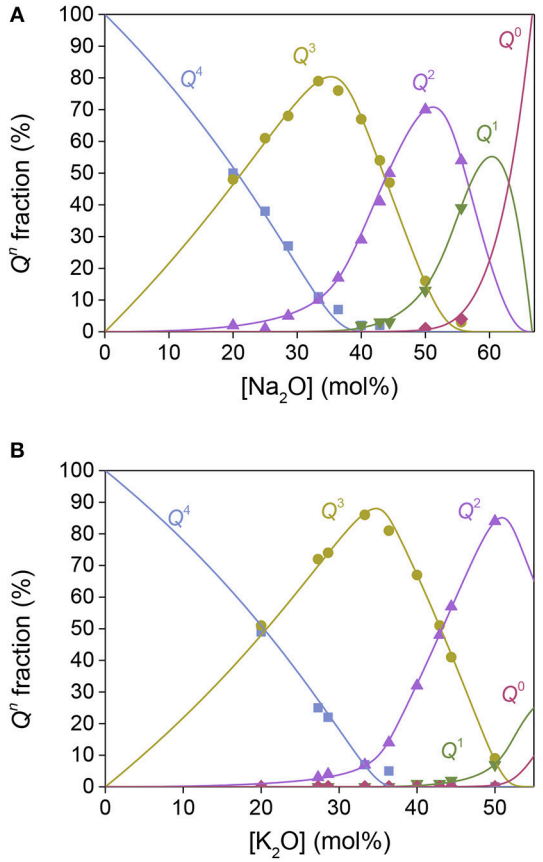

FIGURE 1 | Composition dependence of the fraction of Q^n structural units in **(A)** sodium silicate and **(B)** potassium silicate glasses. The closed symbols represent ^{29}Si MAS NMR experimental data (from Maekawa et al., 1991 for sodium and Schroeder et al., 1973 and Maekawa et al., 1991 for potassium) and the solid lines represent the model predictions.

TABLE 1 | Relative association enthalpies (H_i), where i corresponds to a given structural configuration, for the fitting of the current statistical mechanical model to experimental structure data.

Glass system	Na_2O-SiO_2	K_2O-SiO_2	Na_2O-B_2O_3	K_2O-B_2O_3
H_1 (kJ/mol)	0	0	0	0
H_2 (kJ/mol)	14.1	18.8	8.4	6.0
H_3 (kJ/mol)	22.9	35.2	7.4	21.4
H_4 (kJ/mol)	27.1	32.8	28.5	28.3
α_{B^4/B^2}	–	–	35.5	35.4

The following structural configurations are considered: Q^4, Q^3, Q^2, and Q^1 for $i = 1, 2, 3$, and 4, respectively, in the silicate system and B^3, B^4, B^2, and B^1 for $i = 1, 2, 3$, and 4, respectively, in the borate system. The uncertainty of the association enthalpy parameters is on the order of ±0.05 kJ/mol. α_{B^4/B^2} is the fitted average critical modifier concentration, where Equation (12) starts occurring instead of Equation (11).

Reconciling Structure Data From Experiments and MD Simulations

Simulated quenching of liquid to glasses using MD requires the use of high cooling rates, in turn yielding higher T_f values for MD glasses compared to experimental glasses. In other words, the structure freezes in at a higher temperature and becomes more entropically controlled. Assuming that the enthalpic contributions to the modifier-former interactions are the same for experimental and MD simulated glasses, the present statistical mechanical model should be able to predict the structural evolution in a MD simulated glass system based on the difference in fictive temperature. **Figure 2A** shows the Q^n speciation in a $35Na_2O$-$65SiO_2$ glass as a function of T_f, including model predictions, experimental data from ^{29}Si NMR spectroscopy (Maekawa et al., 1991), and simulations data from a previous MD study (Adkins and Cormack, 2011). The good agreement between model and data confirms the hypothesis that the present model can be used to describe the MD simulated structure of oxide glasses based on experimentally obtained NMR data (or vice versa) with only T_f as the free parameter. Likewise, **Figure 2B** shows the fraction of four-fold coordinated boron (B^4) in a $40Li_2O$-$60B_2O_3$ glass as a function of T_f, including model predictions from our previous study (Bødker et al., 2019) based on the fractions of superstructural units, experimental data from ^{10}B NMR spectroscopy (Feller et al., 1982). Since the fraction of B^4 varies non-monotonically with the fictive temperature according to the model (Bødker et al., 2019), the values of B^4 fraction from NMR and MD are almost identical, in agreement with previous studies (Xu et al., 1988; Ohtori et al., 2001).

In **Figure 1A**, the structural units in the Na_2O-SiO_2 system are plotted against the modifier concentration, where the solid symbols represent ^{29}Si NMR data (Maekawa et al., 1991) and the lines as model predictions with known T_g values (MacDonald et al., 1985; Belova et al., 2015) with the resulting H_i parameters as reported in **Table 1**. Next, we use the obtained H_i values from the binary sodium silicate glasses (**Table 1**) to predict the structural evolution of the MD simulated Na_2O-SiO_2 glasses (Du and Cormack, 2004; Adkins and Cormack, 2011), with only

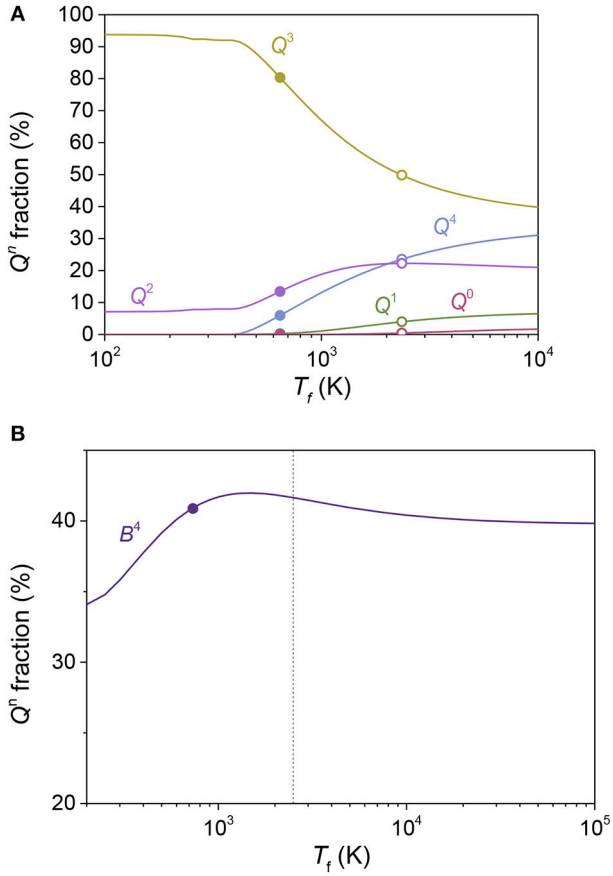

FIGURE 2 | The fraction of structural units in **(A)** $35Na_2O$-$65SiO_2$ and **(B)** $40Li_2O$-$60B_2O_3$ glasses as a function of fictive temperature (T_f). **(A)** The closed symbols represent ^{29}Si MAS-NMR experimental data (Maekawa et al., 1991), the open symbols represent MD simulated data (Adkins and Cormack, 2011), and the solid lines represent the model predictions. **(B)** The closed symbol represent ^{10}B NMR experimental data (Feller et al., 1982) and the dashed line is an estimate of T_f of the MD simulated glass. The solid line represents the model prediction.

an adjustable conversion factor from experimental T_g values to predicted T_f values (**Figure 3**). The excellent agreement suggests that we can predict MD simulated structures based on input from experimental structure data and the thermal history of the MD simulated glasses. With the link established between experimental and MD simulated glass structures, we are now able to utilize the proposed model to predict realistic glass structures of alkali borosilicates based only on knowledge of MD simulated glass structures. As it will be shown below, this becomes useful for multicomponent systems with composition fluctuations, phase separation, uncertain NMR deconvolutions, etc.

Structure Model for Sodium Borosilicate Glasses

^{29}Si NMR data of silica-containing glasses can be challenging to deconvolute, e.g., due to the bond angle distribution contributing to very broad and overlapping peaks (Mahler and Sebald, 1995).

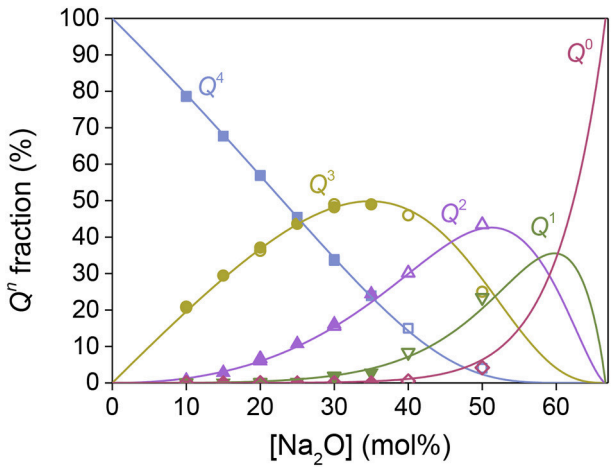

FIGURE 3 | Composition dependence of the fraction of Q^n structural units in sodium silicate glasses. The closed and open symbols represent MD simulated data obtained by Du and Cormack (2004) and Adkins and Cormack (2011), respectively. The solid lines represent model predictions, using the same bonding preferences parameter, but a different fictive temperature compared to **Figure 1A**.

In binary alkali silicate glasses, the chemical composition of the glasses may be used to constrain the deconvolution by assuming neutral charge balance in the glass and that all modifiers interact with the structure, significantly improving the accuracy of the deconvolution. However, in borosilicate glasses, determination of the boron speciation typically only involves quantification of the boron coordination number with no distinction of symmetric (only BO) and asymmetric (one or more NBO) trigonal boron units. In this case, the chemical composition of the glasses cannot be used to constrain the ^{29}Si NMR deconvolution, since the fraction of modifier associated with the boron species is unknown. **Figure 4A** shows the statistical mechanics-based model predictions compared to experimental data obtained by ^{11}B and ^{29}Si NMR spectroscopy techniques (Bhasin et al., 1998; Nanba et al., 2004) in the sodium borosilicate system. These predictions were made with only the relative Si/B weighting factor ($w_{Si,B}$) as a free parameter. All H_i values and α_{B^4/B^2} were transferred from the binary silicate and borate glasses, as reported in **Table 1**. The compositional evolution of Q^n and B^n speciation are shown in **Figures 4B,C**, respectively, for glasses with $K = 2$. Model vs. experiments comparisons for other B/Si ratios (i.e., K value) are shown in **Figure S2**. Overall we find that although the major trends in Q^n and B^n with composition are captured by the model (with only one adjustable parameter), there are relatively large deviations in the absolute values Q^n and B^n between model and experiments.

To overcome the abovementioned experimental uncertainties associated with structure determination in borosilicate glasses, we next attempt to predict the composition dependence of silicon and boron speciation in MD simulated sodium borosilicate glasses, again based on the relative H_i values obtained separately in sodium silicate and sodium borate glasses (**Table 1**). **Figure 5A** shows the comparison of model predictions with MD simulated

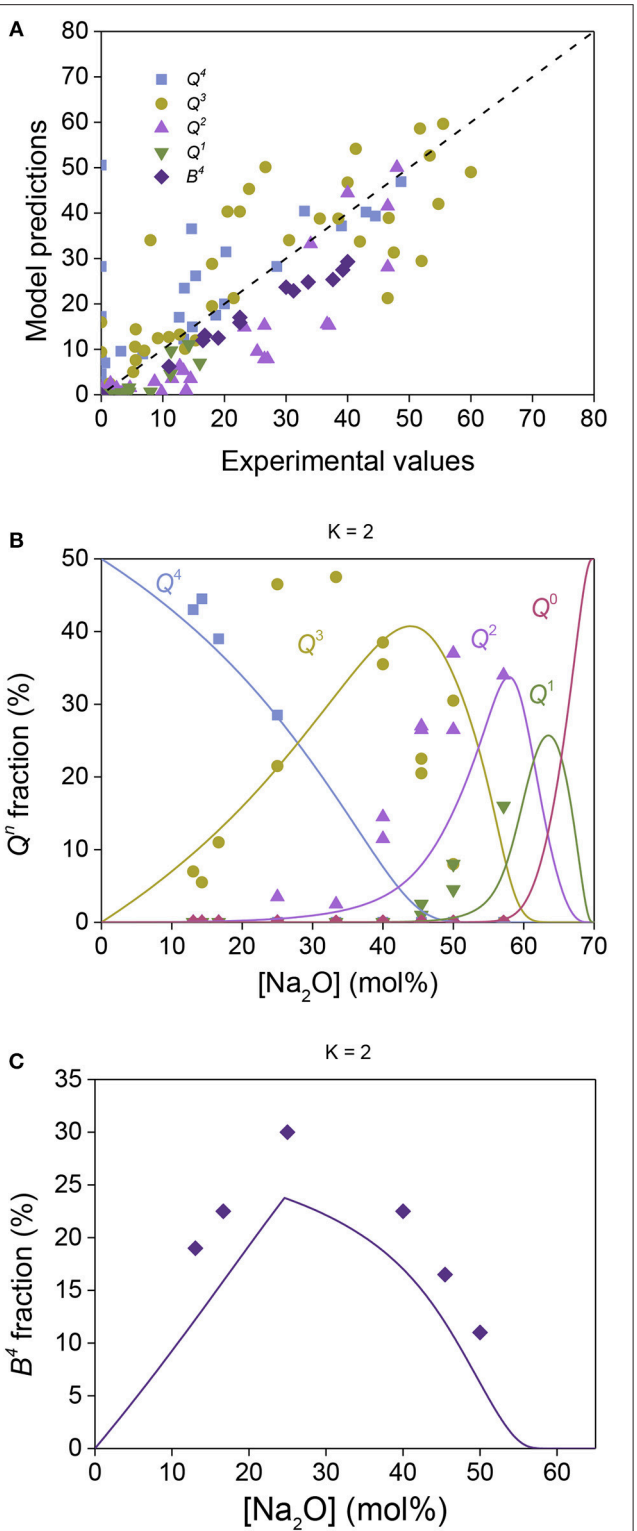

FIGURE 4 | Sodium borosilicate structural data obtained by ^{29}Si and ^{11}B MAS NMR (Bhasin et al., 1998; Nanba et al., 2004) compared to model predictions. **(A)** All experimental data plotted against the model predictions, with the dashed line showing a one-to-one correlation. **(B)** Composition dependence of Q^n fractions in sodium borosilicate glasses with $K = 2$, where the symbol represents experimental data by ^{29}Si MAS NMR and the lines are

(Continued)

FIGURE 4 | model predictions. **(C)** Composition dependence of the fraction of four-fold coordinated boron (B^4) in sodium borosilicate glasses with $K = 2$ as obtained by ^{11}B MAS-NMR (symbols) and the model predictions (line).

data (Deng and Du, 2018), obtained with only $w_{Si,B}$ as a fitting parameter found to be 0.16. The compositional evolution of Q^n and B^n speciation are shown in **Figures 5B,C**, respectively, for glasses with $K = 2$, with additional comparisons given in **Figure S3**. Overall, we observe excellent agreement between the model predictions and MD data with only one adjustable parameter, supporting the assumption that the H_i values can be transferred from simple binary systems to multi-component systems containing the same interactions as in the binary glasses.

Structure Prediction of Potassium Borosilicate Glasses Without Free Parameters

To further test the validity and universality of the present model, the obtained $w_{Si,B}$ weighting factor from the sodium borosilicate glasses is transferred (along with the H_i values from **Table 1**) to predict the structural evolution in potassium borosilicate glasses. The structure data for these glasses are determined based on the MD simulations performed in this study (see section Molecular Dynamics Simulations). **Figure 6A** illustrates the general agreement between model predictions and MD data, while **Figures 6B,C** show the predicted Q^n and B^n speciation, respectively, as a function of the modifier concentration for $K = 2$ (similar plots for $K = 4$ and 6 are shown in **Figure S4**). All the parameters used in the model have been obtained from different systems, namely, H_i and α_{B^4/B^2} values from potassium silicate and potassium borate glasses (**Table 1**) and $w_{Si,B} = 0.16$ from the sodium borosilicate glasses (section Structure model for sodium borosilicate glasses). In other words, no fitting is needed to obtain the model predictions. We note that a small amount of four-fold coordinated boron with one NBO is observed in the MD simulations (up to ~2% of the structure), but since this unit is not observed in the experimental data, it has been included as three-fold coordinated boron with two NBOs. This discrepancy is likely due to the use of the Buckingham potential and the higher fictive temperatures of the MD simulated glasses, resulting in a higher probability for energetically unfavorable structures.

To correct for the thermal history difference, the T_f values for the MD simulated glasses have been determined by extrapolating experimental data (Grandjean et al., 2008) the same way as shown in **Figure 2A**, i.e., all T_f values have been scaled with a constant relative to the experimental values. The predicted T_f values by this method are generally in good agreement with those determined by using the method of Liu et al. (2018) (see **Figure S5**).

Perspectives

Taking alkali borosilicate glasses as an example, we have found good agreement between the predicted values and those determined by MD simulations and also established a link

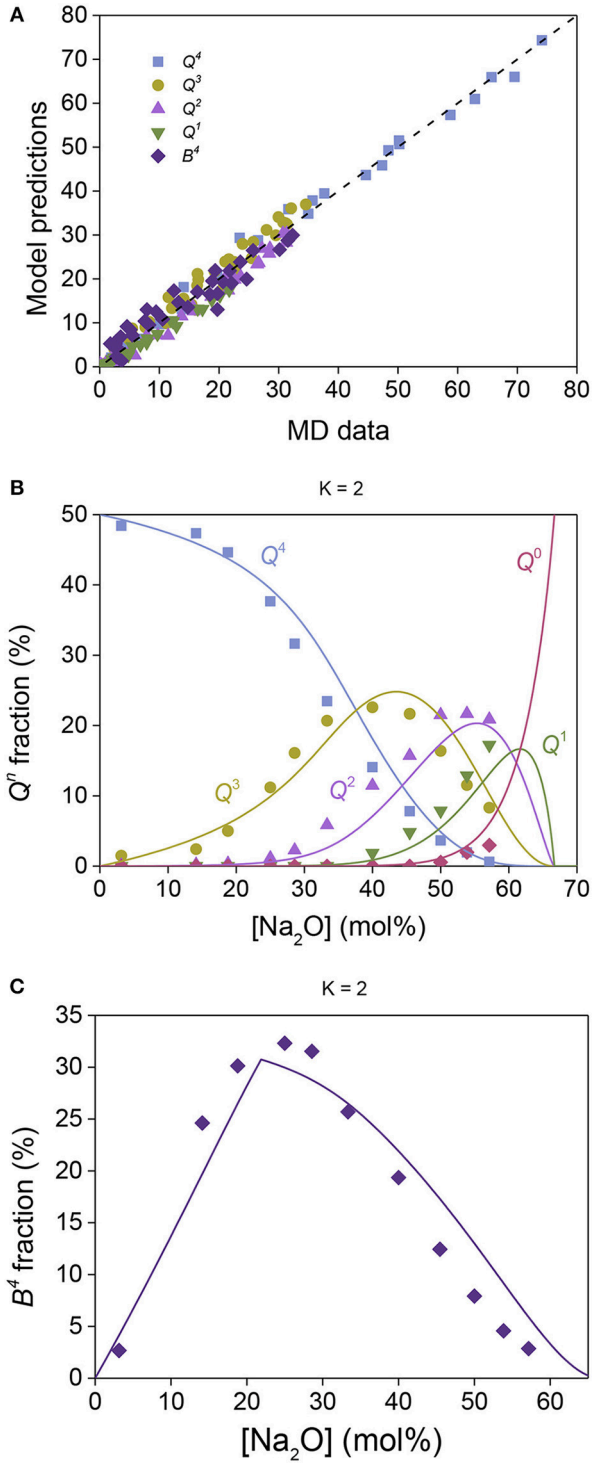

FIGURE 5 | Sodium borosilicate structural data obtained by MD simulations (Deng and Du, 2018) compared to model predictions. **(A)** All experimental data plotted against the model predictions, where the dashed line shows the one-to-one correlation. **(B)** Q^n fractions for silicate structural groups (symbols) and model predictions (lines) plotted against the overall modifier concentration for glasses with $K = 2$. **(C)** Fraction of four-fold coordinated boron as obtained by MD simulations (symbols) and the model predictions (line) against the overall modifier concentration for glasses with $K = 2$.

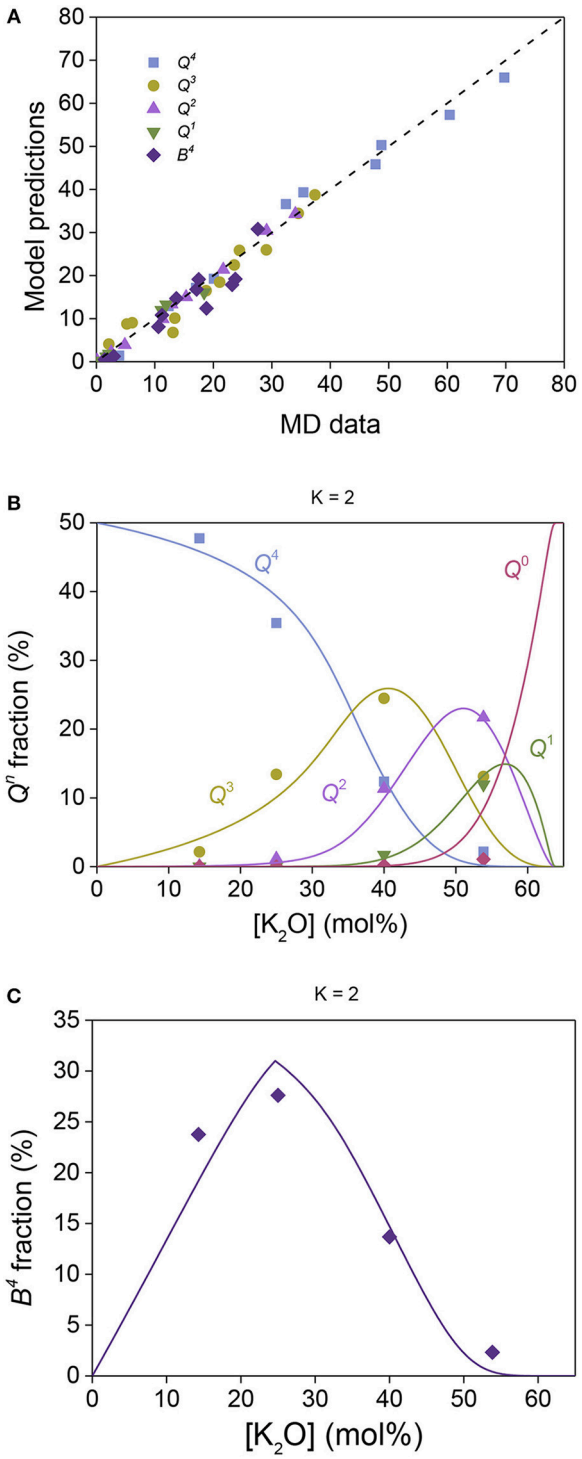

FIGURE 6 | Potassium borosilicate structural data obtained by MD simulations compared to model predictions with zero free parameters. **(A)** All experimental data plotted against the model predictions, where the dashed line shows the one-to-one correlation. **(B)** Q^n fractions for silicate structural groups (symbols) and model predictions (lines) plotted against the overall modifier concentration for glasses with $K = 2$. **(C)** Fraction of four-fold coordinated boron as obtained by MD simulations (symbols) and model predictions (line) plotted against the overall modifier concentration for glasses with $K = 2$.

between MD simulated structures in glasses and their melt-quenched counterparts. We expect this approach can be applied to predict the structure of various multicomponent glasses based on knowledge of the structure of the binary glasses that they are constituted by. This would greatly reduce the experimental or simulation time needed to predict the composition-structure evolution in multicomponent glasses. In this study, we included model predictions of glasses that contained two or three of the following four components: Na_2O, K_2O, B_2O_3, and SiO_2. This required model simulations on four types of binary glasses, namely, Na_2O-SiO_2, K_2O-SiO_2, Na_2O-B_2O_3, and K_2O-B_2O_3. Building on these four simulations, we would in principle be able to predict seven different glass systems, such as K_2O-Na_2O-B_2O_3-SiO_2, K_2O-B_2O_3-SiO_2, K_2O-Na_2O-SiO_2, etc. However, to predict the composition-structure evolution in all these systems, the effect of mixing different types of modifiers on the structure should be accounted for. The probability distributions of interactions in mixed modifier systems have already been developed (Goyal and Mauro, 2018), but still need to be verified experimentally. Another limitation of the model is the T_f dependence of the predicted structural units. If the model is used to predict the structural evolution in compositions not yet established by MD or experiments, a model of thermal history dependence must be incorporated to iteratively estimate the structural evolution and evolution of T_f simultaneously.

As the number of oxide components increases, the number of required simulations would increase linearly, whereas the number of systems predicted from the simulations would increase exponentially. This makes the present approach a promising tool for screening the atomic scale structure of many multicomponent oxide-based glasses. Such prediction would especially be useful when it is coupled with a relevant structure-property model. Finally, we note that the present approach predicts the mean structures of a given composition. Recently, Kirchner et al. (2018) and Kirchner and Mauro (2019) proposed a statistical mechanics-based method to explore topological fluctuations in the glass structure and properties, which would be interesting to couple with the present composition-structure model for borosilicate glasses in future work.

CONCLUSIONS

We have shown that a structure model based on the Boltzmann distribution can be used to predict the structure of ternary borosilicate glasses by transferring model parameters from simpler glasses with some of the same components. We started by using experimental structure data for sodium silicate and sodium borate glasses to determine the relative enthalpy values for sodium to interact with each structural group within the network. Using these values, we then applied the model to predict the structural evolution in sodium borosilicate glass system with only one free parameter to account for the relative propensity for the sodium modifier to interact with the silicate and borate part of the network. This parameter is required since the determined enthalpy values are relative, not absolute. With the $w_{Si,B}$ parameter established for the sodium borosilicate

system, we used the model to accurately predict the structural evolution in potassium borosilicate glasses without any free parameters, in this case building on transferred enthalpy values from experimental data of potassium silicate and potassium borate glasses. Finally, we have also shown that the statistical mechanical model is able to predict both experimental and MD structure data using only the fictive temperature as the scaling parameter.

DATA AVAILABILITY

The datasets generated for this study are available on request to the corresponding author.

AUTHOR CONTRIBUTIONS

MS and MB designed the study. MB performed the statistical mechanical modeling and Python programming. SS performed the MD simulations. MB and MS wrote the manuscript with revisions from JM and SS. All authors participated in discussing the data.

FUNDING

This work was supported by the Independent Research Fund Denmark (grant no. 7017-00019). Computational resources were provided by the DeIC National HPC Center (ABACUS 2.0) at the University of Southern Denmark and funded by Aalborg University.

ACKNOWLEDGMENTS

We thank Sushmit Goyal (Corning Inc.), Randall E. Youngman (Corning Inc.), Jincheng Du (University of North Texas), and Mathieu Bauchy (University of California, Los Angeles) for valuable discussions.

SUPPLEMENTARY MATERIAL

The Supplementary Material for this article can be found online at: https://www.frontiersin.org/articles/10.3389/fmats.2019.00175/full#supplementary-material

REFERENCES

Adkins, L., and Cormack, A. (2011). Large-scale simulations of sodium silicate glasses. *J. Non Cryst. Solids* 357, 2538–2541. doi: 10.1016/j.jnoncrysol.2011.03.012

Almutawa, F., Vandal, R., Wang, S. Q., and Lim, H. W. (2013). Current status of photoprotection by window glass, automobile glass, window films, and sunglasses. *Photodermatol. Photoimmunol. Photomed.* 29, 65–72. doi: 10.1111/phpp.12022

Araujo, R. J. (1980). Statistical mechanical model of boron coordination. *J. Non Cryst. Solids* 42, 209–230. doi: 10.1016/0022-3093(80)90023-X

Bauchy, M. (2019). Deciphering the atomic genome of glasses by topological constraint theory and molecular dynamics: a review. *Comput. Mater. Sci.* 159, 95–102. doi: 10.1016/j.commatsci.2018.12.004

Belova, E. V., Kolyagin, Y. A., and Uspenskaya, I. A. (2015). Structure and glass transition temperature of sodium-silicate glasses doped with iron. *J. Non Cryst. Solids* 423–424, 50–57. doi: 10.1016/j.jnoncrysol.2015.04.039

Bhasin, G., Bhatnagar, A., Bhowmik, S., Stehle, C., Affatigato, M., Feller, S., et al. (1998). Short range order in sodium borosilicate glasses obtained via deconvolution of ^{29}Si MAS NMR spectra. *Phys. Chem. Glass.* 39, 269–274.

Bødker, M. S., Mauro, J. C., Goyal, S., Youngman, R. E., and Smedskjaer, M. M. (2018). Predicting Q-speciation in binary phosphate glasses using statistical mechanics. *J. Phys. Chem. B* 122, 7609–7615. doi: 10.1021/acs.jpcb.8b04604

Bødker, M. S., Mauro, J. C., Youngman, R. E., and Smedskjaer, M. M. (2019). Statistical mechanical modeling of borate glass structure and topology: prediction of superstructural units and glass transition temperature. *J. Phys. Chem. B* 123, 1206–1213. doi: 10.1021/acs.jpcb.8b11926

Bray, P. J. (1985). Structural models for borate glasses. *J. Non Cryst. Solids* 75, 29–36. doi: 10.1016/0022-3093(85)90198-X

Day, D. E., Tomsia, A. P., Jung, S. B., Sonny Bal, B., Fu, Q., Rahaman, M. N., et al. (2011). Bioactive glass in tissue engineering. *Acta Biomater.* 7, 2355–2373. doi: 10.1016/j.actbio.2011.03.016

Deng, L., and Du, J. (2018). Development of boron oxide potentials for computer simulations of multicomponent oxide glasses. *J. Am. Ceram. Soc.* 102, 2482–2505. doi: 10.1111/jace.16082

Du, J., and Cormack, A. N. (2004). The medium range structure of sodium silicate glasses: a molecular dynamics simulation. *J. Non Cryst. Solids* 349, 66–79. doi: 10.1016/j.jnoncrysol.2004.08.264

Eckert, H. (2018). Spying with spins on messy materials: 60 years of glass structure elucidation by NMR spectroscopy. *Int. J. Appl. Glas. Sci.* 9, 167–187. doi: 10.1111/ijag.12333

Feller, S. A., Dell, W. J., and Bray, P. J. (1982). ^{10}B NMR studies of lithium borate glasses. *J. Non Cryst. Solids* 51, 21–30. doi: 10.1016/0022-3093(82)90186-7

Fischer, H. E., Barnes, A. C., and Salmon, P. S. (2006). Neutron and x-ray diffraction studies of liquids and glasses. *Rep. Prog. Phys.* 69, 233–299. doi: 10.1088/0034-4885/69/1/R05

Goyal, S., and Mauro, J. C. (2018). Statistical mechanical model of bonding in mixed modifier glasses. *J. Am. Ceram. Soc.* 101, 1906–1915. doi: 10.1111/jace.15364

Grandjean, A., Malki, M., Montouillout, V., Debruycker, F., and Massiot, D. (2008). Electrical conductivity and 11B NMR studies of sodium borosilicate glasses. *J. Non Cryst. Solids* 354, 1664–1670. doi: 10.1016/j.jnoncrysol.2007.10.007

Jones, E., Oliphant, T., and Peterson, P. (2001). *SciPy: Open Source Scientific Tools for Python*. Available online at: http://www.scipy.org/ (accessed May 15, 2019).

Kirchner, K. A., Kim, S. H., and Mauro, J. C. (2018). Statistical mechanics of topological fluctuations in glass-forming liquids. *Phys. A Stat. Mech. Appl.* 510, 787–801. doi: 10.1016/j.physa.2018.07.028

Kirchner, K. A., and Mauro, J. C. (2019). Statistical mechanical model of the self-organized intermediate phase in glass-forming systems with adaptable network topologies. *Front. Mater.* 6:11. doi: 10.3389/fmats.2019.00011

Lelong, G., Cormier, L., Hennet, L., Michel, F., Rueff, J. P., Ablett, J. M., et al. (2017). Lithium borate crystals and glasses: how similar are they? A non-resonant inelastic X-ray scattering study around the B and O K-edges. *J. Non Cryst. Solids* 472, 1–8. doi: 10.1016/j.jnoncrysol.2017.06.012

Lima, M. M., and Monteiro, R. (2001). Characterisation and thermal behaviour of a borosilicate glass. *Thermochim. Acta* 373, 69–74. doi: 10.1016/S0040-6031(01)00456-7

Liu, Z., Hu, Y., Li, X., Song, W., Goyal, S., Micoulaut, M., et al. (2018). Glass relaxation and hysteresis of the glass transition by molecular dynamics simulations. *Phys. Rev. B* 98:104205. doi: 10.1103/PhysRevB.98.104205

MacDonald, W. M., Anderson, A. C., and Schroeder, J. (1985). Low-temperature behavior of potassium and sodium silicate glasses. *Phys. Rev. B* 31, 1090–1101. doi: 10.1103/PhysRevB.31.1090

Maekawa, H., Maekawa, T., Kawamura, K., and Yokokawa, T. (1991). The structural groups of alkali silicate glasses determined from 29Si MAS-NMR. *J. Non Cryst. Solids* 127, 53–64. doi: 10.1016/0022-3093(91)90400-Z

Mahler, J., and Sebald, A. (1995). Deconvolution of 29Si magic-angle spinning nuclear magnetic resonance spectra of silicate glasses revisited -

some critical comments. *Solid State Nucl. Magn. Reson.* 5, 63–78. doi: 10.1016/0926-2040(95)00027-N

Martens, R., and Müller-Warmuth, W. (2000). Structural groups and their mixing in borosilicate glasses of various compositions - an NMR study. *J. Non Cryst. Solids* 265, 167–175. doi: 10.1016/S0022-3093(99)00693-6

Massobrio, C., Du, J., Bernasconi, M., and Salmon, P. S. (2015). *Molecular Dynamics Simulations of Disordered Materials*. Cham: Springer International Publishing.

Mauro, J. C. (2011). Topological constraint theory of glass. *Am. Ceram. Soc. Bull.* 90, 31–37.

Mauro, J. C. (2013). Statistics of modifier distributions in mixed network glasses. *J. Chem. Phys.* 138:12A522. doi: 10.1063/1.4773356

Mauro, J. C. (2014). Grand challenges in glass science. *Front. Mater.* 1:20. doi: 10.3389/fmats.2014.00020

Mauro, J. C., and Smedskjaer, M. M. (2014). Statistical mechanics of glass. *J. Non Cryst. Solids* 396–397, 41–53. doi: 10.1016/j.jnoncrysol.2014.04.009

Mauro, J. C., Tandia, A., Vargheese, K. D., Mauro, Y. Z., and Smedskjaer, M. M. (2016). Accelerating the design of functional glasses through modeling. *Chem. Mater.* 28, 4267–4277. doi: 10.1021/acs.chemmater.6b01054

Micoulaut, M. (2016). Concepts and applications of rigidity in non-crystalline solids: a review on new developments and directions. *Adv. Phys. X* 6149, 1–29. doi: 10.1080/23746149.2016.1161498

Nanba, T., Nishimura, M., and Miura, Y. (2004). A theoretical interpretation of the chemical shift of ^{29}Si NMR peaks in alkali borosilicate glasses. *Geochim. Cosmochim. Acta* 68, 5103–5111. doi: 10.1016/j.gca.2004.05.042

Naumis, G. G. (2005). Energy landscape and rigidity. *Phys. Rev. E Stat. Nonlin. Soft Matter Phys.* 71:026114. doi: 10.1103/PhysRevE.71.026114

Neuville, D. R., de Ligny, D., and Henderson, G. S. (2014). Advances in Raman spectroscopy applied to earth and material sciences. *Rev. Mineral. Geochem.* 78, 509–541. doi: 10.2138/rmg.2013.78.13

Ohtori, N., Takase, K., Akiyama, I., Suzuki, Y., Handa, K., Sakai, I., et al. (2001). Short-range structure of alkaline-earth borate glasses by pulsed neutron diffraction and molecular dynamics simulation. *J. Non Cryst. Solids* 293–295, 136–145. doi: 10.1016/S0022-3093(01)00662-7

Plimpton, S. (1995). Fast parallel algorithms for short-range molecular dynamics. *J. Comput. Phys.* 117, 1–19. doi: 10.1006/jcph.1995.1039

Plodinec, M. J. (2000). Borosilicate glasses for nuclear waste imobilisation. *Glas. Technol.* 41, 186–192.

Rahman, I. A., and Padavettan, V. (2012). Synthesis of silica nanoparticles by sol-gel: size-dependent properties, surface modification, and applications in silica-polymer nanocomposites—a review. *J. Nanomater.* 2012:132424. doi: 10.1155/2012/132424

Schroeder, J., Mohr, R., Macedo, P., and Montrose, C. (1973). Rayleigh and Brillouin scattering in K_2O-SiO_2 glasses. *J. Am. Ceram. Soc.* 10, 510–514. doi: 10.1111/j.1151-2916.1973.tb12399.x

Schuch, M., Trott, C., and Maass, P. (2011). Network forming units in alkali borate and borophosphate glasses and the mixed glass former effect. *RSC Adv.* 1, 1370–1382. doi: 10.1039/c1ra00583a

Schwabl, F. (2006). *Statistical Mechanics. 2nd Edn*. Garching: Springer US.

Shelby, J. E. (1983). Thermal expansion of alkali borate glasses. *J. Am. Ceram. Soc.* 66, 225–227. doi: 10.1111/j.1151-2916.1983.tb10023.x

Smedskjaer, M. M., Hermansen, C., and Youngman, R. E. (2017). Topological engineering of glasses using temperature-dependent constraints. *MRS Bull.* 42, 29–33. doi: 10.1557/mrs.2016.299

Smedskjaer, M. M., Mauro, J. C., Youngman, R. E., Hogue, C. L., Potuzak, M., and Yue, Y. (2011). Topological principles of borosilicate glass chemistry. *J. Phys. Chem. B* 115, 12930–12946. doi: 10.1021/jp208796b

Tomozawa, M., Hong, J. W., and Ryu, S. R. (2005). Infrared (IR) investigation of the structural changes of silica glasses with fictive temperature. *J. Non Cryst. Solids* 351, 1054–1060. doi: 10.1016/j.jnoncrysol.2005.01.017

Uhlmann, D. R., and Shaw, R. R. (1969). The thermal expansion of alkali borate glasses and the boric oxide anomaly. *J. Non Cryst. Solids* 1, 347–359. doi: 10.1016/0022-3093(69)90018-0

Wang, M., Anoop Krishnan, N. M., Wang, B., Smedskjaer, M. M., Mauro, J. C., and Bauchy, M. (2018). A new transferable interatomic potential for molecular dynamics simulations of borosilicate glasses. *J. Non Cryst. Solids* 498, 294–304. doi: 10.1016/j.jnoncrysol.2018.04.063

Xu, Q., Kawamura, K., and Yokokawa, T. (1988). Molecular dynamics calculations for boron oxide and sodium borate glasses. *J. Non Cryst. Solids* 104, 261–272. doi: 10.1016/0022-3093(88)90397-3

Yiannopoulos, Y. D., Chryssikos, G. D., and Kamitsos, E. I. (2001). Structure and properties of alkaline earth borate glasses. *Phys. Chem. Glas.* 42, 164–172.

Youngman, R. (2018). NMR spectroscopy in glass science: a review of the elements. *Materials* 11, E476. doi: 10.3390/ma11040476

Zhong, J., and Bray, P. J. (1989). Change in boron coordination in alkali borate glasses, and mixed alkali effects, as elucidated by NMR. *J. Non Cryst. Solids* 111, 67–76. doi: 10.1016/0022-3093(89)90425-0

Conflict of Interest Statement: The authors declare that the research was conducted in the absence of any commercial or financial relationships that could be construed as a potential conflict of interest.

frontiers in Materials

ORIGINAL RESEARCH
published: 14 August 2019
doi: 10.3389/fmats.2019.00196

Competition Between Entropy and Energy in Network Glass: The Hidden Connection Between Intermediate Phase and Liquid-Liquid Transition

J. Quetzalcóatl Toledo-Marín[1] *and Le Yan*[2]*

[1] Departamento de Sistemas Complejos, Instituto de Física, Universidad Nacional Autónoma de México, Mexico City, Mexico, [2] Kavli Institute for Theoretical Physics, University of California, Santa Barbara, Santa Barbara, CA, United States

In network glass including chalcogenides, the network topology of microscopic structures can be tuned by changing the chemical compositions. As the composition is varied, an intermediate phase (IP) singularly different from the adjacent floppy or rigid phases on sides has been revealed in the vicinity of the rigidity onset of the network. Glass formers in the IP appear to be reversible at glass transition and strong in dynamical fragility. Meanwhile, the calorimetry experiments indicate the existence of a first-order liquid-liquid transition (LLT) at a temperature above the glass transition in some strong glass-forming liquids. How are the intermediate phase and the liquid-liquid transition related? Recent molecular dynamic simulations hint that the intermediate phase is thermodynamically distinct that the transitions to IP as varying the chemical composition in fact reflect the LLT: out of IP, the glass is frozen in vibrational entropy-dominated heterogeneous structures with voids; while inside IP, energy dominates and the microscopic structures of liquids become homogeneous. Here we demonstrate such first-order thermodynamic liquid-liquid transition numerically and analytically in an elastic network model of network glass and discuss possible experimental approaches to testify the connection.

Keywords: rigidity transition, intermediate phase, liquid-liquid transition, network glasses, vibrational entropy

OPEN ACCESS

Edited by:
Punit Boolchand,
University of Cincinnati, United States

Reviewed by:
John C. Mauro,
Pennsylvania State University, United States
Stefan Karlsson,
RISE Research Institutes of Sweden, Sweden

***Correspondence:**
Le Yan
lyan@kitp.ucsb.edu

Specialty section:
This article was submitted to Glass Science, a section of the journal Frontiers in Materials

Received: *17 May 2019*
Accepted: *29 July 2019*
Published: *14 August 2019*

Citation:
Toledo-Marín JQ and Yan L (2019) Competition Between Entropy and Energy in Network Glass: The Hidden Connection Between Intermediate Phase and Liquid-Liquid Transition. Front. Mater. 6:196. doi: 10.3389/fmats.2019.00196

1. INTRODUCTION

In network glass, the material properties relying on structures can be tuned by changing the chemical compositions that have different abilities to make covalent connections with its neighbor atoms. In chalcogenides $Ge_xAs_ySe_{1-x-y}$, for example, selenium (Se) forms only two bonds while arsenic (As) and germanium (Ge) form three and four respectively. First pointed out by Maxwell (1864), a general network will lose rigidity as the network connectivity is reduced to below certain critical connectivity when the average number of constraints per atom, n, is equal to the degrees of freedom, i.e., $n_c = d$ in spatial dimension d. This rigidity loss also applies to the chalcogenides when selenium concentration is high, predicted by Phillips in Phillips (1979) and Thorpe (1985), where he showed that counting both radial and angular constraints of covalent bonds gives $n_{\mathrm{Se}} = 2$, $n_{\mathrm{As}} = 9/2$, and $n_{\mathrm{Ge}} = 7$, indicating a chalcogenide glass is marginally rigid at a composition with average number of covalent bonds $r_c = 2.4$. Since then, more and more works have shown that the thermodynamic and dynamic features of glass-forming liquids (not limited to

chalcogenides) are strongly regulated by the rigidity transition of the microscopic networks (Hall and Wolynes, 2003; Shintani and Tanaka, 2008; Mauro et al., 2009; Yan et al., 2013). One of the most interesting discoveries is the intermediate phase (IP) near r_c (Boolchand et al., 2001; Wang et al., 2005; Rompicharla et al., 2008; Bhosle et al., 2012), which remains a big puzzle.

The intermediate phase appears to be singularly distinct from the adjacent rigid or floppy phases: the non-reversible heat, a glass-transition equivalent of the latent heat, vanishes (Boolchand et al., 2001); the stress heterogeneity disappears (Wang et al., 2005; Rompicharla et al., 2008); the molar volume and fragility are sharply smaller (Bhosle et al., 2012). All available pieces of evidence suggest that the glass undergoes some transitions when entering IP from either side (Bhosle et al., 2012). However, both, Maxwell's rigidity theorem and the rigidity percolation theory that takes into account fluctuations of random networks (Jacobs and Thorpe, 1995, 1996; Barré et al., 2005) predict only a single transition in network constraint number n. Noticed the interval of the two rigidity transition points in two theories, Thorpe and his colleagues proposed a self-organized transition scenario, which predicts a rigidity window in between two transitions—one corresponding to the loss of percolating rigidity as in the rigidity percolation theory and the other corresponding to the loss of ability to relax stress as in the Maxwell's theorem (Thorpe et al., 2000; Chubynsky et al., 2006). This stress-free rigidity window relies on a subtle balance between the fluctuation or entropy facilitating the rigidity percolation and the energy eliminating the stress throughout the range, which is, however, fragile to the ubiquitous perturbations such as Van der Waals (VdW) forces and temperature (Yan and Wyart, 2014). Despite in a more recent paper (Kirchner and Mauro, 2019), Kirchner and Mauro provide a robust approach of computing the constraint number to determine IP in the presence of finite temperature, the heterogeneous nature captured by a diverging correlation length at $n = n_c$ (Brière et al., 2007), in fact, still contradicts the observations of a homogeneous IP.

An alternative set of theoretical insights on IP is from the molecular dynamics simulations (Micoulaut and Bauchy, 2013; Bauchy et al., 2014; Bauchy and Micoulaut, 2015), where a similar intermediate range of homogeneous structures is revealed by continuously tuning the pressure instead of composition. In the simulation, as the pressure gradually increases, the amorphous structure undergoes a liquid-liquid transition (LLT) from a more structured low-modulus low-density amorphous phase to a more homogeneous rigid high-density phase (Yildirim et al., 2018). When the composition is varied, the transition pressure shows a non-monotonic pattern with a lower value in an intermediate range near r_c, same as the pattern of the stress percolation pressure in chalcogenides (Wang et al., 2005). In addition, in experiments, a transition between two thermodynamically different liquids is indicated by a lambda peak in specific heat at a temperature above the glass transition in some strong glass-formers close to the rigidity threshold, including silica (SiO_2) (Angell, 2008, 2011; Wei et al., 2011, 2013). These materials imply that the glass in IP may be rather in a different thermodynamic phase resulted from a transition above the glass transition and the transitions to IP directly reflect such liquid-liquid transitions. So what are the two different liquid phases in network glass?

In the previous work (Yan, 2018), one of the authors showed with a network model that the vibrational entropy facilitates the rigid-floppy separated heterogeneous network structures close to the rigidity transition n_c as floppy modes store large amounts of vibrational entropy (Naumis, 2005) while cost little configurational entropy in marginally rigid networks. On the opposite, the elastic energy is lower in homogeneous structures with stresses evenly distributed (Yan and Wyart, 2014). So under cooling, a network near n_c inevitably undergoes a first-order transition from an entropy-dominated heterogeneous phase to an energy-dominated homogeneous phase. The interplay of the glass transition temperature T_g and the LLT temperature T_{LLT} would then be key in determining which liquid phase the material is frozen in at the glass transition and all the consequential features. Here, we investigate the transition separating the two liquid phases by studying the thermodynamics of the same network model. We show that the network undergoes a first-order phase transition where free energy crosses over, associated energy and entropy are discontinuous, and specific heat jumps in the thermodynamic limit. Finally, we discuss how this liquid-liquid transition could be probed in experiments in order to understand the intermediate phase.

2. MODEL

We consider a two-dimensional triangular lattice of N particles with periodic boundary conditions (Yan and Wyart, 2014, 2015; Yan, 2018), where a small regular deformation of the lattice is imposed to avoid non-generic singular modes. We model all radial and angular constraints of covalent interactions by $N_s = Nn$ linear springs of stiffness k, connecting the nearest neighbors on a triangular lattice, as shown in **Figure 1**. We incorporate quenched disorder of glassy energy landscape by rest length mismatches of springs to the lattice bond lengths: $l_\gamma = l_{\gamma,0} + \epsilon_\gamma$ for spring γ. Mismatches $\{\epsilon_\gamma\}$ are i.i.d. random Gaussian variables with mean zero and variance ϵ^2. By setting $k_B = 1$, $k\epsilon^2 = 1$ defines the unit of, both, energy and temperature. Furthermore, we include also the weak VdW interactions by adding weak fixed springs of stiffness $k_w \ll k$ connecting any particle to all its six next-nearest neighbors as shown in **Figure 1**. The mean-field effect of these weak long-range non-specific interactions can be captured by a control parameter $\alpha = 3k_w/k \ll 1$ (Yan et al., 2013; Yan and Wyart, 2015).

In the model, the microscopic configuration depends on how the network is connected or which lattice bonds are occupied by strong springs, denoted by $\Gamma \equiv \{\gamma \leftrightarrow (i,j)\}$, for particle i and j connected by spring γ. Given Γ, when particles deviate from the mechanical equilibrium by $|\delta\mathbf{R}\rangle$, the elastic energy potential to the linear order is,

$$V(\Gamma, |\mathbf{R}\rangle) = H(\Gamma) + \frac{1}{2}\langle\delta\mathbf{R}|\mathcal{M}(\Gamma)|\delta\mathbf{R}\rangle, \tag{1}$$

where H is the energy of the inherent structure of configuration Γ and the second term corresponds to the vibration from

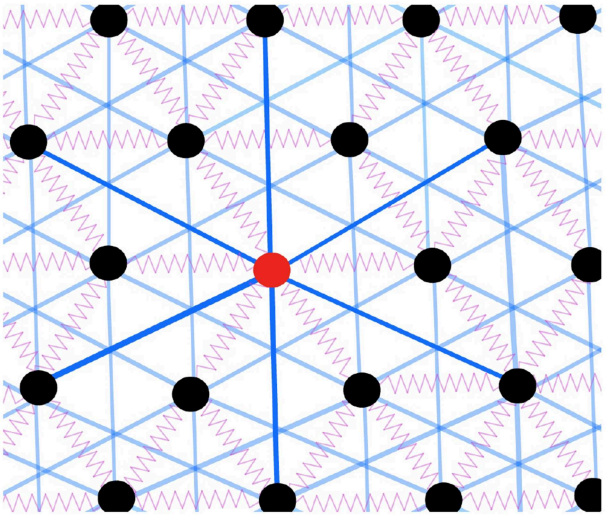

FIGURE 1 | Sketch of the model. The black circles represent the particles, the purple springs represent the strong interaction between nearest neighbors while the blue lines represent the VdW interactions between next nearest neighbors. We color one of the particles in red with bold blue lines for illustration purposes.

equilibrium with $\mathcal{M}$ being the Hessian matrix of energy H. We thus perform a Metropolis Monte Carlo simulation (Newman and Barkema, 1999) to sample the configurations according to their Boltzmann weight $e^{-F(\Gamma)/T}$ with free energy,

$$F(\Gamma) = H(\Gamma) - TS_{\text{vib}}(\Gamma), \tag{2}$$

with the volume of thermal vibrations counted in the vibrational entropy,

$$S_{\text{vib}}(\Gamma) = n_c N \ln T - \frac{1}{2}\ln \det \mathcal{M} = -\sum_{\omega} \ln \omega(\Gamma) + c, \tag{3}$$

where ω^2 are the eigenvalues of the Hessian matrix.

Without loss of generality, we assume the independence of mismatch ϵ_γ on the particle distances of the distorted lattice r_{ij} so that the Hessian matrix becomes only a function of the occupation $\{\sigma\}$, where $\sigma_{ij} = 1$ if particle i and j are connected by a spring and $\sigma_{ij} = 0$ otherwise. The stress energy of the network at mechanical equilibrium can thus be computed by,

$$H(\Gamma) = \frac{1}{2}\langle \epsilon | \mathcal{K} - \mathcal{K}\mathcal{S}\mathcal{M}^{-1}\mathcal{S}^T\mathcal{K} | \epsilon \rangle \ , \tag{4}$$

where $\mathcal{K}$ is the diagonal spring stiffness matrix and $\mathcal{S}$ is the structural matrix, both depending only on occupation $\{\sigma\}$. The detailed derivations and expressions of these matrices and the numerical implementation are documented in the **Supplementary Notes 1**, **2**.

3. RESULTS

3.1. Network Structures

As proven in Yan (2018) and directly inferred by Equation (3), vibrational entropy is large for floppy modes with a vanishing ω. When the total number of constraints is fixed, the total entropy can gain from additional floppy modes in phase separation of a very rigid subnetwork where the springs cluster and a very floppy counterpart where floppy modes cluster. This phase separation is shown in the snapshot of a system of 576 particles at high temperature in the left panel of **Figure 2**. On the contrary, networks with constraints homogeneously distributed store lower elastic energy than other configurations given the number of springs, as shown in Yan and Wyart (2014). At low temperature, when elastic energy dominates, homogeneous microscopic structures with no rigid-floppy phase separation will be sampled, as shown in the right panel of **Figure 2**. In the following, we will show that these heterogeneous and homogeneous structures correspond to two distinct thermodynamic liquid phases that are separated by a first-order liquid-liquid transition at a critical temperature T_{LLT}. We will further argue that depending on the relation between T_{LLT} and the glass transition temperature T_g, the liquid can be frozen into different thermodynamic phases, which could be the origin of the singular intermediate phase in network glass.

3.2. Thermodynamics

The numerical results of thermodynamics of the model are shown in **Figure 3** together with the theoretical predictions of both heterogeneous and homogeneous phases. In the upper left panel of **Figure 3**, for a given connectivity $n = 2.06$, we find the total free energy of the networks equilibrated at given temperature T can be perfectly fitted by the theoretical predictions of heterogeneous networks at high temperature end (in red) and of homogeneous networks at low temperature end (in blue). Moreover, the numerics and the free energy prediction of heterogeneous networks are consistently lower than the prediction of the homogeneous phase when the temperature is higher than certain transition temperature $T_{LLT} \approx 0.2$. At the free energy crossover T_{LLT}, marked in **Figures 3B–D**, we are also observing the convergence to discontinuous jumps at the transition in the thermodynamic limit $N \to \infty$ from a higher value in high temperature heterogeneous phase to a lower value in the low temperature homogeneous phase in stress energy, vibrational entropy, and the specific heat. This result demonstrates that the heterogeneous and homogeneous structures are thermodynamical phases, separated by a first-order phase transition where, both, energy and entropy are discontinuous.

In **Figure 3**, the data points of energy $E = \overline{H}^T$ in the upper right panel of **Figure 3** and vibrational entropy $S_v = \overline{S_{\text{vib}}}^T$ in the lower left panel of **Figure 3** are averages of Equations (3) and (4) over the Monte Carlo courses at given temperature T. The specific heat C in the lower right panel of **Figure 3** is obtained from the mean energy fluctuation over the Monte Carlo courses normalized by temperature squared, $C = (\overline{H^2}^T - E^2)/T^2$. Finally, the main numerical result of free energy F in the upper left panel

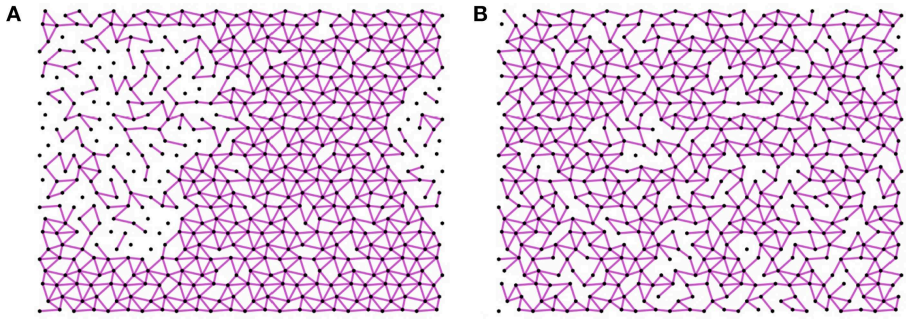

FIGURE 2 | Snapshot of the system above **(A)** and below **(B)** the critical temperature for a system of 576 particles with the constraint number $n = 2.06 > n_c$. The purple lines represent the springs. **(A)** Heterogeneous structure: At high temperature $T = 10$, the entropy dominates over the internal stress energy, in particular, the vibrational entropy maximizes by phase separating into rigid and floppy regions. **(B)** Homogeneous structure: At low temperature $T = 0.001$ the energy of the inherent structures dominates over the internal energy, this energy minimizes by a homogeneous distribution of constraints.

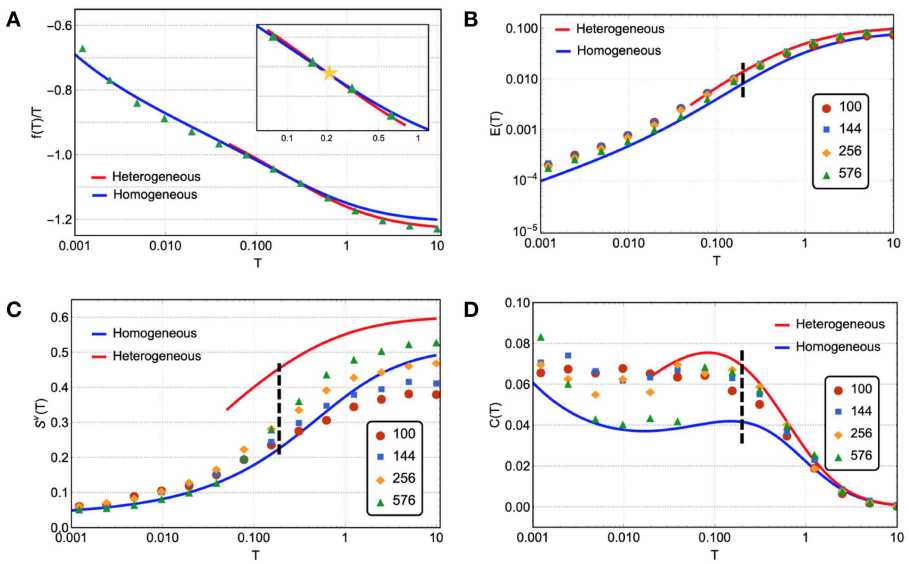

FIGURE 3 | Thermodynamics of the network model near the rigidity transition $n = 2.06$. The thermodynamics is characterized by the basic thermodynamic quantities, including free energy, internal energy, entropy, and specific heat, shown vs. temperature in markers for simulation results and in curves for analytical predictions. The simulations are done for different system sizes N (see legends) and the analytical predictions are obtained in the thermodynamic limit $N \to \infty$ for homogeneous networks in blue and heterogeneous networks in red (see **Supplementary Notes 3**, **4** for detailed descriptions). **(A)** The numerical results of free energy follow the prediction of a homogeneous network at low temperatures until the homogeneous-heterogeneous first order phase transition around $T \approx 0.2$ and then cross over to the prediction of a heterogeneous network. The yellow star in the inset marks this crossover. **(B)** Data points follow the homogeneous and heterogeneous predictions in the same low and high temperature ranges corresponding to the free energy, while separated by a discrete transition that the numeric result is converging to in the thermodynamic limit. **(C)** Similarly, the vibrational entropy results also converge to a discrete jump at the crossover of free energy. **(D)** At the phase transition, the specific heat is also characterized by has a jump, seen in the largest system size.

of **Figure 3** combines both direct measurement of energy E and the inferred total entropy $S = S_v + S_c$ by integrating over the specific heat C,

$$S(T) = S(\infty) - \int_T^\infty \frac{C(T)}{T} dT, \tag{5}$$

as $F = E - TS$. The theory derivations and the way we consistently fit parameters are fully documented in the **Supplementary Notes 3–5** or see Yan and Wyart (2015) for homogeneous networks and Yan (2018) for heterogeneous networks.

3.3. Spatial and Temporal Correlations

We have shown the existence of two distinct thermodynamic liquid phases of networks with the basic thermodynamic quantities. Among these quantities, the specific heat is a good experimental indicator to detect the two liquid phases and the transition: one can look for a lambda divergence or a peak in

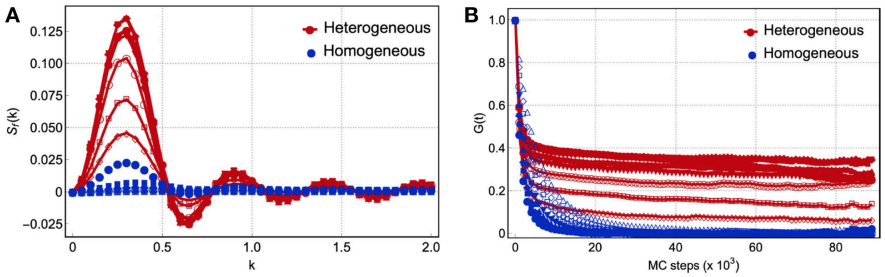

FIGURE 4 | (A) Spatial correlation function and **(B)** time correlation function for $N = 576$. Red curves correspond to temperatures $T(m) = 10/2^m$ with $m = \{0, ..., 5\}$ and blue curves correspond to temperatures $T(m)$ with $m = \{6, ..., 16\}$. The blue open symbols correspond to temperatures $T \lesssim \alpha$, i.e., of the order of the weak interactions. The wavenumber k has been averaged over three different directions. The time correlation function was computed using samples taken every 10^3 Monte Carlo steps.

specific heat above glass transition T_g, as found in certain strong-type glass-forming liquids and water (Angell, 2008, 2011; Wei et al., 2011, 2013). Here we present also the spatial and temporal correlation profiles of the two phases that could be directly measured in experiment to probe the transition. The spatial and temporal correlations are investigated by the structure factor and the time autocorrelation function as shown in **Figure 4**. They are defined by the occupation $\{\sigma\}$ as,

$$S_f(k) = \frac{1}{3N(3N-1)} \sum_{ij \neq kl} (\sigma_{ij} - \bar{\sigma})(\sigma_{kl} - \bar{\sigma}) e^{ikr_{ij,kl}}, \quad (6)$$

$$G(t) = \frac{1}{T_{tot} - t} \sum_{\tau} \frac{1}{3N} \sum_{ij} [\sigma_{ij}(\tau) - \bar{\sigma}][\sigma_{ij}(\tau + t) - \bar{\sigma}], \quad (7)$$

where $\bar{\sigma} = n/3$.

For temperatures higher than the transition temperature $T_{LLT} \approx 0.2$, we observe a plateau to finite correlation in the time range scanned in simulation and a strong signal in structure factor averaged over that time scale, which reflects the heterogeneous phase as in the snapshot in the left panel of **Figure 2**. On the contrary, for temperatures lower than T_{LLT}, we observe normal homogeneous liquid, where the correlation quickly relaxes to zero with no special structure in wave vector space after averaged over time, as in the snapshot in the right panel of **Figure 2**. In the left panel of **Figure 4**, we also notice that the systems in the heterogeneous phase yield two relaxation times: the system first relaxes to a plateau rapidly, yet in this plateau, the system is also relaxing but with a much larger characteristic time. It implies that the rigid and floppy clusters are not held fixed in a given position and the structural features in $S_f(k)$ will also vanish when averaged at the time longer than the second relaxation as in liquids. These features of spatial and temporal correlations emerging at an intermediate time scale should be looked for in distinguishing the two liquid phases and detecting the transition.

3.4. Dependence on Network Topology

Finally, we derive the liquid-liquid transition temperature T_{LLT} for varying constraint number n but close to n_c where a heterogeneous phase exists at high temperature, shown in **Figure 5A**[1]. Unlike the glass transition temperature T_g, which increases monotonically with n, T_{LLT} varies non-monotonically and is maximal at $n = n_c$, which is also consistently shown by numerical results of the model as data points in **Figure 5A**. This result implies that for certain range of parameters, the networks undergo LLT to a thermodynamic homogeneous phase before they are dynamically trapped in glass, when $T_{LLT}(n) > T_g(n)$ or $n_f < n < n_r$, which is likely to occur in the vicinity of the rigidity threshold n_c due to the different dependences of T_{LLT} and T_g on n. The liquids frozen in homogeneous networks become glass in the IP, while the network glass out of the IP is then frozen in the heterogeneous network structures as the glass transition happens first under cooling, as illustrated in **Figure 5B**. The transitions to the IP are thus transitions between different frozen thermodynamic liquid phases in this picture.

4. DISCUSSION

Relying on how and where T_g and T_{LLT} intersect with each other, this new picture of the intermediate phase is potent to explain some of the material features in the experiments. First, depending on the relative strength of the Van der Waals forces, the constraint numbers where T_g and T_{LLT} intersect vary, which leads to different widths and locations of the intermediate phase when changing the chemical compositions (Boolchand et al., 2001; Yan, 2018). Second, as the dynamics have shown to be much less fragile in a liquid with homogeneous structures, the liquid-liquid transition from the high-temperature heterogeneous to low-temperature homogeneous phase implies the dynamics of a liquid in the intermediate phase potentially undergoes a fragile to strong transition under cooling as observed in water (Angell, 2011) and *in-silico* silica (Horbach and Kob, 1999; Sastry

[1]Notice that the temperature predicted here is in the unit of covalent bond bending and stretching energy. For instance, in the case of silica with an average constraint number $n_{SiO_2} = 3.67$, the liquid-liquid phase transition temperature has been experimentally reported at $T_{LLT} \approx 1820K$ (Brueckner, 1970; Horbach and Kob, 1999) and glass transition at $T_g \approx 1425K$. The bond energy is estimated at 621.7 kJ/mol (Jutzi and Schubert, 2007), and the bond bending/stretching energy can be estimated by Lindemann's criterion with $k\epsilon^2 = 2 \times 0.3^2 \times 621.7 \approx 112kJ/mol$. We then have $T_{LLT} \approx 0.14$ and $T_g \approx 0.11$ in the unit of $k\epsilon^2$ for silica.

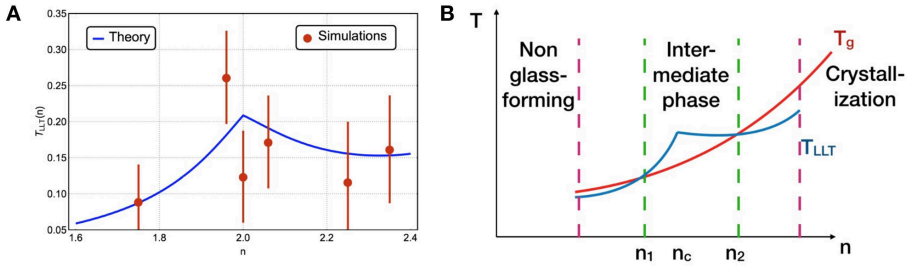

FIGURE 5 | (A) Liquid-liquid transition temperature vs. number of constraints, predicted by theory (blue line) and measured numerically for the network model for $N = 256$ (data points). Details of the theory and numerical extraction of T_{LLT} are documented in **Supplementary Note 6**. **(B)** Illustration of different dependence of T_{LLT} and glass transition T_g on the number of constraints n. When n is close to n_c where T_{LLT} becomes $>T_g$, liquid is frozen in a homogeneous intermediate phase at T_g.

and Angell, 2003). Finally, as a byproduct of our theory, the disappearance of heterogeneous phases at very high and very low n may explain the transitions beyond the intermediate phase far from the rigidity threshold (Bhosle et al., 2012), as depicted in **Figure 5B**.

To test this picture of the intermediate phase experimentally, one could look for direct signals of the liquid-liquid transition, including a lambda peak in the specific heat and loss of structural features from the scattering experiments under cooling. The direct evidence should be most likely to be found in compounds close to the boundaries of the intermediate phase, where the liquid-liquid transition temperature is comparable to the glass transition temperature. As the glass transition reflects the dynamic aspect while the liquid-liquid transition reflects the thermodynamic aspect of the material, one could also tune one of the transitions by increasing the cooling rate, or adding a small amount of impurities, or exerting a certain amount of pressure to check if the range of the intermediate phase can be perturbed in a predictable way.

5. CONCLUSIONS

In this paper, we have shown with an elastic network model that the microscopic structure of a network glass undergoes a liquid-liquid transition from an entropy-dominated heterogeneous phase to an energy-dominated homogeneous phase under cooling. At this first-order transition, the specific heat diverges, structural features disappear, and relaxation plateau vanishes. The transition temperature scales as the average frustration energy stored in covalent bonds and varies non-monotonically on the network connectivity. As the glass transition temperature scales positively with the connectivity, the two transition temperatures could cross at two constraint numbers. Inside the two constraint numbers, we would observe the liquid-liquid transition first under cooling and obtain homogeneous network glass at glass transition as in the intermediate phase.

DATA AVAILABILITY

All datasets generated for this study are included in the manuscript and/or **Supplementary Files**.

AUTHOR CONTRIBUTIONS

JT-M and LY contributed conception and design of the study, developed the theory and performed the statistical analysis, and drafted the manuscript. JT-M implemented simulation. Both authors contributed to manuscript revision, read, and approved the submitted version.

FUNDING

JT-M acknowledges a doctoral fellowship from CONACyT as well as support from DGAPA-UNAM project IN102717. LY was supported by the Gordon and Betty Moore Foundation under Grant No. GBMF2919. This research was supported in part by the National Science Foundation under Grant No. NSF PHY-1748958.

ACKNOWLEDGMENTS

We gratefully thank G. G. Naumis and M. Wyart for discussions. We thank the editors for invitation to contribute to the topic.

SUPPLEMENTARY MATERIAL

The Supplementary Material for this article can be found online at: https://www.frontiersin.org/articles/10.3389/fmats.2019.00196/full#supplementary-material

REFERENCES

Angell, C. A. (2008). Insights into phases of liquid water from study of its unusual glass-forming properties. *Science* 19, 582–587. doi: 10.1126/science.1131939

Angell, C. A. (2011). "Heat capacity and entropy functions in strong and fragile glass-formers, relative to those of disordering crystalline materials," in *Glassy, Amorphous and Nano-crystalline Materials* (Springer), 21–40.

Barré, J., Bishop, A. R., Lookman, T., and Saxena, A. (2005). Adaptability and "intermediate phase" in randomly connected networks. *Phys. Rev. Lett.* 94:208701. doi: 10.1103/PhysRevLett.94.208701

Bauchy, M., Kachmar, A., and Micoulaut, M. (2014). Structural, dynamic, electronic, and vibrational properties of flexible, intermediate, and stressed rigid as-se glasses and liquids from first principles molecular dynamics. *J. Chem. Phys.* 141:194506. doi: 10.1063/1.4901515

Bauchy, M., and Micoulaut, M. (2015). Densified network glasses and liquids with thermodynamically reversible and structurally adaptive behaviour. *Nat. Commun.* 6:6398. doi: 10.1038/ncomms7398

Bhosle, S., Gunasekera, K., Boolchand, P., and Micoulaut, M. (2012). Melt homogenization and self-organization in chalcogenides-part II. *Int. J. Appl. Glass Sci.* 3, 205–220. doi: 10.1111/j.2041-1294.2012.00092.x

Boolchand, P., Georgiev, D., and Goodman, B. (2001). Discovery of the intermediate phase in chalcogenide glasses. *J. Optoelectr. Adv. Mater.* 3, 703–720.

Brière, M.-A., Chubynsky, M. V., and Mousseau, N. (2007). Self-organized criticality in the intermediate phase of rigidity percolation. *Phys. Rev. E* 75:056108. doi: 10.1103/PhysRevE.75.056108

Brueckner, R. (1970). Properties and structure of vitreous silica. I. *J. Non-crystalline solids* 5, 123–175.

Chubynsky, M. V., Brière, M.-A., and Mousseau, N. (2006). Self-organization with equilibration: a model for the intermediate phase in rigidity percolation. *Phys. Rev. E* 74:016116. doi: 10.1103/PhysRevE.74.016116

Hall, R. W., and Wolynes, P. G. (2003). Microscopic theory of network glasses. *Phys. Rev. Lett.* 90:085505. doi: 10.1103/PhysRevLett.90.085505

Horbach, J., and Kob, W. (1999). Static and dynamic properties of a viscous silica melt. *Phys. Rev. B* 60:3169. doi: 10.1103/PhysRevB.60.3169

Jacobs, D. J., and Thorpe, M. F. (1995). Generic rigidity percolation: the pebble game. *Phys. Rev. Lett.* 75:4051–4054.

Jacobs, D. J., and Thorpe, M. F. (1996). Generic rigidity percolation in two dimensions. *Phys. Rev. E* 53:3682–3693.

Jutzi, P., and Schubert, U. (2007). *Silicon Chemistry: From the Atom to Extended Systems*. Weinheim : John Wiley & Sons.

Kirchner, K. A., and Mauro, J. C. (2019). Statistical mechanical model of the self-organized intermediate phase in glass-forming systems with adaptable network topologies. *Front. Mater.* 6:11. doi: 10.3389/fmats.2019.00011

Mauro, J. C., Allan, D. C., and Potuzak, M. (2009). Nonequilibrium viscosity of glass. *Phys. Rev. B* 80:094204. doi: 10.1103/PhysRevB.80.094204

Maxwell, J. (1864). L. On the calculation of the equilibrium and stiffness of frames. *Philos. Mag.* 27, 294–299. doi: 10.1080/14786446408643668

Micoulaut, M., and Bauchy, M. (2013). Anomalies of the first sharp diffraction peak in network glasses: Evidence for correlations with dynamic and rigidity properties. *Phys. Stat. Solidi B* 250, 976–982. doi: 10.1002/pssb.201248512

Naumis, G. G. (2005). Energy landscape and rigidity. *Phys. Rev. E* 71:026114. doi: 10.1103/PhysRevE.71.026114

Newman, M., and Barkema, G. (1999). *Monte Carlo Methods in Statistical Physics Chapter 1-4*. New York, NY: Oxford University Press.

Phillips, J. C. (1979). Topology of covalent non-crystalline solids i: Short-range order in chalcogenide alloys. *J. Non-Crystalline Solids* 34, 153–181.

Rompicharla, K., Novita, D. I., Chen, P., Boolchand, P., Micoulaut, M., and Huff, W. (2008). Abrupt boundaries of intermediate phases and space filling in oxide glasses. *J. Phys.* 20:202101. doi: 10.1088/0953-8984/20/20/202101

Sastry, S., and Angell, C. (2003). Liquid–liquid phase transition in supercooled silicon. *Nat. Mater.* 2, 739–743. doi: 10.1038/nmat994

Shintani, H., and Tanaka, H. (2008). Universal link between the boson peak and transverse phonons in glass. *Nat. Mater.* 7:870–877. doi: 10.1038/nmat2293

Thorpe, M. (1985). Rigidity percolation in glassy structures. *J. Non-Crystalline Solids* 76, 109–116.

Thorpe, M., Jacobs, D., Chubynsky, M., and Phillips, J. (2000). Self-organization in network glasses. *J. Non-Crystalline Solids* 266-269 (Pt 2), 859 – 866. doi: 10.1016/S0022-3093(99)00856-X

Wang, F., Mamedov, S., Boolchand, P., Goodman, B., and Chandrasekhar, M. (2005). Pressure raman effects and internal stress in network glasses. *Phys. Rev. B* 71:174201. doi: 10.1103/PhysRevB.71.174201

Wei, S., Gallino, I., Busch, R., and Angell, C. A. (2011). Glass transition with decreasing correlation length during cooling of fe 50 co 50 superlattice and strong liquids. *Nat. Phys.* 7, 178–182. doi: 10.1038/nphys1823

Wei, S., Yang, F., Bednarcik, J., Kaban, I., Shuleshova, O., Meyer, A., et al. (2013). Liquid–liquid transition in a strong bulk metallic glass-forming liquid. *Nat. Commun.* 4:2083. doi: 10.1038/ncomms3083

Yan, L. (2018). Entropy favors heterogeneous structures of networks near the rigidity threshold. *Nat. Commun.* 9:1359. doi: 10.1038/s41467-018-03859-9

Yan, L., Düring, G., and Wyart, M. (2013). Why glass elasticity affects the thermodynamics and fragility of supercooled liquids. *Proc. Natl. Acad. Sci. U.S.A.* 110, 6307–6312. doi: 10.1073/pnas.1300534110

Yan, L., and Wyart, M. (2014). Evolution of covalent networks under cooling: contrasting the rigidity window and jamming scenarios. *Phys. Rev. Lett.* 113:215504. doi: 10.1103/PhysRevLett.113.215504

Yan, L., and Wyart, M. (2015). Adaptive elastic networks as models of supercooled liquids. *Phys. Rev. E* 92:022310. doi: 10.1103/PhysRevE.92.022310

Yildirim, C., Raty, J. Y., and Micoulaut, M. (2018). Decoding entangled transitions: polyamorphism and stressed rigidity. *J. Chem. Phys.* 148:244505. doi: 10.1063/1.5034500

Conflict of Interest Statement: The authors declare that the research was conducted in the absence of any commercial or financial relationships that could be construed as a potential conflict of interest.

frontiers in Materials

ORIGINAL RESEARCH
published: 04 September 2019
doi: 10.3389/fmats.2019.00213

Topological Constraint Theory for Network Glasses and Glass-Forming Liquids: A Rigid Polytope Approach

Sabyasachi Sen and Jeremy K. Mason*

Department of Materials Science and Engineering, University of California, Davis, Davis, CA, United States

A variation of the topological constraint theory is proposed where an atomic network is modeled as a collection of rigid polytopes, and which explicitly distinguishes the bond angle constraints as well as rigid bond angles from flexible ones. The proposed theory allows for direct quantitative estimation of the fraction f of zero-frequency or floppy modes of the network. A preliminary model is proposed to connect the theory to the two key experimental observables that characterize glass-forming liquids, i.e., the glass transition temperature T_g and fragility m. The predicted values are tested against the literature data available for binary and ternary chalcogenides in the Ge-As-Se system. The T_g is related to f in this model by the activation entropy associated with the bond scission-renewal dynamics that is at the heart of transport and relaxation in glass-forming liquids. On the other hand, the large and temperature-dependent conformational entropy contribution of the 1-polytopes, i.e., the selenium chain elements in these chalcogenide glass-forming liquids, plays a key role in controlling the variation of m with f.

Keywords: supercooled and glassy state, rigid polytope, activation entropy, glass transition, fragility, topological constraint theory

OPEN ACCESS

Edited by:
Matthieu Micoulaut, Sorbonne Universités, France

Reviewed by:
Gerardo Naumis, National Autonomous University of Mexico, Mexico
Yann Gueguen, University of Rennes 1, France

****Correspondence:***
Sabyasachi Sen
sbsen@ucdavis.edu

Specialty section:
This article was submitted to Glass Science, a section of the journal Frontiers in Materials

Received: *15 May 2019*
Accepted: *14 August 2019*
Published: *04 September 2019*

Citation:
Sen S and Mason JK (2019) Topological Constraint Theory for Network Glasses and Glass-Forming Liquids: A Rigid Polytope Approach. Front. Mater. 6:213. doi: 10.3389/fmats.2019.00213

1. INTRODUCTION

The deformability, entropy and even temperature-dependent disintegration modes of a random atomic network are largely determined by the network's rigidity. Seminal works by Phillips (1979), Phillips (1981), Thorpe (1983), and He and Thorpe (1985) have shown the existence of a floppy-to-rigid transition in such networks in the form of rigidity percolation. The prevailing model suggests that the network is floppy when the number of degrees of freedom per atom exceeds the number of interatomic force field constraints, and the transition to rigidity occurs when these two quantities are equal. The network's rigidity therefore depends on the average coordination number $\langle r \rangle$, and various arguments suggest that the floppy-to-rigid transition occurs at the critical value $r_p = 2.4$. Although Phillips (1979) and Phillips (1981) originally attempted to relate the glass-forming ability of a network to its entropy and deformability, Thorpe (1983) placed the idea of network rigidity on more formal footing by considering the number of zero-frequency vibrational modes, i.e., continuous deformations with no energy penalty. The fraction f of such modes is predicted to decrease with increasing $\langle r \rangle$ to zero at or near r_p where rigidity percolates, and increasing the connectivity further only serves to overconstrain the network.

The rigidity percolation model suggests that there could be an underlying universal dependence of the physical properties of glasses on composition that is effectively insensitive to their chemical details. The chalcogenide glasses provide an ideal testbed in this regard, being characterized by energetically similar covalent bonds and a wide range of network connectivity. As it is practically

impossible to directly obtain f for these complex amorphous networks, typical studies in the literature instead report the variation of physical properties with $\langle r \rangle$ (Tanaka, 1989; Kamitakahara et al., 1991; Yang et al., 2010, 2013; Wang et al., 2014; Sen et al., 2019). However, it remains unclear what would be the signature of the rigidity percolation in the physical properties of amorphous networks as a function of the connectivity. In fact, a wide variety of physical properties including elastic moduli, refractive index and the glass transition temperature T_g of glasses in the Ge-Se system show continuous and monotonic change through r_p (Yang et al., 2013). On the other hand, Boolchand and coworkers have suggested that the floppy-to-rigid transition may not be sharp at r_p, but rather that the network is optimally constrained and therefore stress-free over a range of $\langle r \rangle$ around the threshold value of 2.4 (Wang et al., 2000; Boolchand et al., 2001, 2005; Chakravarty et al., 2004). These authors used modulated differential scanning calorimetry (MDSC) to show that Ge-Se glasses with such optimally constrained networks are characterized by vanishing non-reversing enthalpy, and identified this as a property of the "Intermediate Phase" (IP). It was further suggested that these IP glasses would be completely resistant to aging or relaxation below T_g. However, subsequent direct aging studies of IP glasses in the Ge-Se and Si-Se systems by other researchers showed the presence of both structural and enthalpy relaxation (Edwards and Sen, 2011; Zhao et al., 2013; Marple et al., 2019), thus questioning the validity of the existence of such IP.

Considering that T_g depends strongly on the connectivity of a network, its monotonic variation with $\langle r \rangle$ raises further questions about the use of the average coordination number as a governing variable for rigidity percolation. For example, the Gibbs–DiMarzio model of the chain polymer glass transition (Gibbs and DiMarzio, 1958; DiMarzio and Gibbs, 1964) predicts that T_g (along with the available free volume, chain stiffness and degree of polymerization) is described by the monotonic function $T_g = T_0/(1 - \kappa X)$ where X is the cross-linking density of the chains and κ is a universal constant. Note that while the chain length in chain polymers is not affected by cross-linking, this does result in progressively shorter chains for chalcogenides. Despite this difference, Sreeram et al. (1991) found that for chalcogenide networks the compositional variation of T_g could be described by the same equation if κX is replaced by $\beta(\langle r \rangle - 2)$ where β is a system-dependent parameter. Naumis (2006) and Naumis (2015) included the effect of floppy modes on the vibrational density of states to provide theoretical justification for this observation by suggesting that the Lindemann criterion for atomic displacements at the melting point could also be applied to the glass transition. Other previous studies (Buchenau et al., 2014; Toledo-Marín and Naumis, 2017) have shown the existence of a fundamental connection between the temperature dependence of the atomic mean square displacement and viscous flow or shear relaxation in glass-forming liquids. However, the glass transition is not a true thermodynamic transition and is only significant for the fact that, by definition, the structural relaxation timescale at T_g is on the order of ~ 100 s. Therefore, the validity of applying the Lindemann criterion to the glass transition remains questionable.

On the other hand, several studies have reported sharp changes in the activation energy of viscous flow near T_g, or in the related fragility parameter (Angell, 1991):

$$m = \left. \frac{\partial \log_{10} \eta}{\partial (T_g/T)} \right|_{T=T_g} \tag{1}$$

where η is the viscosity, in the vicinity of T_g. That said, the original form of the rigidity percolation model cannot explain temperature-dependent dynamics in supercooled liquids because it does not include any mechanism for the thermal energy to overcome the interatomic constraints. Gupta and Mauro (2009) attempted to address this by explicitly introducing temperature-dependent network constraints in the rigidity model. This involves assigning each network constraint a switching temperature such that the constraint becomes active only when the system temperature drops below the switching point. Although this approach is used extensively in the literature to model the compositional variation of the thermophysical properties of a wide range of glass-formers, direct experimental verification of the key assumption about the switching behavior has yet to be made.

Naumis (2005) and Naumis (2015) attempted to connect the rigidity percolation model to statistical mechanics by suggesting that the floppy modes provide channels in the potential energy landscape that serve as pathways for the network to explore many local minima, and hence make a contribution S_c to the configurational entropy. This entropy was calculated as $S_c = fNk_B \ln \Omega$, where Ω is the number of accessible microstates per atomic degree of freedom and is independent of f. Floppy modes indeed provide an important source of entropy, though their connection with structural relaxation is not obvious from the standpoint of the energy landscape where metabasin hopping and vibrational excitations within the metabasins are expected to be temporally decoupled. A possible connection between the short- and long- timescale processes has been proposed by Dyre and coworkers with their elastic "shoving" model, where the rapid increase with cooling of the activation energy for structural relaxation in a fragile glass-forming liquid is attributed to a corresponding anharmonic increase of the high-frequency shear modulus (Dyre, 2006). Additionally, an exact solvable glass transition model by Toledo-Marín and Naumis (2017) has related the short-time process to the frequency of probing transition states of the energy landscape, while the long-time relaxation process represents the transition between metastable states.

The rigidity percolation model is undoubtedly useful as means to understand the behavior of random networks around the glass transition. Nevertheless, the model makes some predictions that are not consistent with experimental observations, and the average atomic coordination number $\langle r \rangle$ is not always an appropriate measure of the network connectivity (section 2.1 gives an example), at least not without qualifications described by Thorpe (1983). Moreover, a connection between the model and the statistical mechanics of glass-forming liquids has yet to be conclusively established. That is to say, the topological

constraint theory of glasses should not be considered complete and inviolable.

This article proposes a variation of the topological constraint theory where, for the purposes of calculating the available degrees of freedom, the network is considered as being constructed from a collection of rigid polytopes. This view is supported by, e.g., Sidebottom's observation that the mean connectivity of a network's weakest links is more closely related to the fragility than the mean coordination number (Sidebottom, 2015, 2019), and is related to the concept of rigid unit modes in the context of negative thermal expansion materials (Evans, 1999; Fang et al., 2014). The theory is motivated and developed in section 2, along with a preliminary model that relates the available degrees of freedom to the relaxation time of a glass-forming liquid. The resulting equations are tested and evaluated for the family of chalcogenide glasses in section 3, and suggest that this variation of the topological constraint theory could be useful more generally.

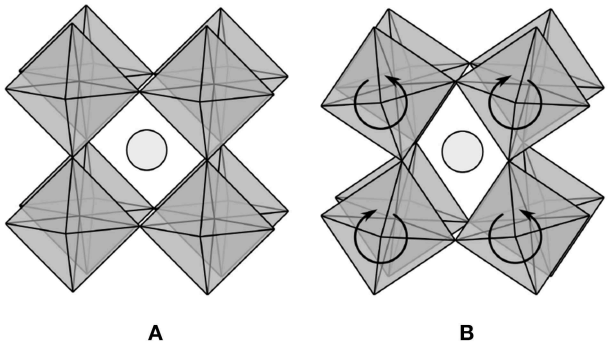

FIGURE 1 | (A) Perovskite materials with formula ABO_3 contain a regular network of corner-sharing BO_6 octahedra, with the position of the A atom in light gray. **(B)** Patterns of octahedral tilting (Glazer, 1972) are low-frequency modes of the network.

2. NETWORKS OF RIGID POLYTOPES

This section revisits the rigidity percolation model. First, the limits of this model are explored using the example of an octahedral network, with the purpose of reinforcing that the underlying assumptions in the model are more subtle than is sometimes believed. Second, a variation on the topological constraint theory is derived where rigid polytopes are considered as the structural units of the network instead of atoms. This follows from the conceptual separation of the degrees of freedom into three classes, namely, those that are directly constrained by strong interatomic bonds, those that are constrained by the connectivity of the network, and those that are unconstrained. Apart from offering more flexibility in the application of the model, the resulting formula for the fraction of unconstrained degrees of freedom is quantitatively different from Thorpe (1983). Third, the implications of the revised model for the dynamical properties of supercooled liquids in the immediate vicinity of the glass transition are explored. The predictions of this model are compared with experiments in section 3.

2.1. Limits of the Rigity Percolation Model

Thorpe's rigidity percolation model (Thorpe, 1983) begins by classifying atoms in a random network by the number of bonds in which they participate, without distinguishing bonds of different types. If n_r is the number of atoms with r bonds, then $3\sum_r n_r$ is the number of degrees of freedom. Specifying the bond lengths and bond angles around an atom with r bonds imposes $r/2$ and $2r-3$ constraints, respectively, on the degrees of freedom. If all of these constraints are independent, then the fraction of unconstrained degrees of freedom f is given by:

$$f = \frac{3\sum_r n_r - \sum_r n_r[r/2 + (2r-3)]}{3\sum_r n_r}. \tag{2}$$

The average coordination number $\langle r\rangle$ is defined to be $\sum_r n_r r/\sum_r n_r$ (despite the misprint in Thorpe, 1983), reducing this to the standard equation:

$$f = 2 - 5\langle r\rangle/6. \tag{3}$$

Since $f = 0$ when $\langle r\rangle = 2.4$, the model is often believed to predict that rigidity should percolate through the network and various properties of the system should be discontinuous around this critical value. Thorpe's original article included several qualifications to this conclusion that are unfortunately not consistently discussed in the literature, but that indicate that the situation is more nuanced than suggested by Equation (3).

Consider applying this model to the regular network of corner-sharing octahedra in a perovskite material, as shown in **Figure 1A**. If the formula for this material is ABO_3, then a single octahedron contains one B atom with six bonds and three O atoms with two bonds each. The average coordination number for the octahedral network is then three, and the model would seem to predict that the network is not only rigid but highly overconstrained. Nonetheless, it is widely recognized that various patterns of octahedral tilting (Glazer, 1972), including the one in **Figure 1B**, are low-frequency modes of the network. In fact, such soft modes are believed to be responsible for displacive phase transitions and negative thermal expansion in a number of systems (Evans, 1999; Fang et al., 2014). Possible resolutions to this apparent contradiction are considered below to help to clarify the limitations of the model as frequently interpreted, and to suggest refinements to be included in the subsequent derivation.

Our first attempt begins with the observation that the symmetry of the ideal system allows only a constant number of octahedral tilting modes, independent of the number of atoms. Hence, as the system size approaches the thermodynamic limit, the fraction of zero-frequency modes goes to zero and the model gives the expected result. This argument is not entirely satisfying though; the number of octahedral tilting modes is constant because they extend throughout the entire network, but it is difficult to exclude the possibility of localized zero-frequency modes whose number scales with the size of a disordered system.

Thorpe (1983) discussed this possibility, saying that "the number of zero frequency modes is not zero at $\langle r \rangle = r_p$ because floppy inclusions still exist". Perhaps then the presence of localized zero-frequency modes is less relevant to the system properties than a percolating network of identical ideally rigid bonds. The difficulty with this is that bonds in physical systems are neither identical nor ideally rigid; van der Waals forces allow systems with $\langle r \rangle < r_p$ at room temperature to solidify at low temperatures, and bond breaking allows systems with $\langle r \rangle > r_p$ at room temperature to liquify at high temperatures. The conclusion here is the same as the one arrived at by Thorpe (1983), namely, one should neither expect to observe discontinuous behavior in the number of zero-frequency modes, nor in the properties of glass-forming liquids, at any particular value of the average coordination number.

Our second attempt considers the possibility that the number of constraints is overestimated in Equation (3). Initially observe that if the bond angles of the oxygens at the corners of the octahedra were fixed, then the octahedra would not be able to tilt. Thorpe (1983) anticipated this possibility as well: "For example in Si_xO_{1-x}...it is reasonable *not* to count the angular force at the oxygen atoms". Since the bond angle constraints do not explicitly appear in Equation (3), such a modification needs to be performed using Equation (2). Unfortunately, excluding the oxygen bond angle constraints is insufficient to make f nonnegative, and only increases the apparent value from -0.5 to -0.25. This idea should instead be taken much further, with only *independent* constraints included in Equation (2) (Thorpe, 1983). The difficulty with this is that while many constraints are dependent for the octahedral network, distinguishing the dependent from the independent ones is not at all obvious due to the interactions being nonlocal (e.g., a set of bonds could form a ring). While there do exist approaches to identifying the set of independent constrains (e.g., the pebble game; Jacobs and Thorpe, 1995, 1996), these require much more detailed knowledge of the network configuration than is generally available in practice.

Perhaps since all of the quantities in Equation (2) are defined using only local information, f is more closely related to the properties of an average local environment than the overall network. Indeed, f could be interpreted as an estimate for the average fraction of unconstrained degrees of freedom *per atom*. A value of $f = -0.25$ for the octahedral network could then be rationalized as a consequence of the atoms at the centers of the octahedra being highly overconstained. If f is truly a local quantity though, one should not expect it to provide any information about the existence of nonlocal zero-frequency modes. That is, interpreting f in this way resolves the apparent contradiction introduced as motivation for this section, but raises the question of whether there is some other property that would be more relevant to the experimental properties of the system.

A revised topological constraint theory would ideally address the several concerns identified in the preceding discussion:

1. There is more than one kind of atomic interaction, and the model should distinguish rigid bond angles from flexible ones.
2. Bond angle constraints should be explicit in the model, and included only where dictated by intuition.
3. The model should suggest a connection to the nonlocal properties of the system that is explicit and consistent with experiments.

Section 2.2 proposes a revised topological constraint theory that is motivated by the first and second points, while the third is the subject of section 2.3.

2.2. Revised Topological Constraint Theory

The concept of a metabasin requires separating two types of relaxations in glass-forming liquids, namely, local rearrangements of particles and substantial structural relaxations (Stillinger, 1995). If the available kinetic energy is such that the system is confined to a single metabasin, then the system is expected to behave as a solid. Conversely, a system that often experiences the substantial structural relaxations associated with transitions between metabasins explores more of the configuration space and is expected to behave as a liquid. This suggests that characterizing the metabasins is essential to understanding the glassy state, and much effort has been expended in this direction (Doliwa and Heuer, 2003; Heuer, 2008).

Suppose that the local rearrangements in this picture can be identified with operations involving a small number of covalent bonds, and structural relaxations with changes to the network conformation or connectivity. Constraints associated with individual bonds would then be less relevant to understanding the glass transition than constraints imposed by the network connectivity on larger structural units. This serves as motivation for the topological constraint theory developed in this section, where the network is considered as being composed of rigid polytopes rather than individual atoms, and any relaxations involving bonds within a rigid polytope are explicitly not considered. While others have used rigid polytopes for this purpose before (Cooper, 1978, 1982; Gupta and Cooper, 1990), and even general networks composed of multiple types of rigid polyhedra with edge and face sharing (Gupta, 1993), those authors specifically considered the restricted question of whether topologically-disordered networks could exist. Moreover, those theories consider the number of degrees of freedom per vertex (rather than the fraction of unconstrained degrees of freedom) and require considerably more detailed knowledge of the constituent polyhedra than the theory developed here.

A polytope is a generalization of polygons and polyhedra to any nonnegative dimension. More precisely, an i-polytope is a finite region of i-dimensional space that is bounded by a finite set of $(i-1)$-dimensional hyperplanes. The boundary of a polytope is itself comprised of polytopes, and a j-polytope of this type is called a j-facet[1]. For example, a polyhedron (3-polytope) is bounded by faces (2-facets), the faces can join at edges (1-facets), and the edges can join at vertices (0-facets). This article only considers i-polytopes for $0 \leq i \leq 3$, and requires two polytopes to intersect on a shared facet or not at all. For example, two tetrahedra could intersect on a 0-polytope (corner sharing), a

[1]Formally, a i-polytope is its own i-facet.

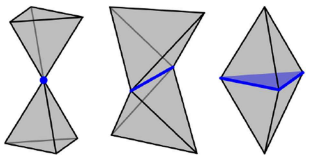

FIGURE 2 | Two tetrahedra could intersect not at all, on a 0-polytope **(Left)**, on a 1-polytope (center), or on a 2-polytope **(Right)**, corresponding to corner sharing, edge sharing and face sharing.

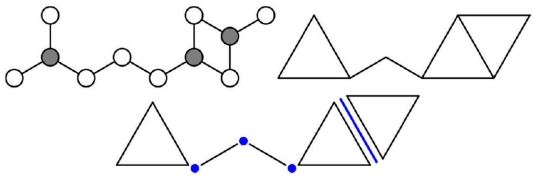

FIGURE 3 | A portion of an atomic network **(Top left)** contains 2- and 3-coordinated white and gray atoms, respectively. The same network can be modeled using rigid polytopes **(Top right)**, where the bonds around gray atoms are replaced by triangles and the remaining bonds by line segments. More precisely **(Bottom)**, the network is composed of five direct polytopes (two 1-polytopes and three 2-polytopes) and four intersection polytopes (three 0-polytopes and one 1-polytope).

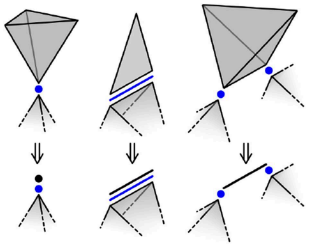

FIGURE 4 | A direct d-polytope can contribute fewer than $\phi(d)$ degrees of freedom. For a direct 3-polytope connected to a single intersection 0-polytope (left), the two orientational variables do not affect the network's behavior, and the direct polytope can safely be replaced by a direct 0-polytope. More generally, only the connection of a direct polytope to an intersection polytope affects the network behavior, and the direct polytope can be replaced by the convex hull of the connected intersection polytopes.

1-polytope (edge sharing), or a 2-polytope (face sharing), as indicated in **Figure 2**.

Following the discussion above, a network of atomic bonds is represented as a network of rigid polytopes. The construction of the polytopes is flexible by design and not entirely algorithmic, but there are several general principles to follow. A polytope is usually constructed as the convex hull of a set of contiguous bonds. Substantial changes to the angles of bonds within the set should be energetically expensive since the polytopes are assumed to be rigid, and any internal degrees of freedom are explicitly ignored. This construction implies that every polytope vertex coincides with some atom; if the system contains one or more atomic species for which the bond angles are not entirely fixed (e.g., oxygen), then these should be placed at the vertices.

Figure 3 considers an example fragment of an atomic network containing two types of atoms, one 3-coordinated and the other 2-coordinated (bonds to the surroundings are omitted for simplicity). If the bond angles around the gray atoms are fixed and those around the white atoms are not, then the atomic network can be represented as a network of rods and triangles. The polytopes constructed as convex hulls of sets of atomic bonds (i.e., the rods and triangles) are called *direct* polytopes. The facets where direct polytopes intersect are called *intersection* polytopes, and encode any constraints imposed by the connectivity of the network on the motion of the direct polytopes. For example, the network in **Figure 3** contains three intersection 0-polytopes, the existence of which requires the adjoining direct polytopes to share a vertex. Alternatively, one could imagine being given a collection of direct and intersection polytopes, and having to join direct polytopes along the intersection polytopes (with none left over) to create a facsimile of the atomic network.

The objective of a topological constraint theory is to estimate f, the fraction of unconstrained degrees of freedom available to the network. The direct polytopes contribute degrees of freedom whereas the intersection polytopes contribute constraints; if the number of degrees of freedom contributed by a direct polytope and the number of constraints contributed by an intersection polytope are known, and every constraint is assumed to be independent, then f is straightforward to estimate. This reduces the objective of this section to the calculation of the number of degrees of freedom or constraints contributed by a given polytope.

Consider a single direct polytope. A 0-polytope requires three variables to specify the three spatial coordinates. A 1-polytope requires five variables, three for a 0-facet and two for the orientation of the attached edge. A 2- or 3-polytope requires six variables, five for a 1-facet and one for the rotation angle about that facet. For notational purposes, let d be the dimension of a direct polytope and define:

$$\phi(d) = \begin{cases} 3 & d = 0 \\ 5 & d = 1 \\ 6 & d = 2, 3 \end{cases} .$$

It is tempting to say that $\phi(d)$ is the number of degrees of freedom made available to the network by a direct d-polytope, but this is not necessarily the case; **Figure 4** shows several situations where a direct d-polytope contributes fewer than $\phi(d)$ degrees of freedom. For example, the direct 3-polytope on the right constrains the distance between the connected intersection 0-polytopes, but can rotate about the relevant edge without affecting the configurations available to the network (direct polytopes not connected by intersection polytopes do not interact). That is, this direct 3-polytope effectively functions as a direct 1-polytope. Along with the other examples in **Figure 4**, this suggests that a direct d-polytope actually contributes only $\phi(\delta)$ degrees of freedom, where $\delta \leq d$ is the dimension of the

convex hull of the connected intersection polytopes and is called the *reduced dimension*.

For the intersection polytopes, the configurational variables of a single intersection d-polytope contribute $\phi(d)$ degrees of freedom. Connecting an intersection d-polytope to a direct polytope imposes $\phi(d)$ constraints on the direct polytope though, since the relevant configurational variables of the intersection and direct polytopes must be the same. There could be k additional angular constraints associated with the intersection polytope as well (counted only after reducing the dimension of the connected direct polytopes). An intersection d-polytope connected to j direct polytopes would therefore contribute a total of $(j-1)\phi(d)+k$ constraints. For example, the intersection 0-polytope on the left of **Figure 4** contributes three positional degrees of freedom, imposes three positional constraints on each of the connected direct polytopes, and has zero associated angular constraints for a total of three constraints.

At this point, the number of unconstrained degrees of freedom can be estimated by substracting the sum of the constraints imposed by intersection polytopes from the sum of the degrees of freedom contributed by direct polytopes. Let n_i be the number of direct polytopes with reduced dimension i, and m_{ijk} be the number of intersection i-polytopes with j connections to direct polytopes and k associated angular constraints. Then the proposed topological constraint theory gives the following estimate for the fraction of unconstrained degrees of freedom:

$$f = \frac{\sum_i n_i\phi(i) - \sum_i \sum_j \sum_k m_{ijk}[(j-1)\phi(i)+k]}{\sum_i n_i\phi(i)}. \quad (4)$$

The use of this equation can be clarified with several examples. For SiO_2, a network with n direct 3-polytopes (SiO_2 tetrahedra) would have $2n$ intersection 0-polytopes (oxygen atoms), each with two connections to direct polytopes and no associated angular constraints. Evaluating Equation (4) indicates that $f = 0$ for the SiO_2 network, in agreement with the conventional model. For the octahedral network in **Figure 1**, a network with n direct 3-polytopes would have $3n$ intersection 0-polytopes with the same properties as those for SiO_2. Evaluating Equation (4) for this network gives $f = -0.5$, a quantitatively different value from the -0.25 given by Equation (2) (modified to remove angular constraints on the oxygen atoms). Since the numerators of Equations (2) and (4) are both the number of unconstrained degrees of freedom (a property of the network that is independent of the model), the difference should be caused by the denominators. That is, there is a quantitative difference that results from choosing atoms or rigid polytopes as the structural units of the network. The preferred choice should depend on whether Equations (2) or (4) is more strongly correlated with the experimental data.

2.3. A Model for Entropy and Relaxation

Ideally, the relevance of the topological constraint theory developed in section 2.2 to physical systems would be established by connecting the fraction of unconstrained degrees of freedom f to an experimentally-observable quantity, and comparing the predicted and experimental values of that quantity. The purpose of this section is to motivate and derive an equation for the relaxation time τ of a glass-forming liquid that depends explicitly on f. This will imply functional dependencies of the glass transition temperature T_g and the fragility m on f that will be compared with experiments in section 3.

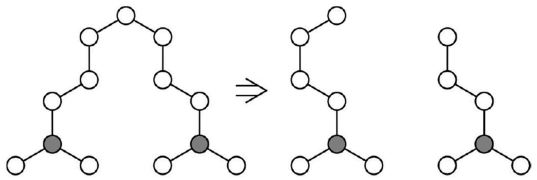

FIGURE 5 | Consider part of a network containing only chains of length n, with v chains connected to a single gray atom **(Left)**. One possible bond-breaking event would convert one of these chains into two chains of length $\sim n/2$ **(Right)**, increasing the entropy of the system.

Given a single primary relaxation mechanism, a relaxation time τ can be modeled as having an Arrhenius dependence on temperature, at least over a limited temperature range near T_g. The relaxation time τ can then be simply written as:

$$\tau = \tau_0 \exp\left(\frac{\Delta G}{k_B T}\right).$$

The free energy of activation ΔG can be written in terms of an activation enthalpy and entropy. If only the activation entropy ΔS depends explicitly on f, the expression for τ can be re-written as:

$$\tau = \tau_0 \exp\left(-\frac{\Delta S(f)}{k_B}\right)\exp\left(\frac{\Delta H}{k_B T}\right). \quad (5)$$

This leaves only the construction of a model for $\Delta S(f)$ to be able to relate f to an experimental observable.

For this purpose, assume that the configurational entropy of a network containing chain-like moieties cross-linked by pyramidal or tetrahedral units is dominated by the conformational entropy of the chains. A simple model of such a network could contain 2-coordinated white atoms and v-coordinated gray atoms with all of the white atoms participating in chains of length n, as on the left of **Figure 5**. A single chain can be modeled as a self-avoiding walk (SAW), with a number of configurations approximately given by:

$$Z(n) = A\mu^n n^{\gamma-1}$$

where A, μ and γ are constants (Madras and Sokal, 1988; Schram et al., 2017). Using Boltzmann's formula $S = k_B \ln Z$, the conformational entropy of a single chain depends on n as:

$$S(n) = k_B[\ln A + n\ln\mu + (\gamma-1)\ln n]$$

where k_B is Boltzmann's constant. Since entropy is an extensive quantity, the change in configurational entropy when breaking a

bond to convert one chain of length n into two chains of length $\sim n/2$, as on the right of **Figure 5**, is:

$$\begin{aligned}\Delta S &= 2S(n/2) - S(n) \\ &= k_B[(\gamma - 1)\ln(n/4) + \ln A]. \end{aligned} \quad (6)$$

This is interpreted as the activation entropy for the bond scission-renewal dynamics. While many distinct microscopic events are expected to contribute to the effective bond-breaking mechanism in practice, the reasoning above is intended only to motivate the form of the dependence of ΔS on n.

The dependence of n on f for the system on the left of **Figure 5** can be established using Equation (4). Specifically, a single chain contributes n direct 1-polytopes $(n-1)$, intersection 0-polytopes with two connections to direct polytopes along the chain, and $2/\nu$ intersection 0-polytopes with ν connections to adjoining chains. Evaluating Equation (4) gives:

$$f = \frac{2}{5} - \frac{3 - 6/\nu}{5n}$$

for the fraction of unconstrained degrees of freedom f as a function of n. Solving instead for n gives:

$$n = \frac{3 - 6/\nu}{2 - 5f} \quad (7)$$

which indicates that the chain length diverges as $f \to 0.4$. Since repeating the derivation with the chain segments as 3-polytopes instead of 1-polytopes and not using the reduced dimension makes the chain length diverge as $f \to 0.5$, a significant change is expected in the properties of most glass-forming liquids in the interval $0.4 \leq f \leq 0.5$. Substituting Equation (7) into Equation (6) gives:

$$\begin{aligned}\Delta S(f) &= -k_B\left\{(\gamma - 1)\ln(0.4 - f) - \left[(\gamma - 1)\ln\left(\frac{3 - 6/\nu}{20}\right) + \ln A\right]\right\} \\ &= -k_B[a\ln(b - f) - c]\end{aligned}$$

for the change in configurational entropy, where a, b and c are constants. The value of a is expected to be around 0.157 from the literature (Madras and Sokal, 1988; Schram et al., 2017), and b is expected to be in the interval $0.4 \leq b \leq 0.5$ by the above reasoning. Finally, substituting the equation for $\Delta S(f)$ into Equation (5) gives:

$$\tau = \tau_0'(b - f)^a \exp\left(\frac{\Delta H}{k_B T}\right) \quad (8)$$

for the relaxation time, where $\tau_0' = \tau_0 \exp(-c)$. If there is a characteristic relaxation time $\tau_g \approx 100\,\text{s}$ that is a universal constant at the glass transition temperature T_g, then Equation (8) can be inverted to find T_g as a function of f:

$$T_g = \frac{\Delta H/k_B}{\ln(\tau_g/\tau_0') - a\ln(b - f)}. \quad (9)$$

The fragility m, on the other hand, is related by the Adam-Gibbs model of relaxation (Adam and Gibbs, 1965) to the temperature dependence of the configurational entropy S_c:

$$m \propto \left.\frac{\partial S_c}{\partial T}\right|_{T=T_g}. \quad (10)$$

Sidebottom (2015) has recently suggested that the temperature dependence of S_c is governed by the connectivity of a network. Estimating the conformational entropy of a network formed via progressive cross-linking of chains indicated an abrupt rise in m as the average chain length n between cross-linking points increased beyond ~ 3. Substituting this value of n into Equation (7) gives $0.30 \leq f \leq 0.33$ for $3 \leq \nu \leq 4$, values typical for chalcogenide glasses. Taken together, these results suggest that fragility m is expected to rise abruptly as f increases beyond 0.3. These predictions for the dependence of T_g and m on f are compared with experimental results for chalcogenide systems in section 3 below.

3. CONNECTION WITH EXPERIMENTS

For the examination of select thermophysical properties of glass-forming networks as a function of f, we restrict ourselves to binary and ternary compositions in the Ge-As-Se system ranging from pure chalcogen Se to up to the stoichiometric compositions along the $GeSe_2$-As_2Se_3 join. This system is chosen as it represents a simple compositional evolution from a chain-like structure for pure Se to a 3-dimensional network for the stochiometric compositions. There is the additional advantage that the nature and strength of the homopolar Se-Se and heteropolar Ge/As-Se bonds in this system are similar, which ensures that their effects on the network rigidity can be considered comparable. Although other chalcogenide systems, i.e., the sulfides and the tellurides, share similarities in the compositional variation of their physical properties, the increasingly ionic behavior in sulfides and metallic behavior in tellurides result in significant differences in the nature of the homopolar and heteropolar bonds (Wei et al., 2017). The analysis of S-rich glasses is further complicated by the presence of S_8 rings that do not participate in the network (Zhu et al., 2018). The chalcogen-deficient glass-forming compositions are not considered either, since such networks are over-constrained and the estimation of f for such networks is not physically sensible. Moreover, the structure of chalcogen-deficient Ge-As-Se networks is known to be complicated by the formation of molecular elements of the type As_4Se_3, As_4Se_4 and As_4, as well as the appearance of Ge-Ge bonds in ethane-like $Se_{3/2}$-Ge-Ge-$Se_{3/2}$ units and Ge-As bonds (Sen and Aitken, 2002; Yang et al., 2010; Kaseman et al., 2014). The quantitative estimation of the relative concentrations of these structural units and their effects on the network rigidity are not straightforward and will be considered in the future. Finally, it is well known that the $GeSe_{4/2}$ tetrahedral units in the structural network of Ge_xSe_{1-x} glasses over the composition range $0 \leq x \leq 0.33$ are predominantly corner-sharing, but a small fraction (15–35%) that increases monotonically with x form edge-sharing tetrahedral units

(Salmon, 2007; Edwards and Sen, 2011). Sidebottom (2015) suggested that the edge-sharing tetrahedra provide more degrees of freedom to the network compared to their corner-sharing counterparts since the shared edge does not participate in the connectivity of the rest of the network. However, this does not account for the fact that edge-sharing between tetrahedra or other rigid polytopes can severely over-constrain the local degrees of freedom of the polytope itself (Gupta and Cooper, 1990; Marple et al., 2019). Here we assume that these effects approximately cancel, and that all of the tetrahedra are corner-sharing at the concentrations considered below.

Now consider the fractional degrees of freedom f of a chalcogenide network with composition $Ge_xAs_ySe_{1-x-y}$ that contains n_a atoms and n_d direct polytopes. Let α be the fraction of direct polytopes that are $GeSe_{4/2}$ tetrahedra (3-polytopes), β be the fraction that are $AsSe_{3/2}$ triangles (reduced 2-polytopes), and $(1-\alpha-\beta)$ be the fraction that are $Se_{2/2}$ line segments (1-polytopes). The first step to calculate f is to find expressions for the direct polytope fractions α and β in terms of the atomic fractions x and y. Equating the number of Ge, As, and Se atoms with those that appear in the direct polytopes gives the following system of equations:

$$\begin{aligned} xn_a &= \alpha n_d \\ yn_a &= \beta n_d \\ (1-x-y)n_a &= (1+\alpha+0.5\beta)n_d \end{aligned}$$

Solving for the number of direct polytopes n_d as a function of x and y and substituting the result into the first and second equations gives:

$$\begin{aligned} \alpha &= \frac{x}{1-2x-1.5y} \\ \beta &= \frac{y}{1-2x-1.5y} \end{aligned}$$

for the fractions of direct 3-polytopes and direct 2-polytopes. The second step to calculate f is to find the types and numbers of all intersection polytopes. Given the assumption that all direct polytopes are corner sharing, the network contains only intersection 0-polytopes, each with two connections to direct polytopes and no associated angular constraints. Since there is precisely one intersection 0-polytope for every Se atom, the number n_i of intersection 0-polytopes is:

$$\begin{aligned} n_i &= (1-x-y)n_a \\ &= \frac{1-x-y}{1-2x-1.5y} n_d. \end{aligned}$$

Evaluating Equation (4) for a network containing αn_d direct 3-polytopes, βn_d direct 2-polytopes, $(1-\alpha-\beta)n_d$ direct 1-polytopes, and n_i intersection 0-polytopes gives:

$$f = \frac{2-6x-3.5y}{5-9x-6.5y} \tag{11}$$

for the fraction of unconstrained degrees of freedom.

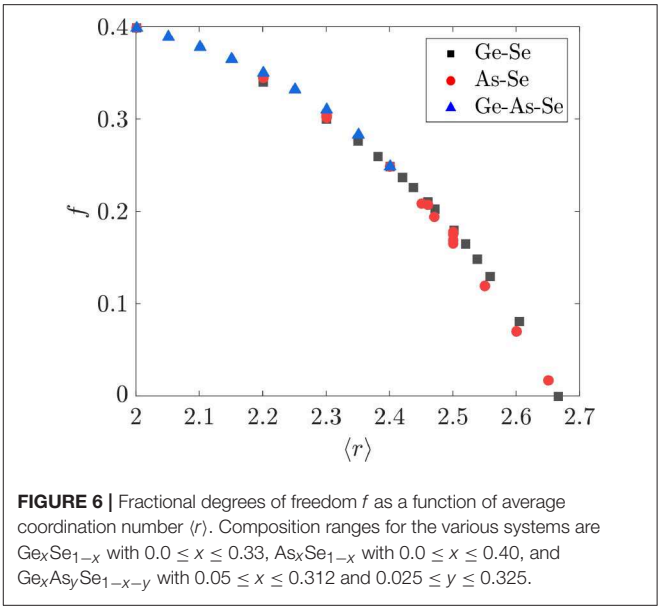

FIGURE 6 | Fractional degrees of freedom f as a function of average coordination number $\langle r \rangle$. Composition ranges for the various systems are Ge_xSe_{1-x} with $0.0 \le x \le 0.33$, As_xSe_{1-x} with $0.0 \le x \le 0.40$, and $Ge_xAs_ySe_{1-x-y}$ with $0.05 \le x \le 0.312$ and $0.025 \le y \le 0.325$.

The value of f is compared with the average coordination number $\langle r \rangle = 2x + y + 2$ in **Figure 6** for the binary and ternary Ge-As-Se compositions considered in this study. That f should nearly be a function of $\langle r \rangle$ is surprising, given that both f and $\langle r \rangle$ are functions of two independent variables relating to the number of tetrahedral and pyramidal cross-linking elements. It is also immediately apparent that the variation of f with $\langle r \rangle$ is quite different from that obtained by Thorpe using Equation (3), since that version of f decreases linearly with $\langle r \rangle < r_p$ until the sharp transition at $r_p = 2.4$. The f obtained using Equation (11) is instead nearly a nonlinear function of $\langle r \rangle$ that goes to zero at $r_p = 2.67$. As a result, the model developed in section 2.2 predicts that As_2Se_3 and $GeSe_4$ with $\langle r \rangle = 2.4$ are underconstrained networks, whereas Equation (3) predicts that they are isostatically rigid; the source of this difference is in the application of the angular constraints around Se atoms. This prediction of our model calls into question the existence of the IP as defined elsewhere (Wang et al., 2000; Boolchand et al., 2001, 2005; Chakravarty et al., 2004). Furthermore, one should expect a rapid increase in the elastic moduli beyond $r_p = 2.67$ as the network is increasingly over constrained; such behavior is indeed observed for a wide variety of binary and ternary Ge-As/Sb-S/Se chalcogenide glasses (Tanaka, 1989; Yang et al., 2013).

The glass transition temperature T_g for glass-forming liquids represents an isoviscous temperature where the viscosity is $\sim 10^{12}$ Pa · s and the relaxation time is ~ 100 s, and is expected to be a monotonic function of the average connectivity of a network. Since the bond strengths of the homopolar Se-Se and heteropolar Ge-Se and As-Se bonds are comparable, the T_g of Ge-As-Se glasses should monotonically decrease with f. This is borne out in **Figure 7**, which shows a nearly universal and linear decrease in T_g with increasing f in these glasses. The black line in **Figure 7** is given by fitting Equation (9) to the data using $\tau_g = 100$ s, $\tau_0' = 10^{-13}$ s, $b = 0.45$, and a standard conjugate

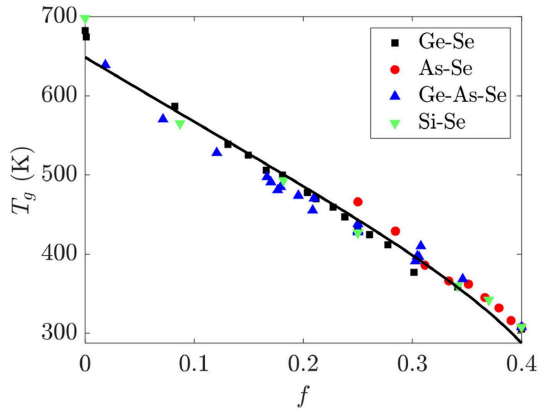

FIGURE 7 | The glass transition temperature T_g for binary Ge-Se, As-Se, Si-Se and ternary Ge-As-Se glasses is nearly a linear function of the fractional degrees of freedom f. The black line is a fit using Equation (9) for the parameter values reported in the text. T_g data are from Bernatz et al. (2002), Yang et al. (2010), Musgraves et al. (2011), Wang et al. (2014), Marple et al. (2017), Zeidler et al. (2017).

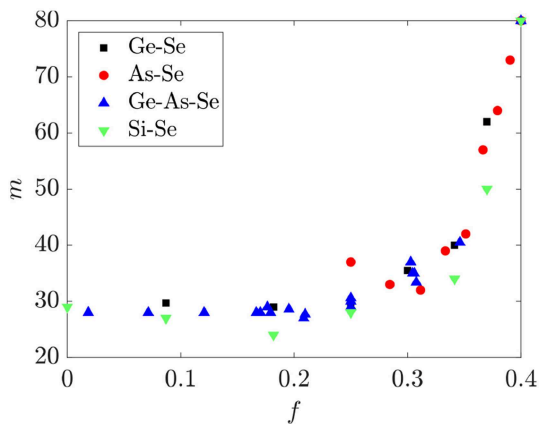

FIGURE 8 | The fragility m for binary Ge-Se, As-Se, Si-Se and ternary Ge-As-Se glasses as a function of the fractional degrees of freedom f. Fragility data are from Bernatz et al. (2002), Koštál and Málek (2010), Gueguen et al. (2011), Musgraves et al. (2011), Wang et al. (2014), Svoboda and Málek (2015), Marple et al. (2019).

gradient minimization algorithm for the remaining parameters. This procedure gives $\Delta H = 3.552 \pm 0.001$ eV and $a = 36.32 \pm 0.02$, with parameter uncertanties estimated by calculating the Hessian matrix at the minimum. An activation enthalpy ΔH of around twice the bond energy is reasonable enough for a scission event given the simplicity of the model developed in section 2.3, and is roughly consistent with the value of ∼2.7 eV for the Ge_xSe_{1-x} system as reported in the literature (Gueguen et al., 2011). The deviation of a from the expected value of 0.157 is more dramatric, with the activation entropy being ∼200 times larger than expected. This could be related to the number of configurations in SAW models generally being calculated for chains on lattices rather than in continuous space, or to the neglect of the effect of a scission event on the conformations available to the surrounding network components.

The dependence of the fragility m on f for the same Ge-As-Se liquids is shown in **Figure 8**. A nearly universal functional dependence between m and f is again observed for glass-forming liquids in this system, where m is nearly constant ∼30 for $0 \leq f \leq 0.3$ and rapidly increases to ∼80 for $0.3 \leq f \leq 0.4$. Recent studies have suggested that this behavior is related to the disappearance of the conformational entropy of the selenium chain segments as their average length is reduced to ∼3 (Naumis, 2015; Sidebottom, 2015), and is consistent with the prediction made in section 2.3 for the corresponding threshold value of $0.30 \leq f \leq 0.33$. By comparison, the onset of the sharp rise in m coincides with $\langle r \rangle \approx 2.3$, below where the conventional topological constraint theory predicts a transition.

4. CONCLUSIONS

A rigid polytope model of glass structure is developed and used to calculate the relative fraction of unconstrained degrees of freedom f, the result having a fundamentally different dependence on $\langle r \rangle$ than that originally obtained by Thorpe (1983) using a mean-field approximation. The variation of T_g and m of binary and ternary chalcogenide glass-forming liquids in the Ge-As-Se system shows nearly universal dependence on f over a wide range of compositions. While T_g decreases almost linearly with f, m does not vary significantly in the range $0 \leq f \leq 0.3$ but increases rapidly with f for $0.3 \leq f \leq 0.4$. The variation of T_g with f can be explained by considering the change in the conformational entropy associated with the bond scission-renewal process of chain segments as the primary mode of structural relaxation of the glassy network. On the other hand, following Sidebottom (Sidebottom, 2015), the rapid increase in m for $f > 0.3$ is ascribed to the corresponding rise in the conformational entropy of the selenium chain segments as their average length increases beyond ∼3 Se atoms.

DATA AVAILABILITY

The datasets generated for this study are available on request to the corresponding author.

AUTHOR CONTRIBUTIONS

SS suggested the idea of using rigid polytopes to calculate topological constraints. JM developed the theoretical construct and performed all calculations. SS and JM analyzed the results and wrote the manuscript.

FUNDING

SS was supported by the National Science Foundation under Grant No. DMR 1855176. JM was supported by the National Science Foundation under Grant No. DMR 1839370.

REFERENCES

Adam, G., and Gibbs, J. H. (1965). On the temperature dependence of cooperative relaxation properties in glass-forming liquids. *J. Chem. Phys.* 43, 139–146.

Angell, C. (1991). Relaxation in liquids, polymers and plastic crystals—strong/fragile patterns and problems. *J. Non-Crystall. Solids* 131, 13–31.

Bernatz, K., Echeverría, I., Simon, S., and Plazek, D. (2002). Characterization of the molecular structure of amorphous selenium using recoverable creep compliance measurements. *J. Non-Crystalline Solids* 307, 790–801. doi: 10.1016/S0022-3093(02)01522-3

Boolchand, P., Georgiev, D., and Goodman, B. (2001). Discovery of the intermediate phase in chalcogenide glasses. *J. Optoelectr. Adv. Mater.* 3, 703–720. Available online at: https://joam.inoe.ro/arhiva/Pdf3_3/Boolchand.pdf

Boolchand, P., Lucovsky, G., Phillips, J., and Thorpe, M. (2005). Self-organization and the physics of glassy networks. *Philos. Magaz.* 85, 3823–3838. doi: 10.1080/14786430500256425

Buchenau, U., Zorn, R., and Ramos, M. (2014). Probing cooperative liquid dynamics with the mean square displacement. *Phys. Rev. E* 90:042312. doi: 10.1103/PhysRevE.90.042312

Chakravarty, S., Georgiev, D., Boolchand, P., and Micoulaut, M. (2004). Ageing, fragility and the reversibility window in bulk alloy glasses. *J. Phys. Conden. Matt.* 17:L1. doi: 10.1088/0953-8984/17/1/L01

Cooper A. R. Jr. (1982). WH Zachariasen-the melody lingers on. *J. Non-Crystalline Solids* 49, 1–17. doi: 10.1016/0022-3093(82)90105-3

Cooper, A. (1978). Zachariasen's rules, Madelung constant, and network topology. *Phys. Chem. Glass.* 19, 60–68.

DiMarzio, E., and Gibbs, J. (1964). On the second-order transition of a rubber. *J. Res. Nat. Bur. Stand. A* 68, 611–617.

Doliwa, B., and Heuer, A. (2003). Energy barriers and activated dynamics in a supercooled Lennard-Jones liquid. *Phys. Rev. E* 67:031506. doi: 10.1103/PhysRevE.67.031506

Dyre, J. C. (2006). Colloquium: the glass transition and elastic models of glass-forming liquids. *Rev. Mod. Phys.* 78, 953–972. doi: 10.1103/RevModPhys.78.953

Edwards, T., and Sen, S. (2011). Structure and relaxation in germanium selenide glasses and supercooled liquids: a Raman spectroscopic study. *J. Phys. Chem. B* 115, 4307–4314. doi: 10.1021/jp202174x

Evans, J. S. (1999). Negative thermal expansion materials. *J. Chem. Soc. Dalton Trans.* 19, 3317–3326.

Fang, H., Dove, M. T., and Phillips, A. E. (2014). Common origin of negative thermal expansion and other exotic properties in ceramic and hybrid materials. *Phys. Rev. B* 89:214103. doi: 10.1103/PhysRevB.89.214103

Gibbs, J. H., and DiMarzio, E. A. (1958). Nature of the glass transition and the glassy state. *J. Chem. Phys.* 28, 373–383.

Glazer, A. (1972). The classification of tilted octahedra in perovskites. *Acta Crystallogr. Sec. B Struct. Crystallogr. Crystal Chem.* 28, 3384–3392.

Gueguen, Y., Rouxel, T., Gadaud, P., Bernard, C., Keryvin, V., and Sangleboeuf, J.-C. (2011). High-temperature elasticity and viscosity of Ge x Se 1-x glasses in the transition range. *Phys. Rev. B* 84:064201. doi: 10.1103/PhysRevB.84.064201

Gupta, P., and Cooper, A. (1990). Topologically disordered networks of rigid polytopes. *J. Non-Crystalline Solids* 123, 14–21.

Gupta, P. K. (1993). Rigidity, connectivity, and glass-forming ability. *J. Am. Ceram. Soc.* 76, 1088–1095.

Gupta, P. K., and Mauro, J. C. (2009). Composition dependence of glass transition temperature and fragility. I. A topological model incorporating temperature-dependent constraints. *J. Chem. Phys.* 130:094503. doi: 10.1063/1.3077168

He, H., and Thorpe, M. F. (1985). Elastic properties of glasses. *Phys. Rev. Lett.* 54:2107.

Heuer, A. (2008). Exploring the potential energy landscape of glass-forming systems: from inherent structures via metabasins to macroscopic transport. *J. Phys. Conden. Matt.* 20:373101. doi: 10.1088/0953-8984/20/37/373101

Jacobs, D., and Thorpe, M. (1996). Generic rigidity percolation in two dimensions. *Phys. Rev. E* 53:3682.

Jacobs, D. J., and Thorpe, M. F. (1995). Generic rigidity percolation: the pebble game. *Phys. Rev. Lett.* 75:4051.

Kamitakahara, W., Cappelletti, R., Boolchand, P., Halfpap, B., Gompf, F., Neumann, D., et al. (1991). Vibrational densities of states and network rigidity in chalcogenide glasses. *Phys. Rev. B* 44:94.

Kaseman, D. C., Hung, I., Gan, Z., Aitken, B., Currie, S., and Sen, S. (2014). Structural and topological control on physical properties of arsenic selenide glasses. *J. Phys. Chem. B* 118, 2284–2293. doi: 10.1021/jp412451h

Koštál, P., and Málek, J. (2010). Viscosity of selenium melt. *J. Non-Crystalline Solids* 356, 2803–2806. doi: 10.1016/j.jnoncrysol.2010.09.032

Madras, N., and Sokal, A. D. (1988). The pivot algorithm: a highly efficient Monte Carlo method for the self-avoiding walk. *J. Statist. Phys.* 50, 109–186.

Marple, M., Hung, I., Gan, Z., and Sen, S. (2017). Structural and topological evolution in Si x Se1–x glasses: results from 1D and 2D 29Si and 77Se NMR spectroscopy. *J. Phys. Chem. B* 121, 4283–4292. doi: 10.1021/acs.jpcb.7b01307

Marple, M. A., Yong, V., and Sen, S. (2019). Fragility and aging behavior of SixSe1-x glasses and liquids. *J. Chem. Phys.* 150:044506. doi: 10.1063/1.5080225

Musgraves, J. D., Wachtel, P., Novak, S., Wilkinson, J., and Richardson, K. (2011). Composition dependence of the viscosity and other physical properties in the arsenic selenide glass system. *J. Appl. Phys.* 110:063503. doi: 10.1063/1.3638122

Naumis, G. G. (2005). Energy landscape and rigidity. *Phys. Rev. E* 71:026114. doi: 10.1103/PhysRevE.71.026114

Naumis, G. G. (2006). Variation of the glass transition temperature with rigidity and chemical composition. *Phys. Rev. B* 73:172202. doi: 10.1103/PhysRevB.73.172202

Naumis, G. G. (2015). Low-frequency vibrational modes anomalies and rigidity: a key to understanding the glass and the electronic properties of flexible materials from a topological perspective. *Front. Mater.* 2:44. doi: 10.3389/fmats.2015.00044

Phillips, J. (1981). Topology of covalent non-crystalline solids II: Medium-range order in chalcogenide alloys and A? Si (Ge). *J. Non-Crystalline Solids* 43, 37–77.

Phillips, J. C. (1979). Topology of covalent non-crystalline solids I: short-range order in chalcogenide alloys. *J. Non-Crystalline Solids* 34, 153–181.

Salmon, P. S. (2007). Structure of liquids and glasses in the Ge–Se binary system. *J. Non-Crystalline Solids* 353, 2959–2974. doi: 10.1016/j.jnoncrysol.2007.05.152

Schram, R. D., Barkema, G. T., Bisseling, R. H., and Clisby, N. (2017). Exact enumeration of self-avoiding walks on BCC and FCC lattices. *J. Statist. Mech. Theory Exp.* 2017:083208. doi: 10.1088/1742-5468/aa819f

Sen, S., and Aitken, B. (2002). Atomic structure and chemical order in Ge-As selenide and sulfoselenide glasses: an x-ray absorption fine structure spectroscopic study. *Phys. Rev. B* 66:134204. doi: 10.1103/PhysRevB.66.134204

Sen, S., Xia, Y., Zhu, W., Lockhart, M., and Aitken, B. (2019). Nature of the floppy-to-rigid transition in chalcogenide glass-forming liquids. *J. Chem. Phys.* 150:144509. doi: 10.1063/1.5092841

Sidebottom, D. (2019). Connecting glass-forming fragility to network topology. *Front. Mater.* 6:144. doi: 10.3389/fmats.2019.00144

Sidebottom, D. L. (2015). Fragility of network-forming glasses: a universal dependence on the topological connectivity. *Phys. Rev. E* 92:062804. doi: 10.1103/PhysRevE.92.062804

Sreeram, A., Swiler, D., and Varshneya, A. (1991). Gibbs-DiMarzio equation to describe the glass transition temperature trends in multicomponent chalcogenide glasses. *J. Non-Crystalline Solids* 127, 287–297.

Stillinger, F. H. (1995). A topographic view of supercooled liquids and glass formation. *Science* 267, 1935–1939.

Svoboda, R., and Málek, J. (2015). Kinetic fragility of Se-based binary chalcogenide glasses. *J. Non-Crystalline Solids* 419, 39–44. doi: 10.1016/j.jnoncrysol.2015.03.041

Tanaka, K. (1989). Structural phase transitions in chalcogenide glasses. *Phys. Rev. B* 39:1270.

Thorpe, M. F. (1983). Continuous deformations in random networks. *J. Non-Crystalline Solids* 57, 355–370.

Toledo-Marín, J. Q., and Naumis, G. G. (2017). Short time dynamics determine glass forming ability in a glass transition two-level model: a stochastic approach using Kramers' escape formula. *J. Chem. Phys.* 146:094506. doi: 10.1063/1.4977517

Wang, T., Gulbiten, O., Wang, R., Yang, Z., Smith, A., Luther-Davies, B., et al. (2014). Relative contribution of stoichiometry and mean coordination to the fragility of Ge–As–Se glass forming liquids. *J. Phys. Chem. B* 118, 1436–1442. doi: 10.1021/jp412226w

Wang, Y., Boolchand, P., and Micoulaut, M. (2000). Glass structure, rigidity transitions and the intermediate phase in the Ge–As–Se ternary. *EPL* 52:633. doi: 10.1209/epl/i2000-00485-9

Wei, S., Coleman, G. J., Lucas, P., and Angell, C. A. (2017). Glass transitions, semiconductor-metal transitions, and fragilities in Ge-V-Te (V= As, Sb) liquid alloys: the difference one element can make (vol 7, 034035, 2017). *Phys. Rev. Appl.* 8:049901. doi: 10.1103/PhysRevApplied.8.049901

Yang, G., Bureau, B., Rouxel, T., Gueguen, Y., Gulbiten, O., Roiland, C., et al. (2010). Correlation between structure and physical properties of chalcogenide glasses in the As x Se 1-x system. *Phys. Rev. B* 82:195206. doi: 10.1103/PhysRevB.82.195206

Yang, G., Gueguen, Y., Sangleboeuf, J.-C., Rouxel, T., Boussard-Plédel, C., Troles, J., et al. (2013). Physical properties of the GexSe1-x glasses in the 0<x<0.42 range in correlation with their structure. *J. Non-Crystalline Solids* 377, 54–59. doi: 10.1016/j.jnoncrysol.2013.01.049

Zeidler, A., Salmon, P. S., Whittaker, D. A., Pizzey, K. J., and Hannon, A. C. (2017). Topological ordering and viscosity in the glass-forming Ge–Se system: The search for a structural or dynamical signature of the intermediate phase. *Front. Mater.* 4:32. doi: 10.3389/fmats.2017.00032

Zhao, H., Koh, Y., Pyda, M., Sen, S., and Simon, S. (2013). The kinetics of the glass transition and physical aging in germanium selenide glasses. *J. Non-Crystalline Solids* 368, 63–70. doi: 10.1016/j.jnoncrysol.2013.02.025

Zhu, W., Lockhart, M. J., Aitken, B. G., and Sen, S. (2018). Rheology of the λ transition in liquid sulfur: insights from arsenic sulfide liquids. *J. Chem. Phys.* 148:244506. doi: 10.1063/1.5037719

Conflict of Interest Statement: The authors declare that the research was conducted in the absence of any commercial or financial relationships that could be construed as a potential conflict of interest.

frontiers in Materials

ORIGINAL RESEARCH
published: 25 October 2019
doi: 10.3389/fmats.2019.00264

Topological Constraint Theory Analysis of Rigidity Transition in Highly Coordinate Amorphous Hydrogenated Boron Carbide

*Bradley J. Nordell[1], Thuong D. Nguyen[1], Anthony N. Caruso[1], William A. Lanford[2], Patrick Henry[3], Han Li[3], Liza L. Ross[3], Sean W. King[3] and Michelle M. Paquette[1]**

[1] Department of Physics and Astronomy, University of Missouri-Kansas City, Kansas City, MO, United States, [2] Department of Physics, University at Albany, Albany, NY, United States, [3] Logic Technology Development, Intel Corporation, Hillsboro, OR, United States

Topological constraint theory (TCT) has revealed itself to be a powerful tool in interpreting the behaviors of amorphous solids. The theory predicts a transition between a "rigid" overconstrained network and a "floppy" underconstrained network as a function of connectivity or average coordination number, $\langle r \rangle$. The predicted results have been shown experimentally for various glassy materials, the majority of these being based on 4-fold-coordinate networks such as chalcogenide and oxide glasses. Here, we demonstrate the broader applicability of topological constraint theory to uniquely coordinated amorphous hydrogenated boron carbide (a-BC:H), based on 6-fold-coordinate boron atoms arranged into partially hydrogenated interconnected 12-vertex icosahedra. We have produced a substantial set of plasma-enhanced chemical vapor deposited a-BC:H films with a large range of densities and network coordination, and demonstrate a clear threshold in Young's modulus as a function of $\langle r \rangle$, ascribed to a rigidity transition. We investigate constraint counting strategies in this material and show that by treating icosahedra as "superatoms," a rigidity transition is observed within the range of the theoretically predicted $\langle r \rangle_c$ value of 2.4 for covalent solids with bond-stretching and bond-bending forces. This experimental data set for a-BC:H is unique in that it represents a uniform change in connectivity with $\langle r \rangle$ and demonstrates a distinct rigidity transition with data points both above and below the transition threshold. Finally, we discuss how TCT can be applied to explain and optimize mechanical and dielectric properties in a-BC:H and related materials in the context of microelectronics applications.

Keywords: boron carbide, amorphous hydrogenated boron carbide, amorphous solids, topological constraint theory, rigidity theory

OPEN ACCESS

Edited by:
Matthieu Micoulaut, Sorbonne Universités, France

Reviewed by:
Normand Mousseau, Université de Montréal, Canada
Roger Jay Loucks, Alfred University, United States

****Correspondence:***
Michelle M. Paquette
paquettem@umkc.edu

Specialty section:
This article was submitted to Glass Science, a section of the journal Frontiers in Materials

Received: *20 June 2019*
Accepted: *10 October 2019*
Published: *25 October 2019*

Citation:
Nordell BJ, Nguyen TD, Caruso AN, Lanford WA, Henry P, Li H, Ross LL, King SW and Paquette MM (2019) Topological Constraint Theory Analysis of Rigidity Transition in Highly Coordinate Amorphous Hydrogenated Boron Carbide. Front. Mater. 6:264. doi: 10.3389/fmats.2019.00264

INTRODUCTION

Understanding the fundamental science of amorphous solids remains an essential problem in condensed matter physics (Billinge and Levin, 2007; Berthier and Biroli, 2010; Huang et al., 2013; Mauro, 2018). This problem has percolated to the forefront with the increasing demand for materials that are tunable (Baldus and Jansen, 1997; Medvedeva et al., 2017; Paquette et al., 2017; Mauro, 2018), manufacturable using gentle processing, and resilient to extreme conditions

(Deb et al., 2001; Chen et al., 2003; Wilding et al., 2006; Lin et al., 2011). With expensive *ab initio* solutions still generally out of reach, one theory that has shown success in explaining and predicting behavior in covalently bonded random networks is topological constraint theory (TCT) or rigidity theory (Thorpe et al., 2002; Mauro, 2011; Micoulaut, 2016). As an extension to Maxwell's work on the rigidity of structural trusses (Maxwell, 1864), TCT was advanced by Phillips and Thorpe as a model for understanding the mechanical properties of amorphous glasses as a function of average atomic constraints (Phillips, 1979; Thorpe, 1983; Phillips and Thorpe, 1985; Thorpe et al., 2002). They showed that the rigidity of an amorphous network can be evaluated by comparing atomic constraints to atomic degrees of freedom, with constraints arising from bond-stretching and bond-bending forces determined by the average coordination of the network, $\langle r \rangle$, and degrees of freedom equivalent to the dimensionality of the network, i.e., three in most cases. The TCT model predicts a rigidity transition at a critical average coordination value, $\langle r \rangle_c$, when the number of atomic degrees of freedom equals the number of atomic constraints −2.4 in 3D covalent networks—demarcating a threshold between an underconstrained or "floppy" network and an overconstrained or "rigid" network, with properties scaling above the rigidity threshold as a function of network coordination (He and Thorpe, 1985).

Rigidity theory has been applied most extensively to chalcogenide glasses, such as the Ge_xSe_{1-x} or $Ge_xAs_ySe_{1-x-y}$ systems (Boolchand et al., 2001). These systems are uniquely suitable for studying rigidity theory due to their covalent bonding and the "mix-and-match" coordination numbers of the atomic constituents (Se = 2, As = 3, Ge = 4), allowing for a range of network coordination to be achieved by varying stoichiometry. The theory has been supported computationally via the calculation of elastic constants and zero-frequency modes, which has demonstrated clear thresholds at $\langle r \rangle \approx 2.4$ (He and Thorpe, 1985; Franzblau and Tersoff, 1992; Plucinski and Zwanziger, 2015). The existence of a rigidity transition has been supported experimentally by probing vibrational and/or structural features in stoichiometrically varying glassy systems via Mössbauer spectroscopy (Bresser et al., 1986; Boolchand et al., 1995), Raman spectroscopy (Feng et al., 1997), and neutron scattering (Kamitakahara et al., 1991), with evidence of threshold behavior. A variety of thermal measurements probing glassy behavior have also corroborated such a threshold (Tatsumisago et al., 1990; Senapati and Varshneya, 1995). In terms of more direct experimental evidence, elastic constants/moduli have been measured, however with a vast majority of studies showing a lack of compelling support for the anticipated rigidity transition. In some cases, data sets feature no or only a small number of samples above or below the predicted threshold; in other cases, the data feature materials from different families, obscuring conclusions; and in yet other cases, the predicted effects are either not observed or are very subtle, requiring "guides to the eye" to highlight the desired interpretation (Tanaka, 1989; Yun et al., 1989; Kamitakahara et al., 1991; Sreeram et al., 1991; Srinivasan et al., 1992; Guin et al., 2009; Das et al., 2012). Some data showcase deviations from the theory which may apply to real material systems, such as a shift in $\langle r \rangle_c$ (Tanaka, 1986; Duquesne and Bellessa, 1989) or the presence of multiple transitions (Wang et al., 2013), the latter being ascribed to the existence of an intermediate phase (Boolchand et al., 2001).

Rigidity threshold phenomena have also been investigated in other classes of materials wherein the incorporation of terminal hydrogen atoms or other groups is used to alter network connectivity, including a-Si:H (Kuschnereit et al., 1995), a-C:H (Boolchand et al., 1996), a-C:F (Ghossoub et al., 2010), a-SiC:H (King et al., 2013), a-SiCN:H (Gerstenberg and Taube, 1989), and a-SiOC:H (Ross and Gleason, 2005; Trujillo et al., 2010), with a few of these studies (Ross and Gleason, 2005; Trujillo et al., 2010; King et al., 2013) showing a convincing transition point, including via experimental modulus data. Finally, rigidity thresholds have been demonstrated in more complex materials such as proteins (Rader et al., 2002), zeolites (Sartbaeva et al., 2006), and cements (Bauchy et al., 2015), albeit only computationally. Overall, while the literature taken together provides plenty of evidence for rigidity threshold phenomena related to network coordination, there is only a small amount of compelling direct experimental data—particularly elastic data—corroborating the predicted result, which has been limited to a relatively small number of materials classes.

Here, we apply rigidity theory to a unique and unusually coordinated material, boron carbide. This material has garnered interest for a variety of applications, including nuclear reactor coatings (Greuner et al., 2004; Buzhinskij et al., 2009), neutron detection (Robertson et al., 2002; Caruso, 2010; Gervino et al., 2013), low-*k* dielectrics and related layers for integrated circuits (Han et al., 2002; Nordell et al., 2016b, 2017), and various specialized coatings (Keski-Kuha et al., 1998; Chen et al., 2006; Hu and Kong, 2014; Azizov et al., 2015; Störmer et al., 2016). The particular amorphous hydrogenated boron carbide (a-BC:H) variant described here was produced in the form of thin films by plasma-enhanced chemical vapor deposition (PECVD) from a single-source molecular *ortho*-carborane (*o*-$C_2B_{10}H_{12}$) precursor to form a disordered polymeric carborane-based network. The material consists of nominally 6-fold-coordinate boron (and carbon!) atoms arranged into 12-vertex icosahedral $C_2B_{10}H_x$ subunits. These icosahedral subunits are then—we believe (Paquette et al., 2011)—cross-linked either directly to each other (**Figure 1A**) or via hydrocarbon linkers (**Figure 1B**), where the total amount of 1-fold-coordinate atomic hydrogen contained within the material correlates with decreased overall network coordination through the termination of icosahedral vertices and decreased cross-linking. By varying PECVD conditions, we have produced a substantial set of a-BC:H films with a vast range of densities, hydrogen concentrations, and effective network coordination (**Figure 2A**; Nordell et al., 2015, 2016a,b). We have observed a clear threshold in Young's modulus [and other properties (Nordell et al., 2015, 2016a,b)] as a function of density/hydrogen concentration (**Figure 2B**), which we attribute to a rigidity transition. In the present study, we describe and compare a number of constraint counting strategies and show how

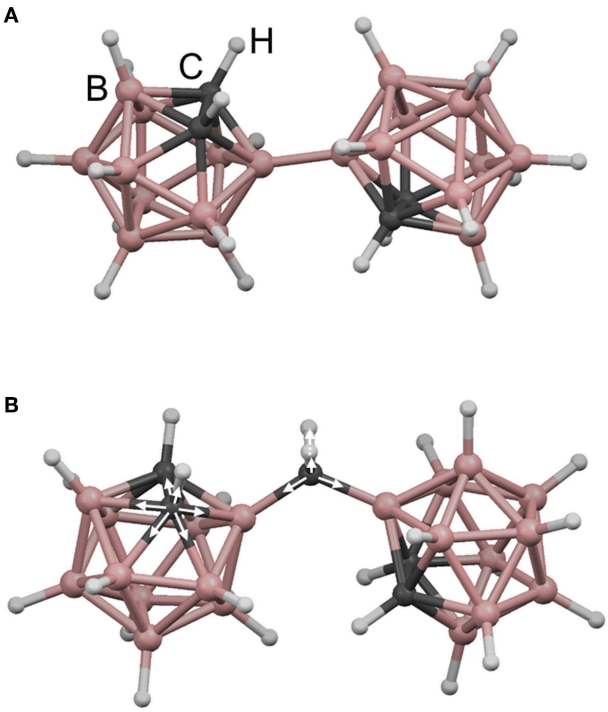

FIGURE 1 | Illustration of possible cross-linking modes in amorphous hydrogenated boron carbide (a-BC:H): **(A)** directly between icosahedra and **(B)** via intericosahedral carbon. In **(B)** are shown both 6-fold-coordinate intraicosahedral carbon and 4-fold-coordinate extraicosahedral carbon environments.

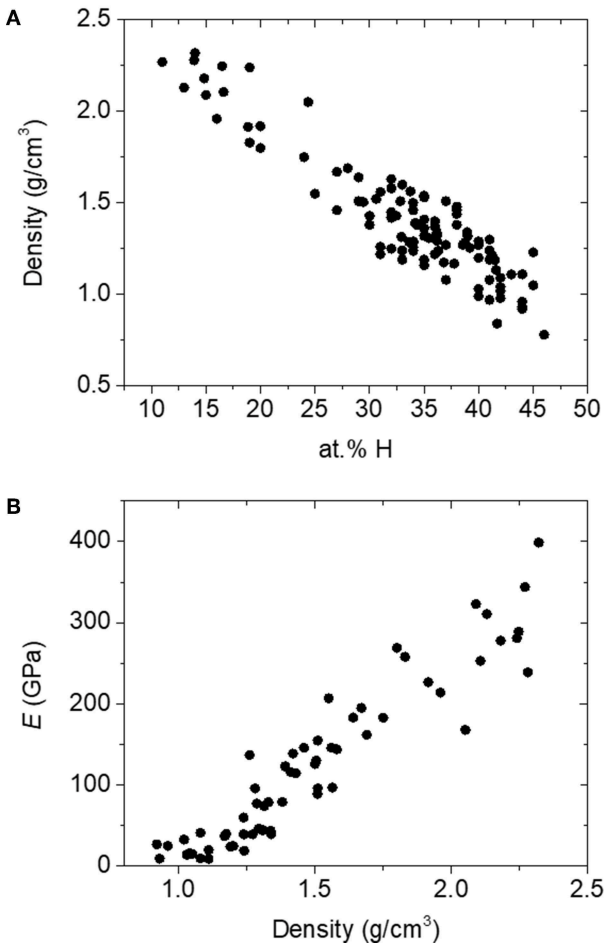

FIGURE 2 | (A) Range of density and atomic concentration hydrogen in amorphous hydrogenated boron carbide films. **(B)** Young's modulus (*E*) as a function of density in a-BC:H films.

a-BC:H adheres to traditional TCT predictions if we apply a "superatom" approach and treat individual icosahedra as independently constrained units. Further, we discuss how TCT can be used to predict and optimize material properties of technological relevance. Importantly, the data span the "floppy," "transition," and "rigid" regimes, and—assuming no underlying phase transition exists—represent a direct change in network coordination and connectivity not obscured by additional chemical or structural ordering contributions. This result is an essential contribution in supporting the generality and versatility of TCT for predicting and understanding the properties of amorphous solids.

RESULTS AND DISCUSSION

Topological constraint theory allows us to determine the number of zero-frequency modes or floppy modes, f, within a network—which can be related to its rigidity and glass properties—based on the difference between its atomic degrees of freedom, n_d, and atomic constraints, n_c. The constraint counting rules developed by Phillips and Thorpe can be applied with a simple knowledge of network coordination. Every r-coordinated atom accounts for $r/2$ bond-stretching constraints (since two atoms share each bond) and $2r - 3$ bending constraints (since a 2-fold-coordinate atom involves one angle, with each additional bond introducing two new angles). If we take the average coordination number, $\langle r \rangle$, the average number of atomic constraints is then given as $n_c = \langle r \rangle/2 + (2\langle r \rangle - 3)$. For a three dimensional network, the number of floppy modes goes to zero when $n_c = n_d = 3$ at a critical coordination number, $\langle r \rangle_c$, of 2.4, which represents the rigidity transition point and optimal glass-forming region.

In extending these constraint counting principles to amorphous hydrogenated boron carbide, we must first revisit the nature of the bonding in this material. The present study is based on multiple series' of a-BC:H films (Nordell et al., 2015, 2016a,b), including some fabricated as part of this work, grown by plasma-enhanced chemical vapor deposition from the single molecular precursor, *ortho*-carborane (o-$C_2B_{10}H_{12}$). We can differentiate the resulting amorphous solid from the more well-known and heavily studied crystalline B_xC variant, which is known to be comprised of B_{12} or $B_{11}C$ icosahedra and C–C–C or C–B–C chains within a densely packed rhombohedral lattice (Domnich et al., 2011). In contrast, evidence from previous work suggests that the PECVD carborane a-BC:H product, while still based on icosahedral units, forms a very

different disordered polymeric network comprised of *ortho*-carborane $B_{10}C_2H_x$ units, cross-linked to varying degrees, either directly to each other or via extraicosahedral hydrocarbon linkers (e.g., B–CH_2-B; **Figure 1**). Solid-state NMR and FTIR characterization (Paquette et al., 2011; Nordell et al., 2017) is consistent with the presence of hydrogenated *ortho*-carborane and sp^3 hydrocarbon functionalities within the network. We assume that all carborane vertices that are not cross-linked are terminated by hydrogen atoms. What our previous characterization does not show evidence for are other types of boranes (e.g., partial cages), extraicosahedral boron (e.g., C–B–C chains), or B–H–B bonding. It is possible that these moieties could still be present and simply not observed due to the expected weak signal, but if so they would exist in minimal quantities.

On the basis of this information, we assume that all of the boron atoms are bonded within an icosahedral environment, and thus can be considered 6-fold coordinate. It is possible that some boron could exist in partial cages, C–B–C chains, or a form of boron oxide (Li and Qiu, 2007), but these have not been observed spectroscopically, and therefore if such compositions exist, they would most likely be present in a very small amount and would not contribute significantly to the mean coordination of the solid. The carbon within the a-BC:H network, on the other hand, exists as both intraicosahedral carbon and extraicosahedral sp^3 hydrocarbon and can be considered to be in a non-traditional 6-fold-coordinate environment in the former case and a traditional 4-fold-coordinate environment in the latter (**Figure 1B**). Although it is possible that some sp (2-fold-coordinate) or sp^2 (3-fold-coordinate) hydrocarbon exists, this has not been observed by NMR and FTIR and would again be present in minimal quantities if at all. Finally, hydrogen atoms exhibit 1-fold-coordinate bonding, either terminating carborane vertices or satisfying hydrocarbon valencies. Hydrogen is known to exhibit rare bridging B–H–B bonding in amorphous boron-based solids (Anan'ev et al., 2002), but since this is not observed spectroscopically, we assume its contribution is absent or negligible. Finally, we would be remiss to not mention oxygen, which is inevitably present in these a-BC:H films in concentrations ranging from ∼1–10% (Driver et al., 2012; Nordell et al., 2015). This element is found to exist in the form of OH groups, CO groups, and/or boron-oxide-based species, and is generally considered 2-fold coordinate. We have found that including oxygen in our constraint counting has a negligible effect on the result, and therefore because it is considered a contaminant we do not include it here.

Armed with knowledge of the atomic structure and coordination environments, we can calculate the mean network coordination for each film based on the concentrations of the atomic species: [B], [C], and [H]. Atomic concentrations were measured via combined Rutherford backscattering spectroscopy (RBS) and nuclear reaction analysis (NRA) methods (Nordell et al., 2015, 2016a,b). In our accounting, we assume that all boron is present within carborane units and that all carborane units maintain $B_{10}C_2$ stoichiometry. Therefore, for each 10 boron atoms, 2 icosahedral C atoms ($[C_{icosahedral}]$) must be accounted for, with the remaining C atoms assumed to exist as sp^3 hydrocarbon species ($[C_{sp3}]$). The average coordination of the network, $\langle r \rangle$, is thus defined as:

$$\langle r \rangle = \frac{r_B[B] + r_{C(icosahedral)}[C_{icosahedral}] + r_{C(sp3)}[C_{sp3}] + r_H[H]}{[B] + [C_{icosahedral}] + [C_{sp3}] + [H]} = \frac{6[B] + 6[C_{icosahedral}] + 4[C_{sp3}] + 1[H]}{[B] + [C_{icosahedral}] + [C_{sp3}] + [H]} \quad (1)$$

We distinguish this first constraint counting strategy as the "atomic model," because it considers the coordination environment of each individual atom. **Figure 3** displays plots of Young's modulus (E), measured via nanoindentation (Nordell et al., 2015, 2016a,b), vs. coordination number ($\langle r \rangle$) (a) as well as the associated log–log plot (b). The data appear to show three distinct regions beginning at high Young's modulus: a first region with E decreasing steadily with decreasing $\langle r \rangle$ until $E \approx 130$ GPa and $\langle r \rangle \approx 4.3$ (light blue region), a steep fall off in E between $\langle r \rangle \approx 4.3$ and 4.1 centered at 4.2 (medium blue region), and a relative plateau below this with $E \approx 20$ GPa (darker blue region).

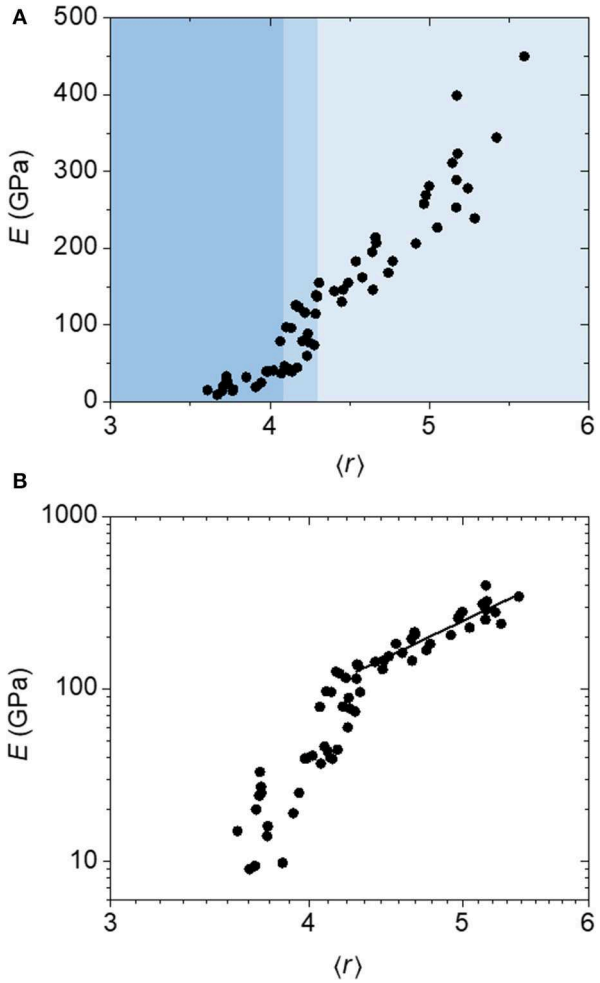

FIGURE 3 | (A) Linear and **(B)** log plots of Young's modulus (E) as a function of average coordination number ($\langle r \rangle$) calculated using an atomic constraint counting method for a-BC:H films. The data above the transition region is fit to a power-law function to yield an exponent of 4.4.

To assess the merit of the constraint counting model, we compare the results with two predictions from TCT: (1) the existence of a critical threshold, and (2) the observation of a power law behavior in Young's modulus as a function of $\langle r \rangle$ above the threshold.

For a typical covalent 3D network, the predicted critical coordination is 2.4. However, for a network containing 1-fold-coordinate (OFC) atoms, a correction must be introduced to account for these as they do not impose the same constraints (Boolchand and Thorpe, 1994). The predicted threshold can thus be calculated based on the formula established by Boolchand and Thorpe, where the threshold coordination is effectively adjusted for the fraction of 1-fold-coordinate (hydrogen) atoms as:

$$\langle r \rangle_{c(OFC)} = 2.4 - 0.4\left(\frac{[\mathrm{H}]}{[\mathrm{B}]+[\mathrm{C}]+[\mathrm{H}]}\right) \quad (2)$$

For the a-BC:H samples, the predicted $\langle r \rangle_{c(OFC)}$ ranges between 2.1 and 2.2 as a function of the actual H concentration of each sample. The experimental data does show a transition, but the center of this transition at $\langle r \rangle = 4.2$ is not consistent with the value of 2.4 predicted by TCT theory. Interestingly, it is closer to the value predicted based on the bond percolation (BP) threshold, p_c, for a simple 6-fold-coordinate cubic 3D lattice (vs. that for a 4-fold-coordinate tetrahedral lattice). Assuming a p_c value of ~0.25 (Vyssotsky et al., 1961; Phillips and Thorpe, 1985; Galam and Mauger, 1996), $\langle r \rangle_{c(BP)}$ is obtained as $\langle r \rangle_{c(BP)} = z - z(p_c) = 4.5$, with $z = 6$. Although Vyssotsky et al. (1961) do report that the lattice type does not have a significant effect relative to lattice dimensionality and coordination number, it is unclear whether a-BC:H can be appropriately modeled by this theory, not only due to it not forming a cubic lattice but also due to the nature of its bonding (*vide infra*).

As for the second TCT prediction, He and Thorpe demonstrated that there is a power-law type behavior in the elasticity of network glasses (He and Thorpe, 1985), where the elastic constants (C) exhibit a power law with exponent ν as a function of mean coordination above $\langle r \rangle_c$ as $C \propto (\langle r \rangle - \langle r \rangle_c)^{\nu}$. Using a modified diamond lattice, they computed this exponent to be 1.5. Franzblau and Tersoff expanded on this work, showing that the exponent can range between 1.35 and 1.89 depending on the ratio of the bond-stretching and bond-bending force constants, α and β (Franzblau and Tersoff, 1992). In the a-BC:H data, the Young's modulus does exhibit a power law response above $\langle r \rangle_{c(experimental)}$; however, the calculated exponent is 4.4, which does not match the theoretical prediction. The mismatch between experiment and theory suggests that perhaps the constraint counting strategy can be improved.

In revisiting our constraint counting method, we first recognize that boron exhibits non-traditional bonding. From a valence bond perspective, boron is known to form 3 center−2 electron (3c−2e) bonds as opposed to the 2 center−2 electron (2c−2e) bonds most commonly observed. Thus, within an icosahedron, the electron density is located, not between sets of two boron atoms, but at the center of groups of three boron atoms. At the vertices of the icosahedra, we find more traditional outward-pointing 2c−2e sigma bonds (Emin, 1987). From a molecular orbital (MO) perspective, an icosahedron contains 13 internally bonding molecular orbitals and 12 externally bonding MOs. Within the internally bonding MOs, the electron density is delocalized across the surface of the icosahedron, which is considered to be aromatic (King, 2001). For an icosahedron composed of 12 boron atoms, each atom contributes three bonding electrons, for a total of 36. Twelve of these are reserved for external bonding at each vertex, which leaves 24 to fill the 13 internally bonding MOs, coming up 2 short. This explains why the C_2B_{10} icosahedron is particularly stable (relative to the unstable B_{12} icosahedron) as the carbon atoms contribute these two additional electrons.

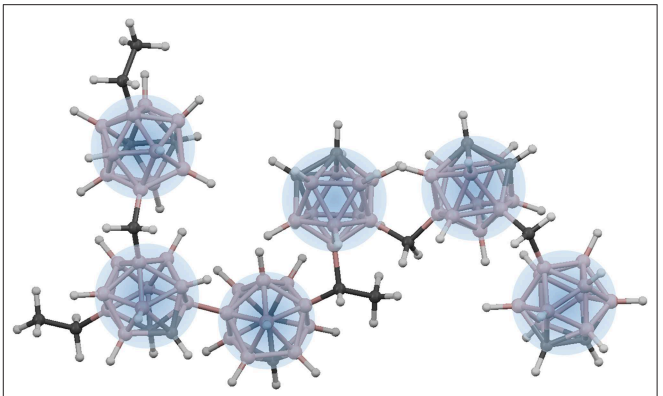

FIGURE 4 | "Superatom"-based network in polymeric a-BC:H (with minimal cross-linking shown for simplicity). Each icosahedron is treated as a constrained superatom with a total possible coordination of 12.

Thus, from a bonding perspective, it may not be appropriate to treat the constraint counting within icosahedra based on a "ball and stick" bonding model when the electron density is not located between pairs of atoms but rather delocalized across the entire cluster. A similar breakdown in constraint counting is described by Robertson in relation to amorphous carbon (Robertson, 1992). However, *between* icosahedra, the connectivity is based on the more traditional sigmoidal bonding. Thus, given the overconstrained and strongly bound nature of the individual icosahedra, it is attractive to treat these as rigid "superatom" units (Castleman and Khanna, 2009), and rather than consider the degree of connectivity between individual atoms, instead consider the degree of connectivity between icosahedra (**Figure 4**). In this modified "superatom" constraint counting strategy, we therefore count individual icosahedra as independently constrained units with a hypothetical coordination number of 12, and then count the remaining extraicosahedral carbon atoms (recall we assume that all boron is contained within icosahedra, and that for each 10 icosahedral B atoms, there must be two associated intraicosahedral C atoms) as 4-fold coordinate, and all H atoms as 1-fold coordinate (Equation 3).

$$\begin{aligned}\langle r \rangle &= \frac{r_{\mathrm{icosahedron}}[\mathrm{B_{10}C_2}] + r_{\mathrm{C(sp3)}}[\mathrm{C_{sp3}}] + r_{\mathrm{H}}[\mathrm{H}]}{[\mathrm{B_{10}C_2}] + [\mathrm{C_{sp3}}] + [\mathrm{H}]} \\ &= \frac{12\,[\mathrm{B_{10}C_2}] + 4\,[\mathrm{C_{sp3}}] + 1[\mathrm{H}]}{[\mathrm{B_{10}C_2}] + [\mathrm{C_{sp3}}] + [\mathrm{H}]}\end{aligned} \quad (3)$$

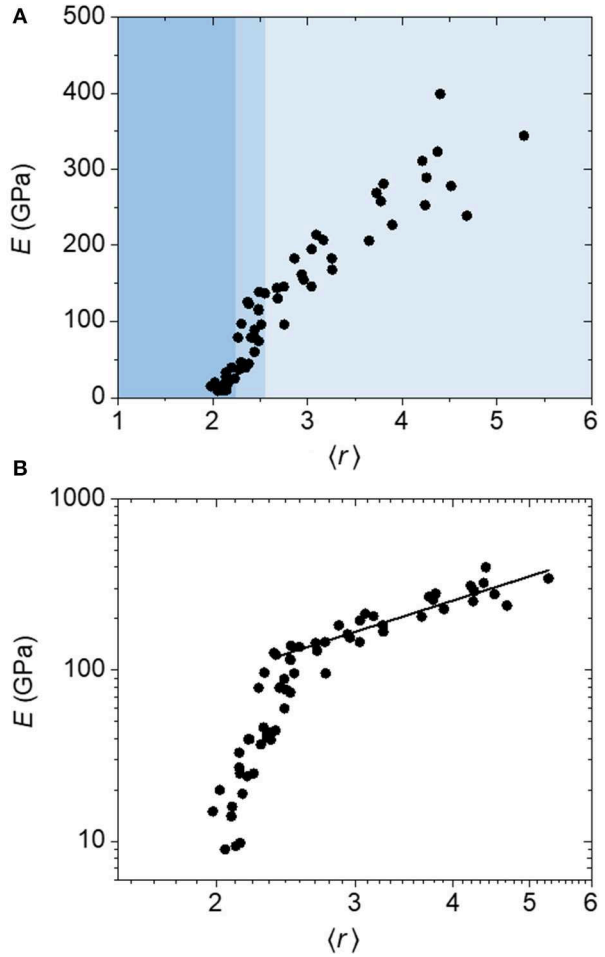

FIGURE 5 | (A) Linear and **(B)** log plots of Young's modulus (*E*) as a function of average coordination number (⟨*r*⟩) calculated using a "superatom" constraint counting method for a-BC:H films. The data above the transition region is fit to a power-law function to yield an exponent of 1.5.

The results of this constraint counting scheme are given in **Figure 5**. Once again we observe a clear transition region for *E* (medium blue shading) separating high ⟨*r*⟩ (lighter blue shading) and low ⟨*r*⟩ regions (darker blue shading), but in this case it is spanning an ⟨*r*⟩ range of 2.2–2.6, centered at $\langle r \rangle = 2.4$ (**Figure 5A**). A log–log plot (**Figure 5B**) clearly shows a distinct linear relationship above this transition region, demonstrating a power law fit with an exponent of 1.5, exactly consistent with He and Thorpe's prediction. The distinction between the transition region and the low ⟨*r*⟩ region is less clear than in the atomic model, although there does still appear to be a rapid change in *E* with ⟨*r*⟩ (∼30–130 GPa) in the transition region distinct from a more gradual change in *E* with ⟨*r*⟩ below this (∼10–30 GPa). The central rigidity threshold value of 2.4 is now in line with that predicted by theory, although slightly higher than the value of 2.1–2.2 predicted for a-BC:H when applying the 1-fold-coordinate atom correction. (We note that in computing the critical coordination for the superatom network, we take the degrees of freedom for each icosahedron to be 3 as we are assuming spherical symmetry.) However, the initial onset of the steep rigidity increase is very close to the prediction.

The observation of an experimental transition point slightly higher than predicted by theory is quite common, and has been shown in several amorphous systems, albeit for different reasons. Most work on topological constraint theory has focused on chalcogenide glasses, and the demonstration of a rigidity transition via the measurement of elastic properties has yielded ambiguous results. A majority of studies do not show a clear transition in elastic constants or modulus at $\langle r \rangle = 2.4$, but many do show a transition at $\langle r \rangle \approx 2.7$ (or a cutoff at 2.7, which can neither confirm nor deny the existence of said transition). (Tanaka, 1986; Duquesne and Bellessa, 1989; Yun et al., 1989; Kamitakahara et al., 1991; Sreeram et al., 1991; Yang et al., 2010) Early explanations posited that this effect could be due to underlying Van der Waals (VDW) forces which are unaccounted for in the theory, that can shift and/or "wash out" the rigidity transition (Tanaka, 1986, 1989; Thorpe et al., 2002). It also became clear that these transition points corresponded to distinct changes in ordering (layers/clusters, and cross-linking thereof) of the material (Duquesne and Bellessa, 1989; Yun et al., 1989). For example, in the Ge–Se system, $\langle r \rangle = 2.4$ corresponds to a $GeSe_4$ stoichiometry, at which point Se chains are fully cross-linked by Ge atoms, whereas $\langle r \rangle = 2.67$ corresponds to a $GeSe_2$ stoichiometry, whereupon Ge–Ge bonds begin to form (Rouxel, 2007). These changes are still related to coordination number, though highlight distinct changes in network structure. The most current, yet still controversial (Micoulaut, 2016), interpretation of this phenomenon is that in systems where there is underlying ordering, the two transition thresholds represent the delineation of the so-called "intermediate phase" between floppy and stressed–rigid states, where the system is rigid yet optimally constrained (Boolchand et al., 2001; Sartbaeva et al., 2007). We note that although these two transitions are generally not observed in elastic modulus data, they are observed through other experimental probes such as differential scanning calorimetry and Raman spectroscopy (Boolchand et al., 2001). Of course, other effects beyond network coordination can influence elastic properties, including bond strength and packing density (Rouxel, 2007), and the changes in stoichiometry and medium-range order in chalcogenide glasses as a function of ⟨*r*⟩ therefore convolute the interpretation of network-coordination-based results for these systems to some extent. Tichý, for example, ascribes the transitions instead to chemical thresholds (Tichý and Tichá, 1994).

In terms of other material systems that demonstrate rigidity thresholds, in SiO_2 the rigidity transition is also shifted to 2.67 due to the broken bond-bending forces of the oxygen atoms (Zhang and Boolchand, 1994; Boolchand et al., 2001). The a-BC:H system studied here is perhaps most similar, however, to other partially hydrogenated networks such as a-SiC:H and a-SiOC:H, in which rigidity transitions have been observed at $\langle r \rangle \approx 2.4$ (Ross and Gleason, 2005; Trujillo et al., 2010; King et al., 2013). Consistently, these transition points are similarly ∼0.2–0.3 coordination units higher than theoretically predicted if one accounts for the 1-fold-coordinate

correction. This could potentially be due to oxygen-based bonding in the case of a-SiOC:H or VDW bonding in the case of a-SiC:H. In a-BC:H, VDW and other weak forces may likewise cause a slight shift in the experimentally observed transition threshold.

Another point of discussion concerns the region below the rigidity threshold. Although basic rigidity theory predicts that the elastic modulus goes to zero below $\langle r \rangle_c$, this is not the case in experiment due to the presence of dihedral angle and VDW forces that contribute an underlying elasticity (He and Thorpe, 1985). In other hydrogenated/fluorinated materials, the Young's modulus/hardness tends toward zero at $\langle r \rangle_c$ in the case of a-C:H/a-C:F (Ghossoub et al., 2010; King et al., 2013) or finite yet very low values below $\langle r \rangle_c$ in the case of a-SiC:H/a-SiOC:H (Ross and Gleason, 2005; Trujillo et al., 2010; King et al., 2013), yet in a-BC:H, it remains relatively high. This "superatom" system is unique in that, in addition to VDW and related forces, we must also consider the intrinsic rigidity of the icosahedra as well as the fact that boron-based covalent bonds are extremely strong. Further, in a-BC:H, the elastic modulus does not stabilize below $\langle r \rangle_c$ but instead continues to decrease, the most straightforward reason for which is due to the decrease in network density associated with further decreases in $\langle r \rangle$. This effect is not typically captured in simulations due to these being based on the removal of bonds rather than both atoms and bonds or the substitution of atom types. Finally, regarding the transition region, it is unclear whether the behavior of the data between $\langle r \rangle = 2.2$ and 2.6 represents some form of "intermediate phase" or is simply the experimental broadening of a sharp transition. As mentioned above, the elastic constants for simple non-ordering networks are predicted to gradually approach zero with decreasing $\langle r \rangle$ until $\langle r \rangle_c$ (He and Thorpe, 1985; Plucinski and Zwanziger, 2015). Based on experimental work for materials which are said to possess an intermediate phase, we might anticipate a plateau in this region; vibrational markers tend to plateau, for example (Boolchand et al., 2001). In a rare example reported by Wang et al. where two elastic thresholds are observed experimentally in a chalcogenide glass, the data also reveal a plateau between the two (Wang et al., 2009). However, in this study the change in elastic modulus essentially mirrors the change in density, which decreases over this same region, highlighting the convolution of the effect of packing density and coordination on modulus. In a-BC:H, on the other hand, at the transition point, rather than a plateau, we instead observe a steep fall off from ∼130 to ∼30 GPa over a narrow range of $\langle r \rangle$. This change is not associated with an abrupt change in density, which varies smoothly with coordination number. If we base our interpretation on the assertion that it is the structural variability or the ability of a network to self-organize that leads to the intermediate phase (Micoulaut and Phillips, 2007; Sartbaeva et al., 2007), then the smooth transition in network connectivity predicted in a-BC:H may suggest that what we are observing is indeed a sharp transition associated with a significant loss in rigidity at the threshold.

Importantly, not only does a-BC:H stand out in that it demonstrates a distinct rigidity transition with a large number of data points both above and below the threshold, but it may also represent a unique example system where there is, in fact, a smooth variation in network connectivity independent from changes in medium-range ordering or chemical stoichiometry. In this way, despite its perceived complexity, the superatom a-BC:H network may actually be quite similar to the most simple theoretical network models such as the modified diamond lattice studied by He and Thorpe. One question that might arise is whether our simplified structural model of a-BC:H is truly an accurate representation of this system. To probe this question, we attempted constraint counting with several different variations. In addition to the superatom constraint counting strategy described above, we applied a second strategy where we neglected extraicosahedral carbon entirely, and only considered the ratio of 12-fold-coordinate icosahedral superatoms to 1-fold-coordinate hydrogen atoms. Using a third strategy, we assumed all extraicosahedral carbon was present in the form of CH_2 groups, and treated CH_2 groups as constrained 2-fold-coordinate units. In all three cases, the results were nearly identical to those shown in **Figure 5**, with the same transition point and power-law exponents, and only very slight deviations in the scatter of the data. Thus, we can conclude that the core connectivity of the lattice is by and large dependent on the degree of cross-linking between icosahedra, primarily determined by the degree of hydrogenation, and that the detailed structure and connectivity of the extraicosahedral carbon, which we admittedly do not fully understand, does not play a significant role.

In addition to investigating the relationship between Young's modulus and average network coordination, we can also look at the Young's modulus–density relationship. Here too, we see a power-law relation above a clear transition point at a density of ∼1.3 g/cm^3 (**Figure 6**). Similarly to what we have shown for a subset of this data (Nordell et al., 2016b), a power law fit above this threshold gives an exponent of 2.0, which is consistent with

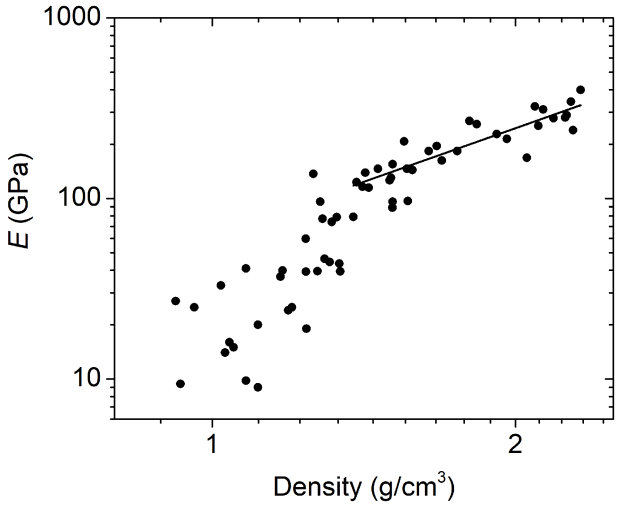

FIGURE 6 | Logarithmic plot of Young's modulus as a function of density for a-BC:H films yielding an $E \propto D^{2.0}$ relationship above 1.3 g/cm^3.

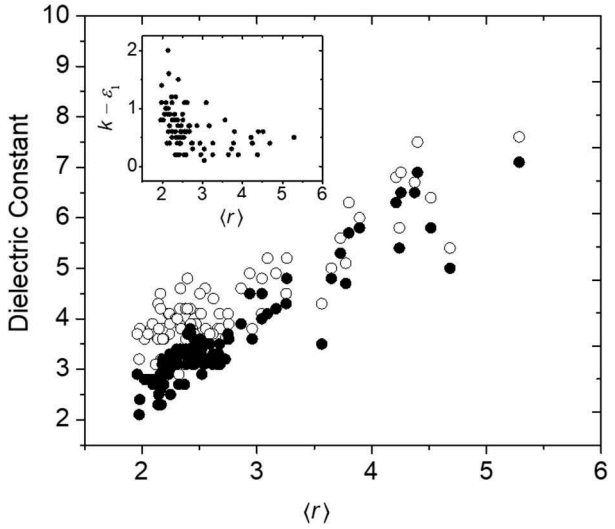

FIGURE 7 | High- (ε_1, 4.6 × 10^{14} Hz, •) and low- (k, 100 kHz, ○) frequency relative permittivity as a function of $\langle r \rangle$ for a-BC:H films. The inset displays the difference between k and ε_1 as a function of $\langle r \rangle$.

the quadratic scaling relationship expected for cellular solids, as well as with that observed for disordered nanoporous silica (Jain et al., 2001; Fan et al., 2007; Meza et al., 2014). At ∼1.3 g/cm^3, the modulus drops sharply, and below 1.2 g/cm^3, the data display significantly increased scatter.

Another property of a-BC:H that may be influenced by the rigidity regime of the a-BC:H network is its permittivity, a frequency-dependent quantity related to a material's polarizability. A material's polarization may be broken into three contributions: (1) the electronic polarization (movement of electrons) at high (optical) frequencies, (2) the distortion polarization (vibration of bonds) at moderate (infrared) frequencies, and (3) the orientation polarization (movement of permanent dipoles) at low (micro-/radio-wave) frequencies (Maex et al., 2003; Kohl, 2011). In **Figure 7** is shown the high-frequency (10^{14} Hz) relative permittivity, ε_1, which represents the electronic contribution only, as well as the low-frequency (10^5 Hz) or "total" permittivity, k (also commonly referred to as the dielectric constant), which represents the sum of the electronic, distortion, and orientation contributions, as a function of $\langle r \rangle$. While we observe a clear trend in ε_1 as a function of $\langle r \rangle$, which we attribute primarily to a decrease in network density (and therefore electronic density), this trend breaks down for k at low $\langle r \rangle$. This is highlighted by the k – ε_1 difference term (**Figure 7**, inset), which increases below $\langle r \rangle \approx 2.4$. We hypothesize that this is due to the expected increase in floppy modes below the rigidity transition which would contribute to distortion and orientation polarization effects (Palin, 1967). We note that we have previously found no relationship between k – ε_1 and oxygen concentration (Nordell et al., 2016b), and therefore the increased polarity of oxygen-based bonds does not appear to be the cause of this effect. For low-dielectric-constant or low-k materials, a key strategy for decreasing k involves decreasing material density, both by using lower-Z elements (containing fewer electrons) and lower volume density (i.e., higher porosity or free volume). A common challenge is the deterioration in mechanical properties associated with the latter approach (Grill et al., 2014; Michalak et al., 2015). The result described here suggests that not only does weak network connectivity decrease mechanical properties, but may also result in higher-than-anticipated k values. Thus, establishing low-density yet highly connected lattices will be essential to attaining both optimal mechanical *and* dielectric properties.

CONCLUSIONS

We have shown that amorphous hydrogenated boron carbide (a-BC:H) exhibits a transition in elastic properties as a function of average network coordination. By treating the lattice as a network of rigid icosahedral "superatoms," the rigidity transition falls at a critical coordination of $\langle r \rangle = 2.4$ (within a range of 2.2–2.6), essentially consistent with the Phillips–Thorpe topological constraint theory prediction with modifications for the contribution from 1-fold-coordinate atoms. Further, above the rigidity transition, the Young's modulus obeys a power law behavior as a function of $\langle r \rangle$ with an exponent of 1.5, again consistent with the original predictions by He and Thorpe and others. We have discussed how the rigidity theory framework can be used to optimize properties, such as Young's modulus and dielectric constant, for microelectronic applications. Additional analysis remains to better understand this system. In terms of constraint counting, using a molecular dynamics approach such as that described by Bauchy (2019) would be illuminating toward developing a more rigorous understanding of the constraints present in the network. Further, studying additional properties, such as glass transition temperature from differential scanning calorimetry and vibrational modes from Raman scattering, particularly in the region of $\langle r \rangle_c$, could provide valuable complementary insight into the nature of the transition. Overall, this is one of the largest and broadest sets, if not the largest/broadest, of elastic modulus data as a function of coordination number that we are aware of, and therefore represents a compelling result in directly supporting the existence of the theoretically predicted rigidity transition, in addition to supporting the generalizability of topological constraint theory to a range of materials.

DATA AVAILABILITY STATEMENT

The data sets generated for this study are available on request to the corresponding author.

AUTHOR CONTRIBUTIONS

BN and TN completed thin-film depositions and characterization. WL performed RBS/NRA measurements and analysis. PH, HL, and LR performed nanoindentation

measurements and analysis. BN, MP, and SK completed data analysis and interpretation. BN and MP prepared figures. SK and AC provided technical support, both for experiment and analysis. MP wrote the manuscript, with contributions and revisions from BN and SK. All authors have approved the submission of this work.

FUNDING

The authors are grateful for financial support by Intel (contract no. 2012-IN-2313), the Defense Threat Reduction Agency (grant no. HDTRA1-10-1-0092), and the National Science Foundation (award no. 1729227).

REFERENCES

Anan'ev, A. S., Kon'kov, O. I., Lebedev, V. M., Novokhatski, A. N., Terukov, E. I., and Trapeznikova, I. N. (2002). Fabrication and properties of amorphous hydrogenated boron carbide films. *Semiconductors* 36, 941–943. doi: 10.1134/1.1500477

Azizov, E., Barsuk, V., Begrambekov, L., Buzhinsky, O., Evsin, A., Gordeev, A., et al. (2015). Boron carbide (B_4C) coating. Deposition and testing. *J. Nucl. Mater.* 463, 792–795. doi: 10.1016/j.jnucmat.2015.01.015

Baldus, H.-P., and Jansen, M. (1997). Novel high-performance ceramics—amorphous inorganic networks from molecular precursors. *Angew. Chem. Int. Ed. Engl.* 36, 328–343. doi: 10.1002/anie.199703281

Bauchy, M. (2019). Deciphering the atomic genome of glasses by topological constraint theory and molecular dynamics : a review. *Comput. Mater. Sci.* 159, 95–102. doi: 10.1016/j.commatsci.2018.12.004

Bauchy, M., Qomi, M. J. A., Bichara, C., Ulm, F. J., and Pellenq, R. J. M. (2015). Rigidity transition in materials: hardness is driven by weak atomic constraints. *Phys. Rev. Lett.* 114, 1–5. doi: 10.1103/PhysRevLett.114.125502

Berthier, L., and Biroli, G. (2010). Theoretical perspective on the glass transition and amorphous materials. *Rev. Mod. Phys.* 83:587. doi: 10.1103/RevModPhys.83.587

Billinge, S. J. L., and Levin, I. (2007). The problem with determining atomic structure at the nanoscale. *Science* 316, 561–565. doi: 10.1126/science.1135080

Boolchand, P., Bresser, W., Zhang, M., Wu, Y., Wells, J., and Enzweiler, R. N. (1995). Lamb-Mössbauer factors as a local probe of floppy modes in network glasses. *J. Non. Cryst. Solids* 182, 143–154. doi: 10.1016/0022-3093(94)00540-0

Boolchand, P., Georgiev, D. G., and Goodman, B. (2001). Discovery of the intermediate phase in chalcogenide glasses. *J. Optoelectron. Adv. Mater.* 3, 703–720.

Boolchand, P., and Thorpe, M. F. (1994). Glass-forming tendency, percolation of rigidity, and onefold-coordinated atoms in covalent networks. *Phys. Rev. B* 50, 10366–10368. doi: 10.1103/PhysRevB.50.10366

Boolchand, P., Zhang, M., and Goodman, B. (1996). Influence of one-fold-coordinated atoms on mechanical properties of covalent networks. *Phys. Rev. B* 53, 11488–11494. doi: 10.1103/PhysRevB.53.11488

Bresser, W., Boolchand, P., and Suranyi, P. (1986). Rigidity percolation and molecular clustering in network glasses. *Phys. Rev. Lett.* 56, 2493–2496. doi: 10.1103/PhysRevLett.56.2493

Buzhinskij, O. I., Barsuk, V. A., and Otroshchenko, V. G. (2009). Renewable boron carbide coating in plasma shots of tokamak T11-M. *J. Nucl. Mater.* 390–391, 996–999. doi: 10.1016/j.jnucmat.2009.01.261

Caruso, A. N. (2010). The physics of solid-state neutron detector materials and geometries. *J. Phys. Condens. Matter* 22:443201. doi: 10.1088/0953-8984/22/44/443201

Castleman, A. W. Jr., and Khanna, S. N. (2009). Clusters, superatoms, and building blocks of new materials. *J. Phys. Chem. C.* 113, 2664–2675. doi: 10.1016/S1571-0785(07)12010-1

Chen, M., McCauley, J. W., and Hemker, K. J. (2003). Shock-induced localized amorphization in boron carbide. *Science* 299, 1563–1566. doi: 10.1126/science.1080819

Chen, Y., Chung, Y.-W., and Li, S.-Y. (2006). Boron carbide and boron carbonitride thin films as protective coatings in ultra-high density hard disk drives. *Surf. Coatings Technol.* 200, 4072–4077. doi: 10.1016/j.surfcoat.2005.02.164

Das, C., Kiran, M. S. R. N., Ramamurty, U., and Asokan, S. (2012). Manifestation of intermediate phase in mechanical properties: Nano-indentation studies on Ge-Te-Si bulk chalcogenide glasses. *Solid State Commun.* 152, 2181–2184. doi: 10.1016/j.ssc.2012.09.020

Deb, S. K., Wilding, M., Somayazulu, M., and Mcmillan, P. F. (2001). Pressure-induced amorphization and an amorphous-amorphous transition in densified porous silicon. *Nature* 414, 528–530. doi: 10.1038/35107036

Domnich, V., Reynaud, S., Haber, R. A., and Chhowalla, M. (2011). Boron carbide: structure, properties, and stability under stress. *J. Am. Ceram. Soc.* 94, 3605–3628. doi: 10.1111/j.1551-2916.2011.04865.x

Driver, M. S., Paquette, M. M., Karki, S., Nordell, B. J., and Caruso, A. N. (2012). The electronic and chemical structure of the a-$B_3CO_{0.5}$:H_y-to-metal interface from photoemission spectroscopy: implications for Schottky barrier heights. *J. Phys. Condens. Matter* 24:445001. doi: 10.1088/0953-8984/24/44/445001

Duquesne, J. Y., and Bellessa, G. (1989). Ultrasonic study of percolation rigidity in Se-Ge glasses. *Europhys. Lett.* 9, 453–458. doi: 10.1209/0295-5075/9/5/008

Emin, D. (1987). Icosahedral boron-rich solids. *Phys. Today* 40, 55–62. doi: 10.1063/1.881112

Fan, H., Hartshorn, C., Buchheit, T., Tallant, D., Assink, R., Simpson, R., et al. (2007). Modulus–density scaling behaviour and framework architecture of nanoporous self-assembled silicas. *Nat. Mater.* 6, 418–423. doi: 10.1038/nmat1913

Feng, X., Bresser, W., and Boolchand, P. (1997). Direct evidence for stiffness threshold in chalcogenide glasses. *Phys. Rev. Lett.* 78, 4422–4425. doi: 10.1103/PhysRevLett.78.4422

Franzblau, D. S., and Tersoff, J. (1992). Elastic properties of a network model of glasses. *Phys. Rev. Lett.* 68, 2172–2175. doi: 10.1103/PhysRevLett.68.2172

Galam, S., and Mauger, A. (1996). Universal formulas for percolation thresholds. *Phys. Rev. E* 53, 2177–2181. doi: 10.1103/PhysRevE.53.2177

Gerstenberg, K. W., and Taube, K. (1989). Measurement of the Young's modulus for structural characterization of amorphous Si:C:N:H-films. *Fresenius Z. Anal. Chem.* 333, 313–314. doi: 10.1007/BF00572312

Gervino, G., Balma, M., Devona, D., Lavagno, A., Palmisano, C., Zamprotta, L., et al. (2013). Preliminary results of a new boron coated neutron detector. *Nucl. Instrum. Methods Phys. Res. Sect. A* 718, 143–144. doi: 10.1016/j.nima.2012.08.092

Ghossoub, M. G., Lee, J. H., Baris, O. T., Cahill, D. G., and Sinha, S. (2010). Percolation of thermal conductivity in amorphous fluorocarbons. *Phys. Rev. B* 82, 195441. doi: 10.1103/PhysRevB.82.195441

Greuner, H., Balden, M., Boeswirth, B., Bolt, H., Gadow, R., Grigull, P., et al. (2004). Evaluation of vacuum plasma-sprayed boron carbide protection for the stainless steel first wall of WENDELSTEIN 7-X. *J. Nucl. Mater.* 329–333, 849–854. doi: 10.1016/j.jnucmat.2004.04.214

Grill, A., Gates, S. M., Ryan, T. E., Nguyen, S. V., and Priyadarshini, D. (2014). Progress in the development and understanding of advanced low k and ultralow k dielectrics for very large-scale integrated interconnects—state of the art. *Appl. Phys. Rev.* 1:011306. doi: 10.1063/1.4861876

Guin, J.-P., Rouxel, T., Sanglebœuf, J.-C., Melscoët, I., and Lucas, J. (2009). Hardness, toughness, and scratchability of germanium-selenium chalcogenide glasses. *J. Am. Ceram. Soc.* 85, 1545–1552. doi: 10.1111/j.1151-2916.2002.tb00310.x

Han, L. M., Yi, X., Xie, J. Z., Zhou, M. S., and Chooi, S. (2002). *Use of Boron Carbide as an Etch-Stop and Barrier Layer for Copper Dual Damascene Metallization.* U.S. Patent No 6,424,044 B1. Washington, DC: U.S. Patent and Trademark Office.

He, H., and Thorpe, M. (1985). Elastic properties of glasses. *Phys. Rev. Lett.* 54, 2107–2110. doi: 10.1103/PhysRevLett.54.2107

Hu, H., and Kong, J. (2014). Improved thermal performance of diamond-copper composites with boron carbide coating. *J. Mater. Eng. Perform.* 23, 651–657. doi: 10.1007/s11665-013-0780-z

Huang, P. Y., Kurasch, S., Alden, J. S., Shekhawat, A., Alemi, A., a, McEuen, P. L., et al. (2013). Imaging atomic rearrangements in two-dimensional silica glass: watching silica's dance. *Science* 342, 224–227. doi: 10.1126/science.1242248

Jain, A., Rogojevic, S., Gill, W. N., Plawsky, J. L., Matthew, I., Tomozawa, M., et al. (2001). Effects of processing history on the modulus of silica xerogel films. *J. Appl. Phys.* 90, 5832–5834. doi: 10.1063/1.1412266

Kamitakahara, W. A., Cappelletti, R. L., Boolchand, P., Halfpap, B., Gompf, F., Neumann, D. A., et al. (1991). Vibrational densities of states and network rigidity in chalcogenide glasses. *Phys. Rev. B* 44, 94–100. doi: 10.1103/PhysRevB.44.94

Keski-Kuha, R. A., Blumenstock, G. M., Fleetwood, C. M., and Schmitt, D.-R. (1998). Effects of space exposure on ion-beam-deposited silicon-carbide and boron-carbide coatings. *Appl. Opt.* 37, 8038–8042. doi: 10.1364/AO.37.008038

King, R. B. (2001). Three-dimensional aromaticity in polyhedral boranes and related molecules. *Chem. Rev.* 101, 1119–1152. doi: 10.1021/cr000442t

King, S. W., Bielefeld, J., Xu, G., Lanford, W. A., Matsuda, Y., Dauskardt, R. H., et al. (2013). Influence of network bond percolation on the thermal, mechanical, electrical and optical properties of high and low-k a-SiC:H thin films. *J. Non. Cryst. Solids* 379, 67–79. doi: 10.1016/j.jnoncrysol.2013.07.028

Kohl, P. A. (2011). Low–dielectric constant insulators for future integrated circuits and packages. *Annu. Rev. Chem. Biomol. Eng.* 2, 379–401. doi: 10.1146/annurev-chembioeng-061010-114137

Kuschnereit, R., Fath, H., Kolomenskii, A. A., Szabadi, M., and Hess, P. (1995). Mechanical and elastic properties of amorphous hydrogenated silicon films studied by broadband surface acoustic wave spectroscopy. *Appl. Phys. A* 61, 269–276. doi: 10.1007/BF01538192

Li, Y., and Qiu, T. (2007). Oxidation behaviour of boron carbide powder. *Mater. Sci. Eng. A* 444, 184–191. doi: 10.1016/j.msea.2006.08.068

Lin, Y., Zhang, L., Mao, H., Chow, P., Xiao, Y., Baldini, M., et al. (2011). Amorphous diamond: A high-pressure superhard carbon allotrope. *Phys. Rev. Lett.* 107:175504. doi: 10.1103/PhysRevLett.107.175504

Maex, K., Baklanov, M. R., Shamiryan, D., Lacopi, F., Brongersma, S. H., and Yanovitskaya, Z. S. (2003). Low dielectric constant materials for microelectronics. *J. Appl. Phys.* 93, 8793–8841. doi: 10.1063/1.1567460

Mauro, J. C. (2011). Topological constraint theory of glass. *Am. Ceram. Soc. Bull.* 90, 31–37.

Mauro, J. C. (2018). Decoding the glass genome. *Curr. Opin. Solid State Mater. Sci.* 22, 58–64. doi: 10.1016/j.cossms.2017.09.001

Maxwell, J. C. (1864). On the calculation of the equilibrium and stiffness of frames. *Philos. Mag.* 27, 294–299. doi: 10.1080/14786446408643668

Medvedeva, J. E., Buchholz, D. B., and Chang, R. P. H. (2017). Recent advances in understanding the structure and properties of amorphous oxide semiconductors. *Adv. Electron. Mater.* 3:1700082. doi: 10.1002/aelm.201700082

Meza, L. R., Das, S., and Greer, J. R. (2014). Strong, lightweight, and recoverable three-dimensional ceramic nanolattices. *Science* 345, 1322–1327. doi: 10.1126/science.1255908

Michalak, D. J., Blackwell, J. M., Torres, J. M., Sengupta, A., Kreno, L. E., Clarke, J. S., et al. (2015). Porosity scaling strategies for low-k films. *J. Mater. Res.* 30, 3363–3385. doi: 10.1557/jmr.2015.313

Micoulaut, M. (2016). Concepts and applications of rigidity in non-crystalline solids: a review on new developments and directions. *Adv. Phys. X* 6149, 1–29. doi: 10.1080/23746149.2016.1161498

Micoulaut, M., and Phillips, J. C. (2007). Onset of rigidity in glasses: from random to self-organized networks. *J. Non. Cryst. Solids* 353, 1732–1740. doi: 10.1016/j.jnoncrysol.2007.01.078

Nordell, B. J., Karki, S., Nguyen, T. D., Rulis, P., Caruso, A. N., Purohit, S. S., et al. (2015). The Influence of hydrogen on the chemical, mechanical, optical/electronic, and electrical transport properties of amorphous hydrogenated boron carbide. *J. Appl. Phys.* 118:035703. doi: 10.1063/1.4927037

Nordell, B. J., Keck, C. L., Nguyen, T. D., Caruso, A. N., Purohit, S. S., Lanford, W. A., et al. (2016a). Tuning the properties of a complex disordered material: Full factorial investigation of PECVD-grown amorphous hydrogenated boron carbide. *Mater. Chem. Phys.* 173, 268–284. doi: 10.1016/j.matchemphys.2016.02.013

Nordell, B. J., Nguyen, T. D., Caruso, A. N., Purohit, S. S., Oyler, N. A., Lanford, W. A., et al. (2017). Carbon-enriched amorphous hydrogenated boron carbide films for very-low-k interlayer dielectrics. *Adv. Electron. Mater.* 3:1700116. doi: 10.1002/aelm.201700116

Nordell, B. J., Nguyen, T. D., Keck, C. L., Dhungana, S., Caruso, A. N., Lanford, W. A., et al. (2016b). Conquering the low-k death curve: Insulating boron carbide dielectrics with superior mechanical properties. *Adv. Electron. Mater.* 2:1600073. doi: 10.1002/aelm.201600073

Palin, G. R. (1967). "Chapter 4: electrical properties of of plastics," in *Plastics for Engineers: An Introductory Course* (New York, NY: Pergamon Press), 40–48.

Paquette, M. M., Li, W., Sky Driver, M., Karki, S., Caruso, A. N., and Oyler, N. A. (2011). The local physical structure of amorphous hydrogenated boron carbide: insights from magic angle spinning solid-state NMR spectroscopy. *J. Phys. Condens. Matter* 23:435002. doi: 10.1088/0953-8984/23/43/435002

Paquette, M. M., Nordell, B. J., Caruso, A. N., Sato, M., Fujiwara, H., and King, S. W. (2017). Optimization of amorphous semiconductors and low-/high-k dielectrics through percolation and topological constraint theory. *MRS Bull.* 42, 39–44. doi: 10.1557/mrs.2016.297

Phillips, J., and Thorpe, M. (1985). Constraint theory, vector percolation and glass formation. *Solid State Commun.* 53, 699–702. doi: 10.1016/0038-1098(85)90381-3

Phillips, J. C. (1979). Topology of covalent non-crystalline solids I: short-range order in chalcogenide alloys. *J. Non Cryst. Solids* 34, 153–181. doi: 10.1016/0022-3093(79)90033-4

Plucinski, M., and Zwanziger, J. W. (2015). Topological constraints and the Makishima-Mackenzie model. *J. Non. Cryst. Solids* 429, 20–23. doi: 10.1016/j.jnoncrysol.2015.08.029

Rader, A. J., Hespenheide, B. M., Kuhn, L. A., and Thorpe, M. F. (2002). Protein unfolding: Rigidity lost. *Proc. Natl. Acad. Sci. U.S.A.* 99, 3540–3545. doi: 10.1073/pnas.062492699

Robertson, B. W., Adenwalla, S., Harken, A., Welsch, P., Brand, J. I., Dowben, P. A., et al. (2002). A class of boron-rich solid-state neutron detectors. *Appl. Phys. Lett.* 80, 3644–3646. doi: 10.1063/1.1477942

Robertson, J. (1992). Mechanical properties and coordinations of amorphous carbons. *Phys. Rev. Lett.* 68, 220–223. doi: 10.1103/PhysRevLett.68.220

Ross, A. D., and Gleason, K. K. (2005). Effects of condensation reactions on the structural, mechanical, and electrical properties of plasma-deposited organosilicon thin films from octamethylcyclotetrasiloxane. *J. Appl. Phys.* 97:113707. doi: 10.1063/1.1923163

Rouxel, T. (2007). Elastic properties and short-to medium-range order in glasses. *J. Am. Ceram. Soc.* 90, 3019–3039. doi: 10.1111/j.1551-2916.2007.01945.x

Sartbaeva, A., Wells, S. A., Huerta, A., and Thorpe, M. F. (2007). Local structural variability and the intermediate phase window in network glasses. *Phys. Rev. B* 75:224204. doi: 10.1103/PhysRevB.75.224204

Sartbaeva, A., Wells, S. A., Treacy, M. M. J., and Thorpe, M. F. (2006). The flexibility window in zeolites. *Nat. Mater.* 5, 962–965. doi: 10.1038/nmat1784

Senapati, U., and Varshneya, A. K. (1995). Configurational arrangements in chalcogenide glasses: A new perspective on Phillips' constraint theory. *J. Non. Cryst. Solids* 185, 289–296. doi: 10.1016/0022-3093(94)00534-6

Sreeram, A. N., Varshneya, A. K., and Swiler, D. R. (1991). Molar volume and elastic properties of multicomponent chalcogenide glasses. *J. Non. Cryst. Solids* 128, 294–309. doi: 10.1016/0022-3093(91)90467-K

Srinivasan, A., Madhusoodanan, K. N., Gopal, E. S. R., and J., P. (1992). Observation of a threshold behavior in the optical band gap and thermal diffusivity of Ge-Sb-Se glasses. *Phys. Rev. B* 45, 8112–8115. doi: 10.1103/PhysRevB.45.8112

Störmer, M., Siewert, F., and Sinn, H. (2016). Preparation and characterization of B_4C coatings for advanced research light sources. *J. Sync. Radiat.* 23, 50–58. doi: 10.1107/S1600577515020901

Tanaka, K. (1986). Elastic properties of covalent glasses. *Solid State Commun.* 60, 295–297. doi: 10.1016/0038-1098(86)90469-2

Tanaka, K. (1989). Structural phase transitions in chalcogenide glasses. *Phys. Rev. B* 39, 1270–1279. doi: 10.1103/PhysRevB.39.1270

Tatsumisago, M., Halfpap, B. L., Green, J. L., Lindsay, S. M., and Angell, C. A. (1990). Fragility of Ge-As-Se glass-forming liquids in relation to rigidity percolation, and the Kauzmann Paradox. *Phys. Rev. Lett.* 64, 1549–1552. doi: 10.1103/PhysRevLett.64.1549

Thorpe, M. F. (1983). Continuous deformations in random networks. *J. Non. Cryst. Solids* 57, 355–370. doi: 10.1016/0022-3093(83)90424-6

Thorpe, M. F., Jacobs, D. J., Chubynsky, N. V., and Rader, A. J. (2002). "Generic rigidity of network glasses," in *Rigidity Theory and Applications*, eds M. F. Thorpe and P. M. Duxbury (New York, NY: Kluwer Academic/Plenum Publishers), 239–277.

Tichý, L., and Tichá, H. (1994). On the chemical threshold in chalcogenide glasses. *Mater. Lett.* 21, 313–319. doi: 10.1016/0167-577X(94)90196-1

Trujillo, N. J., Wu, Q., and Gleason, K. K. (2010). Ultralow dielectric constant tetravinyltetramethylcyclotetrasiloxane films deposited by initiated chemical vapor deposition (iCVD). *Adv. Funct. Mater.* 20, 607–616. doi: 10.1002/adfm.200900999

Vyssotsky, V. A., Gordon, S. B., Frisch, H. L., and Hammersley, J. M. (1961). Critical percolation probabilities (bond problem). *Phys. Rev.* 123, 1566–1567. doi: 10.1103/PhysRev.123.1566

Wang, R. P., Smith, A., Luther-Davies, B., Kokkonen, H., and Jackson, I. (2009). Observation of two elastic thresholds in $Ge_xAs_ySe_{1-x-y}$ glasses. *J. Appl. Phys.* 105:056109. doi: 10.1063/1.3079806

Wang, T., Wei, W. H., Shen, X., Wang, R. P., Davies, B. L., and Jackson, I. (2013). Elastic transition thresholds in Ge-As(Sb)-Se glasses. *J. Phys. D. Appl. Phys.* 46:165302. doi: 10.1088/0022-3727/46/16/165302

Wilding, M. C., Wilson, M., and McMillan, P. F. (2006). Structural studies and polymorphism in amorphous solids and liquids at high pressure. *Chem. Soc. Rev.* 35, 964–986. doi: 10.1039/b517775h

Yang, G., Bureau, B., Rouxel, T., Gueguen, Y., Gulbiten, O., Roiland, C., et al. (2010). Correlation between structure and physical properties of chalcogenide glasses in the As_xSe_{1-x} system. *Phys. Rev. B* 82:195206. doi: 10.1103/PhysRevB.82.195206

Yun, S. S., Li, H., Cappelletti, R. L., Enzweiler, R. N., and Boolchand, P. (1989). Onset of rigidity in $Se_{1-x}Ge_x$ glasses: ultrasonic elastic moduli. *Phys. Rev. B* 39, 8702–8706. doi: 10.1103/PhysRevB.39.8702

Zhang, M., and Boolchand, P. (1994). The central role of broken bond-bending contraints in promoting glass formation in the oxides. *Science* 266, 1355–1357. doi: 10.1126/science.266.5189.1355

Conflict of Interest: The authors declare that the research was conducted in the absence of any commercial or financial relationships that could be construed as a potential conflict of interest.

frontiers in Materials

ORIGINAL RESEARCH
published: 12 November 2019
doi: 10.3389/fmats.2019.00283

Signature of Coordination Defects in the Vibrational Spectrum of Amorphous Chalcogenides

Matthieu Micoulaut[1]* *and Punit Boolchand*[2]

[1] *Laboratoire de Physique Théorique de la Matière Condensée, Sorbonne Université, Paris, France,* [2] *School of Electronics and Computing Systems, College of Engineering and Applied Science, University of Cincinnati, Cincinnati, OH, United States*

Using model structures obtained from molecular dynamics simulations, we calculate the Infrared (IR) spectrum of amorphous and liquid As_2Se_3. The calculated spectrum is in rather good agreement with the experimental counterpart and contains the signatures of coordination defects represented by quasi-tetrahedral $Se{=}AsSe_{3/2}$ units which dominate the vibrational spectrum beyond 300 cm^{-1} with a typical vibration for the As=Se bond near 370 cm^{-1}. Conversely, the most prominent peaks around 100 and 200 cm^{-1} are mainly due to vibrations of As atoms in pyramidal geometry. The study of the thermal behavior indicates that such defects increase with temperature so that their presence in the glass is reminiscent of the liquid state. They are, furthermore, metastable in character, as are other defects such as 1- and 3-fold Se, and relax to a few percent on the picosecond timescale once an instantaneous quench has been achieved from high temperature to room temperature.

Keywords: As-Se glasses, molecular simulations, rigidity transitions, structure of disordered networks, vibrational analysis

OPEN ACCESS

Edited by:
Morten M. Smedskjaer, Aalborg University, Denmark

Reviewed by:
Roger Jay Loucks, Alfred University, United States
Bishal Bhattarai, Washington University in St. Louis, United States

***Correspondence:**
Matthieu Micoulaut
mmi@lptmc.jussieu.fr

Specialty section:
This article was submitted to Glass Science, a section of the journal Frontiers in Materials

Received: *09 July 2019*
Accepted: *22 October 2019*
Published: *12 November 2019*

Citation:
Micoulaut M and Boolchand P (2019) Signature of Coordination Defects in the Vibrational Spectrum of Amorphous Chalcogenides. Front. Mater. 6:283. doi: 10.3389/fmats.2019.00283

1. INTRODUCTION

Chalcogenide glasses are of great technological importance due to their potential applications in rewritable optical media, electronic nonvolatile memories, electrolytes and infrared waveguides (Adam, 2014). Among such materials, As-Se systems are among the most widely studied given their use as starting material for multicomponent alloys with targeted properties (Chen et al., 2010; Yang et al., 2010; Musgraves et al., 2011; Adam, 2014). In spite of numerous studies, the structural properties of amorphous As-Se glasses are still being debated. The molecular structure in the Se-rich region between x = 0 % (pure Selenium) and x = 40 % (As_2Se_3) has been described as a network of Se chains randomly cross-linked by Arsenic atoms in a $AsSe_{3/2}$ pyramidal structure (PYR) (Adam, 2014) (**Figure 1**). However, while a three-fold coordination can be reliably inferred from different techniques (Bureau et al., 2003; Xin et al., 2008) and represents undoubtedly the dominant local structure, coordination defects such as quasi-tetrahedral (QT) $Se{=}AsSe_{3/2}$ units (**Figure 1C**) have been proposed to also exist (Georgiev et al., 2000), and these contain a double As=Se bond. The presence of miscoordinated species is not specific to As-Se glasses since many other chalcogenides display the tendency to form local structures that do not fully conform to the octet rule, as revealed by e.g., molecular simulation techniques. In certain chalcogenides, these defects have been used to interpret vibrational and photoelectron spectroscopic measurements (Diemann, 1979) of e.g., As_2S_5, and used subsequently for the interpretation of experimental data of As-Se glasses (Wagner and Kasap, 1996). There have been theoretical and experimental investigations (Mauro and Varshneya, 2007; Hosokawa et al., 2013) indicating that 4-fold As might be present in the glass

through possible homopolar As-As defects, and a calculated coordination number was found to be larger than three (n_{As} = 3.29) which is another indication that such defects might be present in the glassy state. Recently, first principles molecular dynamics (FPMD) simulations (Bauchy et al., 2013, 2014) have also shown that As_2Se_3 displays a significant number of homopolar As-As and Se-Se bonds, together with the presence of QT units, albeit the fraction is rather small, typically less than 10%. Moreover, the results from such structural models lead to partial correlations seem to agree with those obtained experimentally from anomalous X-ray scattering (Hosokawa et al., 2013). Nevertheless, the question remains subject to large uncertainties given that the structural picture using QT is in contrast with the analysis of Raman spectroscopy on limited frequency range (Kostadinova, 2009) and Nuclear Quadrupole Resonance (Ahn et al., 2006).

Experimentally, signatures of As in QT sites have been assigned to specific features of the Raman spectrum of chemical analogs such as P_2Se_5 (Georgiev et al., 2003), and different Raman peaks in As-Se were tentatively assigned (Chen et al., 2010) to vibrational modes of $Se{=}AsSe_{3/2}$ but their origin and thermodynamic stability has been largely overlooked. Therefore, a compelling identification of QT Arsenic has not yet been given. From a more general viewpoint, the question of coordination defects is also central for the understanding for light-induced effects which are typical of chalcogenides (Li and Drabold, 2000). Electronic excitations reduce, indeed, the HOMO-LUMO band gap, the reduction being enhanced when valence-alternation pairs (Zhang and Drabold, 1998; Simdyankin et al., 2005) can be promoted. In this respect, the question of alternative coordinations to three-fold As, their underlying stability and their behavior across the glass-liquid transition is crucial.

In the present contribution, we provide theoretical evidence that such coordination defects exist in the archetypal network former As_2Se_3. These QT units appear to be reminiscent of the liquid state where they represent the dominant local structures with a fraction of about 40%. We show that all specific local molecular structures with detectable vibrational modes such as the $AsSe_{3/2}$ (PYR) and the $Se{=}AsSe_{3/2}$ (QT) unit contribute to the total infrared absorption spectrum of the glass and the liquid, that is calculated using linear response theory. Such modes can be only identified from first-principles calculations permitting to obtain their typical vibrational frequency, and a complementary assignment from local clusters permits to identify typical frequencies (at $\simeq$380 cm^{-1}) with the QT unit. The latter depends strongly on temperature and its thermal stability is examined.

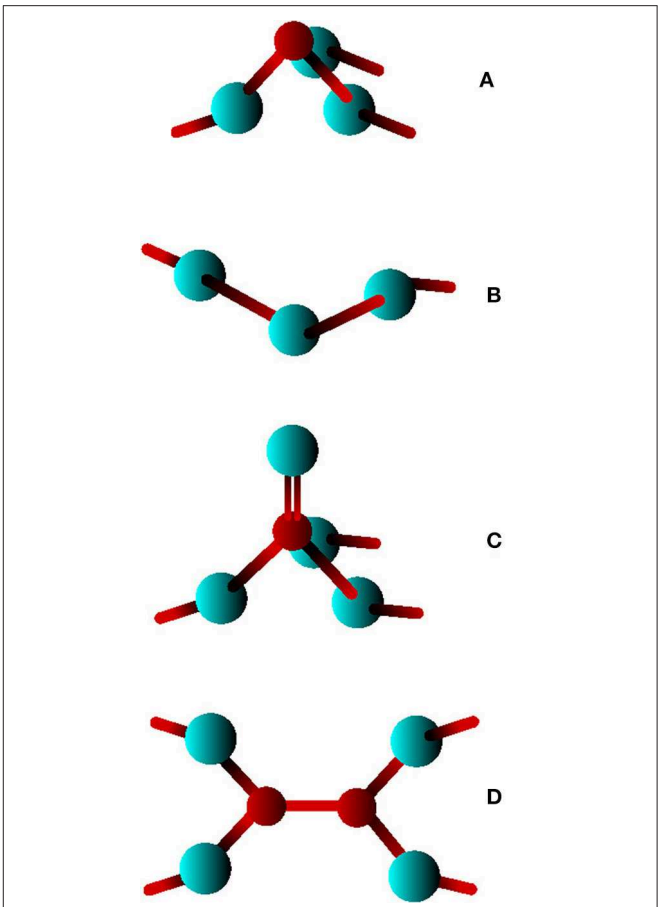

FIGURE 1 | Possible local structures in amorphous As_2Se_3: **(A)** a pyramidal $AsSe_{3/2}$ (PYR), **(B)** a Se chain-like fragment, **(C)** a quasitetrahedral $Se_{3/2}As{=}Se$ unit, **(D)** a homopolar As-As bond.

2. NUMERICAL METHODS

For the simulation of the present As_2Se_3 glasses and liquids, we used density functional theory (DFT) in combination with plane wave basis sets, from the Car-Parrinello molecular dynamics (CPMD) package. The electronic scheme has been chosen after a series of methodological investigations on different liquid and amorphous chalcogenides (Ge-Se) showing that (i) a generalized gradient approximation (GGA) for the exchange-correlation energy improves substantially (Massobrio et al., 1999) the description of both short and intermediate range order when compared to the local density approximation (LDA), (ii) an alternative exchange-correlation functional (with respect to Massobrio et al., 1999), derived after PW Becke (B) for the exchange energy (Becke, 1988) and Lee, Yang and Parr (LYP) for the correlation energy (Lee et al., 1988) leads to a structure with a reduced number of miscoordinated atoms and metallic character, and improves the reproduction of vibrational spectra (Giacomazzi et al., 2011) or Nuclear Magnetic resonance (NMR) properties (Kibalchenko et al., 2010). These simulations have been found to lead to structural models able to reproduce a variety of structure functions (pair correlation, structure factor) for various compositions in the As-Se binary that have been successfully compared to experiments (Bauchy et al., 2013, 2014).

A periodically repeated cubic cell containing 200 atoms was used, corresponding to the number density (18.06 Å) of the glass (Chen et al., 2010) and the time step for the integration of the equation of motion was chosen to be 0.12 fs with a fictitious mass of 200 a.u. Valence electrons were treated explicitly, in

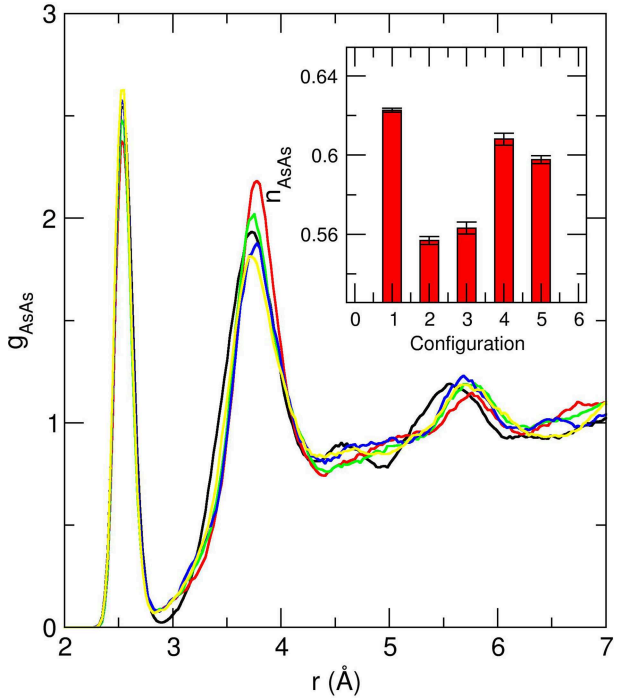

FIGURE 2 | Calculated As-As partial pair correlation function g_{AsAs} for five independent quenched configurations of amorphous As_2Se_3. The inset shows the corresponding obtained AsAs coordination number n_{AsAs} for the five configurations.

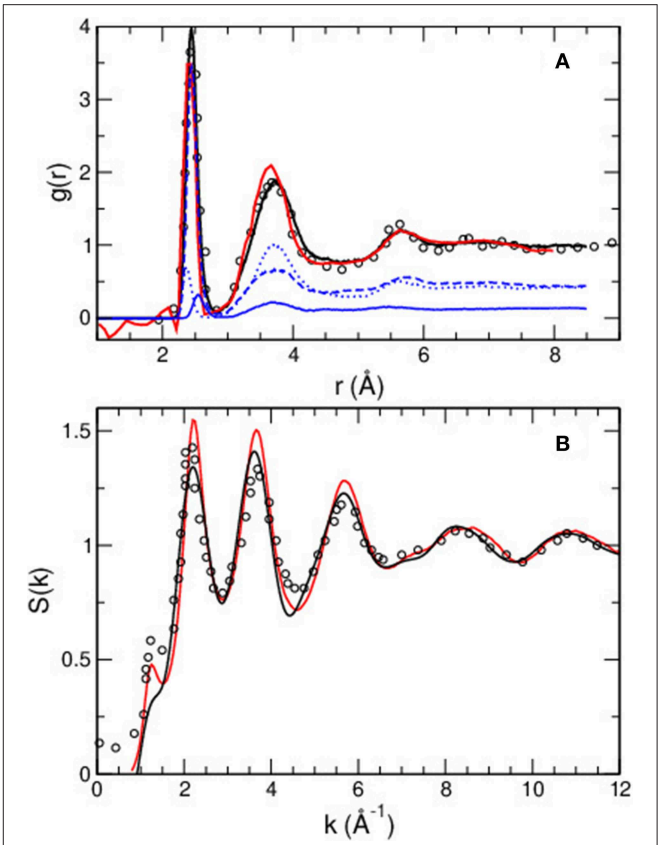

FIGURE 3 | (A) Total calculated pair correlation function $g(r)$ of amorphous As_2Se_3 (black curve), compared to experimental data from neutron diffusion (red curve Xin et al., 2008, circles Fabian et al., 2010). **(B)** Simulated structure factor $S_T(k)$ (black curve) compared to experimental data from Fabian et al. (2010) (circles) and Xin et al. (2008) (red curve). A decomposition into partial structure factors is shown in panel a), weighted by the appropriate neutron coherence lengths and concentrations of the species: As-As (solid curve), As-Se (broken curve), Se-Se (dotted curve).

conjunction with normconserving pseudopotentials to account for core-valence interactions. The wave functions were expanded at the Γ point of the supercell and the energy cutoff was set at 20 Ry. Finally, it should be noted that the amorphous structures result from five independent quenches (10K/ps) in order to increase the statistical accuracy of the models. The starting configurations of these independent quenches are separated by 5 ps at 1,000 K. Given the small system size of 200 atoms, there are, indeed, increased thermal history effects that can alter the overall results as highlighted by **Figure 2** which shows a difference for the obtained inherent structures displaying a clear variability in short range order and manifests by a different amplitude for the As-As homopolar prepeak at 2.45 Å and different bonding distances for the second correlation (3.71–3.78 Å). By ultimately performing the averages over such inherent structures, it is implicitly assumed that the resulting "*average*" structure will be a more realistic model of the glassy state, as confirmed below from the inspection of the calculated structure factor or pair correlation function, and their comparison with experiments.

3. RESULTS

3.1. Structure

The obtained structural properties in real and reciprocal space are given in **Figure 3**. The total pair correlation function $g(r)$ is represented in panel a. When compared to available experimental data (Xin et al., 2008; Fabian et al., 2010), one acknowledges an excellent agreement for all typical features: position, width and intensity of the principal peak at r = 2.44 Å defining the first correlation or bond distance dominated by As-Se correlations (experimentally 2.39–2.41 Å Renninger and Averbach, 1975; Mastelaro et al., 1992; Xin et al., 2008), and the secondary peak at r = 3.71 Å (experimentally 3.62–3.68 Å from various probes Renninger and Averbach, 1975; Xin et al., 2008), a slight overestimation of the bond distances being acknowledged when compared to experimental findings. The origin of the principal peak is essentially due to As-Se correlations with a moderate contributions from As-As and Se-Se bonds which is an indication of broken chemical order that has been also evidenced in another stoichiometric chalcogenide (Petri et al., 2000). The partial correlations (As-As, As-Se, Se-Se) are, indeed, also represented and two small contributions at 2.55 and 2.37 Å signal the presence of homopolar As-As and Se-Se bonds, respectively (blue curves in **Figure 3A**).

In **Figure 3B** the total structure factor $S_T(k)$ is represented and compared to corresponding experimental data (Xin et al., 2008; Fabian et al., 2010). The agreement between experiments and simulation is found to be excellent for all momentum transfers k, and the two principal peaks at k_{PP1}=2.2 Å^{-1} and k_{PP2}=3.7 Å^{-1} are very well reproduced, as are also the peaks obtained at higher k ($k > 6$ Å^{-1}). Note that the first sharp diffraction peak (FSDP), while rather small in experiments (Xin et al., 2008), reduces in the simulations to a simple shoulder on the low wavevector side of the principal peak at 2.1 Å^{-1}. In contrast to similar chalcogenides ($GeSe_2$), we are not aware of a full resolution of partial structure factors from isotopic substituted neutron diffraction. However, it has been pointed out (Bauchy et al., 2014) that the partial resolution from anomalous X-ray scattering (Hosokawa et al., 2001, 2006) can be also very well reproduced. Such experiments reveal, furthermore, that only an As-related partial displays a FSDP at $k \simeq$1.2 Å^{-1}, which is an indication that correlations in medium range order (i.e., at low k) mainly arise from As atoms. Many other physical and chemical properties can be inferred from the simulated structure and the dynamics (Bauchy et al., 2013, 2014; Micoulaut and Bauchy, 2013).

3.2. Infrared Properties

Following a strategy developed for Ge-Se glasses (Micoulaut et al., 2013), the infrared (IR) absorption spectrum can be determined from dipole-dipole correlations. During the DFT calculation, the total dipole moment **M**(t) is directly calculated (Silvestrelli et al., 1997) and contributes *via* the Fourier transform of the dipole-dipole autocorrelation function to the IR absorption spectrum using the maximum entropy inversion method (Silver et al., 1990):

$$\alpha(\omega) = \frac{4\pi \tanh(\beta\hbar\omega/2)}{3\hbar c V n(\omega)} \int_0^\infty e^{-i\omega t} \langle \mathbf{M}(t)\mathbf{M}(0)\rangle dt, \qquad (1)$$

where V is the volume, β=1/k$_B$T, and $n(\omega)$ the refractive index. **Figure 4** shows the computed IR spectra $\alpha(\omega)n(\omega)$ for different temperatures. As in previous investigations of chalcogenides (Micoulaut et al., 2013), the main features are qualitatively reproduced from the simulation such as the main peak at 150-200 cm^{-1} and the broad band between 50 and 130 cm^{-1}, these two features being detected experimentally (Lucovsky et al., 1975), as well as the shoulder peak at 250 cm^{-1}. It should be noted that the reproduction of IR properties have been found to be highly sensitive to the method employed and a previous methodological study for Ge-Se glasses has shown that a direct calculation inspired by linear response theory and the time dependence of the dipolar momentum $\mathbf{M}(t)$ was much more accurate than an alternative method (Giacomazzi et al., 2007, 2011). The latter builds on the response to a finite electrical field in conjunction with the computation of coupling tensors (dynamical Born charge Resta, 1994) based on the first derivative of the atomic forces with respect to the electrical field.

With increasing temperature, the entire spectra shifts to lower frequencies, which is consistent with an overall temperature induced softening of the vibrational motion, the main peak shifting from $\simeq$ 180 cm^{-1} at room temperature to about 160 cm^{-1} at 800 K. One furthermore notes the vanishing of the low-frequency bands at 50–130 cm^{-1} (barely detectable at 600 K) and the emergence of a shoulder peak at $\simeq$ 300–360 cm^{-1} which is visible at 300 K, albeit minuscule (arrows). The detail of the typical mode vibrations can be analyzed to further decode the IR spectra, in relationship with structural features.

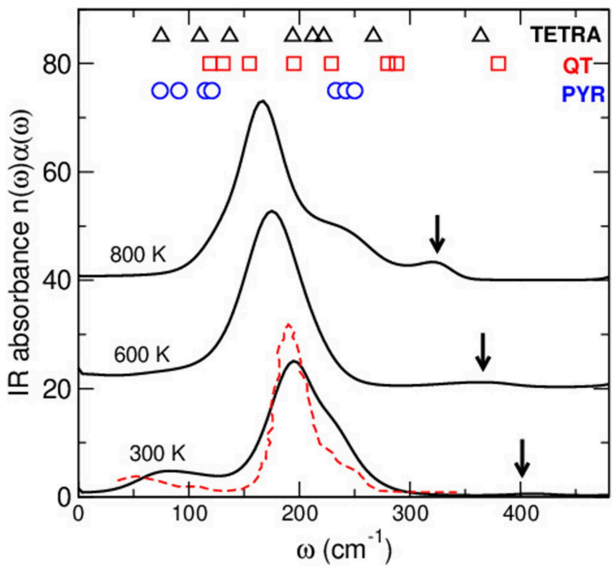

FIGURE 4 | Calculated IR absorbance spectra in amorphous and liquid As_2Se_3, compared to the measured spectra for As_2Se_3 (Lucovsky et al., 1975) (broken red curve). On top are reminded the location of the typical vibrational modes of a pyramidal unit $AsSe_{3/2}$ (PYR), the quasi-tetrahedral unit $Se{=}AsSe_{3/2}$ (QT) unit and a tetrahedral As (see numbers in **Table 1**).

4. DISCUSSION

4.1. Typical Mode Frequencies

The IR spectrum can be analyzed from a vibrational cluster analysis (**Table 1**) on typical As-centered species. DFT based calculations of the clusters (some of them represented in **Figure 1**) provide a complementary indication and an assignment of the typical bands observed in **Figure 4**. In the present case, three typical clusters have been considered: the PYR unit which is the dominant motif of the network structure, the QT containing the double As=Se bond, and a pure tetrahedral $AsSe_{4/2}$ (TETRA) which has been suggested to be part of the structure in combination with the presence of As-As homopolar bonds (Hosokawa et al., 2013). It is seen that the PYR unit gives essentially rise to bands found in the 70–120 cm^{-1} region, and are associated with bending/stretching and/or deformation modes of the local geometry, the modes at the largest frequencies (250 cm^{-1}) giving rise to umbrella flip modes, while smaller modes are found to be linked with breathing modes.

Interestingly, the analysis of the other clusters (TETRA, QT) indicate additional contributions at higher frequencies (180–260 cm^{-1}), consistently with the emergence of additional bands

TABLE 1 | Predicted mode frequencies of the different units present in amorphous As_2Se_3 glasses using DFT calculations.

Unit	Formula	Frequencies (cm^{-1})
PYR	$AsSe_3H_3$	74, 91, 115, 121, 233, 242, 250
QT	$AsSe_4H_3$	119, 131, 155, 195, 229, 280, 288, 380
TETRA	$AsSe_4H_4$	75, 110, 137, 194, 212, 222, 267, 364

in this frequency range with increasing temperature as discussed below. The addition of an extra coordination sphere of Se atoms to As-centered unit brings the calculated frequencies somewhat closer to the experimental values found for the main peak (modes detected in the 180–220 cm^{-1} range), although it cannot be eluded that these modes might also be the result of vibrational motions arising from linkages of elementary PYR units (Lucovsky et al., 1975). Most importantly is the fact that both QT and TETRA have an additional frequency found at $\simeq$365 cm^{-1} which is associated, in the case of the QT, with the vibrational motion of a double As=Se bond, as independently suggested by a Raman mode calculation (Jackson et al., 1999; Ravindren, 2014). This typical frequency is not found from the vibrational analysis of a PYR cluster (**Table 1**), and appears therefore to be specific of the tetrahedral defect coordination.

The calculated Raman active modes reveal, indeed, dominant vibrations at 235 cm^{-1} and 260 cm^{-1} are due to As-Se asymetric (in phase bond stretching) and symmetric stretching, respectively, as found experimentally (Chen et al., 2010), the only mode standing apart from the others with no possible overlap corresponding to a vibration of the Se=As double bond, expected experimentally to be near 360 cm^{-1}. It should be stressed that similar solitary modes have been determined in corresponding P-Se, P-S (Georgiev et al., 2001; Boolchand et al., 2009) and As-S glasses (Chen et al., 2008; Chakravarty et al., 2019) where the presence of P=Se and As=S double bonds could be determined independently, including from NMR (Tullius et al., 1990; Georgiev et al., 2001).

Experimentally, it has been found that the principal modes of the Raman spectrum of As_2Se_3 are spread out contiguously between 190 cm^{-1} and 300 cm^{-1} but with signatures of QT units found at larger frequencies (Chen et al., 2010; Ravindren, 2014) and these typical modes associated with the As=Se double bond do exist besides the main bands and have been identified at 355 cm^{-1} and 475 cm^{-1}. In contrast to the most recent work on As-Se (Chen et al., 2010; Ravindren, 2014), previous experimental studies on Raman (Kostadinova, 2009) or IR (Lucovsky et al., 1975) have not focused (ω <330 cm^{-1}) on this high frequency domain and it would certainly be interesting to probe, at least for the IR absorption, how the present numerical results can be compared.

An inspection of the fraction of r-fold species (**Figure 5**) that is calculated from the network structure indicates that the 600 K and 800 K liquids can contain a large fraction of As^{IV} (i.e., a 4-fold As, Micoulaut and Bauchy, 2013). The structure of the liquids is, thus, at variance with the amorphous structure which is found to

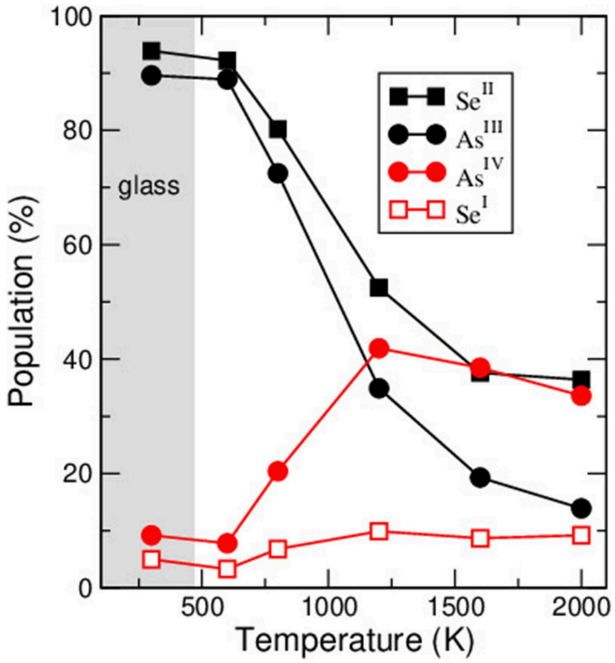

FIGURE 5 | Calculated fraction of *r*-fold species in amorphous and liquid As_2Se_3 (after Micoulaut and Bauchy, 2013). The gray zone corresponds to the glass region with T_g derived from Chen et al. (2010).

be mostly populated by 3-fold PYR units with minority species ($\simeq$10 %) made of As^{IV} that can be determined from different methods (Bauchy et al., 2014). However, as the temperature is increased across the glass transition region, the fraction of such species grows in an important fashion, leading to a fraction of about $\simeq$40% at 1200 K, and representing the dominant motif in the stable liquid. One can thus conclude that the abrupt decrease of 4-fold coordinated As is an important structural feature driving the onset of the glass transition in As_2Se_3. These findings actually contrast those found for Ge-Se liquids where the dominant tetrahedral order prevails over extended ranges in temperature (Massobrio et al., 2001; Salmon, 2007).

4.2. Stability

In order to probe the stability of such tetrahedral motifs, we have calculated their population in the supercooled liquids as well as in the 300 K glass under special numerical preparation condition (see below).

In **Figure 6A** we represent the statistics of As^{IV} in the two target liquids at 600 K and 800 K over the picosecond time domain which corresponds to multiple bond lifetimes. Evolution with time evolves for e.g., the lowest temperature (600 K) around 8 $\pm$ 2.5 % with a bond lifetime that we have calculated to be of about 0.82 ps. The situation is somewhat different for the amorphous system. For the latter, the starting configuration at 300 K has been chosen to be a 1,000 K atomic system containing about 40% As^{IV} and hyperquenched (**Figure 5**), a Nosé-Hoover thermostat being applied with a frequency of

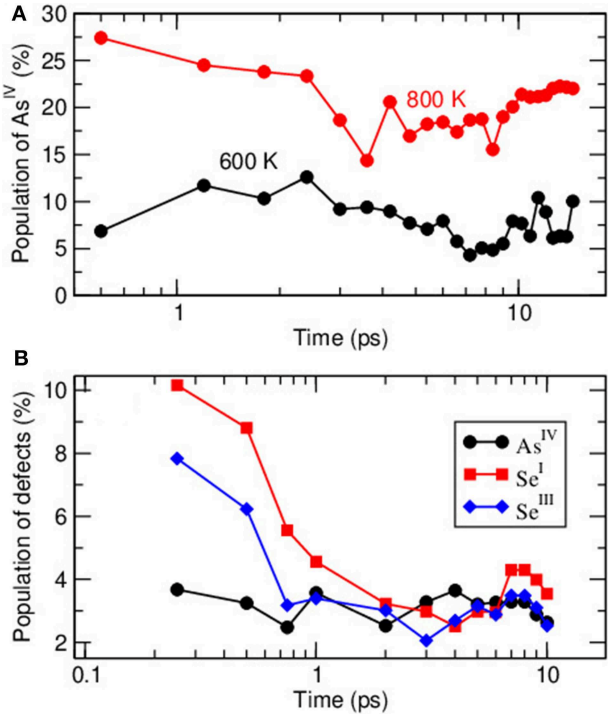

FIGURE 6 | Calculated fraction of As^{IV} in liquid (600 K and 800 K) As_2Se_3 with simulation time **(A)** and time evolution of defect species (As^{IV}, Se^{I}, and Se^{III}) from a hyperquenched stable liquid to 300 K **(B)**.

800 cm^{-1} (corresponding to a relaxation time for the thermostat of 41.69 fs). A subsequent relaxation led to a modification of the structure, and the inspection of **Figure 6B** suggests a rapid evolution of a starting "liquid-like" network with numerous miscoordinated defects containing QT into a structure with the predominant PYR local structure, the evolution being merely fulfilled within the picosecond timescale. For the particular As^{IV} defect, the decrease is linked with a global decrease of As^{IV} having one or two homopolar As-As bonds whose initial probability is in a ratio of nearly 1:1. The trend in all defect coordinated species is found to parallel the energy of the system (not shown) which decreases with the same trend within the first picosecond.

As a result, such defects represent minority species of the As_2Se_3 glass but these give rise, as evidenced from **Figure 4** and **Table 1**, to specific spectroscopic signatures in the high frequency domain of both IR and Raman spectra, as also detected in other Group V chalcogenides (Georgiev et al., 2001; Chen et al., 2008; Boolchand et al., 2009; Chakravarty et al., 2019).

5. SUMMARY AND CONCLUSIONS

In the present contribution, we have investigated vibrational and spectroscopic properties of amorphous As_2Se_3 with a special emphasis on the signature of QT units. Results show that such units must have, like for other Group V chalcogenides, a typical mode located in the high frequency domain as revealed from the calculation of the IR absorption spectra in the glassy and liquid state. This mode is found to blueshift and to increase in amplitude as the temperature is increased, consistently with the growth of the fraction of 4-fold As that is calculated independently. It is found that such species have a large probability of occurrence in the high temperature liquid. The vibrational analysis from clusters indicates that only such higher coordinated species have a typical mode compatible with the obtained IR spectra in the region 350–400 cm^{-1}.

On a more general ground, the present numerical study shows that an amorphous system obtained from a molecular dynamics simulation represents an ultrafast quenched high-temperature liquid. In covalent chalcogenides, it is known that such liquids contain a large number of miscoordinated atoms and defect geometries which are frozen down to low temperature due, in part, to the minuscule relaxation. It would be interesting to probe such methods for other compositions in the As-Se system in order to link the probability of such QT units with documented anomalies in thermal and relaxation properties (Ravindren et al., 2014). Work in this direction is in progress.

DATA AVAILABILITY STATEMENT

The datasets generated for this study are available on request to the corresponding author.

AUTHOR CONTRIBUTIONS

All authors listed have made a substantial, direct and intellectual contribution to the work, and approved it for publication.

REFERENCES

Adam, J. L. (2014). *Chalcogenides: Preparation, Properties and Applications*. Oxford: Woodhead.

Ahn, E., Williams, G. A., and Taylor, P. C. (2006). Nuclear quadrupole resonance study of local bonding in glassy As_xSe_{1x}. *Phys. Rev. B* 74:174206. doi: 10.1103/PhysRevB.74.174206

Bauchy, M., Kachmar, A., and Micoulaut, M. (2014). Structural, dynamic, electronic and vibrational properties of flexible, intermediate and stressed rigid As-Se glasses and liquids from first principles molecular dynamics simulations. *J. Chem. Phys.* 141:194506. doi: 10.1063/1.4901515

Bauchy, M., Micoulaut, M., Boero, M., and Massobrio, C. (2013). Compositional thresholds and anomalies in connection with stiffness transitions in network glasses. *Phys. Rev. Lett.* 110:165501. doi: 10.1103/PhysRevLett.110.165501

Becke, A. D. (1988). Density-functional exchange-energy approximation with correct asymptotic behavior. *Phys. Rev. A* 38:3098. doi: 10.1103/PhysRevA.38.3098

Boolchand, P., Chen, P., and Vempati, U. (2009). Intermediate phases, structural variance and network demixing in chalcogenides: the unusual case of group V sulfides. *J. Non-Cryst. Solids* 355:1773. doi: 10.1016/j.jnoncrysol.2008.11.046

Bureau, B., Troles, J., Floch, M. L., Smektala, F., and Lucas, J. (2003). Medium range order studied in selenide glasses by ^{77}Se NMR. *J. Non-Cryst. Solids* 326-327:58. doi: 10.1016/S0022-3093(03)00377-6

Chakravarty, S., Chbeir, R., Chen, P., Micoulaut, M., and Boolchand, P. (2019). Correlating melt dynamics and configurational entropy change with topological phases of As_xS_{100-x} glasses and the crucial role of melt/glass homogenization. *Front. Mater.* 6:166. doi: 10.3389/fmats.2019.00166

Chen, P., Boolchand, P., and Georgiev, D. G. (2010). Long term aging of selenide glasses: evidence of sub-T_g endotherms and pre-T_g exotherms. *J. Phys. Cond. Matt.* 22:065104. doi: 10.1088/0953-8984/22/6/065104

Chen, P., Holbrook, C., Boolchand, P., Georgiev, D. G., Jackson, K. A., and Micoulaut, M. (2008). Intermediate phase, network demixing, boson and floppy modes, and compositional trends in glass transition temperatures of binary As_xS_{1x} system. *Phys. Rev. B* 78:224208. doi: 10.1103/PhysRevB.78.224208

Diemann, E. (1979). Amorphous arsenic pentasulfide - structure and electronic structure. *Rev. Chim. Miner.* 16:237.

Fabian, M., Sváb, E., Pamukchieva, V., Szekeres, A., Vogel, S., and Ruett, U. (2010). Study of As_2Se_3 and As_2Se_2Te glass structure by neutron- and X-ray diffraction methods. *J. Phys. Cond. Matt.* 253:012053. doi: 10.1088/1742-6596/253/1/012053

Georgiev, D. G., Boolchand, P., Eckert, H., Micoulaut, M., and Jackson, K. (2003). The self-organized phase of bulk PxSe1-x glasses. *Europhys. Lett.* 62, 49–55. doi: 10.1209/epl/i2003-00361-2

Georgiev, D. G., Boolchand, P., and Micoulaut, M. (2000). Rigidity transitions and molecular structure of As_xSe_{1x} glasses. *Phys. Rev. B* 62:R9228. doi: 10.1103/PhysRevB.62.R9228

Georgiev, D. G., Mitkova, M., Boolchand, P., Brunklaus, G., Eckert, H., and Micoulaut, M. (2001). Molecular structure, glass transition temperature variation, agglomeration theory, and network connectivity of binary P-Se glasses. *Phys. Rev. B* 64:134204. doi: 10.1103/PhysRevB.64.134204

Giacomazzi, L., Massobrio, C., and Pasquarello, A. (2007). First-principles investigation of the structural and vibrational properties of vitreous $GeSe_2$. *Phys. Rev. B* 75:174207. doi: 10.1103/PhysRevB.75.174207

Giacomazzi, L., Massobrio, C., and Pasquarello, A. (2011). Vibrational properties of vitreous $GeSe_2$ with the Becke-Lee-Yang-Parr density functional. *J. Phys. Cond. Matt.* 23:295401. doi: 10.1088/0953-8984/23/29/295401

Hosokawa, S., Kawakita, Y., Pilgrim, W. C., and Hensel, F. (2001). Local structures in glassy and liquid As_2Se_3 - an anomalous X-ray scattering study. *J. Non-Cryst. Solids* 293–295:153. doi: 10.1016/S0022-3093(01)00665-2

Hosokawa, S., Koura, A., Bérar, J. F., Pilgrim, W. C., Kohara, S., and Shimojo, F. (2013). Does the 8-N bonding rule break down in As_2Se_3 glass? *Europhys. Lett.* 102:66008. doi: 10.1209/0295-5075/102/66008

Hosokawa, S., Wang, Y., Pilgrim, W. C., Bérar, J. F., Mamedov, S., and Boolchand, P. (2006). Partial structure analysis of glassy As_2Se_3 using anomalous X-ray scattering. *J. Non-Cryst. Solids* 352:1517. doi: 10.1016/j.jnoncrysol.2005.12.026

Jackson, K., Briley, A., Grossman, S., Porezag, D. V., and Pederson, M. R. (1999). Raman-active modes of $aGeSe_2$ and $aGeS_2$: a first-principles study. *Phys. Rev. B* 60:R14985. doi: 10.1103/PhysRevB.60.R14985

Kibalchenko, M., Yates, J. R., Massobrio, C., and Pasquarello, A. (2010). Structural assignments of NMR chemical shifts in Ge_xSe_{1x} glasses via first-principles calculations for $GeSe_2$, Ge_4Se_9, and GeSe crystals. *Phys. Rev. B* 82:020202. doi: 10.1103/PhysRevB.82.020202

Kostadinova, O. (2009). (Ph.D. thesis). University of Patras, Patras, Greece.

Lee, C., Yang, W., and Parr, R. G. (1988). Development of the Colle-Salvetti correlation-energy formula into a functional of the electron density. *Phys. Rev. B* 37:785. doi: 10.1103/PhysRevB.37.785

Li, J., and Drabold, D. A. (2000). Direct calculation of light-induced structural change and diffusive motion in glassy As_2Se_3. *Phys. Rev. Lett.* 85:2785. doi: 10.1103/PhysRevLett.85.2785

Lucovsky, G., Nemanich, R. J., Solin, S. A., and Keezer, R. C. (1975). Coordination dependent vibrational properties of amorphous semiconductors alloys. *Solid State Commun.* 17:1567. doi: 10.1016/0038-1098(75)90997-7

Massobrio, C., Pasquarello, A., and Car, R. (1999). Intermediate range order and bonding character in disordered network-forming systems. *J. Am. Chem. Soc.* 121:2943. doi: 10.1021/ja9808447

Massobrio, C., Pasquarello, A., and Car, R. (2001). Short- and intermediate-range structure of liquid $GeSe_2$. *Phys. Rev. B* 64:144205. doi: 10.1103/PhysRevB.64.144205

Mastelaro, V., Dexpert, H., Benazeth, S., and Ollitrault-Fichet, R. (1992). Structure of the Ag-As-Se chalcogenide glasses: the AsSe-Ag_2Se line. *J. Solid State Chem.* 96:301. doi: 10.1016/S0022-4596(05)80263-4

Mauro, J. C., and Varshneya, A. K. (2007). Multiscale modeling of arsenic selenide glass. *J. Non-Cryst. Solids* 353:1226. doi: 10.1016/j.jnoncrysol.2006.09.067

Micoulaut, M., and Bauchy, M. (2013). Structure of As_2Se_3 and As-Se network glasses: evidence for coordination defects and homopolar bonding. *J. Non-Cryst. Solids* 377:34. doi: 10.1016/j.jnoncrysol.2013.01.019

Micoulaut, M., Kachmar, A., Bauchy, M., Roux, S. L., Massobrio, C., and Boero, M. (2013). Structure, topology, rings, vibrational and electronic properties of Ge_xSe_{1-x} glasses across the rigidity transition: a numerical study. *Phys. Rev. B* 88:054203. doi: 10.1103/PhysRevB.88.054203

Musgraves, J. D., Wachtel, P., Novak, S., Wilkinson, J., and Richardson, K. (2011). Composition dependence of the viscosity and other physical properties in the arsenic selenide glass system. *J. Appl. Phys.* 110:063503. doi: 10.1063/1.3638122

Petri, I., Salmon, P. S., and Fischer, H. E. (2000). Defects in a disordered world: the structure of glassy $GeSe_2$. *Phys. Rev. Lett.* 84:2413. doi: 10.1103/PhysRevLett.84.2413

Ravindren, S. (2014). (Ph.D. thesis). University of Cincinnati.

Ravindren, S., Gunasekera, K., Tucker, Z., Diebold, A., Boolchand, P., and Micoulaut, M. (2014). Crucial effect of glass processing and melt homogenization on the fragility of non-stoichiometric chalcogenides. *J. Chem. Phys.* 140:134501. doi: 10.1063/1.4869107

Renninger, A. L., and Averbach, B. L. (1975). Atomic radial distribution functions of As-Se glasses. *Phys. Rev. B* 8:1507. doi: 10.1103/PhysRevB.8.1507

Resta, R. (1994). Macroscopic polarization in crystalline dielectrics: the geometric phase approach. *Rev. Mod. Phys.* 66:899. doi: 10.1103/RevModPhys.66.899

Salmon, P. S. (2007). Structure of liquids and glasses in the Ge-Se binary system. *J. Non-Cryst. Solids* 353:2959. doi: 10.1016/j.jnoncrysol.2007.05.152

Silver, R. N., Silvia, D. S., and Gubernatis, J. E. (1990). Maximum-entropy method for analytic continuation of quantum Monte Carlo data. *Phys. Rev. B* 41:2380. doi: 10.1103/PhysRevB.41.2380

Silvestrelli, P. L., Bernasconi, M., and Parinello, M. (1997). Ab initio infrared spectrum of liquid water. *Chem. Phys. Lett.* 277:478. doi: 10.1016/S0009-2614(97)00930-5

Simdyankin, S., Niehaus, T. A., Natarajan, G., Frauenheim, T., and Elliott, S. R. (2005). New type of charged defect in amorphous chalcogenides. *Phys. Rev. Lett.* 94:086401. doi: 10.1103/PhysRevLett.94.086401

Tullius, M., Lathrop, D., and Eckert, H. (1990). Glasses in the system phosphorus-sulfur: a phosphorus-31 spin-echo and high-speed MAS-NMR study of atomic distribution and local order. *J. Phys. Chem.* 94:2145. doi: 10.1021/j100368a075

Wagner, T., and Kasap, S. O. (1996). Glass transformation, heat capacity and structure of As_xSe_{1-x} glasses studied by modulated temperature differential scanning calorimetry experiments. *Philos. Mag. B* 74:667. doi: 10.1080/01418639608241069

Xin, S., Lu, J., and Salmon, P. S. (2008). Structure of Cu–As–Se glasses investigated by neutron diffraction with copper isotope substitution. *Phys. Rev. B* 78:064207. doi: 10.1103/PhysRevB.78.064207

Yang, G., Gulbiten, O., Gueguen, Y., Bureau, B., Sangleboeuf, J. C., Roiland, C., et al. (2010). Correlation between structure and physical properties of chalcogenide glasses in the As_xSe_{1x} system. *Phys. Rev. B* 82:195206. doi: 10.1103/PhysRevB.82.195206

Zhang, X., and Drabold, D. A. (1998). Evidence for valence alternation, and a new structural model of amorphous selenium. *J. Non-Cryst. Solids* 241:195. doi: 10.1016/S0022-3093(98)00807-2

Conflict of Interest: The authors declare that the research was conducted in the absence of any commercial or financial relationships that could be construed as a potential conflict of interest.

frontiers in Materials

ORIGINAL RESEARCH
published: 10 January 2020
doi: 10.3389/fmats.2019.00340

Topological Study of Phase-Separated Ag-Conducting Chalcogenide Glasses Using Peak Force Quantitative Nano-Mechanical Characterization

Andrea A. Piarristeguy[1], Rozenn Le Parc[2], Michel Ramonda[3], Raphaël Escalier[1] and Annie Pradel[1]*

[1] ICGM, Univ Montpellier, CNRS, ENSCM, Montpellier, France, [2] Laboratoire Charles Coulomb (L2C), UMR 5221 CNRS-Université de Montpellier, Montpellier, France, [3] Centre de Technologie de Montpellier, Université de Montpellier, Montpellier, France

Peak Force Quantitative Nano-Mechanical property mapping (PF-QNM) was used to explore the nanomechanical properties of binary Ge_ySe_{100-y} glasses and phase-separated $Ag_x(Ge_{0.25}Se_{0.75})_{100-x}$ glasses. The indentation modulus decreases when the selenium content increases in the binary glasses and when the silver content increases in phase-separated ternary glasses as a consequence of the increasing flexibility of the network. At nanoscale level, PF-QNM measurements highlighted a higher indentation modulus for the Ag-rich phase than for the Ag-poor phase, together with a decrease of both local indentation moduli with the increase of silver content in the glass. A model to gain a further insight in the mean coordination numbers and compositions of the Ag-rich and Ag-poor phases, based upon the assumption of a decoupled effect of the variations in Ag and in Ge on the mechanical properties, is described in detail. In the framework of the model, the mean coordination numbers for the Ag-rich phase $<N_R>$ and Ag-poor phase $<N_P>$ keep on decreasing when the total silver content in the glasses increases. The Ge concentration differs in Ag-rich and Ag-poor phases. When the silver content in the glass increases, the Ge concentration decreases in both phases. The result, in turn, indicates that an increase in the conductivity of the Ag-rich phase when the total silver content increases, as shown previously by C-AFM, would not be only explained by an increase in silver content but also by a softening of the network and consequently by an increase of charge carrier mobility.

Keywords: Ag-doped chalcogenide glasses, phase separation, ionic conduction, near field microscopy, nano-mechanical mapping

OPEN ACCESS

Edited by:
Punit Boolchand,
University of Cincinnati, United States

Reviewed by:
Ren Zhang,
Intel, United States
Dave Drabold,
Ohio University, United States

****Correspondence:***
Andrea A. Piarristeguy
andrea.piarristeguy@umontpellier.fr

Specialty section:
This article was submitted to Glass Science, a section of the journal Frontiers in Materials

Received: *15 June 2019*
Accepted: *11 December 2019*
Published: *10 January 2020*

Citation:
Piarristeguy AA, Le Parc R, Ramonda M, Escalier R and Pradel A (2020) Topological Study of Phase-Separated Ag-Conducting Chalcogenide Glasses Using Peak Force Quantitative Nano-Mechanical Characterization. Front. Mater. 6:340. doi: 10.3389/fmats.2019.00340

INTRODUCTION

Owing to their remarkable properties (IR transparency, high ionic conduction, photo-diffusion, etc.), chalcogenide glasses aroused strong interest in both the academic community and private companies. Among potential applications, the Conductive-Bridging Random Access Memories (CB-RAM), susceptible to replace the current flash memories, take advantage of two properties

of chalcogenide films, their sensitivity to photo-diffusion and their high ionic conductivity when doped with silver. A CB-RAM memory typically comprises a Ag-photo-doped glassy thin film of composition $\sim Ge_{0.25}Se_{0.75}$ placed between two electrodes, a silver one and a nickel one for example. The conductivity of the film is reversibly changed by several orders of magnitude when a low voltage is applied ($\sim$0.2V). When applied to nanometric devices (when the thickness of the glassy film is typically 20–30 nm), the phenomenon is characterized by a very short time for commutation ($\sim$10 ns) and a very high cyclability ($>10^6$ cycles) (Kozicki et al., 2005).

In order to explain the operation of this memory and in particular its very short switching time hardly compatible with the mobility of Ag^+ ions, various hypotheses have been proposed and among them, the presence of pre-existing silver-rich zones within the amorphous film—which would be heterogeneous—and the creation of conduction paths between these zones. To confirm this hypothesis and to better understand the phenomena at the origin of the switching from a resistive state to a conductive state in CB-RAM memories, the electrical, structural, and thermal properties of bulk Ag-Ge-Se glasses have been widely studied (Dejus et al., 1988, 1991, 1992; Kawasaki et al., 1999; Mitkova et al., 1999; Iyetomi et al., 2000; Piarristeguy et al., 2000, 2003, 2007a, 2012; Ureña et al., 2003, 2005; Wang et al., 2003; Cervinka et al., 2005; Tafen et al., 2005; Cuello et al., 2007; Prasai and Drabold, 2011; Le Parc et al., 2013; Stellhorn et al., 2016a,b; Zeidler et al., 2016, 2018). It was shown that the conductivity of $Ag_x(Ge_{0.25}Se_{0.75})_{100-x}$ glasses with $1 < x < 30$ at. % increases suddenly by seven to eight orders of magnitude at 7–10 at. % Ag.

Insight into the microstructure of these glasses was clearly needed. However, owing to the ease of diffusion of silver in these materials (Kolobov and Elliott, 1991), the use of classical microscopy techniques to probe the structure of Ag-based glasses is tricky; a risk of altering the Ag-centered local structures exists if the light or electron beam energy is too high. As a matter of fact, few papers on the electrical properties of chalcogenide glasses report attempts to get insights into the homogeneity of the materials.

Gutenev et al. (1991) and Wang et al. (2003) indicated for the first time that the glasses were phase separated according to optical microscopy and modulated differential scanning calorimetry (MDSC) experiments, respectively. However, these experiments cannot provide insight on, for example, the evolution of the composition or the conductivity of each phase with increasing silver content. Several years later, the ability and the complementarity of near field microscopy techniques provided insight into the intrinsic electrical properties of each phase present in bulk $Ag_x(Ge_{0.25}Se_{0.75})_{100-x}$ glasses and their composition dependence (Balan et al., 2006; Piarristeguy et al., 2007b, 2010a,b). Electrostatic force microscopy (EFM) was indeed used to get images of electrical contrasts (dielectric permittivity) in phase separated glasses. Combined with electrical conductivity measurements using complex impedance spectroscopy, EFM helped in understanding the jump in conductivity at 7–10 at% in $Ag_x(Ge_{0.25}Se_{0.75})_{100-x}$ glasses. While a Ag-rich phase is embedded in a Ag-poor phase for the low conductivity region ($x <$ 7–10 at. % Ag), the reverse is true for high conductivity region ($x >$ 7–10 at. % Ag) with the Ag-rich phase controlling the silver diffusion throughout the material. The percolation of the Ag-rich phase was at the origin of a sudden jump in conductivity (Balan et al., 2006; Piarristeguy et al., 2007b).

Recently another near field microscopy technique, i.e., the Contact Resonance Atomic Force Microscopy (CR-AFM) in combination with Raman mapping was used to get additional information on the phase compositions in bulk $Ag_x(Ge_{0.25}Se_{0.75})_{100-x}$ glasses (Piarristeguy et al., 2018). The results suggested a different Ge/Se ratio in Ag-poor and Ag-rich phases, the first one being richer in selenium than the second one.

In this work, an innovative and complementary technique, the Peak Force Quantitative Nano-Mechanical mapping (PF-QNM) was used to explore the nano-mechanical properties of Ge_ySe_{100-y} and $Ag_x(Ge_{0.25}Se_{0.75})_{100-x}$ glasses and get information on the topology of these phase-separated glasses. A model, based upon the assumption of a decoupled effect of the variations in Ag and in Ge on the mechanical properties, helped to gain a further insight in the mean coordination numbers and compositions of the Ag-rich and Ag-poor phases.

MATERIALS AND METHODS

Sample Preparation and Characterization

Bulk Ge_ySe_{100-y} glasses (y = 15, 20, 25, 30, and 33 at. %) and $Ag_x(Ge_{0.25}Se_{0.75})_{100-x}$ glasses (x = 0, 7, 15, and 20 at. %) were synthesized from a mixture of high-purity starting elements [Ag (Aldrich, 99.9 %), Ge (Aldrich, 99.999 %) and Se (Aldrich, 99.99 %)] Three grams of the stoichiometric powders were placed in a cylindrical quartz ampoule (11 mm inner diameter, 1 mm thick) sealed under secondary vacuum (10^{-5} mbar). The tube was subsequently heated with a low heating rate of 6°C/h up to 600°C for $Ge_{15}Se_{85}$, 700°C for $Ge_{20}Se_{80}$ and 850°C for $Ge_{30}Se_{70}$ and $Ge_{33}Se_{67}$, held at this temperature for 12 h, and finally quenched in air. For the $Ag_x(Ge_{0.25}Se_{0.75})_{100-x}$ glasses, the powder was heated up to 950°C with a 10°C/h heating rate and kept at this temperature for 8 h for homogenization before being quenched in a salt-ice-water mixture. The samples were named Agx according to the concentration of Ag (in at. %) and the nomenclature R-Agx and P-Agx was used for the Ag-rich and Ag-poor phases, respectively.

The amorphous nature of the ingots was confirmed by performing X-Ray diffraction using a PANalytical X'Pert diffractometer. A Cu (Kα) source (λ = 1.5406Å) was used with an operating voltage of 40 kV and a beam current of 30–40 mA.

Peak Force Quantitative Nano-Mechanical Property Mapping (PF-QNM)

The mechanical characterization was performed with a Multimode AFM instrument (from Bruker Corporation, USA) upgraded with Nanoscope V using PF-QNM imaging mode and a special RTESPA-525-30 (BatchA050 wafer1 Box9 probe#3) (Bruker) probe with a lever spring constant of 167 N/m and a tip radius of 34 nm. A FSILICA-12M sample from Bruker Instruments was first used to calibrate sensitivity deflection and sync distance QNM. The calibration was checked by

measuring a sample (given by Arnould et al., 2017) consisting in a mixture of resin and fiber of K28 grade Kevlar, providing indentation moduli of around 4 GPa ± 0.4 GPa and 23 GPa ± 4 GPa, respectively, in agreement with the data of Arnould et al. (2017). The applied maximum load was set at 200 nN for all the measurements. Different mechanical properties, i.e., adhesion force, elastic modulus, deformation, energy dissipation, were obtained by a real time analysis of the "force versus separation" curves. The well-known Derjaguin-Muller-Toporov (DMT) model (Derjaguin et al., 1975) was used to fit the retract curves and calculate the indentation moduli (Poisson coefficient set at 0).

Measurements were performed on the surfaces of freshly fractured glass to avoid any problem due to surface oxidation. The experiments were carried out within the following hours.

RESULTS

Ge-Se Glasses

PF-QNM experiments allowed getting information about the mechanical properties of glasses. The indentation moduli, reported for glasses for the first time, were estimated from data recorded over 5 × 5 μm images. **Figure 1** shows the indentation moduli for the different Ge_ySe_{100-y} glasses. A monotonous increase in modulus with increasing germanium concentration (y) is observed, which is in agreement with Vickers and Meyer's hardness and Young's modulus measured by conventional mechanical techniques (Guin et al., 2002). The insert in **Figure 1** shows both the indentation moduli obtained by PF-QNM measurements and the Young's moduli for the same glassy compositions (Guin et al., 2002). Similar trends are observed, which allows to validate the PF-QNM technique to evaluate realistic glass indentation moduli.

Because of similar Se-Se and Se-Ge bond strengths (223 and 230 kJ/mol, respectively) and only slightly weaker Ge-Ge bond strength (186 kJ/mol), Guin et al. (2002) claimed that the source for the increase of the hardness has to be topological in nature. Consequently, the continuous increase of hardness is of the same origin as the increase of the elastic moduli, and it results from the increasing number of strong covalent bonds with increasing Ge concentration.

Ag-Ge-Se Glasses

Figure 2 shows the topography and the indentation modulus images (PF-QNM) for the $Ag_x(Ge_{0.25}Se_{0.75})_{100-x}$ glasses. These images (**Figures 2b,d,f**) clearly show heterogeneous domains, which indicates that the PF-QNM technique is sensitive to modulation of mechanical properties at the local stage. The heterogeneous domains are similar to those already reported for this family of glasses using Electrostatic Force Microscopy (EFM) and Conductive-Atomic Force Microscopy (C-AFM) (Balan et al., 2006; Piarristeguy et al., 2007b, 2010a,b). For glassy compositions belonging to the low-conductivity region (x < 10 at. % Ag, **Figure 2b**), nodules of a Ag-rich (R-Agx) phase (light region) are embedded in a connected Ag-poor (P-Agx) phase (dark region). At the opposite, for the glassy compositions belonging to the high conductivity region

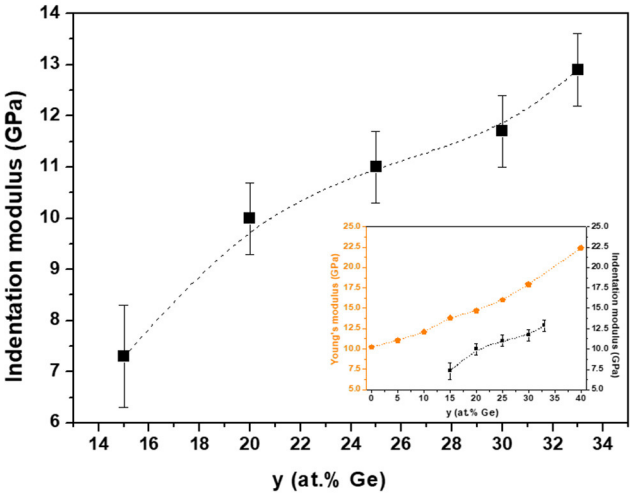

FIGURE 1 | Indentation moduli for bulk Ge_ySe_{100-y} glasses. Insert shows the comparison between Young's modulus (Guin et al., 2002) and indentation modulus obtained by PF-QNM measurements. The broken lines are drawn as guides for the eye. The indentation modulus values and the error bars were calculated from an average of three PF-QNM measurements and standard deviation evaluation.

(x = 15 and 20), a connected R-Agx phase contains nodules of P-Agx phase (**Figures 2d,f**). Depending upon the quenching conditions, spinodal or nucleation/growth phase separation can occur in these glasses (Piarristeguy et al., 2018). In this work, the images show a morphology typical of nucleation/growth phase separation.

As an example, the analysis of a small zone of the indentation modulus mapping for a typical phase-separated $Ag_{20}(Ge_{0.25}Se_{0.75})_{80}$ glass is detailed (**Figure 3**). This glass presents nodules of about 0.7 μm (P-Agx phase) immersed in a conductive matrix (R-Agx phase). The indentation moduli of both phases are visible in **Figure 3A**. The variation of modulus along the white line in **Figure 3A** is shown in **Figure 3B**. The modulus of the R-Agx phase, i.e., ∼9 GPa, corresponds to the domains of the line from 0 to ∼0.5 μm and from ∼1.3 to 2 μm. The modulus for the R-Agx phase between ∼0.5 and ∼1.3 μm has a value of ∼7.2 GPa.

Three different values of indentation modulus for each of these phase-separated glasses were extracted from the PF-QNM experiments. The first one corresponds to an average value and is evaluated by taking into account the whole region included in the blue parallelepiped in **Figure 4**, the second one corresponds to the indentation modulus for the R-Agx phase and is obtained from regions included in the red parallelepiped in **Figure 4**, the third one corresponds to the P-Agx phase (regions in the green parallelepiped in **Figure 4**). The average indentation modulus, estimated from data recorded over the whole 5 × 1.5 μm image is equivalent to a "macroscopic measurement." At least thirty different regions were taken into in the PF-QNM image to estimate the value of and the uncertainty on the indentation modulus for each phase.

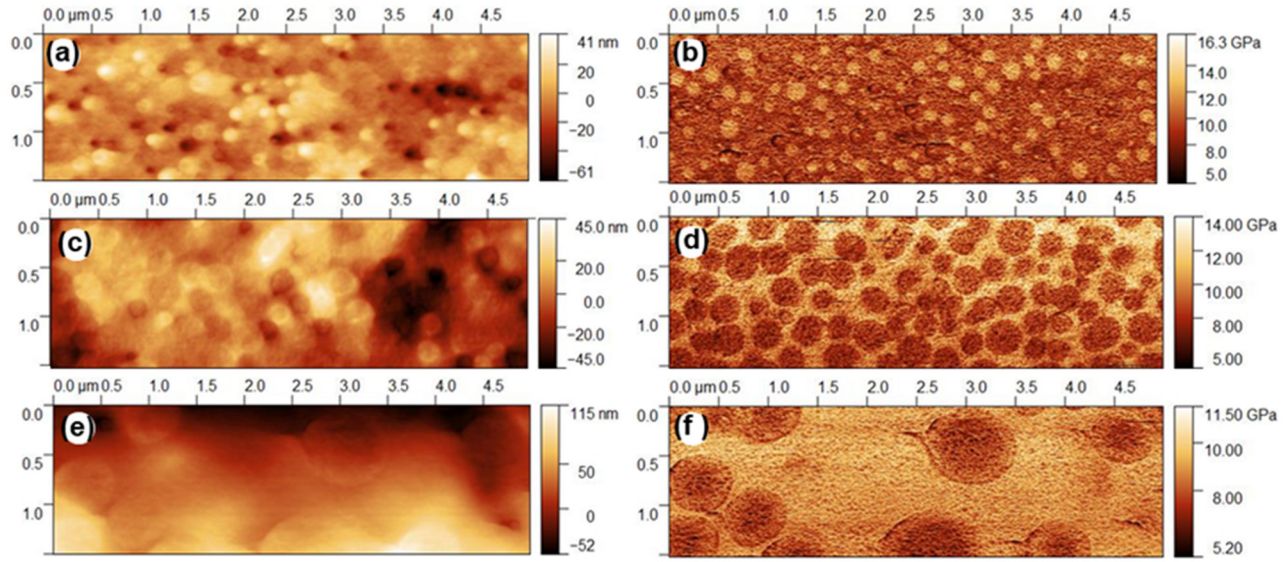

FIGURE 2 | PF-QNM mapping of the $Ag_x(Ge_{0.25}Se_{0.75})_{100-x}$ glasses: **(a)** $x = 7$, topography, **(b)** $x = 7$, indentation modulus, **(c)** $x = 15$, topography, **(d)** $x = 15$, indentation modulus, **(e)** $x = 20$, topography and **(f)** $x = 20$, indentation modulus.

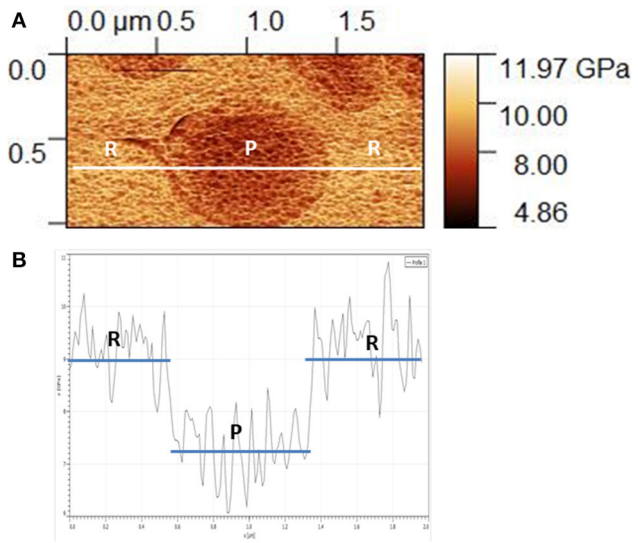

FIGURE 3 | (A) Detailed mapping of indentation modulus for the $Ag_{20}(Ge_{0.25}Se_{0.75})_{80}$ glass and **(B)** variation of the indentation modulus along the profile drawn in **(A)**. In both images, "R" and "P" correspond to R-Agx and P-Agx phases, respectively.

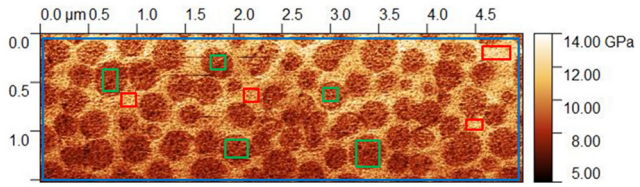

FIGURE 4 | PF-QNM mapping of indentation modulus for $Ag_{15}(Ge_{0.25}Se_{0.75})_{85}$ glass. The blue, red and green regions correspond to the average (or macroscopic) indentation modulus, the R-Agx phase and the P-Agx phase modulus, respectively.

The indentation moduli for R-Agx and P-Agx phases as well as the "average modulus" as a function of the silver content are presented in **Figure 5**. The "average modulus" decreases with the increase of silver concentration in the glass, which is in agreement with previous Vickers microhardness measurements (Piarristeguy et al., 2018). This decrease is a consequence of the structural changes induced by the introduction of Ag in the $Ge_{25}Se_{75}$ glass. Introduction of silver affects the tetrahedral network through changes in bond angles, eventual ES to CS tetrahedra transformation associated to network disruption and selenium chains breaking. At high silver content, a high flexibility of the network is expected as a consequence of depolymerization of the glass network. Based on this statement, the local mechanical measurements present an apparent contradiction since the indentation modulus value is higher for the R-Agx phase than for the P-Agx phase (it will be discussed in the next section). A decrease of both local indentation moduli with the increase of the silver content in the glass is also observed.

DISCUSSION

Mean Coordination Number and Composition

The results above show a decrease in the "average" indentation modulus M (symbols in blue, **Figure 5**) when the Ag content increases in the glasses. However, for a given Ag content, the

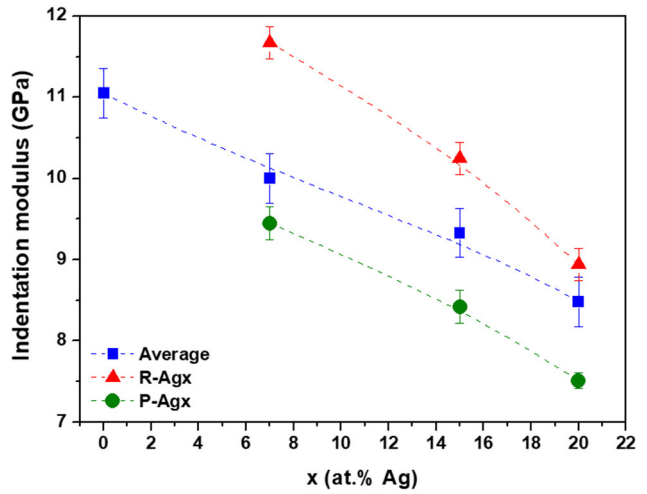

FIGURE 5 | Indentation moduli for bulk $Ag_x(Ge_{0.25}Se_{0.75})_{100-x}$ glasses. Blue, red and green symbols correspond to the "average modulus," R-Agx and P-Agx phases moduli, respectively. The broken lines are drawn as guides for the eye. The indentation modulus values and the error bars were calculated from: i) an average of three PF-QNM measurements and standard deviation evaluation for the "average modulus" and ii) an average of PF-QNM measurements over thirty different regions (see green and red regions in **Figure 4**) and subsequent standard deviation evaluation for the Ag-rich and Ag-poor phases.

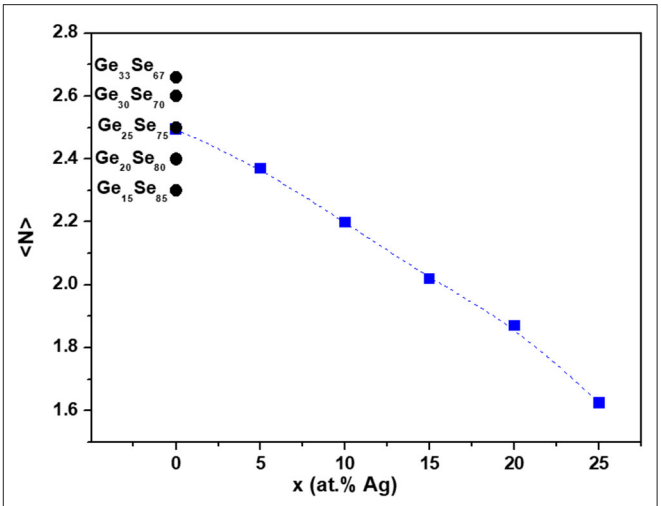

FIGURE 6 | Mean coordination number <N> for $Ag_x(Ge_{0.25}Se_{0.75})_{100-x}$ glasses estimated using Zeidler et al. (2016). For comparison, mean coordination number <N> for Ge_ySe_{100-y} glasses are presented assuming $<N_{Ge}> = 4$ and $<N_{Se}> = 2$ for the mean coordination numbers of Ge and Se, respectively.

R-Agx phase systematically exhibit a higher modulus than the P-Agx phase. The explanation has to be searched in difference in compositions and, consequently in average coordination numbers, between R-Agx and P-Agx.

In Ge_ySe_{100-y} glasses, assuming $<N_{Ge}> = 4$ and $<N_{Se}> = 2$ for the mean coordination numbers of Ge and Se, respectively, the mean coordination number can be estimated

$$< N >_{Ge-Se} = \frac{y}{100} < N_{Ge} > + \frac{100 - y}{100} < N_{Se} > \qquad (1)$$

In $Ag_x(Ge_{0.25}Se_{0.75})_{100-x}$ glasses, when ionic bonds are participating to the structure, the determination of the mean coordination is more complex. Zeidler et al. (2018) have estimated the nearest-neighbor coordination numbers $<N_{ij}>$ extracted from neutron diffraction experiments on glasses along the $Ag_x(Ge_{0.25}Se_{0.75})_{100-x}$ tie line. Taking into account that the first coordination sphere implies only $<N_{GeSe}>$, $<N_{SeSe}>$, and $<N_{SeGe}>$, the mean coordination number for this family of glasses can be estimated

$$< N >_{Ag-Ge-Se} = \frac{0.25(100 - x)}{100} < N_{GeSe} > + \frac{0.75(100 - x)}{100} [< N_{SeGe} > + < N_{SeSe} >] \qquad (2)$$

Figure 6 shows the mean coordination number <N> for Ge_ySe_{100-y} and $Ag_x(Ge_{0.25}Se_{0.75})_{100-x}$ glasses. As expected, we observe that the mean coordination number decreases monotonously with the increase of silver content in the glass, with values comprised between $<N> = 2.50$ for Ag0 to $<N> = 1.62$ for Ag25. Silver incorporation is expected to depolymerize the network, searching for selenium to compensate its positive charge, leading to inter-tetrahedral Ge-Se-Ge, and selenium chains breaking. Therefore, the introduction of silver is expected to introduce some flexibility into the network.

An attempt to gain a further insight into the mean coordination numbers of the R-Agx and P-Agx phases in $Ag_x(Ge_zSe_{1-z})_{100-x}$ glasses is described below.

As a first approximation, the dependence of the indentation modulus M_{Ge} on Ge content in Ge_ySe_{100-y} glasses, shown in **Figure 7** (black symbols), can be taken as linear with

$$\Delta M_{Ge} = 14.04\Delta < N > \qquad (3)$$

In the same way, the dependence of the indentation modulus M_{Ag} on Ag content for $Ag_x(Ge_{0.25}Se_{0.75})_{100-x}$ glasses, shown in **Figure 7** (blue symbols), can be taken as linear with

$$\Delta M_{Ag} = -3.94\Delta < N > \qquad (4)$$

On the whole, the effect of Ge modulation is almost three times more impacting on the indentation modulus than the evolution of the average Ag content and evolves in the opposite direction.

With the assumption that the difference of indentation moduli ΔM_{R-P} = M(R-Agx)-M(P-Agx) between the Ag-rich phase $(Ag_{x'}(Ge_{z'}Se_{1-z'})_{100-x'})$ and the Ag-poor phase $(Ag_{x''}(Ge_{z''}Se_{1-z''})_{100-x''})$, for a given glass composition, can be related to the decoupled effect of both the variation in Ag content, $\Delta_{x'x''} = x' - x''$, and the variation in Ge content, $\Delta_{z'z''} = 100.z' - 100.z''$, one can write

$$\Delta M_{R-P} = \Delta M_{x'x''} + \Delta M_{z'z''} \qquad (5)$$

where $\Delta M_{x'x''}$ is the modulus difference related to a Ag variation $\Delta_{x'x''}$ and $\Delta M_{z'z''}$ a modulus difference related to Ge variation $\Delta_{z'z''}$.

Taking into account Equations (3–4), the equation (5) can be written

$$\Delta M_{R-P} = 14.04\Delta < N > -3.94\,\Delta < N >= 10.06\Delta < N > \quad (6)$$

The modulus difference between R-Agx and P-Agx phases, ΔM_{R-P}, for a given glass, can be calculated from the experimental data shown in **Figure 5**. These values are 2.33, 1.85, 1.43, for Ag7, Ag15, and Ag20 glasses respectively, which corresponds (see Equation 6) to Δ <N> values of 0.23, 0.18, and 0.14 with the Ag content increasing in the glass.

Additional information can help to estimate the mean coordination number for R-Agx (<N_R>) and P-Agx (<N_P>) phases. The PF-QNM images (**Figures 2b,d,f**) indeed allow to calculate the surface percentage for the R-Agx (% R) and P-Agx (% P) phases. Assuming that the volume percentage is equivalent to the surface percentage, the mean coordination number is therefore a linear combination of the mean coordination number in R-Agx and P-Agx phases:

$$< N >= (\%P) < N_P > + (\%R) < N_R > = (\%P) < N_P > + (\%R)(< N_P > +\Delta < N >) \quad (7)$$

where we have assumed that <N_R> = <N_P> + Δ <N> because R-Agx phase presents a high indentation modulus in comparison with the P-Agx phase. The mean coordination numbers <N_R> and <N_P> are presented in **Figure 7**.

It can be seen that, consistently with the average coordination number, both <N_R> and <N_P> decrease with increasing Ag content. These decreases in coordination number can be understood by a decrease in Ge (z′, z″) and/or an increase of Ag (x′, x″). The differences <N_R> – <N_P> for a specific Agx composition decreases when Ag content increases (respectively equal to 0.23, 0.18, 0.14 for Ag7, Ag15, and Ag20). Interestingly, depending upon the preparation procedure, the glass Ag 25, not measured here, is either homogeneous or shows only very small inhomogeneities.

As a matter of fact, compositions of the P-Agx and R-Agx phases should not only differ in Ag composition (x′, x″), but also in Ge composition (z′, z″) as already suggested by the results from CR-AFM data shown in a previous (Piarristeguy et al., 2018). Indeed, one expects a R-Agx phase with a higher Ge content (z′) than the P-Agx one (see **Figure 8**).

In the following, we aim at gaining a further insight in the compositions of the R-Agx phase ($Ag_{x'}(Ge_{z'}Se_{1-z'})_{100-x'}$) and of the P-Agx phase ($Ag_{x''}(Ge_{z''}Se_{1-z''})_{100-x''}$). As already mentioned, according PF-QNM images (**Figures 2b,d,f**), the average composition is a linear combination of the compositions in R-Agx and P-Agx phases:

$$Ag_x(Ge_{0.25}Se_{0.75})_{100-x} = (\%R)\,Ag_{x'}\left(Ge_{z'}Se_{1-z'}\right)_{100-x'} + (\%P)\,Ag_{x''}\left(Ge_{z''}Se_{1-z''}\right)_{100-x''} \quad (8)$$

with

$$x = (\%R)\,x' + (\%R)\,x'' \quad (9)$$

$$0.25\,(100-x) = (\%R)\;z'\left(100-x'\right) + (\%P)\;z''\left(100-x''\right) \quad (10)$$

where (% R) and (% P) correspond, respectively to the surface percentage for R-Agx and P-Agx phases.

Combining these equations leads to a great number of potential compositions, however further restrictions on the

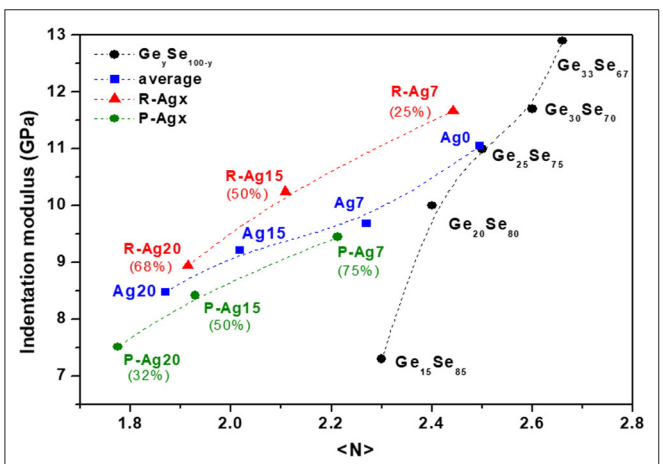

FIGURE 7 | Indentation moduli in function of the mean coordination number for Ge_ySe_{100-y} glasses (black symbols), $Ag_x(Ge_{0.25}Se_{0.75})_{100-x}$ glasses (bleu symbols), and R-Agx (red symbols) and P-Agx (green symbols) phases. Percentages correspond to the proportion of R-Agx and P-Agx phase for each composition Agx. The broken lines are drawn as guides for the eye.

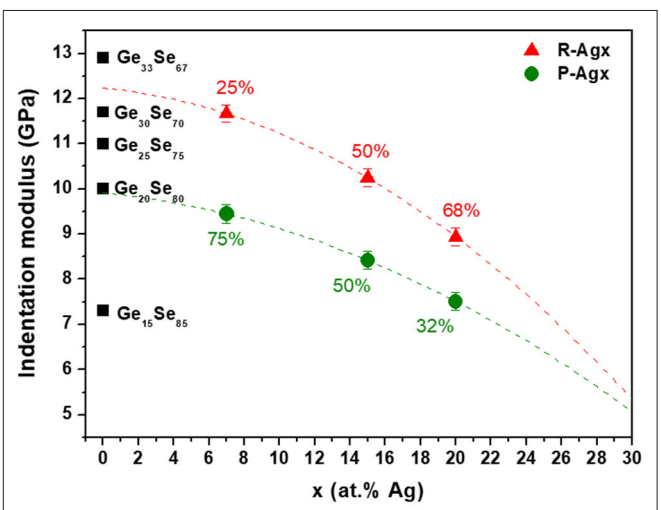

FIGURE 8 | Indentation moduli for R-Agx (red symbols) and P-Agx (green symbols) phases in $Ag_x(Ge_{0.25}Se_{0.75})_{100-x}$ glasses and for Ge_ySe_{100-y} glasses (black symbols). Percentages correspond to the proportion of R-Agx and P-Agx phases for each composition Agx. The broken lines are drawn as guides for the eye.

Ge content can be considered and reduce the number of suitable compositions.

At first, the Ge content for the R-Agx phase (z′) has to be larger than 0.25 since it was shown that the R-Agx phase is richer in Ge than the P-Agx one, and obviously to the average composition (z). A second set of restrictions can be estimated from the difference of indentation moduli ΔM_{R-P} = M(R-Agx)-M(P-Agx) between R-Agx and P-Agx phases, assuming once again that the modulus dependence on Ag and Ge can be decoupled (Equation 5).

$$\Delta M_{R-P} = -0.12\Delta_{x'x''} + 0.28\Delta_{z'z''} \quad (11)$$

where $\Delta M_{Ge} = 0.28\ \Delta y = 0.28\ \Delta_{z'z''}$ and $\Delta M_{Ag} = -0.12\ \Delta x = -0.12\ \Delta_{x'x''}$ were obtained from a linear dependences of the indentation modulus M_{Ge} on Ge content in Ge_ySe_{100-y} glasses (**Figure 1**) and the indentation modulus M_{Ag} on Ag content for $Ag_x(Ge_{0.25}Se_{0.75})_{100-x}$ glasses, shown in **Figure 5** (blue symbols).

With the above information, it is possible to access to the possible values $\Delta_{z'z''}$ for each Agx composition. **Figure 9** shows the indentation modulus differences ΔM_{R-P} predicted as a function of $\Delta_{x'x''}$ in the form of several linear curves, each one corresponding to possible values of $\Delta_{z'z''}$. Intercepts between experimental ΔM_{R-P} and the line network give access to the potential $\Delta_{z'z''}$ values for each Agx composition. On can deduce that

- For Ag 7: $\Delta_{x'x''}$ = [0-7], ΔM_{R-P} = 2.33 and $\Delta_{z'z''}$ = [8.2–11.3]
- For Ag 15: $\Delta_{x'x''}$ = [0-15], ΔM_{R-P} =1.85 and $\Delta_{z'z''}$ = [6.5–13]
- For Ag 20: $\Delta_{x'x''}$ = [0-20], ΔM_{R-P} = 1.43 and $\Delta_{z'z''}$ = [5–13.7]

Taking into account all the previous constraints that include $z' > 0.25$, $x' > x$, $0 < x'' < x$, Equations (8–11) and $\Delta_{z'z''}$ estimated from **Figure 9**, several compositions for the R-Agx phase (x′ and z′) and for the P-Agx phase (x″ and z″) can be proposed. They are reported in **Figure 10**. Among these compositions, some might not be realistic, in particular if they do not contain a sufficient Se ratio to compensate the positive charges brought by Ge and Ag (compositions not shown in **Figure 10**).

Therefore, a last restriction is proposed inspired from the limit of $Ag_x(Ge_{0.25}Se_{0.75})_{100-x}$ glass forming ability proposed by Zeidler et al. (2018). This limit corresponds to the consumption of all Se-Se homopolar bonds, can be estimated when the concentration of Ge, Se, and Ag lead to the mean coordination number associated to the number of Se-Se bonds $\overline{n}_{Se}^{Se} = 0$. Then $\overline{n}_{Se}^{Se}$ can be calculated from this relation

$$\overline{n}_{Se}^{Se} = Z_{Se} - Z_{Ge} * \left[\frac{y}{(1-y)}\right] - 2\overline{N}_{Broken} * \left[\frac{2x}{(1-y)(100-x)}\right] \quad (12)$$

where Z_{Se} and Z_{Ge} are the overall coordination numbers of Se and Ge equal to 2 and 4 respectively, and $\overline{N}_{Broken}$ is the mean number of broken Se-Se bonds per silver atoms estimated around 0.33 (Zeidler et al., 2018). The criteria of $\overline{n}_{Se}^{Se} = 0$ has been used to find the limit between the compositions lying within the glass forming ability and those beyond. The composition limit is shown in **Figure 10**. Most compositions found for R-Agx and P-Agx phases are in the glass forming compositions.

An exact value of Ag concentration in R-Agx and P-Agx phases cannot be given from the previous analyses but some interesting information can be brought: (i) the Ge concentration differs in R-Agx and P-Agx phases with Ge concentration being larger in R-Agx phase, (ii) when the average silver content increases, the Ge concentration decreases in both phases, (iii) z′ and z″ lie in the range 19–31 at. % Ge.

Conductivity

The PF-QNM images (**Figure 2**) show a nucleation/growth type phase separation in the $Ag_x(Ge_{0.25}Se_{0.75})_{100-x}$ glasses, in

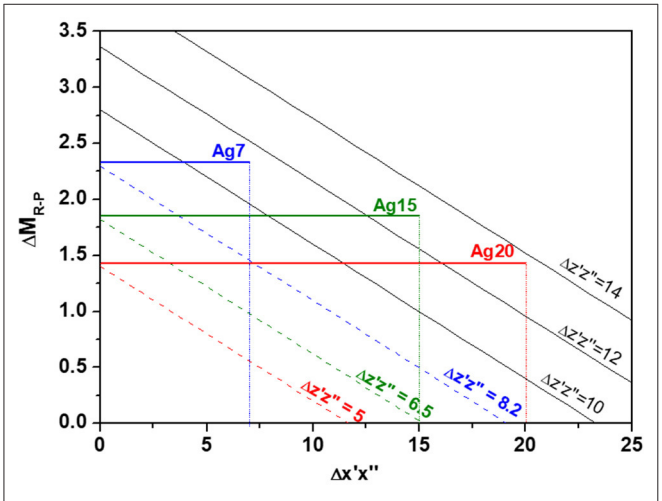

FIGURE 9 | Indentation modulus differences ΔM_{R-P} predicted as a function of $\Delta_{x'x''}$ in the form of several linear curves each one corresponding to possible values of $\Delta_{z'z''}$. Horizontal lines correspond to experimental ΔM_{R-P} for Ag7, Ag15, and Ag20.

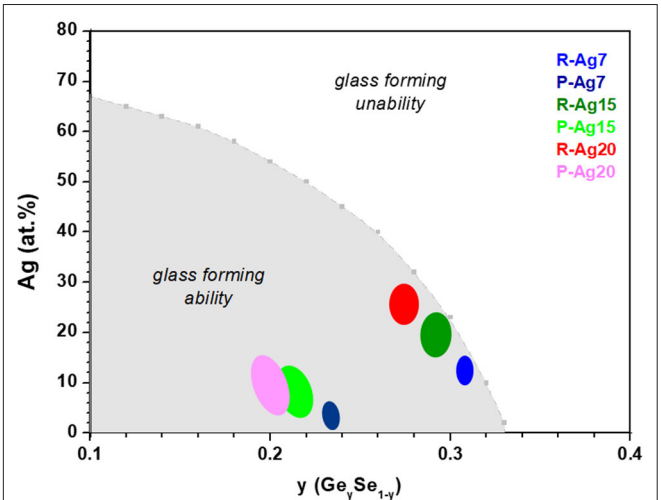

FIGURE 10 | Curve showing the limiting values of x (Ag) for each composition y (Ge) on the basis of the validity of criteria of $\overline{n}_{Se}^{Se} = 0$. Color regions show compositions found for R-Agx and P-Agx phases.

agreement with previous papers (Balan et al., 2006; Piarristeguy et al., 2007b, 2010a,b, 2018). The heterogeneous structure has been used to explain the sudden jump in conductivity by 8 orders of magnitude at a silver content lying in the range 7–10 at. % Ag. Indeed, while the Ag-rich phase is embedded in a Ag poor phase for the low conductivity region ($x < 7$–10% at Ag), the reverse is true for the high conductivity region ($x > 7$–10% at Ag), with the silver rich phase then controlling the silver diffusion throughout the material. Additional nanoscale electrical characterization of the R-Agx phases by conductive atomic force microcopy (C-AFM) showed that the conductivity increased in R-Agx phases with the increase in total Ag content of the glass (x) (Piarristeguy et al., 2010a). Such an increase can be explained by the increase in the Ag content of the R-Agx phase (x′) (see blue, dark green, and red regions in **Figure 10**). However, the present data also show that with increasing Ag content, a softening of the network in R-Agx phases occurs due to a decrease in Ge (z′). Such a softening could also contribute to an increase in conductivity due to an increase in charge carrier mobility. This proposal agrees with Micoulaut et al. (2009) that states "The ease of conduction in an ion conducting glass could indeed be related to the mechanical nature of the host network."

CONCLUSION

Peak Force Quantitative Nano-Mechanical (PF-QNM) mapping was used to characterize a series of binary Ge_ySe_{100-y} glasses and phase-separated $Ag_x(Ge_{0.25}Se_{0.75})_{100-x}$ glasses. This technique proved to be efficient to obtain mechanical information at the nanoscale in a system where information at the nanoscale are difficult to obtain due to the fast silver photo-diffusion under energetic (light or electron beam) stimulus, leading to modification of Ag-centered local structures. As expected, a decrease in the indentation modulus when the selenium content increased in the binary glasses and when the silver content increased in phase-separated ternary glasses, as a consequence of the increasing flexibility of the network, was observed. At nanoscale level, the sensitivity of PF-QNM measurements allowed to observe a difference in the indentation moduli of the two phases, i.e., high and low for Ag-rich (R-Agx) and Ag-poor (P-Agx) phases, respectively.

A model that contributes to a better understanding of the topology of this phase-separated system has been proposed. It is based on the assumption that the change in nanomechanical properties of the Ag-rich and Ag-poor phases depends on the change in Ag and Ge in an independent way. Within this assumption, the mean coordination numbers and compositions for Ag-rich (R-Agx) and Ag-poor (P-Agx) phases can be qualitatively estimated from PF-QNM data. When the silver content in the glass increases, the mean coordination numbers of the R-Agx phase $<N_R>$ and P-Agx phase $<N_P>$ decrease continuously. This is accompanied with a decrease of the Ge concentration in both phases but with the average Ge concentration remaining equal to 25.

Finally, these data helped in providing new information about the increase of conductivity in the Ag-rich (R-Agx) phase when silver content increases in the glasses, as observed by C-AFM measurements. As a matter of fact, it would not only be explained by an increase in silver content in the Ag-rich phase but also by a softening of the network and consequently by an increase of charge carrier mobility.

These promising results provide prospects likely to contribute to the understanding of the topology of phase-separated glasses as well as other bi-phase systems such as glass ceramics or composite materials.

DATA AVAILABILITY STATEMENT

All datasets generated for this study are available on request to the corresponding author.

AUTHOR CONTRIBUTIONS

All authors listed have made a substantial, direct and intellectual contribution to the work, and approved it for publication.

ACKNOWLEDGMENTS

The authors acknowledge M. Bigot for its help in sample preparation and O. Arnould and R. Arinero for fruitful discussions on PF-QNM image analysis.

REFERENCES

Arnould, O., Siniscalco, D., Bourmaud, A., Le Duigou, A., and Baley, C. (2017). Better insight into the nano-mechanical properties of flax fibre cell walls. *Industr. Crops Prod.* 97, 224–228. doi: 10.1016/j.indcrop.2016.12.020

Balan, V., Piarristeguy, A., Ramonda, M., Pradel, A., and Ribes, M. (2006). Phase separation and ionic conductivity: an electric force microscopy investigation of silver chalcogenide glasses. *J. Optoelectron. Adv. Mater.* 8, 2112–2116.

Cervinka, L., Bergerová, J., Tichý, L., and Rocca, F. (2005). A contribution to the structure of Ge–Se–Ag glasses. *Phys. Chem. Glasses* 46, 444–450.

Cuello, G. J., Piarristeguy, A. A., Fernández-Martínez, A., Fontana, M., and Pradel, A. (2007). Structure of chalcogenide glasses by neutron diffraction. *J. Non-Cryst. Solids* 353, 729–732. doi: 10.1016/j.jnoncrysol.2006.12.036

Dejus, R. J., Le Poire, D. J., Susman, S., Volin, K. J., and Price, D. L. (1991). Dynamics of vitreous Ag-Ge-Se. *Phys. Rev. B* 44, 11705–11713. doi: 10.1103/PhysRevB.44.11705

Dejus, R. J., Susman, S., Volin, K. J., Montague, D. G., and Price, D. L. (1992). Structure of vitreous AgGeSe. *J. Non-Cryst. Solids* 143, 162–180. doi: 10.1016/S0022-3093(05)80565-4

Dejus, R. J., Susman, S., Volin, K. J., Price, D. L., and Montague, D. G. (1988). The structure of silver/germanium/selenium glass. *J. Non-Cryst. Solids* 106, 34–37. doi: 10.1016/0022-3093(88)90222-0

Derjaguin, B. V., Muller, V. M., and Toporov, Y. P. (1975). Effect of contact deformations on the adhesion of particles. *J. Colloid Interface Sci.* 53, 314–326. doi: 10.1016/0021-9797(75)90018-1

Guin, J., Rouxel, P., Sangleboeuf, T. J.-C., Melscoet, I., and Lucas, J. (2002). Hardness, toughness, and scratchability of germanium–selenium chalcogenide glasses. *J. Am. Ceram. Soc.* 85 1545–1552. doi: 10.1111/j.1151-2916.2002.tb00310.x

Gutenev, M., Tabolin, A., and Rykova, A. (1991). Dielectric loss in Ag-Ge-Se system glasses. *Fiz. Khim. Stakla* 17, 36–40.

Iyetomi, H., Vashishta, P., and Kalia, R. K. (2000). Incipient phase separation in Ag/Ge/Se glasses: clustering of Ag atoms. *J. Non-Cryst. Solids* 262, 135–142. doi: 10.1016/S0022-3093(99)00692-4

Kawasaki, M., Kawamura, J., Nakamura, Y., and Aniya, M. (1999). Ionic conductivity of $Ag_x(GeSe_3)_{1-x}$ ($0 \leq x \leq 0.571$) glasses. *J. Non-Cryst. Solids* 123, 259–269. doi: 10.1016/S0167-2738(99)00117-4

Kolobov, A. V., and Elliott, S. R. (1991). Photodoping of amorphous chalcogenides by metals. *Adv. Phys*. 40, 625–684. doi: 10.1080/00018739100101532

Kozicki, M. N., Balakrishnan, M., Gopalan, C., Ratnakumar, C., and Mitkova, M. (2005). "Programmable metallization cell memory based on Ag-Ge-S and Cu-Ge-S solid electrolytes," in *Procedings of Symposium Non-Volatile Memory Technology* (Dallas, TX), 83–89. doi: 10.1109/NVMT.2005.1541405

Le Parc, R., Piarristeguy, A. A., Frolet, N., Pradel, A., and Ribes, M. (2013). Ag–Ge–Se glasses: a vibrational spectroscopy study. *J. Raman Spectrosc.* 44, 1049–1057. doi: 10.1002/jrs.4320

Micoulaut, M., Malki, M., Novita, D. I., and Boolchand, P. (2009). Fast-ion conduction and flexibility and rigidity of solid electrolyte glasses. *Phys. Rev. B* 80, 184205-1–184205-10. doi: 10.1103/PhysRevB.80.184205

Mitkova, M., Wang, Y., and Boolchand, P. (1999). Dual chemical role of Ag as an additive in chalcogenide glasses. *Phys. Rev. Lett*. 83, 3848–3851. doi: 10.1103/PhysRevLett.83.3848

Piarristeguy, A., Conde Garrido, J. M., Ureña, M. A., Fontana, M., and Arcondo, B. (2007a). Conductivity percolation transition of $Ag_x(Ge_{0.25}Se_{0.75})_{100-x}$ glasses. *J. Non-Cryst. Solids* 353, 3314–3317. doi: 10.1016/j.jnoncrysol.2007.05.078

Piarristeguy, A., Cuello, G. J., Fernández-Martínez, A., Cristiglio, V., Johnson, M., Ribes, M., et al. (2012). Short range order and Ag diffusion threshold in $Ag_x(Ge_{0.25}Se_{0.75})_{100-x}$ glasses. *Phys. Status Solidi B* 249, 2028–2033. doi: 10.1002/pssb.201200384

Piarristeguy, A., Fontana, M., and Arcondo, B. (2003). Structural considerations about the $(Ge_{0.25}Se_{0.75})_{100-x}Ag_x$ glasses. *J. Non-Cryst. Solids* 332, 1–10. doi: 10.1016/j.jnoncrysol.2003.09.011

Piarristeguy, A., Le Parc, R., Ramonda, M., Escalier, R., Grillo, I., Cuello, G. J., et al. (2018). Local vibrational and mechanical characterization of Ag conducting chalcogenide glasses. *J. Alloys Compounds* 762, 906–914. doi: 10.1016/j.jallcom.2018.05.280

Piarristeguy, A., Ramonda, M., Frolet, N., Ribes, M., and Pradel, A. (2010a). High resolution electrical characterisation of Ag-conducting heterogeneous chalcogenide glasses. *Solid State Ionics* 181, 1205–1208. doi: 10.1016/j.ssi.2010.06.050

Piarristeguy, A., Ramonda, M., and Pradel, A. (2010b). Local electrical characterization of Ag conducting chalcogenide glasses using electric force microscopy. *J. Non-Cryst. Solids* 356, 2402–2405. doi: 10.1016/j.jnoncrysol.2010.03.024

Piarristeguy, A., Ramonda, M., Ureña, A., Pradel, A., and Ribes, M. (2007b). Phase separation in Ag–Ge–Se glasses. *J. Non-Cryst. Solids* 353, 1261–1263. doi: 10.1016/j.jnoncrysol.2006.09.065

Piarristeguy, A. A., Mirandou, M., Fontana, M., and Arcondo, B. (2000). X-ray analysis of GeSeAg glasses. *J. Non-Cryst. Solids* 273, 30–35. doi: 10.1016/S0022-3093(00)00141-1

Prasai, B., and Drabold, D. A. (2011). Ab initio simulation of solid electrolyte materials in liquid and glassy phases. *Phys. Rev. B* 83, 094202-1–094202-8. doi: 10.1103/PhysRevB.83.094202

Stellhorn, J. R., Hosokawa, S., Kawakita, Y., Gies, D., Pilgrim, W. C., Hayashi, K., et al. (2016a). Local structure of room-temperature superionic Ag–$GeSe_3$ glasses. *J. Non- Cryst. Solids* 431, 68–71. doi: 10.1016/j.jnoncrysol.2015.02.027

Stellhorn, J. R., Hosokawa, S., Pilgrim, W. C., Kawakita, Y., Kamimura, K., Kimura, K., et al. (2016b). Structural aspects of the superionic conduction mechanism in Ag-$GeSe_3$ glasses. *Z. Phys. Chem*. 230, 369–386. doi: 10.1515/zpch-2015-0667

Tafen, D. N., Drabold, D. A., and Mitkova, M. (2005). Silver transport in Ge_xSe_{1-x}:Ag materials: Ab initio simulation of a solid electrolyte. *Phys. Rev. B* 72, 054206-1–054206-9. doi: 10.1103/PhysRevB.72.054206

Ureña, M. A., Fontana, M., Arcondo, B., and Clavaguera-Mora, M. T. (2003). Crystallization processes of Ag–Ge–Se superionic glasses. *J. Non-Cryst. Solids* 320, 151–167. doi: 10.1016/S0022-3093(03)00022-X

Ureña, M. A., Piarristeguy, A. A., Fontana, M., and Arcondo, B. (2005). Ionic conductivity (Ag^+) in AgGeSe glasses. *Solid State Ionics* 176, 505–512. doi: 10.1016/j.ssi.2004.09.008

Wang, Y., Mitkova, M., Georgiev, D. G., Mamedov, S., and Boolchand, P. (2003). Macroscopic phase separation of Se-rich ($x < 1/3$) ternary $Ag_y(Ge_xSe_{1-x})_{1-y}$ glasses. *J. Phys.: Condens. Matter.* 15, S1573–S1584. doi: 10.1088/0953-8984/15/16/307

Zeidler, A., Salmon, P. S., Piarristeguy, A., Pradel, A., and Fischer, H. E. (2016). Structure of glassy Ag–Ge–Se by neutron diffraction with isotope substitution. *Z. Phys. Chem*. 230, 417–432. doi: 10.1515/zpch-2015-0727

Zeidler, A., Salmon, P. S., Whittaker, D. A. J., Piarristeguy, A., Pradel, A., Fischer, H. E., et al. (2018). Structure of semiconducting versus fast-ion conducting glasses in the Ag–Ge–Se system. *R. Soc. Open Sci.* 5, 171401–171421. doi: 10.1098/rsos.171401

Conflict of Interest: The authors declare that the research was conducted in the absence of any commercial or financial relationships that could be construed as a potential conflict of interest.

Advantages of publishing in Frontiers

OPEN ACCESS
Articles are free to read for greatest visibility and readership

FAST PUBLICATION
Around 90 days from submission to decision

HIGH QUALITY PEER-REVIEW
Rigorous, collaborative, and constructive peer-review

TRANSPARENT PEER-REVIEW
Editors and reviewers acknowledged by name on published articles

Frontiers
Avenue du Tribunal-Fédéral 34
1005 Lausanne | Switzerland

Visit us: www.frontiersin.org
Contact us: info@frontiersin.org | +41 21 510 17 00

REPRODUCIBILITY OF RESEARCH
Support open data and methods to enhance research reproducibility

DIGITAL PUBLISHING
Articles designed for optimal readership across devices

FOLLOW US
@frontiersin

IMPACT METRICS
Advanced article metrics track visibility across digital media

EXTENSIVE PROMOTION
Marketing and promotion of impactful research

LOOP RESEARCH NETWORK
Our network increases your article's readership